



HAL
open science

Multi-scale biomechanics of healthy and pathological cornea

Chloé Giraudet

► **To cite this version:**

Chloé Giraudet. Multi-scale biomechanics of healthy and pathological cornea. Biomechanics [physics.med-ph]. Institut Polytechnique de Paris, 2022. English. NNT: 2022IPPAX038. tel-03815130

HAL Id: tel-03815130

<https://theses.hal.science/tel-03815130>

Submitted on 14 Oct 2022

HAL is a multi-disciplinary open access archive for the deposit and dissemination of scientific research documents, whether they are published or not. The documents may come from teaching and research institutions in France or abroad, or from public or private research centers.

L'archive ouverte pluridisciplinaire **HAL**, est destinée au dépôt et à la diffusion de documents scientifiques de niveau recherche, publiés ou non, émanant des établissements d'enseignement et de recherche français ou étrangers, des laboratoires publics ou privés.

Multi-scale biomechanics of healthy and pathological cornea

Thèse de doctorat de l'Institut Polytechnique de Paris
préparée à l'École polytechnique

École doctorale n°626 École doctorale de l'Institut Polytechnique de
Paris (EDIPP)

Spécialité de doctorat: Mécanique des fluides et des solides, acoustique

Thèse présentée et soutenue à Palaiseau, le 22 Juin 2022, par

Chloé Giraudet

Composition du Jury :

François Hild Research Director, CNRS (LMPS)	Président
Stéphane Avril Professor, Mines de Saint-Etienne (STBio)	Rapporteur
Marie-Christine Ho Ba Tho Professor, UTC (BMBI)	Rapporteuse
Lucie Bailly Research Associate, CNRS (INSIS)	Examinatrice
Julie Diani Research Director, CNRS (LMS)	Examinatrice
Anna Pandolfi Professor, Politecnico di Milano (Department of Civil and Environmental Engineering)	Examinatrice
Patrick Le Tallec Professor, Ecole Polytechnique (LMS)	Directeur de thèse
Jean-Marc Allain Professor, Ecole Polytechnique (LMS)	Co-directeur de thèse

La recherche, c'est faire avancer des trucs qui marchent pas.

Anonyme

Remerciements

Ces travaux de thèse, ainsi que tout ce qui m'a occupé pendant 4 ans, n'auraient bien évidemment pas pu être menés à bien sans l'appui et le soutien scientifique (et pas que) de toutes les personnes qui ont gravité autour du projet.

Étant dans une équipe conjointe X/Inria, les remerciements vont comprendre bon nombre de pauses café ! Peut-être une habitude héritée d'un de mes directeurs de thèse... Ne m'en tenez pas rigueur, tous ceux qui m'ont croisé pendant ces 4 années savent que c'est un de mes moments préférés.

Tout d'abord, je tiens à remercier tous les membres du jury qui ont gentiment accepté d'évaluer ce petit manuscrit que je leur ai transmis, ainsi que tout mon travail de recherche.

À Stéphane et Marie-Christine, un grand merci d'avoir rapporté cette thèse, pour vos remarques pertinentes, constructives et pour la bienveillance avec laquelle vous avez lu mon travail.

À Julie et François, merci de m'avoir accompagné à ces deux cruciaux jalons que sont le comité de thèse et la soutenance finale. Julie, merci pour tes conseils affutés et François, merci infiniment pour ta prévenance, tes expertises expérimentales, ta relecture plus qu'approfondie de mon manuscrit et bien évidemment pour la présidence du dernier jalon.

To Anna, thank you for your welcome during this stay of 2019 in Milan, I will not forget your kindness and your professionalism. Also thanks a lot for attending my defense, it was a great pleasure to see you there and it meant a lot to me.

À Lucie, merci beaucoup d'être venue de Grenoble discuter de mes travaux, le futur fera que l'on se recroisera peut-être et j'en serai ravie.

Ensuite, il me semble que des remerciements s'imposent pour les personnes qui dirigent la boutique au quotidien.

Je commence donc par la personne qui fut à la fois directeur de labo et de thèse. À Patrick, un immense merci du soutien que tu m'as apporté durant ces 3 ans (et un peu plus) même lorsque tu étais encore directeur du LMS, surtout dans le numérique et l'analytique. Tu resteras à jamais l'homme de la microsphère ! J'ai également été ravie que tu m'embarques dans le processus d'admission des Bachelors cette année.

À Andrei, merci du travail que tu as déjà mené et que tu mènes encore à la tête du labo !

À Philippe, merci de m'avoir accueilli dans cette équipe qui ne serait définitivement pas la même sans toi ! Ne perds jamais l'attention que tu portes à tes collègues, elle est précieuse !

Enfin, celui qui a probablement fait le plus avancer le schmilblick pendant ces 4 ans. À Jean-Marc : 4 ans à travailler ensemble, tout ça ... Je pense que vu tout ce qu'on a partagé, toutes les heures à discuter de choses plus ou moins scientifiques (probablement moins que plus d'ailleurs), tu sais ce que ça représente pour moi. Ma plus grande déception, ne pas réussir à trouver un petit jeu de mots à écrire dans ces quelques lignes Allain'star de tout ceux que tu as pu me faire subir pendant ces années, alors je te dirai juste un grand MERCI pour tous ces bons moments, que je ne saurais énumérer quand bien même je le voudrais, tellement ils furent nombreux !

Bien évidemment, toute cette aventure n'aurait jamais été la même sans tous les collègues que j'ai pu rencontré durant toutes ces années, ainsi je vais essayer de ne pas en oublier :)

À Jérôme, mon presque co-bureau. Je me souviendrais toujours de cette interview d'immuno et ce boulot pour JM où tu me montrais déjà ta folie du numérique, du MoReFEM drinking game (auquel on n'a jamais joué), de l'orga du week-end M3DISIM et de toutes les heures que j'ai pu passer dans ce bureau qui n'était pas le mien... Bref, tu as été un sacré collègue pendant toutes ces années, merki !

Aux commères de M3DISIM, Cécile et Fred, ces moments papotes / ragots n'ont absolument rien apporté à ma thèse et pourtant... Ces liens de commérages sont maintenant indéfectibles et vous allez devoir me supporter encore longtemps.

À la team BGA qui se reconnaîtra (je dénoncerai quand même Guillaume ici) et qui m'a bien aidé à supporter les longues heures de confinement !

À mes co-bureaux, Cécile dIV., Nicole, Nicolas A., Vincenzo, Mahdi et Alice, ce fut un plaisir de partager ce bureau avec vous. Nicolas, Vincenzo, on a partagé un directeur de thèse, ce lien qui nous unit est impérissable ! Mahdi, I will not forget you! Alice, tu ne m'as pas supporté bien longtemps, mais probablement pendant la pire période, tu as été d'un soutien immense et tu ne peux pas savoir à quel point notre cohabitation était bénéfique ! Je peux dire que tu es arrivée collègue et je suis repartie amie.

Aux autres doctorants, post-doc et stagiaires de M3DISIM et du LMS que j'ai pu croiser tout au long de ces 4 années : Andrei, Jessica, Tiphaine, Colin, Mathieu, Maria, Hajer, Francesco, Federica, Arthur, Anna, Louis-Pierre, Camille D., Laura, Camille P. et ta chatonne, Filippo, Clément, Nicolas D., Martin, Jérémie, Nick et tous les autres que j'oublie mais que je n'oublie pas – c'était super cool !! Les raclettes party, le week-end M3DISIM et les barbecues qu'on a partagé – ce sont vraiment des supers moments qui resteront gravés !!

A special thanks for you, Giulia, who accepted to work with me for 9 months and pursued the adventure in the team after, it was a great pleasure to share this experience with you and to become friends afterwards !! Thank you so much =)

Aux collègues de M3DISIM, Martin, Sébastien, Dominique – merci pour l’ambiance, Frédérique pour l’instauration du tour du lac et François pour les heures que tu as passé à me supporter pendant ces années.

Aux collègues du LMS également, avec une attention spéciale pour Laurence, avec qui j’ai pu mouler, remouler et remouler encore pendant tout un été; Manas, avec qui je reprendrai volontiers un verre =>) et Emmanuelle qui m’a si bien accompagné dans les entretiens de Bachelors.

Aux collègues ingé du LMS, Simon et Hakim qui m’ont accompagné au tout début de cette aventure, je n’oublierai jamais cette soirée mémorable à la cave – et toutes les pauses cafés sur la table du LMS qui ont suivi cet été là et même encore après =>). J’ajouterai Vincent, qui a su déjouer toutes les péripéties de l’injecteur et enfin Alex pour ses précieux conseils en permaculture ! Et bien évidemment Sylvain, Éric et Estève, pour ces moments papotes autour d’un café ou au détour d’un couloir. Je n’oublie pas non plus nos deux chers collègues partis à la retraite depuis Jean-Christophe et Pascal – bon vent à eux !

À toutes les collègues de l’administration, Alex, Anna, Christiane, Catherine, Valérie et Danièle – merci pour votre bonne humeur et votre efficacité qui rendent la vie au labo tellement plus agréable – les pauses café avec vous en haut sont toujours un plaisir =>) Un remerciement spécial aussi à Fattah, qui abat le travail de 4 personnes mais toujours avec le sourire et une volonté de rendre service et de bien faire ! Et bien sûr je n’oublie pas Bahar, du côté de l’Inria, merci !

Aux collègues du LOB qui ont rendu cette aventure encore plus passionnante de par leur enthousiasme et leur savoir et savoir-faire sur des sujets qui m’étaient complètement inconnus : Marie-Claire, Gaël, Karsten, merci ! Un remerciement spécial pour Clothilde et Maëlle qui étaient toujours dispo pour discuter de cornée ou d’OCT quand j’en avais besoin. Un grand merci également aux collègues des 15-20, Pr Borderie et Juliette, pour votre expertise et votre patience. Et finalement, un dernier merci aux différents collaborateurs de la BFY, avec une attention particulière à Tassadit pour son aide sur les cornées.

À Elsa, avec qui toute cette aventure a commencé et qui m’a donné le goût de l’expérimental.

Aux nouveaux copains de l’UTC et du LadHyx, avec qui l’organisation de cet après-midi de débat fut un véritable plaisir et a permis de nouer des liens pro et même un peu plus : à Thibaut, Aude et Sabrina. Un remerciement spécial à Dominique qui nous a réunis et à Kat’ qui est venu assister et fêter la soutenance !

Aux collègues qui m’ont accompagné avec joie et toujours beaucoup d’enthousiasme dans l’enseignement : Nicolas F., Olivier et Sophie – merci à vous, ce fut réellement un plaisir de travailler à vos côtés et de partager ces heures d’enseignement aux X et aux Bachelors !

À toutes les personnes de la com’ avec qui j’ai pu discuter et travailler : Chloé, Alice, Astrid, Sylvain, Antoine, Christine et Marc sur les différents projets de médiation scientifique. Une attention spéciale

pour toi, Chloé, qui m'a pris sous ton aile sur ces différents sujets, les vidéos seront une réussite j'en suis sûre !

Enfin, cette aventure étant aussi bien professionnelle que personnelle, il me reste quelques personnes à remercier pour le soutien indéfectible dont elles ont fait preuve.

À mes parents, qui ont toujours soutenu toutes les décisions, même les plus farfelues, que j'ai pu prendre dans ma vie professionnelle. Il y en a eu des stupides, mais celle-là était probablement une des meilleures, vous ne trouvez pas ?

À mon frangin, qui est toujours là au besoin.

À Granny, qui du haut de ses quelques printemps est toujours aussi fringante et partante pour les vacances en Thalasso !

À mon Bichon, qui est là à mes côtés depuis presque ... années déjà (on taira le chiffre =)), t'es ma coupine de toujours !

À Rémy, tu partages ma vie depuis une décennie et pourtant, le quotidien d'une cavalière c'est pas toujours évident ! Tu es mon roc ! Tu es mon pic ! Tu es mon cap ! Que dis-je ? ... Je m'égare ... Bref, tu as accepté de vivre cette aventure avec moi et on dirait qu'on s'en tire pas trop mal. A tout ce qu'il nous reste à partager !

Enfin, cela va paraître bizarre pour bon nombre de ceux qui liront ces lignes (jusqu'ici) mais ceux qui me connaissent savent qu'ils font partis de la famille : à mon Poneyrose, mon Mousse et ma Brunette, mon échappatoire au quotidien !

Contents

1	Introduction	5
1.1	Structure of the cornea	6
1.1.1	Anatomy of the cornea	6
1.1.2	Stroma	8
1.1.3	The keratoconus	12
1.2	Optical Coherence Tomography (OCT) and Image analysis	14
1.2.1	Optical Coherence Tomography	14
1.2.2	Image analysis and strain measurement techniques	21
1.3	Mechanical characterization of the human cornea	25
1.3.1	<i>Ex-vivo</i> mechanical characterization of cornea	26
1.3.2	<i>In-vivo</i> mechanical characterization of cornea	36
1.3.3	Summary of the mechanical characterization of the cornea	42
1.4	Mechanical modeling of the human cornea	43
1.4.1	Mechanical response of cornea	43
1.4.2	The case of the keratoconus	52
1.5	Inverse problems and identification process	54
1.5.1	Principle	54
1.5.2	Minimization of cost function: choice of the new set of parameters	56
	Thesis outline	58
2	Multiscale mechanical model based on patient-specific geometry: application to early keratoconus development	61
	Foreword	62
	Main conclusions	62
2.1	Introduction	64
2.2	Methods	66
2.2.1	Patient - specific geometry	66
2.2.2	Mechanical equilibrium of the cornea: variational formulation	68
2.2.3	Constitutive behavior	69
2.2.4	Parameters of the mechanical model	73
2.2.5	Stress-free configuration	76
2.2.6	simK determination	76
2.3	Results	77
2.3.1	Parameter estimation	77

CONTENTS

2.3.2	Keratoconus: geometrical and mechanical effect	78
2.3.3	Induced keratoconus	80
2.4	Discussion	82
2.5	Conclusions	84
	Supplementary Materials	85
2.6	Sensitivity analysis	85
2.7	Mechanical parameters used in the computation	86
2.8	Stresses representation	88
2.8.1	Keratoconus: geometrical and mechanical effect	88
2.8.2	Induced keratoconus	92
3	Full field measurements of the cornea under pressure using Digital Image/Volume Correlation on 2D/3D Optical Coherence Tomography images	95
3.1	Introduction	96
3.2	Methods	97
3.2.1	Specimen preparation	97
3.2.2	Experimental apparatus	97
3.2.3	Mechanical tests on the cornea	98
3.2.4	Image analysis	100
3.2.5	Uncertainties quantification	105
3.3	Results	111
3.3.1	Creep test at physiological pressure	111
3.3.2	Creep test at high pressure	127
3.3.3	Comparison of creep tests	142
3.3.4	Inflation tests	144
3.3.5	Summary of the results and discussion	161
3.4	Extension of the hyperelastic model	165
3.4.1	First model: elastic model of auxetic cornea	165
3.4.2	Second model: elasticity coupled with osmotic pressure	167
3.4.3	Superposition of auxetic and osmotic material	169
3.4.4	Summary of model results and discussion	170
3.5	Conclusion	172
	Conclusions and Perspectives	175
A	General framework of the multiscale modeling of the cornea	I
A.1	Continuum mechanics framework	I
A.1.1	Classical kinematics	I
A.1.2	Weak formulation	II
A.2	Parametrization with B-splines	III
A.2.1	Knot vector	IV
A.2.2	B-splines basis	IV
A.2.3	B-spline surfaces	V
A.3	Minimization of cost function: choice of the new set of parameters	VI

A.3.1	Gradient-descent algorithm	VI
A.3.2	Covariance MAtrix Evolution Strategy (CMA-ES)	VII
B	Mesh Calculation	IX
B.1	Data used for the mesh creation	IX
B.2	Creation of the in-plane coordinates of the mesh	XII
B.2.1	Contour of the real space D	XII
B.2.2	Point in computational space	XIII
B.2.3	Transfinite generation	XIV
B.3	Creation of the 3D mesh	XIV
C	Technical developments related to the multiscale modeling of the cornea	XVII
C.1	Computation of the anisotropic 2 nd Piola-Kirchhoff tensor	XVII
C.2	Computation of the quadrature used in the micro-sphere model	XVIII
C.2.1	Quadrature used in the FEM code to calculate the fiber contribution	XVIII
C.2.2	Summary of the quadrature for Piola-Kirchhoff tensor	XXIV
C.2.3	First five Hermite polynomials, associated roots and weights	XXV
C.3	Technical development related to the identification process	XXVI
C.3.1	Reduction of the number of parameters to be identified using B-splines	XXVII
C.3.2	Cost function	XXIX
D	Supplementary experimental methods	XXXI
D.1	Data on the corneas	XXXI
D.2	Computation of the strain error due to difference of refractive index	XXXII
E	Supplementary experimental results	XXXV
E.1	Uncertainty quantification	XXXV
E.2	Supplementary results of the creep tests at physiological pressure	XXXVIII
E.2.1	Histograms of the distributions	XXXVIII
E.2.2	Time dependence analyses	XL
E.3	Supplementary results of creep tests at high pressure	XLIV
E.3.1	Histograms	XLIV
E.3.2	Time dependence analyses	XLVI
E.4	Supplementary results for the comparison of the two creep tests	LII
E.4.1	Histograms	LII
E.5	Supplementary results of the inflation tests	LIV
E.5.1	Histograms	LIV

CONTENTS

E.5.2	Pressure dependence	LX
E.5.3	Pressure - limit strain curves	LXVI
F	Technical developments on the modeling of cornea following the experimental results	LXXI
F.1	First hypothesis: a simple elastic model of an auxetic material	LXXI
F.1.1	Infinitesimal strain tensor	LXXI
F.1.2	Boundary conditions	LXXII
F.1.3	Equilibrium	LXXII
F.1.4	Constitutive law and computation of the strain	LXXII
F.2	Second hypothesis: existence of an osmotic pressure	LXXIV
F.2.1	Form of $J(z, t)$	LXXV

Résumé de la thèse

La cornée est la partie extérieure et transparente de l'œil et un des tissus essentiels à la vision. En effet, elle procure les 2/3 du pouvoir optique de l'œil en focalisant les rayons lumineux sur la rétine tout en résistant aux variations de pression intraoculaire journalière auxquelles elle est soumise. Elle est également la première barrière contre les agressions oculaires extérieures. La cornée est étudiée à travers le prisme des chirurgiens ophtalmologistes depuis des siècles, cependant ce n'est que depuis quelques décennies que les mécaniciens s'intéressent de près à ce tissu. Le dialogue entre les deux communautés a, dans notre cas, débouché sur les travaux de cette thèse qui tentent de répondre à la question suivante : **peut-on donner quelques clés de lecture sur le développement d'une pathologie de la cornée – le kératocône – grâce à l'étude de la mécanique cornéenne ?**

Le kératocône est une dystrophie cornéenne idiopathique caractérisée par une ectasie (déformation de la cornée, dont la géométrie saine est quasi-sphérique) et un amincissement progressif du tissu dans la zone touchée par la pathologie. Cette déformation géométrique entraîne des défauts de vision, qui, dans le cas d'un kératocône sévère, ont pour conséquence la nécessité d'une greffe cornéenne. A ce jour, il n'existe pas d'origine claire et identifiée de la maladie. Une des hypothèses avancées est le changement de géométrie induit par un frottement oculaire répété. Cette contrainte mécanique cyclique sur la cornée entraînerait une modification de sa microstructure, et avec elle sa résistance mécanique. Cependant, il est impossible de savoir aujourd'hui si le kératocône apparaît parce que les propriétés mécaniques de la cornée sont altérées ou si les propriétés mécaniques sont modifiées à la suite du changement de géométrie.

Les propriétés mécaniques de la cornée sont liées à la microstructure très particulière de son stroma en contreplaqué de lamelles de collagène et il a été clairement identifié que cette microstructure se désorganise dans le cas d'un kératocône. De nombreux modèles mécaniques ont été développés pour prendre en compte cette microstructure, dans des cas sains et pathologiques, cependant il n'existe à ce jour que très peu de données expérimentales sur la réponse mécanique macroscopique de la cornée pour les valider.

L'objectif de cette thèse est donc de caractériser la mécanique cornéenne afin de mieux comprendre l'apparition de la pathologie. Deux voies parallèles sont utilisées : (i) **un modèle mécanique multi-échelle est développé et implémenté dans un code éléments finis afin de simuler la réponse mécanique de la cornée à la pression intraoculaire** et (ii) **des essais expérimentaux couplés à de la tomographie par cohérence optique sont réalisés afin de caractériser la réponse mécanique macroscopique de la cornée.**

Dans un premier temps, un modèle multi-échelle et à géométrie patient-spécifique incluant la microstructure cornéenne est développé et implémenté dans un code éléments finis (MoReFEM) développé dans l'équipe MΞDISIM. La réponse mécanique prend en compte la réponse isotrope de la matrice ainsi que la quasi-incompressibilité du tissu. La réponse anisotrope des fibres de collagène est intégrée via une approche par intégration angulaire – la microsphère. Le modèle est validé sur les données expérimentales disponibles dans la littérature dans le cas de tissus sains et les paramètres sont adaptés dans le cadre de cornées kératocôniques.

Dans un second temps, une étude expérimentale de la réponse mécanique macroscopique de la cornée est menée à bien. La cornée est placée sur une chambre de pression dans laquelle est injectée du fluide. Le changement de volume est contrôlé et la pression appliquée sous la cornée mesurée.

Trois essais différents sont réalisés : (i) un test de fluage à pression physiologique (15 mmHg ou 20 mbar) est réalisé afin de mimer la réponse d'un greffon après une transplantation, (ii) un test de fluage à haute pression (113 mmHg ou 150 mbar) est réalisé afin d'étudier la réponse mécanique de la cornée à une forte contrainte et enfin (iii) un test de gonflement est effectué afin de caractériser la réponse mécanique de la cornée à un large champ de pressions. Tout au long des essais, des images 2D et 3D de la cornée sous pression sont réalisées par tomographie en cohérence optique. Elles sont ensuite analysées grâce à des techniques de corrélation d'images 2D et 3D afin de calculer des cartes de déformations.

Les principaux résultats de ces travaux sont les suivants : (i) l'étude numérique réalisée sur les cornées pathologiques montre l'importance de l'affaiblissement des lamelles de collagène dans l'apparition du kératocône tandis que le changement de géométrie ne serait pas un facteur déterminant, (ii) la cornée sous pression physiologique a tendance à gonfler, ce qui pourrait être expliqué par des échanges osmotiques, (iii) à l'inverse la cornée sous haute pression a tendance à se « vider » de son eau, (iv) dans tous les cas la cornée peut être subdivisée en trois parties qui ont chacune une réponse différente à la pression et (v) l'étude expérimentale réalisée permet aujourd'hui d'avoir des cartes de déformations 3D de référence pour des futurs travaux d'identification de paramètres.

Summary of the thesis

The cornea is the external and transparent part of the eye and one of the essential tissues for vision. It provides 2/3 of the optical power of the eye by focusing the light rays on the retina while resisting the daily variations of intraocular pressure to which it is subjected. It is also the first barrier against external ocular aggression. The cornea has been studied through the prism of ophthalmic surgeons for centuries, but it is only in the last few decades that mechanical researchers have taken a close interest in this tissue. The dialogue between the two communities has, in our case, led to the work of this thesis which attempts to answer the following question: **can we provide some keys to the development of a corneal pathology - the keratoconus - through the study of corneal mechanics?**

Keratoconus is an idiopathic corneal dystrophy characterized by ectasia (deformation of the cornea, whose healthy geometry is almost spherical) and a progressive thinning of the tissue in the area affected by the pathology. This geometrical deformation leads to visual defects which, in the case of severe keratoconus, result in the need for corneal graft. To date, there is no clear and identified origin of the disease. One of the hypotheses put forward is the change in geometry induced by repeated eye rubbing. This cyclic mechanical stress on the cornea would lead to a modification of its microstructure, and with it its mechanical resistance. However, it is impossible to know today if keratoconus occurs because the mechanical properties of the cornea are altered or if the mechanical properties are altered as a result of the change in geometry.

The mechanical properties of the cornea are linked to the very particular microstructure of its stroma, which is structured as a plywood of collagen lamellae, and it has been clearly identified that this microstructure becomes disorganized in the case of keratoconus. Numerous mechanical models have been developed to take into account this microstructure, in healthy and pathological cases, however, there are to date very little experimental data on the macroscopic mechanical response of the cornea to validate them.

The objective of this thesis is therefore to characterize the corneal mechanics in order to better understand the onset of the pathology. Two parallel paths are used: **(i) a multiscale mechanical model is developed and implemented in a finite element code to simulate the mechanical response of the cornea to intraocular pressure and (ii) experimental tests coupled with optical coherence tomography are performed to characterize the macroscopic mechanical response of the cornea.**

First, a multiscale model with a patient-specific geometry including the corneal microstructure is developed and implemented in a finite element code (MoReFEM) developed in the MEDISIM team. The mechanical response takes into account the isotropic response of the matrix and quasi-incompressibility of the tissue. The anisotropic response of collagen fibers is integrated via an angular integration approach - the microsphere. The model is validated on experimental data available in the literature in the case of healthy tissue and the parameters are adapted in the context of keratoconus corneas.

Then, an experimental study of the macroscopic mechanical response of the cornea is carried out. The cornea is placed on a pressure chamber in which fluid is injected. The volume change is controlled and the pressure applied under the cornea is measured. Three different tests are performed: (i) a creep test at physiological pressure (15 mmHg or 20 mbar) is carried out to mimic the response of

a graft after transplant, (ii) a creep test at high pressure (113 mmHg or 150 mbar) is done to study the mechanical response of the cornea to high stress and finally (iii) an inflation test is conducted to characterize the mechanical response of the cornea to a wide range of pressures. Throughout the tests, 2D and 3D images of the cornea under pressure are acquired by optical coherence tomography. They are then analyzed using 2D and 3D image correlation techniques to compute strain maps.

The main results of this work are as follows: (i) the numerical study carried out on pathological corneas shows the importance of the weakening of the collagen lamellae in the appearance of keratoconus while the change in geometry would not be a determining factor, (ii) the cornea under physiological pressure tends to inflate, which could be explained by osmotic exchanges, (iii) conversely, the cornea under high pressure tends to "empty" itself of its water, (iv) in all cases the cornea can be subdivided into three parts, each of which has a different response to pressure, and (v) the experimental study carried out now provides 3D deformation maps for future work on identifying parameters.

Chapter 1

Introduction

Contents

1.1	Structure of the cornea	6
1.1.1	Anatomy of the cornea	6
1.1.2	Stroma	8
1.1.3	The keratoconus	12
1.2	Optical Coherence Tomography (OCT) and Image analysis	14
1.2.1	Optical Coherence Tomography	14
1.2.2	Image analysis and strain measurement techniques	21
1.3	Mechanical characterization of the human cornea	25
1.3.1	<i>Ex-vivo</i> mechanical characterization of cornea	26
1.3.2	<i>In-vivo</i> mechanical characterization of cornea	36
1.3.3	Summary of the mechanical characterization of the cornea	42
1.4	Mechanical modeling of the human cornea	43
1.4.1	Mechanical response of cornea	43
1.4.2	The case of the keratoconus	52
1.5	Inverse problems and identification process	54
1.5.1	Principle	54
1.5.2	Minimization of cost function: choice of the new set of parameters	56
	Thesis outline	58

1.1 Structure of the cornea

1.1.1 Anatomy of the cornea

Macroscopic description The cornea is the external part of the eye (Fig. 1.1.a). It is a transparent medium that transmits light inside the eye and protects it from external aggression. Accounting for $2/3$ of the refractive power of the eye (around 40 diopters over 60), the cornea forms with the crystalline lens the ocular dioptr, whose function is to focus the light on the retina. The cornea is attached to the eyeball through the sclera, the white tissue surrounding it (Fig. 1.1.a). Its posterior surface (Fig. 1.1.c – anterior and posterior surfaces are the external and internal ones, respectively) is in contact with the aqueous humor (refractive index $n_{aqh} = 1.3375$ [152]), a transparent liquid composed of 99% water, which plays a key role in regulating intraocular pressure (IOP) – between 10 and 20 mmHg (1333.2 and 2666.5 Pa respectively) in healthy conditions [66] – and providing nutritional metabolic function to the lens and the cornea.

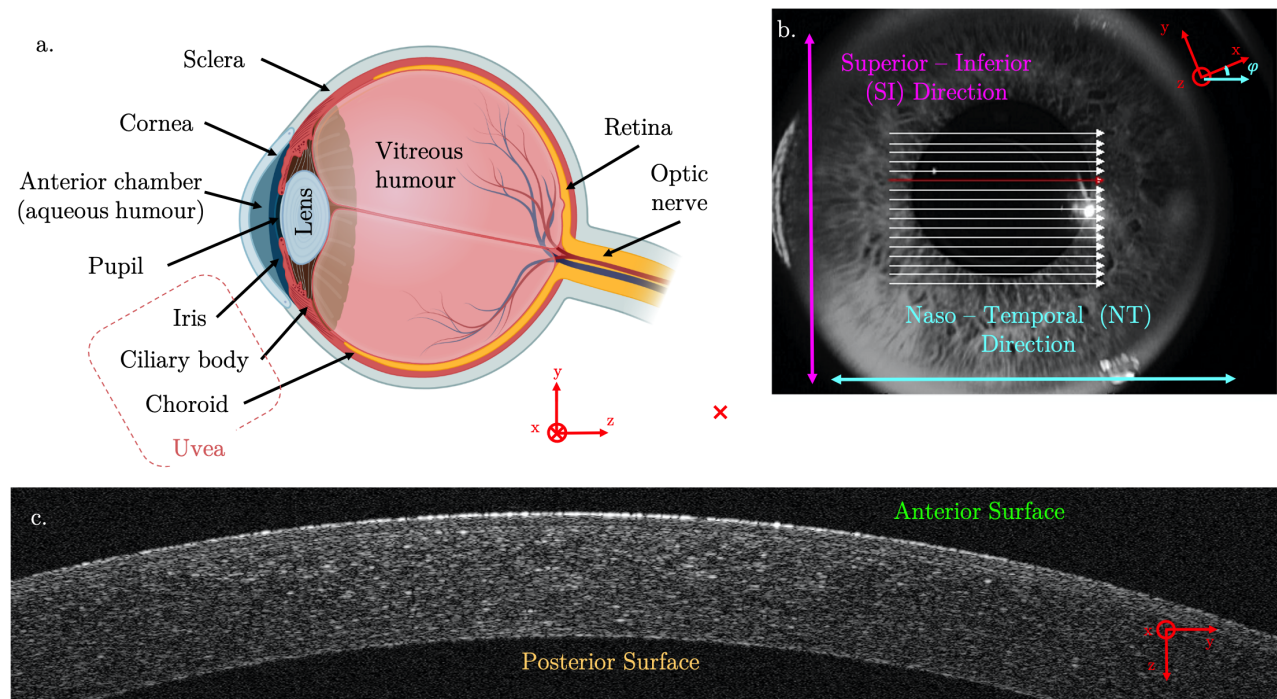


Figure 1.1: a. Schematic view of the eye: the cornea is the external part of the eye, surrounded by the sclera and forming the optical dioptr with the crystalline lens – [Created with BioRender.com]. b. Photo of an eye viewed from the front with the classical directions used in ophthalmology: Superior–Inferior in pink and Naso–Temporal in blue. c. Optical Coherence Tomography (OCT) image of a cornea defining the anterior and posterior surfaces. The coordinate system is the same in all the scheme/images.

Geometry The corneal shape is close to a spherical cap. Typical dimensions of the cornea are around 1 cm in diameter, a thickness between approximately $500 \mu\text{m}$ in the central part and $600 \mu\text{m}$ in the periphery, and radii of curvature around 7.8 mm for the anterior surface and 6.5 mm for the posterior surface [98]. The geometry of the healthy cornea is regular and well described by a parametric quadratic equation [55]. Placing the apex of the cornea at the origin of a coordinate system with the z-axis oriented vertically and downwards (Fig 1.1.c for the representation of the axes), the anterior

and posterior surfaces of the cornea are described by the biconic function [76]:

$$z(x, y, R_x, R_y, Q_x, Q_y) = z_0 + \frac{\frac{x^2}{R_x} + \frac{y^2}{R_y}}{1 + \sqrt{1 - (1 + Q_x)\frac{x^2}{R_x^2} - (1 + Q_y)\frac{y^2}{R_y^2}}}, \quad (1.1)$$

where R_x and R_y are the curvature radii of the flattest (x axis) and the steepest (y axis) meridians of the cornea, Q_x and Q_y are the associated asphericities. Note that the x and y directions can be rotated by an angle ϕ from the classical naso-temporal (N-T) and inferior-superior (I-S) axes (Fig. 1.1.b). Finally, z_0 is an arbitrary translation with respect to the z axis origin.

Considering this approximation of the geometry of the cornea, the local diopter of the cornea is computed using:

$$D = \frac{n_{aqh} - n_{air}}{R_{ant}} \quad (1.2)$$

with $n_{aqh} = 1.3375$ and $n_{air} = 1.0000$ the refractive index of the aqueous humor and the air respectively and R_{ant} the local steepest curvature radius of the anterior surface.

Mesoscopic organization The cornea is composed of six layers (a histological section is presented Fig. 1.2) described hereafter from the most external layer to the most internal one.

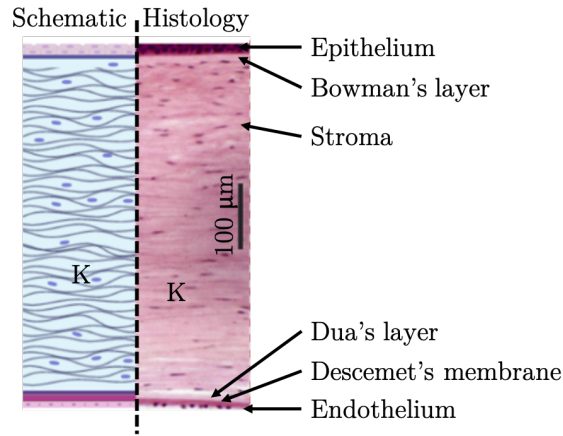


Figure 1.2: Schematic view (left – [Schematic created with BioRender.com]) and histological section (right – from [118]) of the cornea.

The epithelium is the external part, composed of a few layers of epithelial cells (50-90 μm thick), and plays the role of a barrier against external aggression and a facilitator for the dispersion of the tears. Bowman's membrane is a non cellular homogeneous layer (approximately 10 μm thick) composed of collagen fibrils [67], which has the particularity to not regenerate after destruction. The stroma is the main part of the cornea and will be described in more detail in the following section (Sec. 1.1.2). The fourth layer is Dua's layer, which was only discovered in 2013 [40]. It is around 15 μm thick and located between the stroma and Descemet's membrane. Its role is not yet clear because it has only been recently located. Descemet's membrane is a base membrane of the endothelium – and therefore plays the role of a joint between the stroma and the endothelium – and is mostly composed of a type VIII collagen network [47]. It grows over life from 3-4 μm thick at childhood to around

$12\ \mu\text{m}$ for adults [21]. Finally, the endothelium is a single layer of endothelial cells approximately $5\ \mu\text{m}$ thick. The endothelial density is between 3000 to 4000 cells/ mm^2 for a new born and decreases down to approximately 2000 cells/ mm^2 at old age [21]. The endothelial cells do not regenerate so that when one of them dies, the surrounding cells enlarge to fill up the void. The endothelium acts like a pump between the aqueous humor and the cornea to maintain constant hydration – and with its transparency – of the tissue [107]. It is commonly admitted that below a certain cell density (between 400 and 700 cells/ mm^2 [79]), the endothelium does not longer fulfill its pumping role and then stromal edemas appear.

1.1.2 Stroma

The stroma represents about 90% of the cornea and is composed mainly of type I et V collagen fibrils arranged in lamellae anchored in a matrix of keratocytes (corneal fibroblasts) and proteoglycans [47]. It provides the cornea its mechanical strength and optical performance (transparency and optical power) due to the particular arrangement of collagen inside the tissue [102; 147]. Hereafter are defined and described the multiple scales of collagen arrangement, from smallest (the triple helix) to largest (lamellae). The bigger ones are detailed more precisely (see Fig. 1.9 for a summary of all scales).

1.1.2.a Smallest scales of stromal collagen: the triple helix, the microfibril and the fibril of collagen

The triple helix of collagen (Fig. 1.3.a) is one of the smallest observable arrangement of collagen monomers, with a diameter of only 1.5 nm. X-ray diffraction scattering is one of the techniques available to observe the triple helix of collagen. It has been first applied on kangaroo tails (Fig. 1.3.b) and led to a founding article on the organization of collagen at the smallest scale. It allows patterns of the arrangement of the collagen to be distinguished when looking at the different layers (e.g. alternation of black and white on the scattering gives a periodic pattern), but it is necessary to add amino acid composition and physicochemical data to obtain the classical 7/2-helical model (7 different amino acid per 2 turns of helix – Fig. 1.3.c) found in [126].

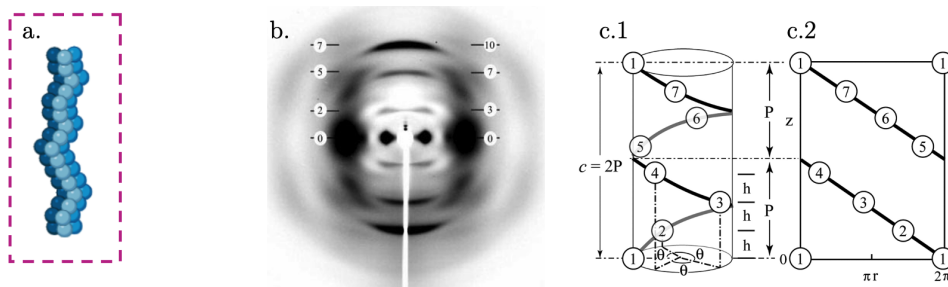


Figure 1.3: a. Schematic view of the triple helix of collagen [Created with BioRender.com]. b. X-ray diffraction scattering (from [125]) of the triple helix of collagen in a kangaroo tail. c. schematic representation of the monomer of the triple helix (from [126]).

Multiple triple helices of collagen pack to form 4 nm diameter microfibrils of collagen which axial arrangement is represented in Fig. 1.4.a and c. Electron microscopy (Fig. 1.4.b from [96]) and tomography (Fig. 1.4.c [68]) allow microfibrils of collagen of bovine cornea to be observed (orange boxes).

It allows the diameter of the microfibrils to be measured and their arrangement to be deduced, which follows an alternation of overlap and gap zones with a period of 670 Å.

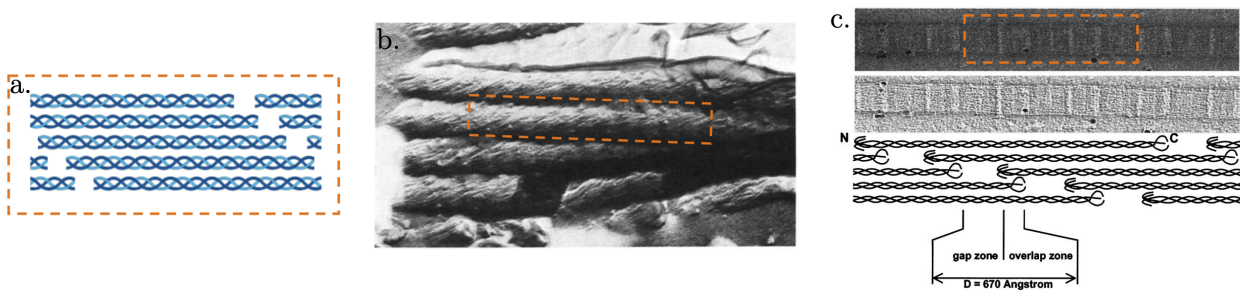


Figure 1.4: a. Schematic view of a microfibril of collagen [Created with BioRender.com]. b. Electron microscopy (from [96] - 80000X). c. Electron tomography image (from [68] - 20000X) of the microfibrils of collagen of a bovine cornea.

The microfibrils of collagen are themselves packed in fibrils of collagen (Fig. 1.5) of around 30 nm in diameter. Figure 1.5.b presents Transmission Electron Microscopy (TEM) images where the fibrils of collagen can be distinguished. TEM images also show that the direction of the fibrils of collagen alternates through the thickness of the cornea – from top to bottom three layers of fibrils of collagen and a keratocyte (corneal fibroblasts) can be distinguished.

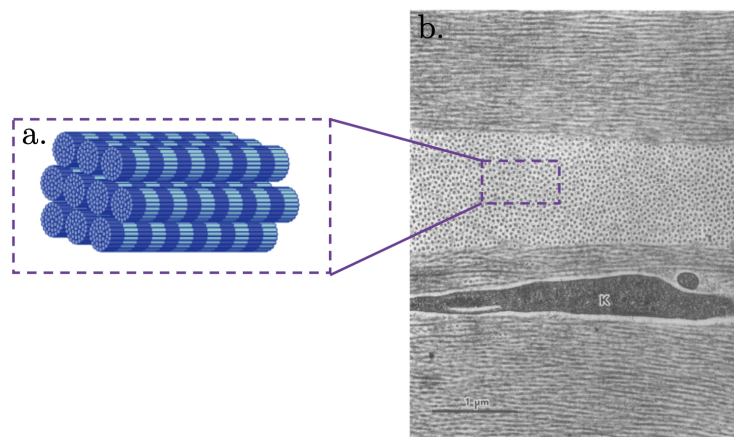


Figure 1.5: a. Schematic view [Created with BioRender.com] and b. TEM image (from [87]) of the fibrils of collagen of a human cornea. K = keratocyte. Scale bar: 1 μm.

1.1.2.b Collagen lamellae

The packing of collagen fibrils forms collagen lamellae, which are the largest scale of collagen arrangement found in the cornea. This is the scale of interest for mechanical modeling. Collagen lamellae are arranged like a plywood with an alternation of lamellae with two perpendicular main directions (Fig. 1.6.a). Scanning Electron Microscopy (SEM) and Second Harmonic Generation (SHG) microscopy images (Fig. 1.6.b and c) reveal the presence of the lamellae (red "L's" on the images). The SEM image also shows that the lamellae are intertwined rather than superimposed on top of each other, whereas the SHG image points out that the angles between the different lamellae are not

exactly 90° .

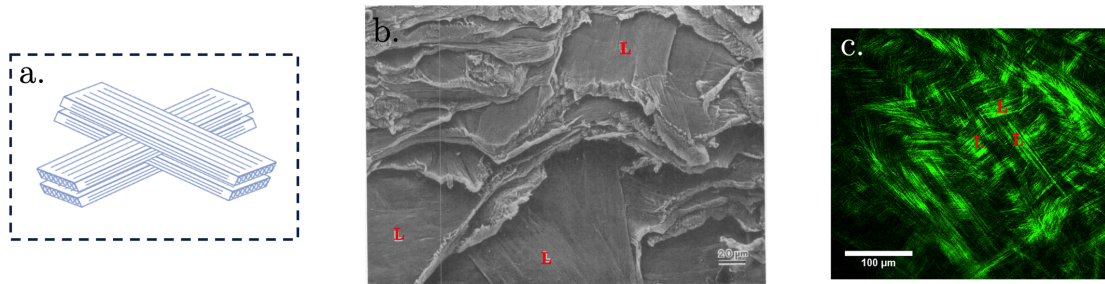


Figure 1.6: a. Schematic view of the lamellae of collagen [Created with BioRender.com]. b. SEM image of the cornea (from [87]) – scale bar: $20\ \mu\text{m}$. c. SHG image of the cornea (from [14]) – scale bar: $100\ \mu\text{m}$.

The scale of the collagen lamellae is generally used in the mechanical modeling field, where materials reinforced by fibers are extensively studied (Sec. 1.4). From now on "collagen fibers" or "collagen lamellae" will be used to refer to the same collagen arrangement. X-ray imaging (Fig. 1.7.a) and SHG microscopy (Fig. 1.7.b) have been used to determine the 3D orientation of collagen lamellae. X-ray imaging allows X-ray scattering pattern of the collagen lamellae to be obtained, averaged over the thickness of the tissue [101; 103]. Fig. 1.7.a presents the results of X-ray image analysis, with a polar plot (butterfly diagram) of the lamella direction at each point of measurement, which gives an in-plane information on the average orientation of the lamella through thickness. The radial extent of the polar plot shows the relative number of collagen lamella aligned in a particular direction, i.e. the longer the wing of the butterfly, the more lamellae along that direction. The width of the butterfly wings represents their scatter. The colors of the different butterflies indicate the factor with which the polar plots have been scaled down on the representation of Fig. 1.7.a. Two main observations are drawn from this analysis. First, the lamellae in the center are oriented in the naso-temporal (N–T) and superior-inferior (S–I) directions with an angle of approximately 90° , while in the peripheral zone, the lamellae are mostly oriented in the circumferential direction of polar coordinates. Second, fewer lamellae (in orange, i.e. with no scaling) are oriented in the central area than in the peripheral one (mostly in dark red, black and green so with a scale down factor of 2, 3 or 4 on the representation). Although X-ray image analysis gives valuable information on the in-plane distribution of the lamellae, it does not give any insight into the out-of-plane distribution. To this end, SHG images (from [175]) have been studied by Petsche and Pinsky [134] to build a model of the out-of-plane dispersion of the collagen lamellae. They show that the maximum out-of-plane angle of the collagen lamellae varies with depth – decreasing from approximately 30° on the anterior part of the cornea to almost 0° on the posterior stroma – while no heterogeneity has been noted in the other two directions. Those two analyses allow 3D maps of the orientation of the collagen lamellae in healthy corneas to be built. Their modeling will be studied in Sec. 1.4.1.b. In the case of keratoconic corneas, the arrangement of the collagen lamellae is disorganized (see Sec. 1.1.3 – Fig. 1.11), which alters the mechanical strength and optical properties of the tissue, therefore causing a loss of vision.

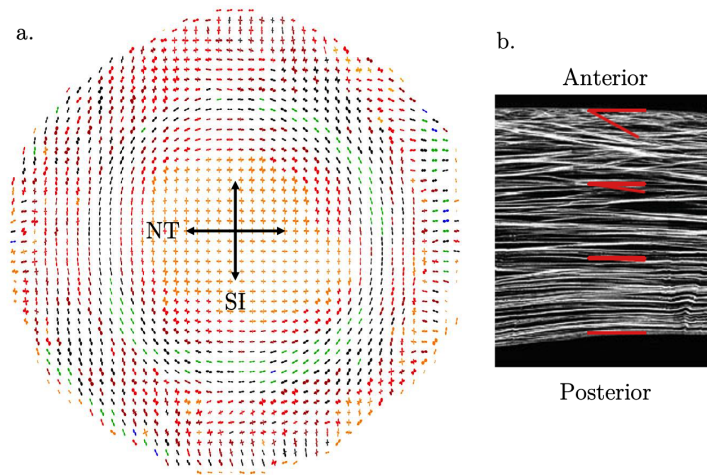


Figure 1.7: a. In-plane and b. out-of-plane (right) distributions of the orientation of the collagen lamellae. The in-plane orientations have been determined by analyzing X-ray diffraction scattering observation (from [1; 18]) (down scale factor: orange – 1, red – 1.5, dark red – 2, black – 3, green – 4, blue – 5), and the out-of-plane orientations use SHG images (from [134; 175]).

1.1.2.c Stromal striae

At tissue scale, "X-shape" linear structures appear both on Optical Coherence Tomography (OCT) images (Fig. 1.8) and on histological cuts [118]. They are called Vogt or stromal striae, and are detected both in healthy and pathological corneas [62]. Stromal striae are less visible as pressure increases, meaning that the corneal wrinkles fade with pressure (like a balloon that loses its ripples as it inflates). This suggests that the striae may protect the collagen fibrils from damage induced by a sudden increase in pressure (when the eyes receive mechanical shocks for instance) [62].

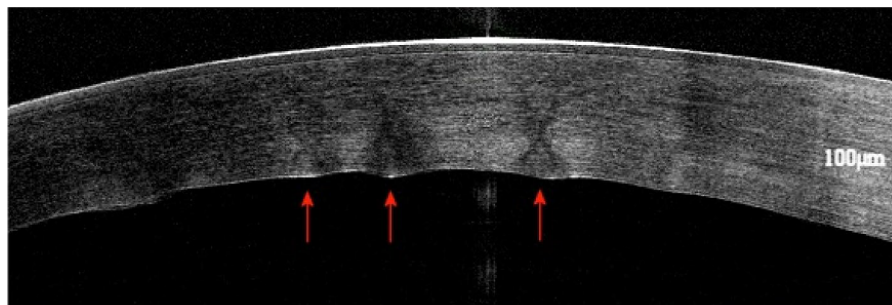


Figure 1.8: Vogt striae in a human cornea on OCT imaging (top) and histology (bottom). The arrows indicate the most conspicuous 'X-shaped' structures. Scale bar – 100 μm (extracted from [118]).

1.1.2.d Summary of all scales

Figure 1.9 summarizes the different scales of the components of the cornea, especially the different scales of collagen found in the stroma.

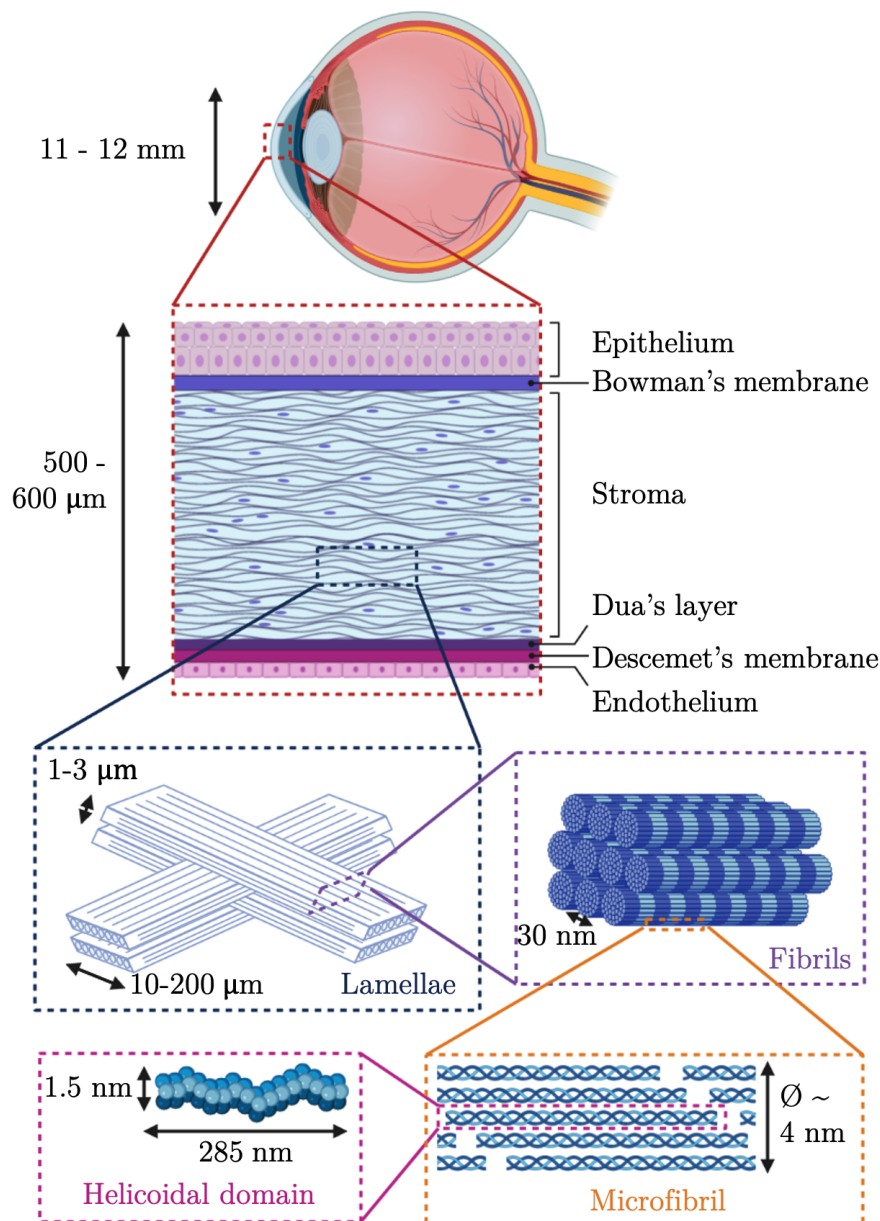


Figure 1.9: Schematic view of the different scales of the components of the cornea. Top: eye scale. Red box: different layers composing the cornea – tissue scale. Blue box: collagen lamellae – micrometric scale. Violet box: fibrils of collagen – micro- to nanometric scale. Orange box: single microfibril of collagen – nanometric scale. Pink box: triple helix of collagen – nanometric scale. [Created with BioRender.com]

1.1.3 The keratoconus

Keratoconus is an idiopathic pathology characterized by ectasia (corneal deformation) and progressive non-inflammatory localized thinning of the cornea. In other words, the cornea changes its shape during the progression of the pathology, from a quasi-spherical shape to an irregular conical ones (Fig. 1.10). This condition affects approximately 1/2000 to 1/500 more people each year. The keratoconus usually appears at the end of adolescence and affects both eyes, but not necessarily with the same severity nor in the same area of the eye. Although there is no clear origin of the disease, some risk factors have been identified such as family history (no specific gene has yet been identified), presence of

allergy in the patient or regular eye rubbing [117]. Four stages of the disease can usually be identified (Krumeich's classification [114]): from the least advanced stage (stage I or frustrated stage: visual discomfort, decrease in visual acuity with astigmatism) to the most advanced stage (stage IV or severe stage: thinning associated with a loss of transparency – scars or opacities at the top of the cone – and risk of acute keratoconus). The evolution from a stage to another is not systematic, not symmetric and not linear with time. For example, the keratoconus can evolve from a stage to another and then stop its progression.

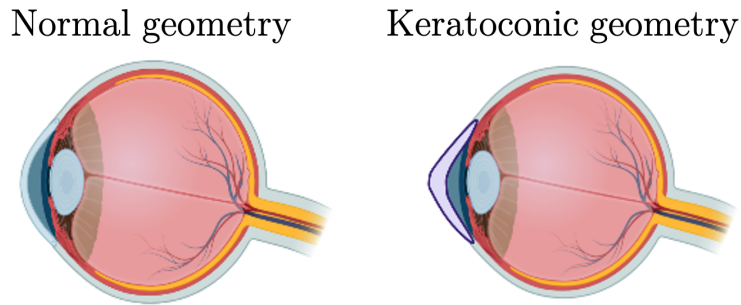


Figure 1.10: Schematic representation of a keratoconus: the shape of the cornea changes from a spherical to a conical one [Created with BioRender.com]

Treating keratoconus involves two parallel tasks: improving the patient's vision and stopping the progression of the disease. To stabilize the keratoconus, the corneal cross-linking technology can be used. It is based on the photo-polymerization of collagen lamellae and riboflavin previously impregnated on the cornea. The improvement of the patient's vision implies first the use of glasses, then the use of therapeutic contact lenses and in case of failure of those two approaches, corneal surgery is needed. In the latter case, two options are considered: the placement of intra-corneal rings or corneal transplant (only 1% of the patient with a known keratoconus go through the latter). Intra-corneal rings are used to delay grafting. They are placed in the thickness of the cornea to tighten the central cornea. This technology increased with the rise of femto-second lasers, which make it possible to dig tunnels with extreme precision in the cornea, through which the surgeons introduce the intra-corneal rings. Another type of laser can be used to treat the keratoconus: the "Excimer" laser. It allows the cornea to be remodeled by photo-ablation of the tissue and the visual accuracy of the patient to be increased, who will need a smaller visual correction. This technique is called LASIK surgery (Laser In Situ Keratomileusis) and is usually coupled with cross-linking to stop the progression of the disease. Finally, when all those techniques have failed, the only choice that remains is transplant. In the case of a keratoconus, surgeons perform a deep anterior lamellar graft, which keeps the posterior part of the patient's cornea and only transplants the anterior part of the donor's cornea.

The change of shape of the cornea in case of a keratoconus comes with an alteration of the collagen lamellae. Figure 1.11 presents the orientation of the lamellae of collagen in one healthy and one stage III keratoconic cornea, taken at the central part of the cornea (Fig. 1.11.a and b). In the case of a healthy cornea, it confirms that the lamellae are mostly parallel to the surface of the cornea (greenish and blueish colors on Fig. 1.11.c) which is emphasized by the large peak near 0 on the histogram of out-of-plane orientations (Fig. 1.11.e). On the other hand, the keratoconic cornea presents more

diverse colors than the control one (Fig. 1.11.d) – which is in agreement with the scatter in orientation angle in the middle stroma observed in the histograms on the right (Fig. 1.11.f). SHG images also show that the lamellae are curved in the case of the keratoconic cornea, while they are straight for healthy cornea. Those structural changes in the tissue lead to different mechanical responses of the corneal stroma, which will be studied in Sec. 1.4.2. In this work, we will also try to address the chicken and egg question: does the keratoconus appear because the mechanical properties of the cornea are altered, or does the change in mechanical properties come after the change in geometry?

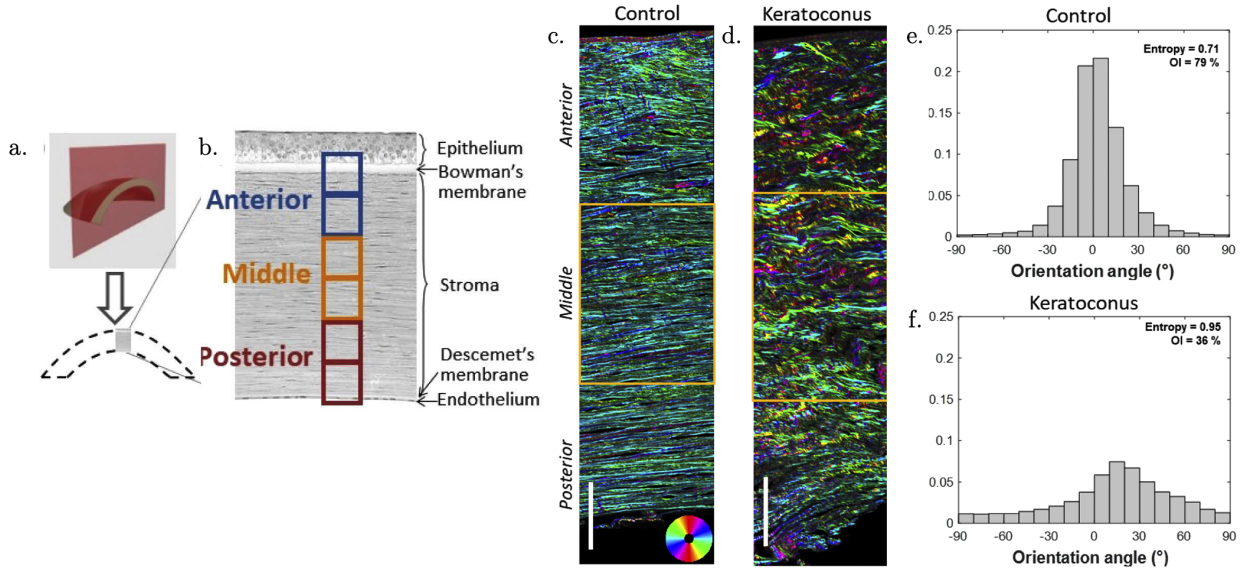


Figure 1.11: Orientation distribution of collagen lamellae in control and stage III keratoconic corneas on samples located in the central part of the cornea (from [145]). a, b. Location of the imaged samples. The anterior, middle and posterior stroma of the central part of the cornea are imaged. c, d: Typical out-of-plane orientation maps obtained from P-SHG images of transverse sections of the same control c. and keratoconic d. human corneas – scale bars: $100\ \mu\text{m}$ – and e, f: histograms of the collagen out-of-plane orientation in the middle stroma of the e. control and f. keratoconic corneas displayed in c and d.

1.2 Optical Coherence Tomography (OCT) and Image analysis

1.2.1 Optical Coherence Tomography

A variety of imaging techniques have emerged in the literature regarding tomography – the imaging technique allowing to look inside a material – and especially for biological tissues imaging. X-ray computed tomography, confocal microscopy, magnetic resonance imaging (MRI) or Optical Coherence Tomography (OCT) are the most used in hospitals today. They each have their specificities (resolution, field of application...) and are based on different theories. In the case of the eye, the reference technology is OCT, which is widely used in clinics to image the retina and the cornea.

1.2.1.a Principle of OCT

This section is largely based on [33; 39; 61]. It details the principle of the most widely used OCT systems.

General principle Optical coherence tomography (OCT) systems are non-contact and non-invasive systems using light scattering (particularly the reflectivity) of the imaged sample. The incident light is partially reflected by the internal structures of the sample (Fig. 1.12). The characteristics of the reflected waves (amplitude and travel time) are then analyzed to compute a reflectivity map of the sample.

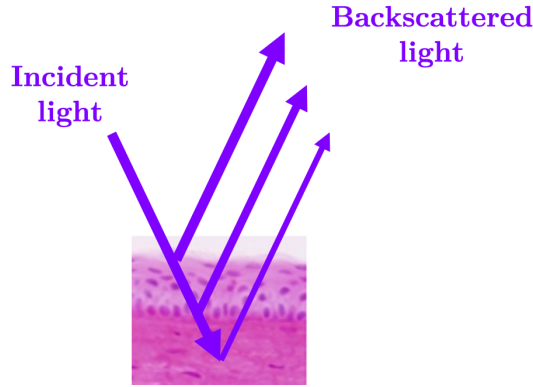


Figure 1.12: General principle of Optical Coherence Tomography (OCT) systems. The incident light is reflected by the internal structures of the samples and the reflected waves are analyzed to create the reflectivity map (adapted from [33]).

Since it is not possible to capture the reflected waves directly with sensors (the speed of light being too fast), another method – interferometry – has to be used. In the case of OCT systems, a Michelson interferometer is used to image the sample, taking advantage of the low coherence property of the light source to create localized interference. Figure 1.13 presents the principle of the different OCT systems commonly used in hospitals today.

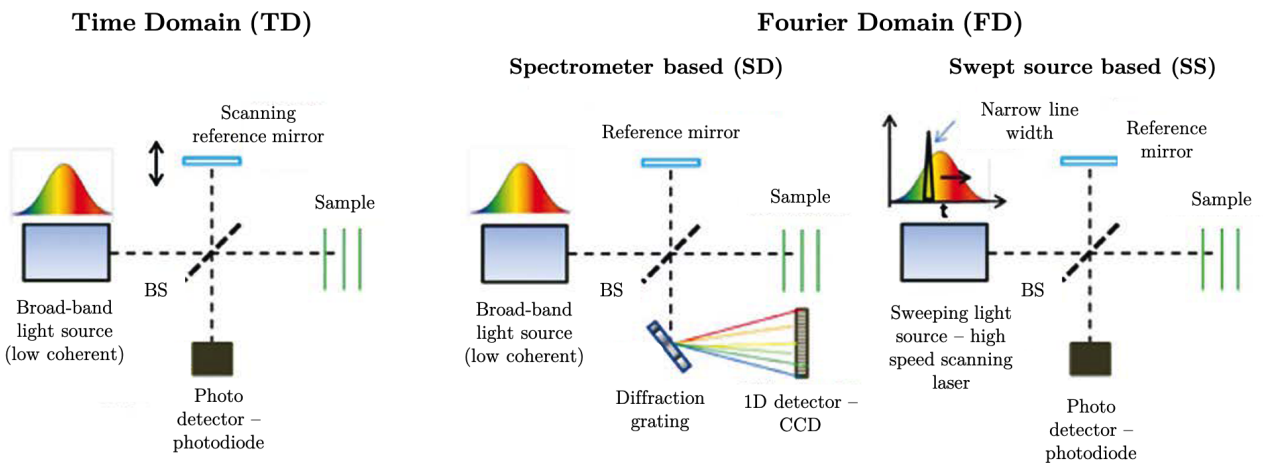


Figure 1.13: Optical Coherence Tomography (OCT) systems can be divided into Time Domain (TD) and Fourier Domain (FD) systems, which can themselves be separated into two types, the spectrometer based and the swept source based systems (adapted from [39]).

First, the light is split using a beam splitter (BS in Fig. 1.13) between the reference and the sample arms. Then the signal is reflected both by the reference mirror and the reflective interfaces of the sample. The back-reflected signals create interferences when the optical path lengths are the same (within the coherence length) and then they are captured by a detector. With the optical path

of the reference arm known, the interference signal is processed to generate images of the sample interfaces, and with that, reflectivity depth-profiles named A-scan. The axial (depth) resolution of the interferometer is determined by the so-called coherence length, which is classically defined by:

$$l_c = \frac{2 \ln 2}{\pi} \frac{\lambda_0^2}{\Delta\lambda} \quad (1.3)$$

with λ_0 the central wavelength of the spectrum and $\Delta\lambda$ the width of the spectrum. Note that the wider the spectrum, the smaller the coherence length and therefore the better the resolution. A simplified version of the intensity at the output of the interferometer (as the sum of the reference and object arm intensities) is [33]:

$$I(z) = \frac{I_0}{4} [R_{inc}(z) + R_{coh}(z) + R_{ref} + 2\sqrt{R_{ref}R_{coh}(z)}V_{coh}(z) \cos(\Delta\phi(\lambda_0, z))] \quad (1.4)$$

with $R_{coh}(z)$ the proportion of coherent back-scattered photons, $R_{inc}(z)$ the proportion of incoherent back-scattered photons, R_{ref} the reflectivity of the reference surface, $\Delta\phi$ the phase shift between the two arms of the interferometer and $V_{coh}(z)$ the Gaussian envelope of the wave, centered on the plane of zero step difference.

Looking at the intensity (Eq. (1.4)), and more particularly at the phase:

$$\Delta\phi(\lambda_0, z) = \frac{2n\pi}{\lambda_0} z \quad (1.5)$$

with n the refractive index and z the reference mirror position, the intensity (Eq. (1.4)) can be seen either as an oscillating wave of frequency λ_0 with a variable z or as an oscillating wave of frequency z with a variable λ_0 . These two different approaches will give the two types of OCT systems used today: Time Domain (TD-OCT) and Fourier Domain (FD-OCT) OCT systems (see Fig. 1.13).

TD- and FD-OCT TD-OCT systems use a broad-band light source (such as white light generated by optical fiber) with low coherence. This requires having very close optical paths between the two arms to obtain interferences. In this case, the position of the reference mirror changes (z in Eq. (1.5)) to create the interference with the different reflected interfaces of the sample and create an A-scan. Figure 1.14.a presents typical interferograms for two reflected interfaces of the sample. The envelope of the interferogram gives information on the material: the peak of intensity is related to the refractive power of the sample at that location. At the maximum intensity, constructive interferences appear – the image on the detector is reconstructed as white. Considering all the different intensity peaks, one can reconstruct the different gray levels of the A-scan. To distinguish two different interfaces of the sample, the two associated interferograms should be distinguishable. Thus, the coherence length of the source gives the limitation for the axial resolution of OCT. Once the A-scan is completed, a lateral sweeping (B-scan) is done to obtain a 2D image of the sample, and with a stack of 2D images, a 3D reconstruction of the sample can be obtained.

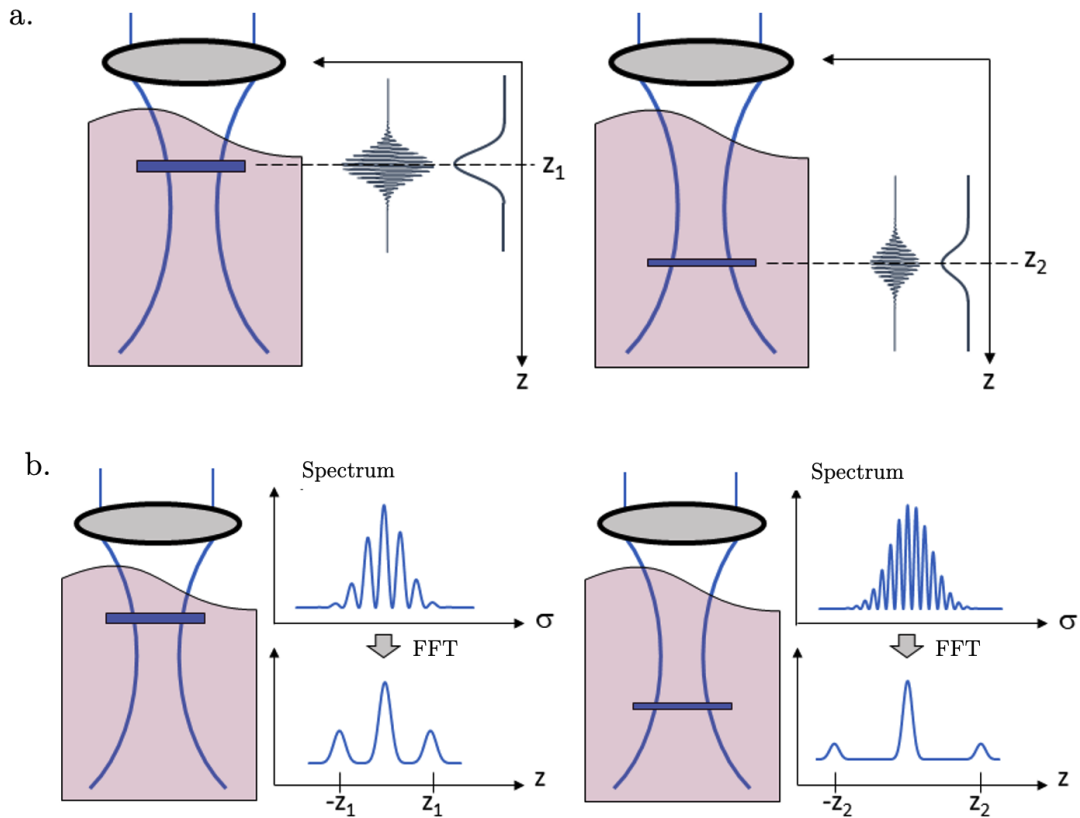


Figure 1.14: a. Typical interferograms of TD-OCT systems and b. typical spectrum of FD-OCT systems (adapted from [33]).

In the case of FD-OCT, the reference arm does not move, but the wavelength changes. The spectrum of the back-scattered signal is analyzed in the frequency domain. Depending on the type of spectrum analysis, FD-OCT systems are split into two categories: spectrometer based (SD-OCT) and swept source based (SS-OCT) systems. In the first case, a broad-band light source is used and the reflected signal is diffracted with a diffraction grating or a prism, and detected by a 1D detector such as a CCD (charge coupled device), or the grating spectrometer is directly used as detector. In the case of the swept source based system, the source is a frequency scanning light source, in which case a simple photo detector (photo-diode) is sufficient to capture the interference at the end of the process. In both cases, the axial resolution is limited by the spectral bandwidth of the light source.

Figure 1.14.b presents the typical spectrum detected for a sample with two reflective structures, which presents grooves due to the interference between reference and reflective light. The modulation frequency is proportional to the optical path difference and therefore to the distance (z_1 or z_2 on Fig. 1.14.b) to the coherency plane. So different grooves mean different depths of the reflective structures. Fast Fourier Transform (FFT) of the spectrum allows three components (three peaks on the FFT of the spectrum Fig. 1.14.b) to be found, one of which is interesting: the positive peak (in z_1 and z_2 on Fig. 1.14.b) gives the corresponding depth of the refractive surface – its height gives the amplitude of the back-scattered signal and its width the signal range. For a real sample, the signal is way more complex as the system captures one A-scan (the whole depth profile) at a time, but extracting positive peaks of FFT allows all the positions of the reflective structures of the sample to be found.

TD-OCT systems capture the A-scan pixel by pixel, whereas FD-OCT systems can capture one A-scan at a time. This gives the FD-OCT system a great advantage in speed and a better signal-to-noise ratio (SNR) [39]. However, capturing the whole depth in one shot (A-scan) requires the lens to have a wide field of view to light up the whole measured depth of the sample. A compromise must be found between acquisition speed, SNR and field of view size. Today, most surgeons use FD-OCT, which is the reason why, in this work, an FD-OCT – and more precisely an SD-OCT – with a low coherence source will be used to study corneas *ex-vivo*.

1.2.1.b Use of OCT in hospitals

This section is mainly based on [144; 166]. It details the main uses of OCT in clinics, especially on the cornea. Most of the figures are clinical images where the scale bar is therefore absent.

OCT in hospitals was first used to image the posterior chamber of the eye (especially retina) but it has proven to be a very effective tool to image the anterior chamber too, especially cornea. Ophthalmic OCT uses mainly infrared sources with wavelength typically between 800 and 900 nm for the retina and 1310 nm for the anterior chamber. With the emergence of FD-OCT systems, the scanning speed and axial resolution have increased due to the use of shorter wavelength. Commercial OCT systems achieve axial resolution of less than $5\ \mu\text{m}$ for ultra-high resolution mode.

In hospitals, TD-OCT have been gradually replaced by FD-OCT systems to image anterior segments. For example it can help detect ocular surface lesion, diagnose pathologies (macular degeneration, keratoconus, tumor or retinal lesions), choose between different treatments (in particular different types of surgeries) or quantify some anterior segment parameters (such as the anterior chamber angle between the scleral spur and the iris). We will focus here on the imaging of the cornea and the detection of its pathologies, and particularly the keratoconus. Figure 1.15 presents a typical 2D OCT image of a normal cornea. Epithelium, stroma and endothelium are easily distinguished by the difference in contrast between the three regions of the cornea.

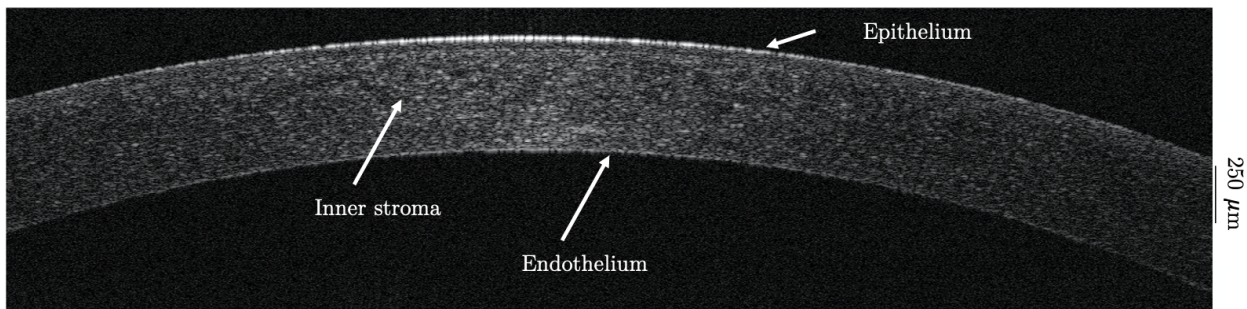


Figure 1.15: Optical Coherence Tomography (OCT) image of a normal cornea. Scale bar – $250\ \mu\text{m}$. (kindly provided by V. Borderie from 15-20 hospital).

Detecting keratoconus Figure 1.16.a presents a pachymetry (map of corneal thicknesses over a 10 mm-diameter circle) of a keratoconic cornea obtained using an OCT. Central thinning is detected with a minimum thickness of $422\ \mu\text{m}$ in the central zone (in red) of 2 mm in diameter, which may indicate a fruste keratoconus. Figure 1.16.b shows a 2D OCT scan of a cornea presenting a scarring

(the tissue appears whiter on the image in the affected area) and a thinning in the region pointed by the white arrow, also revealing a keratoconus. These two images show that pachymetry and 2D scans of corneas can be helpful to detect keratoconus.

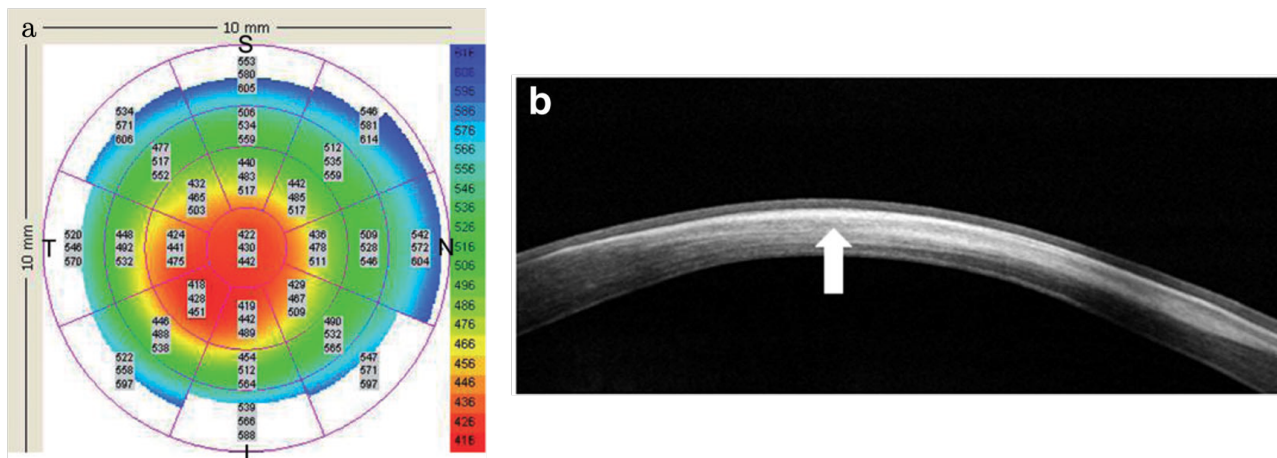


Figure 1.16: a. Pachymetry (map of the corneal thicknesses) of a keratoconic cornea obtained using a Visante OCT (extracted from [144]). b. OCT images of a keratoconic cornea showing a corneal scarring and thinning (arrow) (extracted from [166]).

Intrastromal rings Figure 1.17.b–c present OCT cross-section images of keratoconic corneas after the implant of intrastromal corneal rings (Fig.1.17.a for the picture of the eye implanted with the corneal rings). Ophthalmic surgeons use those images post-operative to verify the depth and position of the implantation (Fig. 1.17.c for a correct implantation). If the implants are too deep, they may perforate the anterior chamber (Fig. 1.17.b) and if they are not deep enough, it may lead to serious complications on both the stroma and/or the epithelium.

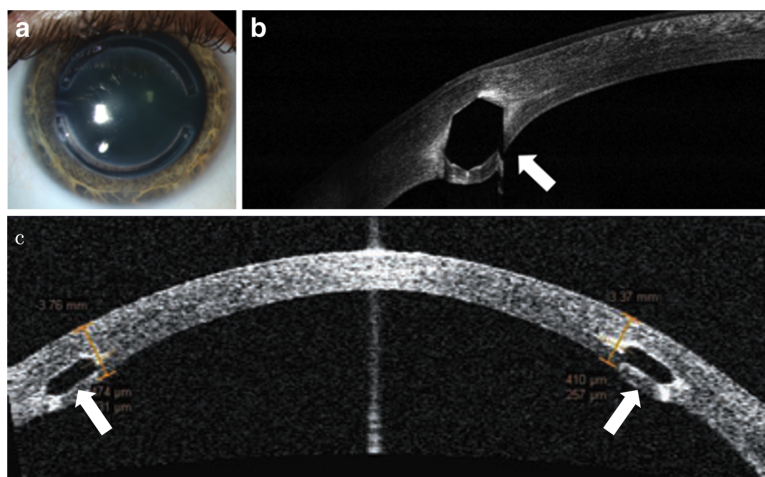


Figure 1.17: Intrastromal ring segments. a. Photograph of intrastromal ring segments (extracted from [166]). b-c. OCT images of intrastromal ring segments (arrow) (extracted from [144; 166]).

LASIK surgery Figures 1.18.a shows an OCT scan after LASIK surgery. It shows a $198\ \mu\text{m}$ flap – a cap created from the epithelium and a bit of stroma which is removed before LASIK surgery to access deeper stroma (where laser treatment is performed) and put back after the treatment – which was unexpectedly thick in this case and put the cornea at risk for ectasia. Here, OCT imaging helps

the surgeon adapt the treatment rapidly. Figure 1.18.b presents an OCT scan of a cornea after cross-linking treatment. The arrow points toward the demarcation line between the non-penetrated and the penetrated tissue. In this case, OCT images help measure the penetration depth of the collagen cross-linking treatment, and to study the influence of this depth on the response of the patient to the treatment.

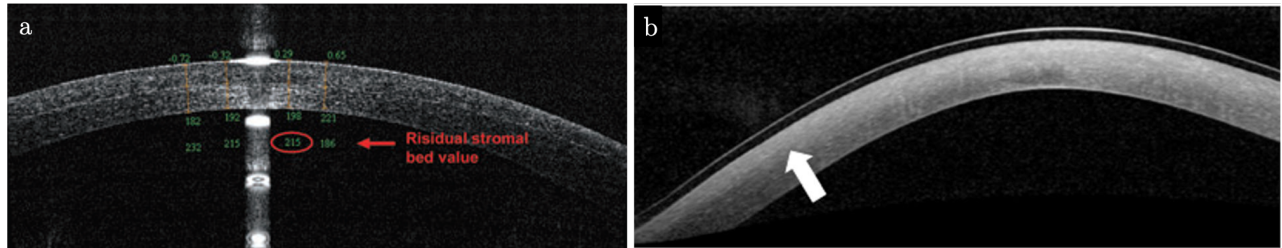


Figure 1.18: OCT images after laser surgery and cross-linking. a. LASIK flap of $198 \mu\text{m}$ and residual stromal bed at $215 \mu\text{m}$, (extracted from [144]). b. Corneal haze three days after corneal collagen cross linking. The arrows point at the demarcation line in the corneal haze (extracted from [166]) .

Corneal transplant Figure 1.19 presents OCT scans of a cornea after keratoplasty (corneal transplant). Fig. 1.19.a shows a cornea and the graft after Descemet Stripping Automated Endothelial Keratoplasty (DSAEK), a type of lamellar transplant. The demarcation line between the graft and the original cornea is clearly visible on the OCT scan, allowing for a control of the interface and anticipating graft detachment. When the keratoplasty fails, OCT scan allows the graft edge detachment (red arrow on Fig. 1.19.b) to be rapidly localized and the necessary action for the proper recovery of the eye to be taken.

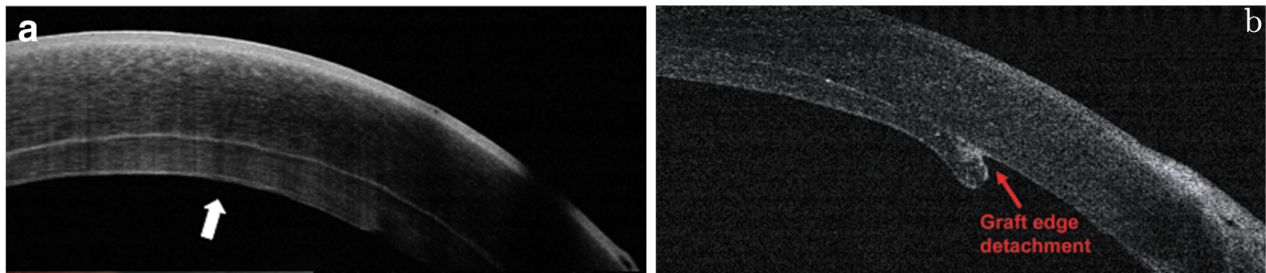


Figure 1.19: OCT images after keratoplasty. a. OCT image of an attached DSAEK graft (arrow) post-operative (extracted from [166]). b. OCT scan of a cornea after transplant showing a detachment of the graft. (extracted from [144]).

Conclusion In recent years, OCT has proven to be a very powerful tool for physicians. It allows both anterior and posterior chambers to be imaged (statically), pathologies such as keratoconus to be detected and the tissue pre- and post-operative to be imaged. The FD-OCT having a very high imaging speed, it opens a field of application on the characterization of the dynamics of the cornea in hospital. Finally, it can also be used to characterize the mechanics of the cornea using elastography coupled techniques (Sec. 1.3.2.b). Although the resolution of OCT in hospitals may be lower than OCT used in the laboratory, clinical OCT images are used in this work to describe the geometry of a patient's cornea at physiological pressure, particularly via the pachymetry maps and especially in the case of keratoconus.

1.2.2 Image analysis and strain measurement techniques

Ophthalmologists use OCT techniques to measure and control the health of the eyes. Therefore, they produce a huge amount of images, which data are not fully exploited at the moment. New techniques, such as Optical Coherence Elastography (Sec. 1.3.2.b), combining OCT with mechanical testing, have emerged to compute mechanical properties such as stiffness of the cornea. They rely mainly on two distinct types of image analysis: wavelength scanning interferometry and image correlation, introduced hereafter.

1.2.2.a Phase contrast and Wavelength Scanning Interferometry (WSI)

This part is mainly based on [28; 148].

The phase contrast or phase difference technique is a method to compute the displacement of a material between two interferogram-based images. The suitability of this approach has been highlighted by Ruiz and his colleagues [28; 148] using the technique of wavelength scanning interferometry (WSI). It relies on the existing relationship between the phase difference surface/volume $\underline{\Phi}$ and the displacement \underline{r} : $\underline{\Phi} = \underline{S}\Delta\underline{r}$ through the sensitivity matrix \underline{S} , which is related to the source and therefore considered known or at least easily measurable. The unknown is the displacement \underline{r} , while the phase differences $\underline{\Phi}$ are measured using WSI.

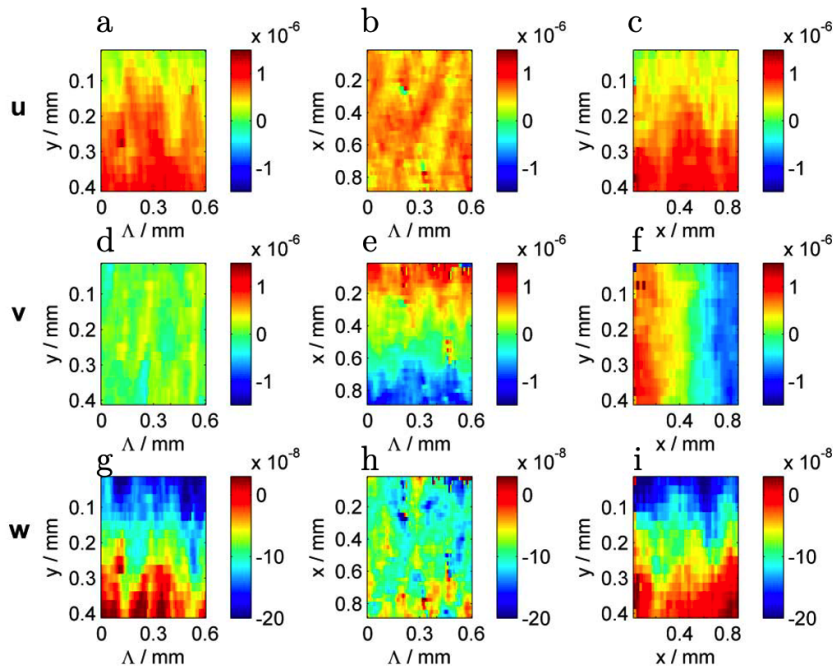


Figure 1.20: Cross sections of the measured 3D displacement field corresponding to an epoxy sample under in-plane rotation and out-of-plane tilt. The rows indicate the three displacement components u , v , and w . The columns show sections of the data volume on different planes. Displacements are in meters. (Extracted from [28]).

WSI is based on the same principles as the FD-OCT systems. A source with multiple wavelengths is used to image a sample at two different times. The source can be of different kinds: a low coherent source (like for OCT) associated with a prism, a swept source (considered the most expensive choice)

or an optic splitter that divides power equally between the output channels. Interference is created using the different frequencies of the source. A Fourier Transform is then applied on the detected signal. Images can be reconstructed, but it is the reconstruction of the phase between the two images Φ that is interesting in our case. Combining three non co-planar sources, the phase shifts can be measured in three different directions, allowing displacement maps to be computed such as Fig. 1.20, which presents the three components (u, v, w) of the displacement (rows) for different planes of the sample (columns) after an in-plane rotation and a out-of-plane tilt. Fig. 1.20.a, c, e and f show a gradient in the u and v components, which is expected from the in-plane rotation. Fig. 1.20.g and i present also an expected gradient from the out-of-plane tilt.

The same principle of phase contrast will be applied with OCT systems to compute displacement fields in the case of Optical Coherence Elastography (Sec. 1.3.2.b) [143; 171].

1.2.2.b Digital Image/Volume Correlation (DIC/DVC)

This part is mainly based on [24; 127].

Context Digital Image Correlation (DIC) is a commonly used technique to compute surface strain maps of a material under load. It became very popular with the evolution of digital camera technology, allowing for higher resolution, and also with the evolution of computing power, allowing for faster computation on many images corresponding to the material loading stages. It is usually based on the tracking and matching of speckled samples between a reference and a deformed state. Figure 1.21 presents an example of the experimental methodology for a classical traction test on Achilles' tendon (from [94]). First, the sample was dyed with methylene blue (Fig. 1.21.a). Then, it was speckled with white paint (Fig. 1.21.b) to give random contrast to the tissue. Finally, the longitudinal strain map was computed between two levels of load using DIC (Fig. 1.21.c) .

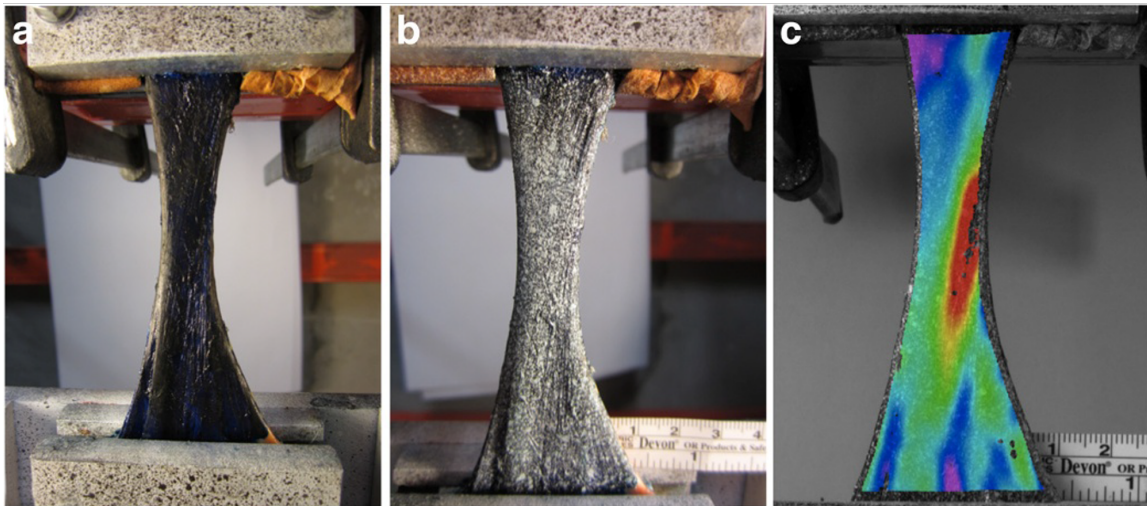


Figure 1.21: Example of DIC on Achilles' tendon. a. The Achilles' tendon in the clamps dyed with methylene blue, b. speckled with white paint and c. longitudinal strain map computed by DIC (extracted from [94]).

Principle Figure 1.22 presents the principle of DIC. A correlation domain (framed in pink on Fig. 1.22) is composed of a certain number of pixels (here 9) associated with gray levels in the

reference configuration. The goal is to track the evolution of this correlation domain in the deformed configuration, using the gray levels of the pixels in the so-called search domain of the deformed configuration. Denoting $f(\underline{x})$ and $g(\underline{x})$ the known gray levels of the pixels on the reference and deformed configurations respectively, image correlation relies on the existence of a displacement field $\underline{u}(\underline{x})$ such that:

$$g(\underline{x} + \underline{u}(\underline{x})) = f(\underline{x}) \quad (1.6)$$

with \underline{x} the location of the pixel. Figure 1.22 illustrates an idealized, simple case of DIC (with a simple field $\underline{u}(\underline{x})$ of a vertical displacement leading to a vertical strain), which hides the complexity that entail actual experimental setups. First, the displacement $\underline{u}(\underline{x})$ can be of any values, especially, there is no reason for it to be an integer multiple of pixels, resulting in the need to compute the displacement at the sub-pixel scale, to allow displacements of less than a pixel. Then, to have a precise computation, a large range of image gray dynamic should be used. In particular in each correlation domain and between a correlation domain and its neighbors, the gray levels must be varied enough so that the pattern can be easily recognizable between the reference and the deformed configuration. In practice, it means that the quality of the image should be sufficient and the speckling of the sample should be randomly distributed, so that the contrast of the image can be sufficient to perform the correlation. Finally, even if sub-pixel gray level computation is done and contrast is good, images are naturally noisy. Even for two images taken at the same levels of load (i.e. where $\underline{u}(\underline{x})$ should be $\underline{0}$), f and g are not perfectly equal and the difference between them is related to the noise coming from the experimental apparatus.

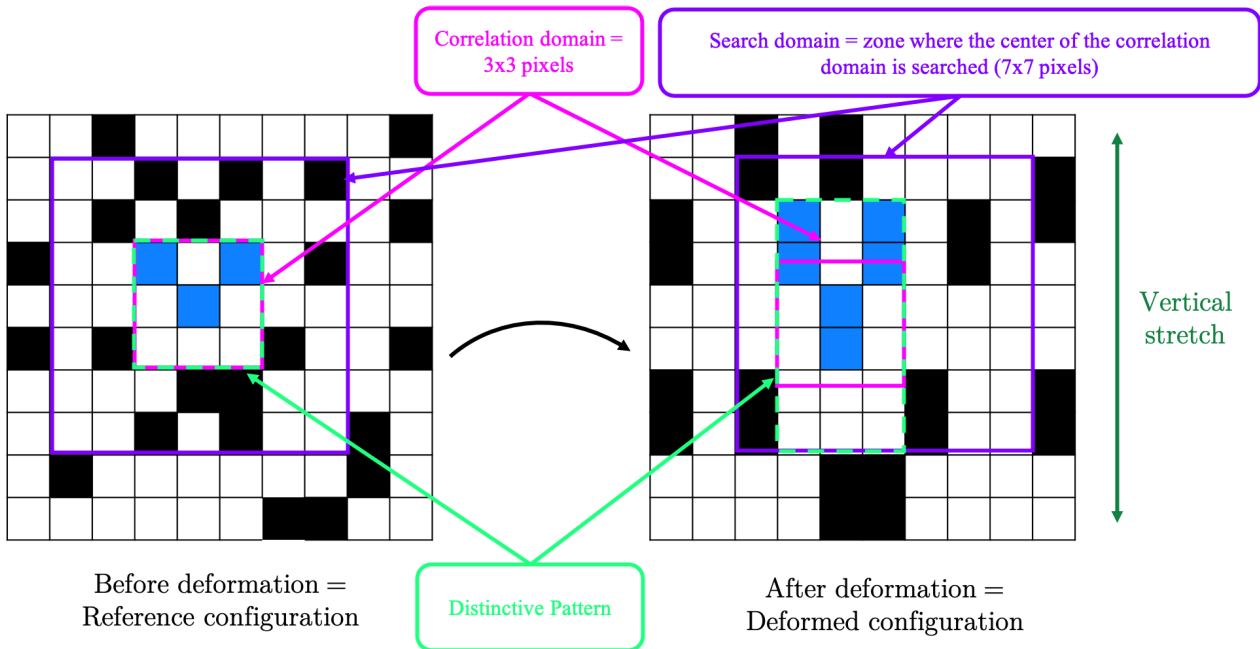


Figure 1.22: DIC Principle. The distinctive pattern of pixels of the reference correlation domain (pink square), will be compared using gray levels and correlation criterion with the deformed configuration pack of pixels. Then the correlation domain of the deformed configuration can be computed and with it the displacement between the two configuration.

To compare f and g taking into account these issues, a correlation criterion is created, estimating the similarity of the correlation domain of the reference configuration with the corresponding area

of pixels in the deformed configuration (the center of the correlation reference domain is searched in the deformed configuration within the search domain). A typical correlation criterion on a square correlation domain of $(2M + 1) \times (2M + 1)$ pixels is the zero-normalized cross-correlation criterion C_{ZNCC} defined as:

$$C_{ZNCC} = \sum_{i=-M}^M \sum_{j=-M}^M \frac{[f(x_i, y_j) - \bar{f}][g(x'_i, y'_j) - \bar{g}]}{\Delta f \Delta g} \quad (1.7)$$

with (x_i, y_j) and (x'_i, y'_j) the positions of the same pixel in the reference and the deformed configurations, respectively,

$$\bar{f} = \frac{1}{(2M + 1)^2} \sum_{i=-M}^M \sum_{j=-M}^M f(x_i, y_j), \quad \bar{g} = \frac{1}{(2M + 1)^2} \sum_{i=-M}^M \sum_{j=-M}^M g(x'_i, y'_j)$$

the mean values of the gray levels and

$$\Delta f = \sqrt{\sum_{i=-M}^M \sum_{j=-M}^M [f(x_i, y_j) - \bar{f}]^2} \quad \text{and} \quad \Delta g = \sqrt{\sum_{i=-M}^M \sum_{j=-M}^M [g(x'_i, y'_j) - \bar{g}]^2}.$$

A ZNCC criterion close to 1 corresponds to a very good correlation whereas a ZNCC criterion tending to -1 means a very poor correlation. Most DIC softwares allow a minimal acceptable value for the correlation criterion to be given, to consider that the correlation is good enough.

Local and global DIC Local DIC consists in correlating each correlation domain between its reference state and its deformed state. A global DIC can be done by looking at the region of interest as a whole. One of the main advantage is that it ensures the continuity of the measured displacement. Also a regularization process can be added when looking at materials for which there is an a priori on the displacement. Global DIC will not be detailed here as local DIC/DVC has been used in this work, mainly because we have no simple preconception of the behavior of the cornea and also because the image/volume correlation software in the laboratory handles local image correlation.

From DIC to DVC DIC is a surface method applied to 2D images. Historically, only such images provided enough contrast (due to the speckling for example). With the emergence of 3D imaging techniques in the 2000s however, such as X-ray tomography [11] or OCT [53], 3D images of materials with internal contrast are now available. The methodology of DIC can then be easily transposed to the third spatial dimension. Pixels become voxels, DIC becomes Digital Volume Correlation (DVC) and 2D cross-correlation algorithms become 3D.

Figure 1.23 presents the typical results for 3D displacements (A-C), 3D normal strain (D-F) and 3D shear strains (G-I) of chicken breast tissue under vertical compression obtained by DVC (using C_{ZNCC} correlation criterion) on 3D SS-OCT images [105]. During the test, muscle fibers were aligned along the x-direction. Results show an anisotropy in the mechanical deformation of the breast tissue (linear reduction along the z-direction, diagonal linear distribution along the x-direction and a near linear distribution along the y-direction).

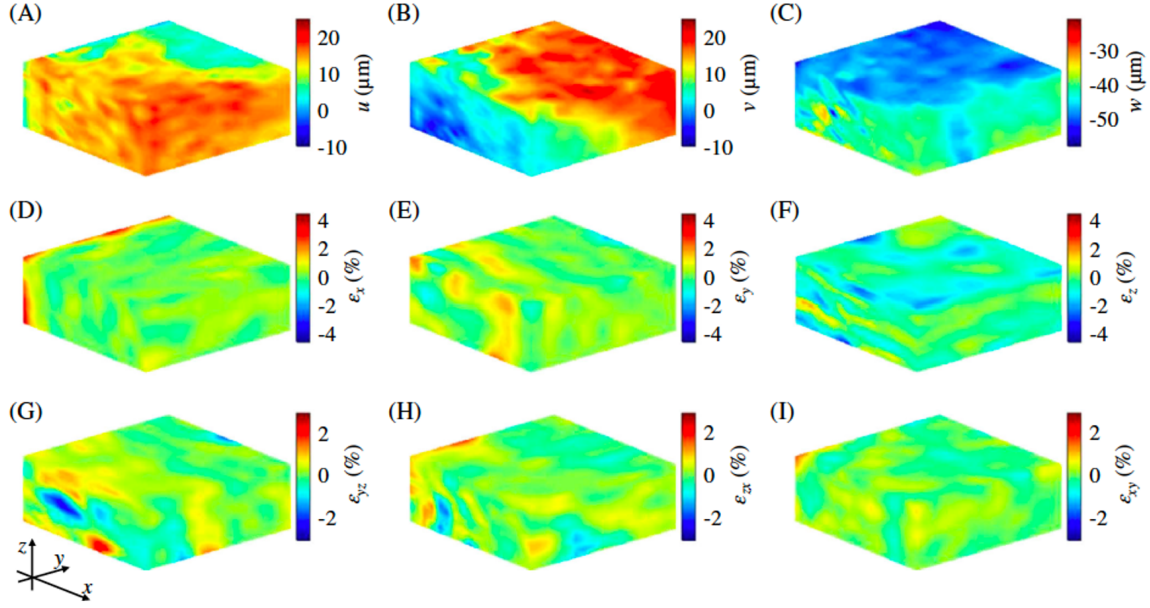


Figure 1.23: Example of DVC on SS-OCT images of chicken breast tissue under vertical compression. (A-C) the 3D displacements in the x, y and z directions, respectively, (D-F) the 3D normal strains ε_x , ε_y and ε_z in the x, y and z directions respectively and (G-I) the 3D shear strains ε_{yz} , ε_{zx} and ε_{xy} (extracted from [105]).

With the development of imaging techniques came the development of strain field measurement techniques. WSI and DVC are two techniques allowing 3D displacement of a material under loading to be measured, thereby offering the possibility to characterize the response of a material to those loads. Anisotropy in the three directions can be detected, which is interesting for a material reinforced by one or two varying families of fibers, such as collagen-based tissues (muscle, tendon, cornea...). While WSI is more commonly used in optics laboratories, DVC is well implemented in the mechanics field. In this work, DVC will be used to compute local displacement of the cornea under mechanical loading.

1.3 Mechanical characterization of the human cornea

In order to model the response of the cornea to pressure, one needs values for the mechanical parameters of the tissue, such as stiffness, viscous modulus... To do so, one of the newest experimental approach is called Elastography. It can be defined as any imaging process allowing to extract elasticity or stiffness of a material. It usually couples a mechanical exciter to create a perturbation in the tissue, with an imaging apparatus to measure the induced perturbation. Finally, to extract the mechanical properties of the material, one needs a model of the tissue, generally based on simplified constitutive law.

Even though it is usually easier to perform mechanical tests *ex-vivo* (repeatability of experimental conditions, sampling, availability of samples and the experimental apparatus, larger range of experimental conditions...), the cornea is a tissue that has the advantage of being accessible *in-vivo*. As a result, although the classical characterization tests of healthy tissues are usually performed *ex-vivo*, the characterization of pathological corneas can be done *in-vivo* thanks to new elastography techniques, which compare their properties with healthy ones. In this work, we will focus on the

characterization of bank corneas, thus healthy and *ex-vivo*.

1.3.1 *Ex-vivo* mechanical characterization of cornea

This section presents the most common tests performed *ex-vivo* on corneas to measure and characterize the mechanical properties of the tissue. The inflation test is the experiment that mimics best the physiological action of pressure on the cornea. Strip extensometry has been used for decades to measure Young's modulus of all types of materials. Nanoindentation and acoustic radiation force elasticity microscopy (ARFEM) are two more modern techniques allowing for the evaluation of the Young's modulus, and the latter has the advantage of being non destructive.

1.3.1.a Inflation test

Principle of the method The inflation test is an experimental method to characterize the mechanical properties of cornea. It mimics the action of intraocular pressure on the tissue. Elsheikh's group has studied the mechanical properties of porcine and human corneas using the experimental apparatus represented in Fig. 1.24 [46]. The cornea is attached to a pressure chamber by the sclera, and saline solution is injected under the cornea via the pressure chamber to put the tissue under pressure. The pressure in the chamber is monitored using a pressure sensor and the displacement of the apex of the cornea is measured via a laser displacement sensor. The biomechanics of the cornea is then analyzed using the pressure with apex displacement curve.

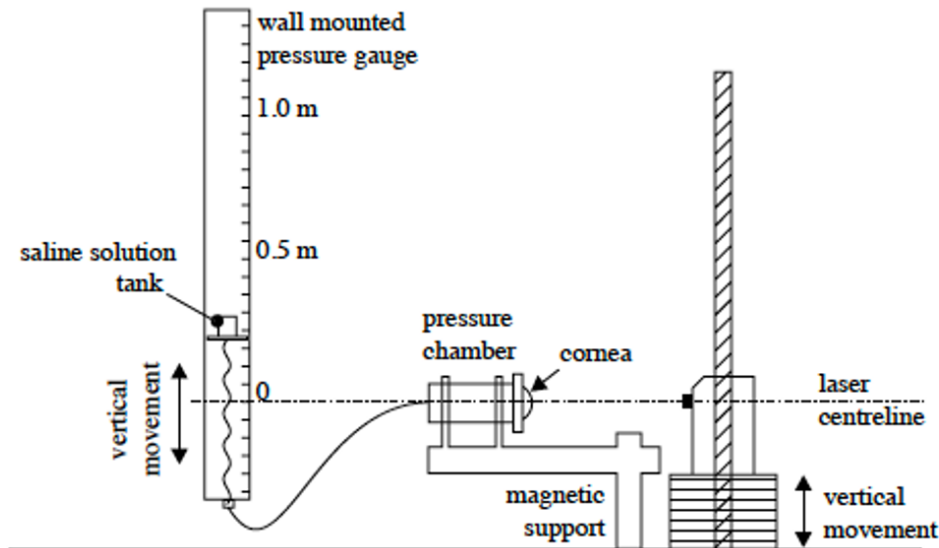


Figure 1.24: Schematic view of the different components of the inflation test (extracted from [46])

Main results Figure 1.25 presents the pressure with apical rise curves for six human corneas [45]. At low pressure (under approximately 15 mmHg), the cornea exhibits a low stiffness. Then, with the increasing pressure, a sudden change of stiffness (corresponding to an abrupt change of slope) appears. Elsheikh and Anderson explain these two regimes by a domination of the mechanical response by the matrix (of low stiffness) at low pressure, and a domination by the collagen lamellae (high stiffness) at higher pressures [46].

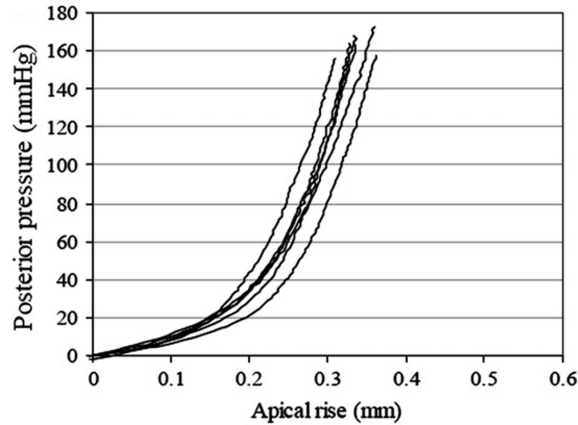


Figure 1.25: Pressure with apical rise during inflation test for 6 human corneas (from [45]).

In the same article [45], the authors also show that porcine and human corneas do respond the same way to pressure (low stiffness at low pressure and sudden change of stiffness at higher pressure consistent with the exponential response) but that human corneas are stiffer than porcine ones, and also that human corneas stiffen with age.

Although the article of Elsheikh's group proposes a first global mechanical behavior of the cornea using the displacement of the apex, it may seem reductive to consider that the whole biomechanics of the cornea is governed by what happens at the highest point, in particular in view of the complex microstructure. That's why other groups – particularly Boyce's group [23] – measured the displacement of the whole anterior surface of the cornea by stereo-correlation (a 3D displacement field measurement of a surface). Figure 1.26.a presents the results for the out-of-plane displacement (in the z-axis direction of Fig. 1.26.a) at a particular pressure (60 mmHg). Fig. 1.26.b presents the results for the out-of-plane displacement for various location over a loading cycle. Those maps show that the out-of-plane displacement is homogeneous for the central part of the bovine cornea at 60 mmHg and also relatively homogeneous over the loading cycle (the displacement at the different locations is similar).

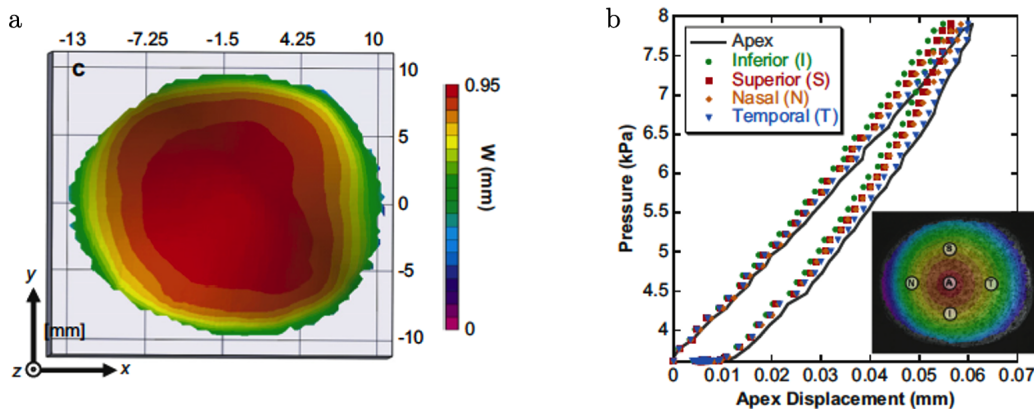


Figure 1.26: a. Typical out-of-plane displacement at a pressure of 8 kPa (60 mmHg) for bovine cornea. b. Typical out-of-plane displacement at different locations during a loading cycle over a pressure range of 3.6–8.0 kPa (27–60 mmHg). (Both images are extracted from [23])

It confirms that one could consider the apex displacement as a proxy for the anterior surface displacement of the cornea, at least for bovine eyes, when the surface geometry is known. But there is still a lack of information on the material behavior through thickness. Fu [Fu] tried to tackle this issue by measuring full-field displacement and strain maps using digital volume correlation (DVC) on OCT images of porcine corneas during an inflation test between 2 and 2.5 kPa (15–18.75 mmHg).

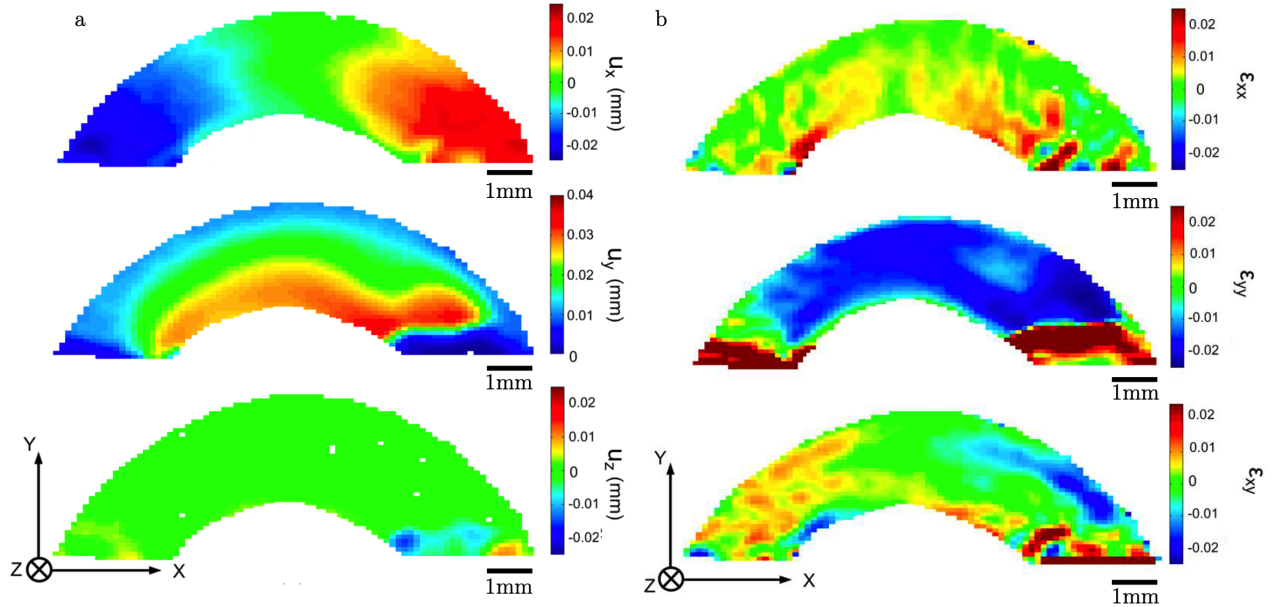


Figure 1.27: a. Displacement and b. strain maps measured with DVC for the central z-slice of a porcine cornea under pressure from 2 to 2.5 kPa (15 to 18.75 mmHg) (extracted from [Fu] – Scale bar: 1 mm)

Figure 1.27.b shows a clear contraction (approximately -2% of ϵ_{yy} strain) of the center of the cornea along the vertical direction (y-axis) while the cornea inflates in the peripheral zone (of approximately 2% also) between the two steps of pressure 15 and 18.75 mmHg. ϵ_{xx} strain maps show an extensional deformation along the x-axis and clear heterogeneity between the anterior and posterior parts (almost all of the deformation appears in the posterior stroma) while the cornea is submitted to shear strain in the periphery (and mostly on the anterior part of the cornea), which may be due to the computation of the strain in Cartesian while the cornea is curved (and thus would have a rather radial deformation). Figure 1.27.a shows displacement maps for the same steps of pressure and the order of magnitude of the vertical displacement u_y at the apex of the cornea seems to be in agreement with the apex displacement found by Elsheikh’s group [45], i.e. approximately 0.01 mm between 15 and 19 mmHg.

Pathological case To our knowledge, there is no mechanical characterization of a whole human cornea (healthy or pathological) using inflation tests. To study the case of pathological corneas, inflation tests have been performed on porcine corneas treated with a riboflavin solution to perform the cross-linking treatment (Sec. 1.1.3). Kling [85] used a Scheimpflug corneal three-dimensional topographer to image the eye and the Young’s modulus was computed using the classical stress-strain relationship where stress is defined as $\sigma = Rp/2d$ (with R the mean radii of curvature, p the applied pressure and d the corneal thickness) and strain is defined as $\epsilon = \Delta R/R$. They show that the Young’s modulus in a cross-linked cornea is significantly higher (1.096 ± 0.30 kPa) than the one found

in non-cross-linked eyes (0.692 ± 0.30 kPa). They also show that the cross-linking treatment influences the thickness of porcine corneas, especially 24 hours after the treatment. A strong dehydration was observed on porcine corneas with classical hyperosmolar riboflavin instillation, while swelling occurred for hyposmolar riboflavin treatment. In another study, Chang [29] found that the shear modulus μ at a stress of 0.03 MPa shows an increase of $43\% \pm 24\%$ in a cornea treated by cross-linking with respect to non treated porcine corneas. One can conclude that the cross-linking process tends to stiffen the tissue and also to influence the thickness of the cornea.

Summary Using the inflation test approach, the literature has shown that (i) the cornea presents two very distinct regimes of mechanical responses depending on the applied pressure, (ii) cross-linking can be a suitable treatment approach for keratoconus because it stiffens the weakened pathological corneas, and (iii) a global characterization of the local properties of the cornea is lacking, which will be studied in this work.

1.3.1.b Strip extensometry

Principle of the method Strip extensometry is one of the most classical experiments designed to obtain mechanical properties of a material and especially the Young's modulus, which is obtained from the slope of the stress-strain curve as $E = \sigma/\varepsilon$ (with σ the axial stress and ε the axial strain). Elsheikh and Anderson [46] have performed tensile tests until rupture on porcine cornea while Boyce's group have carried out creep tests on bovine cornea [22]. Figure 1.28 presents the experimental apparatus used by Boyce's group (Fig. 1.28.a–d) and by Elsheikh and Anderson (Fig. 1.28.e–f). They both cut a strip going through the apex diagonal out of a cornea (bovine and porcine respectively) and applied uniaxial load on the coupon.

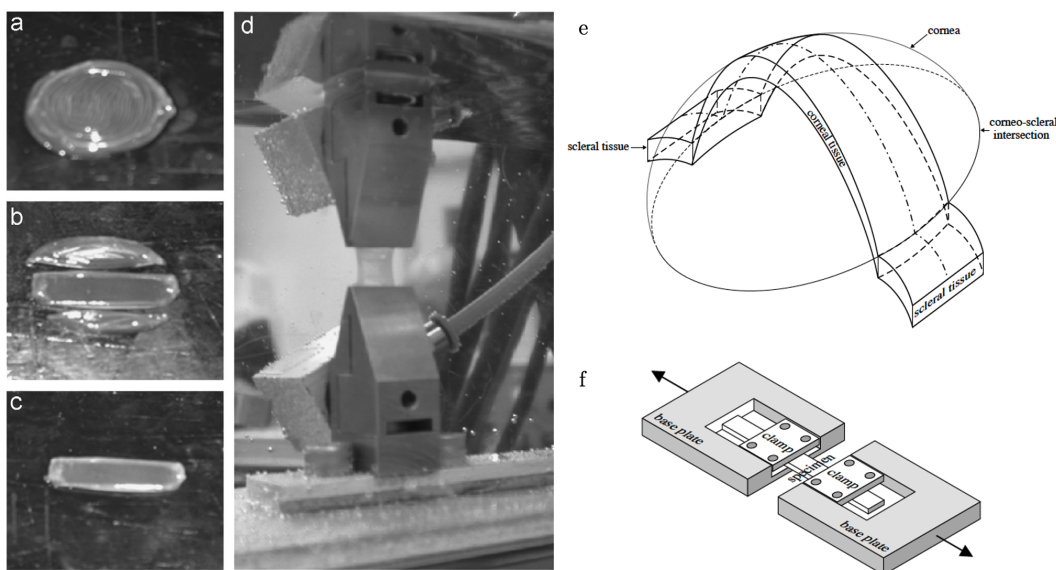


Figure 1.28: a-d. Experimental apparatus used in (and extracted from) [22]. a. Bovine cornea, b. and c. cut of the strip and d. tensile test. e. Schematic of the specimen and f. the strip extensometry test rig used in (and extracted from) [46].

Main results Figure 1.29 presents the stress-strain curve (a and c) and the load-extension curve (b) of the strip extensometry tests. In all the cases, the exponential responses under the two regimes is obtained, similar to the inflation test response. Figure 1.29.c shows the comparison between the averaged stress-strain curve for strip extensometry and inflation tests on porcine corneas. It appears that the strip test exhibits a smaller first regime, the cornea stiffens between 1 and 3% of strain whereas it stiffens between 3 and 5% of strain in the case of the inflation test.

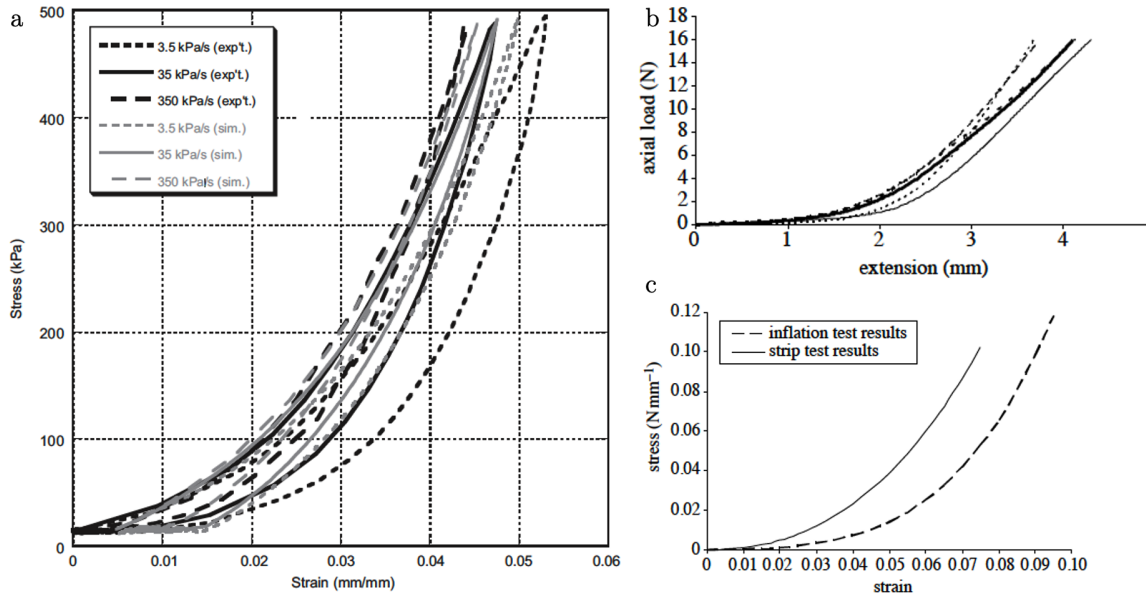


Figure 1.29: a. Average tensile stress–strain response of bovine cornea tissue in the naso-temporal orientation at each of three different strain rates (extracted from [22]). b. Load-elongation behavior of a selection of strip tests on porcine corneas and c. Material constitutive relationship obtained using both inflation and strip tests on porcine corneas (extracted from [46]).

Even though the stress-strain results of the strip extensometry tests are similar to those of the inflation test, three sources of inaccuracy coming from the geometry of the cornea can be identified computing the axial stress ($\sigma = T/A$, with T the axial tension and A the cross-sectional area of the specimen) and axial strain ($\varepsilon = \delta L/L$ with δL the elongation and L the initial length). First, the cornea being almost spherical, the length of the anterior and posterior surfaces of the strip are not equal and so the usual area used has to be adapted to compute the Young’s modulus [46] to take into account the non uniform stress distribution. Second, the corneal strip is flattened, so its initial curvature has to be taken into account in the computation of the Young’s modulus, especially for pre-strain (extensional strain in the posterior surface and contractile strain in the anterior surface). Finally, the thickness is not homogeneous along the strip (the cornea is thinner in the central part than in the periphery) and this third geometrical effect has to be considered in the computation of the area A . Anderson and Elsheikh [46] have built a model to correct the results of the strip extensometry test to match the inflation test results (the difference between the two sets is reduced to 5% in average) so that future work on the characterization of the mechanical properties of the cornea can be done using strip extensometry.

Pathological case In the case of pathological corneas, there is only a few old studies of strip extensometry comparing the Young's modulus of healthy and keratoconic human corneas. Andreassen and his colleagues [6] show that the Young's modulus of a keratoconic cornea is significantly lower than the one of a healthy cornea. However, Nash [119] shows that this assertion is true for high level of stress but not at physiological pressure, where no significant difference is found between healthy and pathological corneas. Finally, Spoerl *et al.* [162] studied very early the effect of cross-linking by using strip extensometry on treated and non treated porcine specimen and showed that the cross-linking resulted in an increased stiffness. More recently, Wollensak *et al.* [177] performed extensometry tests on human and porcine corneas and showed that the Young's modulus was higher when the corneas have been treated with riboflavin (4.5 higher and 1.8 higher, respectively).

Summary Although strip extensometry is easy to perform, assessing the mechanical properties of cornea based on this approach is not straightforward because the transition from plane properties (of the strip) to 3D properties (of the half-sphere) is not obvious. That is why more recent studies do not use strip extensometry anymore for this purpose, but usually prefer the methods described hereafter.

1.3.1.c Nanoindentation

Principle of the method The test of indentation consists in penetrating a tip (the indenter) in a flat surface of the tested material, and monitoring the height of penetration (h in Fig. 1.30) and the applied load (P on Fig. 1.30). The mechanical properties – such as hardness – can then be determined.

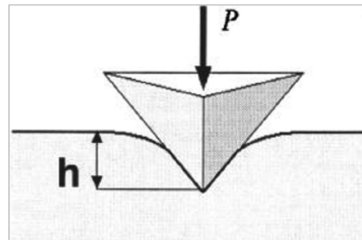


Figure 1.30: The principle of nanoindentation (extracted from [35]).

Main results Dias *et al.* [37] and Last *et al.* [90] measured the Young's modulus of corneal stroma using atomic force microscopy (AFM) as a nanoindentation process. Dias *et al.* found that the posterior stromal elasticity is 39.3% of the anterior stromal elasticity, with an anterior Young's modulus of 281 ± 214 kPa. Last *et al.* on their side measured an anterior stromal Young's modulus of 33.1 ± 6.1 kPa. The difference in the order of magnitude may come from experimental protocols, especially the preparation of the exposition of the anterior stroma. Eberwein *et al.* [42] used a Bioindenter to measure the properties of cornea, limbus and sclera. Figure 1.31 presents the typical force with displacement curve obtained using the Bioindenter on the three tissues. Young's modulus measured for the central cornea was approximately 19 kPa, 10 kPa in the limbal region and 17 kPa in the scleral region.

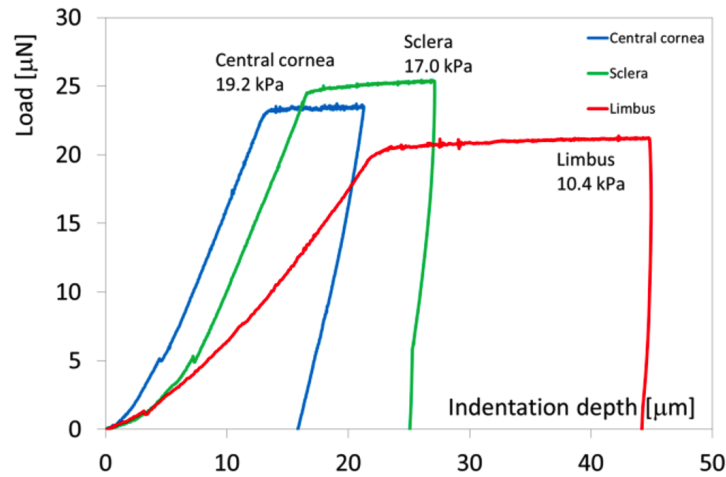


Figure 1.31: Typical force with displacement curves obtained using nanoindentation for the cornea (blue), the limbus (red) and the sclera (green) (extracted from [42]).

Pathological case The same groups used nanoindentation to measure the elasticity of corneas after cross-linking. Dias *et al.* [36] showed that porcine corneas treated with riboflavin were stiffer and less viscous than the control ones. Nohava *et al.* [123] used the Bioindenter on human corneas and measured that the stiffness of the central cornea is two times higher after riboflavin treatment. In both articles, the authors show that the region of higher stiffness is centered around the riboflavin application and does not extend significantly towards the periphery.

1.3.1.d Acoustic Radiation Force Elasticity Microscopy (ARFEM)

One of the most recent techniques used to measure the mechanical properties of the cornea (and other soft tissues) is the acoustic radiation force elasticity microscopy (ARFEM). Figure 1.32 presents the setup used in Mikula's papers [109; 110].

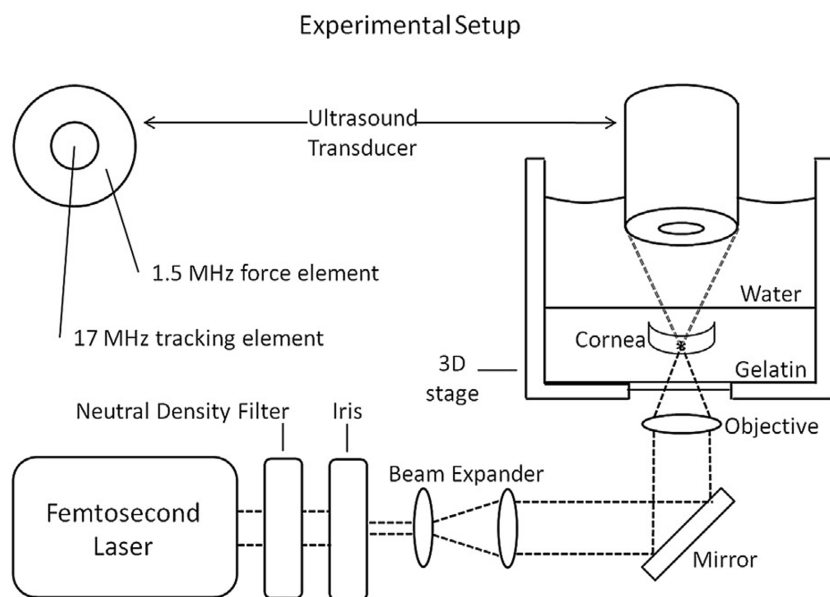


Figure 1.32: ARFEM setup (extracted from [109]).

Details of the experimental apparatus can be found in [109]. Only the main components are described below. A femtosecond laser generates a micro-bubble inside the sample with one pulse. Then an acoustic force (low-frequency, high-intensity) displaces the bubble while an ultrasound probe (high-frequency, low-intensity) monitors the displacement of the bubble. The Young's modulus is related to the displacement of the bubble using the following relationship $E = Ia/2cx_{max}$ [109], where I is the acoustic intensity, a the bubble radius, c the speed of sound in the medium and x_{max} the maximum displacement of the bubble.

With this technique Mikula *et al.* managed to measure the Young's modulus in healthy [111] and keratoconic [110] corneas. They found that the anterior central part is stiffer ($E = 4.2 \pm 1.2$ kPa and $E = 1.67 \pm 0.44$ kPa for healthy and keratoconic corneas, respectively) than the posterior central part of the cornea ($E = 2.3 \pm 0.7$ kPa and $E = 0.970 \pm 0.30$ kPa for healthy and keratoconic corneas, respectively). They also show that keratoconic corneas are significantly less stiff than healthy tissues.

Summary on Nano-indentation and ARFEM Nano-indentation and ARFEM are new techniques that allow direct measurements of the Young's modulus of the anterior and posterior cornea. In this work, despite their large scatter, the results of nano-indentation experiments will be used in the modeling process because the experiments were performed on the anterior and posterior stroma and not on the whole cornea (with the epithelium and Bowman's layer removed).

1.3.1.e Summary of *ex-vivo* mechanical characterization without microscopic imaging

To conclude, although all these techniques give quite different results in terms of numerical values, significant trends emerge with respect to *ex-vivo* measurements.

Figure 1.33 presents a summary of the previous results on characteristic stiffness measured using the different techniques presented, which definition varies across experiments (see Table 1.1 for a summary). First, in all cases, porcine corneas (in pink on Fig. 1.33) are globally less stiff than human corneas (in blue on Fig. 1.33). Then, keratoconic corneas (\triangle on Fig. 1.33) are significantly softer than healthy tissue (\square on Fig. 1.33), but cross-linked corneas (\diamond on Fig. 1.33) are significantly stiffer than healthy tissue. The lack of rigidity of pathological corneas can thus be counterbalanced by the increase of stiffness brought by cross-linking treatment. Finally, anterior stroma (middle blue and pink) is stiffer than posterior stroma (light blue and pink) either for humans and pigs. However, no study compared the measure on the whole cornea to those on anterior and/or posterior parts only.

Based on Fig. 1.33, we conclude that it is difficult to choose a single value for a given mechanical property of the cornea. The scatter across the results available in the literature is very large: the scale of Fig.1.33 being logarithmic, the range of possible values comprises almost four orders of magnitude for human corneas. Furthermore, it shows that there are discrepancies between the anterior and posterior parts and that local information on the whole organ is therefore missing. The experimental part of this work will try to tackle those issues by measuring local information on the whole tissue.

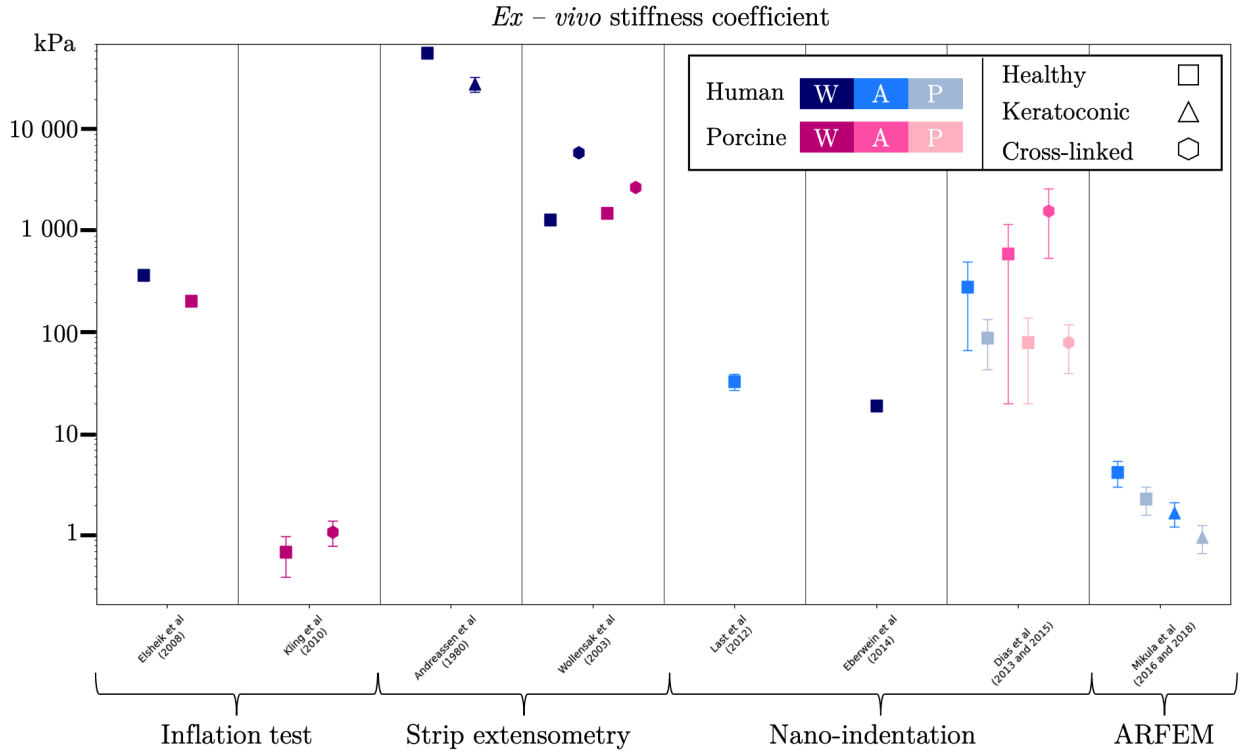


Figure 1.33: *Ex-vivo* measured corneal stiffness coefficient using the different methods previously presented: inflation test (Sec. 1.3.1.a), strip extensometry (Sec. 1.3.1.b), nano-indentation (Sec. 1.3.1.c) and ARFEM technique (Sec. 1.3.1.d). Notation: W = whole cornea, A = anterior stroma, P = posterior stroma.

1.3.1.f Mechanical testing coupled with imaging of the microstructure

Two founding papers have studied the response of the cornea to mechanical load whilst imaging the microstructure: one using Second Harmonic Generation (SHG) microscopy coupled with inflation test [14] and one using X-ray diffraction coupled with strip extensometry [13]. In these papers, microscopic strains are compared to the distribution of the lamellae during the mechanical tests.

Macroscopic strain response Figure 1.34.a.1 presents the scan positions used for the X-ray analysis and Fig.1.34.b.1 the different volumes of interest for the study, in particular Stack#2 (2PEF) that was used to perform the strain analysis.

Figures 1.34.a.2 and b.3 present the local strain results measured by DIC. Fig. 1.34.a.2 shows the computed parallel strain on the strip cut along the vertical meridian at 5% of strain during tensile test [13]. Fig. 1.34.b.3 illustrates the strain on the corneal surface between the loading steps of the inflation test along the two preferential directions of the collagen lamellae φ_1 and φ_2 presented in Fig. 1.34.b.2 [14]. Figure 1.34.a.2 shows a relatively symmetric distribution of strain with respect to the center of the sample with a bigger parallel strain in the center (around 7%) than in its closest periphery (around 3-4% at positions of 6 and 10 mm). The end of the strip is subject to higher strain – up to 10%. Normal strain maps (ϵ_{11} and ϵ_{22} in Fig. 1.34.b.3) and shear strain maps (ϵ_{12}) show, respectively, the progressive stretching and shearing of the cornea along dominant orientations with increasing pressure. The strain appears rather uniform, leading to homogeneous deformations at the sub-millimeter scale.

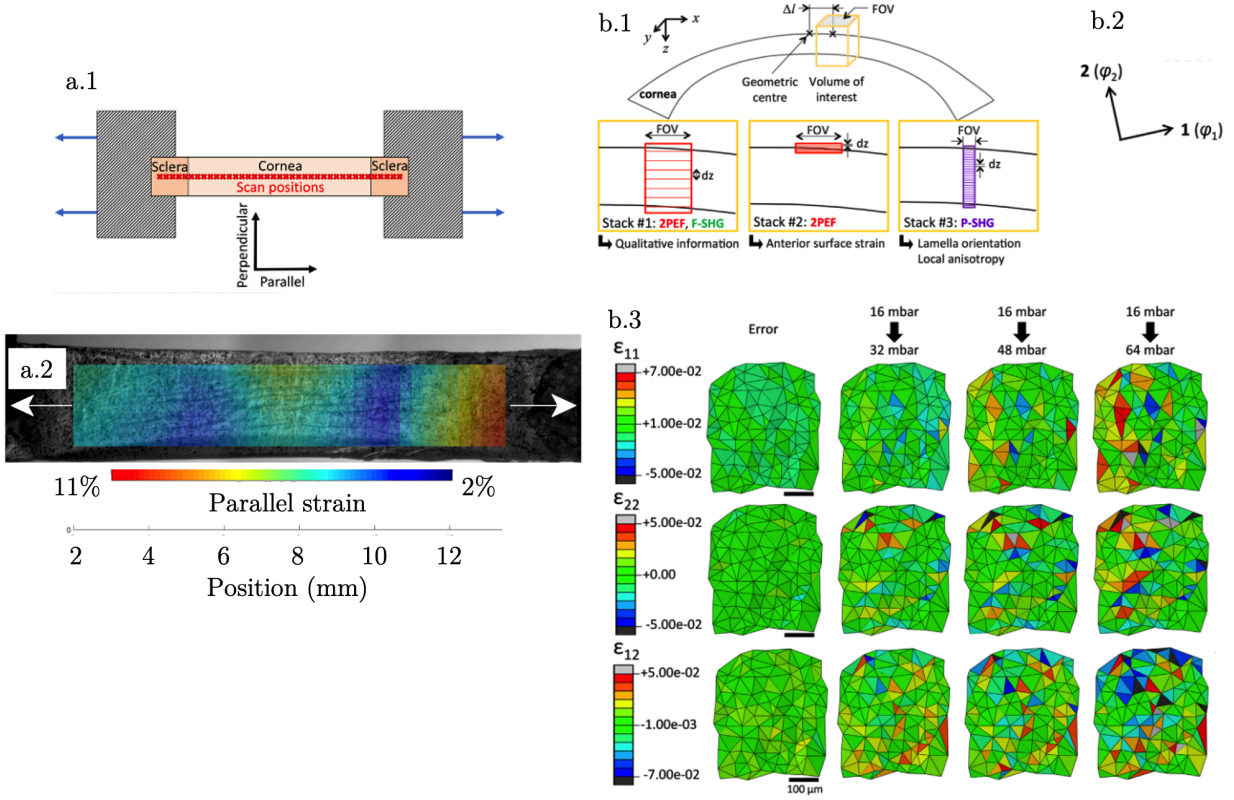


Figure 1.34: a.1. Scan positions used for the X-ray analysis during tensile test. a.2. Parallel strain computed by DIC at 5% of strain – scale bar 11% (red) to 2% (blue) (extracted from [13]). b.1. Volumes of interest considered in the study. b.2. Main direction of the lamellae used to compute b.3. the local normal (ε_{11} and ε_{22}) and shear (ε_{12}) strains (extracted from [14]).

Lamellae orientation Figure 1.35 presents the results on lamellae orientation during the two loading tests. Fig 1.35.a shows the analysis for the tensile test and Fig 1.35.b for the inflation test. WAXS analysis (Fig 1.35.a) shows the polar plot of the aligned collagen lamellae. It features a clear alignment of the lamellae along the stretching direction with increasing strain. The anisotropy value, representing the ratio of maximum parallel collagen to maximum orthogonal collagen peaks, is clearly increasing in the middle of the sample, which leads to a rearrangement of the collagen lamellae along the stretch direction. However, the pattern of the macroscopic strain at 5% is not completely recovered in these WAXS results. In particular, there is no clear difference between the center of the sample and its nearest periphery (around 6 and 10 mm). Figure 1.35.b.1 presents the results of SHG image analysis determining the distribution of the orientation probability of the lamellae on the whole thickness of the cornea and on the anterior, middle and posterior stroma with increasing pressure. It shows first that the main orientation remains the same during the whole experiment and, second, that the probability distribution is changing with pressure, especially in the middle and posterior stroma. Figures 1.35.b.2 and b.3 detail the percentage of lamellae oriented along the two main directions (with a margin of $\pm 15^\circ$) in the same zones of the cornea with increasing pressure. It is interesting to note that the proportion of lamellae oriented along the main direction φ_1 decreases with pressure, whereas the proportion of lamellae oriented along the second main direction φ_2 slightly increases, as if the lamellae reoriented themselves to be less anisotropically distributed. More particularly, this

reorientation happens in the middle and posterior stroma, contrary to the collagen lamellae of the anterior stroma which tend to keep their quasi-isotropic orientation. Again, no direct link can be established between the observed macroscopic strain and the response of the collagen lamellae to increasing pressure.

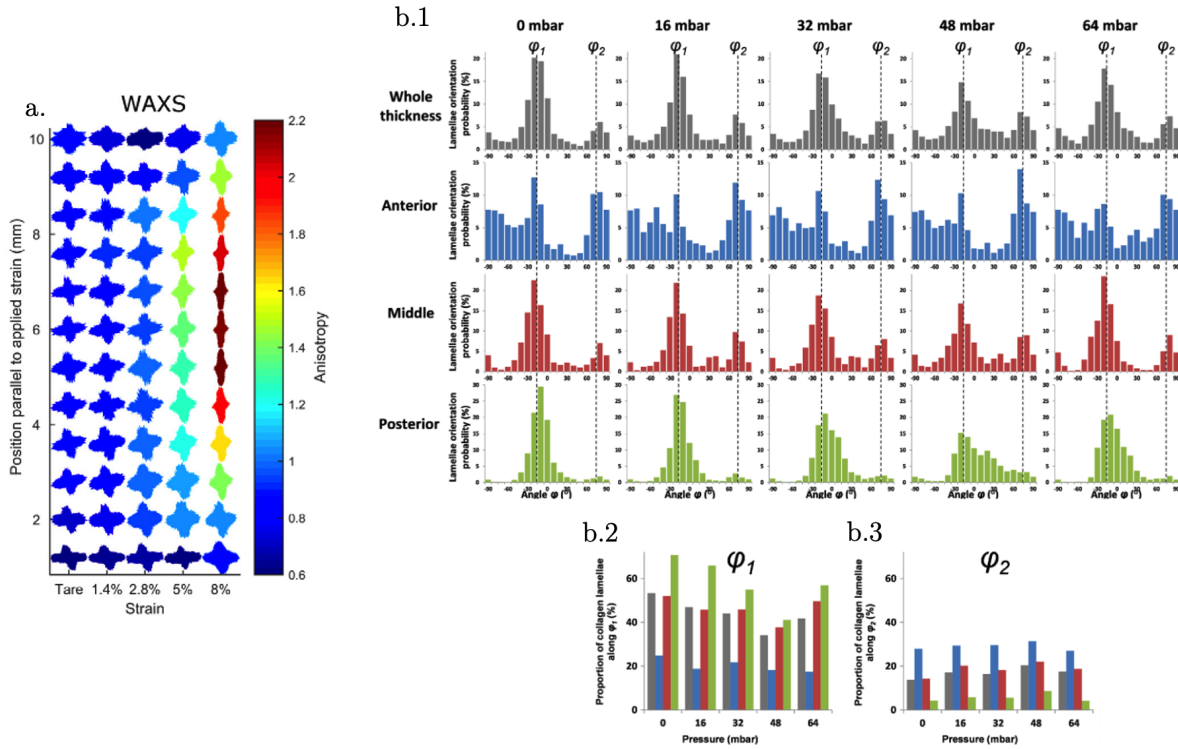


Figure 1.35: a. Polar plot of the lamellae orientation drawn from the X-ray analysis (extracted from [13]). b.1. Distribution of the orientation probability of the collagen lamellae on the whole thickness of the cornea and on the anterior, middle and posterior stroma. φ_1 and φ_2 represent the two main orientations. b.2. and b.3. Proportions of collagen lamellae oriented along φ_1 and φ_2 ($\pm 15^\circ$) (extracted from [14]).

Summary These experiments have shown that collagen lamellae reorganize themselves when the cornea is submitted to mechanical load, in the stretch direction for the tensile test, and with a flip in orientation during inflation test, but in all cases, although the fraction of lamellae changes between the two main orientations, these main directions do not change. However, there is no clear and simple relationship between the reorientation of the lamellae and the macroscopic strain measured by DIC. For this reason, microscopic observations are interesting and suitable when it comes to understanding a part of the response of the cornea, but they do not fully explain the behavior of the tissue.

1.3.2 *In-vivo* mechanical characterization of cornea

Even though *ex-vivo* experiments can give insight into the mechanical properties, *in-vivo* properties are the one ophthalmologists look at to detect pathology in hospitals. In the past few years, two main methods have emerged to measure the response of the cornea to intraocular pressure: Brillouin optical microscopy and optical coherence elastography (OCE). Although it has been shown that these methods can be used *in-vivo*, their clinical development is not yet complete and the authors who

attempted to use it so far only have results on a very limited number of patients, if any.

1.3.2.a Brillouin optical microscopy

Principle of the method Brillouin optical microscopy is a non invasive technique used to characterize the tissue. It has been used for the first time on human by Scarcelli *et al.* [156]. The principle is presented in Fig.1.36 and briefly explained hereafter. A near-infrared laser light is focused on the sample and creates a local thermodynamic acoustic wave. The Doppler Brillouin frequency shift Ω is then analyzed by a confocal spectrometer and can be directly linked to the real part of longitudinal viscoelastic modulus M' [154] using the relationship $M' = \rho\lambda^2\Omega^2/4n^2$ with ρ the density of the material, λ the optical wavelength and n the refractive index. At low frequencies (around 1 Hz), the variation of the longitudinal modulus M' can be easily linked to the variation of the classical Young's modulus E' using this relationship: $\delta E'/E' = (1/a)\delta M'/M'$, with $(1/a)$ a conversion factor dependent on the material.

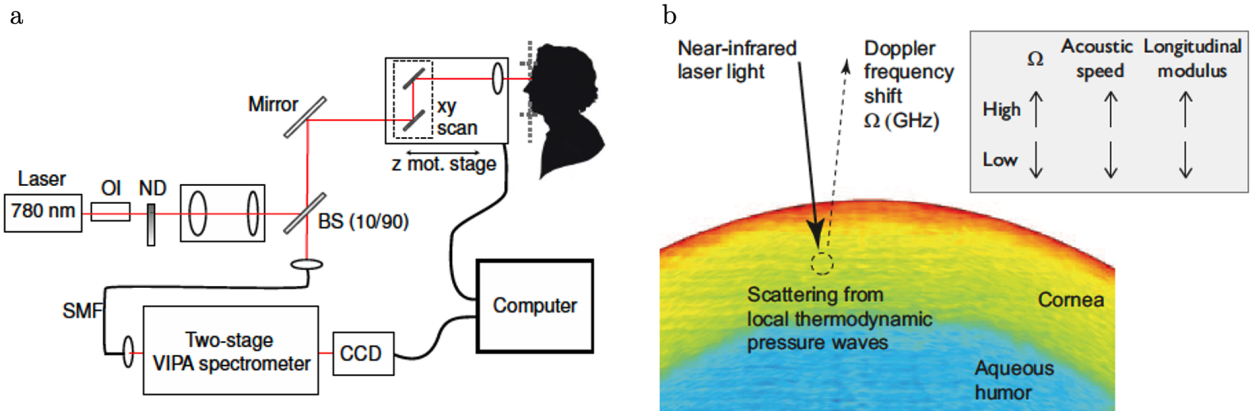


Figure 1.36: a. Brillouin microscopy setup (extracted from [156]) and b. Brillouin microscopy principle (extracted from [178]).

Main results on healthy and pathological cases So far, Brillouin microscopy has not been extensively used to measure the mechanical properties of corneas. A few examples exist however, first *ex-vivo* [155] on healthy and keratoconic corneas and then *in-vivo* [154; 158; 159]. Figure 1.37 presents the typical sagittal curvature (in Diopter), thickness and Brillouin shift maps for a 53-year-old person with normal corneas – Fig. 1.37.a – and a 40-year-old patient with advanced keratoconus – Fig. 1.37.b (extracted from [153]). *In-vivo* data reveal homogeneous Brillouin shift in healthy corneas while keratoconic corneas present an heterogeneous dispersion of the shift. Moreover a statistically significant decrease of Brillouin shift (and with it a decrease of stiffness) was observed in keratoconic corneas compared to healthy corneas [153].

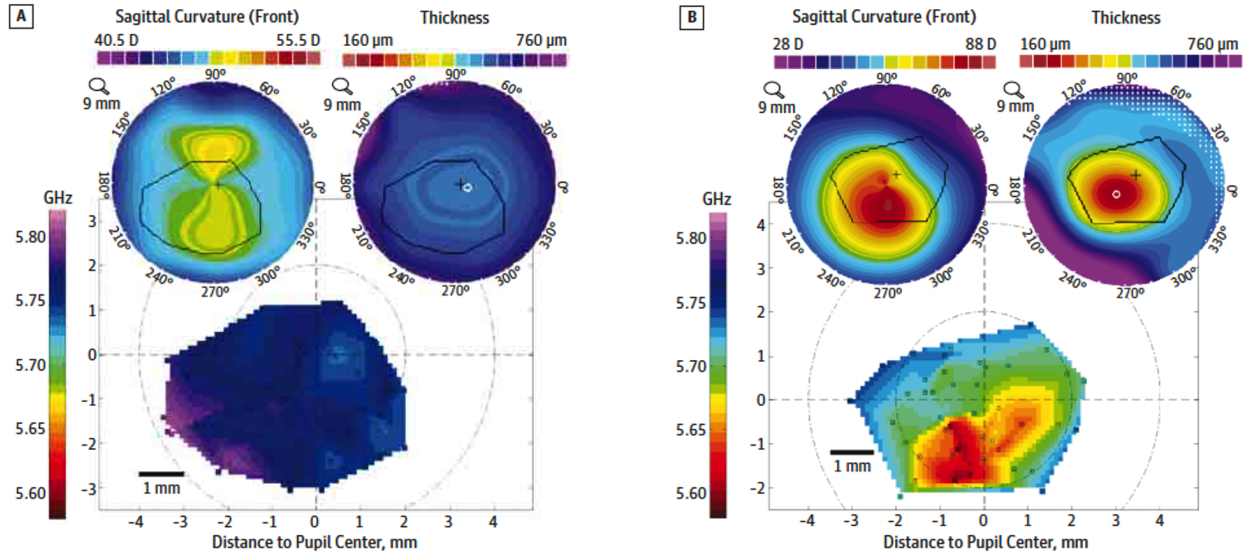


Figure 1.37: Typical sagittal curvature (in Diopter), thickness and Brillouin shift Ω maps for a. a 53-year-old patient with normal corneas and b. a 40-year-old patient with advanced keratoconus (extracted from [153]).

Summary Brillouin microscopy being a non-invasive method showing significant differences in mechanical elasticity of normal and pathological corneas is a promising tool to detect early stage keratoconus. However, it is a relatively new technique that only a few people have expertise on, and is therefore not used in hospitals yet.

1.3.2.b Optical coherence elastography (OCE)

Principle of the method Optical coherence elastography is a class of imaging techniques based on an elastography system, whose imaging device is an Optical Coherence Tomography (OCT) microscope (Sec. 1.2.1). Kennedy *et al.* and Larin and Sampson reviewed the different techniques of OCE [80; 89].

Here the focus is on the methods actually applied to the cornea. The mechanical exciter can be of two main kinds: a compression load (Fig. 1.38.a) or an acoustic wave perturbation (Fig. 1.38.b). The two mechanical perturbations are associated with different constitutive laws, which relate the Young's modulus to a characteristics of the response to the perturbation (the observed strain ε_l – Fig. 1.38.a or the phase velocity c_p – Fig. 1.38.b). In the first case, tissue displacement can be obtained using one of two methods: the OCT speckle-tracking method or the phase-resolved OCT approach [172]. Similarly, phase velocity can be derived from the phase of the complex OCT signals in the case of acoustic wave excitation (details on the computation can be found in [172]).

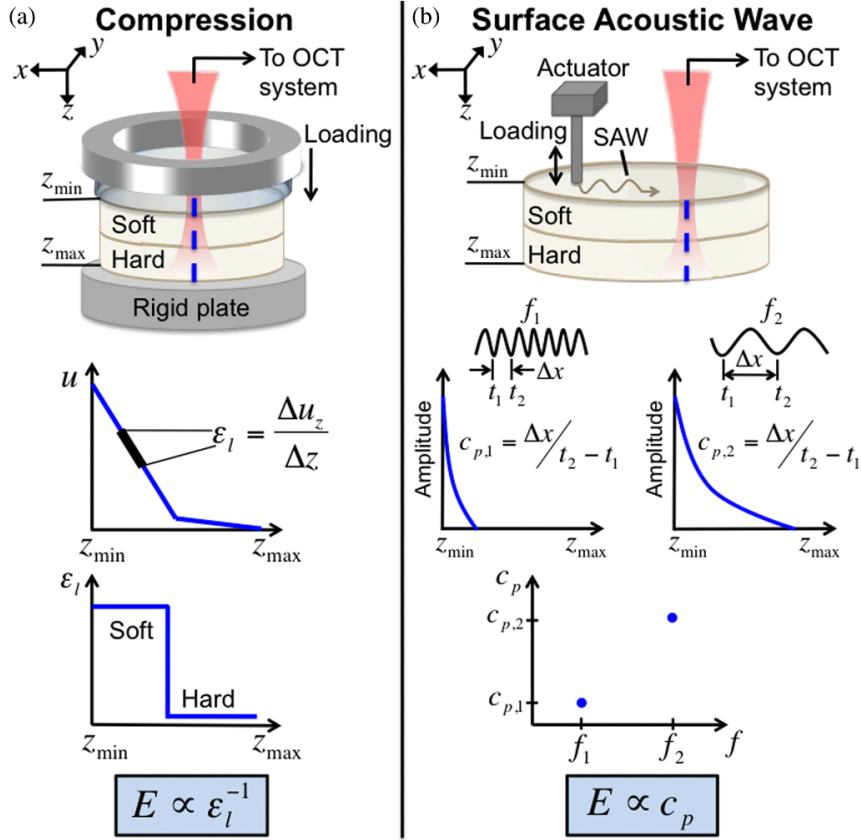


Figure 1.38: Loading schemes and elasticity estimation for the two OCE techniques presented: (a) Compression: a mechanical load is applied and the corresponding strain is measured ϵ_l . (b) Surface Acoustic Wave: an acoustic wave is generated in the tissue and its phase velocity c_p is measured (extracted from [80]).

Main results on healthy and pathological cases Ford *et al.* demonstrated [50] that OCE based on speckle tracking can be used on corneas to produce 2D maps of heterogeneous displacement, using IOP as a mechanical load (Fig. 1.39.a). They used a 2D cross-correlation algorithm to compute the displacement (Fig. 1.39.a). The observed vertical displacement is consistent with the axial displacement they imposed ($20 \mu\text{m}$), and the horizontal displacement shows heterogeneity among the central region and the periphery. In a following study, they used the same speckle tracking procedure to compute the displacement resulting from the application of a flat lens on the corneas, in a clinical study with healthy (21 eyes of 12 patients) and keratoconic (15 eyes of 12 patients) corneas [34]. A biomechanical indicator was created to compare anterior and posterior mechanical responses. They showed that the ratio of anterior to posterior surface stiffness was smaller in keratoconic corneas, creating a novel method, clinically applicable, for the detection of the pathology.

Nahas *et al.* [115] also used speckle-tracking to reveal the presence of two zones in the response of porcine corneas *ex-vivo* at 1% mean strain of deformation (induced by a piston system). Figure 1.39.b shows clearly a difference in the 2D vertical strain maps (computed by digital volume correlation) between the epithelium (1.6% of strain – red color) and the other regions of the cornea (less than 1% of strain). However, this technique has not yet been used *in-vivo*.

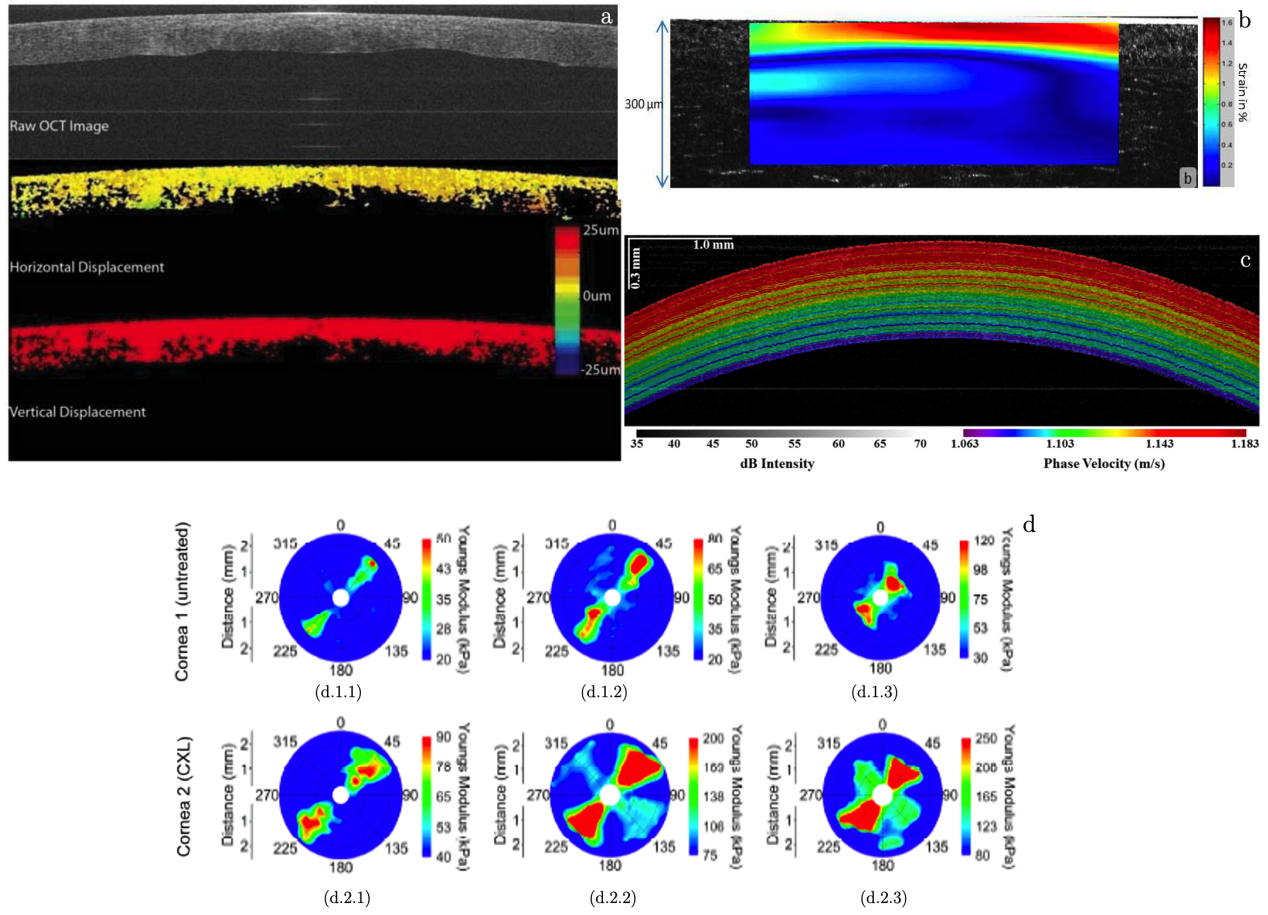


Figure 1.39: Computation of OCE results. a. Horizontal and vertical displacement maps (middle and bottom) computed by a 2D cross-correlation algorithm corresponding to the cornea imaged by OCT (top) and submitted to axial displacement generated by IOP (extracted from [50]). b. Lamb phase velocity computed during air-puff experiment on rabbit eye (extracted from [171]). c. FF-OCT cross-sectional image of porcine cornea superimposed with the corresponding computing strain maps (in %) under a 1% strain application (extracted from [115]). d. Young's modulus for untreated (d.1) and cross-linking-treated (d.2) porcine corneas at 15 (d.1.1 and d.2.1), 20 (d.1.2 and d.2.2) and 25 mmHg (d.1.3 and d.2.3) (extracted from [161]).

Wang and Larin [171] used the clinical air-puff test to create dynamical loading on the cornea, and used spectral analysis of Lamb wave propagation combined with phase signal to compute the displacement of the rabbit eye, first *ex-vivo*. They have highlighted the presence of four regions of different elasticity (refining Nahas' study [115]): the epithelium, the anterior stroma, the posterior stroma and the innermost region. Figure 1.39.c shows the Lamb velocity computed during the experiment. The four regions appear (in accordance with the phase velocity profile [171]): the epithelium corresponds to the dark red, the anterior stroma goes from red to green, the posterior stroma from green to blue, and the innermost region is in purple. Lan *et al.* [88] then conducted a clinical trial on 18 healthy eyes of 9 patients to assess the mechanical properties of human cornea *in-vivo*. A microliter air-pulse stimulator was used to generate corneal displacements, during which the wave velocity was recorded. Corneal elastic speed was found to increase with IOP and to be positively correlated with central corneal thickness. Ramier *et al.* [143] used a similar technique to measure the shear modulus on 12 human corneas *in-vivo* using Rayleigh wave theory instead of Lamb wave theory. The shear modulus was found to be of 72 ± 14 kPa and decreasing with age.

Singh *et al.* [161] managed to obtain Young's modulus maps using an air-pulse delivery system while monitoring the intraocular pressure and imaging porcine corneas *ex-vivo* with an SS-OCT. Figure 1.39.d presents Young's modulus maps at 15, 20 and 25 mmHg for healthy and CXL-treated corneas. They showed that the technique they adopted was able to quantify changes in Young's modulus between healthy and treated corneas and that cross-linked corneas were stiffer than untreated ones. This technique remains to be applied *in-vivo*.

OCE can also be coupled to acoustic/ultrasound methods to determine corneal elasticity. For example Qu *et al.* [140] have coupled Acoustic Radiation Force (ARF – see Sec. 1.3.1.d) to an OCE system to compare healthy and cross-linked rabbit corneas *ex-vivo*. They showed that the elastic wave shift dropped for cross-linked corneas, corresponding to a change of stiffness in the tissue. A few years later, they used Lamb wave model to compute the wave velocity resulting from the ultrasound excitation on rabbit eyes *in-vivo* [77]. They demonstrated in those two papers the interest of the methodology to assess corneal elasticity *in-vivo*.

Summary Similarly to Brillouin microscopy, OCE can be used to detect a pathology. The main limitation to determine actual values of mechanical properties in the case of cornea is that the mechanical excitation may lead to large deformations. Thus, they cannot be captured by simple linear models that are usually used in OCE. Also, most times the tissue is assumed to be homogeneous, which is not the case for cornea, especially for pathological ones. As a result, the models used to describe the mechanical response of the cornea may have to be adapted to tackle these issues.

1.3.2.c Conclusion of *in-vivo* mechanical characterization of the cornea

To conclude, even if all the authors have not yet applied their methods *in-vivo* on human, it is only a question on *when* and not *how*. Brillouin microscopy and OCE are very promising techniques to determine mechanical properties of the cornea *in-vivo*, if not quantitatively, at least qualitatively. To this end, they can be used to detect pathology by comparing the measured data with healthy corneas. But as promising as they are, they cannot be used to measure the parameters that are used in mechanical modeling.

1.3.3 Summary of the mechanical characterization of the cornea

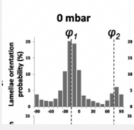

Scale	Imaging Technique	Data measured	Typical measure	Nature of the cornea	Local / Global measure	Stress applied	Stiffness coefficient	Use in this work
Tissue scale	Laser	Apex displacement (VS pressure)	~1/10 mm	Human	Local – on surface	Global	$\sigma = A(e^{B\varepsilon} - 1)$, $E = Cp + D$	Used for calibration / validation.
	Stereo-correlation	Surface displacement (VS pressure)	~1/10 mm	Bovine	Local – on surface	Global	NA	Non used (bovine).
	Strain / stress gauge + camera	Strip displacement / strain (VS force applied)	~1/10 mm / ~%	Porcine / bovine	Global & Local – on surface	Global	$E = \sigma / \varepsilon$	Non used (difference between results for strip extensometry and inflation test are significant + non human).
	Brillouin microscopy	Brillouin shift	~GHz	Human	Local – through thickness	Global	$M = \rho \lambda^2 \frac{\Omega^2}{4n^2}$, $\frac{\delta E}{E} = \left(\frac{1}{a}\right) \frac{\delta M}{M}$	Data non usable as they are and no information in the thickness.
Meso-scale	OCT / OCE	3D displacement / strain	~10 microns / ~%	Porcine / rabbit	Local – through thickness	Global	Based on wave theory or elasticity	Data non available on human, only a proof of concept on porcine and rabbit, and elastic model is limiting.
	Scheimpflug 3D topographer	Corneal deformation - curvature radius	~1/10 mm	Porcine	Local – on surface	Global	$\sigma = \frac{Rp}{2d}$, $\varepsilon = \Delta R / R$	Data non available on human.
	AFM as nanoindenter	Anterior / posterior elasticity	10's kPa	Human	Local – on multiple surfaces	Local	$F = \frac{4E\sqrt{R}}{3(1-\nu^2)} D^{3/2}$	Use to calibrate the isotropic response of the cornea through thickness (18 corneas).
	Bio-indenter	Young's modulus	10's kPa	Human	Local – on surface	Local	$F = \frac{4E\sqrt{R}}{3(1-\nu^2)} D^{3/2}$	No data in the thickness.
	ARFEM	Anterior / posterior Young's modulus	~ kPa	Human	Local – on multiple location through thickness	Local	$E = \frac{Ia}{2cx_{max}}$	Could have been used for calibration but only 6 corneas.
Micro-scale	SHG	Distribution of the lamellae orientation		Human	Local – through thickness	Global	NA	Data available only on a few location.
	X-rays (WAXS)	Mean orientation of the lamellae		Human	Local – averaged on thickness	Global	NA	Non usable as its on a strip extensometry test and also available on only a few location.

Table 1.1: Summary of the different techniques and data measured for the mechanical characterization of the cornea. The pink boxes represent the data used in this manuscript.

1.4 Mechanical modeling of the human cornea

Section 1.3 presented different ways of measuring mechanical properties of cornea. It showed that it is not an easy task to measure them *in-vivo*, especially from a quantitative perspective. On the other hand, Sec. 1.2.2 showed that displacement maps can be obtained from *in-vivo* images. In order to link the displacement field of the tissue under loading to the mechanical response of the cornea, various mechanical models have emerged in the past decades, which can provide insight into the health of the cornea.

1.4.1 Mechanical response of cornea

The stroma is considered to be the main contributor to the mechanical response of cornea. In parallel, there is also a lack of data on the other layers of cornea. As a result, "stroma" and "cornea" will be used indifferently in the framework of mechanical modeling.

1.4.1.a Constitutive behavior of cornea

Cornea is usually considered as a quasi-incompressible material reinforced by fibers – the two families of lamellae can be considered each as a family of fibers – which may sustain very large deformations. As such, it is generally modeled as a hyperelastic material [3; 56; 129; 160; 164] – with the possible addition of viscous terms to introduce history dependence and dissipation [84; 122; 173], when considering the static or dynamic cases, respectively. Dynamic cases are usually used to model air-puff clinical tests. Here the emphasis will be placed on the static response since we will be interested in static inflation tests. In this case, the associated strain energy density ψ is then splitted into three contributions:

$$\psi = \psi^{iso} + \psi^{vol} + \psi^{lam}, \quad (1.8)$$

with an isotropic part ψ^{iso} corresponding to the matrix, the keratocytes and the randomly distributed lamellae, a volumetric part ψ^{vol} penalizing any change of volume and an anisotropic part ψ^{lam} , taking into account the mechanical role of oriented lamellae.

The isotropic part depends generally on the first three invariants I_1 , I_2 and I_3 and reduced invariants ($\bar{I}_1 = I_1 I_3^{-1/3}$, $\bar{I}_2 = I_2 I_3^{-2/3}$) and is usually chosen as a Mooney-Rivlin or neo-Hookean like energy density [3; 129; 160; 164]:

$$\psi^{iso}(\underline{\xi}, \underline{C}) = \frac{1}{2} C_1 (\bar{I}_1 - 3) + \frac{1}{2} C_2 (\bar{I}_2 - 3) \quad (1.9)$$

with C_1 and C_2 two parameters of the model characterizing the isotropic part of the tissue.

The volumic part penalizes any change of volume and can take several forms (which can be based

on the work of P. Ciarlet and G. Geymonat [32]), which depend only on J :

$$\psi^{vol}(\underline{\xi}, \underline{\underline{C}}) = \begin{cases} K \log^2(J) \text{ [3; 129]} \\ \frac{1}{D}(J-1)^2 \text{ [164]} \\ \frac{1}{4}K(J^2 - 1 - 2\log(J)) \text{ [160]} \end{cases} \quad (1.10)$$

with K the bulk modulus (or the corresponding $\frac{1}{D}$). Here, minimizing the energy corresponds to having J close to 1, so that the volume of the material does not change. This is the case for most of the models that consider a high bulk modulus compared to the other moduli of the energy density leading to quasi-incompressibility of the material, with the exception of the model of Studer *et al.* [164] which has a bulk modulus of the same order of magnitude as the isotropic material constant.

For the anisotropic part, there are two classical ways of taking into account the contribution of fibers in biological tissues [71]:

- the ‘generalized structure tensor’ (GST) approach, which is widely used in Holzapfel-like models for many different tissues reinforced by fibers such as arteries or other blood vessels [4; 17; 54; 69], myocardium [70] or skin [78] and cornea [113; 129; 174];
- the ‘angular integration’ (AI) approach, used for arteries [16; 149], cartilage [8; 136] or cornea [121; 164], with 2D data and with 3D data [134].

The anisotropic energy density used in GST models is usually based on the fourth and sixth invariants (I_4 and I_6 respectively, considering each family of fiber). Calling \underline{M}_{01} and \underline{M}_{02} the mean fiber directions on the reference configuration, the reduced invariants are defined as follow: $\bar{I}_4 = \underline{M}_{01} \cdot \underline{\underline{C}} \cdot \underline{M}_{01}$ and $\bar{I}_6 = \underline{M}_{02} \cdot \underline{\underline{C}} \cdot \underline{M}_{02}$ – with $\underline{\underline{C}} = J^{2/3} \bar{\underline{\underline{C}}}$. The associated energy density takes the following form (or a variation there of) [3; 129]:

$$\psi^{lam}(\underline{\xi}, \underline{\underline{C}}) = \frac{k_{11}}{2k_{21}} \{ \exp[k_{21}(\bar{I}_4 - 1)^2] - 1 \} + \frac{k_{12}}{2k_{22}} \{ \exp[k_{22}(\bar{I}_6 - 1)^2] - 1 \} \quad (1.11)$$

An exponential function is generally used to mimic the mean response of the collagen lamellae, as they are considered to behave like collagen fibrils, with a low stiffness response at low strain and a rapid change of response leading to a high stiffness at high strain (Fig. 1.40).

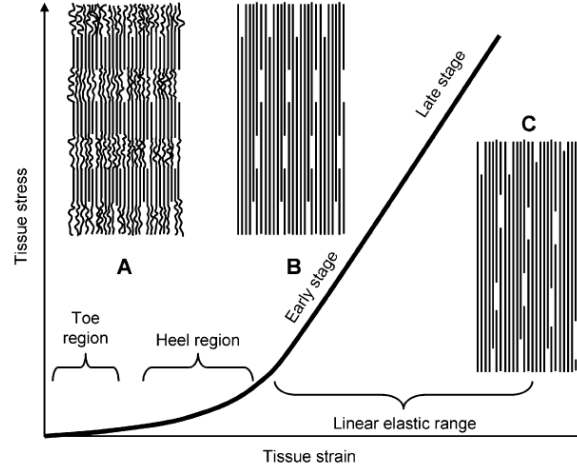


Figure 1.40: Collagen fibril response to tension (from [51]). At low strain, the fibrils are crimped and thus oppose practically no resistance to tension (toe region). In the transitional regime (heel region), fibrils tend to align one next to the other and to straighten. They begin to oppose resistance to tension. In the linear elastic range region, fibrils are not crimped anymore – their stiffness can be measured using a tension test along the direction of the fibrils.

In particular, it allows to have a quasi null response of the collagen lamellae when they are crimped (toe region in Fig. 1.40). It is also consistent with the pressure with apex displacement results from inflation tests [45]. Considering the whole cornea, a parameter (κ in [129]) can be added to take into account the variation of the scatter of the fibers in the tissue. In this approach, at each point of computation, the mean and the scatter of the fiber direction are assessed, and a global mechanical contribution is computed based on these two parameters, for each family of fibers.

In the AI case, the approach is reversed. An elementary response for collagen lamellae $\delta\psi^{lam}$ is considered, and the total mechanical response on a particular location $\psi^{lam}(\underline{\xi}, \underline{C})$ is the integral over the unit sphere ω (for the most complete 3D model [134]) of the elementary contribution weighted by the density distribution $\rho(\underline{\xi}, \theta, \phi)$ of the fiber at this location,

$$\psi^{lam}(\underline{\xi}, \underline{C}) = \int_{\omega} \rho(\underline{\xi}, \theta, \phi) \delta\psi^{lam}(\underline{\xi}, \theta, \phi) d\omega. \quad (1.12)$$

In that case also, all the model found in the literature on cornea for the elementary mechanical response of lamellae $\delta\psi^{lam}$ are based on exponential (or logarithmic) functions:

$$\delta\psi^{lam}(\underline{\xi}, \theta, \phi) = \begin{cases} \frac{\alpha}{\beta} [\exp(\beta\{\lambda_f^2 - 1\}) - \beta\lambda_f^2] & [121] \\ \frac{\alpha_1}{2\alpha_2} [\exp(\alpha_2\{I_4 - 1\}^2) - 1] & [134] \\ \frac{\mu}{\gamma} (\bar{I}_4^{\gamma/2} - 1) - \mu \ln(\bar{I}_4^{1/2}) & [164] \end{cases} \quad (1.13)$$

with

$$\begin{cases} \lambda_f^2 = I_4 = \underline{a} \cdot \underline{C} \cdot \underline{a} \\ \bar{I}_4 = \underline{a} \cdot \bar{\underline{C}} \cdot \underline{a} \\ \underline{a}(\theta, \phi) \quad \text{the local integrating direction} \end{cases} \quad (1.14)$$

In the case of Studer *et al.* [164], they use a modified version of the polynomial Odgen law [97] to include one direction of anisotropy, giving a logarithmic formula, which cannot be linked directly to the collagen fibril response of Fig. 1.40.

Whether using GST or AI approaches, these models do not take into account the energy due to water exchange, except for [30], so that the action of the endothelium is not considered. Also, validations of these models are based on very few experiments – as the quantity of data on cornea is limited – measuring apex displacement ([45; 93] for the human cornea) or 3D displacement of the anterior surface ([23] for bovine cornea), and performed exclusively on healthy subjects.

1.4.1.b Density distribution of fibers

The 3D density distribution of fibers is not available for the whole cornea. However, X-ray diffraction (Fig. 1.7 – [1; 18]) allows a 2D mean representation of the oriented lamellae to be obtained. Two ways of incorporating these data are found in the literature. The first option is to look at the data at each measurement point – an example is given Fig. 1.41. It is well known that the intensity at each point of measurement I_{exp} of X-ray scattering can be represented by a function I_m ,

$$I_m(\phi | \kappa_{ip,1}, \kappa_{ip,2}, \mu_1, \mu_2) = I_{iso} + C_1 \text{VM}_{ip}(\phi | \kappa_{ip,1}, \mu_1) + C_2 \text{VM}_{ip}(\phi | \kappa_{ip,2}, \mu_2), \quad (1.15)$$

depending on I_{iso} , a constant component representing the isotropic part of the measure and C_1 and C_2 , the measures of the number of oriented lamellae in each direction at the point of measure. The distributions of lamellae is described by Von Mises distributions:

$$\text{VM}_{ip}(\phi | \kappa_{ip}, \mu) = \frac{e^{\kappa_{ip} \cos(2(\phi - \mu))}}{C(\kappa_{ip})}, \quad (1.16)$$

where μ is the main direction of the fiber family, κ_{ip} represents a measure of the scatter of the lamellae, and $C(\kappa_{ip})$ is a normalization factor.

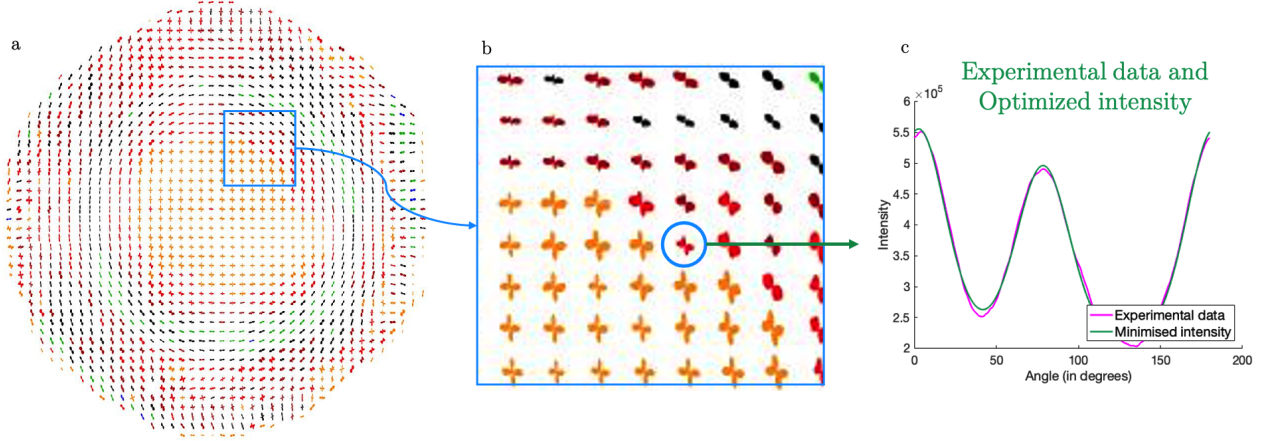


Figure 1.41: Extraction of the 2D density distribution. a. Polar plot of the direction of the lamella [1], b. zoom on a particular measurement point and c. experimental and corresponding optimized intensity.

Minimizing the error $|I_m - I_{exp}|$ at each point of measurement allows the parameters linked to the lamellae to be found: C_i the relative number of oriented lamellae, μ_i their main direction and $\sigma_{ip,i}$ their scatter. Afterwards, the data are interpolated on the whole cornea (i.e. at the nodes, for finite element modeling).

The second technique is based on a model by Pinsky *et al.* [137] (inspired by X-ray images), which gives the probability density function $\Phi(R, \phi|\theta)$, with (R, ϕ) being the polar coordinate of the location (the center of the cornea being the center of the coordinate system and the N-T and S-I directions being the x- and y-axes):

$$\Phi(R, \phi|\theta) = \begin{cases} \Phi_1(R, \phi|\theta) = \cos^{2n}(\theta) + \sin^{2n}(\theta) + c_1 & \text{for } R \in [0, 4] \\ \Phi_2(R, \phi|\theta) = \sin^{2n}(\theta - \phi) + c_2 & \text{for } R \in [5.5, 6.5] \end{cases} \quad (1.17)$$

with a linear combination of the 2 functions for $R \in [4, 5.5]$ to smoothly transition from one to the other. Figure 1.42 presents the results for the case used by Studer *et al.* [164] with $c_1 = 0.45$, $c_2 = 0.72$ and $n = 4$ and the linear combination $\Phi(R, \phi|\theta) = w_1(R)\Phi_1(R, \phi|\theta) + (1 - w_1(R))\Phi_2(R, \phi|\theta)$ in between with $w_1 = \frac{1}{2}\{\cos(\frac{\pi}{1.5}[5.5 - R]) + 1\}$.

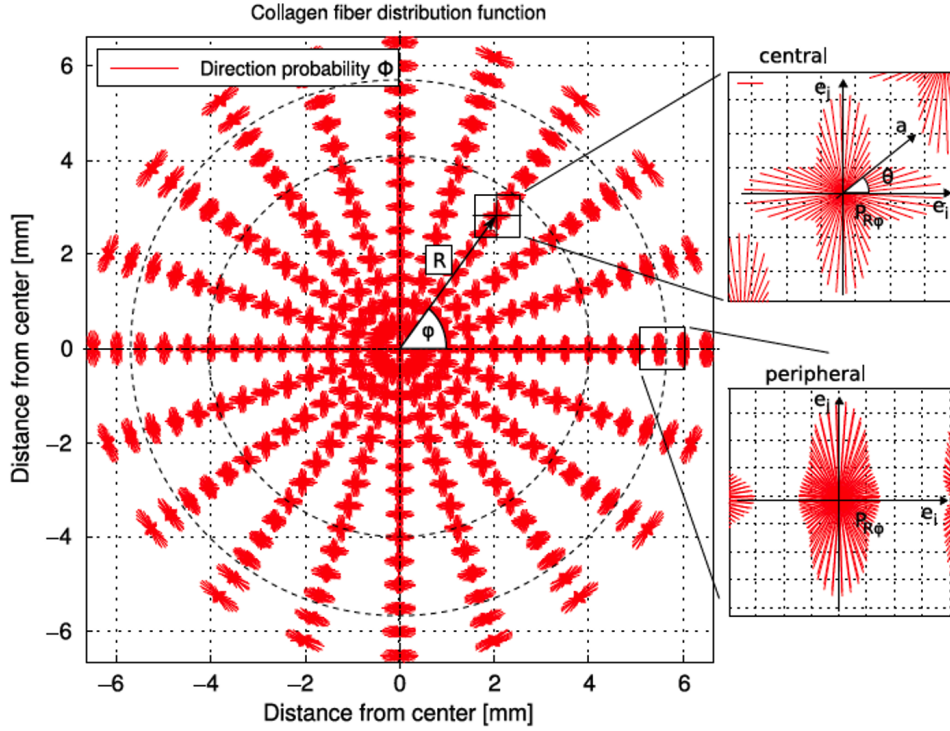


Figure 1.42: Probability distribution map, computed using Eq. (1.17), with $c_1 = 0.45$ and $c_2 = 0.72$. Transitional zone corresponds to radius between 4 and 5.5mm (dashed circles) [164].

Both approaches give information on the so called in-plane orientation of the lamellae, but it gives no information on the out-of-plane distribution. The development of SHG microscopy imaging of cornea made it possible to have a model for the third dimension. Winkler *et al.* [176] imaged the cornea and Petsche and Pinsky [134] built a model of the distribution on the third dimension. SHG images (Fig. 1.43 – middle) are studied to model the out-of-plane scatter of the lamellae. The authors show that there is an exponential dependency of the cut-off-angle ψ_{coa} with depth s , $\psi_{coa}(s) = 28.6^\circ \frac{e^{3.19(1-s)} - 1}{e^{3.19} - 1}$, with a maximum cut-off-angle of 28.6° . No lateral heterogeneity has been measured, so our model does not take into account spatial heterogeneity in the two other directions for the cut-off-angle. Then the out-of-plane distribution of the fibers can be modeled either as a Von Mises distribution

$$VM_t(\theta|\kappa_t, \nu) = \frac{e^{\kappa_t \cos(2\theta)}}{C(\kappa_t)}, \text{ (with } C(\kappa_t) \text{ a normalization factor)}$$

taking into account the depth variation of the maximum out-of-plane angle $\psi(s)$ to characterize the change of the out-of-plane scatter κ_t in thickness, or as a coupled Heaviside function (as in [134])

$$\rho^{SHG}(s, \phi) = H[\phi - \{\frac{\pi}{2} - \psi_{coa}(s)\}] - H[\phi - \{\frac{\pi}{2} + \psi_{coa}(s)\}],$$

with ϕ the local inclination angle.

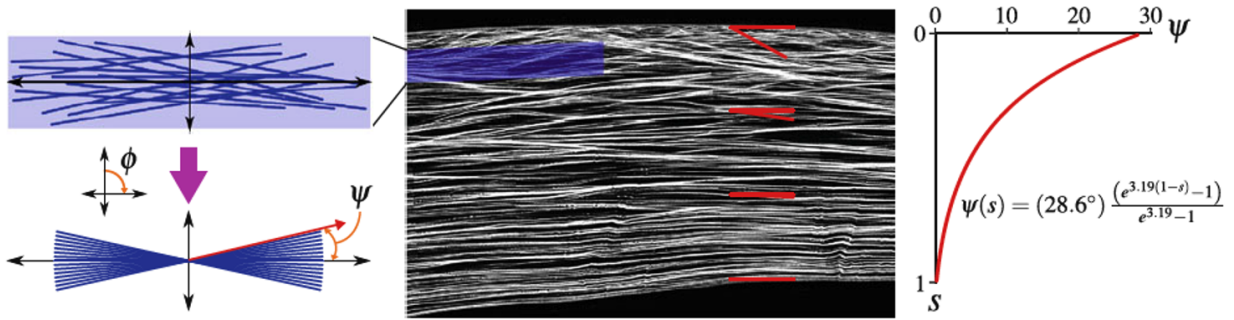


Figure 1.43: Extraction of the 3D density distribution (from [134]). The SHG images allow a model to be built for the out-of-plane angle ψ of the lamellae with depth.

1.4.1.c Summary of the hyperelastic models used for the cornea

	Notation	Reference	Expression	Value of the coefficients	Comments
Isotropic matrix	ψ^{iso}	[Alastrué et al., 2006]	$\frac{C_1}{2}(\bar{I}_1 - 3) + \frac{C_2}{2}(\bar{I}_2 - 3)$	$C_1 = 5 \text{ kPa}$ $C_2 = 0 \text{ kPa}$	The neo-Hookean is mostly used to represent the isotropic matrix, but the Mooney-Rivlin energy allows to take into account second order response, that may exists in the cornea (no experimental data available)
		[Pandolfi et al., 2008]	$\frac{c}{2}(\bar{I}_1 - 3)$	$c = 60 \text{ kPa}$	
		[Simonini et al., 2008]	$\frac{\mu_1}{2}(\bar{I}_1 - 3) + \frac{\mu_2}{2}(\bar{I}_2 - 3)$	$\mu_1 = 60 \text{ kPa}$ $\mu_2 = -10 \text{ kPa}$	
		[Studer et al., 2010]	$\frac{C_{10}}{2}(\bar{I}_1 - 3)$	$C_{10} = 60 \text{ kPa}$	
		[Nguyen et al., 2011]	$\frac{\mu}{2}(\bar{I}_1 - 3)$	$\mu \sim 26.5 \text{ kPa}$	
		[Petsche et al., 2013]	$\frac{\mu}{2}(I_1 - 3)$	$\mu = 5.59 \text{ kPa}$	
Quasi-incompressibility	ψ^{vol}	[Alastrué et al., 2006]	$\frac{1}{D}(\ln(J))^2$	$D = 13.33 \text{ MPa}^{-1}$	As cornea is considered as a quasi-incompressible tissue, the volumetric part of the energy function is here to ensure that the volume is preserved ($J \sim 1$), by penalizing using a relatively huge bulk modulus (at least one order of magnitude higher than the coefficient of the isotropic part)
		[Pandolfi et al., 2008]	$K(\log(J))^2$	$K = 5.5 \text{ MPa}$	
		[Simonini et al., 2008]	$\frac{1}{4}K(J^2 - 1 - 2\log(J))$	$K = 5.5 \text{ MPa}$	
		[Studer et al., 2010]	$\frac{1}{D}(J - 1)^2$	NK	
		[Nguyen et al., 2011]	$\frac{1}{4}K(I_3 - \ln(I_3) - 1)$	NK	
		[Petsche et al., 2013]	$\frac{\lambda}{4}(J^2 - 1) - \left(\frac{\lambda}{2} + \mu\right)\ln(J)$	$\lambda = 500 \text{ kPa}$	
Anisotropic lamellae	ψ^{lam} (GST) or $\delta\psi^{lam}$ (AI)	[Alastrué et al., 2006]	$\frac{k_1}{2k_2}\{\exp[k_2(\bar{I}_4 - 1)^2] - 1\}$ $+\frac{k_3}{2k_4}\{\exp[k_4(\bar{I}_6 - 1)^2] - 1\}$ GST approach	$k_1 = 102.643 \text{ MPa}$ $k_2 = 102.643$ $k_3 = 0.004852 \text{ MPa}$ $k_4 = 102.643$	Two ways of integrating the anisotropic contribution are considered for the lamellar energy: the generalized structure tensor (GST) and the angular integration approach (IA). While the GST approach has a great advantage in term of computational cost, the AI approach allows to take into account the inhomogeneous contribution of the fibers in all the directions of integration at each point of the cornea considered. In the case of the cornea, 2D distribution of lamellae are obtained using X-rays data, while out-of-plane dispersion comes from SHG images. In all cases, exponential functions are often used to mimic the response of a collagen fibril, while considering that the collagen lamellae have the same behavior.
		[Pandolfi et al., 2008]	$\frac{k_{11}}{2k_{21}}\{\exp[k_{21}(\bar{I}_4^* - 1)^2] - 1\}$ $+\frac{k_{12}}{2k_{22}}\{\exp[k_{22}(\bar{I}_6^* - 1)^2] - 1\}$, $\bar{I}_i^* = \kappa_i \bar{I}_i + (1 - 3\kappa_i)\bar{I}_i$ GST approach	$k_{11} = 20 \text{ kPa}$ $k_{21} = 400$ $k_{12} = 20 \text{ kPa}$ $k_{22} = 400$	
		[Simonini et al., 2008]	$\frac{k_{11}}{2k_{21}}\{\exp[k_{21}(\bar{I}_{4,1}^* - 1)^2]\}\{1 + K_1^* \sigma_{\bar{I}_{4,1}^*}^2\}$ $+\frac{k_{12}}{2k_{22}}\{\exp[k_{22}(\bar{I}_{4,2}^* - 1)^2]\}\{1 + K_2^* \sigma_{\bar{I}_{4,2}^*}^2\}$ GST approach	$k_{11} = 40 \text{ kPa}$ $k_{21} = 200$ $k_{12} = 40 \text{ kPa}$ $k_{22} = 200$	
		[Studer et al., 2010]	$\frac{\mu_m}{\gamma_m}\left\{\frac{\gamma_m}{\bar{I}_4^m} - 1\right\} - \mu_m \ln(\bar{I}_4)^{\frac{1}{2}}$ $+\frac{\mu_k}{\gamma_k}\left\{\frac{\gamma_k}{\bar{I}_6^k} - 1\right\} - \mu_k \ln(\bar{I}_6)^{\frac{1}{2}}$ 2D AI approach	$\mu_m = 24 \text{ MPa}$ $\gamma_m = 0.13$ $\mu_k = 95 \text{ MPa}$ $\gamma_k = 0.08$	
		[Nguyen et al., 2011]	$\frac{\alpha}{\beta}\{\exp[\beta(\lambda_f^2 - 1)] - \beta\lambda^2\}$ $\lambda_f^2 = \underline{a} \cdot \underline{C} \cdot \underline{a}$, $\underline{a} = (\cos(\theta), \sin(\theta), 0)$ 2D AI approach	$\alpha \sim 0.12 \text{ kPa}$ $\beta \sim 91$	
		[Petsche et al., 2013]	$\frac{\alpha_1}{2\alpha_2}\{\exp[\alpha_2(I_4 - 1)^2] - 1\}$ 3D AI approach	$\alpha_1 = 638 \text{ kPa}$ $\alpha_2 = 312$	

Table 1.2: Summary of the energy functions and parameters values used in the last paper on modeling of the cornea as an hyperelastic material only. The pink boxes represent the approaches used in this manuscript.

1.4.1.d Validation of models on inflation test

The models are usually validated on inflation tests, against the data of Elsheikh *et al.* [45] (Sec. 1.24), since they are the only available data on human corneas. Finite element models (FEM) are used to compute the mechanical response of cornea to intraocular pressure. Even though the mechanical behavior of cornea and the boundary conditions can change from one author to another, the principle remains the same. The tissue is fixed to the sclera (giving the \mathcal{P}_{BC} term of Eq. A.16 and A.17) and the intraocular pressure is applied to the posterior surface of the cornea (giving the \mathcal{P}_e term of Eq. A.16 and A.17). No other forces are applied. \mathcal{P}_i depends on the chosen model for the mechanical behavior (Sec. 1.4.1.a). The geometry of cornea is described by the biconic function and usually adapted to real patient ones. A spatial discretization is performed to create the mesh used in the FE code. Figure 1.44 presents a typical scheme (Fig. 1.44.a) and mesh (Fig. 1.44.b) used to implement the corneal model in a FE code [56].

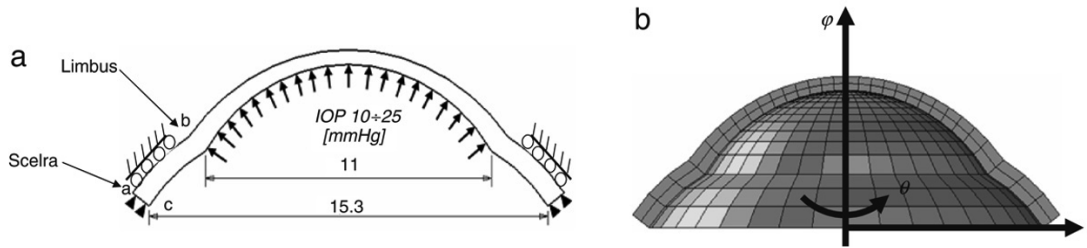


Figure 1.44: FE modeling of the inflation test (extracted from [56]). a. Model description of the forces applied to the cornea (IOP) and of the boundary conditions. b. Typical mesh used to describe the geometry of the tissue.

Figure 1.45 presents the results for three different cases of modeling: one model with AI approach and only in-plane distribution of the lamellae (a.1 and a.2 – [164]), one model with GST approach and only in-plane distribution of the lamellae (b – [129]) and one model with AI approach and 3D distribution of the lamellae (c – [134]). Figure 1.45.a.1, a.2 and c are compared to data from Elsheik’s group study [45] on human cornea. Fig.1.45.b is compared to data from [46] on porcine corneas. It shows that all the models can be calibrated to fit the data of pressure with apex displacement and for both age groups in the first case. The parameters found in the validation process provide insight into the mechanical behavior of healthy cornea *ex-vivo* but they may not be unique and should be adapted for pathological cases.

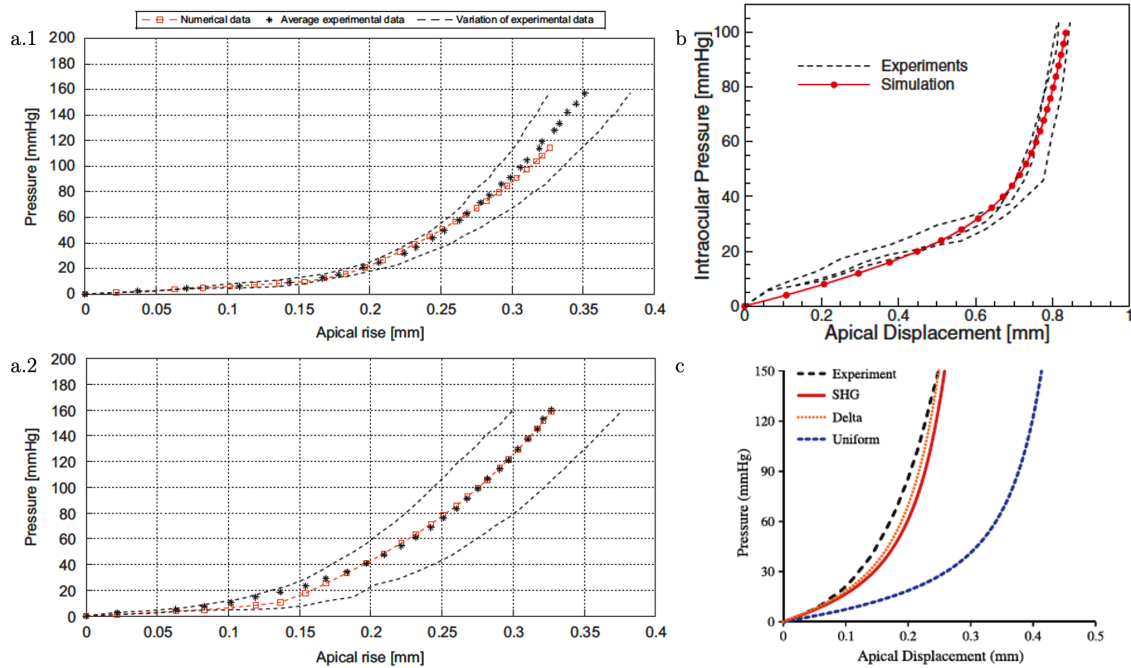


Figure 1.45: Results of inflation test simulations compared with Elsheikh *et al.* [45; 46] data. a.1 and a.2. Results extracted from [164] for two age groups (a.1. 65–79 years old corneas and a.2. 80–95 years old corneas) – model with AI approach and only in-plane distribution of the lamellae compared to [45]. b. Results extracted from [129] – model with GST approach and only in-plane distribution of the lamellae compared to [46]. c. Results extracted from [134] – model with AI approach and 3D distribution of the lamellae (with different cases for the out-of-plane distribution) compared to [45].

In this work (see Chap. 2), an AI approach is used with an in-plane density distribution based on the minimized intensity function I_m and an out-of-plane Von Mises distribution with a varying cut-off-angle. A classical three-part strain energy density will be used with a Mooney-Rivlin energy density for the isotropic part, a J^2 penalizing term and a quadratic elementary contribution of the lamellae. The model will be validated on an inflation test and mechanical properties will be adapted to model pathological corneas.

1.4.2 The case of the keratoconus

The case of keratoconus has been studied numerically through inflation tests by several authors [25; 56; 128; Norouzpour and Mehdizadeh] considering different hypotheses based on the same assumptions: in keratoconic corneas a change of geometry is observed and the stiffness is decreased in the cone region with respect to the rest of the cornea (Sec. 1.3.2). Gefen *et al.* [56] and Carvalho *et al.* [25] studied both the thinning of the region of the cone and the reduction of some mechanical properties of cornea (meridian elastic modulus and shear modulus perpendicular to corneal surface). While Gefen *et al.* [56] show that the main ingredient to keratoconus is the change in shape of cornea [56], Carvalho *et al.* [25] state that the change of local mechanical properties is needed to generate a keratoconus. Figure 1.46 shows the maximum tissue displacement (Fig. 1.46.a) and maximal diopter (Fig. 1.46.b) with increasing IOP for normal and keratoconic cases from Gefen *et al.*'s study [56]. The maximum displacement is more than three times greater in keratoconic corneas than in healthy tissues. For the diopter, while there is no change with pressure for healthy cornea, an increase of 8 diopters is

found for keratoconic cases between 10 and 25 mmHg (the computation of the diopter can be found in App. 1.2).

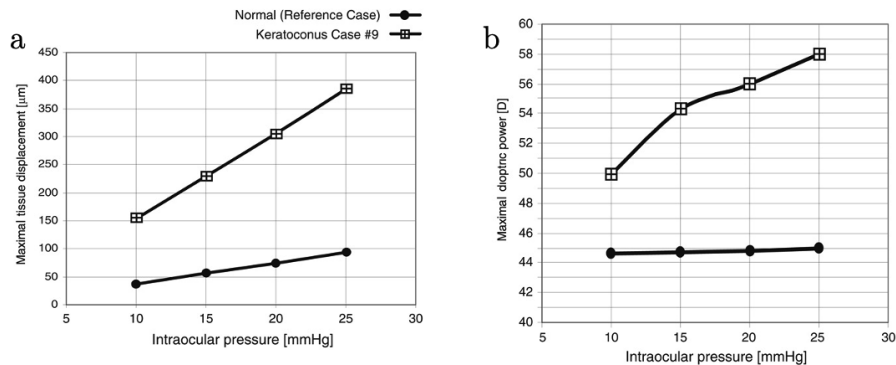


Figure 1.46: a. Maximum corneal tissue displacement with IOP for healthy and keratoconic cases. b. Maximum dioptric power with IOP for normal and keratoconic corneas (extracted from [56]).

Pandolfi *et al.* [128] adopted another approach. Starting from a healthy geometry, the authors created a network of fibrils and cross links (Fig. 1.47.a.2) to represent the lamellae of collagen and their links to each other (glycosaminoglycans or other proteoglycans), and finally decreased the mechanical strength of each part of the fibrils unit cell (Fig. 1.47.a.1).

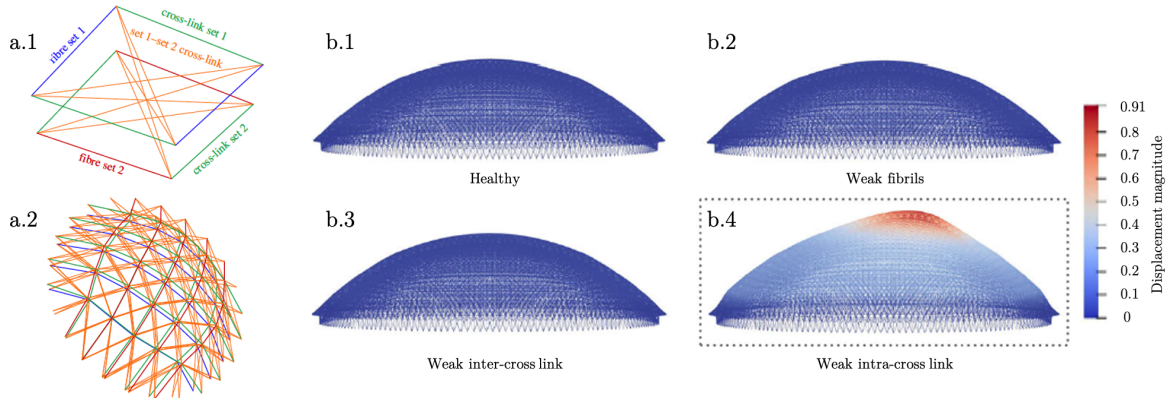


Figure 1.47: a.1. Unit cell of the fibrils and cross links. Fibrils are divided into two sets: fiber set 1 (F1) in blue and fiber set 2 (F2) in red. Two types of cross-links are defined: cross-links between the fibrils of the same set (inter-link: C1 and C2) are in green and between the fibrils of two different sets (intra-link: C12) in orange. a.2. Fibrils and cross-link networks. b.1-4. Comparison of the deformed shape and displacement field between b.1. a healthy cornea, b.2. a cornea weakened only in the F1 and F2 fibril stiffness, b.3. a cornea weakened only in the C1 and C2 cross-link stiffness, and b.4. a cornea weakened only in the C12 cross-link stiffness.

Looking at the displacement results of Fig. 1.47.b.1–4, one must conclude that the weakening of the intra-cross link (in orange on Fig. 1.47.a.1–2) gives a high deformability of the cornea and may lead to thinning and bulging of the tissue in the zone of the cone, as found in keratoconus.

Keratoconus has been studied numerically by various authors with different results regarding the explanation for the inception of the disease: the thinning of the zone (geometrical factor) or the

decreasing of the fibrils stiffness (mechanical weakening) were considered and found to be relevant. While the geometry found for keratoconic corneas are consistent with actual cases of keratoconus, there is however no comparison of quantitative parameters with real data.

1.5 Inverse problems and identification process

Corneal modeling has developed in recent years, with a particular interest in modeling pathological cases (Sec. 1.4.1). Such an approach introduces mechanical parameters, either for the matrix or for the collagen lamellae, which are intra- and inter-patient dependent. In parallel, experiments have been performed to estimate these parameters *ex-* and *in-vivo* (Sec. 1.3). However, like for any tissue – or any material – experimental results do not usually directly give all the parameters needed for modeling. It is therefore necessary to obtain the remaining missing parameters using other techniques. With the expansion of full field measurement techniques, strain maps are becoming available, and with them, a new type of data. Identification processes are then a tool in the chain to extract mechanical parameters of material using the measured experimental strain (or stress) fields.

1.5.1 Principle

This part is largely based on [9].

Modeling a material usually consists in solving the direct mechanical problem. Considering (i) the geometry of the sample, (ii) the mechanical behavior of the material, (iii) the boundary conditions and (iv) the loading applied to it, the direct problem consists in solving the energetic equilibrium ($\mathcal{P}_i = \mathcal{P}_e + \mathcal{P}_{BC}$) in the kinematically admissible displacement space $\mathcal{V}(\Omega_t)$ (Orange square in Fig. 1.48 and App.A.1.1). For this purpose, the finite element method (FEM) is used to solve the discretized equilibrium equations. The outputs of such FE codes can lead to stress and strain maps. We distinguish two sets of parameters: (i) experimentally determined parameters (direct measurements or extracted from the literature) $\underline{\gamma}^{exp}$ and (ii) parameters that cannot be measured and therefore remain to be determined $\underline{\tilde{\gamma}}$.

To determine these missing parameters, the problem is approached the other way around. The strain maps – usually determined experimentally (Sec. 1.2.2) – become the inputs of the new problem and the unknown mechanical parameters $\underline{\tilde{\gamma}}$ become the outputs. This problem is often called the "Inverse Problem" (in the pink square of Fig. 1.48). The goal is to compute – via the FE code – strain maps that are as close as possible to experimental ones. Solving the inverse problem means completing the identification process and thus building a model in which all the parameters have a value either determined experimentally or identified.

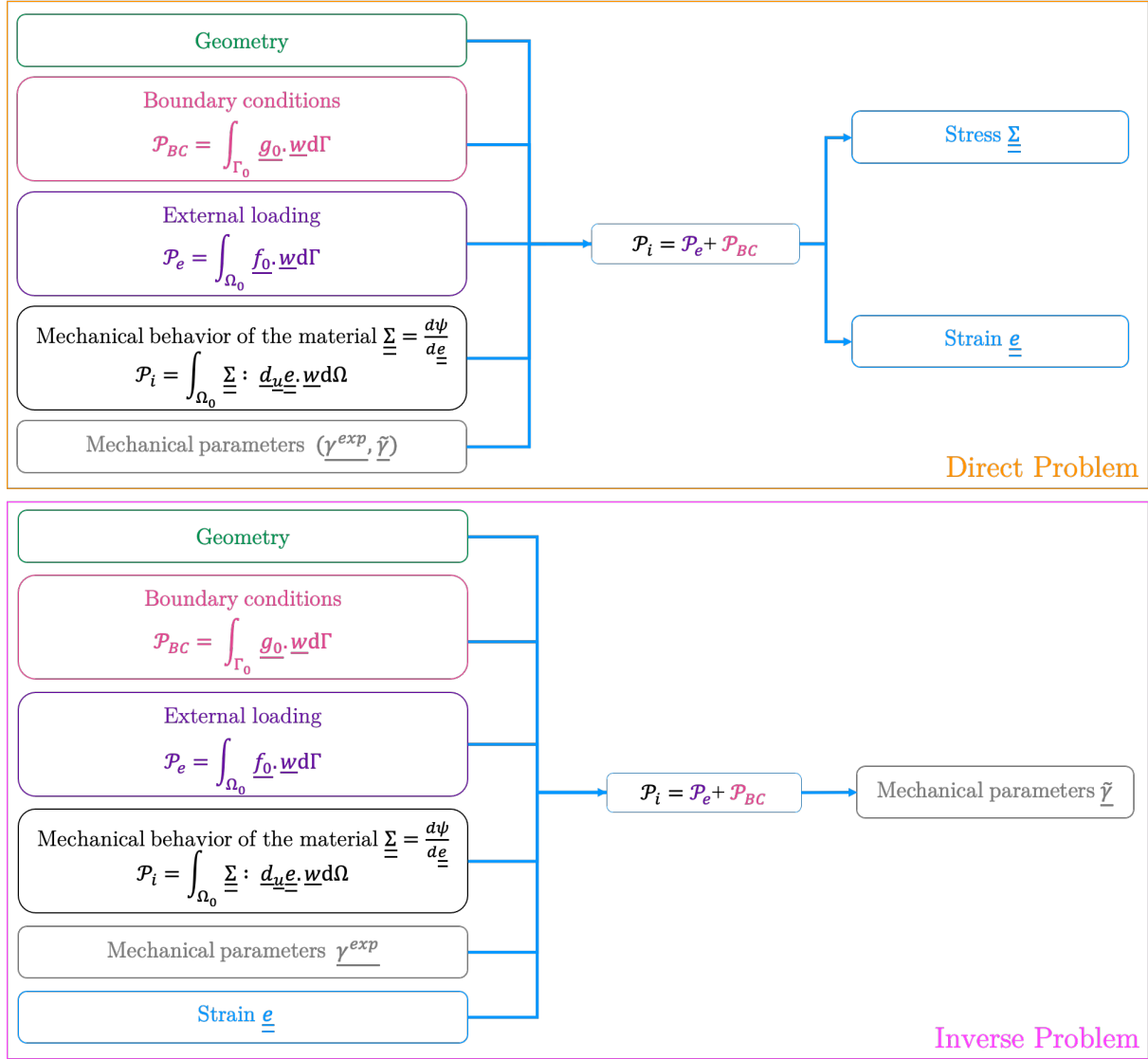


Figure 1.48: Data (inputs) and outputs considered in direct (orange) and inverse (pink) problems.

Several techniques have been developed over the years to perform the identification process using field measurements: (i) the Finite Element Model Updating (FEMU) method, (ii) the Constitutive Equation Gap Method (CEGM), (iii) the Virtual Field Method (VFM), (iv) the Equilibrium Gap Method (EGM) and (v) the Reciprocity Gap Method (RGM). The FEMU method will be used in this work and is detailed hereafter – in particular the FEMU-U approach based on the discrepancy between measured and predicted displacement fields. The other methods are detailed in [9] and the interested reader may refer to it. The FEMU-U method has been chosen because it can be used in the case of full field measurements, it is relatively economical in terms of computation time (with respect to others) and it is well adapted to heterogeneous materials.

The different steps of this identification process are described in Fig. 1.49. They rely on the comparison between the numerically computed \underline{u}^{num} and experimentally measured \underline{u}^{exp} displacement maps, using the cost function J_u , which takes the following form:

$$J_u(\underline{\tilde{\gamma}}) = \frac{1}{2\Omega} \int_{\Omega} (\underline{u}^{exp} - \underline{u}^{num}(\underline{\tilde{\gamma}})) \underline{W}_u (\underline{u}^{exp} - \underline{u}^{num}(\underline{\tilde{\gamma}})) d\Omega \quad (1.18)$$

with \underline{W}_u a symmetric positive definite weighting matrix and Ω the domain considered. Minimizing the cost function $J_u(\tilde{\gamma})$ using the identification loop presented Fig. 1.49 leads to the identified parameters $\tilde{\gamma}$.

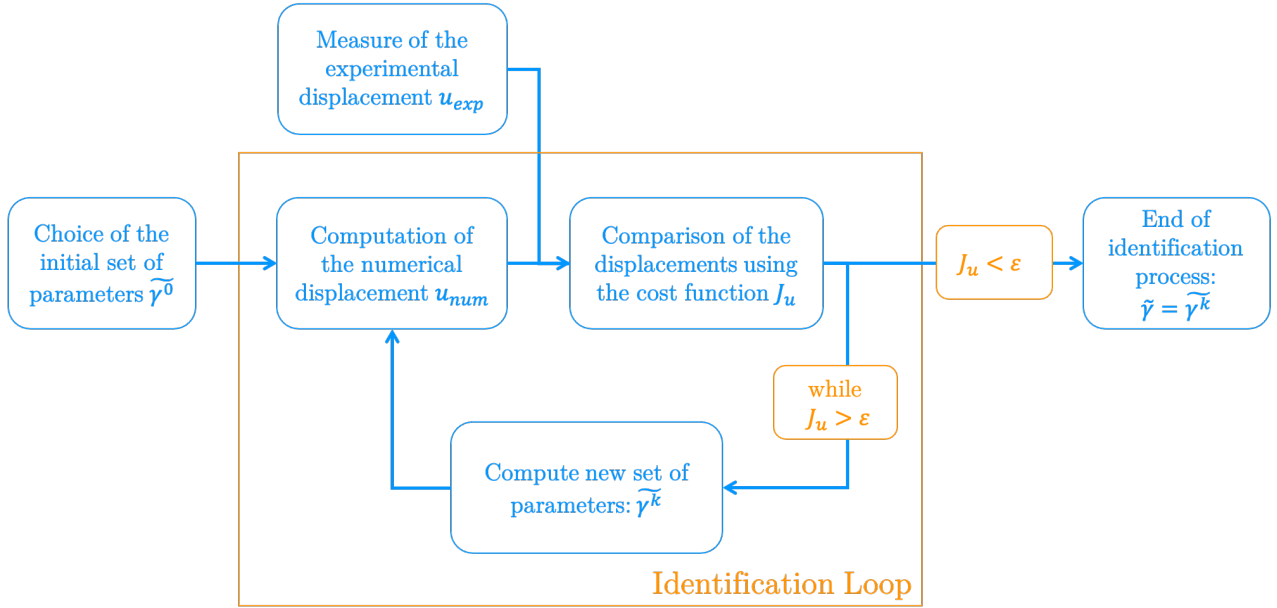


Figure 1.49: Identification loop considered in the FEMU method.

Using a small number of unknown parameters in this identification allows for working without adding a regularisation term in Eq. (1.18). Thus, the identification problem can be reduced to a functional minimization problem. Several algorithms can be used for this step.

1.5.2 Minimization of cost function: choice of the new set of parameters

The minimization of a functional is a whole part of the mathematical literature in itself. Here, the focus is made on two main types of minimization algorithms (see App. A.3 for more details): (i) the most classical ones which are the gradient descent-like methods and (ii) the one we use in this work: the covariance matrix evolution strategy (CMA-ES) [65].

The gradient descent methods (Gauss-Newton, Levenberg-Marquardt...) are all based on the same principle: the choice of the parameter set at iteration $k + 1$ depends on the parameter set at iteration k and the Jacobian J associated to the problem. Gradient descent algorithms (see details in App. A.3.1) are often used in the FEMU methods [9] because they are easy to implement. However, they do not allow a large field of possibilities for the parameter sets to be explored and risk to stop to local optima easily.

The Covariance Matrix Evolution Strategy (CMA-ES) [65] is one of the methods to overcome these weaknesses. It is a stochastic method for real-parameter optimization of non-linear, non-convex functions. It computes the new parameter set $\tilde{\gamma}^{k+1}$ from the old parameter set $\tilde{\gamma}^k$ using a multivariate normal distribution $\mathcal{N}(\underline{m}, \underline{Covar})$ where \underline{Covar} is a positive definite matrix of covariances.

The principle is as follows: at each iteration of the identification loop, a number $\lambda > 1$ of parameter sets $[\tilde{\gamma}_1^k, \dots, \tilde{\gamma}_\lambda^k]$ will be tested, i.e. the cost function will be evaluated for these parameter sets. Parameters

sets which are too far from the solution – i.e. for which the cost function will be the highest – will be discarded for the choice of the new sets of parameters, whose size therefore decreases at each iteration $[\tilde{\gamma}_1^{k+1}, \dots, \tilde{\gamma}_\lambda^{k+1}]$.

This method presents several advantages, the main one being the ability to avoid premature convergence. Even if it does not guarantee to find the global optimum of the function, the stochastic process allows search points to be tested (outside the classical range of the gradient method for example). Moreover, the size of the population (number of experimental points) can be chosen freely. A small population size allows for fast computation, while a large population size helps to find the global optimum, or at least not to stop the convergence process too quickly on the local optima.

The CMA-ES is an excellent candidate for the numerical parameter set selection tool because it allows for the identification of a large number of parameters, and is therefore able to work with a highly heterogeneous material such as the cornea. In addition, since full field measurements allow to work with a large population size, the convergence process has a better chance to find the global minimum of the $J_{\underline{u}}$ functional.

Research question and thesis outline

This thesis tries to tackle a major unresolved question that comes from ophthalmic surgeons: **can we understand the onset and development of keratoconus?**

As seen in Sec. 1.1.3, there is no clear origin of the pathology. One hypothesis, however, is regular rubbing of the patient's eyes [117], so the mechanical origin of the disease may be interesting to look at. The objective of this work is then to characterize the mechanical properties of corneas at different steps of the pathology, in order to identify the key features leading to the development of keratoconus.

First, the mechanical properties of healthy tissue must be studied in order to know the organ as well as possible before any evolution due to any pathology. For these purposes, numerical and experimental studies are possible to characterize the tissue. Numerical studies require modeling the tissue using data available in the literature while experimental studies allow the behavior of the material to be understood and thus valuable information to be extracted for modeling. Looking at the literature, very few data are available, especially on the microstructure and thus make modeling a real challenge even for healthy tissue. Then the pathological tissue can be examined with the same two prisms. In this framework, three main challenges arise. From a numerical and modeling point of view, pathology is often reflected as a change in material parameters or/and geometry that have to be characterized. From an experimental point of view, the supply of pathological samples is always a critical point, thus experiments are often conducted *in-vivo* and therefore the results are incomplete. Finally, to overcome the lack of information, identification is needed as a tool to find parameters not available experimentally.

The cornea is a tissue whose microstructure is complex and whose modeling at different scales for healthy and pathological cases has been growing in the last decades. However, no clear and consensual answer has been found in the literature to the following question: **what are the mechanical parameters that may influence the development of keratoconus?** Chapter 2 will attempt to answer this question through a multi-scale and patient-specific modeling of cornea. The model considered is similar to the ones we can find in the literature with a few but strong differences in its construction. First, real patient geometries are used in both healthy and pathological cases. Then, the mechanical response of the lamellae is considered as quadratic to be in agreement with the tensile response of collagen fibril. Finally, the angular integration approach (the so-called microsphere) is used to incorporate directly the experimental data available in the literature on the microstructure into our homemade finite element code. The model we built allowed us to numerically simulate the response of healthy cornea *ex-vivo*. Once the model was validated on the apex displacement with pressure data [45], we tested the influence of mechanical parameters in the context of *in-vivo* keratoconic corneas.

In parallel to the numerical study, we wanted to explore the local mechanical response of the tissue as the data available in the literature are scarce. The question we asked ourselves was the following: **is it possible to perform experiments to complete the results of the literature by measuring local properties of cornea during an inflation test?** At the same time, we wanted to explore the keratoconic case but as pathological samples are very hard to obtain, we focus our attention on a surgical issue related to the treatment of keratoconus: **how does the cornea**

respond to intraocular pressure after transplant? Chapter 3 will attempt to answer those questions. Corneas from the French eye bank were put under pressure while they were imaged with OCT. Three different types of experiments were performed. The first one tries to mimic the behavior of cornea after transplant (putting a cornea under physiological pressure for a couple of hours), the second one mimics the experiment carried out by Elsheikh's group (with pressure steps) [45] and the third one tries to determine the response of cornea at high pressure. 2D and 3D images are acquired throughout the process and are then analyzed by digital image/volume correlation to measure the local displacements. The results of Elsheikh's group were reproduced and the local strain highlighted an unexpected phenomenon of corneal swelling under pressure, which is not included in the classical representation of cornea. Finally, a theoretical development (see Sec. 3.4) was carried out in order to try to explain the mechanical response of cornea to pressure and more particularly by integrating water flows observed during the experiments.

Chapter 2

Multiscale mechanical model based on patient-specific geometry: application to early keratoconus development

Contents

Foreword	62
Main conclusions	62
2.1 Introduction	64
2.2 Methods	66
2.2.1 Patient - specific geometry	66
2.2.2 Mechanical equilibrium of the cornea: variational formulation	68
2.2.3 Constitutive behavior	69
2.2.4 Parameters of the mechanical model	73
2.2.5 Stress-free configuration	76
2.2.6 simK determination	76
2.3 Results	77
2.3.1 Parameter estimation	77
2.3.2 Keratoconus: geometrical and mechanical effect	78
2.3.3 Induced keratoconus	80
2.4 Discussion	82
2.5 Conclusions	84
Supplementary Materials	85
2.6 Sensitivity analysis	85
2.7 Mechanical parameters used in the computation	86
2.8 Stresses representation	88
2.8.1 Keratoconus: geometrical and mechanical effect	88
2.8.2 Induced keratoconus	92

Foreword

Chapter 2 tries to answer the question: what are the parameters influencing the inception and development of keratoconus? The chapter presents the results described in [58] while following the structure of the article.

The whole technical framework is not included in the core of the chapter but is found in the appendices. Here are listed the main technical points that structure the work of this chapter:

- The multiscale model is developed under the mechanical framework described in App. A.1.
- The patient-specific geometry is based on the generic mesh kindly provided by A. Pandolfi and described in App. B.
- The mechanical response of the lamellae and particularly the anisotropic 2^{nd} Piola-Kirchhoff tensor used in the FE code is computed in App. C.1.
- Finally, an angular integration approach is developed using the microsphere discretization computed in App. C.2 and Hermite's quadrature points of App. C.2.3.

The model built in Chap. 2 involves a large number of parameters, and is therefore difficult to identify. In order to anticipate a future identification process (detailed in App. C.3), a reduction of the number of parameters using B-splines has been implemented during the internship of G. Merlini [108] and can be found in App. C.3.1. At the same time, the cost functions needed to perform the identification process have also been implemented and are found in App. C.3.2.

Main conclusions

In this chapter, we built a multi-scale model based on the geometry of real patient using (i) clinical images kindly provided by ophthalmic surgeons at Hospital 15-20, (ii) a generic mesh kindly provided by A. Pandolfi and (iii) a new methodology developed to adapt the generic mesh so that it becomes patient-specific (see Fig. 2.1).

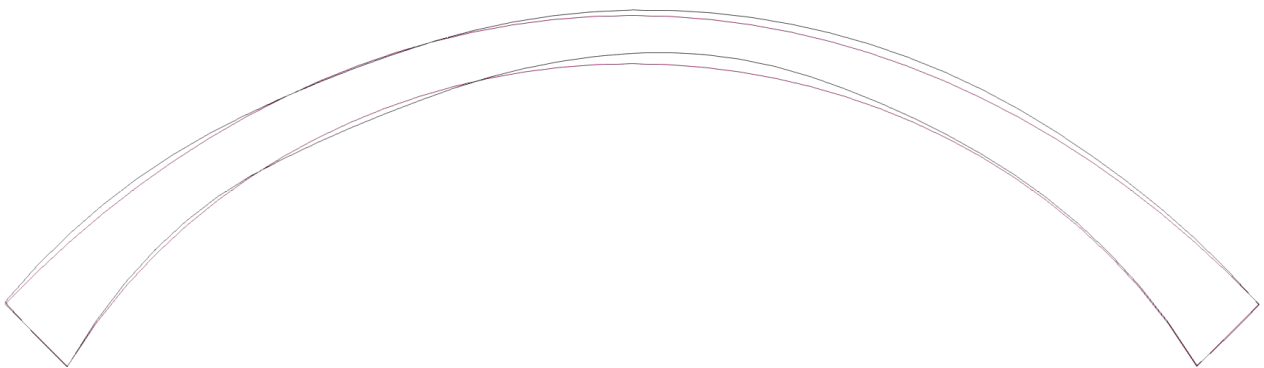


Figure 2.1: Vertical section of idealized (black) and personalized (pink) meshes.

The cornea was modeled as a quasi-incompressible hyperelastic material – represented by a Mooney-Rivlin energy function (to let the possibility to identify the second parameter as no experimental data are available) combined with a quasi-incompressible term – reinforced with collagen

lamellae – having a spring-like behavior. An angular integration approach was used to incorporate non-patient-specific micro-structural data (in-plane and out-of-plane lamellae orientation and dispersion from X-rays and Second Harmonic Generation microscopy imaging) into the FE code. A virtual stress-free configuration (where 0mmHg of pressure is applied on the posterior surface) has been computed to obtain the correct prestrain of the fibers on the reference configuration Ω_0 , via the values of the unfolding elongation.

The main findings of the study performed in this chapter are: (i) the sensitivity study showed that the unfolding stretch of the lamellae – which measures how stretched the lamellae are in the reference configuration – is a parameter of interest when looking at the apex displacement with pressure response of the cornea, (ii) the study of keratoconus development suggests that a change in geometry (all other things remaining unchanged) is not sufficient to show significant changes in SimK – a clinical indicator related to the maximum diopter – whereas a weakening of lamellae stiffness provides the 2-diopter change in SimK reported in [100]. This leads to the suggestion that the development of keratoconus is probably due to a weakening of the collagen lamellae associated with their disorganization – and not necessarily to a weakening of the isotropic matrix – which may result in the observed change of geometry.

The main limitations and perspectives of this work are: (i) the data on lamellae are not specific to each patient but, in the future, could be imaged by SHG as soon as the technique will be ready to non-destructive imaging, (ii) remodeling that occurs during the development of pathology has not been investigated here and would be of great help in understanding the relationship between the weakening of the lamellae and the change in geometry, (iii) as one of the goal was to help to perform laser surgery, remodeling process of wound healing should be taken into account too.

Multiscale mechanical model based on patient-specific geometry: application to early keratoconus development

C.Giraudet^{1,2}, J. Diaz^{2,1}, P. Le Tallec^{1,2}, J.-M. Allain^{1,2}

¹ *Laboratoire de Mécanique des Solides, CNRS, Ecole Polytechnique, Institut Polytechnique de Paris*

² *Inria*

Abstract — Keratoconus is a pathology of the cornea associated with a tissue thinning and a weakening of its mechanical properties. However, it remains elusive which aspect is the leading cause of the disease. To investigate this question, we combined a multiscale model with a patient-geometry in order to simulate the mechanical response of healthy and pathological corneas under intraocular pressure. The constitutive behavior of the cornea is described through an energy function which takes into account the isotropic matrix of the cornea, the geometric structure of collagen lamellae and the quasi-incompressibility of the tissue. A micro-sphere description is implemented to take into account the typical features of the collagen lamellae as obtained experimentally, namely their orientation, their stiffness and their dispersion, as well as the their unfolding stretch, at which they start to provide a significant force. A set of reference parameters is obtained to fit experimental inflation data of the literature. We show that the most sensitive parameter is the unfolding stretch, as a small variation of this parameter induces a major change in the corneal apex displacement. The keratoconus case is then studied by separating the impact of the geometry and the one of the mechanics. We computed the evolution of the SimK (a clinical indicator of cornea curvature) and elevation maps: we were able to reproduce the reported changes of SimK with pressure only by a mechanical weakening, and not by a change in geometry. More specifically, the weakening has to target the lamellae and not the matrix. The mechanical weakening leads to elevations close to early stage keratoconus, but our model lacks the remodeling component to couple the change in mechanics with changes in geometry. Still, these findings indicate that new methods for early diagnosis of keratoconus should focus on the detection of a mechanical weakening, and that stiffening treatments should be appropriate.

Keywords — Cornea mechanics, Patient-specific modeling, Keratoconus.

2.1 Introduction

Cornea is a critical part of the eye providing two thirds of its optical power through its specific lens shape. In keratoconus disease, the shape of the cornea is progressively altered to become conical, leading to optical aberration and thus to a loss of vision [157]. A late detection of the keratoconus imposes a laser surgery with possible complications [72; 112; 167]. Conversely, if the keratoconus is detected at an early stage, appropriated contact lenses can be used to stop its progression [10; 38]. This explains the interest for early diagnosis methods in the literature [26].

Keratoconus origin is not determined as of today: it has been shown to be favored by genetic, but also by mechanical rubbing of the eye [117]. Early keratoconus are associated with both a thinning of the cornea [139] and a decrease of the mechanical properties [5], combined with a loss of the highly

organized structure of the cornea [142]. However, it is not clear if the thinning is due to the weakening of the cornea or comes first. To tackle this question, we propose a modeling approach in which we can change independently the cornea geometry and its mechanical properties from healthy to keratoconic ones.

Patient-specific images of the cornea are obtained by clinicians using topographers. They give morpho-geometric indicators for an early stage of the keratoconus [26; 27; 139], such as corneal thickness, anterior and posterior surfaces geometries, and pachymetry. On the other hand, cornea mechanical properties are difficult to estimate specifically *in-vivo* [44; 84]. They have been investigated *ex-vivo* with inflation tests [14; 45] or strip stretching [46; 179]. They show a response similar to other collagen-rich tissues (as aorta [31], tendon [59] or skin [95]), with a first heel region associated with a low, non-linear, increase of the stress for large stretch, followed by a linear region in which the force increases proportionally to the stretch. Indeed, it has long been known [99] that optical and mechanical properties of the cornea are linked to the micro-structural organization of the stroma [102; 147], a collagen-rich tissue made of a plywood of collagen lamellae anchored in a matrix of proteoglycans and keratocytes. It is classically accepted that the mechanical properties arise from a progressive straightening of the lamellae in the heel region, followed by their stretching in the linear part [7], as reported for tendon [48] for example. Only a few papers have questioned this interpretation, with contradictory observations [13; 14] either due to the probed scales or to the differences in the experimental conditions.

The techniques used today to image the corneal lamellae are either destructive (as X-rays scattering [1; 101; 120]) or with very limited field of view (as transmission electron microscopy [15] and scanning electron microscopy [49; 141], which are also destructive, or Second Harmonic Generation microscopy [91; 106; 175; 182], which is not destructive). The experimental complexity means that the available data are not patient-specific and thus do not represent the variability of the human eyes.

The organization of the lamellae has been shown to be different in the keratoconic corneas compared to healthy ones [2; 104], and so one can expect different mechanical properties. Brillouin microscopy showed that a mechanical loss occurs in the region of the cone in keratoconus [154; 158]. Still, there is no consensus on the difference of rigidity *in-vivo* between healthy and keratoconic corneas [5]. Mechanically, a global difference between healthy and keratoconic cornea has been observed *in-vivo* in the change of the diopter under pressure [100].

Usually, cornea is modeled as an hyperelastic quasi-incompressible material reinforced by fibers [56; 113; 121; 134; 164; 174] representing the two families of lamellae. The validation of these models is only done on a few experiments measuring the displacement of the apex ([45; 93] for human cornea) or the 3D displacement of the anterior surface ([23] in bovine cornea) and exclusively in healthy cases. Note that most models do not include a variation of the mechanical properties through the cornea thickness, while nanoindentation has shown that the anterior part is stiffer than the posterior part [37].

We propose here a multi-scale and heterogeneous model of the cornea, based on the experimental lamellae orientations. This model is calibrated on the available experimental data, showing the high sensitivity of the response to the pre-strain of lamellae. This model is then implemented in a finite element code to simulate variations of intra-ocular pressure (or bulge test) on patient-specific geometries, thanks to clinical keratometer elevation maps. We show that a mechanical weakening of the cornea is needed to reproduce the reported variation of diopter with pressure [100], for both

healthy and keratoconic geometries. On the other hand, the change in geometry without mechanical variation does not reproduce the keratoconus response. We also show that the mechanical weakening tends to induce a keratoconus shape if we start from a stress-free healthy geometry, but the quasi-incompressibility of the cornea does not allow the thinning observed in keratoconus. All of this point towards the importance in a weakening of the mechanical properties in the development of the keratoconus. Particularly, our analysis shows that a weakening of the collagen lamellae is the most likely to induce the pathology. Our observations support the importance of an early measure of the cornea mechanical response, as well as the importance of treatments strengthening the collagen fibers.

2.2 Methods

The mechanical problem we solve is an inflation test where the cornea is fixed on a pressure chamber at its border and put under pressure. A patient-specific mesh is created using clinical elevations and thicknesses maps. The fixation is located at the sclera, the white and very stiff tissue surrounding the cornea. The material response of the cornea is brought by the stroma, modeled as an hyperelastic matrix reinforced by collagen lamellae. The lamellae orientations are extracted from X-rays [1] and SHG images [134; 176].

2.2.1 Patient - specific geometry

To construct a patient-specific mesh, we proceed in two steps. First, we construct an idealized geometry of the cornea using an analytical description: the geometry of the healthy cornea is almost regular and well described by a parametric quadratic equation [55]. Considering the apex of the cornea at the origin of a coordinate system with the z -axis oriented vertically and downwards, the anterior and posterior surfaces of the cornea are described by the biconic function [76]:

$$z(x, y, R_x, R_y, Q_x, Q_y) = z_0 + \frac{\frac{x^2}{R_x} + \frac{y^2}{R_y}}{1 + \sqrt{1 - (1 + Q_x)\frac{x^2}{R_x^2} - (1 + Q_y)\frac{y^2}{R_y^2}}}, \quad (2.1)$$

where R_x and R_y are the curvature radii of the flattest (x axis) and the steepest (y axis) meridians of the cornea, Q_x and Q_y are the associated asphericities. Note that the x and y directions can be rotated of an angle ψ from the classical nasal-temporal (N-T) and inferior-superior (I-S) axes (see Fig. 2.3.b for illustration of the anterior surface). Finally, z_0 is the arbitrary translation with respect to the z axis origin.

To adapt the mesh to real cornea, we use anonymized clinical data obtained by an anterior segment OCT combined with a MS-39 placido type topographer (Dr. J. Knoeri's personal communication). Figures 2.2.a, c, g and i present the maps of clinical anterior and posterior elevations for a healthy (Fig. 2.2.a and c) and a keratoconic cornea (Fig. 2.2.g and i). For each surface, a best fit sphere (BFS) is determined during the acquisition. The distance between the BFS and the real surfaces are called the anterior and posterior elevations (for the exterior and interior surface of the cornea respectively). Figures 2.2.e and k show clinical maps of the thicknesses of the same cornea. We first

do a least square minimization of Eq. (2.1) with respect to the clinical data to find R_x , R_y , Q_x and Q_y . Then, the cornea's thickness at the apex is used to place the anterior surface with respect to the posterior surface. This is used to create an idealized mesh (see Fig. 2.3.a - grey mesh) thanks to the code provided by Pr. A. Pandolfi [130].

This mesh is then corrected to match the real one. First, we adjust the anterior and posterior surfaces to match exactly the clinical observations (see Fig. 2.3.a - pink mesh). This step requires the interpolation of the elevation maps at the node positions, which is done with a bi-dimensional B-spline approximation. Second, the points in the volume of the mesh (so between the interior and exterior surfaces) are corrected to be linearly distributed between the two surfaces. This procedure ensures that the mesh is both realistic and regular.

At the end of the process, elevations (Fig. 2.2.b and d for healthy cornea and Fig. 2.2.h and j for keratoconic cornea) and thicknesses (Fig. 2.2.f for healthy cornea and Fig. 2.2.l for keratoconic cornea) are reproduced on the mesh to be compared to the clinical ones. Although they are determined at different positions and thus cannot be compared directly, we can say that the B-splines approximation captures the clinical data (elevations and thicknesses) pretty well, despite the expected tendency to smooth the shape.

An important point is that this mesh is built in the loaded configuration where the cornea is subjected to the physiological intra-ocular pressure (IOP). We call this configuration Ω_{physio} .

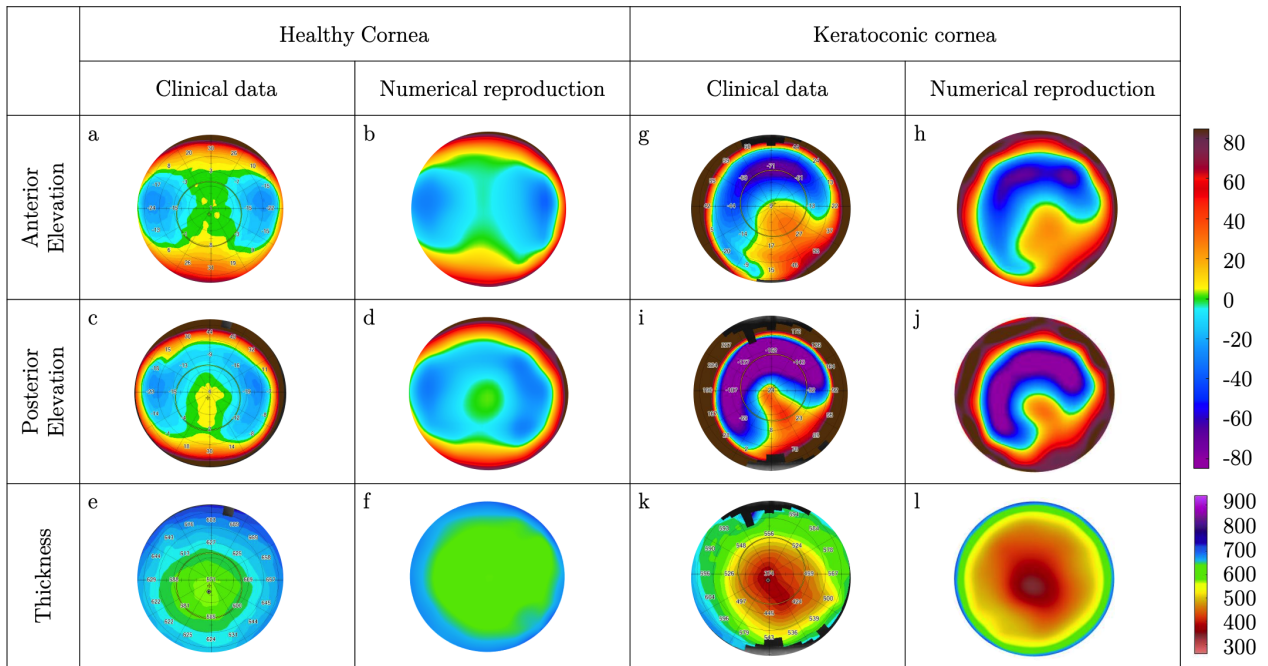


Figure 2.2: Elevation and thickness maps of healthy and keratoconic cornea. (a-f) Clinical and computed maps for a healthy cornea. (g-l) Clinical and computed maps for an advanced stage of keratoconic cornea. (a, c, e, g, i, k) Clinical data obtained by an OCT combined with a MS-39 placido type topographer. (b, d, f, h, j, l) Computed maps at physiological pressure for the same corneas and adapted meshes. (a, b, g, h) Clinical and computed anterior elevations with respect to the best fit sphere (BFS). Scale bar in μm . (c, d, i, j) Clinical and computed posterior elevations with respect to the BFS. Scale bar in μm . (e, f, k, l) Clinical and computed thickness. Scale bar in μm .

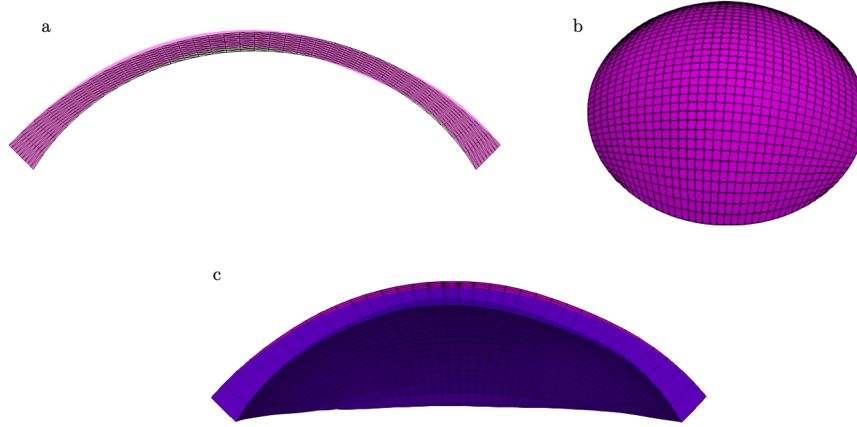


Figure 2.3: Example of a mesh construction for a keratoconic cornea. Mesh parameters: 12250 nodes and 10404 hexahedral elements. (a) Vertical cross-section along the long axis of the cornea of the idealized mesh (grey) and the patient-specific mesh at physiological pressure Ω_{physio} (pink). (b) 3D picture of the patient-specific mesh at physiological pressure Ω_{physio} . (c) Cross-section through the apex of the patient-specific mesh at physiological pressure Ω_{physio} (pink) and in stress-free configuration $\Omega_{0, stress-free}$ (blue) to be defined later.

2.2.2 Mechanical equilibrium of the cornea: variational formulation

We use a weak formulation written in the unknown unloaded configuration Ω_0 to represent the energetic equilibrium, the different terms being summarized in Fig. 2.4. This writes:

$$\mathcal{P}_i = \mathcal{P}_e + \mathcal{P}_{sclera}, \quad (2.2)$$

where \mathcal{P}_i is the inner power, \mathcal{P}_e is the power of external forces and \mathcal{P}_{sclera} is the power associated to the elastic boundary conditions. We look for a quasi-static solution of the problem, where the inertia terms are neglected. We also neglect volumic forces. The external forces are associated to the pressure P applied on the posterior surface of the cornea, producing a virtual power in Lagrangian formalism:

$$\forall \underline{w} \in \mathcal{V}(\Omega_0), \quad \mathcal{P}_e = -P \int_{\Gamma_0^{post}} J \underline{n}_0 \cdot \underline{F}^{-1} \cdot \underline{w} d\Gamma, \quad (2.3)$$

with \underline{w} an admissible test function (satisfying the boundary conditions), $J = \det(\underline{F})$ the change in volume, \underline{F} the gradient of the transformation sending Ω_0 to $\Omega(t)$ and \underline{n}_0 the external normal on the posterior surface in the stress-free configuration. The anterior surface is free of loading. The stiff sclera fixed to the pressure chamber is treated as an elastic support boundary condition, producing the virtual power:

$$\forall \underline{w} \in \mathcal{V}(\Omega_0), \quad \mathcal{P}_{sclera} = - \int_{\Gamma_0^{sclera}} a \underline{u} \cdot \underline{w} d\Gamma, \quad (2.4)$$

with \underline{u} the displacement vector, and a the boundary elastic modulus, assumed to be large with respect to the cornea stiffness. This boundary condition has been chosen to mimic Elsheikh et al. *ex-vivo* inflation test [45], where the cornea and the close surrounding sclera is clamped on the pressure chamber. It could have been interesting to simulate the whole eye (as in [181]) as it allows a deformation of the sclera. But, as our data are limited to cornea (with no information on the sclera motion), the conclusions of a more advanced simulation will have been weakened by an excess of

unknowns.

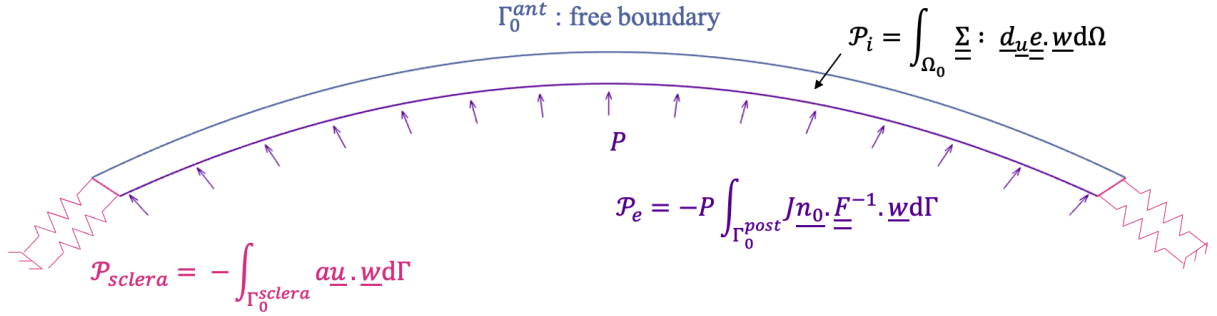


Figure 2.4: Schematic view of the mechanical problem of an inflation test. A pressure P is applied on the posterior surface of the cornea, while the anterior surface of the cornea is stress-free, and the sclera is fixed to a pressure chamber treated as an elastic boundary condition of stiffness a .

Finally, the internal power:

$$\forall \underline{w} \in \mathcal{V}(\Omega_0), \quad \mathcal{P}_i = \int_{\Omega_0} \underline{\underline{\Sigma}} : d_u \underline{e} \cdot \underline{w} d\Omega, \quad (2.5)$$

introduces the 2nd Piola-Kirchhoff stress tensor $\underline{\underline{\Sigma}}$, which is related to the energy function ψ through its derivative with respect to the Green-Lagrange tensor $\underline{e} = \frac{1}{2}(\underline{F}^T \underline{F} - \underline{1})$:

$$\underline{\underline{\Sigma}} := \frac{d\psi}{d\underline{e}}, \quad (2.6)$$

and $d_u \underline{e} \cdot \underline{w} = \frac{1}{2}((\underline{\nabla}_{\underline{\xi}} \underline{w})^T \cdot \underline{F} + \underline{F}^T \cdot \underline{\nabla}_{\underline{\xi}} \underline{w})$, the symmetric part of the gradient tensor of the test function in the current configuration brought back in the reference configuration.

The weak formulation of our mechanical problem leads to the following equilibrium equation in Lagrangian form:

$$\forall \underline{w} \in \mathcal{V}(\Omega_0), \quad \int_{\Omega_0} \underline{\underline{\Sigma}} : d_u \underline{e} \cdot \underline{w} d\Omega = -P \int_{\Gamma_0^{post}} J \underline{n}_0 \cdot \underline{F}^{-1} \cdot \underline{w} d\Gamma - \int_{\Gamma_0^{sclera}} a \underline{u} \cdot \underline{w} d\Gamma. \quad (2.7)$$

2.2.3 Constitutive behavior

We consider that the mechanical resistance of the cornea arises from the stroma, its main layer [131; 160]. The stroma is a collagen-rich tissue that we describe as a hyperelastic material made of fibers in an isotropic matrix viewed as weakly compressible. So, our associated energy function ψ is splitted into three contributions:

$$\psi = \psi^{iso} + \psi^{vol} + \psi^{lam}, \quad (2.8)$$

with an isotropic part ψ^{iso} corresponding to the matrix, the keratocytes and the randomly distributed lamellae, a volumetric part ψ^{vol} penalizing any change of volume and an anisotropic part ψ^{lam} , taking into account the mechanical role of the oriented lamellae.

The isotropic part of the function ψ^{iso} is chosen here as a Mooney-Rivlin function of the reduced invariants $\bar{I}_1 = I_1 I_3^{-1/3}$ and $\bar{I}_2 = I_2 I_3^{-2/3}$ [130; 160] of the Cauchy-green tensor $\underline{C} = \underline{F}^T \underline{F}$:

$$\psi^{iso} := \kappa_1(\bar{I}_1 - 3) + \kappa_2(\bar{I}_2 - 3), \quad (2.9)$$

while the volumetric part ψ^{vol} penalizes any volumic change by a very large bulk modulus K [160]

$$\psi^{vol} := K(J^2 - 1 - 2\log(J)), \quad \text{with } J^2 = I_3. \quad (2.10)$$

The anisotropic contribution is due to the anisotropic distribution of the lamellae. X-ray and SHG observations have shown a two-peak distribution of lamellae (see Fig. 2.5) [1; 91] that we describe by two families of lamellae (lam_1, lam_2). We model their contribution by an angular integration (AI) approach [134; 164]. Other microstructure-based approaches are possible, such as Generalized Structure Tensor (GST) (for example [170]). At each material point of the cornea, the two families of lamellae have a given directional density distribution $(\rho_1(\theta, \phi), \rho_2(\theta, \phi))$. The contribution ψ^{lam} of the two families of lamellae at each point adds local contributions of all possible directions, through the integration on a sphere of radius 1 (called "micro-sphere"):

$$\psi^{lam} := \int_{\theta=0}^{\pi} \int_{\phi=0}^{2\pi} (\rho_1(\theta, \phi) \delta\psi_1^{lam}(\theta, \phi) + \rho_2(\theta, \phi) \delta\psi_2^{lam}(\theta, \phi)) \sin \theta d\theta d\phi \quad (2.11)$$

performed in the local system of coordinates at the given spatial quadrature point $(\underline{e}_r^{lam}, \underline{e}_\theta^{lam}, \underline{e}_\phi^{lam})$ (see Fig. 2.5). At each mesh node, a local Cartesian basis $(\underline{e}_x^{lam}, \underline{e}_y^{lam}, \underline{e}_z^{lam})$ (see Fig. 2.5.d) is created using the main directions of the lamellae extracted from [1]: \underline{e}_x^{lam} is in the direction of one lamellae (chosen as the one which direction is closer to the long axis of the cornea in the central part and the one closer to the tangential direction in the periphery) interpolated at the node from the data at the experimental points; \underline{e}_z^{lam} is normal to the surface at the node and \underline{e}_y^{lam} completes the trihedron. Then, $(\underline{e}_r^{lam}, \underline{e}_\theta^{lam}, \underline{e}_\phi^{lam})$ defines the local spherical system characterizing the direction (θ, ϕ) of a particular quadrature point of the micro-sphere (see Fig. 2.5.e).

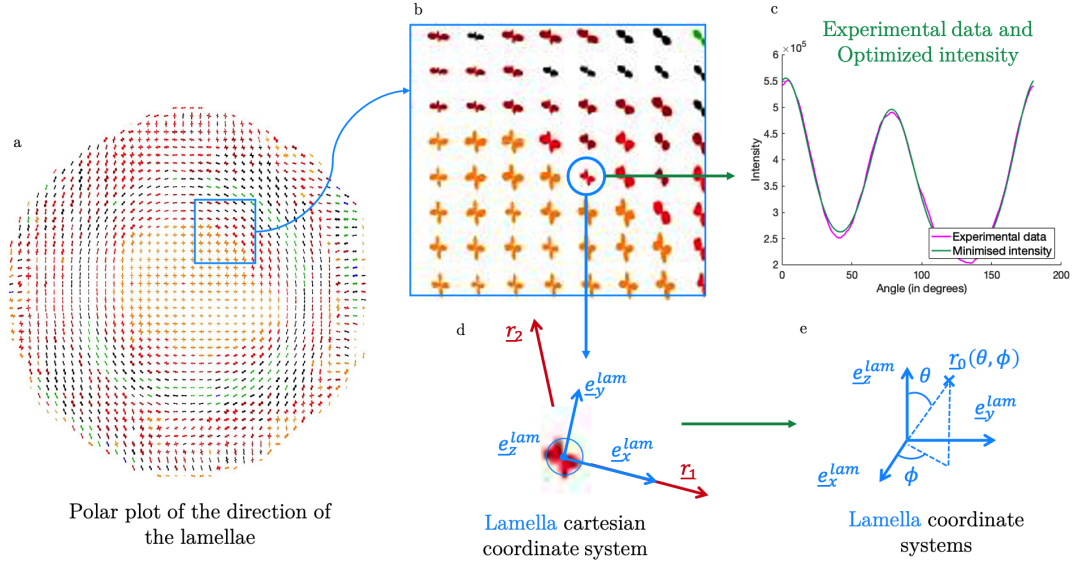


Figure 2.5: Distribution of lamellae orientation in a cornea. (a) Experimental polar plot of the direction of the lamellae obtained from X-ray observation (Figure from [1], kindly provided by S. Hayes and K. M. Meek). (b) Zoom on a sub-region of the cornea. (c) Experimental (pink) and associated optimized angular intensity (green) at one point of measurement. (d-e) Local Cartesian coordinates system (e_x^{lam} , e_y^{lam} , e_z^{lam}) at the same particular point of measurement, and the associated spherical coordinates.

2.2.3.a Elementary response of a lamella $\delta\psi^{lam}$

In many tissue, collagen fibrils are crimped [51], explaining the non-linear response of the tissue, with a heel-region in which the crimps disappear, generating a low force, and a linear region where the fibrils are stretched (and aligned) with a spring-like behavior. In cornea, the collagen fibrils appear very aligned in lamellae [175]. Still, they can buckle, but we expect that this buckling occurs at a stretch smaller than the one at physiological pressure. Note that experiments on cornea strips have shown that the fibrils are tilted and that this tilt decreases in the heel region to create the non-linear response, as the crimps in other tissues [13].

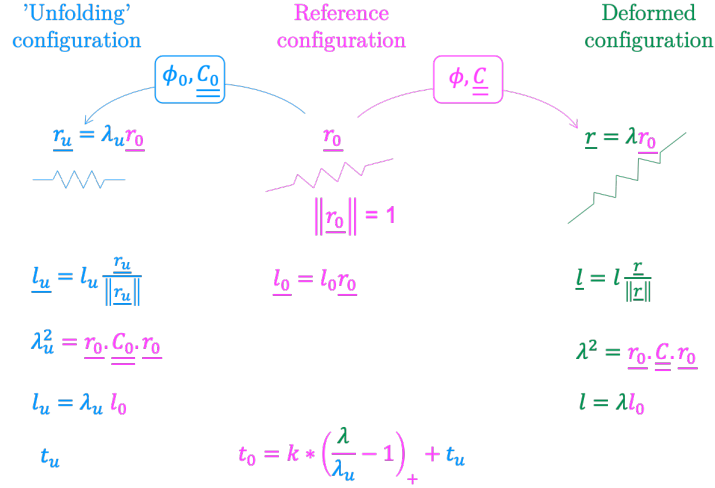


Figure 2.6: Schematic representation of the different configurations of the lamella: the 'unfolding' configuration corresponds to the limit of the lamella in compression, the reference and deformed configuration are those considered in our problem.

We model a collagen lamella as a bi-domain material (see Fig. 2.6). For stretches below an "unfolding" stretch λ_u , the lamella creates a constant prestress t_u , while for higher stretches, the lamella has a spring-like behavior of apparent "stiffness" k . The elementary energy function is therefore given by:

$$\delta\psi_i^{lam}(\theta, \phi) := \frac{1}{2} k_i \lambda_{u,i} l_{0,i} \left(\frac{\lambda_i}{\lambda_{u,i}} - 1 \right)_+^2 + t_{u,i} l_{0,i} \lambda_i, \quad \forall i \in [1 : 2], \quad (2.12)$$

where $()_+$ is the positive absolute value function.

The elongation $\lambda(\theta, \phi)$ of a lamella of reference direction $\underline{r}_0(\theta, \phi)$ is directly obtained under an affine assumption as a function of the Cauchy Green tensor:

$$\lambda(\theta, \phi) := \sqrt{\frac{\underline{r}_0(\theta, \phi) \cdot \underline{C} \cdot \underline{r}_0(\theta, \phi)}{\underline{r}_0(\theta, \phi) \cdot \underline{r}_0(\theta, \phi)}} = \sqrt{\underline{r}_0(\theta, \phi) \cdot \underline{C} \cdot \underline{r}_0(\theta, \phi)} \quad (\|\underline{r}_0\|^2 = 1), \quad (2.13)$$

with $\underline{r}_0(\theta, \phi) := \sin \theta \cos \phi \underline{e}_x^{lam} + \sin \theta \sin \phi \underline{e}_y^{lam} + \cos \theta \underline{e}_z^{lam}$.

2.2.3.b Density functions $(\rho_1(\theta, \phi), \rho_2(\theta, \phi))$

The distribution of each lamellae family is described by a Von Mises distribution (Eq. (2.14)):

$$\text{VM}(\theta, \phi | \kappa_{ip}, \kappa_t, \mu, \nu) := \frac{e^{\kappa_{ip} \cos(2(\phi - \mu))} e^{\kappa_t \cos(2(\theta - \nu))}}{C_{lam}}, \quad (2.14)$$

where C_{lam} is a normalization factor ensuring that the distribution has a total density over the sphere equal to 1. The in-plane κ_{ip} and out-of-plane κ_t concentrations are a measure of the dispersion (the larger the κ the thinner the peak) when μ and ν describe the mean orientations (in-plane and out-of-plane respectively).

To reproduce the X-ray experimental data from [1] at each point of measure (see Fig. 2.5.c), we consider that the diffracted signal is the sum of the two in-plane distributions of the lamellae families,

supplemented by an isotropic contribution:

$$I_m(\phi|\kappa_{ip,1}, \kappa_{ip,2}, \mu_1, \mu_2) = I_{iso} + C_1 VM_{ip}(\phi|\kappa_{ip,1}, \mu_1) + C_2 VM_{ip}(\phi|\kappa_{ip,2}, \mu_2), \quad (2.15)$$

where I^{iso} is a constant component representing the isotropic part of the measure, $\mu_1 + \pi/2$ and $\mu_2 + \pi/2$ the mean directions of the lamellae (the intensity pic is shifted of $\pi/2$ with respect to the main direction of the lamellae [1]), $\kappa_{ip,1}$ and $\kappa_{ip,2}$ the concentrations of the lamellae distributions, and C_1 and C_2 the measures of the number of oriented lamellae in each direction at the point of measurement. The seven fields C_1 , C_2 , $\kappa_{ip,1}$, $\kappa_{ip,2}$, μ_1 , μ_2 and I_{iso} , identified at those experimental points by a least square minimization technique, are then bi-linearly interpolated at each node of the mesh.

The X-rays experiments do not give any indication on the out-of-plane distribution. Using Second Harmonic Generation (SHG), it has been shown that the lamellae have a maximum out-of-plane angle of around 30° for healthy cornea in the anterior region, well represented by a Gaussian distribution [176] and that the maximum out-of-plane angle decreases with the depth [134; 176]. So, we assumed that the out-of-plane Von Mises distribution has a in-plane mean orientation ($\nu = 0$) so that it reduces to $VM_t(\theta|\kappa_t) = \frac{e^{\kappa_t \cos(2\theta)}}{C(\kappa_t)}$, and that the out-of-plane concentration varies exponentially with depth [134]:

$$\kappa_t(s) = (\kappa_{t,min} - \kappa_{t,max}) * \frac{e^{\gamma(1-s)} - 1}{e^\gamma - 1} + \kappa_{t,max}, \quad \text{with} \begin{cases} \gamma = 3.19, \\ \kappa_{t,min} = 7, \\ \kappa_{t,max} = 700, \end{cases} \quad (2.16)$$

where s is the normalized depth (0 at the anterior surface, 1 at the posterior), and $C(\kappa_t)$ normalizes the distribution. $\kappa_{t,min}$ and $\kappa_{t,max}$ have been chosen such that the maximum cut-off-angle is around 30° on the anterior surface ($\kappa_t = \kappa_{t,min}$ and so the peak of the distribution is large) and around 0° (in-plane lamellae) on the posterior surface of the cornea ($\kappa_t = \kappa_{t,max}$ and so the peak of the distribution is tight). No lateral heterogeneity in the lamellae out-of-plane distribution has been reported. Distributions of $\kappa_{ip,1}$, $\kappa_{ip,2}$ and κ_t are represented on Fig. 2.15 in Supplementary Materials Sec. 2.7.

2.2.4 Parameters of the mechanical model

Once the lamellae orientations are known, our model has still 11 parameters to be determined: 2 for the isotropic energy ψ^{iso} (κ_1 and κ_2), 1 for the volumic energy ψ^{vol} (K) and 8 for the anisotropic energy ψ^{lam} (k_i , $\lambda_{u,i}$, $l_{0,i}$ and $t_{u,i}$). Furthermore, all of them except K have to be distributed locally to represent the variation of the micro-structure of the cornea.

The isotropic energy function ψ^{iso} (Eq. (2.9)) involves two parameters: κ_1 and κ_2 . For simplicity, as we have no specific information, we are going to assume that they are proportional with each other:

$$\kappa_2 = \alpha \kappa_1. \quad (2.17)$$

with α a constant to be identified. We will also make the assumption that they are proportional to

the fraction of the isotropic part of the signal I_{iso} (Eq. (2.15)), so they are distributed in space:

$$\kappa_1(x, y, s) = \kappa_1^{apparent} * I_{iso}(x, y, s). \quad (2.18)$$

We consider that this term varies in the cornea's thickness, since the elastic modulus of the posterior stroma is reported to be 39.3% of the modulus of the anterior stroma [37]. We thus apply the same exponential variation as for the out-of-plane angular distribution (Eq. (2.19)), namely:

$$I_{iso}(x, y, s) = (I_{iso}^{ant}(x, y) - I_{iso}^{post}(x, y)) * \frac{e^{\gamma(1-s)} - 1}{e^\gamma - 1} + I_{iso}^{post}(x, y),$$

$$\text{with } \begin{cases} \gamma = 3.19, \\ I_{iso}^{ant}(x, y) \text{ depending of the in-plane position}(x, y) \\ I_{iso}^{post}(x, y) = 39.3\% * I_{iso}^{ant}(x, y). \end{cases} \quad (2.19)$$

Here I_{iso}^{ant} is being obtained by equaling the mean of $I_{iso}(x, y, s)$ in s with the experimental value I_{iso} obtained from the X-ray data. In the end, only $\kappa_1^{apparent}$, a global parameter, needs to be determined to reproduce the experimental data.

The volumetric energy function ψ^{vol} (Eq. (2.10)) involves an independent penalty parameter K to impose volume conservation, which we consider as a global constant parameter, and which needs to be determined through experimental data.

The anisotropic energy functions $\delta\psi_1^{lam}$ and $\delta\psi_2^{lam}$ of the two lamellae families (Eq. (2.12)) involve eight local parameters: $k_1, \lambda_{u,1}, l_{0,1}, t_{u,1}, k_2, \lambda_{u,2}, l_{0,2}$ and $t_{u,2}$ (four per lamellae family). $t_{u,1}$ and $t_{u,2}$ are the forces generated by "undulated" lamellae, which are much smaller than the ones of the stretched ones. So, we are going to neglect them for simplicity, taking $t_{u,1} = t_{u,2} = 0$. Thus, the energy functions (Eq. (2.12)) reduce to:

$$\delta\psi_i^{lam}(\theta, \phi) := \frac{1}{2} k_i \lambda_{u,i} l_{0,i} \left(\frac{\lambda_i}{\lambda_{u,i}} - 1 \right)_+^2, \quad \forall i \in [1 : 2].$$

The product $\lambda_{u,i} l_{0,i}$ of the unfolding elongation and reference length is the unfolding length of a lamellae $l_{u,i}$. We are assuming that all the lamellae are the same and thus have the same unfolding length: $l_{u,1} = l_{u,2} = l_u = Cte$. So the energy function becomes

$$\delta\psi_i^{lam}(\theta, \phi) := \frac{1}{2} k_i l_u \left(\frac{\lambda_i}{\lambda_{u,i}} - 1 \right)_+^2, \quad \forall i \in [1 : 2].$$

The apparent "stiffnesses" k_1 and k_2 are a measure of the relative stiffness of each lamellae. Thus, they are proportional to the number of fibers in the lamellae direction and hence to the coefficients C_1 and C_2 (Eq. (2.15)). Thus, there is a proportionality factor $k_{lamellae,apparent}$ such that:

$$k_i = k_{lamellae,apparent} C_i \quad (2.20)$$

Finally, we can define an effective "stiffness" $k_{lam} = l_u k_{lamellae,apparent}$, so that the energy function becomes:

$$\delta\psi_i^{lam}(\theta, \phi) := \frac{1}{2} C_i k_{lam} \left(\frac{\lambda_i}{\lambda_{u,i}} - 1 \right)_+^2, \quad \forall i \in [1 : 2]. \quad (2.21)$$

and so it leaves only a global constant parameter k_{lam} .

The last parameters are the unfolding stretches $\lambda_{u,1}, \lambda_{u,2}$. The "unfolding" elongations are supposed to depend on the dispersion of the lamellae. Indeed, the more the lamellae are stretched in the reference configuration (i.e. the closer the "unfolding" elongation is to 0), the more the lamellae are aligned, therefore the less they are dispersed (i.e. the greater the κ_{ip}). On the contrary, the less the lamellae are stretched in the reference configuration (i.e. the closer the reference length is to the "unfolding" length), the less the lamellae are aligned, therefore the more they are dispersed (i.e. the smaller the κ_{ip}). In a first approach, they are considered to be linearly inversely proportional $\lambda_u = a/\kappa_{ip} + b$, with coefficients a and b to be determined thanks to the limits:

$$\lambda_{u,min} = \frac{a}{\kappa_{ip,max}} + b, \quad \text{and} \quad \lambda_{u,max} = \frac{a}{\kappa_{ip,min}} + b \quad (2.22)$$

which makes for two new independent parameters $\lambda_{u,max}$ and $\lambda_{u,min}$ the maximum and minimum unfolding elongation of the lamellae in the whole cornea, to be determined experimentally.

Anisotropic contribution (Eq. (2.11)) finally reduces to

$$\psi^{lam} = \int_{\theta=0}^{\pi} \int_{\phi=0}^{2\pi} \sum_{i=1}^2 \frac{1}{2} C_i k_{lam} \left(\frac{\lambda_i(\theta, \phi)}{\lambda_{u,i}} - 1 \right)_+^2 \frac{e^{\kappa_{ip,i} \cos(2(\phi-\mu_i))} e^{\kappa_{t,i} \cos(2\theta)}}{C_i^{lam}} \sin \theta d\theta d\phi \quad (2.23)$$

with only three unknown global parameters left $\lambda_{u,max}$, $\lambda_{u,min}$ and k_{lam} .

Table 2.1 summaries the independent global parameters used in the model, the constitutive equations where they appear and the values determined to reproduce the experimental data from [45] and [100].

Parameter notation	Energy function	Parameter description	Equation	Value
$\kappa_1^{apparent}$	ψ^{iso}	Matrix stiffness	Eq. (2.9), (2.18)	60Pa
α		Proportional factor between the two matrix parameter	Eq. (2.17)	1/4
K	ψ^{vol}	Hyperelastic bulk	Eq. (2.10)	80 kPa
k_{lam}	ψ^{lam}	Apparent stiffness of a collagen lamellae for a given length	Eq. (2.21), (2.23)	65 Pa
$\lambda_{u,max}$		Maximum "unfolding" elongation λ_u in the reference configuration	Eq. 2.22, (2.23)	1.0245
$\lambda_{u,min}$		Minimum "unfolding" elongation λ_u in the reference configuration	Eq. (2.22), (2.23)	1.0195

Table 2.1: Summary of the global parameters of the model, their contribution, where they appear, and their values determined by simulating an inflation test to reproduce the data from [45].

Once we have simplified the model by reducing the number of independent parameters, we use a finite element code - MoReFEM - developed at Inria by the M Ξ DISIM team [57] to solve Eq. (2.7). The Galerkin method is used to do the spatial discretization, using Q1 hexaedric finite elements. To compute the anisotropic part of the 2nd Piola-Kirchhoff tensor at Gauss points, a numerical quadrature is used for the integral (Eq. (2.11)) on the microsphere using a uniform rule with 20 equally distributed points for the in-plane angle ϕ and the Gauss-Hermite quadrature rule with 5th order polynomial and 5 quadrature points for the out-of-plane angle θ . Two loading conditions are used:

- Loading from 2 mmHg to 160 mmHg to mimic the *ex-vivo* experiment of Elsheik et al. [45] on human cornea under pressure: we use this to calibrate the model.

- Loading from 15 mmHg to 30 mmHg to mimic the *in-vivo* experiment of McMonnies and Boneham [100]: we use this to investigate the origin of the keratoconus.

2.2.5 Stress-free configuration

To numerically solve Eq. (2.7), we need to start from a stress-free configuration. However, the patient-specific geometry is obtained under physiological intra-ocular pressure (IOP). As IOP was not determined during this clinical acquisition, we assume that it is the mean IOP of healthy individuals (14.5 mmHg [66]). We then use the patient-specific configuration Ω_{physio} (associated to the positions \underline{x}_{physio}) as the target of a shooting method to determine the stress-free configuration. Starting from an assumed reference configuration $(\Omega_0, \underline{\xi})$, the procedure is the following:

Algorithm 1 Computation of the stress-free configuration

Step 1 - Computation of the deformed configuration under IOP pressure $(\Omega_p, \underline{x}_p)$

Step 2 - Determine the differences $\underline{\Delta}_x = \underline{x}_p - \underline{x}_{physio}$.

Step 3 - While any of the differences $|\underline{\Delta}_x|$ is larger than a tolerance (taken at 10^{-6} mm), update the reference configuration by $\underline{\xi}_{new} = \underline{\xi} - \underline{u}$. Otherwise, we consider that we have found the reference configuration.

Figure 2.3.c presents the two meshes used in the algorithm for a stage 4 keratoconic cornea. The pink one is the corrected mesh under physiological pressure Ω_{physio} and the blue one corresponds to the associated stress-free configuration $\Omega_{0, stress-free}$ mesh (for $P = 0$ mmHg): the two being barely distinguishable. Note that the reference configuration needs to be updated each time you change any mechanical parameter of the model.

2.2.6 simK determination

To compare our data with McMonnies and Boneham [100], we computed the simK of our cornea at different pressures. The simK is the diopter (D) associated to the steepest meridian of the cornea as identified at a small radius ($r = 1.5$ mm - see Fig. 2.7). To compute the simK, we fit the biconic equation (Eq. (2.1)) on the deformed anterior surface inside a 1mm radius from the apex. We obtain the two radii for each level of pressure and from them we can compute the diopter D using the steepest one:

$$D(P) = simK(P) = \frac{n_{aqh} - n_{air}}{R_{steep}(P)} \quad (2.24)$$

where R_{steep} is the radius of the steepest meridian and n_{aqh} and n_{air} are the refraction indexes of the aqueous humor and air (taken at 1.3375 and 1.0000 respectively).

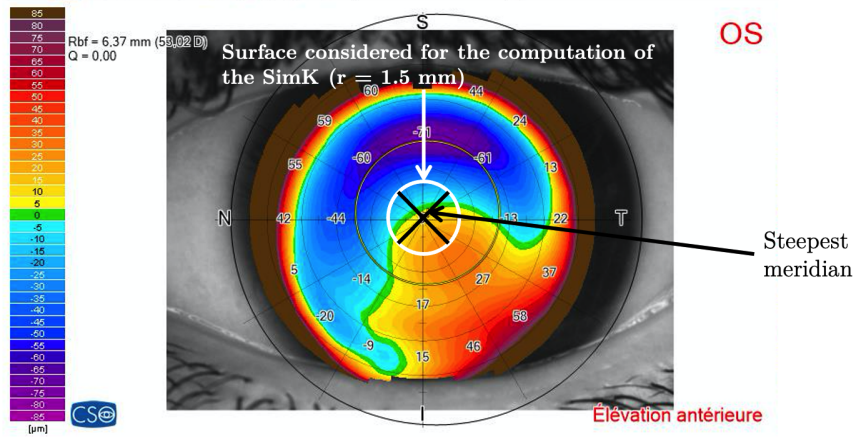


Figure 2.7: Example of the considered surface used to compute the SimK. A subregion of 3 mm in radius of the anterior surface is fitted by a biconic function. The steepest meridian is used to compute the SimK.

2.3 Results

We first determine the values of our model parameters by reproducing experimental data on *ex-vivo* inflation assays [45]: these parameters will be our "reference" parameters used to investigate the origin of the keratoconus.

2.3.1 Parameter estimation

We simulated the experiment by Elsheik et al. [45]. To do so, we used the stress-free geometry $\Omega_{0, stress-free}^{ref}$ of a healthy cornea and applied a pressure from 0 to 160 mmHg while determining the apex displacement. Figure 2.8 shows the envelope of the experimental data (in pink), which comes from inter-cornea variability. The triangular markers are our simulation using the "reference" parameters (see Table 2.1), obtained after manual calibration.

We have then varied each parameter independently by 1%. The most sensitive parameters are the unfolding stretches $\lambda_{u,min}$ and $\lambda_{u,max}$ (the results for the other parameters are presented in appendix 2.6, Fig. 2.14). Figure 2.8 shows that an increase (resp. decrease) of both the unfolding stretches by 1% moves the pressure vs apex displacement curve to the right (resp. to the left), well outside the experimental data range. Unfolding stretch corresponds to the stretch above which the lamellae start to respond elastically. As $\lambda_u > 1$, the lamellae in the reference configuration are folded and do not contribute to the tissue rigidity. Once they become activated, the tissue becomes much stiffer. This explains why a change in the unfolding stretch leads to a shift of the pressure vs apical displacement curve: increasing the unfolding stretch will elongate the heel region, without changing the linear part so much.

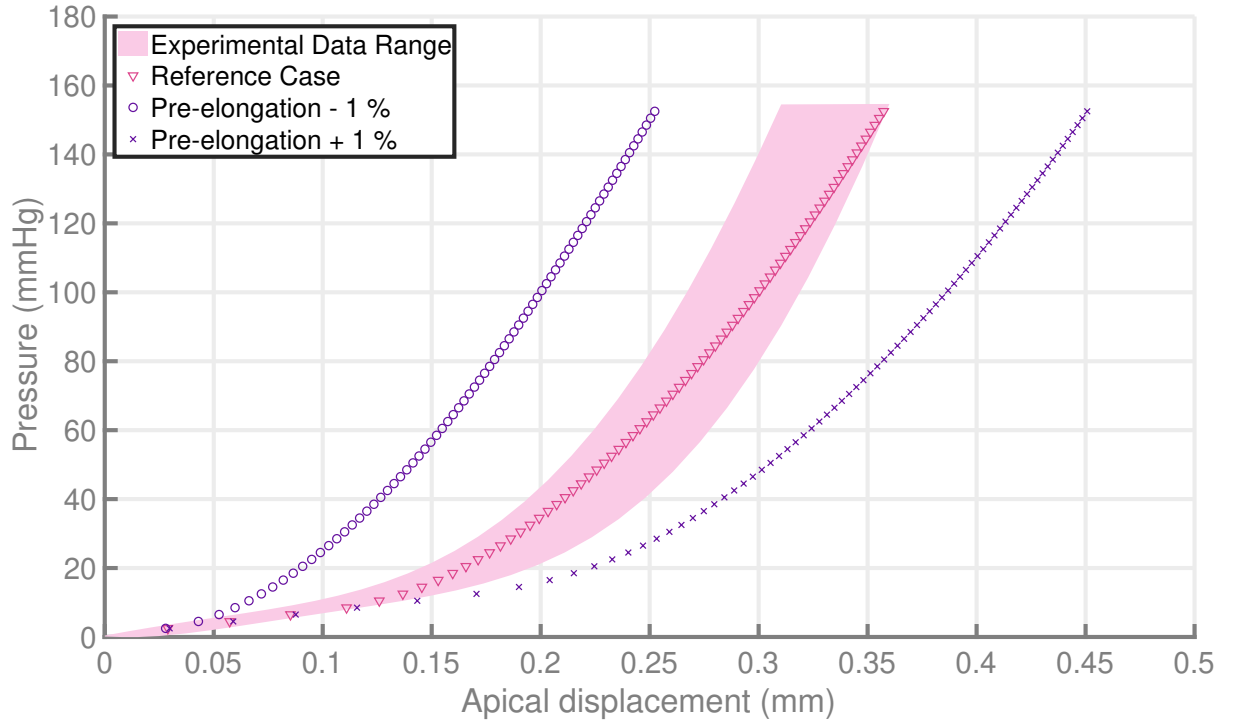


Figure 2.8: Pressure with apical displacement for three different λ_u . Pink zones: envelopes of the experimental data from [45]. '∇': reference case. 'o': 1% decrease of the λ_u . 'x': 1% increase of the λ_u .

2.3.2 Keratoconus: geometrical and mechanical effect

To distinguish between mechanical and geometrical origin of keratoconus, we first simulated a healthy and a stage 4 keratoconic cornea with "reference" mechanical parameters, and compared with the observations from McMonnies and Boneham [100]. They showed that the simK of the healthy corneas does not change significantly for a change of intra-ocular pressure in the range of 15 – 30mmHg whereas the simK of keratoconic corneas increases of 2 diopters. Figure 2.9 shows the simulated keratometry (or simK) as a function of the applied pressure: for the "reference" parameters (∇ symbols, see table 2.3) in both healthy (pink) and keratoconic (purple) corneas, the simK does not change significantly (less than 0.5 diopter). This implies that a modification of the mechanical properties is needed to reproduce the keratoconus response.

Then, we modified the mechanical parameters to obtain a change of keratometry of 2 diopters, by a manual adjustment. We modified separately the non-fibrillar matrix stiffness ($\kappa_1^{apparent}$), the distributed fibril stiffness ($C_i * k_{lam}$), or the pre-elongation (λ_u). The weakening of the cornea (by changing either matrix or fibrillar stiffness) is done using the thickness of the cornea at each nodes: we consider that the thinner the cornea, the smaller the stiffness of the component. The only parameter that gives a significant change of diopter without changing of order of magnitude is the fibril stiffness k_{lam} , the mean values of distributed lamellae stiffnesses ($C_1 * k_{lam}$) and ($C_2 * k_{lam}$) decreasing by around 40 and 30% respectively. Table 2.3 gives the changed parameters of each simulation. To obtain a change of 1 diopter by weakening the matrix, a two orders of magnitude change was needed on $\kappa_1^{apparent}$, and no set of parameters was found to have a change greater than 0.3 diopter thanks to a variation of the pre-elongation parameters λ_u . Figure 2.9 shows the simK variation with pressure

of the reference and weakened fibril stiffness cases. Our results show that the keratoconus pressure response can easily be captured by a change in the mechanical behavior, even if we changed the parameters slightly differently for healthy and keratoconic corneas.

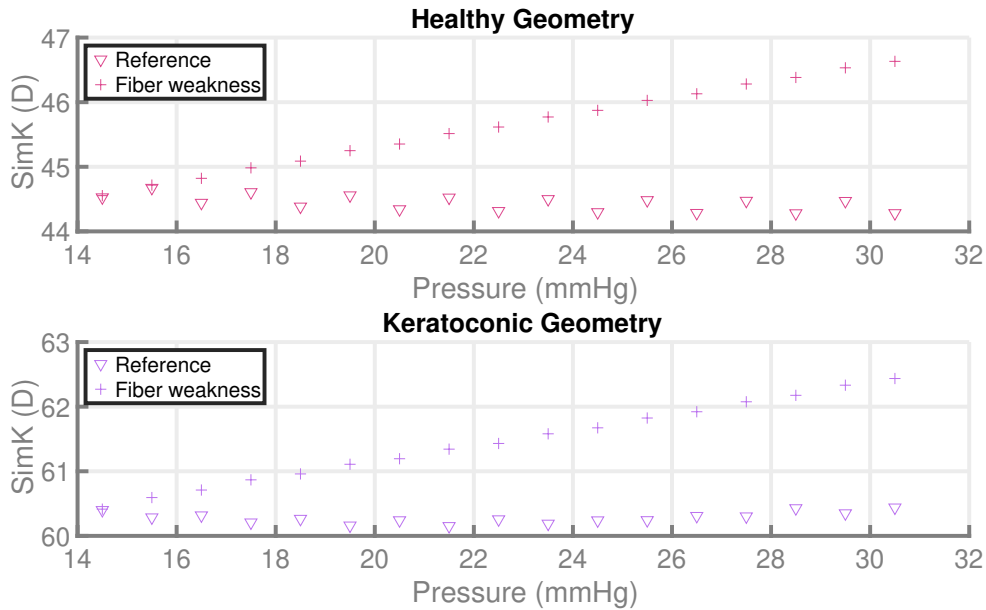


Figure 2.9: Computation of the SimK for the reference and fiber weakness cases considered in table 2.3 with healthy (up) and keratoconic (down) geometries. Modifying the value of the mechanical parameters of the anisotropic part of the cornea, a variation of 2 diopters can be observed.

Figure 2.10 presents the stresses in the Nasal-Temporal (NT) and Superior-Inferior (SI) directions for healthy and keratoconic geometries, without and with mechanical weaknesses at physiological pressure (all the other components of the stress are presented in Supplementary Material 2.8.1, Fig. 2.16 – 2.20). The pattern at the boundary is due to the highly rigid boundary condition, and is heterogeneous in the thickness. Both healthy and keratoconic corneas show a higher concentration of the stress in the central region of the anterior surface (even higher in the keratoconic case), whereas the stress in the posterior surface is quite homogeneous. This means that the geometry has a strong impact on the stress, even if it does not affect the keratometry response. On the contrary, modifications of the mechanical parameters do not affect the pattern strongly - mainly smoothing it. This indicates that the stress distribution is mostly due to the fiber distribution, except at the vicinity of the corneal boundary.

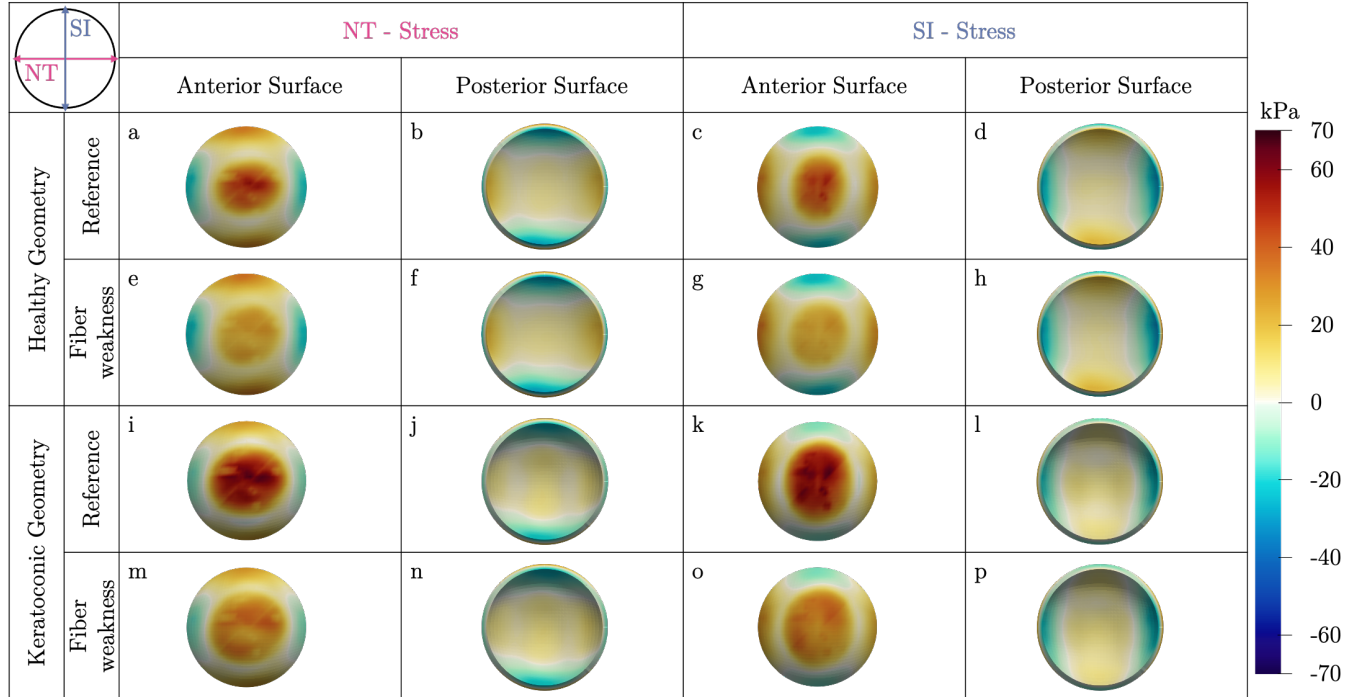


Figure 2.10: Cauchy stress at physiological pressure for different cases of mechanical weaknesses in the cornea with healthy and keratoconic geometries. Fig. 2.10a-h: Naso-Temporal and Superior-Inferior stresses for the healthy geometry (a-d: reference case and e-h: case of the fibril weakness with an increase of 2 diopters between 15 and 31 mmHg) on the anterior and posterior surfaces. Fig. 2.10i-p: Naso-Temporal and Superior-Inferior stresses for the keratoconic geometry on the anterior and posterior surfaces (i-l: reference case and m-p: case of the fibril weakness with an increase of 2 diopters between 15 and 31 mmHg).

2.3.3 Induced keratoconus

So far, we have separated the problem of the geometry and of the mechanical parameters: we have chosen either the healthy parameters and changed the geometry, or chosen an observed geometry and modified the mechanical parameters. In both cases, we show that the change in diopter associated with keratoconus response cannot be explained by the change in geometry but can be reproduced by a decrease in the mechanical properties, in particular of the fiber rigidity. To do so, we started from an observed geometry, and simulated a stress-free configuration, obtained such that it reproduces at physiological pressure the observed geometry, for the chosen set of mechanical parameter. This means that the keratoconic cornea has a stress-free configuration which is different from the healthy cornea. Here, we ask ourselves what will be the geometry of a cornea under pressure if we use the keratoconic mechanical parameters on the healthy-stress cornea geometry: we would like to see if the change of mechanical parameters is able to recreate the keratoconic geometry.

We first determine the stress-free configuration of our reference case (healthy geometry, with reference mechanical parameters), and simulated the response of the cornea at different pressures for weakened fibril stiffness corresponding to a 2 diopter increase.

Figure 2.11 shows the computed SimK for this new case. We also reproduced the simulation of the reference case, which leads to a constant SimK (see Fig. 2.9). The decreased mechanical properties lead to a higher SimK at physiological pressure than for the reference case, although it is smaller than the one for the simulation starting from keratoconic stress-free configuration (around 61 D).

This reflects the fact that a different stress-free configuration will lead to a different geometry under pressure, and is in line with stage-1 keratoconus based on Krumeich's classification [114]. We also observe an increase of 2 diopters, consistent with a keratoconic response.

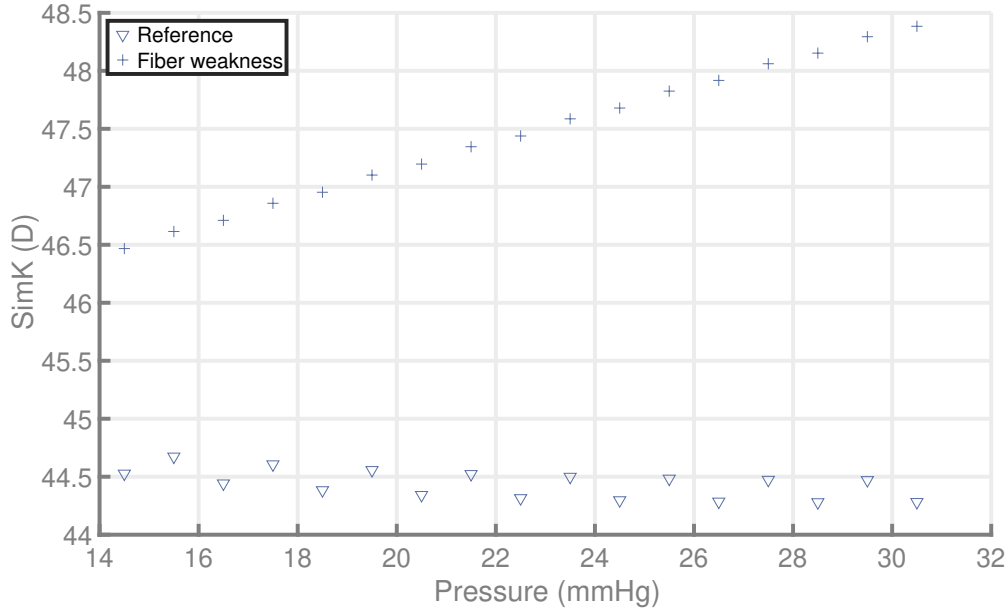


Figure 2.11: SimK computed for the different cases of mechanical weakness on the reference stress-free configuration.

Figure 2.12 presents the NT and SI stress distributions for the reference and mechanical weakness cases (all the other components of the stress are presented in Supplementary Material 2.8.2, Fig. 2.21 – 2.25). The distributions of stresses are very similar to those in Fig. 2.10, in agreement with our previous observation that this stress pattern is more controlled by the fiber distribution than by the cornea geometry.

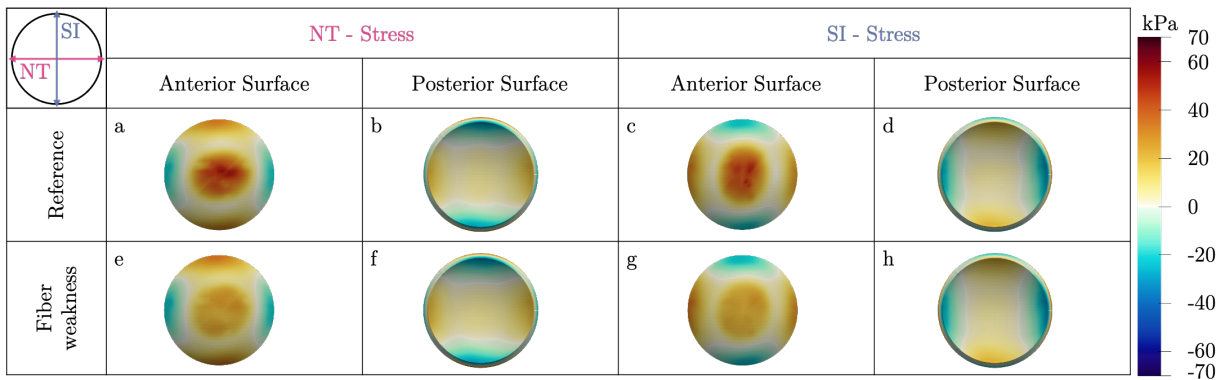


Figure 2.12: Stress at physiological pressure with reference parameters and mechanical weakening of the cornea with healthy geometry and stress-free configuration of the reference case used for every computation. Fig. 2.12a-d: Naso-Temporal and Superior-Inferior stresses for the reference case a, Fig. 2.12e-h: Naso-Temporal and Superior-Inferior stresses for case of the fibril weakness with an increase of 2 diopters between 15 and 31 mmHg.

Figure 2.13 shows the elevation maps obtained at physiological pressure and at $P = 30$ mmHg,

for the reference case and for the weakened mechanical properties. The fibril weakening does not lead to a major change of the elevation, but we can see that in the posterior surface, the elevation in the central region is higher than in the reference case (it is even clearer at 30 mmHg), which can lead to the suspicion of a very early stage of a keratoconus. Those results are coherent with the value of the SimK at physiological pressure previously computed and tend to indicate that the keratoconus may appear following a weakening of the anisotropic part of the cornea. On the other hand, elevation maps do not show an off-centered elevation (neither an off-centered thinning on thickness maps is seen) that could lead to suspect a keratoconus [12; 41]. Indeed the quasi-incompressibility of the cornea does not allow for a significant change in the cornea geometry with a thinning of the cone region, thus it cannot change to become an advanced stage keratoconic cornea, although the change of diopter - and thus the change of curvature radii - is coherent with a keratoconus.

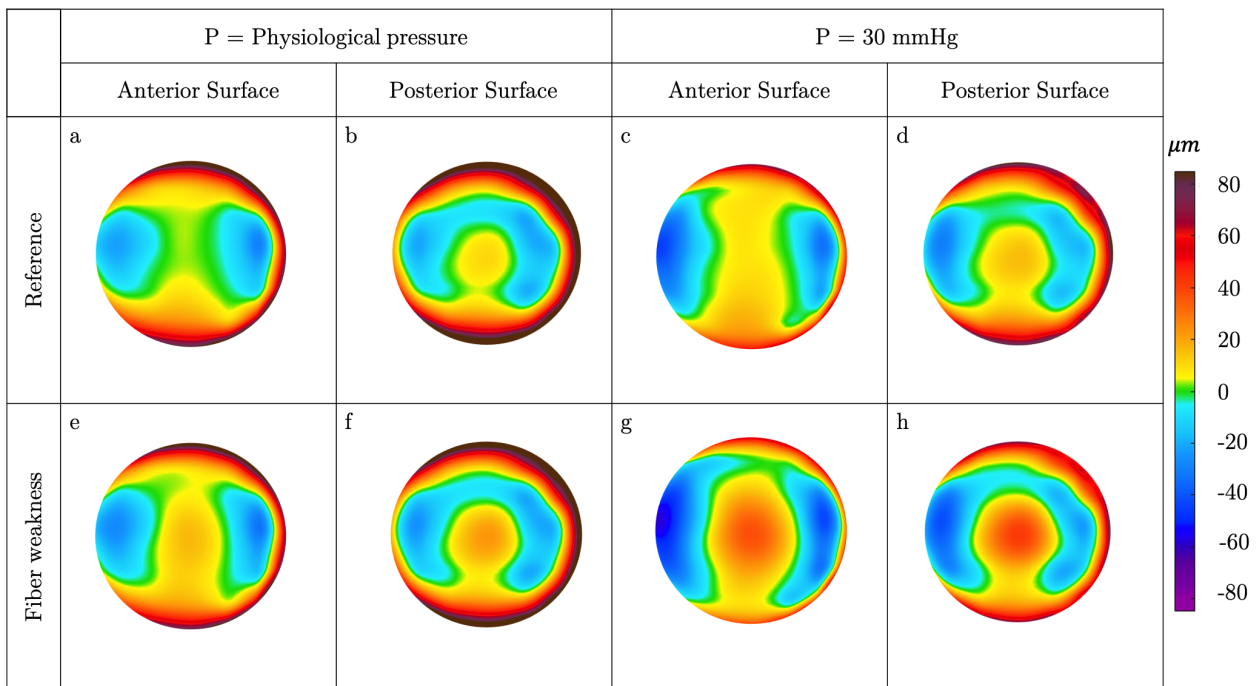


Figure 2.13: Anterior and posterior elevation maps with respect to the best fit spheres for the reference (a-d) and weakened fiber (e-f) cases at physiological pressure (a,b,e,f) and for $P = 30$ mmHg (c,d,g,h).

2.4 Discussion

To investigate the origin of keratoconus, we have compared the effects of a change in geometry and of a change in mechanical properties. To do so, we constructed a patient-specific mesh, which reproduces the geometry measured in clinic. We have built a multi-scale model, which contains explicitly the different contributions (fibrils, isotropic matrix, etc.), but it was not possible to obtain patient-specific data for these parameters. The collagen organization was obtained from experimental observations (X-ray [1] or SHG [176]). The different mechanical stiffnesses were manually calibrated to reproduce the reported data [45]. As we have access only to the displacement of the apex in human cornea, with a variability between corneas, we did not try a proper identification. This implies that our "reference" set of parameters may not be unique. Corneal strain maps have been measured on other animals (as

bovine [23]), but then the keratoconus geometry is not available on the same animal.

We have tested the influence of small variations of each mechanical parameter, and we observed that the most sensitive one is the unfolding stretch, i.e. the stretch at which the fibrils start to generate force. Associated with our observation that the stress distribution corresponds to the fibril distribution (Fig. 2.10), this supports the idea that the forces in the cornea are mainly due to the fibrils, and only partly to the isotropic matrix or the volume variation. Note that the fibers become more and more unfolded as the pressure increases above physiological pressure, contributing to the increase of the tissue stiffness (see Fig. 2.8). This is in agreement with recent results obtained by elastography showing an increase in corneal stiffness (Young's modulus and/or shear modulus) with pressure on porcine [64; 138], bovine [92; 132] or rat [165] corneas. SHG observations of the lamellae show straight fibrils [14; 91]: the unfolding transition may be due to the fibril organization at smaller scale [13]. In any case, it implies that the fibril tensions play a major role in the corneal response, which could have an impact on the recovery of the cornea after a laser surgery. It has been shown that the cornea can become softer after LASIK surgery [63; 82; 133; 146] which can be associated with a destructuring of the collagen lamellae. Our study supports the use of cross-link treatments after surgery, which are known to make the cornea stiff again.

We simulated the inflation of a cornea with a keratoconic geometry. Using directly our reference mechanical parameter fails to reproduce the reported variation of keratometry during the inflation test [100]. This shows that keratoconic geometry alone (thinner cornea) is not enough to have a keratoconic behavior. However, a 30 to 40 % decrease in the average fiber stiffnesses allows our model to reproduce the 2 diopters variations, even for healthy geometries. Thus, our approach shows that mechanical weakening, contrary to the geometry, is able to reproduce the keratoconus changes in SimK, emphasizing the importance of mechanical weakening on the keratoconic response. The weakened parameters reproducing the keratoconus behavior (see Table 2.3) indicate that it requires a relatively small decrease of the fibril stiffness to obtain a 2 diopter variation. This points toward the key role of the collagen lamellae in the development of the keratoconus, in agreement with the proposed treatments by the addition of cross-links.

By using the weakened mechanical parameters on the healthy stress-free configuration (see Fig. 2.13), we were able to reproduce partly a keratoconic shape at physiological pressure. This again supports the idea that the primary motor of the keratoconus is a weakening of the collagen fibrils, consistent with the disorganization of the lamellae observed in [104]. However, access to micro-structural information *in-vivo* is not yet technically possible and so the keratoconus is often detected at a late stage using elevation maps, while new techniques are now able to measure *in-vivo* the local cornea rigidity, such as optical coherence elastography [81]. An early detection of a mechanical weakening is a promising approach for the diagnosis of keratoconus. Coupled to patient-specific geometry, they can be used to simulate the location of the keratoconus as well as the consequence of a stiffening treatment such as riboflavin cross-linking usually used to stop early keratoconus. Still, our obtained shape is not the one of a real keratoconus, with a large elevation peak slightly off-centered. This may come from our quasi-incompressibility assumption, which prevents a thinning of the cornea. But more likely, to go further in the modeling of the keratoconus, we need a better understanding of the remodeling going on inside the tissue.

2.5 Conclusions

In this paper, we have built a multi-scale model of the cornea, coupled to a patient-specific geometry to investigate the origin of the keratoconus. We have first used our model to reproduce the pressure versus apex displacement curve from Elsheikh et al. [45] and determined a reference set of mechanical parameters, describing a healthy cornea. We show that the central element of the mechanical response is the one of the fibrils, and in particular their prestretch.

Our simulation of cornea with keratoconic geometry but healthy mechanical parameters shows that the geometry change is not able to reproduce the response of keratoconic cornea to an increase of the intraocular pressure [100]. In fact, we showed that the keratoconic response is well reproduced when the mechanical properties are altered, whatever the initial geometry, and that the main component involved in this response is the lamellae stiffness. The lamellae weakening is even sufficient to obtain a shape resembling an early-stage keratoconus.

Although they could be completed by a better description of the induced remodeling, our simulations show the importance of a fine measurement of the mechanical properties for the early diagnosis of keratoconus, as it appears to be the motor of the pathology.

Acknowledgment We kindly thank A. Pandolfi for providing the 3D mesh code, K. M. Meek and S. Hayes for the corneal X-ray experimental data and J. Knoeri and V. Borderie for providing elevation and thickness maps.

Authors' contribution C.G. and P.L.T designed the model. C.G. and J.D. implemented the model. C.G. performed the simulations, and analyzed the results. C.G. and J.M.A. discussed the results. J.M.A. supervised the research. All authors read and approved the manuscript.

Competing interests The authors declare no competing interests.

Financial disclosure No funding has been received for this article.

Supplementary Materials

2.6 Sensitivity analysis

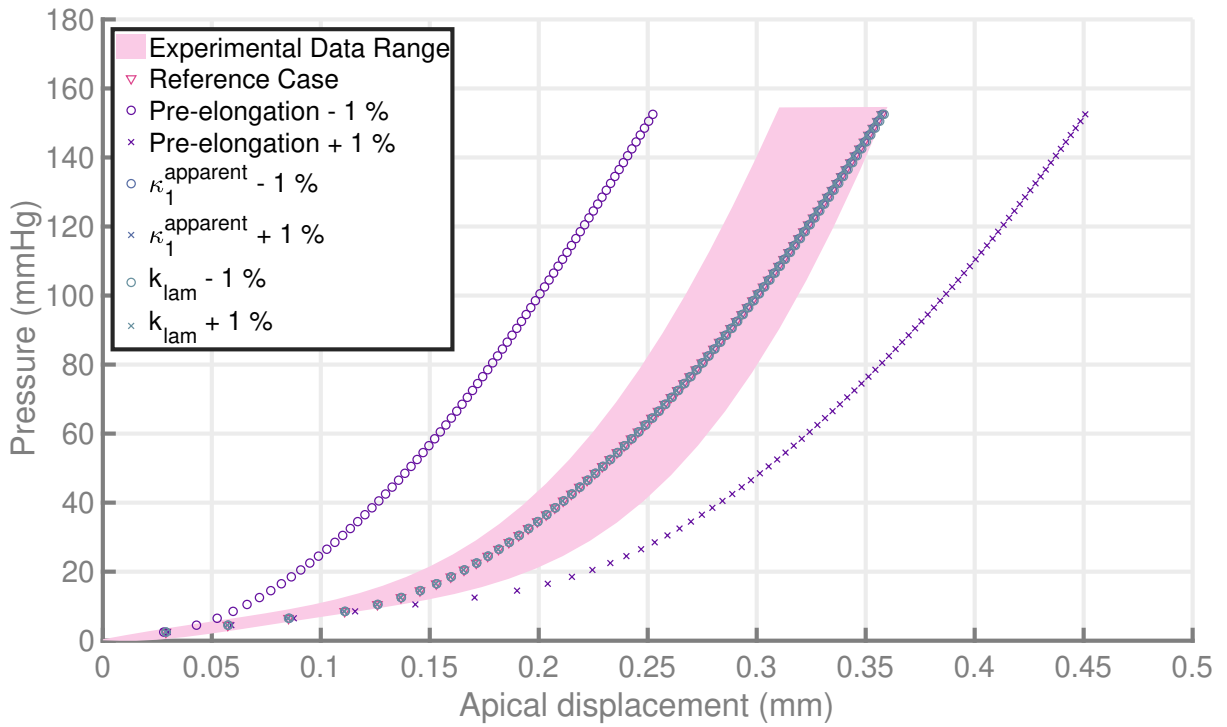


Figure 2.14: Pressure with apical displacement for sensitivity analysis cases. Pink zones: envelopes of the experimental data from [45]. '∇' markers curve: reference case. 'o' violet markers curve: 1% decrease of the λ_u . 'x' violet markers curve: 1% increase of the λ_u . 'o' blue markers curve: 1% decrease of the $\kappa_1^{apparent}$. 'x' blue markers curve: 1% increase of the $\kappa_1^{apparent}$. 'o' green markers curve: 1% decrease of the k_{lam} . 'x' green markers curve: 1% increase of the k_{lam} .

2.7 Mechanical parameters used in the computation

Geometry	Healthy (associated stress-free configuration)	Keratoconic (associated stress-free configuration)
Ref = no mechanical weakness	RefH (Ω_0^{RefH})	RefK (Ω_0^{RefK})
ElongM1 = Pre-elongation minus one percent	ElongM1 ($\Omega_0^{ElongM1}$)	/
ElongP1 = Pre-elongation plus one percent	ElongP1 ($\Omega_0^{ElongP1}$)	/
Fib2 = Mechanical weakness on the lamellae leading to a 2 diopters change	Fib2H (Ω_0^{Fib2H}) and Fib2H2 (Ω_0^{RefH})	Fib2K (Ω_0^{Fib2K})

Table 2.2: Cases considered in the mechanical study of keratoconic cornea (Sec. 2.3.2 and 2.3.3). The reference case for healthy geometry (RefH) corresponds to the ones calibrated on Elsheik's group data (see Sec. 2.3.1). Between brackets are noted the stress-free meshes $\Omega_{0, stress-free}$ used for each computational cases.

Parameter	Case considered				
	RefH / RefK	ElongM1	ElongP1	Fib2H / Fib2H2	Fib2K
Average of distributed isotropic coefficient κ_1 (MPa)	0,97	0,97	0,97	0,97	0,97
Minimum "unfolding" elongation $\lambda_{u,min}$	1,0195	1,0093	1,0297	1,0195	1,0195
Maximum "unfolding" elongation $\lambda_{u,max}$	1,0245	1,0143	1,0347	1,0245	1,0245
Average of distributed anisotropic coefficient $C_1 * k_{lam}$ (MPa)	7,15	7,15	7,15	4,10	4,11
Average of distributed anisotropic coefficient $C_2 * k_{lam}$ (MPa)	18,70	18,70	18,70	12,43	12,76

Table 2.3: Mechanical parameters used in the different computations on the cornea. The different cases are presented in Table 2.2. For the distributed parameters (κ_1 , $C_1 * k_{lam}$ and $C_2 * k_{lam}$) the average values on all over the cornea are given.

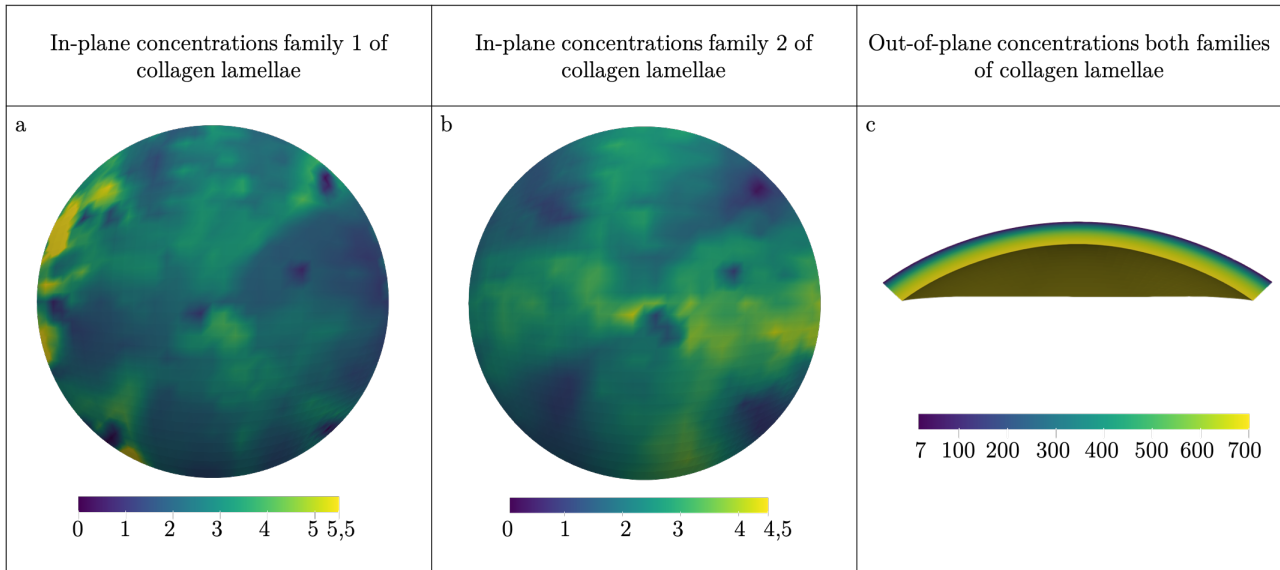


Figure 2.15: In-plane and out-of-plane concentrations of the collagen lamellae. a-b. In-plane concentrations of the two families of fibers. c. Out-of-plane concentration of the two families of collagen lamellae. In all the cases, the greater the concentration κ the smaller the dispersion.

2.8 Stresses representation

2.8.1 Keratoconus: geometrical and mechanical effect

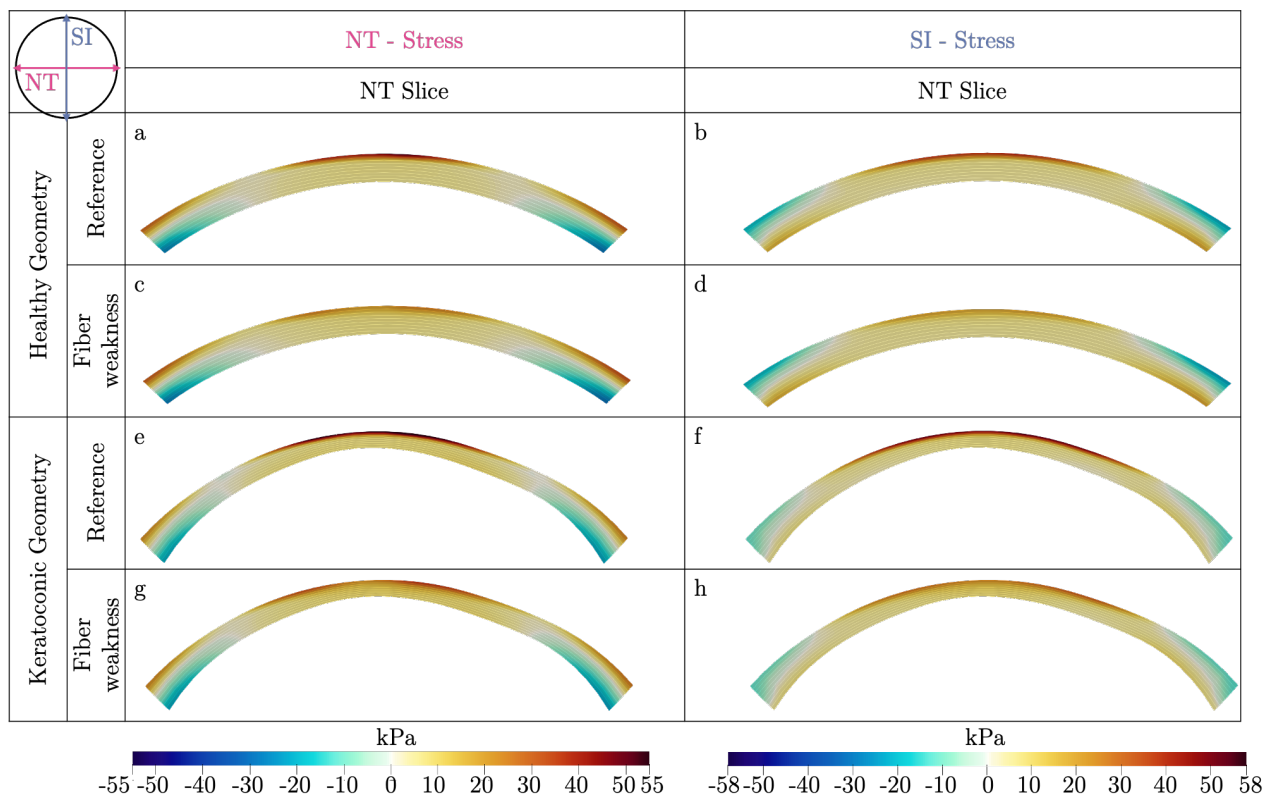


Figure 2.16: Cauchy stress at physiological pressure for different cases of mechanical weaknesses in the cornea with healthy and keratoconic geometries. Fig. 2.16a-d: Naso-Temporal and Superior-Inferior stresses for the healthy geometry (a-b: reference case and c-d: case of the fibril weakness with an increase of 2 diopters between 15 and 31 mmHg) on the central NT slice of the cornea. Fig. 2.16a-f: Naso-Temporal and Superior-Inferior stresses for the keratoconic geometry (e-f: reference case and g-h: case of the fibril weakness with an increase of 2 diopters between 15 and 31 mmHg) on the central NT slice of the cornea.

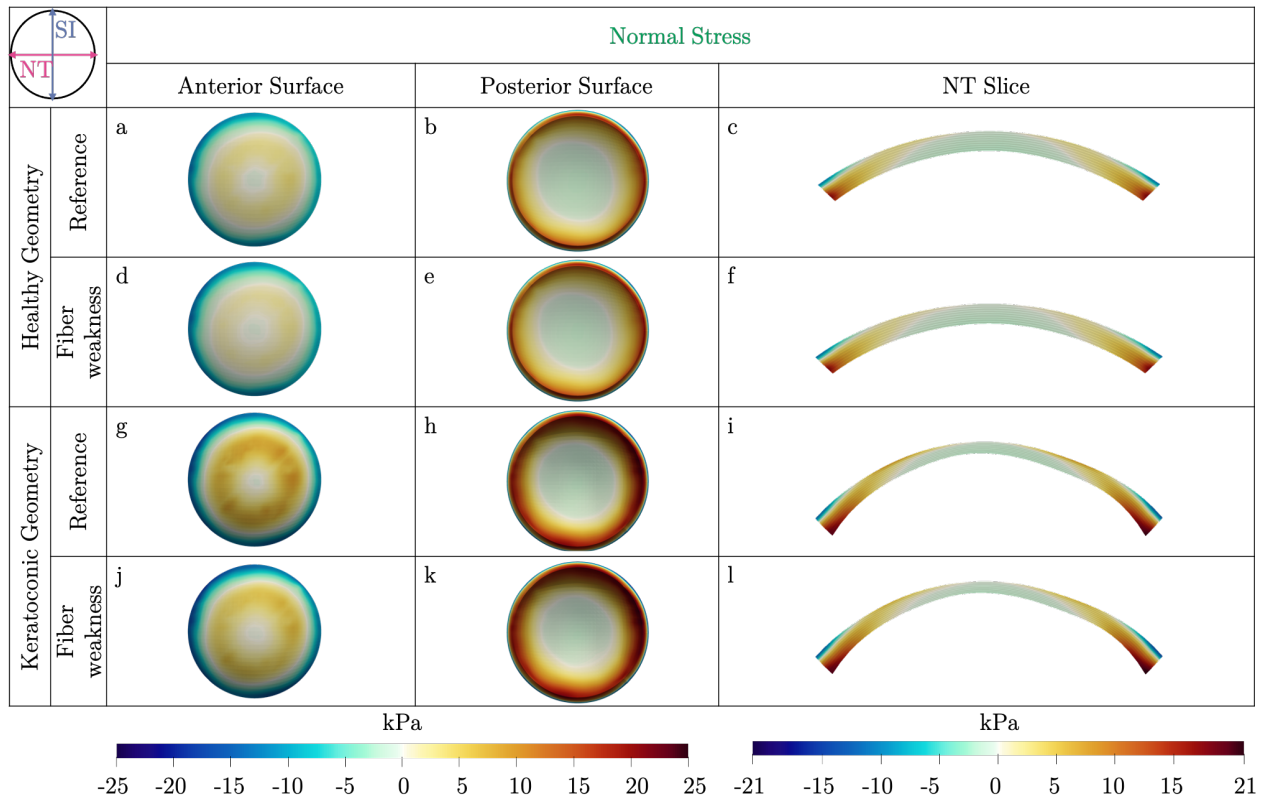


Figure 2.17: Cauchy stress at physiological pressure for different cases of mechanical weaknesses in the cornea with healthy and keratoconic geometries. Fig. 2.17a-f: Normal stress for the healthy geometry (a-c: reference case and d-f: case of the fibril weakness with an increase of 2 diopters between 15 and 31 mmHg) on the anterior (a,d) and posterior (b,e) surfaces and central NT slice (c,f) of the cornea. Fig. 2.17e-h: Normal stress for the keratoconic geometry (g-i: reference case and j-l: case of the fibril weakness with an increase of 2 diopters between 15 and 31 mmHg) on the anterior (g,j) and posterior (h,k) surfaces and central NT slice (i,l) of the cornea.

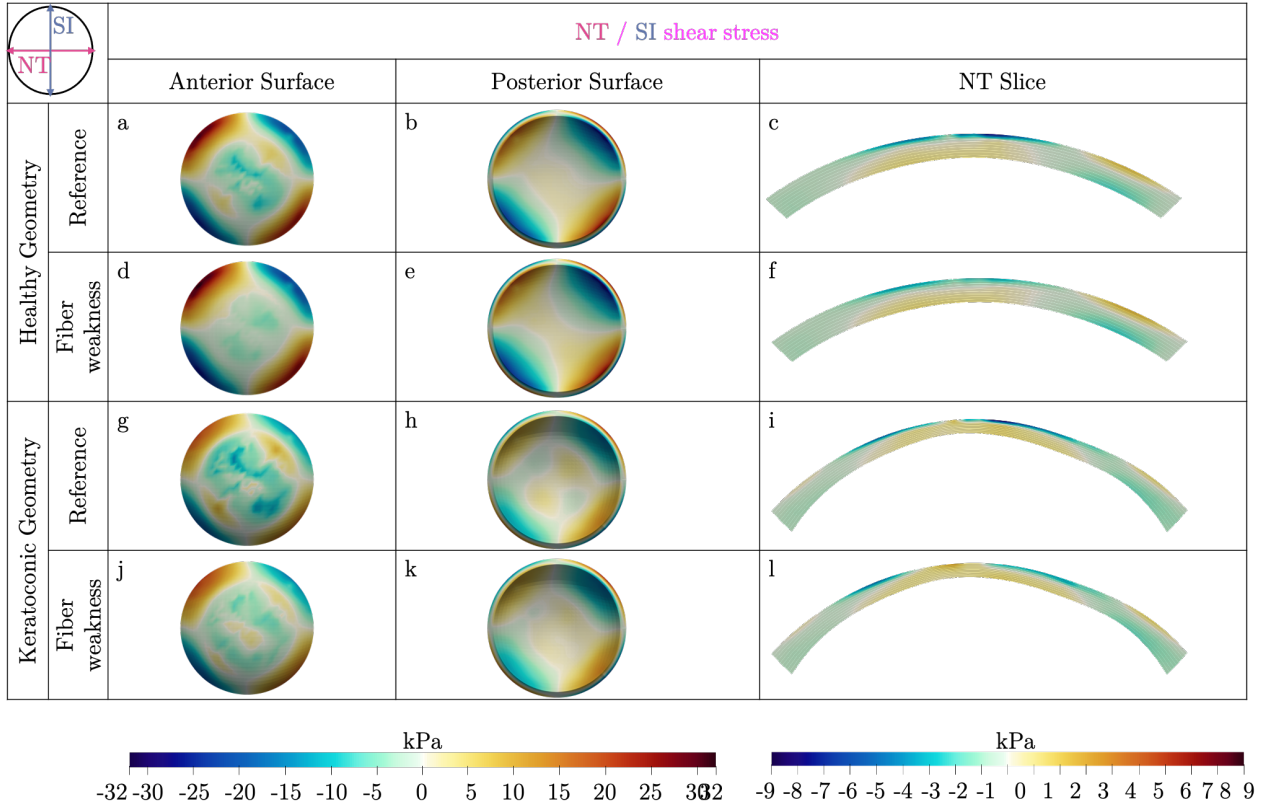


Figure 2.18: Cauchy stress at physiological pressure for different cases of mechanical weaknesses in the cornea with healthy and keratoconic geometries. Fig. 2.18a-f: NT/SI shear stress for the healthy geometry (a-c: reference case and d-f: case of the fibril weakness with an increase of 2 diopters between 15 and 31 mmHg) on the anterior (a,d) and posterior (b,e) surfaces and central NT slice (c,f) of the cornea. Fig. 2.18g-l: NT/SI shear stress for the keratoconic geometry (g-i: reference case and j-l: case of the fibril weakness with an increase of 2 diopters between 15 and 31 mmHg) on the anterior (g,j) and posterior (h,k) surfaces and central NT slice (i,l) of the cornea.

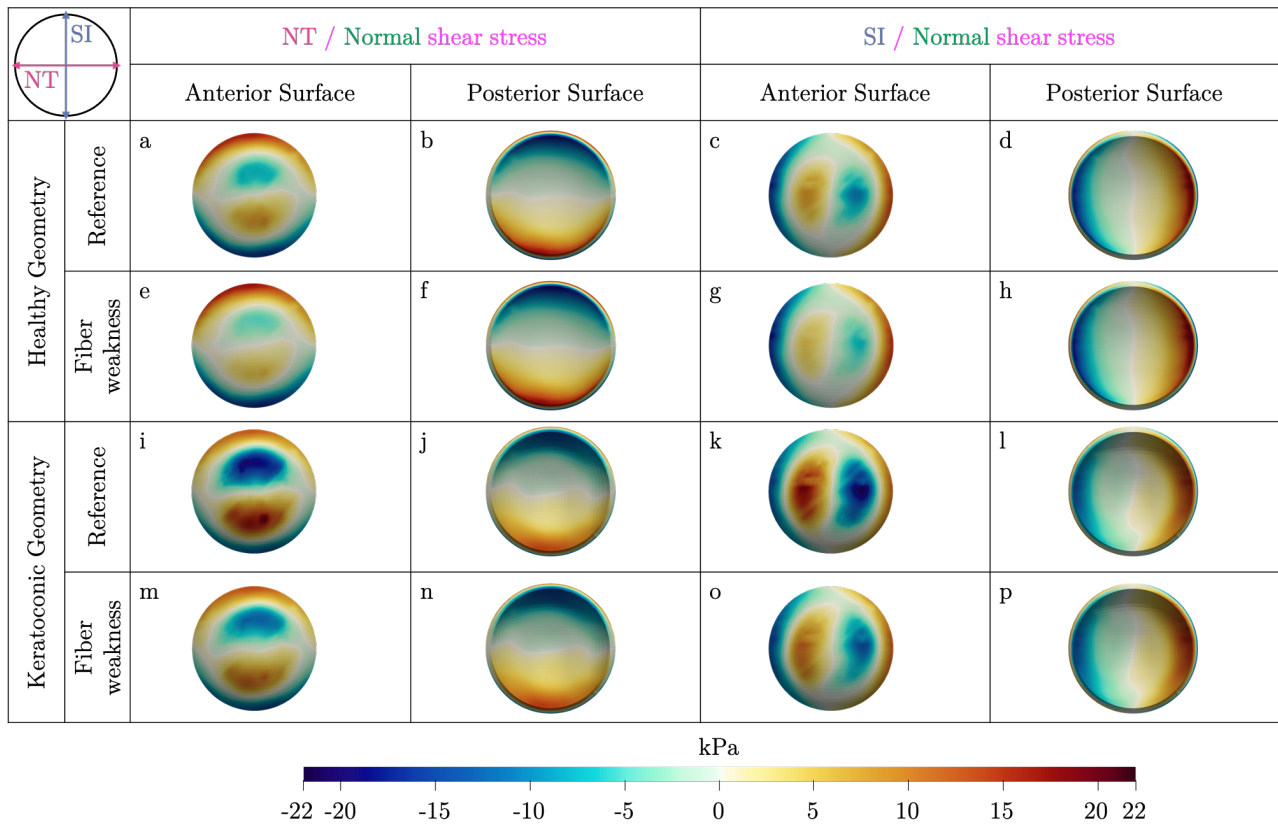


Figure 2.19: Cauchy stress at physiological pressure for different cases of mechanical weaknesses in the cornea with healthy and keratoconic geometries. Fig. 2.19a-h: NT / Normal and SI / Normal shear stresses for the healthy geometry (a-d: reference case and e-h: case of the fibril weakness with an increase of 2 diopters between 15 and 31 mmHg) on the anterior and posterior surfaces. Fig. 2.19i-p: NT / Normal and SI / Normal shear stresses for the keratoconic geometry on the anterior and posterior surfaces (i-l: reference case and m-p: case of the fibril weakness with an increase of 2 diopters between 15 and 31 mmHg).

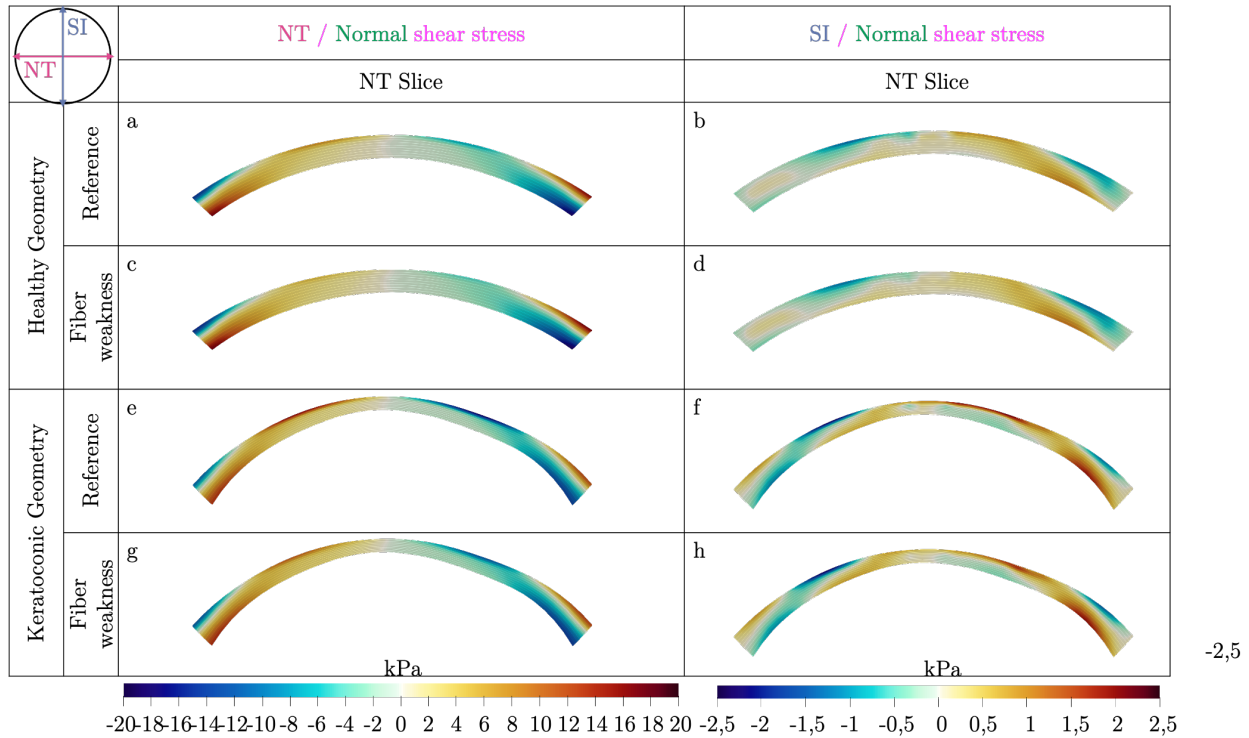


Figure 2.20: Cauchy stress at physiological pressure for different cases of mechanical weaknesses in the cornea with healthy and keratoconic geometries. Fig. 2.20a-d: NT / Normal and SI / Normal shear stresses for the healthy geometry on the central NT slice of the cornea (a-b: reference case and c-d: case of the fibril weakness with an increase of 2 diopters between 15 and 31 mmHg) on the anterior and posterior surfaces. Fig. 2.20a-f: NT / Normal and SI / Normal shear stresses for the keratoconic geometry on the central NT slice of the cornea (e-f: reference case and g-h: case of the fibril weakness with an increase of 2 diopters between 15 and 31 mmHg).

2.8.2 Induced keratoconus

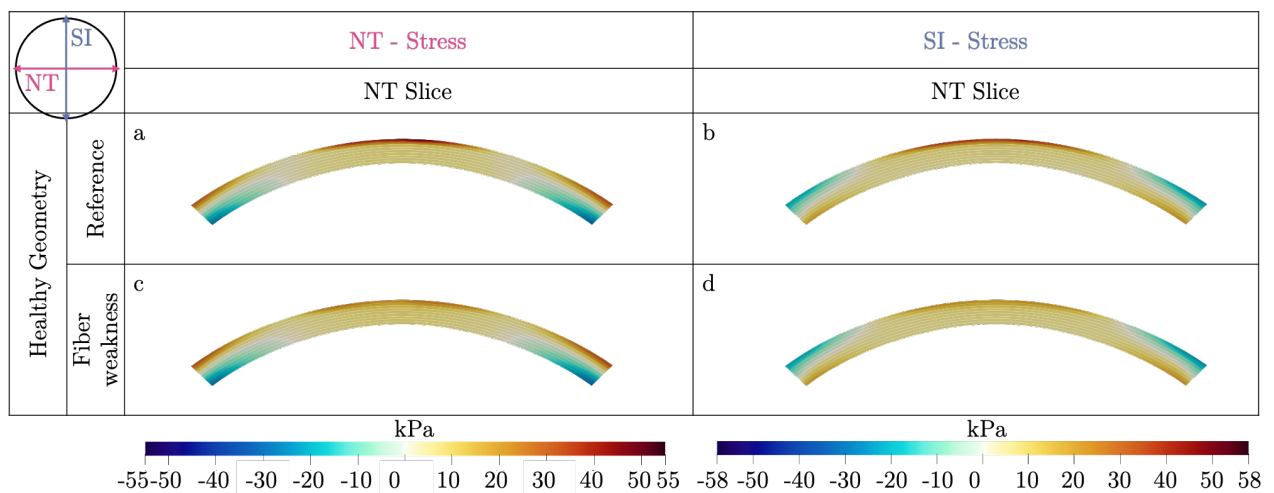


Figure 2.21: Stress at physiological pressure with reference parameters and mechanical weakening of the cornea with healthy geometry and stress-free configuration of the reference case used for every computation. Fig. 2.21a-d: Naso-Temporal and Superior-Inferior stresses for the healthy geometry (a-b: reference case and c-d: case of the fibril weakness with an increase of 2 diopters between 15 and 31 mmHg) on the central NT slice of the cornea.

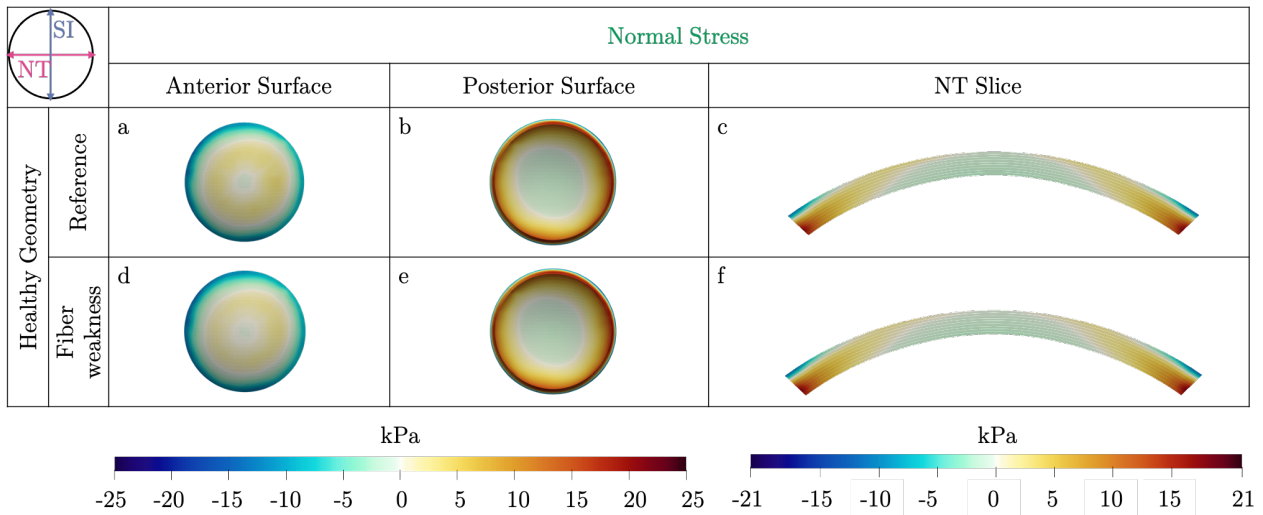


Figure 2.22: Stress at physiological pressure with reference parameters and mechanical weakening of the cornea with healthy geometry and stress-free configuration of the reference case used for every computation. Fig. 2.22a-f: Normal stress for the healthy geometry (a-c: reference case and d-f: case of the fibril weakness with an increase of 2 diopters between 15 and 31 mmHg) on the anterior (a,d) and posterior (b,e) surfaces and central NT slice (c,f) of the cornea.

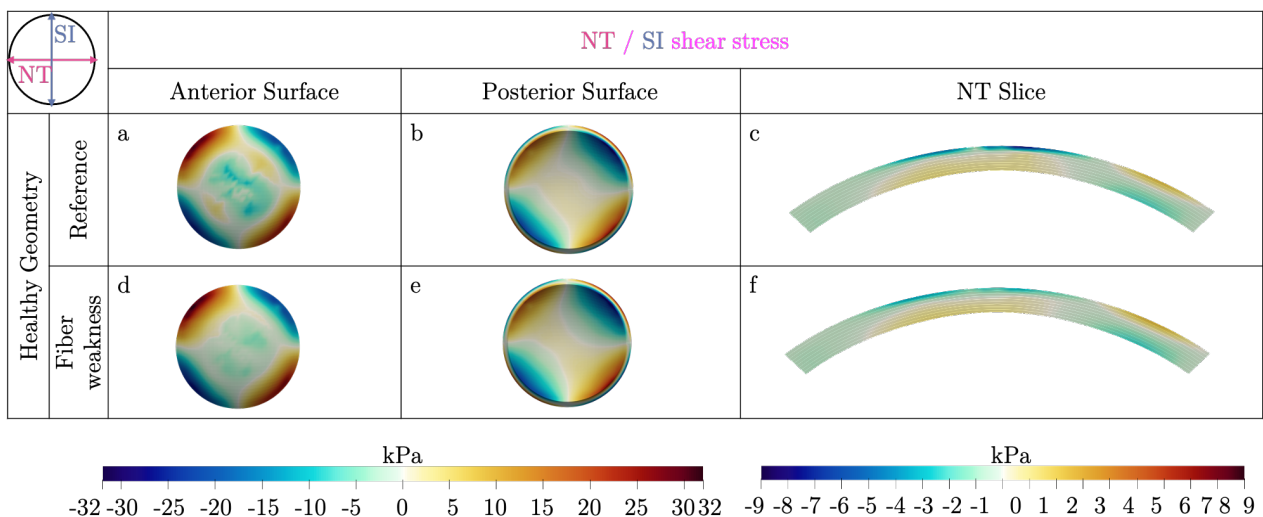


Figure 2.23: Stress at physiological pressure with reference parameters and mechanical weakening of the cornea with healthy geometry and stress-free configuration of the reference case used for every computation. Fig. 2.23a-f: NT/SI shear stress for the healthy geometry (a-c: reference case and d-f: case of the fibril weakness with an increase of 2 diopters between 15 and 31 mmHg) on the anterior (a,d) and posterior (b,e) surfaces and central NT slice (c,f) of the cornea.

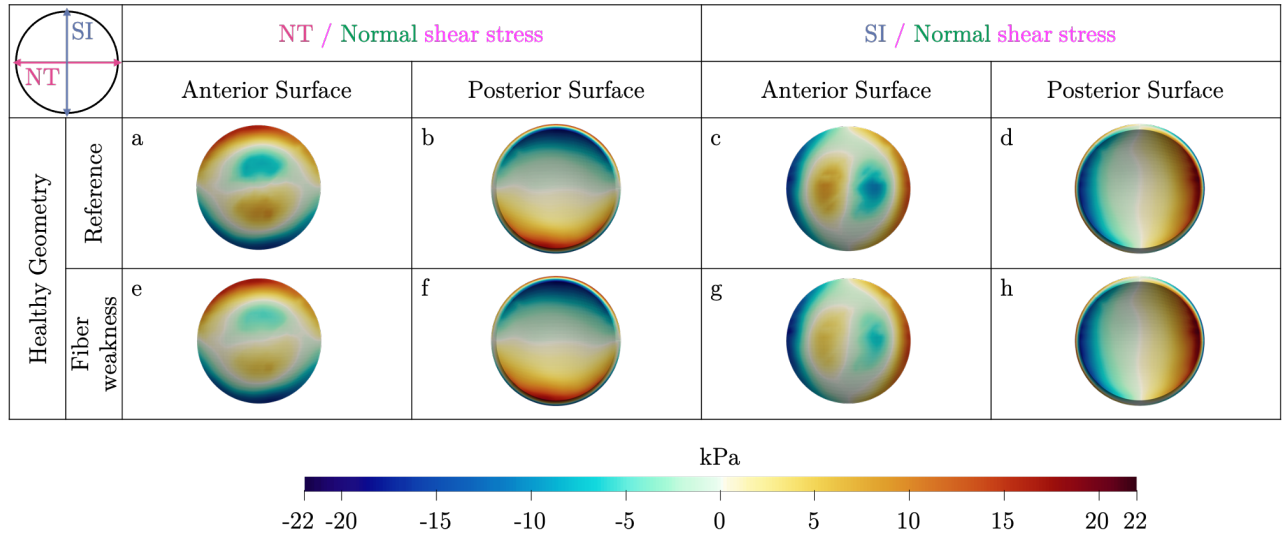


Figure 2.24: Stress at physiological pressure with reference parameters and mechanical weakening of the cornea with healthy geometry and stress-free configuration of the reference case used for every computation. Fig. 2.24a-h: NT / Normal and SI / Normal shear stresses for the healthy geometry (a-d: reference case and e-h: case of the fibril weakness with an increase of 2 diopters between 15 and 31 mmHg) on the anterior and posterior surfaces.

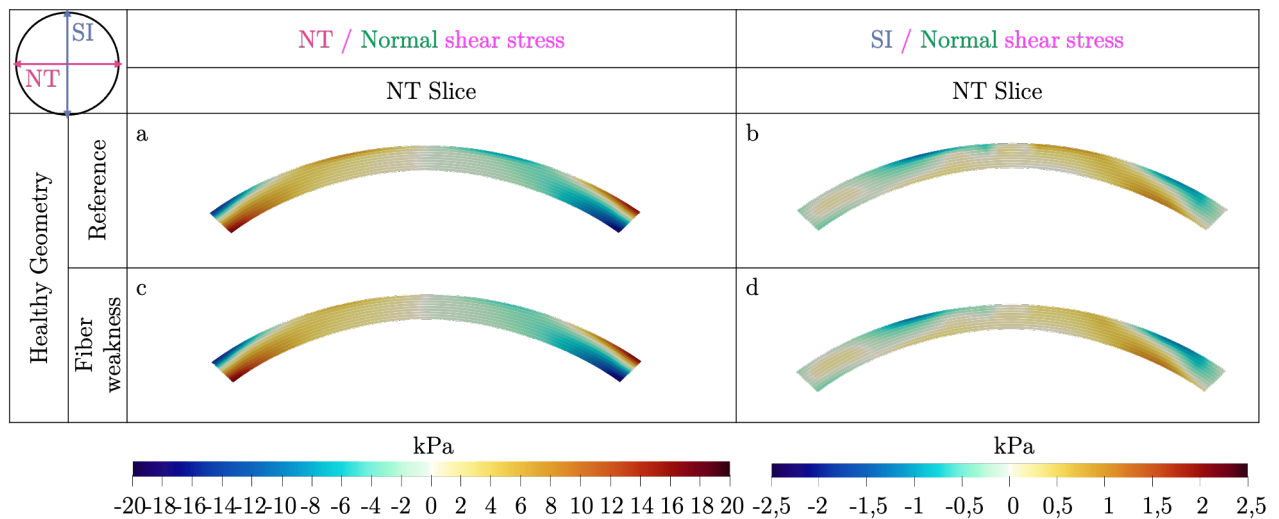


Figure 2.25: Stress at physiological pressure with reference parameters and mechanical weakening of the cornea with healthy geometry and stress-free configuration of the reference case used for every computation. Fig. 2.25a-d: NT / Normal and SI / Normal shear stresses for the healthy geometry on the central NT slice of the cornea (a-b: reference case and c-d: case of the fibril weakness with an increase of 2 diopters between 15 and 31 mmHg) on the anterior and posterior surfaces.

Chapter 3

Full field measurements of the cornea under pressure using Digital Image/Volume Correlation on 2D/3D Optical Coherence Tomography images

Contents

3.1	Introduction	96
3.2	Methods	97
3.2.1	Specimen preparation	97
3.2.2	Experimental apparatus	97
3.2.3	Mechanical tests on the cornea	98
3.2.4	Image analysis	100
3.2.5	Uncertainties quantification	105
3.3	Results	111
3.3.1	Creep test at physiological pressure	111
3.3.2	Creep test at high pressure	127
3.3.3	Comparison of creep tests	142
3.3.4	Inflation tests	144
3.3.5	Summary of the results and discussion	161
3.4	Extension of the hyperelastic model	165
3.4.1	First model: elastic model of auxetic cornea	165
3.4.2	Second model: elasticity coupled with osmotic pressure	167
3.4.3	Superposition of auxetic and osmotic material	169
3.4.4	Summary of model results and discussion	170
3.5	Conclusion	172

3.1 Introduction

Modeling the mechanics of cornea is a valuable tool for the early detection of pathologies, such as keratoconus (Sec. 1.4). Doing so, and more generally modeling the mechanical behavior of a tissue, requires the identification of the relevant parameters (Sec. 1.5.1). In this regard, experiments are key to provide the needed data – such as strain maps or stress/strain curves – for proper parameter identification. In the case of cornea, the available literature is scarce when it comes to experiments, thereby providing a limited amount of data suitable for parameter identification.

As explained in Sec. 1.3, the most commonly used experimental data set for human cornea is the apex displacement with pressure curve [45] although some experiments on strip extensometry [22; 46] or nanoindentation measurements [37; 42; 90] also provided useful data. For human corneas, experiments have been performed mostly *ex-vivo* [13; 14; 37; 42; 45; 90; 110; 111], but *in-vivo* measurements have been performed on animals too, via Optical Coherence Elastography (OCE) for example [115; 140; 161; 171]. On the one hand, OCE has proven that Optical Coherence Tomograph (OCT) is a powerful tool for 2D and 3D corneal imaging. On the other hand, Digital Image/Volume Correlation (DIC/DVC) is a proven technique to derive strain maps from 2D images and 3D volumes (Sec. 1.2.2.b). This method has been successfully used on human hard [169] and soft [94; 180] tissues. However, it generally requires the use of a speckling procedure, in which case the volume correlation is prevented as the speckle alters the image in the third direction, resulting in a usable strain map in two dimensions only. In order to circumvent this limitation and be able to retrieve information on the third dimension, naturally observable patterns emerging from the sample in all directions are a prerequisite [73]. In the case of the cornea, the heterogeneous distribution of the collagen lamellae within the material and the keratocytes provide a distinctive pattern, making it suitable for non-speckling-based measurements. As a result, 2D and 3D OCT images can be used to perform DIC/DVC based on the same approach as in elastography [116]. Although OCE has been widely used recently (Sec. 1.3.2.b), OCT imagery coupled to DIC/DVC [53] has never been attempted to characterize the mechanics of human cornea *ex-vivo* before, to the best of our knowledge.

In the PhD work presented here, I have performed a serie of mechanical tests on human corneas coupled with OCT imaging, which measurements are further analyzed by DIC/DVC. Three different tests are performed: (i) a creep test at physiological pressure to mimic the early mechanical response of the cornea after a transplant, (ii) a creep test at high pressure to characterize the time-dependency of the response of the cornea at high pressure, and (iii) an inflation test to create a reference strain map of the corneal mechanical response to pressure. Strain maps are then computed using DIC/DVC and reveal an unexpected dilatation of the tissue at low and high pressure. In order to better account for the observed behavior and mechanical response of the cornea during the inflation test, I built a model based on an elastic response, including an additional osmotic term similar to [163]. This model suggests that osmotic pressure is a credible hypothesis to model the response of the cornea under pressure, but it does not suffice to capture all the features that were highlighted by the experiments.

3.2 Methods

3.2.1 Specimen preparation

Twenty-one fresh human donor corneas (Fig. 3.1) not suitable for transplant were provided by the Banque Française des Yeux, Paris, France (the data of the corneas are gathered in App. D.1). The corneal button includes the cornea and a 2 to 3 mm of scleral ring, all the other components being removed. For safety reasons, only corneas with a negative serology were selected. Corneas were preserved in a first medium during 7 days after death (Stem α 1; *Stem α , France*) and then transferred to a second medium for a maximum of 21 days (Stem α 2; *Stem α , France*). Both of them make the cornea go in turgescence (swelling of the cornea due to the penetration of water). Finally, 48 hours prior to the experiments, corneas are placed in a third medium (Stem α 3; *Stem α , France*) allowing for their proper deturgescence (i.e. the process by which water is extracted from the cornea so that it recovers its physiological thickness).

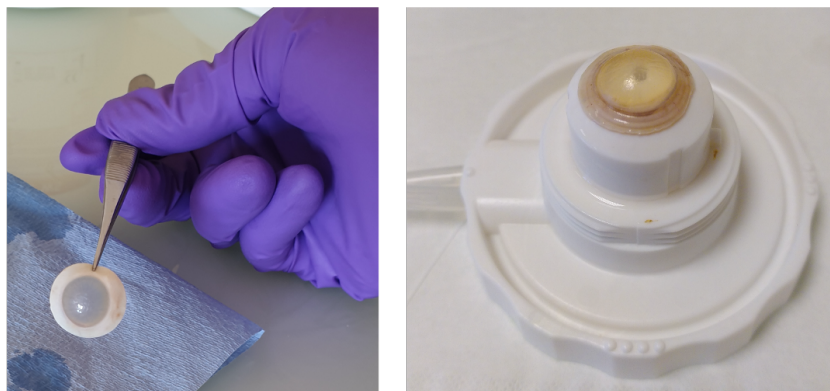


Figure 3.1: Pictures of the cornea prior (left) and after (right) the experiments. On the right picture, the cornea is on the pressure chamber used for the experiments.

3.2.2 Experimental apparatus

The same experimental setup, described in Figure 3.2, was used for all the mechanical tests. The cornea is fixed by the sclera to a pressure chamber (*artificial single-use chamber, Moria, France*) which is filled with Stem α 3 through a bi-valve injector operated by a homemade software. The injected volume (and therefore the flow) is controlled and the pressure at the entrance of the chamber is measured with a pressure sensor (of 1 bar range) accurate to the mbar (*ATM.1ST, STS, France*). 2D and 3D images are acquired using an OCT (*SD-OCT Ganymede – SP5, Thorlabs, Germany*). Parameters used for imaging are as follows: the sensitivity is fixed at 10 kHz and the A-scan images are averaged 4 times. The refractive index is chosen at 1.33 to take into account the ophthalmic gel (Lacrigel 0.2 %, *Europhta Laboratory, Monaco*) used between the tomograph and the cornea to immerse the sample and to maintain hydration of the anterior surface of the tissue. Corneas are placed under the OCT in such a way that the long axis of the cornea is always in the same direction with respect to the field of view.

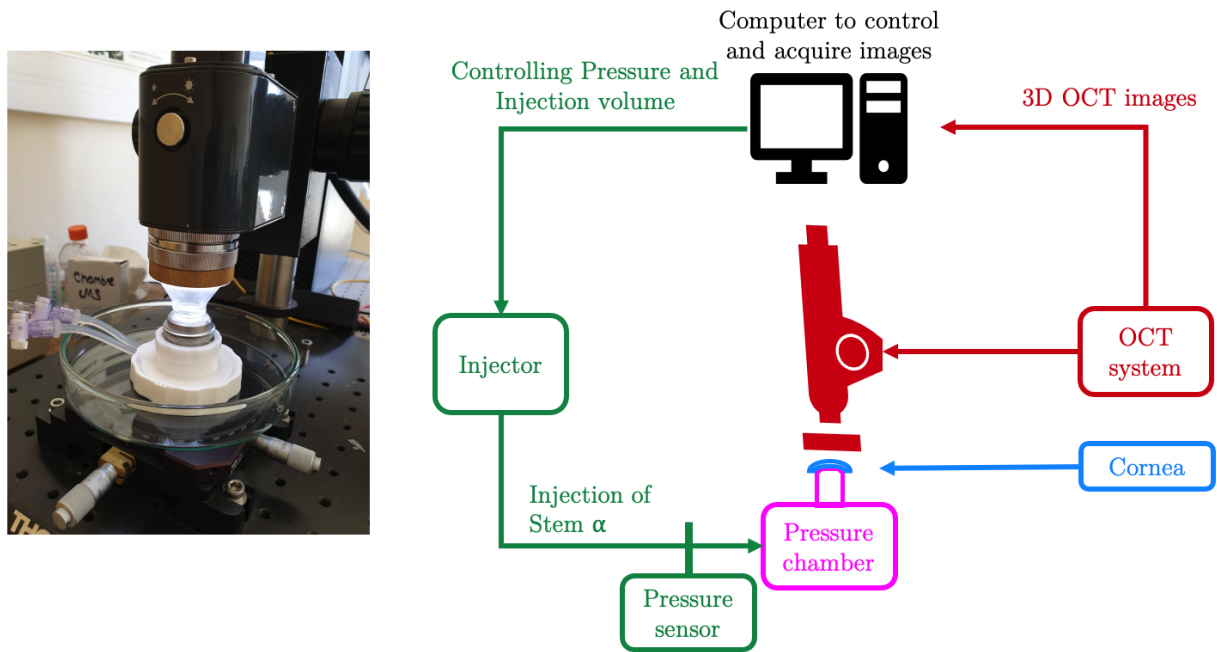


Figure 3.2: Experimental setup: the cornea is put at the top of a pressure chamber, which is filled with Stem α . The fluid is injected through the pressure chamber via an injector controlled by a homemade software. The pressure is measured at the entrance of the pressure chamber using a pressure sensor. The cornea is then imaged in 2D and 3D with an OCT microscope.

3.2.3 Mechanical tests on the cornea

Different mechanical tests have been performed on cornea: (i) creep tests at physiological pressure (between 15 and 20 mmHg), (ii) creep tests at high pressure (150 mbar or 113 mmHg) and (iii) inflation tests until 200 mbar (or 160 mmHg). The same procedure is applied for each of them. First, the pressure chamber is filled with fluid (at a speed of $0.01 \text{ cm}^3/\text{s}$) until the target pressure is reached, so that the pressure is chosen while the volume is controlled. Due to the experimental set-up, this step leads to have at least 15mmHg under the cornea and last for a few tens of seconds (and thus is not detailed in the results). Then images are acquired at regular intervals (between 2 and 10 minutes depending on the test considered) while monitoring that the pressure remains stable. Taking a 2D image is almost instantaneous, whereas 3D images being stacks of hundreds of 2D images, the process takes up to 2 minutes in that case. As the cornea is a rapidly degrading tissue, the experiments do not last for more than 3 hours and a half.

Creep test at physiological pressure The loading path of the creep test at physiological pressure is presented Figure 3.3.a. The cornea is put under physiological pressure for around two hours and images are acquired every 15 minutes. In this experiment the purpose is twofold. First, we want to test the mechanical response of cornea under physiological pressure to mimic early transplant. Second, we want to test the influence of the conditions of the deturgescence process. Seven corneas were put in Stem α 3 for 48 hours at 31°C . Three of them were put in Falcon tubes (which is the classical way to do the deturgescence process) while the other four were placed on a pressure chamber at physiological pressure. Two of those last corneas under pressure did not reach the physiological width after two days (their thicknesses were more than $800 \mu\text{m}$), most probably because of a leak in

the pressure chamber so the corneas were not soaked with fluid the whole time, so they were removed from the study.

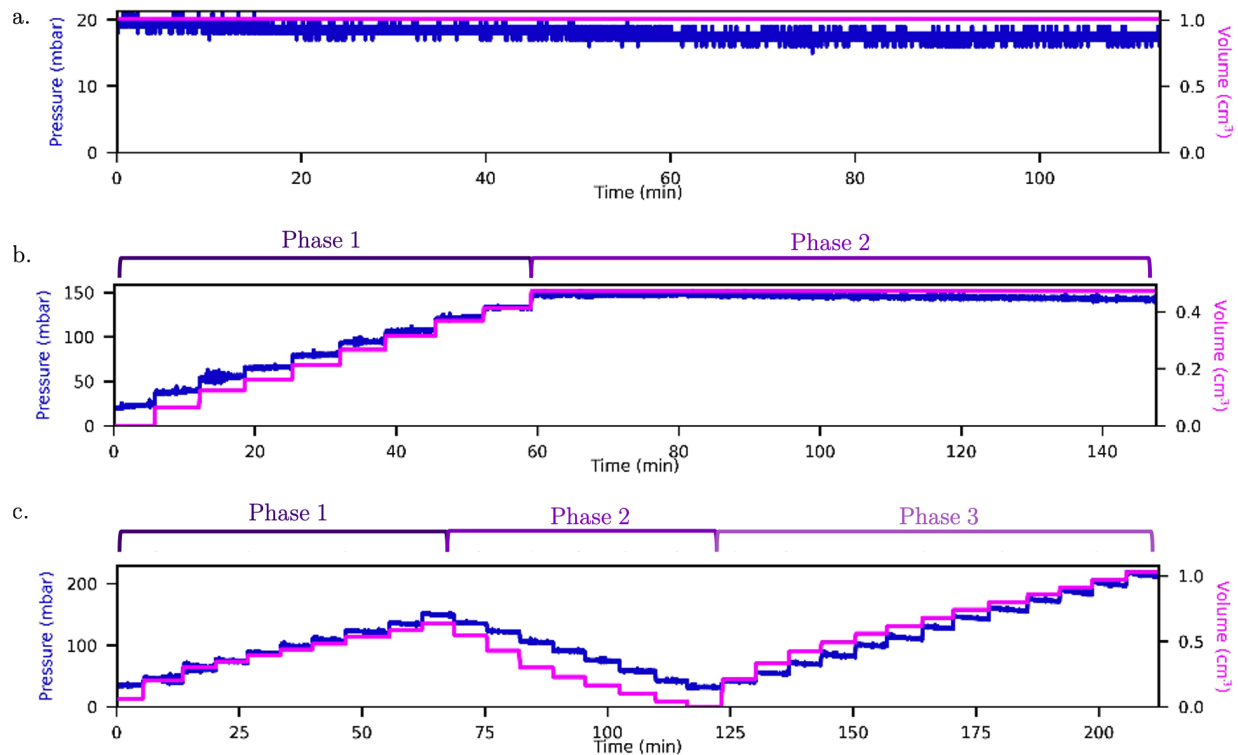


Figure 3.3: Volume (pink) and pressure (blue) evolution with respect to time. a. Creep test at physiological pressure: constant volume over time leading to constant physiological pressure. b. Creep test at high pressure: steps of volume while monitoring the pressure over time until the pressure reaches 150 mbar (phase 1) and constant pressure afterwards (phase 2). c. Inflation test: steps of volume while monitoring the pressure over time. The steps are done in 3 phases: phase 1 corresponds to the first increasing steps of pressure, phase 2 to the decreasing steps of pressure and finally phase 3 corresponds to the second increasing steps of pressure.

Creep test at high pressure The loading path of the creep test at high pressure is presented in Figure 3.3.b. The cornea is brought to high pressure (150 mbar) via steps of pressure (of 10 mbar) that last for 5 to 6 minutes (phase 1 on Fig. 3.3.b), until a pressure of 150 mbar is reached, at which point the volume is kept constant (phase 2 on Fig. 3.3.b). Images are taken at the beginning and at the end of each step of pressure during the ramp-up phase, and every 5 minutes when the pressure is stabilized. The purpose of this test is to characterize the mechanical response of cornea at high pressure with time. Seven corneas underwent the creep test at high pressure.

Inflation test The loading path of the inflation test is presented in Figure 3.3.c. The cornea undergoes a cycle and a half (phases 1 to 3 on Fig. 3.3.c) of steps of pressure (of 10 to 15 mbar) that last for 5 to 6 minutes. Images are acquired at the beginning and end of each step. The goal of this

test is to characterize the mechanical response of cornea under a wide range of pressures, way below the physiological pressure. Seven corneas underwent this inflation test.

3.2.4 Image analysis

Image acquisition All along the mechanical tests, 2D and 3D images are acquired by OCT. The 2D images are acquired along the short (Fig. 3.4.a) and long axis (Fig. 3.4.b) of the cornea – with a section of 6 or 8 mm (1090 or 1333 px) in length and 1.5 mm (1024 px) in depth (for $n = 1.33$). The 3D images are acquired near the apex (Fig. 3.4.c) – with a volume of $2.5 \times 2.5 \times 1.5 \text{ mm}^3$ (416 x 416 x 1024 vx) or $2.5 \times 2.5 \times 1.3 \text{ mm}^3$ (416 x 416 x 885 vx) – the last dimension being the depth of the acquisition. Smallest images were taken for smallest size in GB, without degradation of image quality. Voxel sizes in both horizontal (in-plane) directions are $6 \mu\text{m}$ and $1.47 \mu\text{m}$ in depth (for the chosen refraction index of $n = 1.33$).

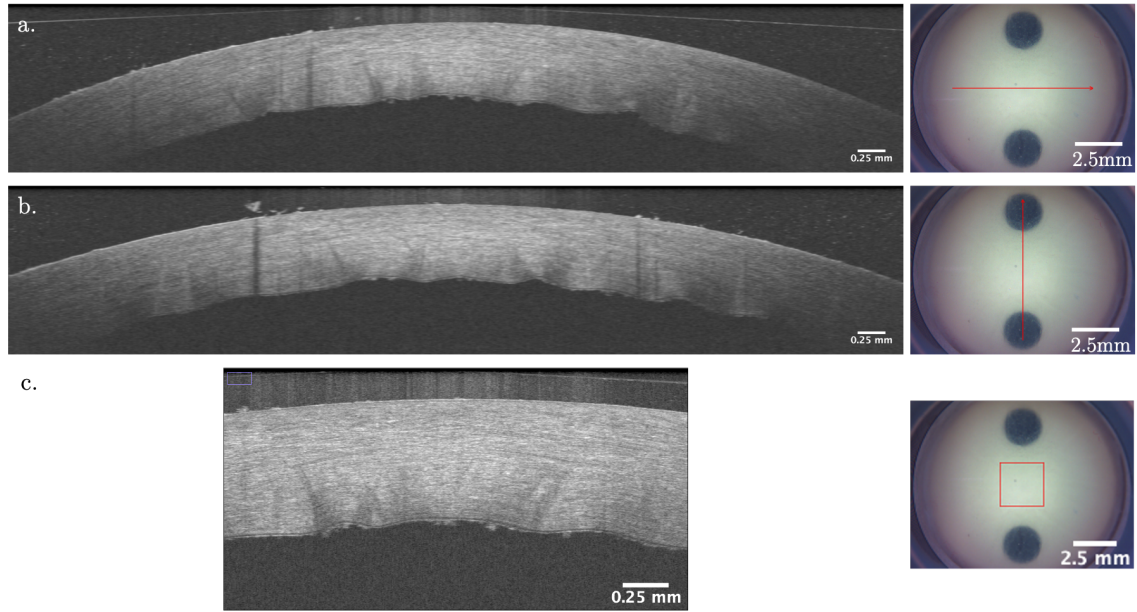


Figure 3.4: Examples of 2D and 3D OCT images with physical pixel ratio. a. Short axis image of the cornea (left) and corresponding camera image (right). b. Long axis image of the cornea (left) and corresponding camera image (right). c. Stack of a 3D OCT image of the cornea (left) and corresponding camera image (right). Scale bars – $250 \mu\text{m}$ for the OCT images and 2.5 mm for the camera images.

Influence of the difference in refractive indices The images are taken with a refractive index fixed to $n = 1.33$ to take into account the Lacrygel (considered as water), and the light rays arrive vertically on the cornea (orange lines on Fig. 3.5). Only one refractive index is taken into account by the OCT, so when the light ray hits the cornea, the image is not recorded accordingly to the change of medium. Descarte's law gives the refracted angle θ_2 with respect of the incident angle θ_1 and the two refractive indices n_1 and n_2 (with $n_1=1.33$ and $n_2=1.37$):

$$n_1 \sin \theta_1 = n_2 \sin \theta_2. \quad (3.1)$$

Considering A a point on the anterior surface of the cornea and I a point in the cornea on the same

vertical line (so that point I would be at its real place on the image if the indices did not change). The real point B can be computed using Descarte's law (Eq. (3.1)) and the relation between the optical paths

$$n_1|AI| = n_2|AB|. \quad (3.2)$$

The error on the real point B comes from two effects due to the index change. Since the index is larger in the cornea than in Lacrygel, (i) the optical path is shorter in reality than in the recorded image (deduced from Eq. (3.2)) and (ii) the refracted angle is smaller than the incident angle (Descarte's law from Eq. (3.1)). We can estimate the error by looking at the center and at the borders of the images and for the entire thickness of the cornea. At the center of the image, as the light ray arrives perpendicular to the anterior surface of the cornea, only the length changes accordingly to Eq. (3.2). The typical thickness measured on the images at the center of the cornea is 600 μm . The real thickness is then around 580 μm . The error on the thickness is therefore less than 3.5 %. At the limbus, the typical thickness of 700 μm on the image gives a real thickness of 675 μm and an error on the thickness of approximately 3.5 %. At the edge of the image, the error will also come from the deviation of the refracted light rays (in red on Fig. 3.5).

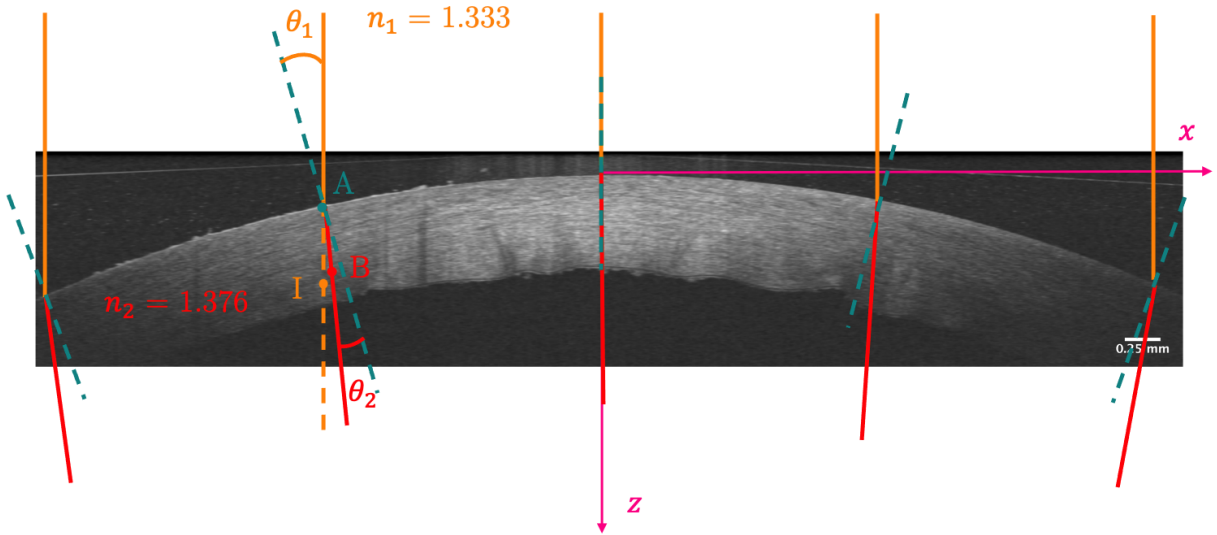


Figure 3.5: Influence of the change of refractive indices. The orange lines represent the incident rays, the red lines represent the refracted rays, the dashed orange line represents the optical path computed by the OCT, i.e. without change of refractive index. The dashed green lines represent the direction of the normal to the anterior surface of the cornea at the point considered. We have emphasized here the deviation for clarity.

Let us approximate the anterior surface of the cornea in 2D with a parabolic function $z = z_0 + \frac{x^2}{R_x}$. The normal to the curve (dashed green line on Fig. 3.5) is then

$$\frac{1}{\sqrt{1 + \frac{x^2}{R_x^2}}} \begin{pmatrix} x/R_x \\ -1 \end{pmatrix} \quad (3.3)$$

and thus the incident angle θ_1 between the normal and the incident ray can be computed using the

scalar product:

$$\cos \theta_1 = \frac{1}{\sqrt{1 + \frac{x^2}{R_x^2}}}. \quad (3.4)$$

Typical value of the curvature radius is $R_x = 7.8$ mm and the edge of the image corresponds to $x = 4$ mm, so that the maximum angle on the image is $\theta_1 = 27^\circ$. The corresponding refracted angle is then $\theta_2 = 25.7^\circ$ and the error is then about 5 % ($\Delta\theta = \theta_1 - \theta_2 = 1.3^\circ$). This gives (using Al Kashi' theorem) a distance between B and I of 24 μm , and using trigonometry formulae we find the vertical difference $z_I - z_B$ will be close to 25 μm while the horizontal difference $x_I - x_B$ will be close to 14 μm .

To conclude, the error in position is summarize in the following table (with an hypothesis of a real thickness of 675 μm and a 8mm image),

Case	$\frac{x_B - x_I}{x_B}$	$\frac{z_B - z_I}{z_B}$
	At the center ($x_I = 0\text{mm}$, $y_I = 600 \mu\text{m}$)	0%
At the border ($x_I = 4\text{mm}$, $y_I = 700 \mu\text{m}$)	<0.35%	<3.5%

Table 3.1: Summary of the position errors in 2D.

To estimate the error on strain, lets consider two correlation domains (see Fig. 3.6) on the same vertical line of the OCT image and for the largest angles θ_1 and θ_2 : I1 and I2 are the position of their center in the reference configuration and I'1 and I'2 their position on the deformed configuration. The corresponding corrected real center are B1 and B2 and B'1 and B'2 respectively for the reference and deformed configuration. Two cases are considered to study the impact of the error in position on the strain measurement within depth (Table 3.2 for the coordinates): (i) one with the two correlation domains the closest to the epithelium (at 0 and 45 μm of depth) and (ii) one with the two correlation domains the closest to the endothelium (at 655 and 700 μm of depth). In each case, the considered deformation is a vertical strain: as the angle $\Delta\theta$ is very small, the largest error due to the difference of refractive index is in the vertical direction.

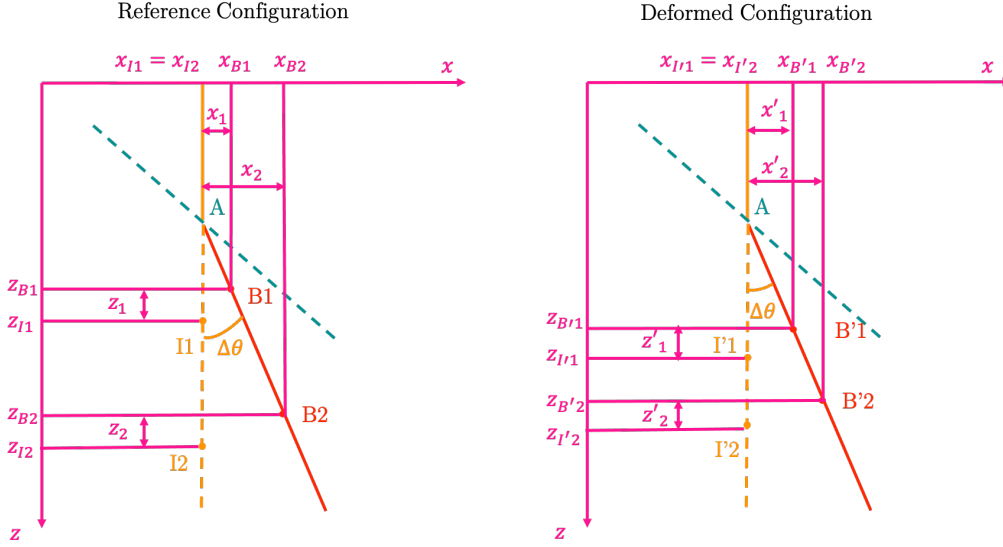


Figure 3.6: Configuration considered to estimate the strain error due to difference of refractive index. Orange and red line are the incident and refracted light ray respectively. Dashed green line is the normal to the cornea (see Fig. 3.5).

Case 1	x	z	Case 2	x	z
I1	0 μm	30 μm	I1	0 μm	655 μm
I2	0 μm	75 μm	I2	0 μm	700 μm
I'1	0 μm	30 μm	I'1	0 μm	655 μm
I'2	0 μm	80 μm	I'2	0 μm	705 μm

Table 3.2: Coordinates of the image points considered in the strain error estimation. Case 1 corresponds to correlation domain under the epithelium while case 2 corresponds to correlation domain above the endothelium.

The strain in the image coordinates system ε_{zz} and the real strain $\tilde{\varepsilon}_{zz}$ are defined by:

$$\begin{cases} \varepsilon_{zz} = \frac{(z_{I'2} - z_{I'1}) - (z_{I2} - z_{I1})}{(z_{I2} - z_{I1})} \\ \tilde{\varepsilon}_{zz} = \frac{(z_{B'2} - z_{B'1}) - (z_{B2} - z_{B1})}{(z_{B2} - z_{B1})} \end{cases} \quad (3.5)$$

Denoting:

$$\begin{cases} \Delta z_I = z_{I2} - z_{I1} \\ \Delta z_1 = z'_1 - z_1, \quad \Delta z_2 = z'_2 - z_2 \end{cases}, \quad (3.6)$$

the real strain reduces to (see App. D.2 for the whole computation):

$$\tilde{\varepsilon}_{zz} = \varepsilon_{zz} \frac{\Delta z_I}{\Delta z_I + (z_2 - z_1)} + \frac{(\Delta z_2 - \Delta z_1)}{\Delta z_I + (z_2 - z_1)}. \quad (3.7)$$

In the cases considered, the vertical strain is around 11% between the reference and deformed configuration. Table 3.3 presents the value of the different quantities of interest to compare the two vertical strains (without or with taking into account the change of index).

Case	Δz_I	$z_2 - z_1$	$\Delta z_2 - \Delta z_1$
Case 1	45 μm	1.3 μm	0.1 μm
Case 2	45 μm	1.3 μm	0.1 μm

Table 3.3: Quantities of interest on the computation of the strain error due to the difference of refractive index.

For both cases, we find $\tilde{\varepsilon}_{zz} = 0.97\varepsilon_{zz} + 0.003 \simeq 0.97\varepsilon_{zz}$. The multiplicative term only depends on the reference configuration, so that when the correlation domains are spaced 45 μm apart, the real strain $\tilde{\varepsilon}_{zz}$ is 97% of the strain computed on the image ε_{zz} along the depth. The added term can be reduced to (using Taylor expansion) $(\Delta z_2 - \Delta z_1)/\Delta z_I$ which is at least one order of magnitude smaller than ε_{zz} and can therefore be neglected. In the theoretical case considered here, $\varepsilon_{zz} = 11\%$, so $\tilde{\varepsilon}_{zz} \simeq 10.7\%$ and the incertitude made is around 0.3%. The error is around 3%, but it is the same at the epithelium and at the endothelium, as the distance between correlation domains are the same everywhere.

To conclude this study, the error on position is bigger on the vertical direction (3.5%) than in the horizontal direction (0.35%), but remains small compared to the observed displacement. As a result, the strain on the image is overvalued compared to the real one (if the measured strain is 11%, the real one should be 10.7%), but as the multiplicative factor (0.97) remains the same along the depth, the strains obtained from image correlations at different depths can be compared directly between them. The error due to the refractive index is at least one order of magnitude smaller than the strain computed (if the measured strain is 11%, the error done on the real strain from the refractive index deviation is around 0.3%), as we are doing local correlation and as the distance between the correlation domain are constant.

Image / Volume correlation These images are then analyzed using a digital volume/image correlation (DIC / DVC - Sec. 1.2.2.b) software developed by M. Bornert, *CMV3D* [19]. 2D/3D correlation domains are taken at 30 x 30 px² and 30 x 30 x 30 vx (Fig. 3.7), with search domains of 15 x 15 px² and 15 x 15 x 15 vx, for 2D and 3D images respectively. For the 2D images, the axes used for the correlation are: (i) the horizontal axis 1 corresponds to either Superior-Inferior direction (Transect 1 – Fig. 3.4.a) or Naso-Temporal direction (Transect 2 – Fig. 3.4.b) and (ii) the vertical axis 2 to the depth direction of cornea. For the 3D images, the axes used for the correlation are: (i) the in-plane axes x and y correspond respectively to the Superior-Inferior and Naso-Temporal directions and (ii) the vertical axis z corresponds to the depth direction of cornea. Results of the correlation present the value of the Green-Lagrangian strain tensor \underline{e} , so that $e_{22} = e_{ZZ}$.

The correlation process differs between 2D to 3D images. Suppose that we want to correlate 10 different steps numerated from 1 to 10. The reference configuration is step 1. For the 2D images, the reference configuration is kept constant (step 1) for all the correlation, thus step 1 is correlated with step j for all j in [2,10]. If, and only if, the correlation between step j and step 1 does not work (for example if images 1 and j are so different that the search domain is not big enough), step j-1 is correlated with step j to give a first guess of the correlation domains of step j. Then the points are re-optimized between step 1 and step j such that the correlation process error does not accumulate. For the 3D images, step j-1 and step j are correlated in pairs for all j in [2,10]. In this case, the

errors accumulate but the re-optimization process only worked for a very low correlation criterion, so I preferred to keep the pairwise correlation rather than the re-optimized one.

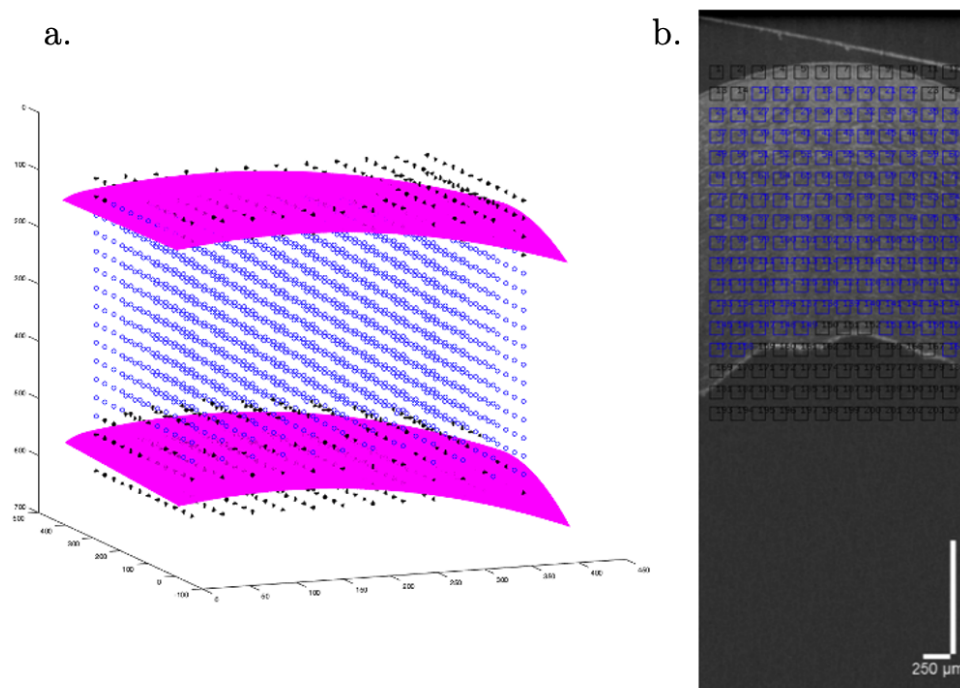


Figure 3.7: a. Complete grid of centers of correlation domains for a cornea in 3D. The pink surfaces represent the anterior and posterior surfaces of the cornea, the blue points correspond to the center of correlation domains used to compute the correlation while black centers are outside the cornea. b. Stack of a 3D OCT image superimposed with the correlation domains computed using the points of Fig. 3.7.a. Scale bar – 250 μm .

3.2.5 Uncertainties quantification

To validate the strain maps measurement, I first tried to quantify the noise of the whole process on a cornea under fixed pressure. As will be seen in Sec. 3.3.1, a non-fixed cornea under pressure cannot be used to assess measurement uncertainties as it will deform between two image acquisitions (one image acquisition can last 5 min for a volume of $2.5 \times 2.5 \times 1.5 \text{ mm}^3$). Consequently, a fixed cornea immersed in ParaFormAldehyde (PFA at 3 % for 2 days and then PFA at 1 %) has been tested with no pressure under it. It appeared that even fixed in PFA, when the cornea was put under the OCT, it compressed (until 5 to 10 % of strain are computed – the compression may be due to the weight of the Lacrygel which is not compensated by an internal pressure), so the uncertainties quantification was not possible either (see App. E.1 for the results of the DVC on a fixed cornea). Finally, I tried to characterize the system with a silicone phantom, where beads were introduced in the manufacturing process in order to introduce a randomized, traceable pattern in the sample (Fig. 3.8), even if the signal origin and the images are very different from cornea.

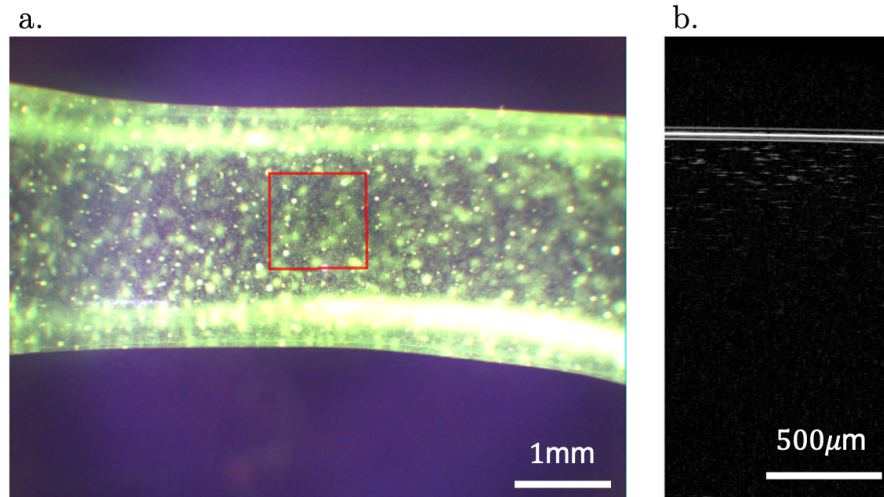


Figure 3.8: a. Camera image and b. OCT image of the silicon phantoms.

Two types of tests were done: a first one where two 3D images are taken consecutively under the same conditions, allowing to quantify the reproducibility of our OCT system. The second one consisted in moving the zone of imaging of the tomograph such that a displacement of $60\ \mu\text{m}$ is observed between the two volumes, allowing to estimate the error due to the rest of the process (interpolation between voxels, optical acquisition aberrations and correlation software error). In this last test, the sample did not move but the OCT imaging zone did, using the displacement of the light source. Each test is done with two different sizes of in-plane voxels (horizontal plane): 6 and $4\ \mu\text{m}$ while the size of the voxel in the vertical direction (depth of the sample) is fixed at $1.95\ \mu\text{m}$ (the minimum size of voxel available with the refraction index of the air).

Volumes 1 – 4	X	Y	Z	Units
Size	166	166	1024	vx
FOV	1.00	1.00	2.00	mm
Pixel size	6.00	6.00	1.95	μm
Volumes 6 – 9	X	Y	Z	Units
Size	250	250	1024	vx
FOV	1.00	1.00	2.00	mm
Pixel size	4.00	4.00	1.95	μm

Table 3.4: Scanned zone information for the two cases of voxel sizes.

Volume 1 and 6 are considered as references for voxel sizes of 6 and $4\ \mu\text{m}$ respectively. Volumes 2 and 7 are taken at the same place (with no displacement of the set-point of the camera), volumes 3 and 8 correspond to a $60\ \mu\text{m}$ translation in the x-direction of the set-point of the camera and volumes 4 and 9 correspond to a $60\ \mu\text{m}$ translation in the y-direction of the set-point of the camera. The number of volumes correspond to their acquisition order. Table 3.4 presents the characteristics of the different volumes considered: (i) the size in voxels of the volume, (ii) the size in mm of the volume (FOV) and (iii) the investigated voxel sizes. Table 3.5 summarizes the different transformations that were analyzed.

	Volume 2	Volume 3	Volume 4
Volume 1: Reference volume	No displacement	+ 60 μm = 10 px in the x-direction	+ 60 μm = 10 px in the y-direction
	Volume 7	Volume 8	Volume 9
Volume 6: Reference volume	No displacement	+ 60 μm = 15 px in the x-direction	+ 60 μm = 15 px in the y-direction

Table 3.5: Volume considered for the uncertainties quantification. Volumes 1 and 6 are taken as reference states while the others are the deformed configurations with respect to volumes 1 and 6.

CMV3D StatTranslat function was used to analyze the displacement for the following cases: V1 vs V2, V1 vs V3, V1 vs V4 and also V6 vs V7, V6 vs V8 and V6 vs V9. The results are given under the form of the mean \bar{T} over all the correlation points, with the associated standard deviation σ and the greatest deviation from the average σ_{max} . All the correlations are done with a 30 x 30 x 30 vx correlation domain and a search domain of 15 x 15 x 15 vx. CMV3D StatTranslat function is used to compute the error in displacement and then this error is used to evaluate the uncertainty of the strain computation. The goal is to estimate the minimum strain that can be measured using the apparatus, hence the need to quantify different possible measurement errors.

Reproducibility errors are summarized in Table 3.6 with $\Delta d = ||\bar{T}| + 2\sigma|$ where Δd is the estimated absolute error, $|\bar{T}|$ is the mean of displacement and σ is the deviation from the mean. Results for 4 μm pixels are similar to those with 6 μm pixels in x and y directions. It results that displacements under 0.5 px are within the error of the correlation process, and that the error is similar in x and y directions, despite the asymmetry between them (x is the A-scan direction and y is the B-scan direction). In the vertical direction, displacements greater than only 0.2 px can be detected (sensitivity direction of the OCT system).

Regarding the strain uncertainties, the normal one is first evaluated using the estimated absolute error in displacement Δd of one correlation domain and the distance between two neighboring correlation domains L_0 . The normal uncertainty is then computed as $2\Delta d^i/2L_0^i = \Delta d^i/L_0^i$, with $i \in \{x, y, z\}$. The error in displacement of the two neighbors adds up when considering the strain (hence the $2\Delta d$). Similarly, the correlation process being done on 8 neighbors, the distance considered is doubled (hence the $2L_0$). Second, the shear strain ε_{ij} uncertainty is computed in the same way using: Shear uncertainty = $1/2 * (\Delta d^i/L_0^j + \Delta d^j/L_0^i)$, with $\{i, j\} \in \{x, y, z\}$.

As for the error on the displacement, x and y directions also feature similar uncertainty margins for the strains, with the impossibility to measure a significant strain below 1.60 %. In the vertical direction, the precision reaches up to 0.56 % of strain. For the shear strain, an interesting measure of the error is ε_{xz} as it is the shear measured while correlating 2D images. In this case, we are able to measure shear strains down to 1.6 %. The other shear strains have also an error smaller than 2.0 % in both cases, with a maximum error for the shear strain ε_{xy} along the in-plane directions.

V1 vs V2	X	Y	Z
\bar{T}	-0.267 vx = -1.602 μm	-0.245 vx = -1.470 μm	0.153 vx = 0.298 μm
σ	0.103 vx = 0.618 μm	0.117 vx = 0.702 μm	0.019 vx = 0.037 μm
σ_{max}	0.488 vx = 2.928 μm	0.495 vx = 2.970 μm	0.053 vx = 0.103 μm
L_0	43 vx = 258 μm	30 vx = 180 μm	34 vx = 66.3 μm
Δd	0.755 vx = 4.530 μm	0.74 vx = 4.440 μm	0.206 vx = 0.402 μm
Normal strain	XX	YY	ZZ
Normal uncertainty (%)	1.10	1.60	0.56
Shear strain	YZ	XZ	XY
Shear uncertainty (%)	1.02	0.92	1.35
V6 vs V7	X	Y	Z
\bar{T}	-0.286 vx = -1.144 μm	-0.487 vx = -1.948 μm	0.110 vx = 0.215 μm
σ	0.199 vx = 0.796 μm	0.024 vx = 0.096 μm	0.227 vx = 0.443 μm
σ_{max}	0.643 vx = 2.572 μm	0.052 vx = 0.208 μm	0.048 vx = 0.094 μm
L_0	35 vx = 140 μm	30 vx = 120 μm	42 vx = 81.9 μm
Δd	0.929 vx = 3.716 μm	0.539 vx = 2.156 μm	0.0158 vx = 0.308 μm
Normal strain	XX	YY	ZZ
Normal uncertainty (%)	1.95	1.78	1.34
Shear strain	YZ	XZ	XY
Shear uncertainty (%)	1.58	1.62	1.90

Table 3.6: Results for the correlation between two images taken at the same place: V1 vs V2 for the 6 μm pixel size in x and y directions and V6 vs V7 for the 4 μm pixel size in x and y directions.

Translation errors are summarized in Table 3.7 (60 μm x-displacement) and Table 3.8 (60 μm y-displacement). This experiment involves a camera displacement, in which case the absolute error becomes $\Delta d = ||\bar{T}| - d_{given} + 2\sigma|$, with $d_{given} = 60$ or 0 μm . In each case, results for 6 μm pixels are more precise than those for 4 μm pixels in x and y directions, except for the y-results of the y-displacement. Errors lesser than 1.6 % in the x-direction were found while they are less than 1.9 % for the y-direction. Here an asymmetry is observed between the three directions, but in summary it is possible to measure strains greater than 3.9 %. Similarly, shear strains greater than 3.0 % can be measured for 6 μm pixels.

V1 vs V3	X	Y	Z
\bar{T}	-10.263 vx = -61.578 μm	0.185 vx = 1.110 μm	-1.242 vx = -2.422 μm
σ	0.212 vx = 1.272 μm	0.191 vx = 1.146 μm	0.034 vx = 0.066 μm
σ_{max}	0.508 vx = 3.048 μm	0.447 vx = 2.682 μm	0.100 vx = 0.195 μm
L_0	43 vx = 258 μm	30 vx = 180 μm	34 vx = 66.3 μm
Δd	0.771 vx = 4.626 μm	0.632 vx = 3.792 μm	1.342 vx = 2.617 μm
Normal strain	XX	YY	ZZ
Normal uncertainty (%)	1.60	1.89	3.85
Shear strain	YZ	XZ	XY
Shear uncertainty (%)	3.02	2.53	1.80
V6 vs V8	X	Y	Z
\bar{T}	-15.200 vx = -60.800 μm	-0.493 vx = -1.972 μm	-1.386 vx = -2.703 μm
σ	0.304 vx = 1.216 μm	0.131 vx = 0.524 μm	0.028 vx = 0.055 μm
σ_{max}	0.589 vx = 2.356 μm	0.827 vx = 3.308 μm	0.095 vx = 0.185 μm
L_0	35 vx = 140 μm	30 vx = 120 μm	42 vx = 81.9 μm
Δd	0.789 vx = 3.156 μm	1.32 vx = 5.280 μm	1.481 vx = 2.888 μm
Normal strain	XX	YY	ZZ
Normal uncertainty (%)	2.31	2.52	3.43
Shear strain	YZ	XZ	XY
Shear uncertainty (%)	3.30	3.02	2.43

Table 3.7: Results for the correlation between two images with a 60 μm displacement in the x direction: V1 vs V3 for the 6 μm pixel size in x and y directions and V6 vs V8 for the 4 μm pixel size in x and y directions

V1 vs V4	X	Y	Z
\bar{T}	-0.474 vx = -2.844 μm	10.459 vx = 62.754 μm	0.313 vx = 0.610 μm
σ	0.039 vx = 0.234 μm	0.105 vx = 0.630 μm	0.027 vx = 0.053 μm
σ_{max}	0.075 vx = 0.450 μm	0.516 vx = 3.096 μm	0.053 vx = 0.103 μm
L_0	43 vx = 258 μm	30 vx = 180 μm	34 vx = 66.3 μm
Δd	0.549 vx = 3.294 μm	0.975 vx = 5.850 μm	0.366 vx = 0.714 μm
Normal strain	XX	YY	ZZ
Normal uncertainty (%)	1.28	2.23	1.08
Shear strain	YZ	XZ	XY
Shear uncertainty (%)	1.60	1.24	1.70
V6 vs V9	X	Y	Z
\bar{T}	-0.311 vx = -1.244 μm	14.501 vx = 58.004 μm	0.160 vx = 0.312 μm
σ	0.280 vx = 1.120 μm	0.059 vx = 0.236 μm	0.022 vx = 0.043 μm
σ_{max}	0.652 vx = 2.608 μm	0.161 vx = 0.644 μm	0.048 vx = 0.094 μm
L_0	35 vx = 140 μm	30 vx = 120 μm	42 vx = 81.9 μm
Δd	0.963 vx = 3.852 μm	0.338 vx = 1.352 μm	0.208 vx = 0.406 μm
Normal strain	XX	YY	ZZ
Normal uncertainty (%)	2.49	1.27	0.49
Shear strain	YZ	XZ	XY
Shear uncertainty (%)	0.79	1.33	2.00

Table 3.8: Results for the correlation between two images with a 60 μm displacement in the y direction: V1 vs V4 for the 6 μm pixel size in x and y directions and V6 vs V9 for the 4 μm pixel size in x and y directions

Finally, in the x-direction displacement case, the errors in the vertical normal strain and also XZ and YZ shear strains are greater than in the other cases (3.85% in the x-displacement case VS 0.56 % in the no-displacement case and 1.08 % for the y-displacement case for the normal strain). This error may come from an unexpected move of the camera in the vertical direction (the mean translation in the z direction is around -1.2 px), which will lead to a change in patterns and thus to a degradation of the correlation.

2D study A similar study have been done in 2D (taking one slice of the 3D volumes) and the results are presented in App. E.1. The conclusions are similar. Voxel size of 6 μm gives better results than 4 μm . As the same set of images have been used the vertical strain error, and so the shear error are bigger than expected in the case of the 60 μm displacement in x-direction. We should expect to measure strain less 2.8 % in 2D.

Conclusion This uncertainties quantification study is not ideal in the sense that the test of the correlation process was not done on a real cornea, but it gives some insight into the order of magnitude of the strain that can be evaluated. It allows to conclude that we are able to separate signal from

noise for strains greater than 3.5 % for the normal strain and 2.7 % for the 2D shear strain ε_{xz} in the case 3D volumes and less than 2 % for 2D images. Images with a 6 μm of in-plane voxel size give better results than 4 μm images. Increasing the voxel size may allow the noise coming from diffraction by averaging it to be reduced and so give better results during the correlation process. This noise is seen on images and comes from the beads incorporated inside the silicon. We can expect the same effects on cornea because it is the reflective surfaces that induce this noise. In addition, the signal to noise ratio should be better because the refractive patterns are more precise in cornea than in the case of the beads incorporated in silicon. However, as the pattern is intrinsic to the tissue, when deforming, the correlation process could be more difficult as the pattern may change between two different images.

3.3 Results

The experimental results presented hereafter rely on 2D and 3D images of cornea. The computed quantities by image/volume correlation represent the components of the Green-Lagrange tensor. Snapshots only are presented in this manuscript, but the time evolution can be found in video format at the following link:

<https://ppi-lms.polytechnique.fr/jean-marc.allain/Giraudet.html>

The result folder is organized as follows: first by test (creep test at physiological or high pressure and inflation test), then by dimension of the images (2 or 3D), then by analysis and finally by corneas.

The results of image and volume correlation have yielded a huge amount of data, which are not easy to present. In the following, they are organized by test and the data analysis is done trying to give some insight into the mechanical response of cornea with time or pressure, whether considering creep or inflation tests.

3.3.1 Creep test at physiological pressure

The goal of the creep test is to simulate the response of the cornea under physiological pressure to mimic a transplant, and to test the two aforementioned deturgescence protocols. In this test, 5 corneas of 3 females and 2 males are submitted to the loading path shown in Fig. 3.3.a, with the following characteristics: 77 ± 4.65 y.o. and with an endothelial cell density of 1900 ± 484 cells/ mm^2 .

3.3.1.a Vertical displacement maps and curvature radii

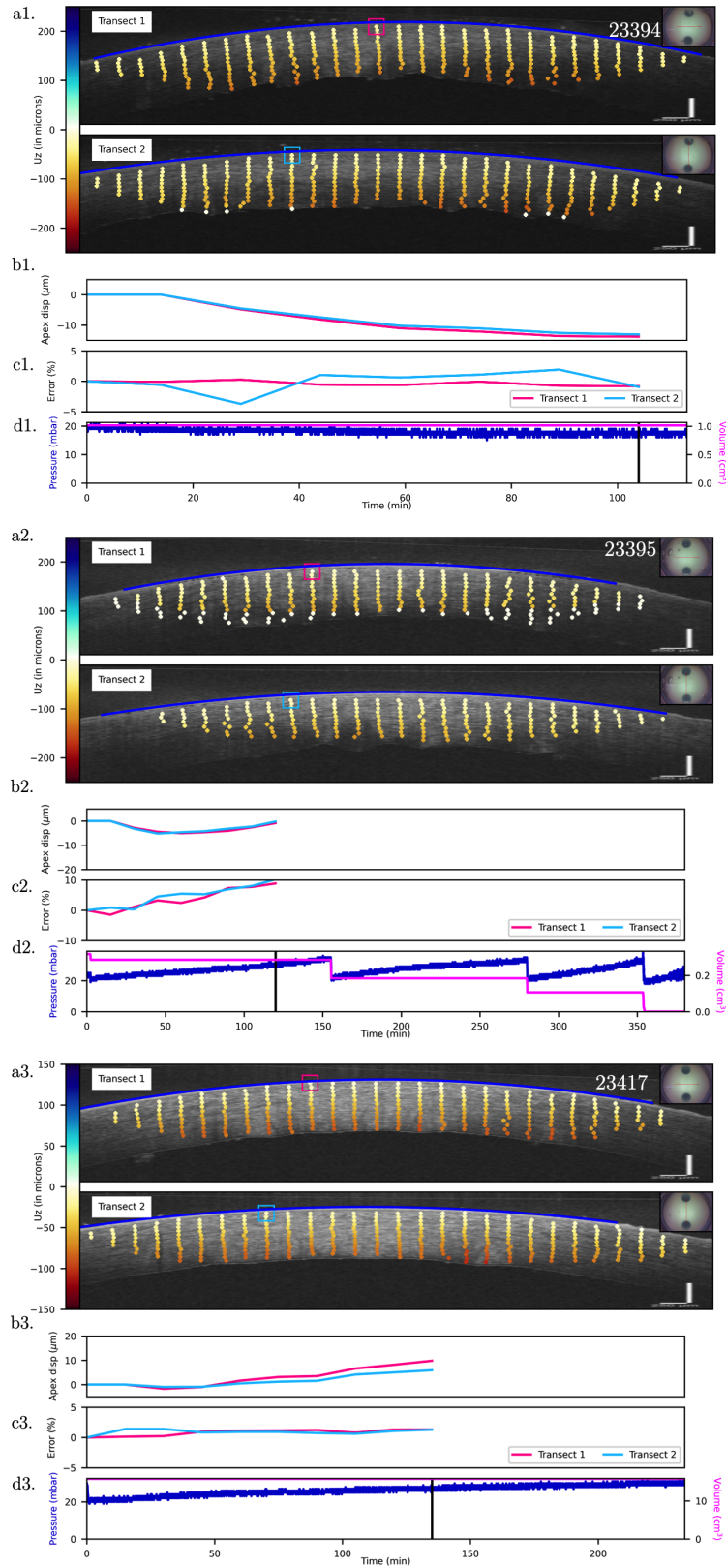


Figure 3.9: Results of the image analysis on two transects (in the direction of minor – Transect 1 – and major – Transect 2 – axis of the cornea) for the creep test at physiological pressure after approximately 2 hours (cornea 23394, 23395 and 23417). a. Vertical displacement U_z - Color bar: [-250 μm , 250 μm]. b. Evolution of the curvature radii with respect to the first ones (in %) c. Internal pressure and volume evolution with time (black bar indicate the considered time).

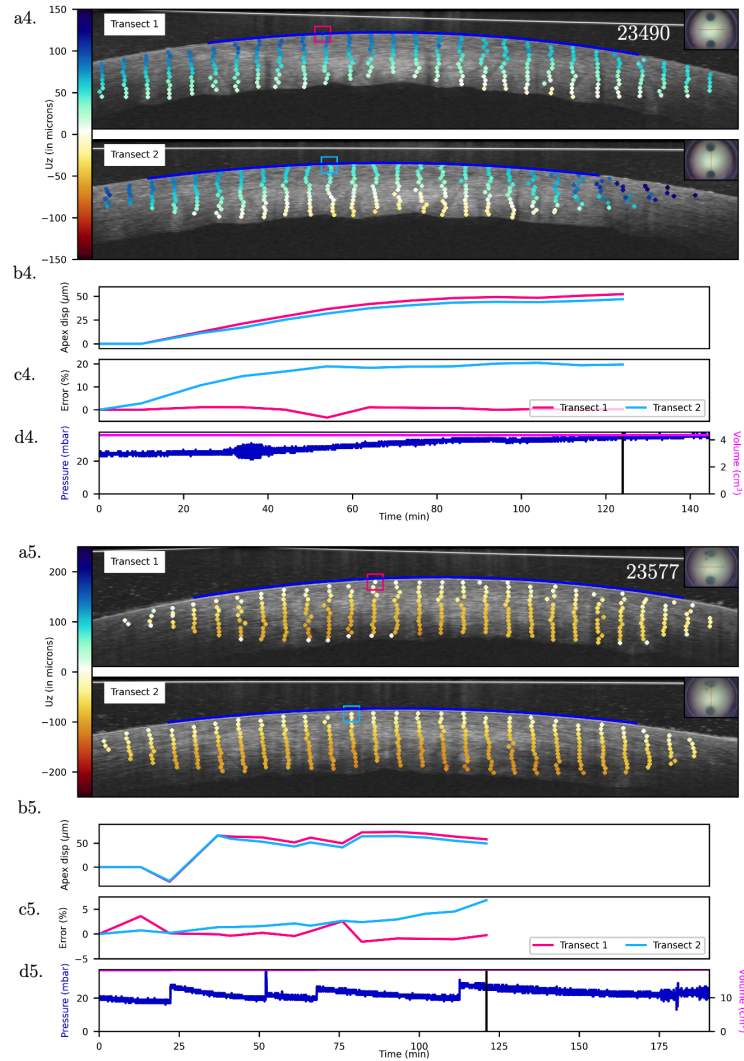


Figure 3.10: Results of the image analysis on two transects (in the direction of minor – Transect 1 – and major – Transect 2 – axis of the cornea) for the creep test at physiological pressure after approximately 2 hours (cornea 23490 and 23577). a. Vertical displacement U_z - Color bar: $[-250 \mu\text{m}, 250 \mu\text{m}]$. b. Evolution of the curvature radii with respect to the first ones (in %) c. Internal pressure and volume evolution with time (black bar indicate the considered time).

Figures 3.9.a and 3.10.a present the results of the vertical displacement U_z at the same time (around 120 min) for the 5 corneas submitted to the creep test at physiological pressure (loading path is recalled on Fig. 3.9.d and 3.10.d). A vertical gradient can be seen on the two transects (Superior-Inferior and Naso-Temporal sections) with almost no displacement in the upper part while the lower part is submitted to a negative displacement (so towards the bottom of the cornea) for four out of five corneas. The only exception is cornea 23490 which exhibits positive displacement under the epithelium while almost none at the endothelium. Figure 3.9.c and Fig. 3.10.c shows the time evolution of the apex displacement (the highest correlation domains on each transect) with results that are dispersed among corneas. No clear tendency can be seen except a stabilization of the apex for most cases. Figure 3.9.c and Fig. 3.10.c shows the time evolution of the two radii of curvature of the anterior surface (represented in dark blue on the images) and defined by:

$$Deviation(\%) = \frac{R - R_0}{R_0} \quad (3.8)$$

with R_0 the radius for the first step. It is interesting to note that the radii of curvature vary very little (less than 5% of change in most cases) during the creep test at physiological pressure. This is the case for 3 of corneas (23394, 23417 and 23577 – transect 1) while for two of them (23395, 23490), the detachment of the epithelium does not allow to make a proper measurement of the variation of the curvature radii. The combination of the vertical displacement map and the constant curvature radii implies that the horizontal normal strain and the 2D shear strain should be less than the vertical normal strain, at least near the epithelium.

3.3.1.b DIC / DVC strain maps

2D and 3D results are discussed here based on snapshots of the experiment, but the evolution throughout the whole test can be found at the following links:

<https://ppi-lms.polytechnique.fr/jean-marc.allain/CTPP2DStrainTime.html> for 2D and <https://ppi-lms.polytechnique.fr/jean-marc.allain/CTPP3D.html> for 3D analyses.

Figure 3.11 presents the results of the creep test (Fig. 3.3.a) after approximately 2 hours for cornea number 23394 with classical deturgescence, i.e. bathing in a liquid that applies a homogeneous pressure force all across the sample. Figures 3.11.a, b and c illustrate, for the last measurement of a given cornea during the creep test, the strain maps (color-maps) computed by DIC along the horizontal, shear and vertical directions, superimposed on the corresponding OCT images, along the short (transect 1) and long axis (transect 2). Figure 3.11.d shows the distribution of each of these strains (in pink for the short axis - transect 1 - and in blue for the long axis - transect 2 - of the cornea). Histogram corresponds to the number of occurrences of a particular level of strain in the image. Figure 3.12 presents the 3D results of the creep test for the same time and the same cornea. Figures 3.12.a–c present the normal strains, while figures 3.12.d–f show the shear strains, both at the end of the creep test. Note that in the 3D representation, the vertical direction corresponds to the z-axis, so that e_{22} on the 2D images corresponds to e_{ZZ} in the 3D analysis.

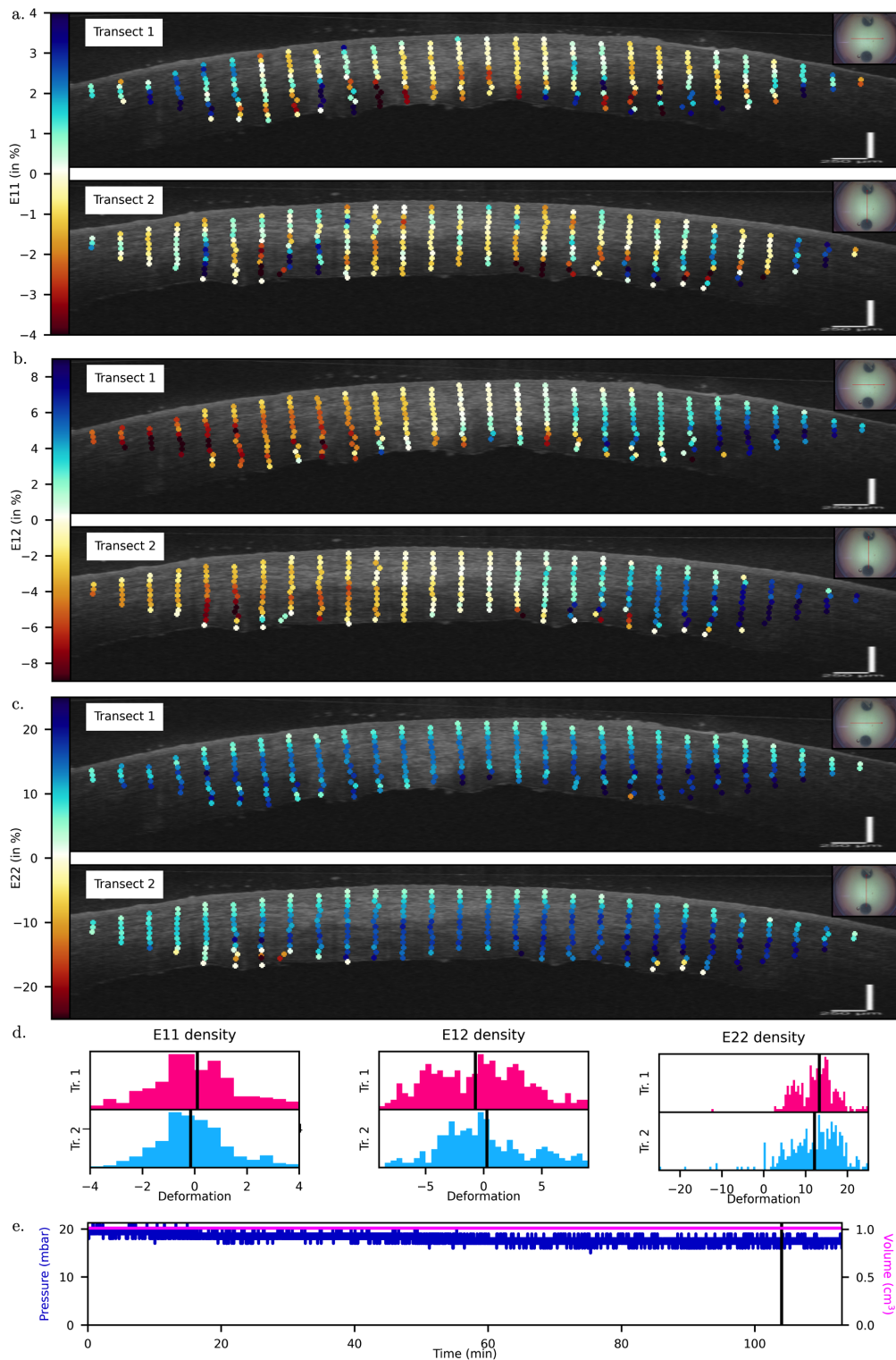


Figure 3.11: Results of image analysis on two transects (in the direction of minor – Transect 1 – and major – Transect 2 – axis of the cornea) for the creep test at physiological pressure after approximately 2 hours (cornea 23394). a. Horizontal strain e_{11} - Color bar: $[-4\%, 4\%]$. b. Shear strain e_{12} - Color bar: $[-9\%, 9\%]$ c. Vertical strain e_{22} - Color bar: $[-25\%, 25\%]$, a-c. scale bar of the OCT image - 250 μm . d. Strain histogram for the particular time of the experiment considered. e. Internal pressure and volume evolution with time (black bar indicate the considered time).

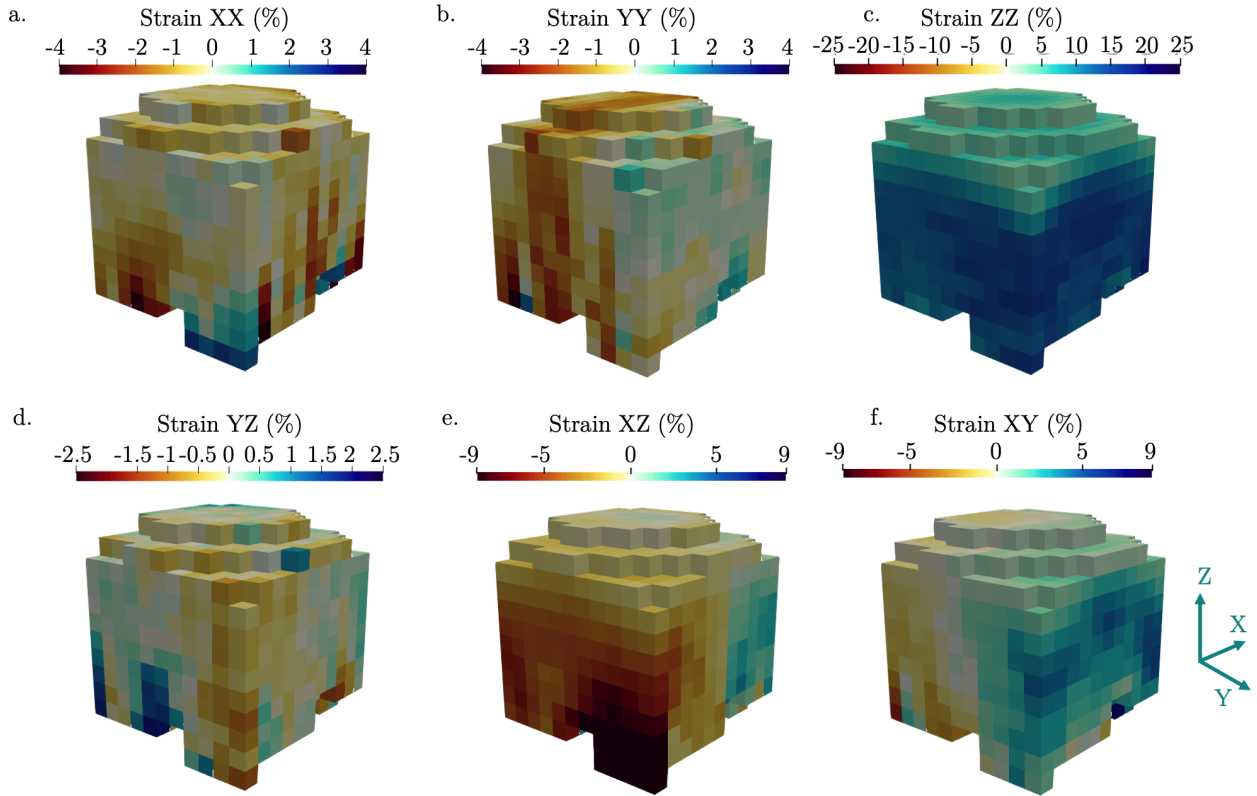


Figure 3.12: Results of the 3D image analysis for the creep test at physiological pressure after approximately 2 hours – same time of measurement as Fig. 3.11 (cornea 23394). Fig. 3.12a – c: normal strains and d – f: shear strains. Note that the vertical direction is the z -axis, so that $e_{ZZ} = e_{22}$ from 2D images. Color bar in%.

Cornea	e_{11}	e_{12}	e_{22}
23394	[-5%, 5%]	[-10%, 9%]	[-5%, 25%]
23395	[-5%, 5%]	[-7%, 7%]	[-6%, 23%]
23417	[-4%, 3%]	[-7%, 7%]	[-1%, 16%]
23490	[-9%, 10%]	[-13%, 7%]	[-11%, 19%]
23577	[-9%, 6%]	[-17%, 14%]	[-14%, 35%]

Table 3.9: Strain range of the creep test at physiological pressure.

Several observations can be made from the analysis of the two (Fig. 3.11) and the three-dimensional (Fig. 3.12) strains measured during the tests of the five samples. Table 3.9 summarizes also the ranges of the values of the strain during the creep test at physiological pressure. Figures 3.13 and 3.14 completes the pictures with the results of the vertical strains for the time 120 min for the five corneas. First, the strain is larger by a factor 3 to 5 approximately along the vertical direction, i.e. through the thickness of the cornea – e_{ZZ} and e_{22} – compared to the horizontal directions – e_{XX} , e_{YY} and e_{11} – as highlighted by Fig. 3.11 and Fig. 3.12. While horizontal strains are mostly contained between -5% and +5%, vertical normal strain can reach up to 25%. In connection, the shear strain – e_{12} – is twice as large as e_{11} , ranging between -10% and 9%. In addition, it is worth noting that

for horizontal normal strains (Fig. 3.11.a and Fig. 3.12.a and b), no discernible pattern emerges, and the distribution of strain is not skewed towards neither contraction nor extension (Fig. 3.11.d). For e_{12} and e_{22} however, the data indicates a different behavior. Figure 3.11.b reveals for e_{12} a negative strain (warm colors) on the left of the image, opposed to a positive strain (cool colors) on its rightmost part, with a neutral strain transition zone at the center of the image (this pattern is not discernible on the 3D images as the zone of imaging is limited). It can be noted that looking at e_{12} histograms in Fig. 3.11.d, two peaks are discernible, one positive and one negative, with a mean close to 0% of strain, which can be observed along both axes of the sample. Contrarily, e_{22} and e_{ZZ} (Fig. 3.11.c and Fig. 3.12) features significantly positive values only throughout the cornea, with a mean strain around 12% (Fig. 3.11.d), except near the epithelium where essentially almost no strain occurs.

With strain levels observed in all three directions, it is interesting to look at the measurement of the volume change J . In Cartesian coordinates systems, the computation of J in 2D and 3D gives

$$\begin{cases} J = [1 + 2(e_{XX} + e_{YY} + e_{ZZ}) + 4(e_{XX}e_{YY} + e_{XX}e_{ZZ} + e_{YY}e_{ZZ} - e_{XY}^2 - e_{XZ}^2 - e_{YZ}^2) \\ + 8(e_{XX}e_{YY}e_{ZZ} - e_{XX}e_{YZ}^2 - e_{YY}e_{XZ}^2 - e_{ZZ}e_{XY}^2)]^{1/2} \end{cases} \quad (3.9)$$

with respect to the components of the 3D Green-Lagrange tensor. At first order, it is approximated by

$$\begin{cases} J \simeq 1 + e_{XX} + e_{YY} + e_{ZZ} \simeq 1 + e_{ZZ} \\ J \simeq 1 + e_{22} \quad (\text{from the 3D analysis}) \end{cases} \quad (3.10)$$

when we look at the order of magnitude of the Green-Lagrange components obtained by DIC/DVC. Therefore, the vertical component $e_{22} = e_{ZZ}$ can be considered as a measure of the volume change of the cornea. In this case, the positive vertical normal strain is observed for both axes of the cornea and can be seen on the 3D representation. It indicates its extension submitted to physiological pressure.

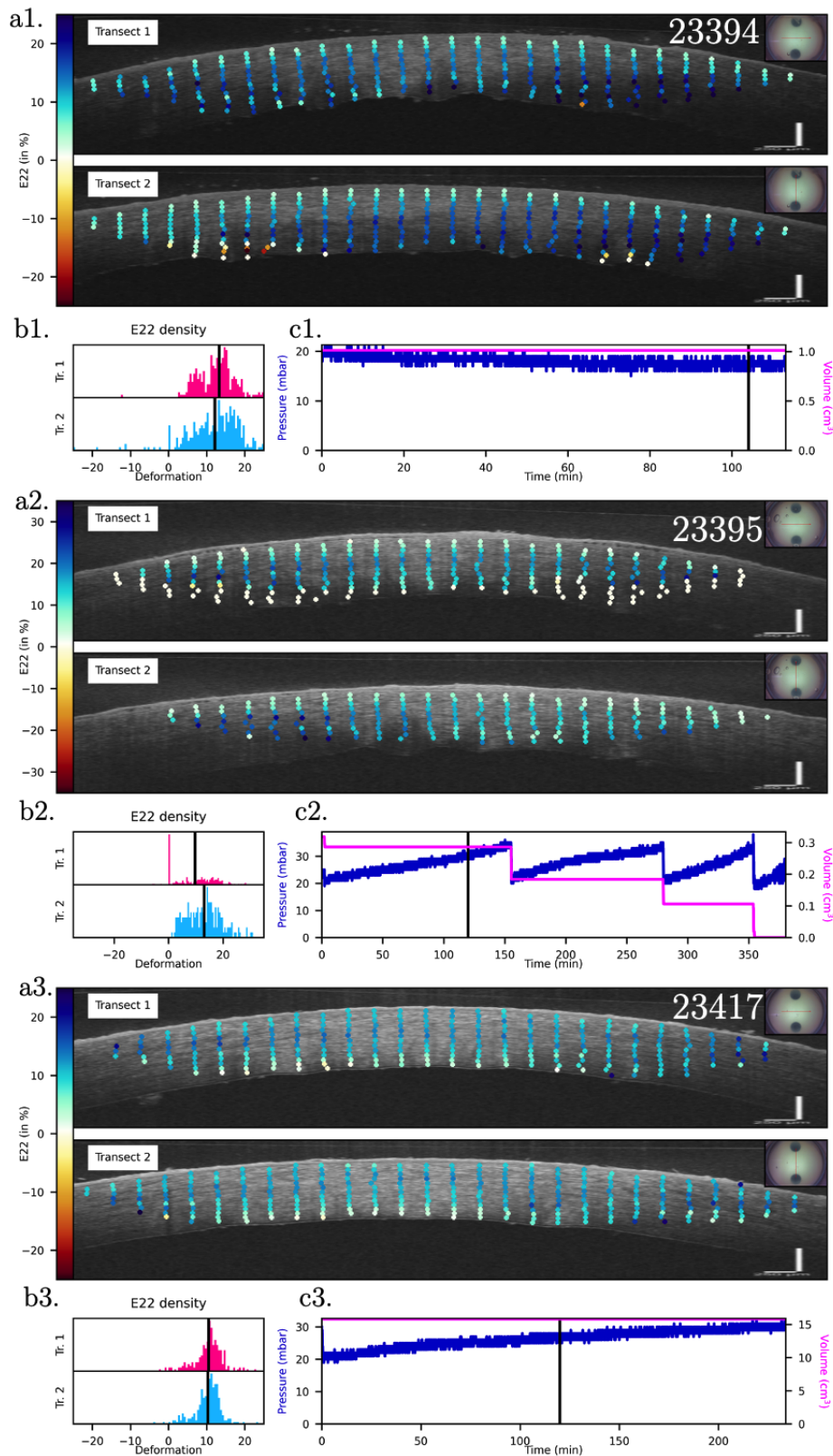


Figure 3.13: Results of the image analysis on two transects (in the direction of minor – Transect 1 – and major – Transect 2 – axis of the cornea) for the creep test at physiological pressure after approximately 2 hours (cornea 23394, 23395 and 23417). a. Vertical strain e_{22} - Color bar: a.1.[-25%, 25%], a.2.[-35%, 35%], a.3.[-25%, 25%]. b. Strain density for the particular time of the experiment considered. c. Internal pressure and volume evolution with time (black bar indicate the considered time)

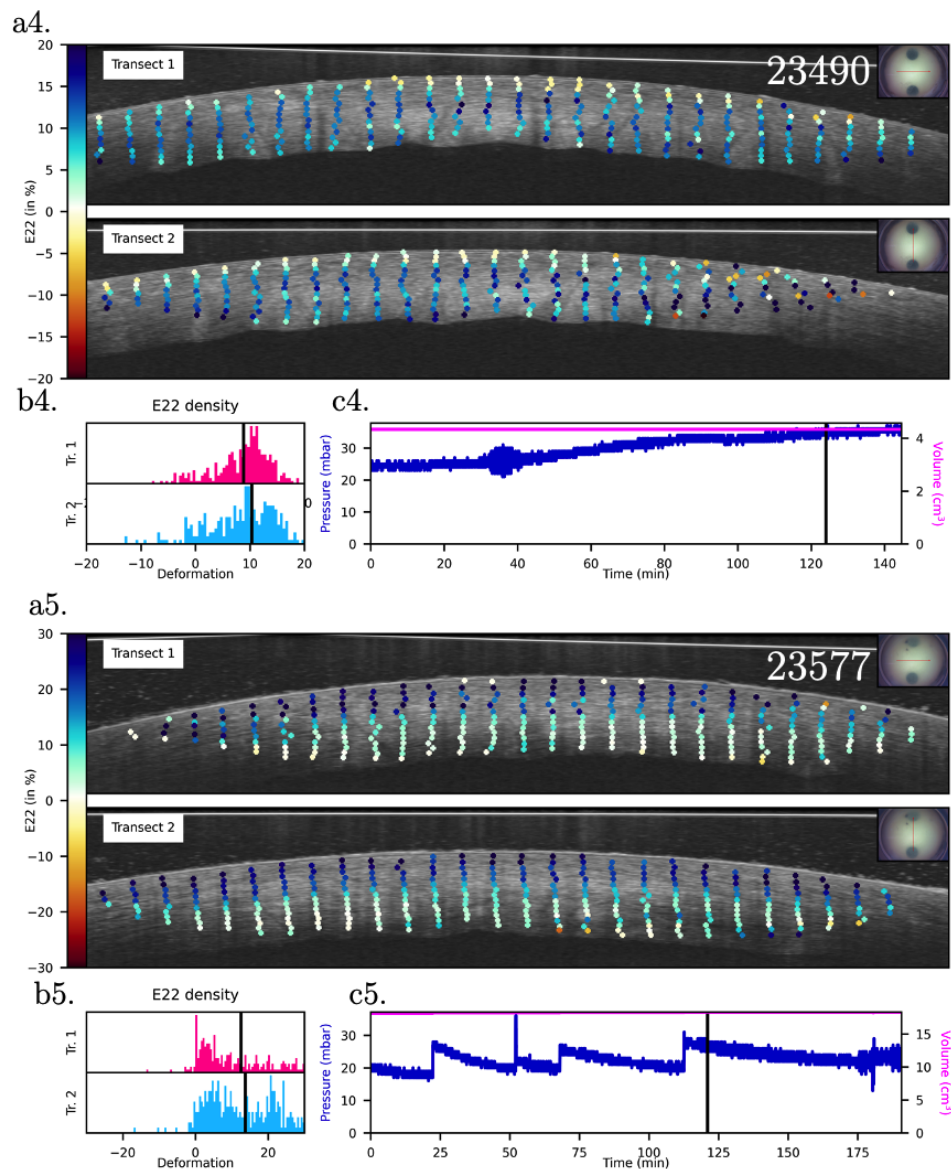


Figure 3.14: Results of the image analysis on two transects (in the direction of minor – Transect 1 – and major – Transect 2 – axis of the cornea) for the creep test at physiological pressure after approximately 2 hours (cornea 23490 and 23577). a. Vertical strain e_{22} - Color bar: a.4.[-20%, 20%], a.5.[-30%, 30%]. b. Strain density for the particular time of the experiment considered. c. Internal pressure and volume evolution with time (black bar indicate the considered time)

3.3.1.c Depth profile of the vertical strain e_{22}

2D results are discussed here based on snapshots of the experiment, but the evolution throughout the whole test can be found at the following links:

<https://ppi-lms.polytechnique.fr/jean-marc.allain/CTPP2DE22Fit.html> for the evolution of the parameters with time,

<https://ppi-lms.polytechnique.fr/jean-marc.allain/CTPP2DE22Profile.html> for the color maps of the depth profile.

Figure 3.11.c reveals a discernible pattern through the thickness for the vertical strain e_{22} . This

pattern will be studied by looking at the depth profile of the strain near the apex of the cornea on both transects. The correlation domain used to study the depth profile are chosen near the apex for two main reasons: (i) first these points are representative of all the depth profile on both transects (the pattern look similar from one column of correlation domain to another) and (ii) the profile near the apex is the less impacted by the error due to the change of refractive index (see Sec. 3.2.4) because the light rays hit the cornea almost perpendicularly.

Transects analysis Figure 3.16 presents the results of the vertical strain profile with time. Figure 3.16.a shows the correlation points used to compute the depth profile, pink and blue are associated to transect 1 and 2 respectively. Figure 3.16.b shows the data and the fit (left) of the depth profile by a three slopes curve defined by:

$$\begin{cases} \alpha_1 z + \beta_1 & \text{for } 0\% < z < z_1 \\ \alpha_2 z + \beta_2 & \text{for } z_1 < z < z_2 \\ \alpha_3 z + \beta_3 & \text{for } z_2 < z < 100\% \end{cases} \quad (3.11)$$

and represented on figure 3.15 (zoom of figure 3.16.b – left).

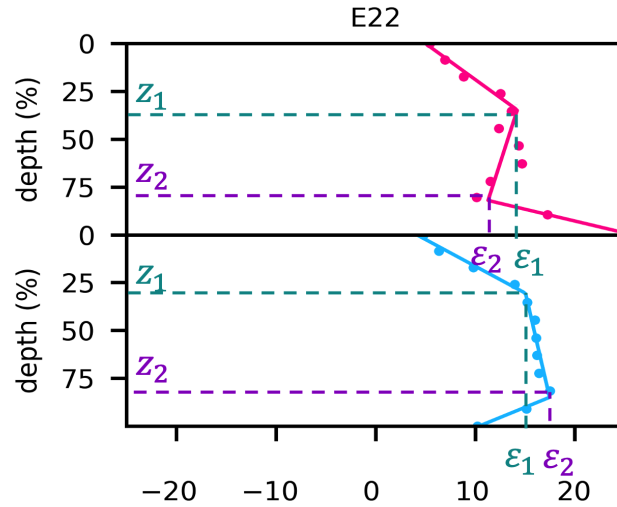


Figure 3.15: Definition of the parameters z_1 , z_2 , ε_1 and ε_2 used to describe the depth profile of the vertical strain. z_1 , z_2 are the so-called limit depths and ε_1 and ε_2 are the limit strains. Epithelium slope α_1 is the slope between the epithelium (0% of depth) and z_1 , middle slope α_2 is the slope between z_1 and z_2 and endothelium slope α_3 is the slope between z_2 and the endothelium (100% of depth).

Two limit depths z_1 and z_2 are observed, associated with two limit strains ε_1 and ε_2 and three slopes α_1 (for $0\% < z < z_1$) – called epithelium slope, α_2 (for $z_1 < z < z_2$) – called middle slope – and α_3 (for $z_2 < z < 100\%$) – called endothelium slope. The corresponding areas distinguished regarding the value of the strain on both the short and long axis transects are: (i) the upper third of the thickness under the epithelium (delimited by the epithelium and z_1), (ii) the central part (delimited by z_1 and z_2) and (iii) the lower quarter of the cornea (delimited by z_2 and the endothelium). Figure 3.16.b shows the time change of the limit depths z_1 and z_2 (middle) and slopes α_1 , α_2 and α_3 (right). The

corresponding along-profile strain with time is shown in Fig. 3.16.c (top for transect 1 and bottom for transect 2). Figure 3.16.d recalls the pressure and volume curves with time associated with the performed experiment.

As seen in Fig. 3.11 and 3.12, the observed strain is positive throughout the whole profile (within a 5-15% range) meaning that the cornea is swelling under physiological pressure. Also, for this case, when looking at the time evolution of the limit depths, we can see large variations on the second one z_2 . This is because the second limit is not as clear in the creep test at physiological pressure as it can be in the two other experiments. The strains in the second and third zones are not so different in this test compared to other two tests. We chose to keep this division into three zones to be consistent within our experiments. As we are dealing with human samples, each one of them is unique so the limits (z_1 and z_2) between the three areas, the associated strains (ε_1 and ε_2) and slopes (α_1 , α_2 and α_3) vary among the five corneas. In the following, we will try to quantify these parameters and assess their temporal variability.

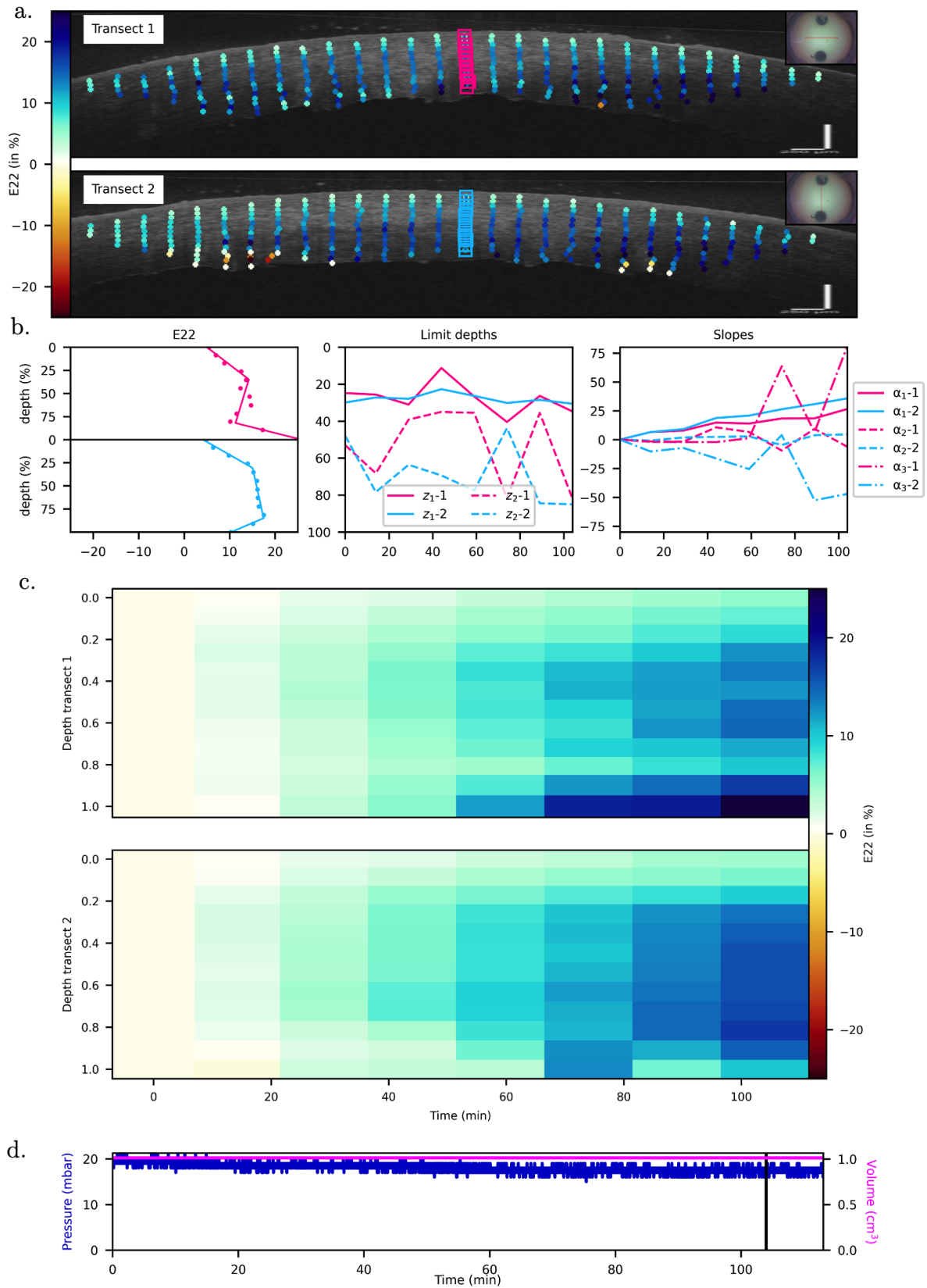


Figure 3.16: Depth profile of vertical strain for creep test at physiological pressure (cornea 23394). a. Depth profiles considered on the two transects (pink and blue squares). b. Vertical strain (in%) of the depth profiles at the considered time – left: data and three-slopes fit, middle: limits depths (in%) and right: slopes (in%) of the fit with time. c. Vertical strain of the depth profile with time for the two transects. d. Internal pressure and volume with time (the black bar indicates the time considered for the images).

Before proceeding to the time dependence analysis, we first wanted to test whether the data from the two transects could be grouped together. The two transects are taken in such a way that the depth profile considered on each of them must be around the apex, thus at almost the same place in the cornea. Thus, the distributions of each data should be similar. We performed a paired by transect t-test (with the python function *t-test_rel*) on the distribution of each parameter between the two transects and also between the two limit depths and strains for each transect. The test measures whether the average score differs significantly across the two transects. A large p-value means that we cannot reject the null hypothesis of identical average scores. Conversely, if the p-value is below the threshold (0.01%, 0.1%, 1% or 5%), then the null hypothesis of equal averages is rejected, and the two transects cannot be considered similar.

Figure 3.17 presents a statistical comparison of a. the limit depths, b. the limit strains and c. the slopes for all the corneas submitted to creep test at physiological pressure for both transects (the associated distributions can be found in App. E.2.1). First, the limit depths are significantly different from each other for both transects, with z_1 around 0.25 and z_2 between 0.5 and 0.7. It is less clear for the limit strain, especially for transect 2 which shows a non-significant difference between ε_1 and ε_2 . Also, it is interesting to note that there is a significant difference between the two transects for almost all parameters except α_1 and α_3 , which was not expected. This is mostly due to a too small data set for this particular experiment. Also, for the second limit depth z_2 and strain ε_2 , it is also because the last two zones (in the middle and near the endothelium) are not so distinct (as they can be in the other two experiments). However, the significance levels obtained for parameters that were not expected to be different are less definitive (p-value always greater than 0.1% according to a T-test). For the experiments that follow, less or non-significant differences between transects are recorded, due to larger data sets, which is more consistent with our expectations.

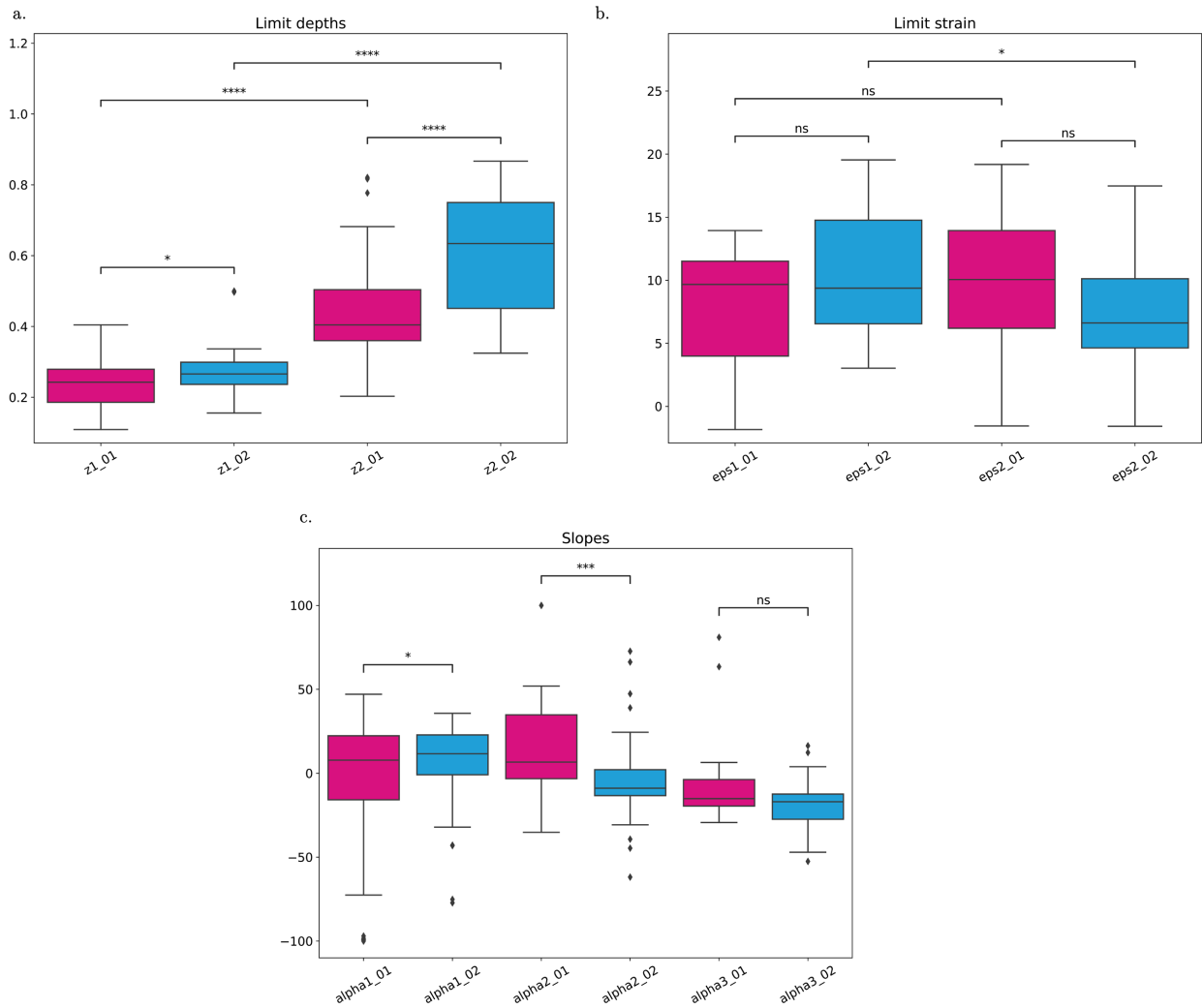


Figure 3.17: a. Limit depths, b. Limit strains (in%) and c. Slopes (in%) of the three-slopes fit of the vertical strain for the creep test at physiological pressure for the two transects. The results for the two transects should be dependent so a paired by transect t-test has been performed to compare the results. Pink box-plots corresponds to transect 1 and blue box-plots to transect 2. The box extends from the lower to upper quartile values of the data, with a line at the median. The whiskers extend from the box to show the range of the data. T-test legend: ns – non-significant, * $p < 5\%$, ** $p < 1\%$, *** $p < 0.1\%$ and **** $p < 0.01\%$.

Figure 3.17 studied the different parameters taken during the whole test. Even if significant differences were found between the two transects, we will regroup the data to try to quantify their time evolution, which will be presented in the next section.

Time dependence analysis Figure 3.18 presents the time evolution of a. the limit depths, b. the limit strains, c. the epithelium slope and d. the middle slope for cornea 23394 (the results for the other corneas can be found in App. E.2.2). The endothelium slope is not studied because the signal deteriorates with depth and therefore the last point (of 100% of depth) is generally not well correlated and as there are only a few points on this part of cornea, it influences a lot the results on the slope. All data are fitted with linear curves. Table 3.10 complements the pictures by giving the mean and standard deviation of the slopes and intercept ordinates for the five corneas tested.

While the two limit depths do not move with time (with $z_1 = 0.25$ and $z_2 = 0.57$ in average), the limit strains ε_1 and ε_2 increase linearly with time by $0.06\%.\text{min}^{-1}$ and $0.13\%.\text{min}^{-1}$ respectively with always positive intercept ordinates. As a result, the middle slope increases with time by $0.31\%.\text{min}^{-1}$. The epithelium slope tends to increase also with time, giving a bigger difference between the limit strain ε_1 and the strain at the epithelium, which does not remain constant but does not increase as fast as ε_1 . The standard deviations are small compared to the mean for the two limit depths and the second limit strain ε_2 , but they are high for the other parameters (of the order of magnitude of the mean), meaning that their scatter between corneas is high.

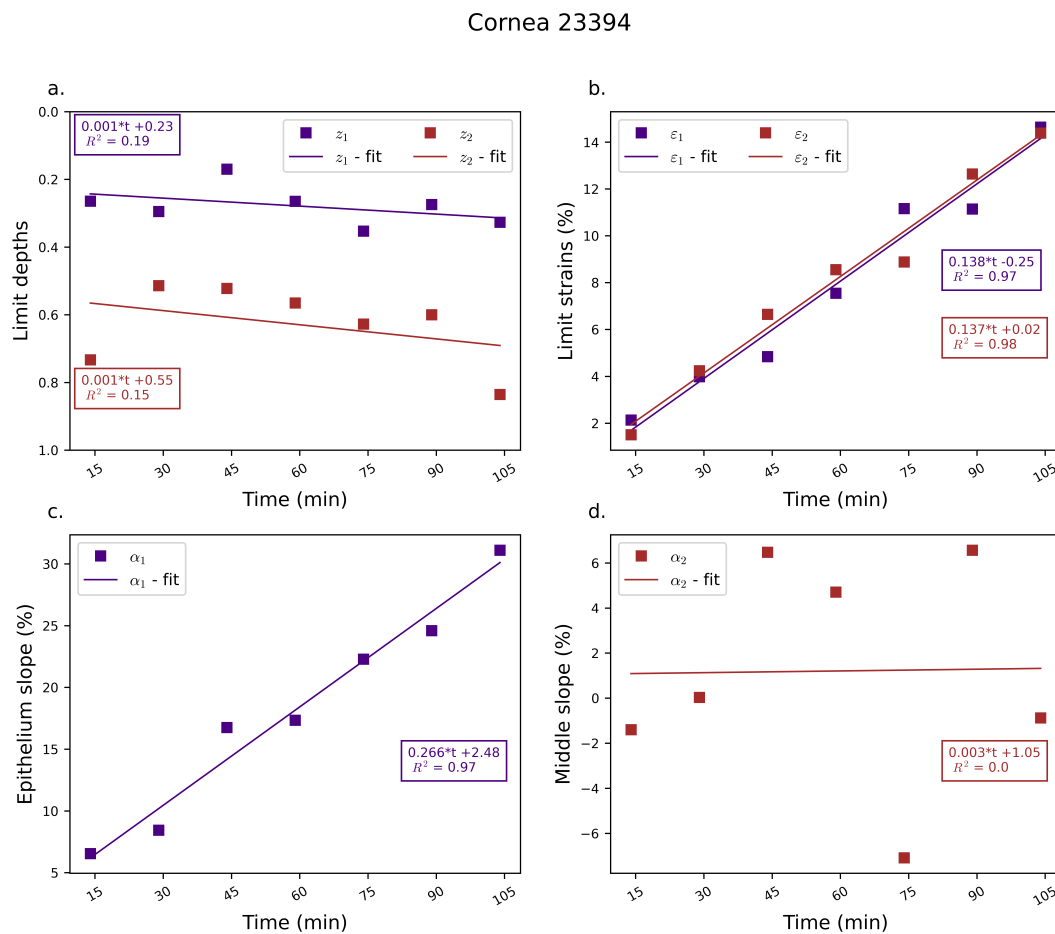


Figure 3.18: Time dependence of the parameters for creep test at physiological pressure (cornea 23394). a. Limits depths, b. Limit strains (purple result indicates limit 1 and dark red indicates limit 2) and c. Epithelium slope and d. Middle slope.

Parameter	Mean Slope	Std Slope	Mean intercept ordinate	Std intercept ordinate
z_1	0.000 min ⁻¹	0.001 min ⁻¹	0.25	0.04
z_2	-0.001 min ⁻¹	0.002 min ⁻¹	0.57	0.10
ε_1	0.06 %·min ⁻¹	0.06 %·min ⁻¹	5.32 %	3.06 %
ε_2	0.13 %·min ⁻¹	0.03 %·min ⁻¹	1.08 %	1.98 %
α_1	0.13 %·min ⁻¹	0.13 %·min ⁻¹	-9.94 %	36.1 %
α_2	0.31 %·min ⁻¹	0.45 %·min ⁻¹	-10.7 %	11.8 %

Table 3.10: Mean and Standard deviation (Std) of the slope and intercept ordinates of the linear fit of the time evolution of the parameters z_1 , z_2 , ε_1 , ε_2 and α_2 for the creep test at physiological pressure.

3.3.1.d Deturgescence protocol

In the previous part, the vertical strain along the depth profile near the apex has been studied to characterize the response of cornea under physiological pressure with time. Looking at this profile gives information on the response of the cornea only on the vertical strain, the deturgescence protocol will be tested in a more global way, considering all 2D strain with time. Looking at the strain maps (as in Fig. 3.11), we can expect similar behavior between the corneas.

Figure 3.19 presents the time evolution of the three components of the 2D strain tensor for the 5 tested corneas. Box plots show the median and standard deviation of each measured component on two representative images: the short and long axis transects. Corneas 23394, 23395 and 23417 followed the classical protocol of deturgescence while corneas 23490 and 23577 were put under pressure during the 48 h. of the deturgescence process. The three components are similar in range and values for the two different cases. As expected, the median strain of component e_{11} and e_{12} is almost 0 while the median of the vertical component e_{22} keeps growing with time, until almost 15%. Except for cornea 23490 – for which the major part of e_{11} rises to almost 4% – horizontal component e_{11} stays small, less than 2% in all cases, while the scatter of the distribution of shear strain e_{12} increases with time, until e_{12} reaches around $\pm 10\%$. The scatter of the vertical component e_{22} also increases with time, and the swelling of the cornea can reach 15% after an hour and a half of experiment.

Irrespective of the deturgescence protocol, the same range of strains and similar patterns are observed when corneas are put under physiological pressure, even if the scatter seems higher in the case of deturgescence under pressure. It may be due either to a lower density of endothelial cells (cornea 23490) for which the cornea would be more permeable, or to a difference in response with age (cornea 23577), which has been shown to be a parameter modifying the behavior of the tissue [45]. In addition, only 2 corneas underwent the deturgescence protocol under pressure, so the results may be biased also by the small number of samples.

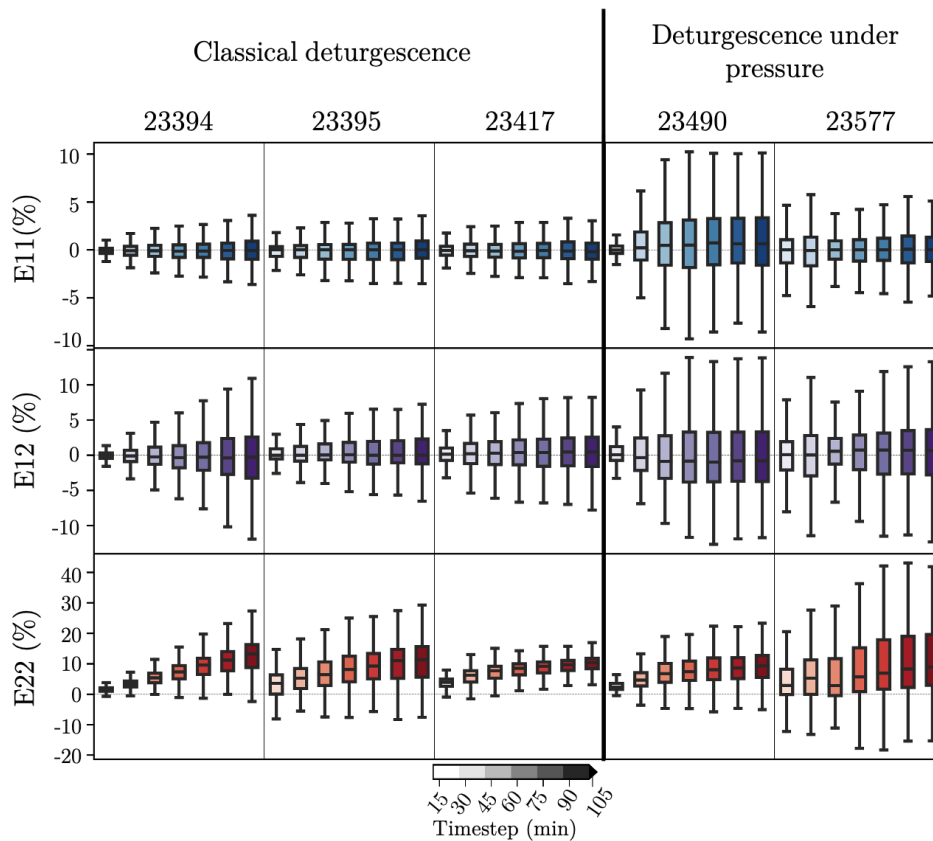


Figure 3.19: Comparison of the deturgescence protocols on the strain distribution of the two transects for the creep test at physiological pressure. Results are presented in the form of a box-plot at each time step on the same two transects presented before: a Naso-Temporal and a Superior-Inferior section through the apex. The box extends from the lower to upper quartile values of the data, with a line at the median. The whiskers extend from the box to show the range of the data. Rows: horizontal e_{11} (blue), shear e_{12} (purple) and vertical e_{22} (red) strains. Columns: considered cornea. Two deturgescence protocols have been tested: corneas 23394, 23395 and 23417 followed the classical deturgescence protocol in a Falcon tube, while corneas 23490 and 23577 were put under pressure during the deturgescence process.

3.3.2 Creep test at high pressure

Once the creep test at physiological pressure has been performed, the response of cornea to high pressure through time was studied. The objective of this second experiment is to assess whether the cornea maintained at high pressure will continue to swell, similar to the physiological pressure case, or not. The cornea was brought to high pressure (around 150 mbar) via 10 mbar pressure steps (Fig. 3.3.b). The purpose of going through small pressure steps was to limit the stress increment applied to the cornea and also to ensure the continuity of the correlation between two steps. 7 corneas of 2 females and 5 males are submitted to this test with the following characteristics: 69.9 ± 14.1 y.o. and with an endothelial cell density of 1996 ± 583 cells/mm².

3.3.2.a Vertical displacement maps and curvature radii

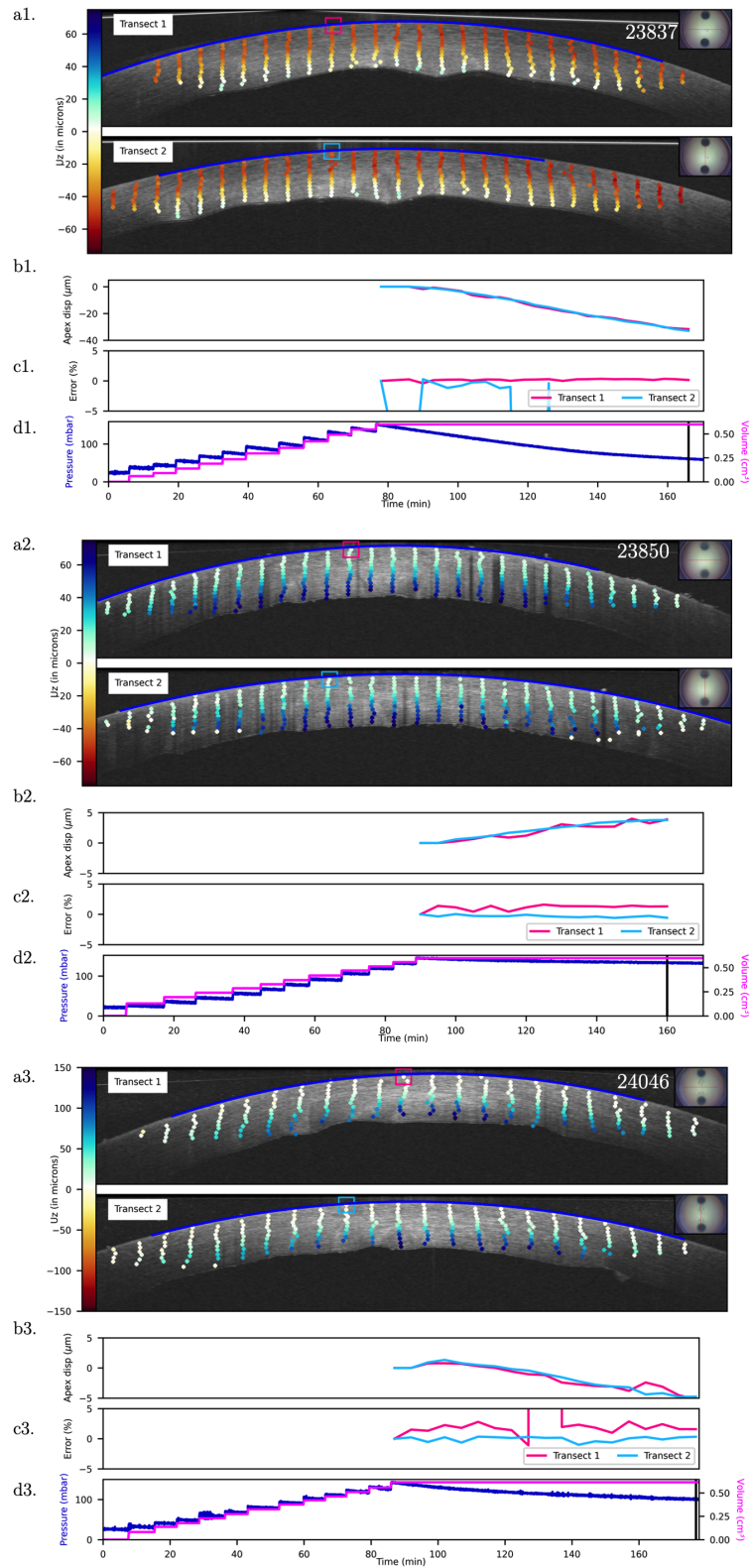


Figure 3.20: Results of the image analysis on two transects (in the direction of minor – Transect 1 – and major – Transect 2 – axis of the cornea) for the creep test at physiological pressure after approximately 2 hours (cornea 23837, 23850 and 24046). a. Vertical displacement U_z - Color bar: a.1.[-250 μm , 250 μm], a.2.[-250 μm , 250 μm], a.3.[-300 μm , 300 μm]. b. Evolution of the curvature radii with respect to the first ones (in %) c. Internal pressure and volume evolution with time (black bar indicate the considered time).

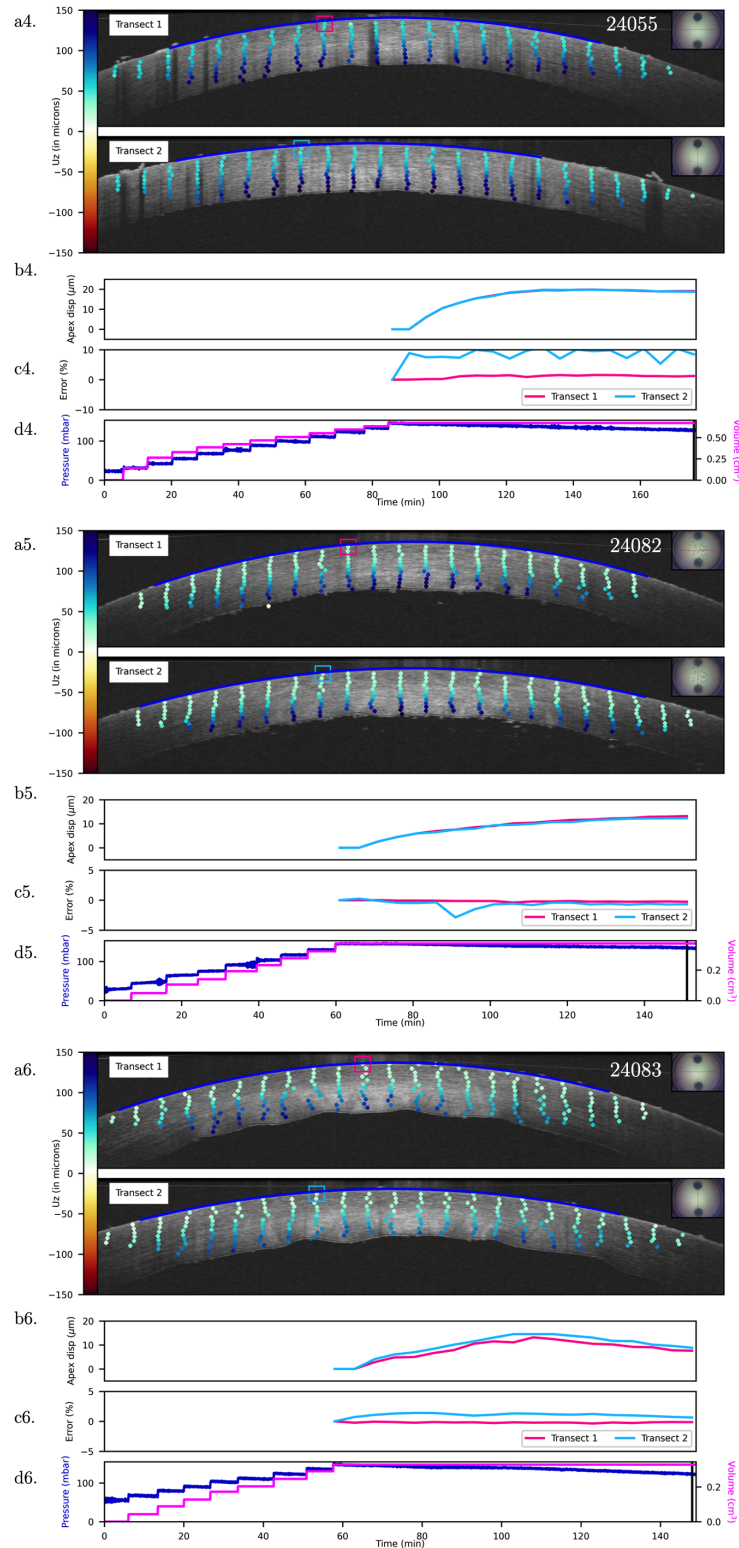


Figure 3.21: Results of the image analysis on two transects (in the direction of minor – Transect 1 – and major – Transect 2 – axis of the cornea) for the creep test at physiological pressure after approximately 2 hours (cornea 24055, 24082 and 24083). a. Vertical displacement U_z - Color bar: a.4. [-350 μm , 350 μm], a.5. [-350 μm , 350 μm], a.6. [-300 μm , 300 μm]. b. Evolution of the curvature radii with respect to the first ones (in %) c. Internal pressure and volume evolution with time (black bar indicate the considered time).

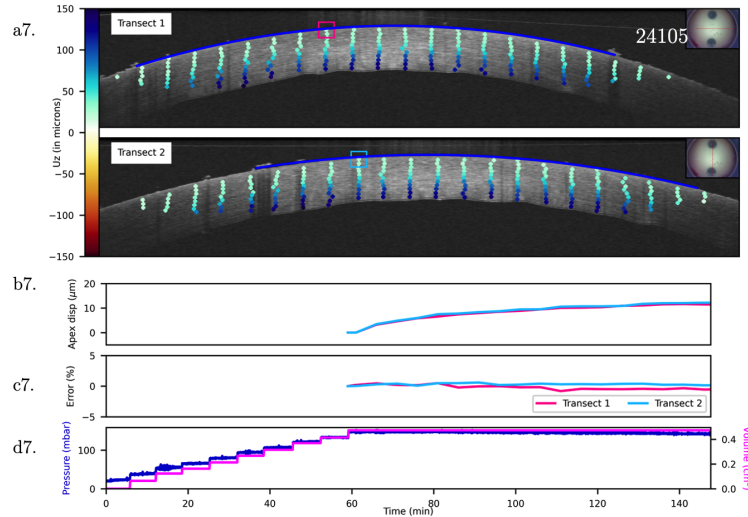


Figure 3.22: Results of the image analysis on two transects (in the direction of minor – Transect 1 – and major – Transect 2 – axis of the cornea) for the creep test at physiological pressure after approximately 2 hours (cornea 24105). a. Vertical displacement U_z - Color bar: [-300 μm , 300 μm]. b. Evolution of the curvature radii with respect to the first ones (in %) c. Internal pressure and volume evolution with time (black bar indicate the considered time).

Figures 3.20.a, 3.21.a and 3.22.a present the results of the vertical displacement U_z at the last time of the creep test at high pressure for the 7 corneas submitted (loading path is recalled on Fig. 3.20.d, 3.21.d and 3.22.d). A vertical gradient can be seen on the two transects (Superior-Inferior and Naso-Temporal sections) with a smaller displacement near the epithelium than in the lower part with positive displacements (so towards the epithelium) for six out of seven corneas. The only exception is cornea 23837 which exhibits negative displacement under the epithelium while almost none at the endothelium. It can be explained by the decreasing pressure observed on the PV with time curve, which may be explained by an leak in the experimental set-up. Figure 3.20.b, 3.21.b and 3.22.b show the time evolution of the two apex displacement. In this case, the apex tends to go upwards for most of the cornea but not more than 20 μm . For the two corneas (23837 and 24046) that has decreasing pressure during the creep test at high pressure, the apex tends to go downwards, which would be coherent with a slight leak of fluid from the chamber. Figure 3.20.c, 3.21.c and 3.22.c show the time evolution of the two radii of curvature of the anterior surface (represented in dark blue on the images) and defined by Eq 3.8. It is interesting to note that the radii of curvature vary very little (less than 5% of change in most cases) during the creep test at high pressure for six corneas out of seven. In this case, cornea 24055 has some bigger variation of the curvature radius for transect 2, which may be due to a poor contrast in the image leading to a bad fit of the surface.

3.3.2.b DIC / DVC strain maps

2D and 3D results are discussed here based on snapshots of the experiment, but the evolution throughout the whole test can be found at the following links:

<https://ppi-lms.polytechnique.fr/jean-marc.allain/CTHP2DStrainTime.html> for 2D and <https://ppi-lms.polytechnique.fr/jean-marc.allain/CTHP3D.html> for 3D analyses.

Figure 3.23 presents the results at the end of the creep test (Fig. 3.3.a – after approximately 150 minutes) for cornea 24105. Figures 3.23.a, b and c illustrate the strain maps (color-maps) computed by DIC for a. the horizontal, b. shear and c. vertical strains, superimposed on the corresponding OCT images, along the short (transect 1) and long axis (transect 2). Figure 3.23.d, shows the histogram of each of these strains (in pink for the short axis - transect 1 - and in blue for the long axis - transect 2 - of the cornea). Fig. 3.23.e presents the pressure with the apex displacement computed using the correlation domain near the apex on both transects and compared to the data found in [45]. Finally, Fig. 3.23.f recalls the pressure and volume with time curve of the creep test.

Figure 3.24 presents some results of the DVC analysis for the vertical strain at chosen times during one creep test at high pressure (cornea 24105). Figure 3.24.a–c show the results for three of the increasing steps of pressure ($p = 20$ mbar, $p = 80$ mbar and $p = 150$ mbar for the first time). Fig. 3.24.d–f present the correlation results for three time steps with stabilized pressure (150 mbar). Note that in the 3D representation, the vertical direction corresponds to the z-axis, so that e_{22} on the 2D images corresponds to e_{ZZ} in the 3D analysis.

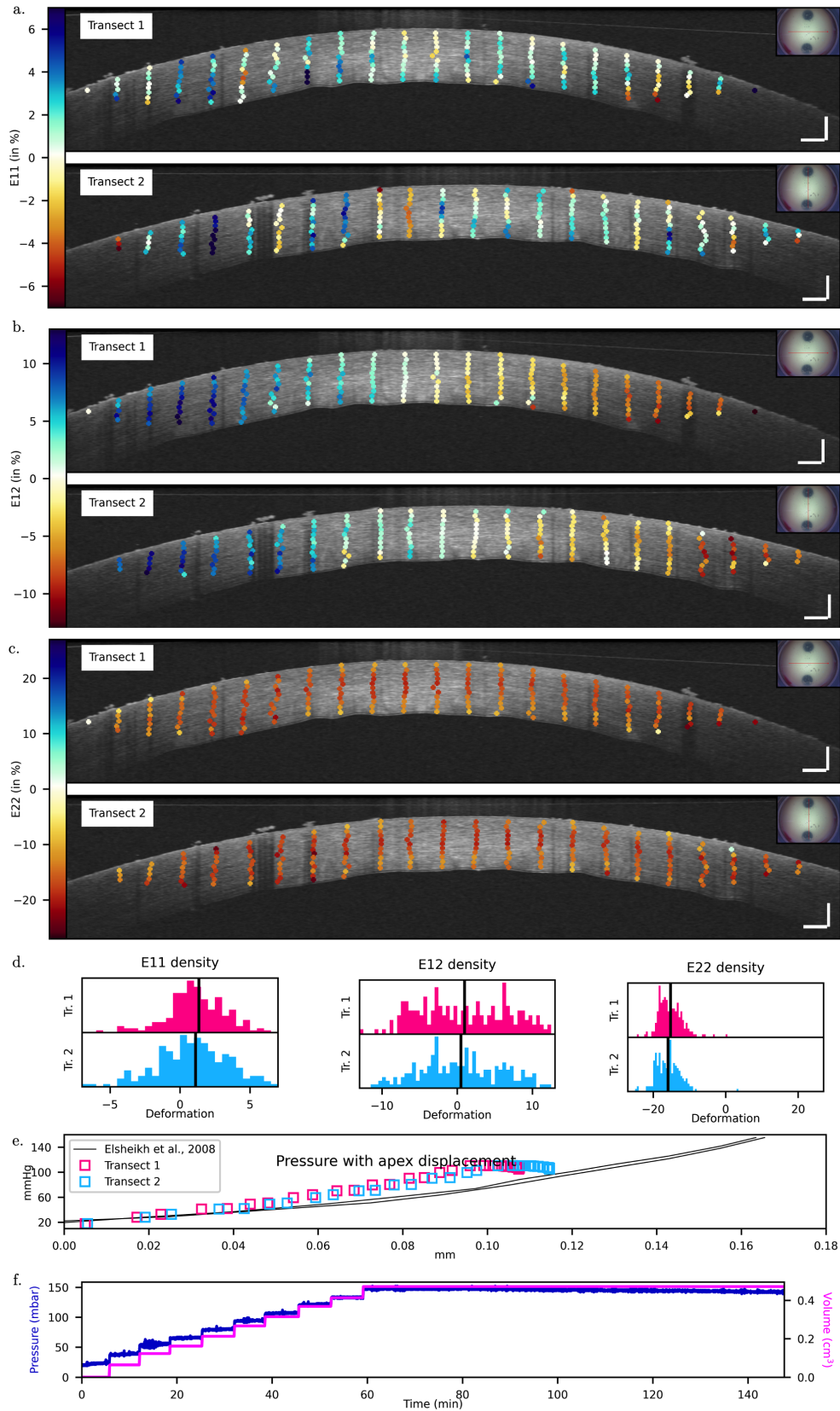


Figure 3.23: Results of the image analysis on two transects (in the direction of minor – Transect 1 – and major – Transect 2 – axis of the cornea) for the creep test at high pressure after approximately 150 minutes (cornea 24105). a. Horizontal strain e_{11} - Color bar: $[-7\%, 7\%]$. b. Shear strain e_{12} - Color bar: $[-15\%, 15\%]$ c. Vertical strain e_{22} - Color bar: $[-27\%, 27\%]$, a–c. scale bar of the OCT image - $250 \mu\text{m}$. d. Strain histogram for a particular time of the experiment. e. Pressure with apex displacement compared to the data found in [45]. f. Internal pressure and volume evolution with time.

Cornea	e11		e12		e22	
	Phase 1	Phase 2	Phase 1	Phase 2	Phase 1	Phase 2
23837	[-5%, 6%]	[-5%, 7%]	[-14%, 11%]	[-16%, 13%]	[-22%, 5%]	[-25%, 2%]
23850	[-5%, 7%]	[-5%, 8%]	[-12%, 10%]	[-14%, 13%]	[-25%, 8%]	[-32%, 3%]
24046	[-6%, 7%]	[-5%, 10%]	[-18%, 17%]	[-21%, 20%]	[-30%, 8%]	[-35%, 2%]
24055	[-7%, 6%]	[-7%, 9%]	[-12%, 9%]	[-15%, 13%]	[-23%, 5%]	[-28%, 1%]
24082	[-4%, 4%]	[-5%, 7%]	[-8%, 9%]	[-13%, 14%]	[-18%, 6%]	[-27%, 4%]
24083	[-11%, 9%]	[-14%, 12%]	[-12%, 10%]	[-16%, 14%]	[-20%, 7%]	[-28%, 5%]
24105	[-4%, 5%]	[-6%, 7%]	[-7%, 7%]	[-11%, 12%]	[-20%, 10%]	[-23%, 6%]

Table 3.11: Strain range of the creep test at high pressure.

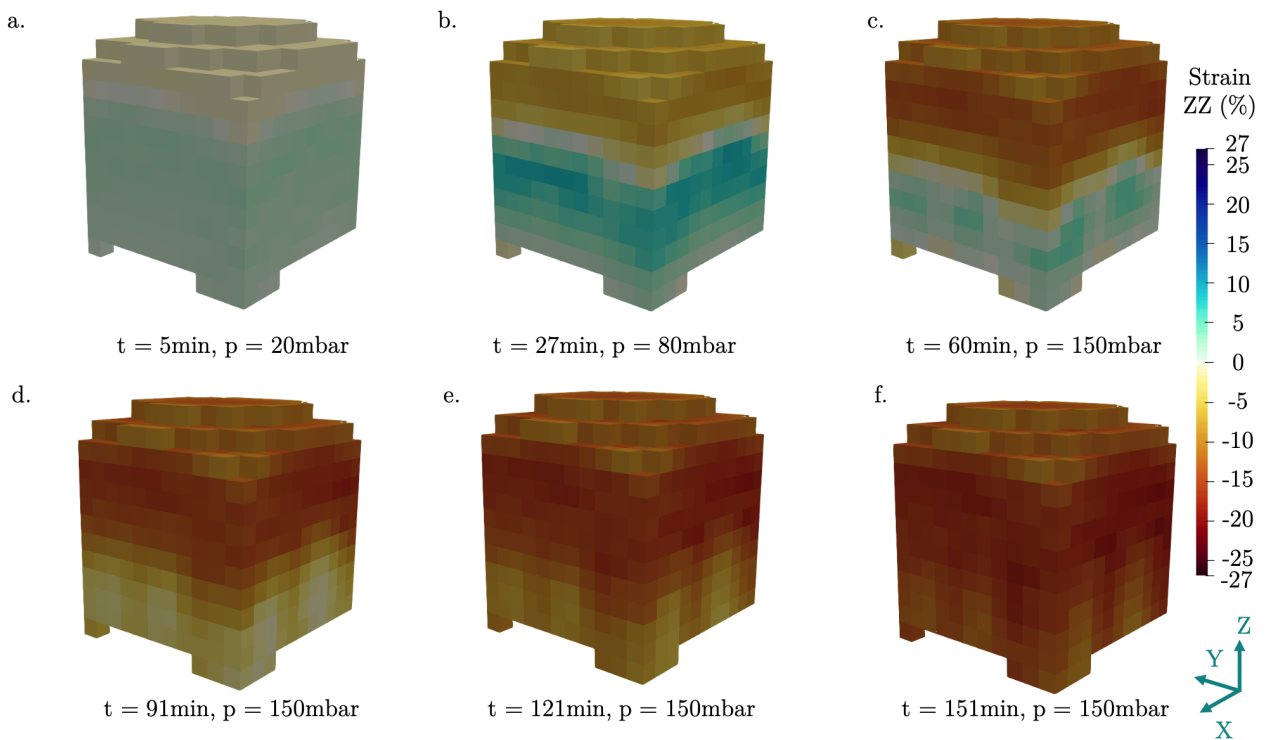


Figure 3.24: Vertical strain e_{ZZ} computed using DVC on 3D images of the cornea under the creep test at high pressure for several time steps and pressures (cornea 24105). Color bar: $[-20\%, 20\%]$. Fig. 3.24.a–c correspond to three of the increasing steps of pressure ($p = 20\text{ mbar}$, $p = 80\text{ mbar}$ and $p = 150\text{ mbar}$ for the first time), and d–f to three following times of stabilized pressure ($p = 150\text{ mbar}$). Fig. 3.24.f corresponds to the same step as Fig. 3.23.c.

The same observations can be made from the analysis of the two (Fig. 3.23) and three-dimensional (Fig. 3.24) strains measured during the tests of the seven samples and also from the values of the strain summarized in Table 3.11 for the creep test at high pressure. Figures 3.25, 3.26 and 3.27 completes the pictures with the results of the vertical strains for the last time of the creep test at high pressure for the seven corneas. First, as in the creep test at physiological pressure, the strain is larger by a factor 3 to 5 approximately along the vertical direction, i.e. through the thickness of the cornea – e_{ZZ} and e_{22} – compared to the horizontal directions – e_{XX} , e_{YY} and e_{11} – as highlighted by Fig. 3.23. While horizontal strains are mostly contained between -6% and +7%, vertical normal

strain can reach up to 23% in absolute value. In connection, the shear strain – e_{12} – is also twice as large as e_{11} , ranging between -11% and 12%. Again, as in creep tests at physiological pressure, for horizontal normal strains (Fig. 3.23.a), no discernible pattern emerges, and the distribution of strain is not skewed towards either contraction nor swelling (Fig. 3.23.d). However, as in the creep test at physiological pressure, for e_{12} and e_{22} , the data indicate a different behavior. Figure 3.23.b reveals for e_{12} a negative strain (warm colors) on the right-hand side of the image, opposed to a positive strain (cool colors) on its leftmost part, with a neutral strain transition zone at the center of the image. At the beginning of the first phase of the creep test (Figure 3.24.a and b), the cornea is in extension in its posterior part (30 to 100% of depth) and in contraction in its anterior part (0 to 30% of depth) and as in the creep test at physiological pressure, the first limit depth is around 30% of depth. Conversely, at the end of the pressure steps (around 60 minutes), e_{22} and e_{ZZ} (Fig. 3.23.c and Fig. 3.24.d–f) feature significantly negative values only throughout the cornea, with a mean strain around -15% for the last time (Fig. 3.23.d). Again, this can be said for both axes of the cornea and seen on the 3D representation, and translates its contraction under high pressure. When the pressure stabilizes (after around 60 minutes), the anterior part of the cornea does not seem to deform anymore, but the contraction continues to propagate in the posterior part of the cornea. Finally, the trend of pressure with apex displacement (Fig. 3.23.e) is similar to [45] when increasing the pressure. Under stabilized pressure, the apex keeps moving upwards, but by less than 20 μm .

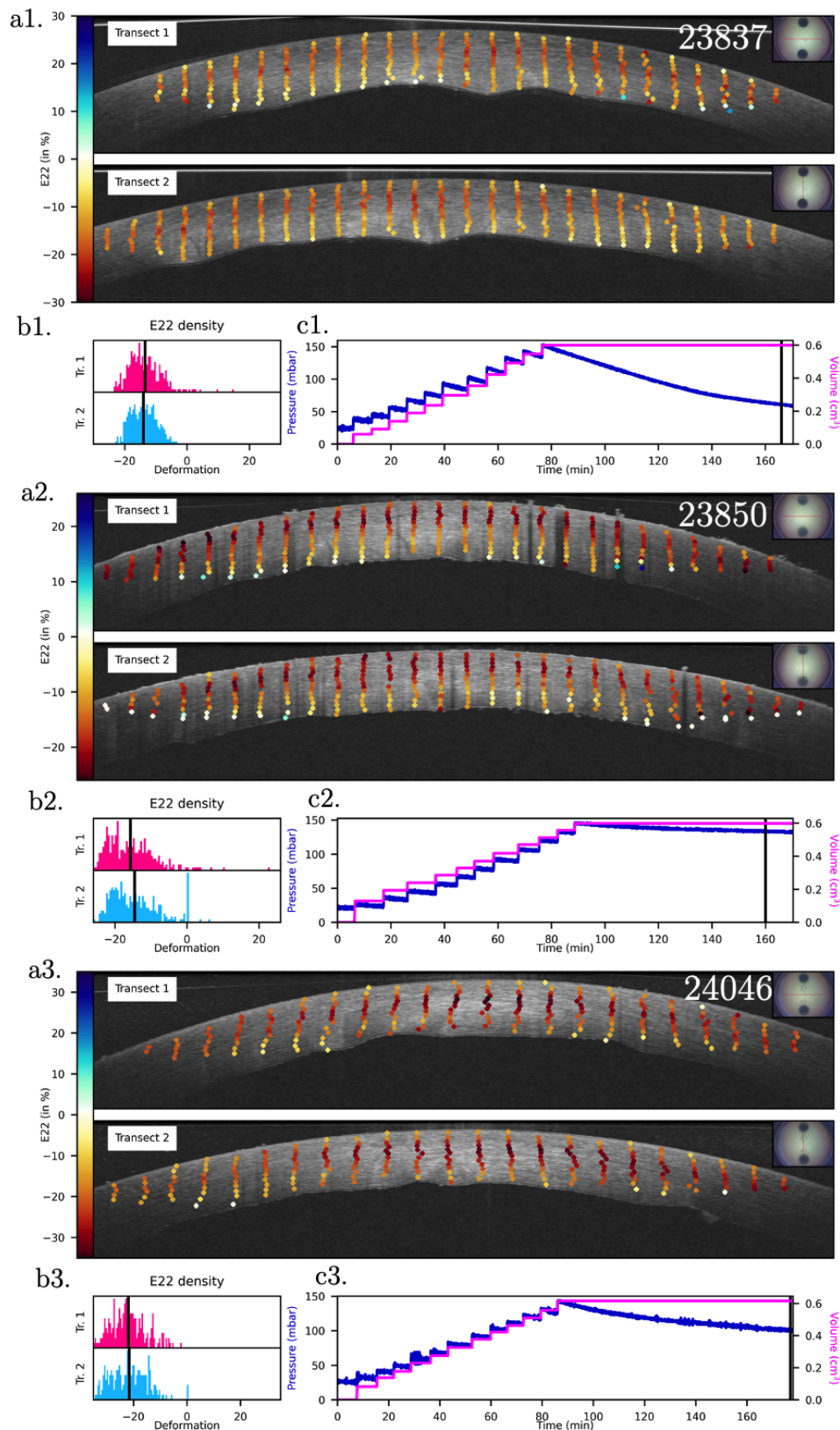


Figure 3.25: Results of the image analysis on two transects (in the direction of minor – Transect 1 – and major – Transect 2 – axis of the cornea) at the end of the creep test at high pressure (cornea 23837, 23850 and 24046). a. Vertical strain e_{22} - Color bar: a.1. $[-30\%, 30\%]$, a.2. $[-26\%, 26\%]$, a.3. $[-35\%, 35\%]$. b. Strain density for the particular time of the experiment considered. c. Internal pressure and volume evolution with time (black bar indicate the considered time)

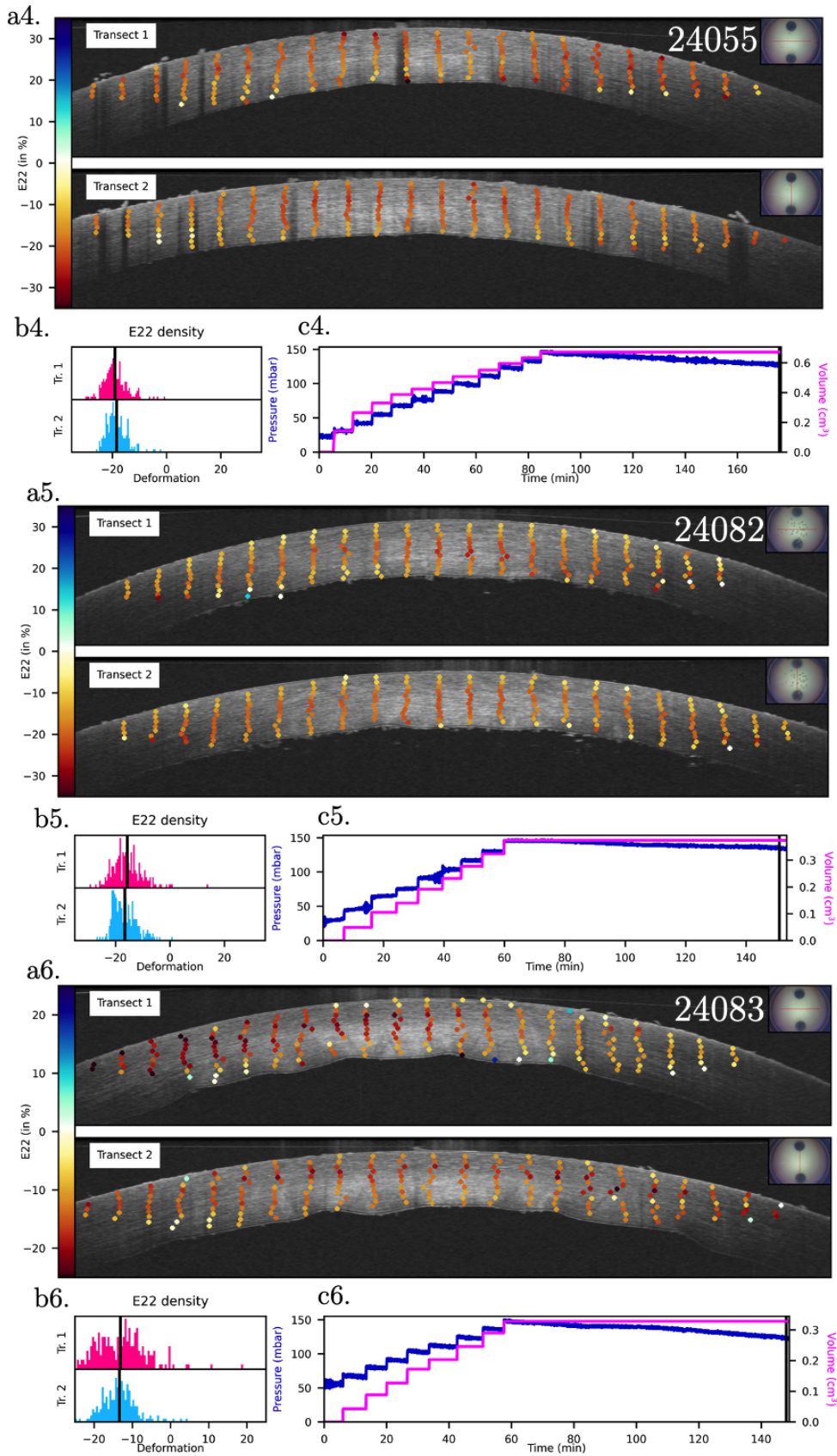


Figure 3.26: Results of the image analysis on two transects (in the direction of minor – Transect 1 – and major – Transect 2 – axis of the cornea) at the end of the creep test at high pressure (cornea 24055, 24082 and 24083). a. Vertical strain e_{22} - Color bar: a.4. $[-35\%, 35\%]$, a.5. $[-35\%, 35\%]$, a.6. $[-25\%, 25\%]$. b. Strain density for the particular time of the experiment considered. c. Internal pressure and volume evolution with time (black bar indicate the considered time)

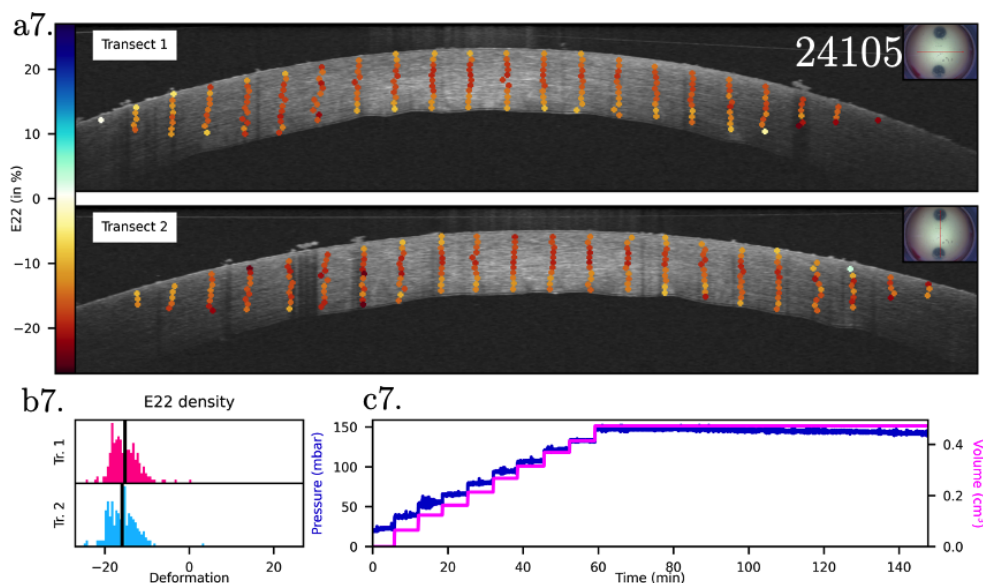


Figure 3.27: Results of the image analysis on two transects (in the direction of minor – Transect 1 – and major – Transect 2 – axis of the cornea) at the end of the creep test at high pressure (cornea 24105). a. Vertical strain e_{22} - Color bar: a.7. $[-27\%, 27\%]$. b. Strain density for the particular time of the experiment considered. c. Internal pressure and volume evolution with time (black bar indicate the considered time)

3.3.2.c Depth profile of the vertical strain e_{22}

2D results are discussed here based on snapshots of the experiment, but the evolution throughout the whole test can be found at the following links:

<https://ppi-lms.polytechnique.fr/jean-marc.allain/CTHP2DE22Fit.html> for the evolution of the parameters with time,

<https://ppi-lms.polytechnique.fr/jean-marc.allain/CTHP2DE22Profile.html> for the color maps of the depth profile.

Figure 3.23.c reveals a discernible pattern through thickness for the vertical strain e_{22} . This pattern will be studied looking at the depth profile of the strain near the apex of the cornea on both transects with the same approach as the study at physiological pressure.

Transects analysis Figure 3.28 presents the results of the vertical strain profile with time. Figure 3.28.a shows the correlation points used to compute the depth profile, pink and blue colors are associated with transect 1 and 2, respectively. Figure 3.28.b shows the data and the fit (left) of the depth profile by the three slopes curve defined in Eq. (3.11). The same decomposition of Fig. 3.15 will be used to have the two limit depths z_1 and z_2 , associated with the two limit strains ε_1 and ε_2 and the three slopes α_1 , α_2 and α_3 . Figure 3.28 shows the time evolution of the limit depths z_1 and z_2 (middle) and slopes α_1 , α_2 and α_3 (right). The corresponding along-profile strain with time is shown in Fig. 3.28.c (top for transect 1 and bottom for transect 2). Figure 3.28.d recalls the pressure and volume curves with time associated with the performed experiment.

As seen in Fig. 3.24, the observed strain is both positive and negative throughout the whole profile at the beginning of the experiment (within a $-10\% - 10\%$ range) reflecting that the cornea swelled in

its deepest part and contracted in its first third under low pressure (during the first steps of phase 1). In addition, the results of the very first step of the creep at high pressure look similar to the first step of the creep test at physiological pressure. Vertical strain is only negative during the second phase (when the pressure is stabilized). Also, for this component, the same three areas can be distinguished regarding the value of the strain on both the short and long axis transects: (i) the upper quarter of the thickness under the epithelium, (ii) the central part and (iii) the lower quarter of the cornea. In this case also, the values of the limits (z_1 and z_2) between the three areas, the associated strains (ε_1 and ε_2) and slopes (α_1 , α_2 and α_3) vary among the seven corneas and the following will try to quantify these parameters and assess their temporal variability.

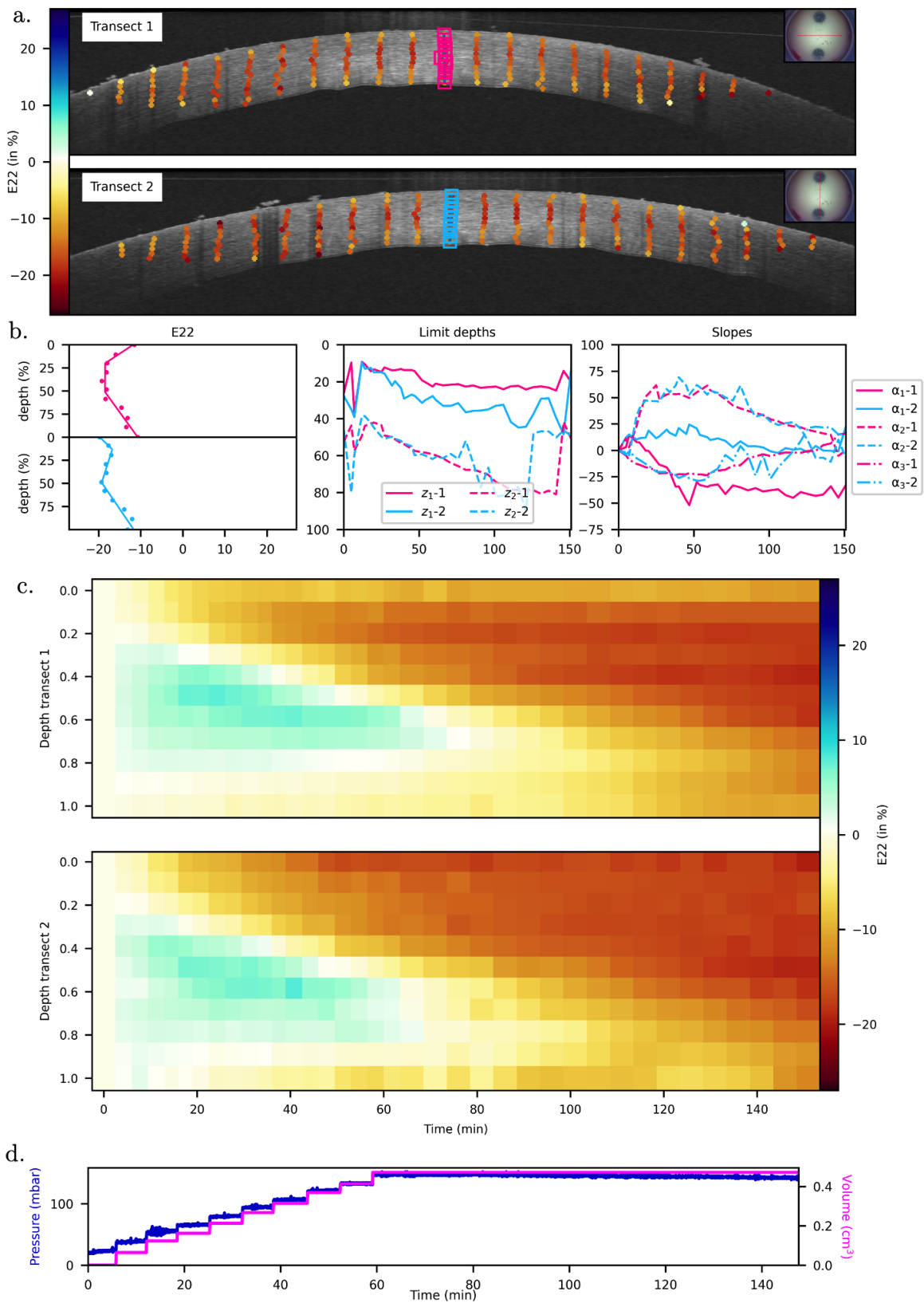


Figure 3.28: Depth profile of vertical strain for creep test at high pressure (cornea 24105). a. Depth profiles considered on the two transects (pink and blue squares). b. Vertical strain (in%) of the depth profiles at the considered time – left : data and three-slopes fit, middle: limit depths (in%) and right : slopes (in%) of the fit with time. c. Vertical strain of the depth profile with time for the two transects. d. Internal pressure and volume with time.

The pressure steps will be studied in the inflation test part (Sec. 3.3.4), and what follows will only concentrate on the second phase of the creep test, during which the pressure is kept constant.

The same paired t-test (as for creep tests at physiological pressure) has been performed on the distributions of the parameters between transects and between the limit depths and strains for each transect (results are presented Fig. 3.29). First, no-significant differences were found between the two transects for z_1 , z_2 , ε_2 and α_2 (t-test with a p-value $< 1\%$). For ε_1 the difference comes from a bigger scatter on transect 2 but the range of value are similar. Again, for the endothelium and epithelium slopes, the differences can be explained by (i) the fact that the considered zones are small (in both cases) and (ii) the loss of signal near the endothelium (for α_3). The two transects are similar for most of the parameters. Consequently, the data obtained for each profile are merged into a single data set, representative of the vertical profile. The time evolution of these parameters is presented in the next section except the endothelium slope, which depends significantly on the correlation domain at 100% depth (as there are only a few points in this area), which is less precise because of loss in signal with depth.

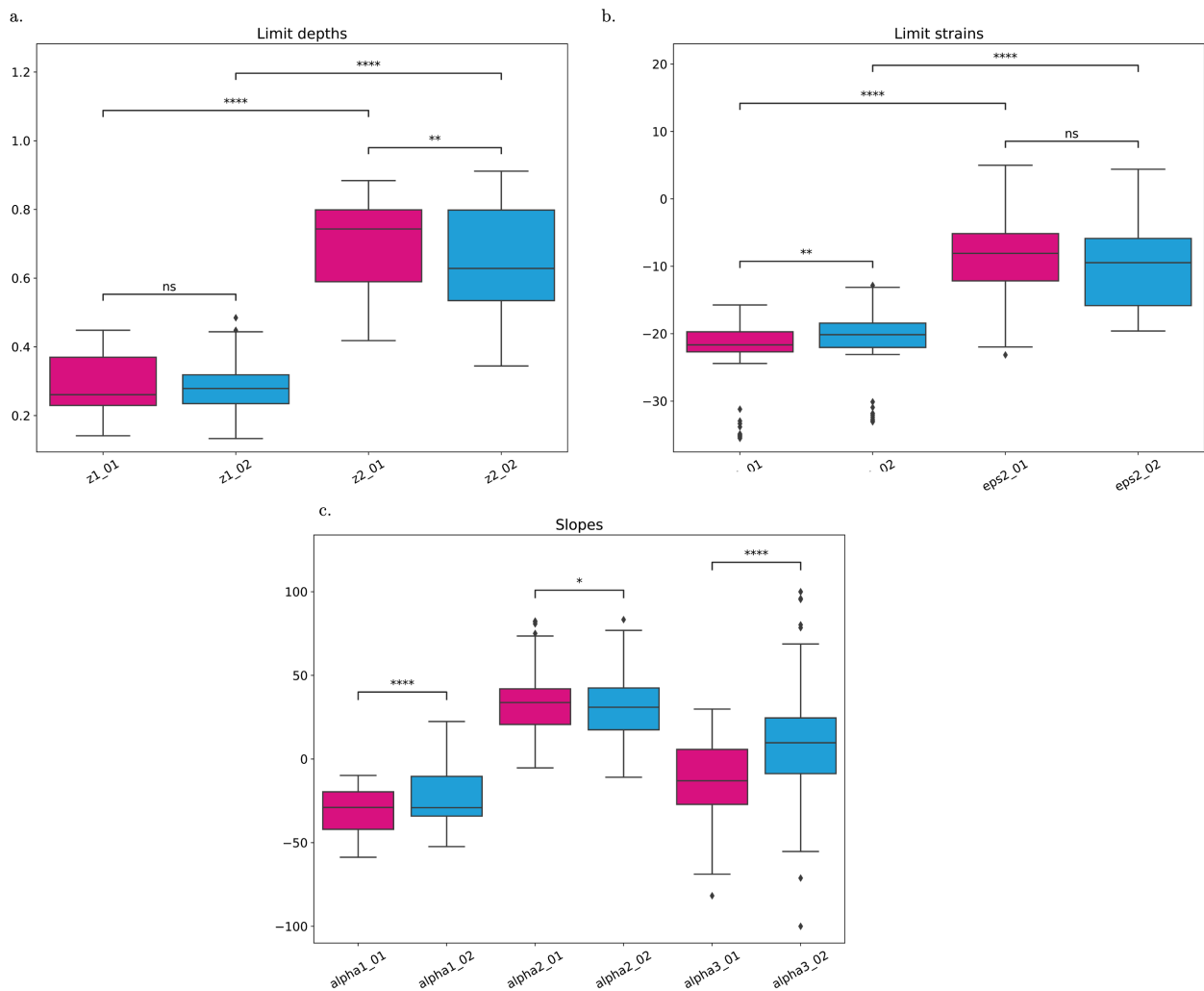


Figure 3.29: a. Limit depths, b. Slopes (in %) and c. Limit strains (in %) of the three-slopes fit of the vertical strain for the creep test at high pressure for the two transects. T-test legend: ns – non-significant, * $p < 5\%$, ** $p < 1\%$, *** $p < 0.1\%$ and **** $p < 0.01\%$.

Time dependence analysis Figure 3.30 presents the time evolution of a. the limit depths, b. the limit strains c. the epithelium slope and d. the middle slope for cornea 24105 (the results for the other corneas can be found in App. E.3.2). All data are fitted with linear curves. Table 3.12 complements the pictures by giving the mean and standard deviation of the slopes and intercept ordinates for the seven corneas tested. While the two limit depths do not move with time (with $z_1 = 0.3$ and $z_2 = 0.6$), the limit strains ε_1 and ε_2 decrease linearly with time by $-0.03\%.\text{min}^{-1}$ and $-0.16\%.\text{min}^{-1}$, respectively, with always negative intercept ordinates, -20.5% and -3.15% respectively). As a result, the middle slope decreases with time by $-0.42\%.\text{min}^{-1}$. This reflects a global contraction of the cornea with first a bigger contraction at depth z_1 than at depth z_2 , and then a progressive homogenization of the values in the central part at the end of the creep test. Those data are consistent with the apparent propagation of the strain observed in Fig. 3.24 d, e, f during phase 2 of the creep test. The epithelium slope does not change much – with a mean slope of $-0.08\%.\text{min}^{-1}$. As the first limit strain is almost constant, this is consistent with the fact that we observe almost no evolution of the strains in the epithelium area. The standard deviations are small compared to the mean for the two limit depths and epithelium slope, but they are quite high for the other parameters (approximately the third of the mean for the slope). This may be due to the variability across human samples, but is less pronounced in this case than in the creep tests at physiological pressure.

Cornea 24105

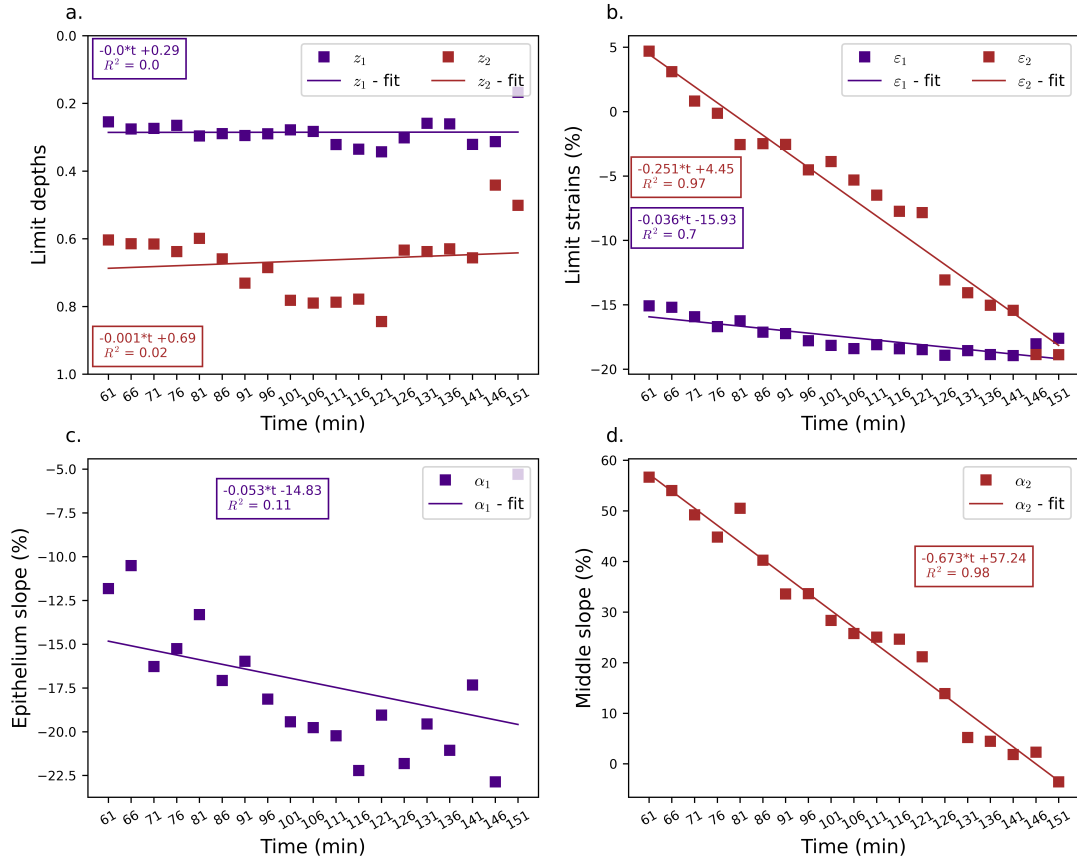


Figure 3.30: Time dependence of the parameters for creep test at high pressure (cornea 24105). a. Limits depths, b. Limit strains (purple results indicates limit 1 and dark red limit 2) and c. Epithelium slope and d. Middle slope.

Parameter	Mean Slope	Std Slope	Mean intercept ordinate	Std intercept ordinate
z_1	0.000 min^{-1}	0.000 min^{-1}	0.27	0.04
z_2	0.001 min^{-1}	0.002 min^{-1}	0.64	0.11
ε_1	$-0.03 \text{ \%}.\text{min}^{-1}$	$0.02 \text{ \%}.\text{min}^{-1}$	-20.5 %	4.74 %
ε_2	$-0.16 \text{ \%}.\text{min}^{-1}$	$0.05 \text{ \%}.\text{min}^{-1}$	-3.15 %	3.47 %
α_1	$-0.08 \text{ \%}.\text{min}^{-1}$	$0.03 \text{ \%}.\text{min}^{-1}$	-25.0 %	12.4 %
α_2	$-0.42 \text{ \%}.\text{min}^{-1}$	$0.15 \text{ \%}.\text{min}^{-1}$	50.1 %	13.9 %

Table 3.12: Mean and Standard deviation (Std) of the slope and intercept ordinates of the linear fit of the time evolution of the parameters z_1 , z_2 , ε_1 , ε_2 and α_2 for the creep test at high pressure.

3.3.3 Comparison of creep tests

A t-test was performed to compare the parameters of the three-slopes function (limit depths, limit strains and slopes) of the two different creep tests. Results are found in Fig. 3.31 (in App. E.4) and the main conclusions are summarized hereafter. The first limit depth z_1 is the most similar parameter

between the two cases. All other parameters, – the second limit depths z_2 , the epithelium slope α_1 , the middle slope α_2 and the limit strains ε_1 and ε_2 – are significantly different at the 99.99% level. It clearly shows that the cornea swells under low pressure, but contracts when submitted to higher pressure, with a first limit depth z_1 slightly higher in the case of high pressure. For the second limit depths z_2 the conclusion are not so clear, as the subdivision of cornea was not so relevant for the creep test at physiological pressure compared to the creep test at high pressure (leading to a huge scatter of z_2 in the creep test at physiological pressure). The epithelium slope comes from a positive to almost null value for the creep test at physiological pressure to a significantly negative value at high pressure. Coupling the epithelium slope with the first limit strain ε_1 shows that in absolute value, the strain is always higher at the first limit depth z_1 than at the epithelium, meaning that the epithelium area deforms less than the central part. For the middle slope, we recover the fact that the cornea swells more (or compress less) around the depth z_2 than around z_1 (with positive slopes). Again the third slope is not studied much because there are only a few points in this area and also for the potential low correlation of the last point (at 100% of depth) which greatly influences the slope.

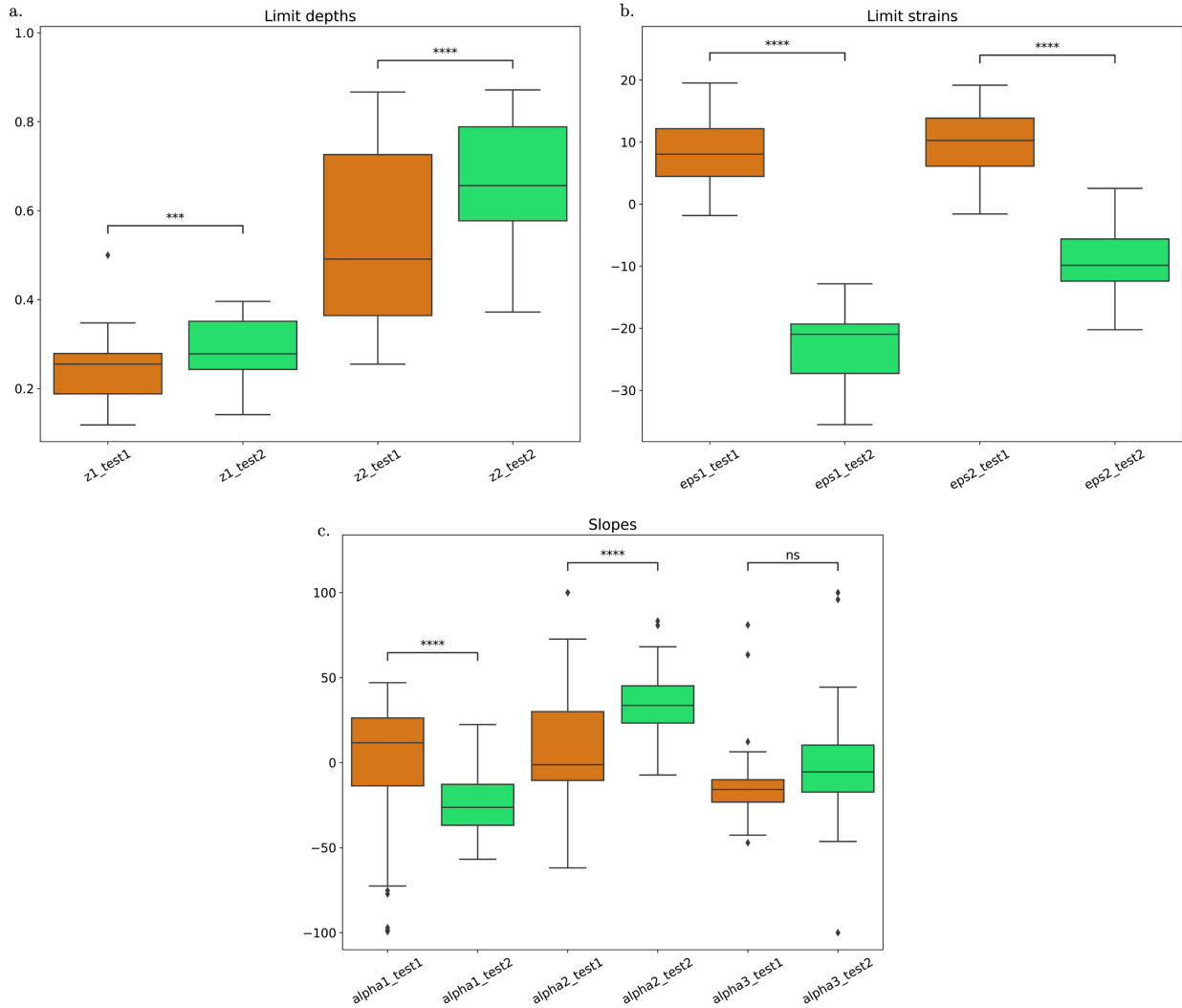


Figure 3.31: Comparison of the a. Limit depths, b. Limit strains (in %) and c. Slopes (in %) of the three-slopes fit of the vertical strain for the two creep tests. Legend: orange corresponds to the creep test at physiological pressure, green is for the creep test at high pressure. T-test legend: ns – non-significant, * $p < 5\%$, ** $p < 1\%$, *** $p < 0.1\%$ and **** $p < 0.01\%$.

The previous sections studied the response of the cornea to creep test at physiological and high pressure, the following section will look at the mechanical behavior of cornea between these two regimes, during the pressure steps.

3.3.4 Inflation tests

The goal of the inflation test is to characterize the mechanical response of cornea under a wide range of pressure. Pressure steps were applied (around 10 mbar each – loading path of Fig. 3.3.c), with an analysis of OCT images based on DIC/DVC. Then, the apex displacement is measured and compared to the data found by [45]. 7 corneas of 3 females and 4 males are submitted to this test with the following characteristics: 76.9 ± 6.5 y.o. and with an endothelial cell density of 2208 ± 420 cells/mm².

3.3.4.a Vertical displacement maps and curvature radii

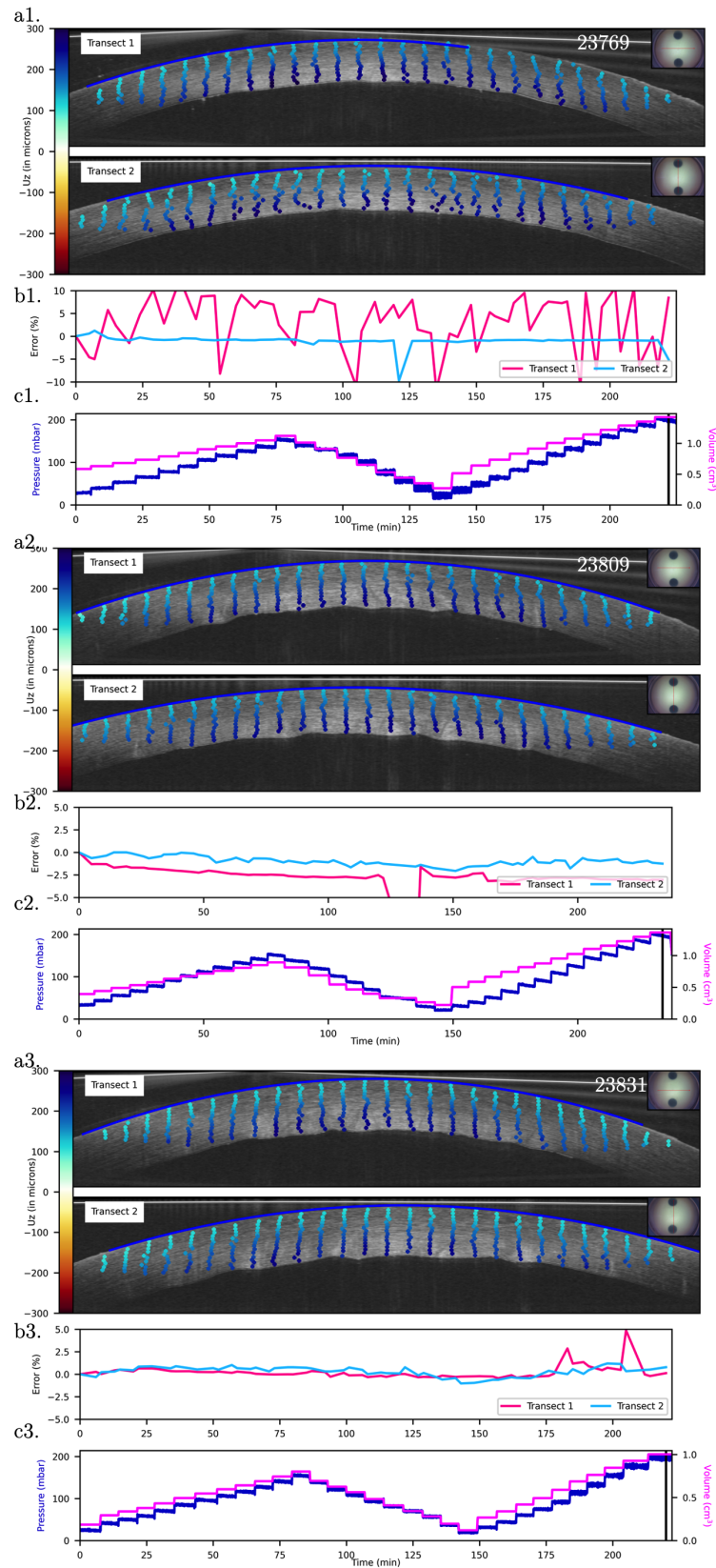


Figure 3.32: Results of the image analysis on two transects (in the direction of minor – Transect 1 – and major – Transect 2 – axis of the cornea) for the creep test at physiological pressure after approximately 2 hours (cornea 23769, 23809 and 23831). a. Vertical displacement U_z - Color bar: a.1–3. [-300 μm , 300 μm]. b. Evolution of the curvature radii with respect to the first ones (in %) c. Internal pressure and volume evolution with time (black bar indicate the considered time). 145

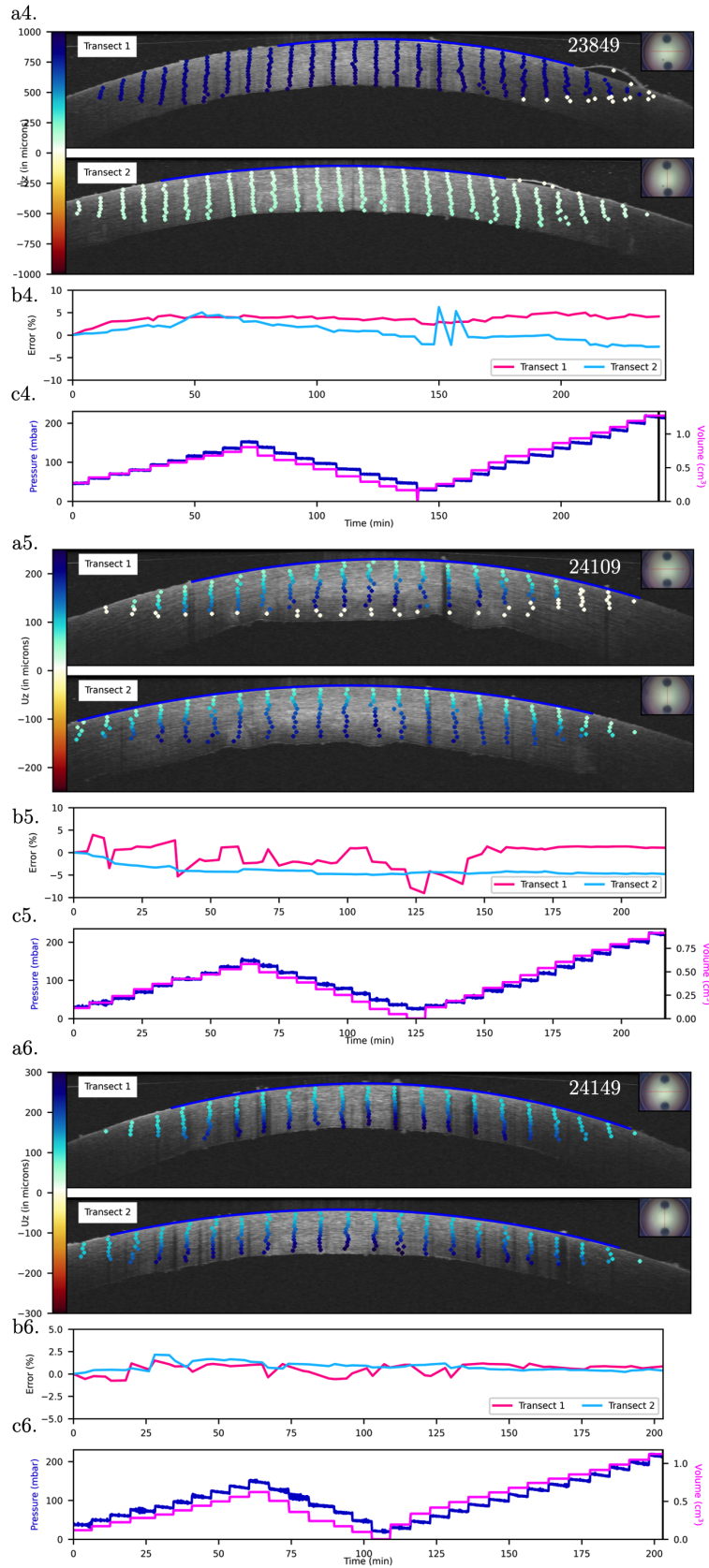


Figure 3.33: Results of the image analysis on two transects (in the direction of minor – Transect 1 – and major – Transect 2 – axis of the cornea) for the creep test at physiological pressure after approximately 2 hours (cornea 23849, 24109 and 24149). a. Vertical displacement U_z - Color bar: a.4.[-1000 μm , 1000 μm], a.5.[-250 μm , 250 μm], a.6.[-300 μm , 300 μm]. b. Evolution of the curvature radii with respect to the first ones (in %) c. Internal pressure and volume evolution with time (black bar indicate the considered time).

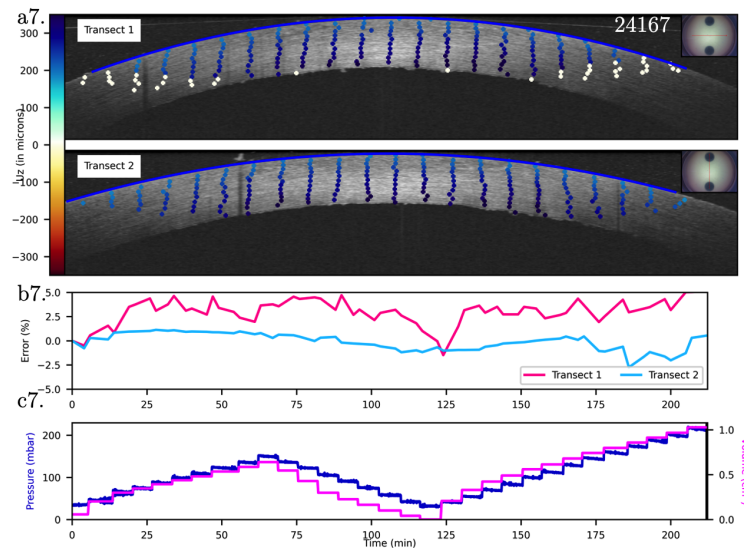


Figure 3.34: Results of the image analysis on two transects (in the direction of minor – Transect 1 – and major – Transect 2 – axis of the cornea) for the creep test at physiological pressure after approximately 2 hours (cornea 24167). a. Vertical displacement U_z - Color bar: a.7.[-350 μm , 350 μm]. b. Evolution of the curvature radii with respect to the first ones (in %) c. Internal pressure and volume evolution with time (black bar indicate the considered time).

Figures 3.32.a, 3.33.a and 3.34.a present the results of the vertical displacement U_z at the last time of the creep test at high pressure for the 7 corneas submitted (loading path is recalled on Fig. 3.32.c, 3.33.c and 3.34.c). A vertical gradient can be seen on the two transects (Superior-Inferior and Naso-Temporal sections) with a smaller displacement near the epithelium than in the lower part with positive displacements (so towards the epithelium) for five out of seven corneas. Two corneas have not the right displacement because of the experimental set-up (some time, I had to change the height of the OCT which led to a vertical displacement of the image). For this reason, the apex displacement curves are not presented here. Figure 3.32.b, 3.33.b and 3.34.b show the time evolution of the two radii of curvature of the anterior surface (represented in dark blue on the images) and defined by Eq 3.8. It is interesting to note that the radii of curvature vary very little (less than 5% of change in most cases) during the inflation test for five corneas out of seven. In this case, corneas 23849 and 24109 have bigger variation of the curvature radii for transect 1, which may be due to a poor contrast in the image leading to a bad fit of the surface.

3.3.4.b DIC / DVC strain maps

2D and 3D results are discussed here based on snapshots of the experiment, but the evolution throughout the whole test can be found at the following links:

<https://ppi-lms.polytechnique.fr/jean-marc.allain/IT2DStrainTime.html> for 2D and

<https://ppi-lms.polytechnique.fr/jean-marc.allain/IT3D.html> for 3D analyses.

Figure 3.35 presents the results at the end of the inflation test (Fig. 3.3.a – after approximately 220 minutes) for cornea 23831. Figures 3.35.a, b and c illustrate the strain maps (color-maps) computed by DIC for a. the horizontal, b. the shear and c. the vertical strains, superimposed on the corresponding OCT images, along the short (transect 1) and long axis (transect 2). Figure 3.35.d shows the density

distribution of each of these strains (in pink for the short axis - transect 1 - and in blue for the long axis - transect 2 - of the cornea). Fig. 3.35.e presents the pressure with apex displacement computed using the correlation domain near the apex on both transects and compared to the data found in [45]. Finally, Fig. 3.35.f recalls the pressure and volume VS time curve of the inflation test.

Figure 3.36 presents results of the DVC analysis for the vertical strain at chosen times during one inflation test (cornea 24167). Figure 3.36.a–c show three of the increasing pressure steps during phase 1, Fig. 3.36.d–f three of the decreasing steps of pressure during phase 2 and Fig. 3.36.g–i three of the increasing pressure steps during phase 3. As before, in the 3D representation, the vertical direction corresponds to the z-axis, so that e_{22} on the 2D images corresponds to e_{ZZ} in the 3D analysis.

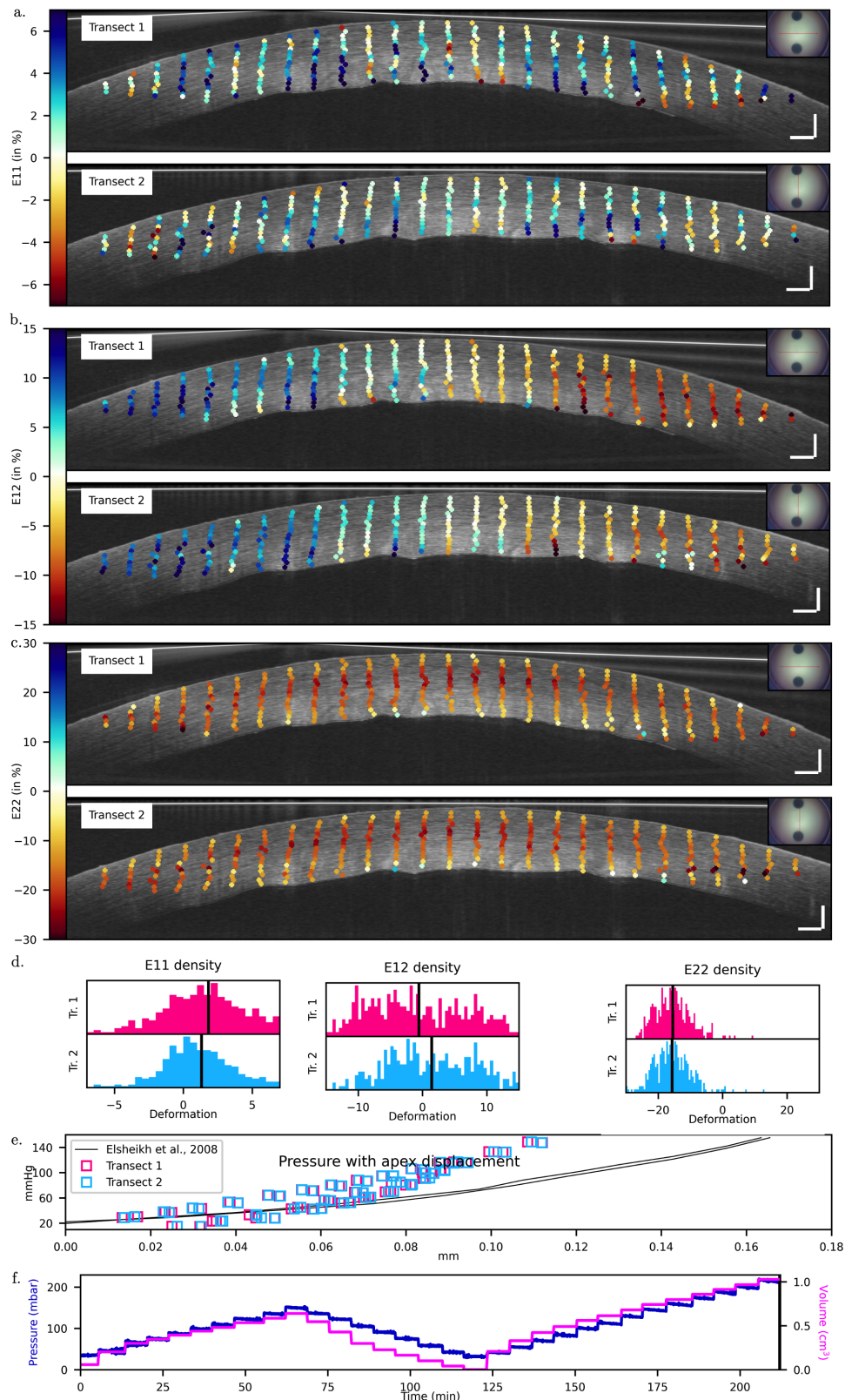


Figure 3.35: Results of the image analysis on two transects (in the direction of minor – Transect 1 – and major – Transect 2 – axis of the cornea) for the inflation test after approximately 220 minutes (cornea 23831). a. Horizontal strain e_{11} - Color bar: $[-7\%, 7\%]$. b. Shear strain e_{12} - Color bar: $[-15\%, 15\%]$ c. Vertical strain e_{22} - Color bar: $[-30\%, 30\%]$, a-c. scale bar of the OCT image - $250 \mu\text{m}$. d. Strain histogram for the particular time of the experiment considered. e. Pressure with apex displacement compared to the data found in [45]. f. Internal pressure and volume evolution with time.

Cornea	e11			e12			e22		
	Phase 1	Phase 2	Phase 3	Phase 1	Phase 2	Phase 3	Phase 1	Phase 2	Phase 3
23769	[-11%, 9%]	[-13%, 11%]	[-15%, 12%]	[-13%, 14%]	[-15%, 16%]	[-18%, 18%]	[-27%, 6%]	[-29%, 3%]	[-34%, -1%]
23809	[-4%, 5%]	[-5%, 6%]	[-6%, 8%]	[-11%, 10%]	[-13%, 11%]	[-17%, 14%]	[-21%, 5%]	[-23%, 2%]	[-27%, -1%]
23831	[-5%, 5%]	[-5%, 6%]	[-6%, 8%]	[-11%, 10%]	[-13%, 12%]	[-16%, 15%]	[-21%, 5%]	[-23%, 3%]	[-27%, -1%]
23849	[-4%, 5%]	[-5%, 6%]	[-6%, 8%]	[-9%, 7%]	[-11%, 9%]	[-14%, 12%]	[-16%, 3%]	[-20%, 0%]	[-28%, -1%]
24109	[-5%, 6%]	[-5%, 6%]	[-6%, 9%]	[-10%, 9%]	[-11%, 10%]	[-14%, 13%]	[-21%, 13%]	[-25%, 13%]	[-32%, 9%]
24149	[-5%, 6%]	[-5%, 7%]	[-7%, 10%]	[-11%, 10%]	[-12%, 11%]	[-17%, 15%]	[-19%, 3%]	[-24%, -1%]	[-32%, -4%]
24167	[-4%, 5%]	[-5%, 6%]	[-7%, 10%]	[-11%, 10%]	[-12%, 12%]	[-17%, 17%]	[-23%, 9%]	[-25%, 9%]	[-30%, 2%]

Table 3.13: Strain range of the inflation test.

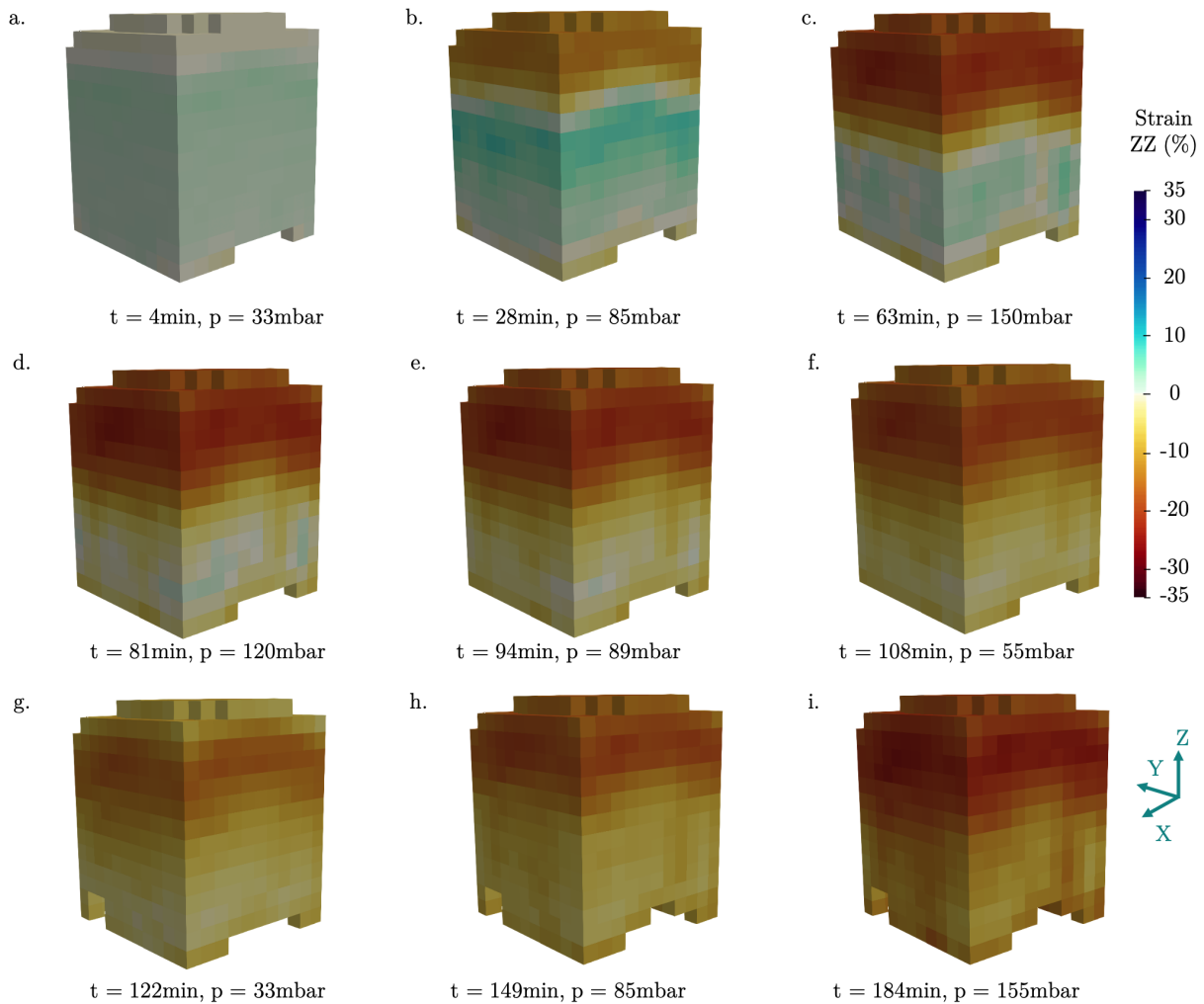


Figure 3.36: Vertical strain e_{zz} computed using DVC on 3D images of the cornea under the inflation test for several times and pressures (cornea 24167). Color bar: $[-35\%, 35\%]$. a–c correspond to three increasing steps of pressure of the first phase ($p = 33$ mbar, $p = 85$ mbar and $p = 150$ mbar), d–f correspond to three steps of decreasing pressure of the second phase ($p = 120$ mbar, $p = 89$ mbar and $p = 55$ mbar) and g–i to three increasing steps of pressure in the third phase ($p = 33$ mbar, $p = 85$ mbar and $p = 155$ mbar).

Several observations can be made from the analysis of the two (Fig. 3.35) and three-dimensional

(Fig. 3.36) strains assessed for the 7 tests. We present here only a few snapshots but the study is generalized from the video of all time steps. Table 3.13 summarizes also all the strain range during the three phases of the inflation test while figures 3.37, 3.38 and 3.39 completes the pictures with the results of the vertical strains for the last time of the creep test at high pressure for the seven corneas. First, as in the other two tests, e_{22} is larger by a factor 3 to 5 approximately compared to e_{11} (Fig. 3.35). While horizontal strains are mostly contained between -7% and +10%, vertical normal strain can reach up to 30% in absolute value. In connection, the shear strain $-e_{12}$ is once again twice as large as e_{11} , ranging between -17% and 17% in this case. In addition, no discernible pattern emerges for horizontal normal strains (Fig. 3.35.a), with a mean of the strain density that suggests a slight swelling. As in the creep test at high pressure, Fig. 3.35.b reveals for e_{12} a negative strain (warm colors) on the right of the image, opposed to a positive strain (cool colors) on its leftmost part, with a neutral strain transition zone at the center of the image. However, in this case, it seems that the radius of the neutral zone is slightly smaller than in the creep test at high pressure. During phase 1 of the inflation test (Figure 3.36.a–c), the cornea is expanding in its posterior part (30 to 100% of depth) and contracting in its anterior part (0 to 30% of depth) and as in phase 1 of creep test at high pressure. Again, the first limit depth is around 30% of depth. Conversely, during phase 2 and 3 of the inflation test (first decrease and second increase of pressure steps), e_{22} and e_{ZZ} (Fig. 3.35.c and Fig. 3.36 d–i) feature almost only negative values throughout the cornea, with a mean strain around -25% for the last step (Fig. 3.35.d). Again, this can be said for both 2D transects of the cornea and seen on the 3D representation, and translates its contraction under high pressure. It also highlights a difference in the response of the cornea between phase 1 and 3 (increasing steps of pressure), so after one cycle of loading. Finally, the trend of pressure with apex displacement (Fig. 3.35.e) is similar to [45] when increasing the pressure, with slightly higher values of pressure for the same displacement in our case.

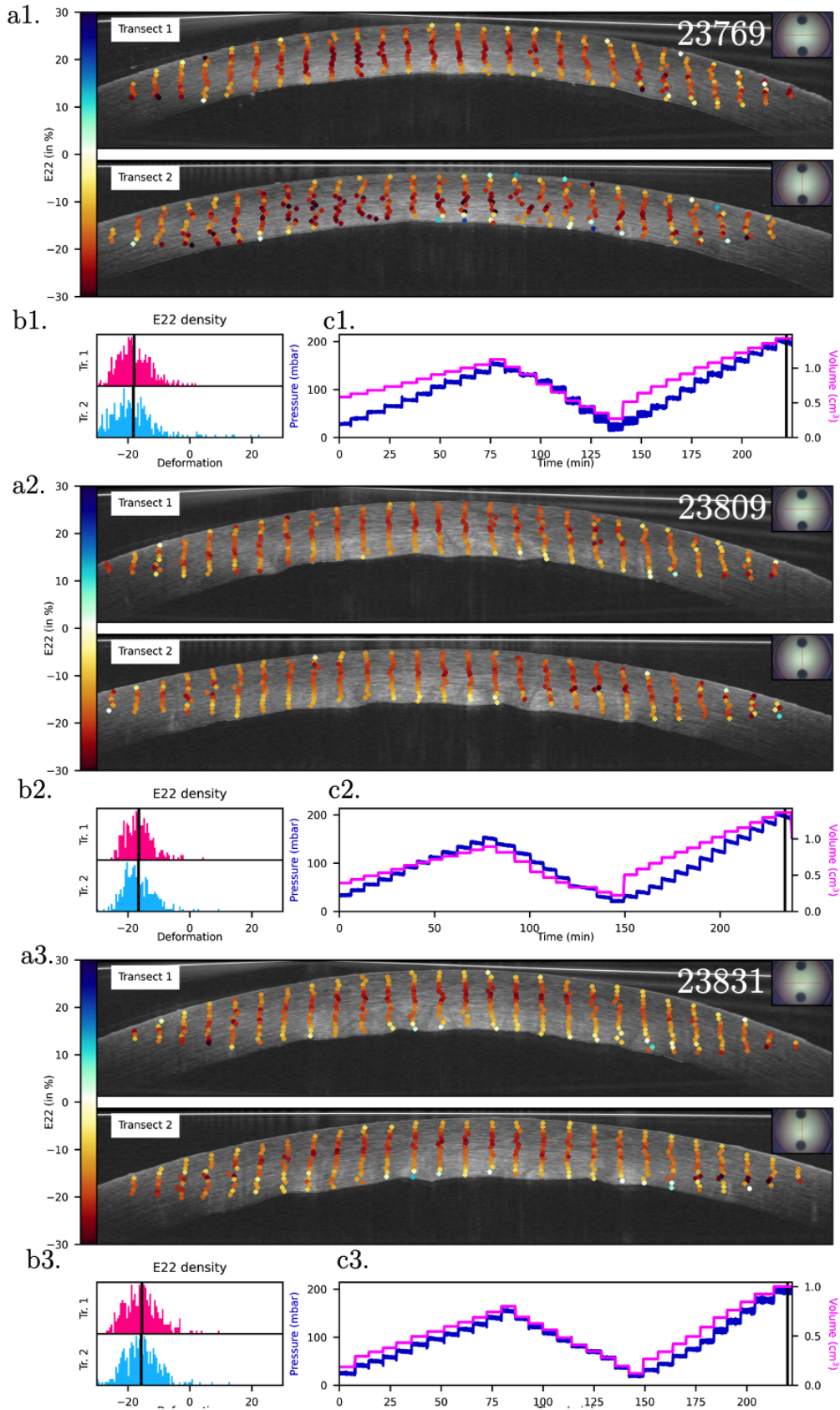


Figure 3.37: Results of the image analysis on two transects (in the direction of minor – Transect 1 – and major – Transect 2 – axis of the cornea) at the end of the creep test at high pressure (cornea 23769, 23809 and 23831). a. Vertical strain e_{22} - Color bar: $[-30\%, 30\%]$. b. Strain density for the particular time of the experiment considered. c. Internal pressure and volume evolution with time (black bar indicate the considered time)

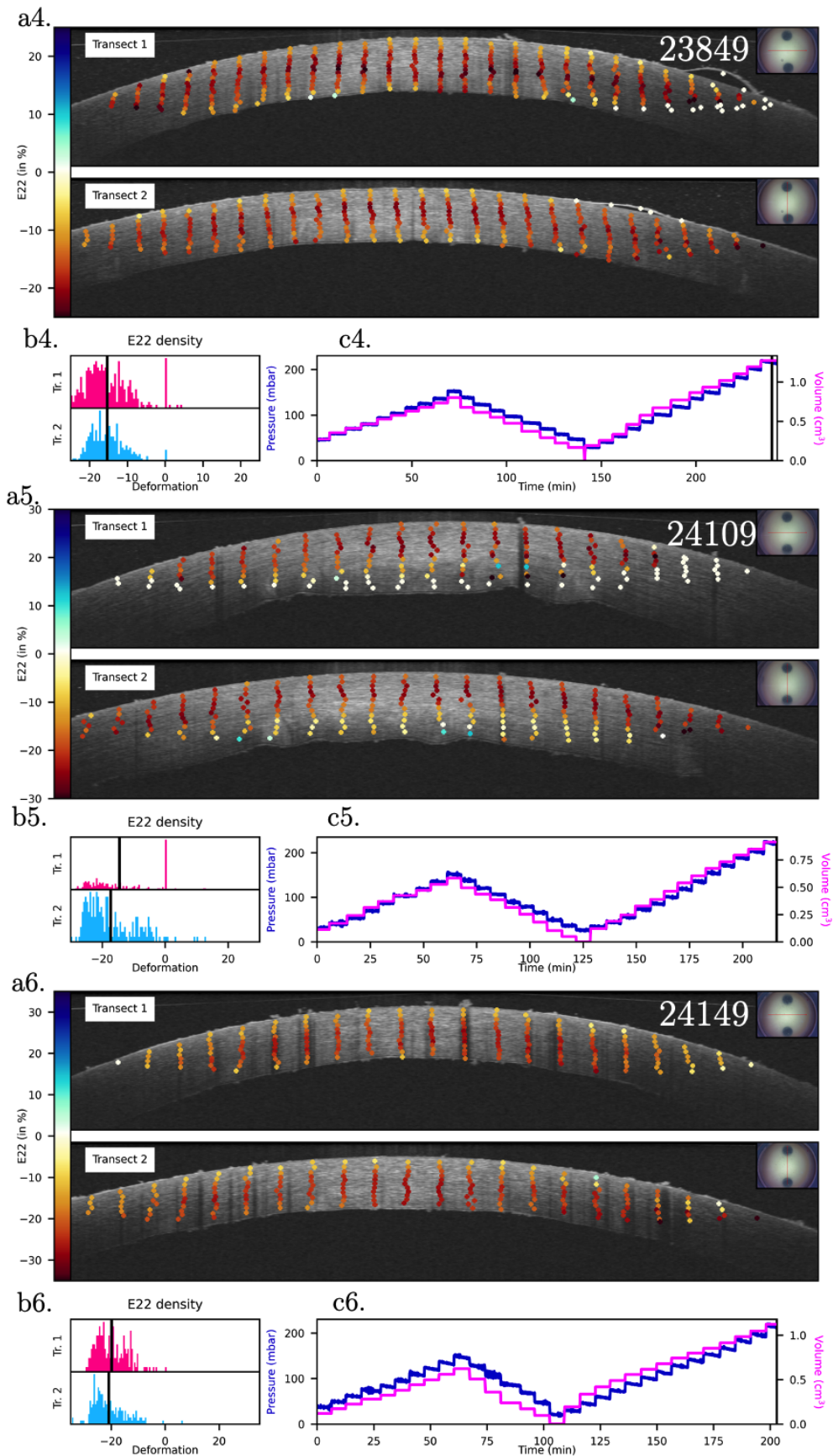


Figure 3.38: Results of the image analysis on two transects (in the direction of minor – Transect 1 – and major – Transect 2 – axis of the cornea) at the end of the creep test at high pressure (cornea 23849, 24109 and 24149). a. Vertical strain e_{22} - Color bar: a.4. [-25%, 25%], a.5. [-30%, 30%], a.6. [-35%, 35%]. b. Strain density for the particular time of the experiment considered. c. Internal pressure and volume evolution with time (black bar indicate the considered time) 153

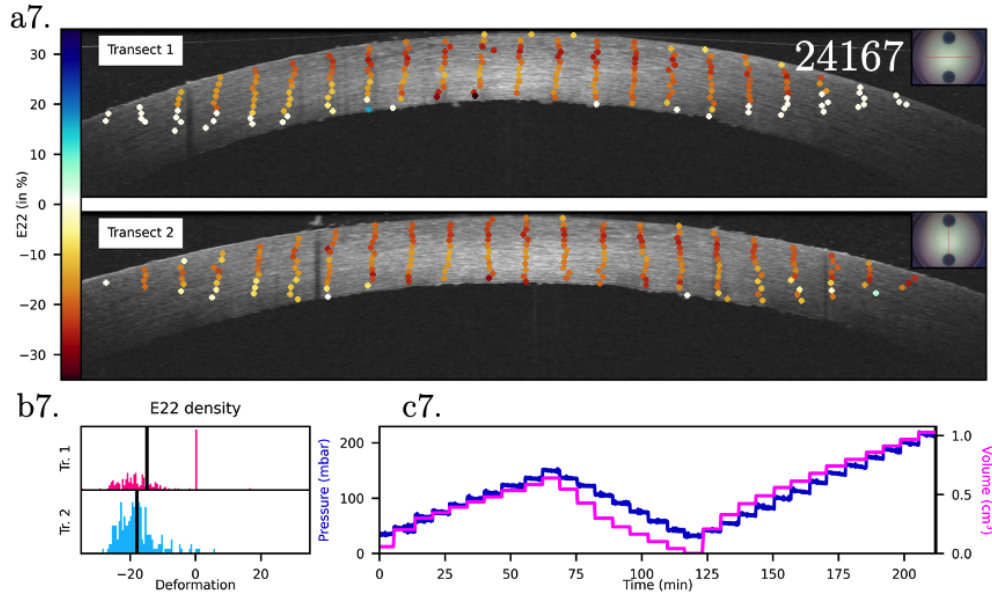


Figure 3.39: Results of the image analysis on two transects (in the direction of minor – Transect 1 – and major – Transect 2 – axis of the cornea) at the end of the creep test at high pressure (cornea 24167). a. Vertical strain e_{22} - Color bar: a.7. $[-35\%, 35\%]$. b. Strain density for the particular time of the experiment considered. c. Internal pressure and volume evolution with time (black bar indicate the considered time)

3.3.4.c Depth profile of the vertical strain e_{22}

2D results are discussed here based on snapshots of the experiment, but the evolution throughout the whole test can be found at the following links:

<https://ppi-lms.polytechnique.fr/jean-marc.allain/IT2DE22Fit.html> for the evolution of the parameters with time,

<https://ppi-lms.polytechnique.fr/jean-marc.allain/IT2DE22Profile.html> for the color maps of the depth profile.

Figure 3.35.c reveals a discernible pattern through the thickness for the vertical strain e_{22} . This pattern will be studied by investigating the depth profile of the strain near the apex of the cornea on both transects, with the same transect analysis as in the other experiments and focusing on the evolution of parameters with pressure.

Transects analysis Figure 3.40 presents the results of the vertical strain profile with time. Figure 3.40.a shows the correlation points used to compute the depth profile, pink and blue being associated to transect 1 and 2 respectively. Figure 3.40.b shows the data and the fit (left) of the depth profile by the three slopes curve defined in Eq. (3.11). The same limit depths z_1 and z_2 represented in Fig. 3.15 are obtained associated with the two limit strains ε_1 and ε_2 (not shown here) and the three slopes α_1 , α_2 and α_3 . Figure 3.40 shows the time evolution of the limit depths z_1 and z_2 (middle) and slopes α_1 , α_2 and α_3 (right). The corresponding along-profile strain with time is shown in Fig. 3.40.c (top for transect 1 and bottom for transect 2). Figure 3.40.d recalls the pressure and volume curves with time associated with the performed experiment.

As seen in Fig. 3.36, the observed strain is both positive and negative throughout the profile

during phase 1 of the experiment (within a $-23\% - 9\%$ range) the cornea swelled in its deepest part and contracted in its first third under low pressure (as in the first phase of creep test at high pressure), and mostly negative during phases 2 and 3. Figure 3.40.c shows clearly the difference between phase 1 and phase 3 with green color associated with positive strains during phase 1 and only orange and red colors associated to negative strains during phase 3. Hence there has been an accommodation of the cornea. Finally, for this component also, the same three areas can be distinguished regarding the value of the strain on both short and long axis transects. Again, as we are dealing with human samples, the limit depths, strains and slopes vary for the seven corneas and the following will try to quantify these parameters and assess their variability with pressure for the three phases of the inflation test.

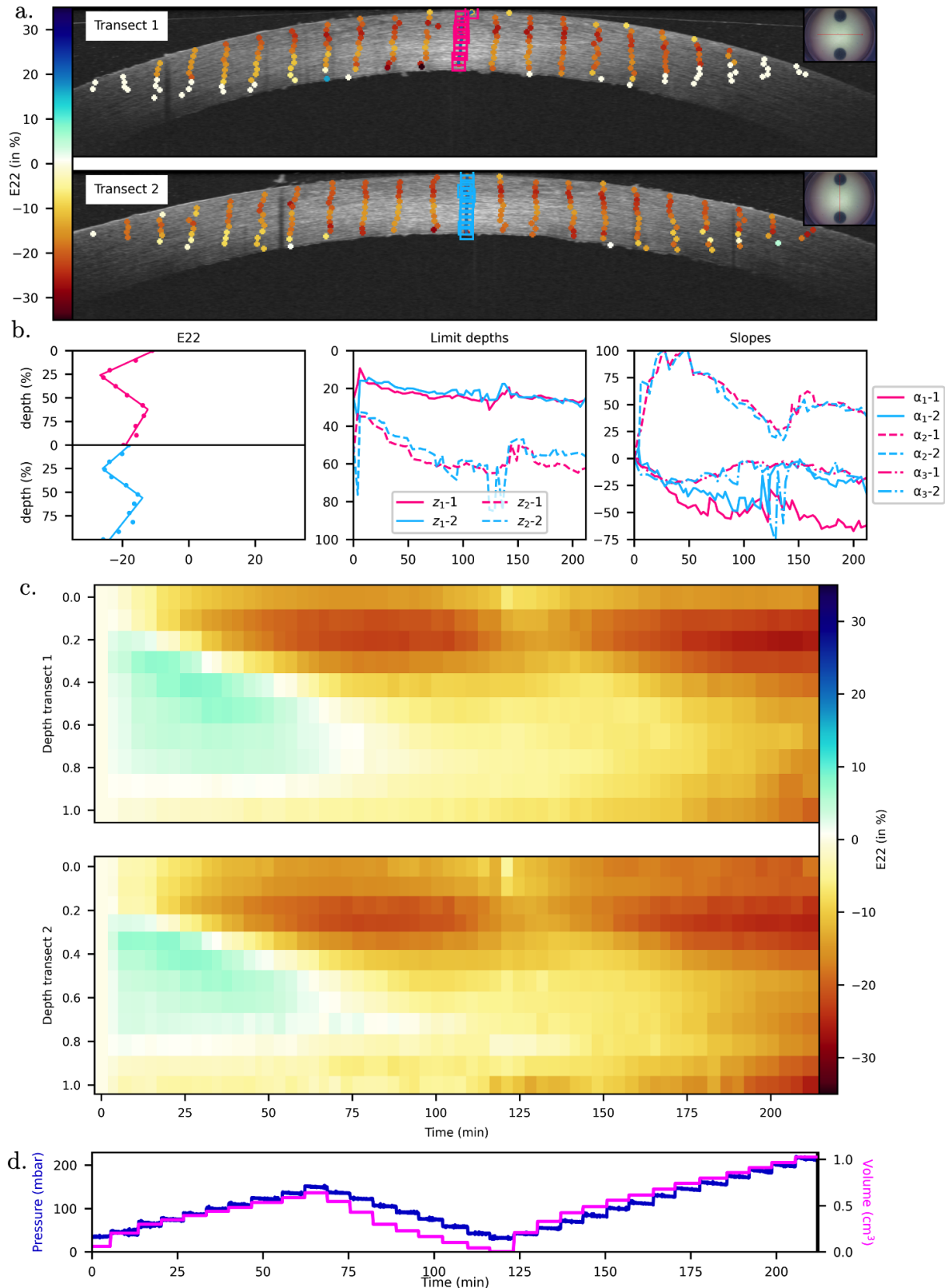


Figure 3.40: Depth profile of vertical strain for the inflation test (cornea 24167). a. Depth profiles considered on the two transects (pink and blue squares). b. Vertical strain (in%) of the depth profiles at the considered time – left : data and three-slopes fit, middle: limits depths (in%) and right : slopes (in%) of the fit with time. c. Vertical strain of the depth profile with time for the two transects. d. Internal pressure and volume with time (the black bar indicates the time considered for the images).

In this case, the data have been separated between phases 1, 2 and 3 and the same paired t-test has been carried out between the transects for each phases. Results of the statistical comparison are presented Fig. 3.41 and summarized hereafter. No-significant differences were found for the limit depths and limit strains between the two transects during the three phases of the inflation test for a p-value $< 1\%$ (except for ε_1 during phase 2). Conversely, significant differences between transects have been found for the epithelium slope and middle slope for the three phases for a p-value $< 1\%$ (except for α_2 during phase 1). Again, for α_3 , this can be due to the fact that the first point of the profile depth (at 0% of depth) can be misplaced and influences a lot the slope as there are only a few points in this area. This analysis shows that the two transects cannot be distinguished from a statistical point of view for most of the parameters. Consequently, the data obtained for each profile will be merged into a single data set, representative of the vertical profile. The next section will provide insights into the parameters evolution during the three phases of the inflation test.

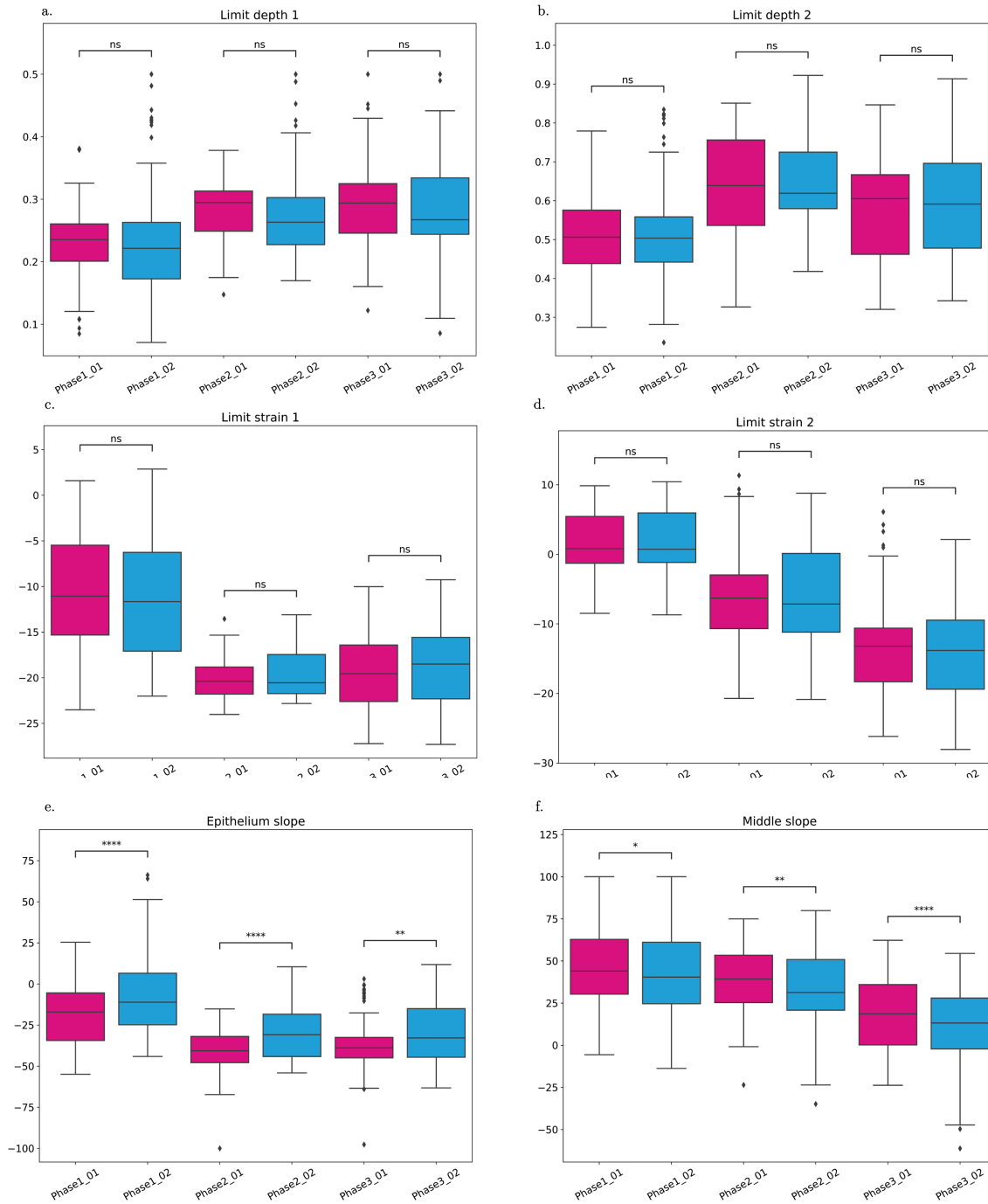


Figure 3.41: a–b. Limit depths, c–d. limit strains (in %) and e–f epithelium and middle slopes of the three-slopes fit of the vertical strain for the three phases of the inflation test for the two transects. T-test legend: ns – non-significant, * $p < 5\%$, ** $p < 1\%$, *** $p < 0.1\%$ and **** $p < 0.01\%$.

Pressure dependence analysis Figure 3.42 details a. the limit depths, b. the limit strains, c. the epithelium slope and d. the middle slope with pressure for cornea 24167 (the results for the other corneas can be found in App. E.5.2). The limit depth z_1 shows a flat curve with a slight difference between phase 1 and the other phases, while z_2 exhibits a different behavior between the three phases. It clearly decreases during the first phase, but remains almost constant during phases 2 and 3. The limit strains ε_1 and ε_2 show different responses between the three phases. More particularly, they tend to decrease with pressure except for ε_2 during phase 2 (red triangles) which seems to be increasing

with pressure. This trend is confirmed on the other corneas. The epithelium slope decreases strongly during phase 1 and then stabilizes during the second phase and finally slightly decrease during phase 3. It is consistent with the fact that the epithelium strain (at 0% of depth) is first really different from the strain at z_1 (during phase 1) and then, the gap is closing in between the two extreme strains of the epithelium area, even becoming almost 0 during phase 2 (the slope is close to 0). Finally, the middle slope α_2 increases with pressure during the three phases with a bigger slope during phase 1, meaning that the difference in limit strains increases with pressure, even more so during phase 1.

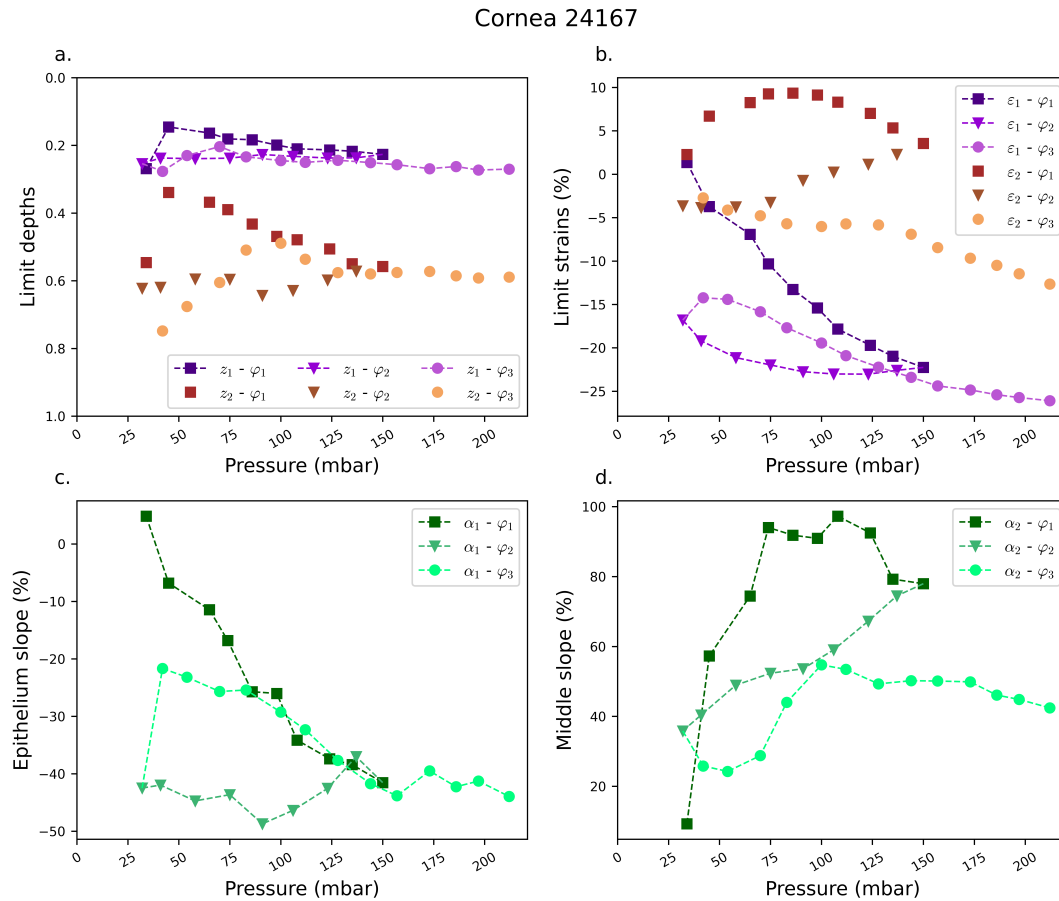


Figure 3.42: Pressure dependency of the parameters for the inflation test during the three phases (cornea 24167). a. Limit depths with pressure, b. Limit strains with pressure and c. Middle slope with pressure. Dark color squares indicate phase 1, middle color triangles indicate phase 2 and light color circles indicate phase 3.

All the data are then fitted with linear curves for the three phases. Tables 3.14 and 3.15 complement the figures by giving the mean and standard deviation of the slopes and intercept ordinates of the fit for the limit depths and the slopes (for the seven corneas tested). The pressure evolution of the limit strains will be studied in the following. The results clearly show that the two depths do not vary much during a given phase but slightly increase between phase 1 and the two following phases. The fact that α_1 stabilizes reflect the homogenization of the vertical strain in the epithelium area. As for α_2 , it tends to increase with pressure for the three phases, with a slope that decreases between phases, leading to a lower difference of limit strains for phase 2 and especially phase 3, where the difference

between the two limit strains is almost constant. It corresponds to the homogeneous contraction of the central zone during phase 3 observed in Fig. 3.40.c. However, the levels of the standard deviation of the slope for α_2 indicate a big variability between corneas, so that the results have to be analyzed cautiously.

	Mean φ_1	Std φ_1	Mean φ_2	Std φ_2	Mean φ_3	Std φ_3
z_1	0.000 mbar ⁻¹	0.001 mbar ⁻¹	0.000 mbar ⁻¹	0.000 mbar ⁻¹	0.000 mbar ⁻¹	0.000 mbar ⁻¹
z_2	0.001 mbar ⁻¹	0.001 mbar ⁻¹	0.000 mbar ⁻¹	0.001 mbar ⁻¹	0.000 mbar ⁻¹	0.001 mbar ⁻¹
α_1	-0.29 %·mbar ⁻¹	0.09 %·mbar ⁻¹	0.05 %·mbar ⁻¹	0.03 %·mbar ⁻¹	-0.05 %·mbar ⁻¹	0.06 %·mbar ⁻¹
α_2	0.37 %·mbar ⁻¹	0.12 %·mbar ⁻¹	0.22 %·mbar ⁻¹	0.08 %·mbar ⁻¹	0.04 %·mbar ⁻¹	0.11 %·mbar ⁻¹

Table 3.14: Mean and Standard deviation (Std) of the slopes of the linear fit of the pressure evolution of parameters z_1 , z_2 , ε_1 , ε_2 and α_2 during the three phases (φ_1 , φ_2 and φ_3) of the inflation tests for all corneas.

	Mean φ_1	Std φ_1	Mean φ_2	Std φ_2	Mean φ_3	Std φ_3
z_1	0.20	0.04	0.28	0.04	0.27	0.05
z_2	0.41	0.10	0.65	0.07	0.58	0.08
α_1	13.4 %	5.35 %	-38.2 %	9.80 %	-27.2 %	9.68 %
α_2	7.51 %	13.6 %	17.0 %	13.2 %	12.0 %	16.6 %

Table 3.15: Mean and Standard deviation (Std) of the intercept ordinates of the linear fit of the pressure evolution of parameters z_1 , z_2 , ε_1 , ε_2 and α_2 during the three phases (φ_1 , φ_2 and φ_3) of the inflation tests for all corneas.

Pressure – limit strain curves To conclude this analysis, the pressure with limit strain curves were fitted for the three phases with linear regression (reverse of Fig. 3.42.b). In this case, the pressure is the global pressure applied to the posterior surface of the corneas and the considered strains are the two local limit strains ε_1 and ε_2 . The slope of the fitted curve is homogeneous to a stiffness, which is denoted k_i^{ap} in Eq. (3.12):

$$\text{for } i \in [1, 2], \quad -p = k_i^{ap} \varepsilon_i - p_i^0, \quad (3.12)$$

with p_i^0 the intercept of the fit. Figure 3.43 presents the resulting curves for the three phases and the two limit strains for cornea 23769 (the results for the six other corneas are in App. E.5.3). The two apparent stiffnesses cannot be compared directly as the effective vertical stresses applied at z_1 and z_2 on the cornea are not the same as the pressure profile through depth is not uniform but can be compared between phases of loading. We find a difference in response between phase 1 and the two others for ε_1 with a clear increase in the values of the slopes. Looking at the response of ε_2 in phase 2, we can see that the slope is negative, which is consistent with Fig. 3.42.b. This is confirmed by the results of Table 3.16 which summarizes the mean and standard deviation of the different apparent stiffnesses computed for the three phases of the seven corneas. k_1^{ap} corresponds to the anterior part of the cornea (at first limit depth z_1) and k_2^{ap} corresponds to the posterior part of the cornea (at second limit depth z_2). The negative apparent stiffness k_2^{ap} found in the second phase φ_2 for the second limit depth z_2 is interesting to look at. It shows that when the pressure decreases, the vertical strain at

depth z_2 increases in absolute value. This indicates a continuous increases of ε_2 with time, associated with an increase of the cornea volume. This effect is due to water pumping, an effect not included in cornea classical description.

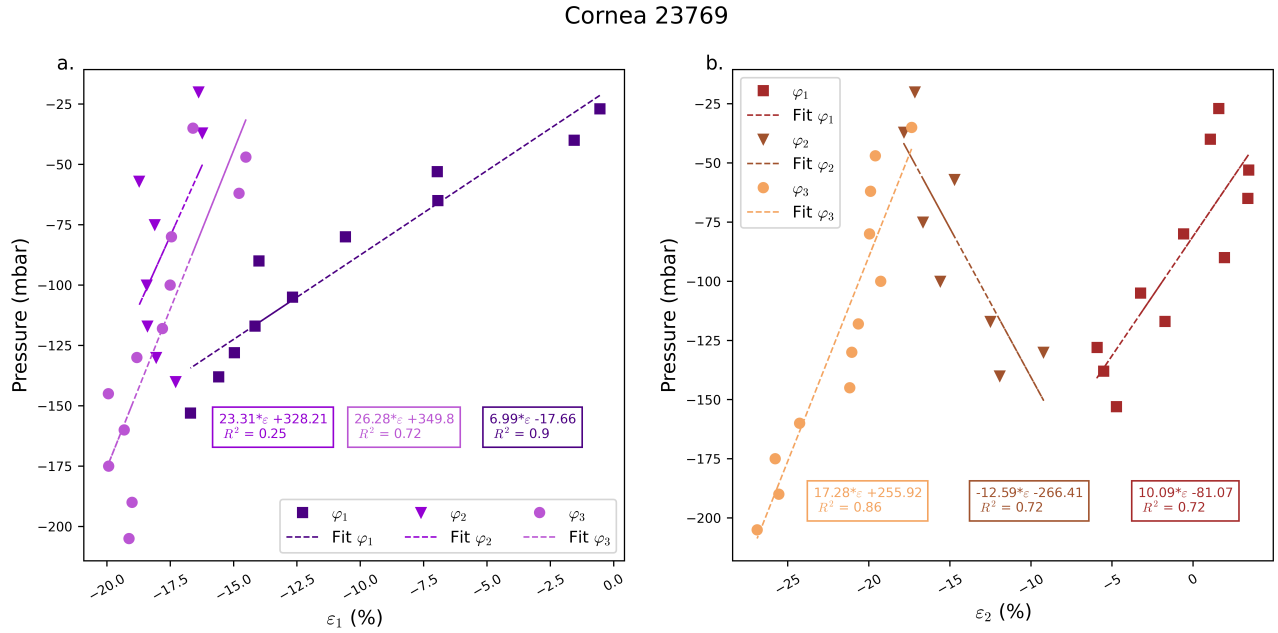


Figure 3.43: Pressure with strain and its linear fit during the three phases of the inflation test (cornea 23769). a. Pressure with the first limit strain and b. Pressure with the second limit strain.

	Mean φ_1	Std φ_1	Mean φ_2	Std φ_2	Mean φ_3	Std φ_3
k_1^{ap} (kPa)	57.7	7.2	220.7	49.8	180.6	48.4
k_2^{ap} (kPa)	81.0	10.4	-169.9	53.3	142.3	37.5

Table 3.16: Mean and Standard deviation (Std) of the apparent stiffness of the linear fit of the pressure with strain curves in kPa for all corneas.

3.3.5 Summary of the results and discussion

The mechanical behavior of cornea has been investigated, through three different tests. The cornea has been put under pressure through the injection of a monitored change of volume of fluid (Stem α 3), simultaneously measuring the pressure at the entrance of the chamber. 2D and 3D OCT images were acquired during the experiments, on which DIC and DVC are used to compute the strain maps. First, creep tests at physiological pressure have been performed to simulate a transplant. Second, creep tests at high pressure (around 150 mmHg) have been completed, and third, an inflation test has been carried out on cornea to characterize the mechanical response of the cornea under a wide range of pressures. The three different tests resulted in several common observations, summarized hereafter.

First, the corneas under low pressure tend to swell in the vertical direction, whereas corneas under high pressure contract. As no particular behavior is noted in the horizontal direction, the vertical strain may be associated with a rearrangement of the lamellae inside the stroma without losing "in-plane" elasticity. So, the swelling may be due to the penetration of water between the lamellae, as

observed for 19 corneas. This increases the diffusion of light, reducing the cornea transparency (or its whiteness at OCT) as observed in our experiments. Such type of water exchange is likely due to a balance between the mechanical state of the cornea and the osmosis equilibrium with the surrounding medium. The observed change of volume cannot be explained by the classical quasi-incompressible hypothesis. Yet, it cannot be determined whether the change in response between low and high pressures comes from a structural inelastic behavior of cornea – due to its particular microstructure of layered collagen lamellae – or from the action of the endothelial cells – which would pump in and out molecules and water [86]. To better understand this mechanism, the pumping action could be quantified monitoring the permeability of the endothelial cells to fluorescein [20].

Second, the cornea can be divided into three parts (through thickness) delimited by two limit depths z_1 and z_2 associated with two limit strains ε_1 and ε_2 and the vertical strain can be described by a three slope (α_1 , α_2 and α_3) linear function. The first limit depths z_1 is relatively constant with time and pressure and is similar for all the experiments (between 20 to 30% of depth). The second limit depth z_2 , on the other hand, varies a bit across experiments and even inside a single experiment (for example it increases between the two last phases of the inflation test). This shows that the anterior and posterior parts of cornea do not have the same response to pressure and may play a different role in the response to intraocular pressure variations. One of the main example of this heterogeneity is given by the epithelium and middle slope. As epithelium slope is close to 0, the upper quarter of cornea seems to deform uniformly. On the contrary, the middle slope is quite high in absolute value (except for phase 3 of the inflation test), meaning that the vertical strain is highly heterogeneous in the middle part of cornea, with usually a higher absolute value of strain at depth z_1 . The occurrence of the distinct zones may emphasize the pumping role of the endothelium, which is permeable to water and molecules [86], and the barrier role of the epithelium [168]. Furthermore, the division of the cornea into three zones is consistent with what is usually done when lamellae are observed with SHG microscopy with equivalent limit depths [134; 145; 175]: the anterior part (above 30% of depth) is significantly different from the middle and posterior stroma in terms of out-of-plane angle and density of branching points (which is a measure of the interconnection between lamellae). The first limit depth would then come from a structural organization of the lamellae, whereas the second limit depth is not as clear, as there is no evidence that the arrangement of the lamellae is so different between the middle and posterior stroma, which brings more variability observed in our experiments.

Third, for tests with several phases, the cornea does not have the same behavior between phases. Apparent posterior stiffness k_2^{ap} defined in the previous section reflects this different responses with an alternation of negative and positive values between phases at depth z_2 . Two hypotheses can be considered for cornea: either cornea has an auxetic behavior (as formulated by [83]) or there are water flows through endothelium that go in the cornea with different speeds with respect to the value of pressure. Also, as the cornea is only globally in contraction after phase 1, it could be an interesting way to tackle the swelling problem of the cornea under physiological pressure in the case of a transplant, which could cause blurry vision. In this case, the effects on the microstructure should be checked by coupling experiments with added microscopic observations – like Second Harmonic Generation (SHG) microscopy for example [91; 176].

Finally, the shear strain seems to highlight a well known property of cornea. The optical power of the tissue does not change during the day, despite variations of intraocular pressure. No shear strain

is observed in the center of the cornea, but opposite values at the two sides on its periphery. This indicates that the cornea tries to maintain its geometry in the central part, by absorbing the strain caused by the variation of the IOP at its periphery.

Interestingly, all of the above phenomenon cannot be explained by either the classical hyperelastic or viscoelastic models which are usually used to simulate the mechanical response of cornea. The previous experiments suggest that some components are missing in these representations. The following section attempts to give some keys to model or adjust existing models of the tissue.

Test	Cornea	e11			e12			e22		
Creep Test at physiological pressure	23394		[-5%, 5%]			[-10%, 9%]			[-5%, 25%]	
	23395		[-5%, 5%]			[-7%, 7%]			[-6%, 23%]	
	23417		[-4%, 3%]			[-7%, 7%]			[-1%, 16%]	
	23490		[-9%, 10%]			[-13%, 7%]			[-11%, 19%]	
	23577		[-9%, 6%]			[-17%, 14%]			[-14%, 35%]	
		Phase 1	Phase 2		Phase 1	Phase 2		Phase 1	Phase 2	
Creep Test at high pressure	23837	[-5%, 6%]	[-5%, 7%]		[-14%, 11%]	[-16%, 13%]		[-22%, 5%]	[-25%, 2%]	
	23850	[-5%, 7%]	[-5%, 8%]		[-12%, 10%]	[-14%, 13%]		[-25%, 8%]	[-32%, 3%]	
	24046	[-6%, 7%]	[-5%, 10%]		[-18%, 17%]	[-21%, 20%]		[-30%, 8%]	[-35%, 2%]	
	24055	[-7%, 6%]	[-7%, 9%]		[-12%, 9%]	[-15%, 13%]		[-23%, 5%]	[-28%, 1%]	
	24082	[-4%, 4%]	[-5%, 7%]		[-8%, 9%]	[-13%, 14%]		[-18%, 6%]	[-27%, 4%]	
	24083	[-11%, 9%]	[-14%, 12%]		[-12%, 10%]	[-16%, 14%]		[-20%, 7%]	[-28%, 5%]	
	24105	[-4%, 5%]	[-6%, 7%]		[-7%, 7%]	[-11%, 12%]		[-20%, 10%]	[-23%, 6%]	
		Phase 1	Phase 2	Phase 3	Phase 1	Phase 2	Phase 3	Phase 1	Phase 2	Phase 3
Inflation test	23769	[-11%, 9%]	[-13%, 11%]	[-15%, 12%]	[-13%, 14%]	[-15%, 16%]	[-18%, 18%]	[-27%, 6%]	[-29%, 3%]	[-34%, -1%]
	23809	[-4%, 5%]	[-5%, 6%]	[-6%, 8%]	[-11%, 10%]	[-13%, 11%]	[-17%, 14%]	[-21%, 5%]	[-23%, 2%]	[-27%, -1%]
	23831	[-5%, 5%]	[-5%, 6%]	[-6%, 8%]	[-11%, 10%]	[-13%, 12%]	[-16%, 15%]	[-21%, 5%]	[-23%, 3%]	[-27%, -1%]
	23849	[-4%, 5%]	[-5%, 6%]	[-6%, 8%]	[-9%, 7%]	[-11%, 9%]	[-14%, 12%]	[-16%, 3%]	[-20%, 0%]	[-28%, -1%]
	24109	[-5%, 6%]	[-5%, 6%]	[-6%, 9%]	[-10%, 9%]	[-11%, 10%]	[-14%, 13%]	[-21%, 13%]	[-25%, 13%]	[-32%, 9%]
	24149	[-5%, 6%]	[-5%, 7%]	[-7%, 10%]	[-11%, 10%]	[-12%, 11%]	[-17%, 15%]	[-19%, 3%]	[-24%, -1%]	[-32%, -4%]
	24167	[-4%, 5%]	[-5%, 6%]	[-7%, 10%]	[-11%, 10%]	[-12%, 12%]	[-17%, 17%]	[-23%, 9%]	[-25%, 9%]	[-30%, 2%]

Table 3.17: Strain range of all tests.

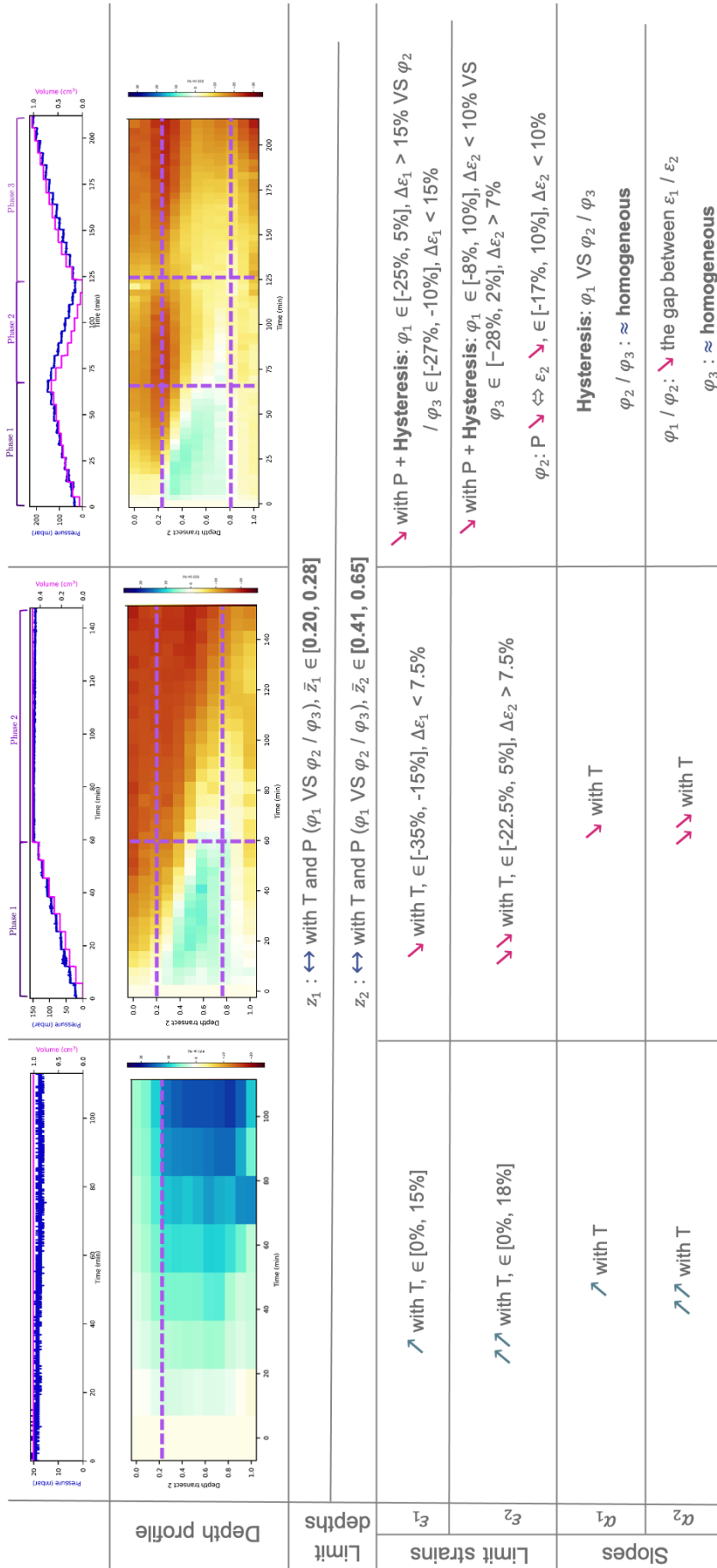


Figure 3.44: Summary of the results for the parameters of the 3-slopes function.

3.4 Extension of the hyperelastic model

Hereafter is an attempt to model analytically the response of cornea that was observed in Sec. 3.3. Two hypotheses are explored: first the cornea is considered as an auxetic material (as in [83]), and then an osmosis effect is introduced (phenomenon which would be related to the flow of water controlled by the endothelium).

3.4.1 First model: elastic model of auxetic cornea

We use a simplified geometry and behavior, a sphere under pressure with an linear response to model the cornea (Fig. 3.45). The intraocular pressure is applied on the posterior surface (internal one) while the anterior surface is kept free of load. The entire computation is available in App. F.1, only the main steps are developed hereafter.

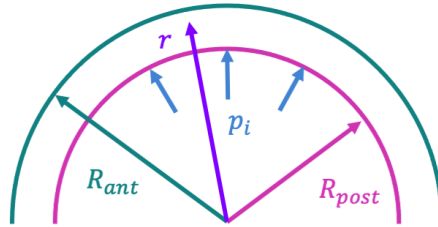


Figure 3.45: Schematic view of the problem considered on a sphere. The sphere is submitted to internal pressure p_i on the posterior surface and is free on the anterior surface.

The problem is considered to depend only on r , and to stay under low strains (to be analytically calculable), so the infinitesimal strain tensor $\underline{\underline{\varepsilon}}$ in spherical coordinate is:

$$\underline{\underline{\varepsilon}} = \begin{pmatrix} \frac{du_r}{dr} & 0 & 0 \\ 0 & \frac{u_r}{r} & 0 \\ 0 & 0 & \frac{u_r}{r} \end{pmatrix}, \quad (3.13)$$

with u_r the radial displacement. The boundary conditions represent the internal pressure applied on the posterior face and the absence of load on the anterior surface:

$$\sigma_{rr}(R_{ant}) = 0 \quad \text{and} \quad \sigma_{rr}(R_{post}) = -p_i. \quad (3.14)$$

The linear momentum balance leads to (in spherical coordinates):

$$\frac{d\sigma_{rr}}{dr} + \frac{2}{r}(\sigma_{rr} - \sigma_{\theta\theta}) = 0. \quad (3.15)$$

The considered constitutive law is the most simple possible; namely, an elastic material is considered with an isotropic Young's modulus E and a Poisson's ratio ν :

$$\underline{\underline{\sigma}} = \frac{E}{1 + \nu} \left(\underline{\underline{\varepsilon}} + \frac{\nu}{1 - 2\nu} \text{tr}(\underline{\underline{\varepsilon}}) \underline{\underline{1}} \right). \quad (3.16)$$

where $\underline{\underline{\sigma}}$ is the Cauchy-stress tensor. The equilibrium equation (3.15) becomes, after computation and defining $K_\nu = \frac{(1-\nu)}{(1+\nu)(1-2\nu)}$:

$$K_\nu E \frac{d(\text{tr}(\underline{\underline{\varepsilon}}))}{dr} = 0 \Leftrightarrow \frac{d(\text{tr}(\underline{\underline{\varepsilon}}))}{dr} = 0. \quad (3.17)$$

Integrating Eq. (3.17) and applying the boundary conditions (3.14), the following form is obtained for the radial displacement u_r and strain ε_{rr} :

$$\begin{cases} u_r = \frac{(1-2\nu)}{E} p_i \frac{R_{post}^3}{R_{ant}^3 - R_{post}^3} r + \frac{1+\nu}{E} p_i \frac{R_{ant}^3 R_{post}^3}{2(R_{ant}^3 - R_{post}^3) r^2} \\ \varepsilon_{rr} = \frac{(1-2\nu)}{E} p_i \frac{R_{post}^3}{R_{ant}^3 - R_{post}^3} - \frac{1+\nu}{E} p_i \frac{R_{ant}^3 R_{post}^3}{(R_{ant}^3 - R_{post}^3) r^3} \end{cases}. \quad (3.18)$$

Figure 3.46 presents the results for the radial strain ε_{rr} during the creep test at physiological pressure (a–b) and the inflation test (c–d) for Poisson’s ratio of $\nu = 0.3$ (a and c) and $\nu = -0.99$ (b and d). The creep test is used to see the spatial heterogeneity in depth of the response of cornea for a particular pressure of the inflation test because the value of the strains computed in the latter tends to smooth out this $1/r^3$ dependency. The other parameters are listed below:

$$\begin{cases} R_{ant} = 8.0 \text{ mm and } R_{post} = 7.5 \text{ mm} \\ E = \frac{E_{post} + E_{ant}}{2} \quad \text{with } E_{ant} = 281 \text{ kPa and } E_{post} = 89.5 \text{ kPa} \end{cases} \quad (3.19)$$

For $\nu = 0.3$, the material reacts as expected in the case of a classical elastic material. The sphere contracts more in the posterior area than in the anterior part (Fig. 3.46.a and b – with a $1/r^3$ dependence), and the strain can go up to a 100% under inflation (which is outside the hypothesis of infinitesimal strains assumed at the beginning). As expected, the strain is constant with time for the creep test and grows in absolute value with pressure in the case of the inflation test (loading path is the same as in Fig. 3.3.c for the inflation test). For $\nu = -0.99$, the material swells but the strain reaches less than 1.0% in the case of the inflation test. With a theoretical Poisson’s ratio of $\nu = -1.5$, we were able to reach 40.0% of strain, but in this case, we are outside of the boundary of linear elasticity of isotropic material (so the results are not presented here). In all cases however, the fact that positive and negative strains can be found in the tissue submitted to pressure is not captured. Moreover, as this type of model does not depend on the loading path, it does not allow our experiments to be reproduced, so we need a more complex model.

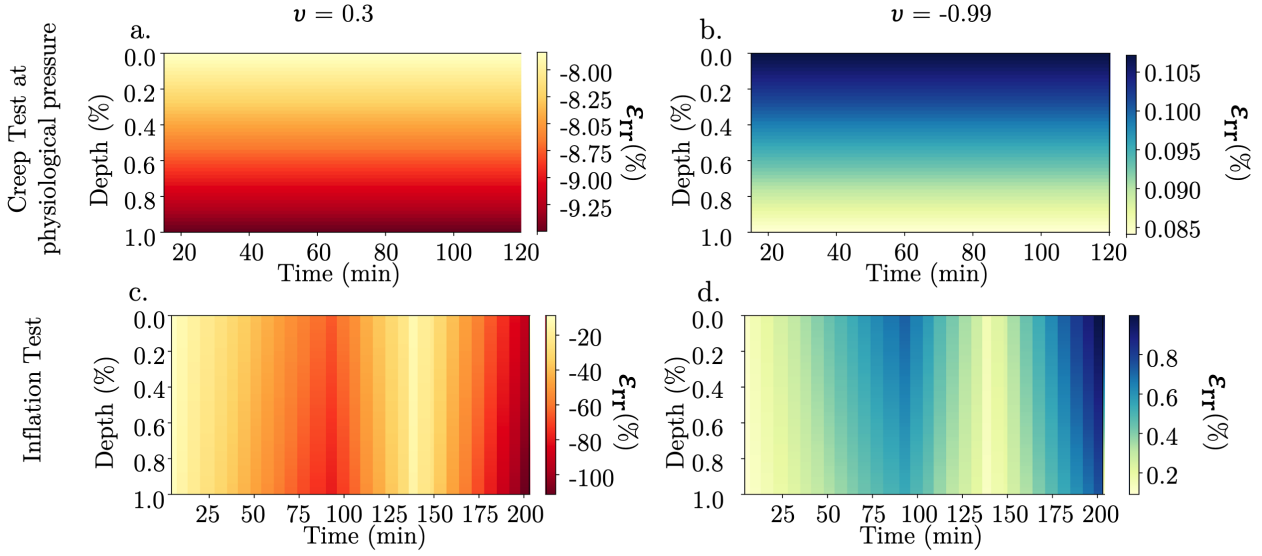


Figure 3.46: Radial strain with time (x-axis) and space (y-axis). a. and b. creep tests at physiological pressure and c. and d. inflation tests, with a Poisson's ratio of $\nu = 0.3$ (a. and c.) and $\nu = -0.99$ (b. and d.).

3.4.2 Second model: elasticity coupled with osmotic pressure

We consider that the contraction and swelling arises from the exchange of water through the endothelium. A term of osmotic pressure is thus introduced in the model. As the analytical computations on a sphere lead to a second order equation with non constant coefficients (not easily solvable analytically), we used a 1D model (in the z-direction) detailed and described in App. F.2 with the following constitutive law:

$$\underline{\underline{\sigma}} = \frac{E}{1 + \nu} (\underline{\underline{\varepsilon}} + \frac{\nu}{1 - 2\nu} \text{tr}(\underline{\underline{\varepsilon}}) \underline{\underline{1}}) - (\mu + \pi(J)) \underline{\underline{1}}, \quad (3.20)$$

with μ the chemical potential of the liquid phase and $\pi(J)$ an osmotic pressure term defined in Eq. (3.21) after [163]:

$$\pi(J) = \beta_0 \left(\frac{1 - \phi_s^{ref}}{J - \phi_s^{ref}} \right)^{\beta_1}, \quad (3.21)$$

where β_0 is the reference osmotic pressure, ϕ_s^{ref} the solid volume fraction per unit reference volume, β_1 is an exponent governing the non-linearity of the curve of the osmotic pressure with J [43]. The complete computation is detailed in App. F.2 but the main steps are presented hereafter. Defining the coefficient K_{osm}

$$K_{osm} = \frac{\beta_0 \beta_1}{1 - \phi_s^{ref}}, \quad (3.22)$$

the osmotic pressure function is linearized under the infinitesimal strains assumption and becomes $\pi(z)$

$$\pi(z) \approx \beta_0 - K_{osm} \text{tr}(\underline{\underline{\varepsilon}}). \quad (3.23)$$

The equilibrium equation then rewrites:

$$\frac{\partial \mu}{\partial z} = (E \cdot K_\nu + K_{osm}) \frac{\partial \text{tr}(\underline{\underline{\varepsilon}})}{\partial z}. \quad (3.24)$$

Using a simplified version of the model described in [163] to link the Jacobian and the chemical potential:

$$\frac{\partial J}{\partial t} = K \frac{\partial^2 \mu}{\partial z^2}, \quad (3.25)$$

which rewrites in terms of the Jacobian:

$$\frac{\partial J}{\partial t} = D \frac{\partial^2 J}{\partial z^2} \quad \text{with } D = K(E.K_\nu + K_{osm}). \quad (3.26)$$

The solution to this equation gives the Jacobian as a function of relative depth \tilde{z} and time t :

$$J(\tilde{z}, t) \simeq J_\alpha + \sum_{k \in \mathbb{N}^*} B_k \sin\left(\frac{k\pi}{2}\tilde{z}\right) e^{-D\left(\frac{k\pi}{2}\right)^2 t} \quad \text{with } B_k = \frac{2(J_\alpha - 1)}{k\pi} ((-1)^k - 1) \quad (3.27)$$

Figure 3.47 presents the results of the vertical strain ε_{zz} computed during the creep test at physiological pressure (Fig. 3.47.a) and during inflation test (Fig. 3.47.b) considering the following parameters:

$$\left\{ \begin{array}{l} \nu = 0.3, E = \frac{E_{post} + E_{ant}}{2} \quad \text{with } E_{ant} = 281 \text{ kPa and } E_{post} = 89.5 \text{ kPa} \\ J_\alpha = 1.2, \beta_0 = 1.518 \text{ kPa}, \beta_1 = 2.0, \psi^{ref} = 0.35 \text{ and } K = 10^{-14} m^4 . N^{-1} . s^{-1} \end{array} \right. \quad (3.28)$$

With these parameters, the vertical strain ε_{zz} can reach 20% either in the creep test at physiological pressure or the inflation test, as the source is infinite and $J_\alpha = 1.2$ makes the material swells by 20%. In this case also, both positive and negative strains cannot be found in the material, but a clear time dependence in the osmotic process is observed. What is not captured are the three zones seen in the experimental results. Here the propagation of the strain comes from the source (the posterior part of the cornea) and diffuses toward the upper part.

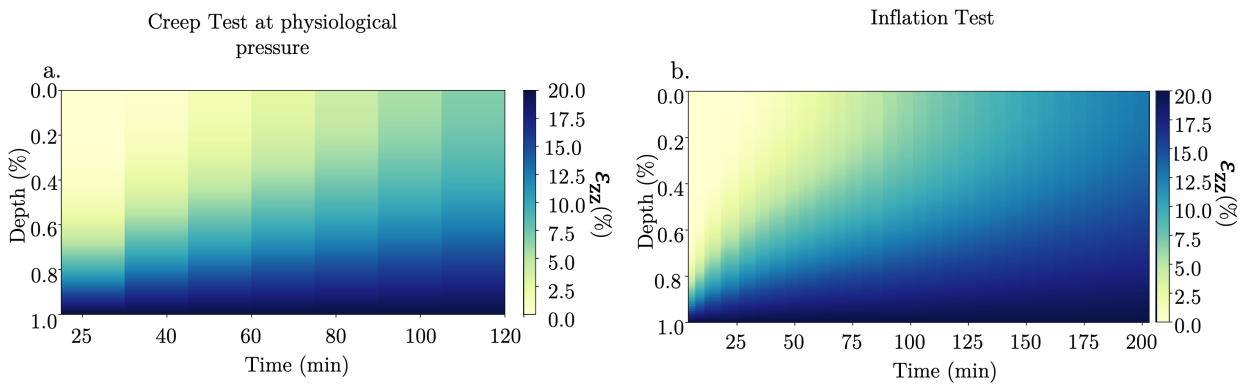


Figure 3.47: Vertical strain with time (x-axis) and space (y-axis) during a. a creep test at physiological pressure and b. an inflation test.

Conclusion Even if the osmotic pressure does not explain every features of the response of cornea, it seems better suited to describe cornea than a purely elastic (even auxetic) material. First, the time dependence is captured and may help to understand the propagation of the swelling in the cornea. Second, the strain levels are of the same order of magnitude as those reached in our experiments,

even if we are supposed to deal with infinitesimal strains. What is missing here again is the spatial heterogeneity that we observe in the experiments: the three areas bounded by the limit depths z_1 and z_2 are completely absent from the computed response in this case as well and also the fact that the strain is higher at the first depth z_1 and seems to propagate from there up and down the cornea, not from the endothelium.

3.4.3 Superposition of auxetic and osmotic material

To allow for swelling and contraction, we would like to superimpose the two effects discussed above. They are combined by taking $\varepsilon = \varepsilon_{rr} + \varepsilon_{zz}$, with ε_{rr} from Sec. 3.4.1 and ε_{zz} from Sec. 3.4.2. We did not do the computation analytically but it is still interesting to consider for future modeling. The parameters used in the computation are the same as before, except for the Young's modulus (here $E = E_{ant} = 281$ kPa). Figure 3.48 presents the results for the strain $\varepsilon = \varepsilon_{rr} + \varepsilon_{zz}$ with time and space during a. a creep test at physiological pressure, b. a creep test at high pressure and c. an inflation test. Using this set of parameters, the model does not reproduce the creep test at physiological pressure (Fig. 3.48.a), while giving satisfying orders of magnitude for the other tests (Fig. 3.48.b and c). The swelling observed in the creep test at physiological pressure – coming for the inflow of water – is not sufficient to balance the elastic material response at the beginning and thus it yields a slight contraction in the anterior part of the cornea. Looking at the response of the creep test at high pressure the values of strains are quite consistent but the three areas are absent, especially the contraction in the endothelium part and the swelling in central part is not really well captured during phase 1. And during phase 2, it seems that the whole cornea contracts quite uniformly, which is really different from our experiments. It is the same for the results of the inflation test regarding the three areas and we can add that the difference in response during phases 1 and 3 is not so clear as in the experiments.

In summary, while the behavior of cornea is globally well captured in terms of strain values with a possibility of having both positive and negative strains, the three zones are absent from the numerical results. The response of the endothelium zone is highly dependent on the osmotic process and does not reflect the compression supported in the creep test at high pressure and the inflation test. Therefore, the central part cannot swell as much as in the experiments (without swelling the endothelial area much more). The homogenization of the response of the epithelial area is not well rendered either.

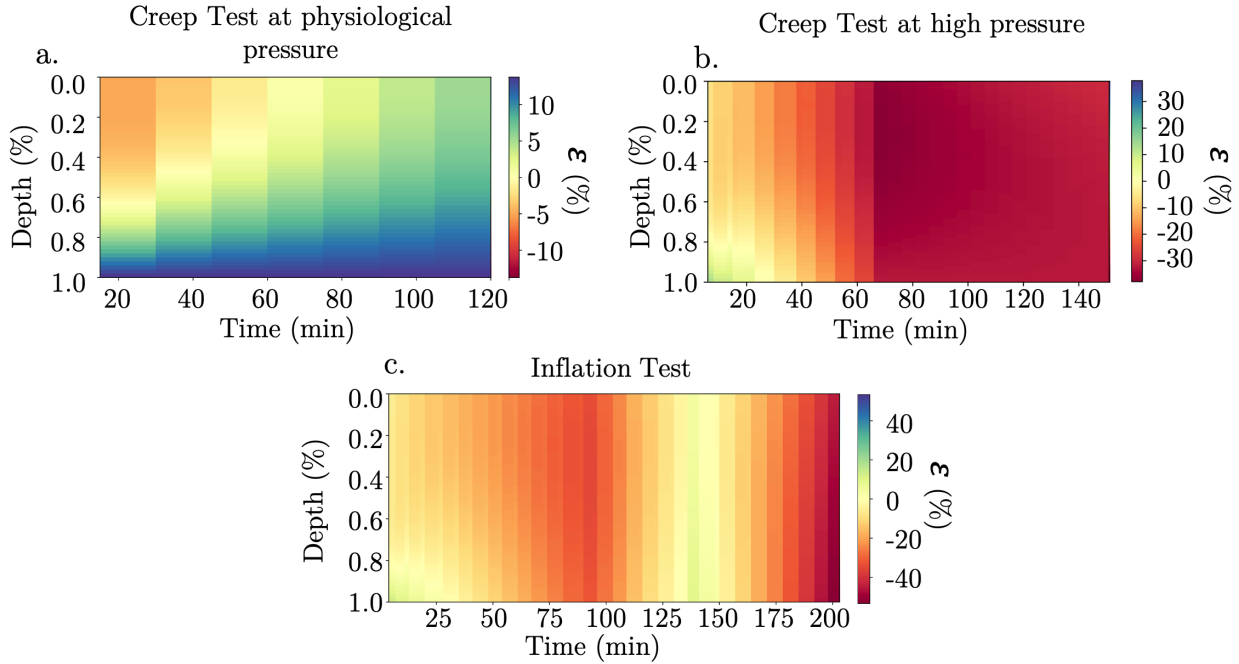


Figure 3.48: Strain with time (x-axis) and space (y-axis) during a. a creep test at physiological pressure and b. an creep test at high pressure and c. an inflation test.

Conclusion on the model Combining the effect of osmotic pressure and the response of an elastic material reproduces some features of our experiments. In particular, it is possible to have simultaneously both swelling and contraction in the tissue under pressure. Also, the osmotic pressure gives a time-dependence to the process that is close from the propagation of the swelling of the cornea. However, this simple model falls short to reproduce the three observed regions which have been brought in to light by the experiments. To further advance, one can assume an effect of the heterogeneity of the Young's modulus. Anterior and posterior parts of the cornea do not have the same stiffness [37]. We did a first try coupling heterogeneous Young's modulus and osmotic pressure but the results were not conclusive in terms of strain evolution in the three regions, so were not presented in this manuscript.

3.4.4 Summary of model results and discussion

Considering an elastic material submitted to osmotic and intraocular pressure, a simple model is built in order to explain the response of cornea under pressure, especially the swelling phenomenon. The model showed that the observed positive strain and the time dependence of the response can come from an osmotic process. Its main limitation is that it does not capture neither the three zones observed in the experiments nor the distribution of strain in the three regions, especially the fact that ε_1 is always higher in absolute value than ε_2 leading to a larger strain at 30% of depth than in the posterior part.

Looking at the microstructure of the cornea, one hypothesis can be formulated regarding the three zones. It has been observed [145; 176] that the lamellae are arranged differently in the first third (0 to 33% of depth) of the cornea than in the two last thirds (33 to 100% of depth). They are more intertwined and less in-plane, the out-of-plane angle being maximum under the epithelium (see upper

third blue out-of-plane lamellae in Fig. 3.49). It may explain that the anterior part of the cornea – where the lamellae form a grid-like network of lamellae – would deform less than the posterior part where the lamellae are more in-plane, which will lead to a heterogeneous rigidity of the cornea in depth.

On the other hand, in the experiments, larger amplitudes of strain at the second limit depths in the different tests are observed than at the first limit depth (for example from +5% to around -15% for ε_2 while only from -15% to -20% for ε_1 during the creep test at high pressure). Looking at the OCT images, the presence of stromal striae mainly in the posterior stroma [62] may lead to think that those structures of the posterior part help supporting the change of pressure (see lower two thirds purple striae in Fig. 3.49). Although it is not clear on a single picture, looking at the whole video of a creep test, the posterior part of the cornea – which is wrinkled at low pressure – tends to unfold under high pressure, especially where the striae are visible. This can also supports the hypothesis of a heterogeneous rigidity within the depth.

These last two points help to understand the difference in response of the tissue between the anterior and posterior parts (above and below the first limit depth, respectively) but it is not sufficient to explain the response of cornea below this first limit depth because it does not explain why the strain seems to homogenize with time from the first limit depth to the endothelium (which can be illustrated for example by the two limit strains ε_1 and ε_2 which converge towards the same value at the end of the creep test at high pressure – Fig. 3.30.b). A two-characteristic-time dependence can be imagined to capture this behavior of cornea (see green and orange arrows in Fig. 3.49). We first observed a rapid response of cornea – which may be due to a fast water flow from inside or outside the cornea – with a characteristic time τ_1 (represented by the green arrows), leading to a larger strain (in absolute value) at the first limit depth z_1 than at depth z_2 . We then observed a slow diffusion process (homogenization) in the anterior and especially posterior parts of the cornea from the first limit depth (represented by the orange arrows), with a characteristic time $\tau_2 \gg \tau_1$. The different organization of the microstructure, with out-of-plane lamellae above the first limit depth and mainly in-plane lamellae coupled to stromal striae below, also leads to a different response during this second phase between the anterior and posterior parts of cornea, as the process seems to be more pronounced in the posterior part.

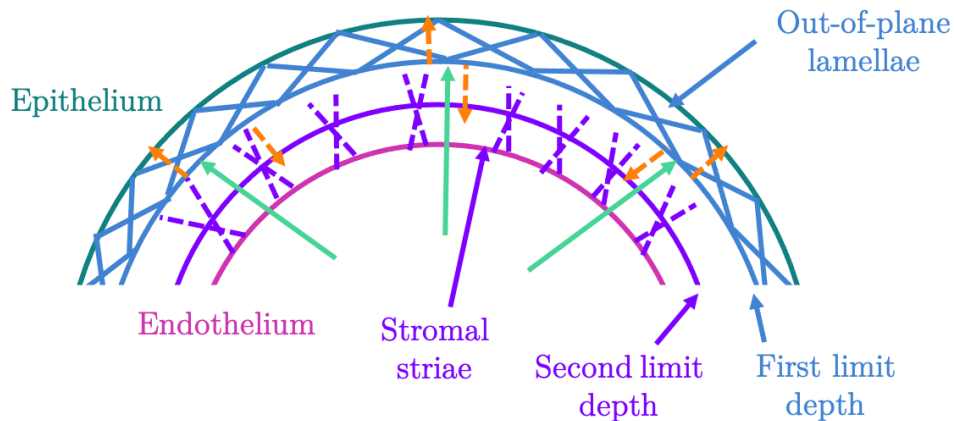


Figure 3.49: Scheme of a possible model using osmotic process with two characteristic times and a heterogeneous microstructure.

3.5 Conclusion

The corneal response under pressure has been explored using creep tests under physiological and high pressure, and inflation tests, monitoring the injected volume and measuring the pressure. Strain maps were computed using DIC/DVC analyses on 2D/3D OCT images and are ready to be used for the identification process. They provided us a huge amount of data that is difficult to present and analyze. They showed that the behavior of cornea differs at low and high pressure (respectively swelling and contraction) and that the most interesting strain to look at is the vertical component. The latter showed a division of the cornea by thickness into three regions: (i) the upper third (below the epithelium), (ii) the central part and (iii) the lower quarter (above the endothelium). Interestingly, the central part has the greatest heterogeneity in strain values, with generally a large difference between 30 and 70% of depth.

A mechanical model has been built to try to understand the discrepancy in the mechanical response of the cornea under the different tests. It showed that the most likely hypothesis for having simultaneously swelling and contraction is to have an osmotic exchange through the endothelium between the cornea and the external fluid. This hypothesis does not explain the division into three regions and some components are still missing.

As the different tests and models show that the mechanical responses of cornea are not easily interpreted, future research may need to build a complex model including a large number of parameters to represent the tissue in a more realistic manner. The data provided here may eventually not be sufficient to identify all the parameters. In particular, there is no clear threshold pressure where the cornea begins to only contract (and not swell anymore), indicating that, for example, the parameters used in the model could not be unique but cornea-specific. In the same spirit, one of the main limitations of the experiments presented herein is the complete lack of information on the microstructure response during the different tests. As it is essential to model properly the cornea – especially in the case of pathological corneas, where the collagen lamellae are altered [142; 145] – it can be interesting to look at what happens at the micro scale. In this view, mechanical tests coupled with SHG images

may lead to a better understanding of the micro-mechanics of cornea (rearrangement of the lamellae) and therefore to a better understanding of the macroscopic behavior.

Conclusions and Perspectives

This thesis aimed to answer one of the questions that ophthalmic surgeons have asked themselves for a long time: can we understand the onset of keratoconus? Since one of the favored hypothesis is the effect of eye rubbing on the cornea, a mechanical origin of the disease was investigated. Two parallel studies were conducted: (i) a numerical study to characterize *in-silico* the onset of the pathology and (ii) an *ex-vivo* experimental study on corneas from eye bank to try to better understand the mechanical response of healthy tissue, for which the literature is quite scarce to date. Hereafter are recalled the main conclusions drawn from those studies. The perspectives that result from this work and the questions that remain unsolved are also discussed.

Numerical and experimental studies

Conclusion on the numerical study A multiscale model based on patient-specific geometry has been built to explore the mechanical response of the cornea. A methodology has been developed to create a mesh as close as possible to the real geometry of the patient using ophthalmic data. The cornea has been modeled as an hyperelastic quasi-incompressible matrix reinforced by anisotropic fibers – the collagen lamellae. An original angular integration approach – the microsphere, allowing for a non-affine transformation (not studied here) between the evolution of the lamellae distribution and the macroscopic response of the cornea – was used to take into account the experimental results of the fiber organization. The numerical study explored the influence of the different parameters of the model, leading to consider the unfolding stretch as the most sensitive parameter in the pressure versus apex displacement response (which can be interesting for the study of the prestress applied on the whole structure). The set of parameters was chosen such that the numerical simulations fit the results of the pressure versus apex displacement curve of [45]. The SimK, an ophthalmic indicator of the diopter in the center of the eye whose evolution with pressure varies in the case of healthy or keratoconic corneas, was then investigated to determine the mechanical parameters affecting the response of the tissue in the case of the pathology. I showed that, in order to have the 2 diopter variations of SimK with pressure found in keratoconic corneas by McMonnies' group [100], the collagen lamellae should be weakened, regardless of the considered geometry. Conversely, a keratoconic geometry with healthy parameters does not lead to a significant change in SimK.

To conclude this study, the question "who appears first: the thinning or the destructuring of the microstructure?" still remains open. The numerical study was not sufficient to make a decision. Yet, the weakening of the lamellae that goes with the destructuring can be an indicator of the pathology. Thus, measuring local stiffness differences could help detect the pathology at an early stage but how remains to be determined.

Perspectives of the numerical study My model does not take into account the remodeling process that occurs as keratoconus progresses. It would seem interesting to start with a geometry and parameters of a healthy cornea, to apply a mechanical remodeling (caused for example by eye rubbing) and to manage to simulate the appearance of the keratoconic geometry with also the associated change of parameter. It would go a step further in trying to answer the question "which comes first between remodeling and weakening?" To complement this kind of study, imaging at different stages of keratoconic microstructure could be very helpful. However, to this day, there is no non destructive imaging technique that allows the microstructure *in-vivo* to be observed. Furthermore, obtaining

samples of keratoconic corneas for mechanical testing is a real challenge as the extraction is usually done before transplant and then the pathological tissue is kept for histological tests.

The numerical study has also demonstrated sensitivity to the unfolding elongation, a parameter that is linked to the length of the lamellae. Experiments show that when a human cornea is cut with a scalpel it does not collapse onto itself (Fig. 3.50), like a porcine cornea would. This observation proves that the lamellar arrangement is capable of supporting the entire structure even when it is cut by a quarter, and thus may be interesting to study in order to determine the prestress and prestrain of the structure. This property is useful in the case of LASIK surgery, which consists in remodeling the stroma (mostly posterior) using a laser – and thus cutting the lamellae. It would be very interesting to image the lamellae of a cornea before and after a LASIK incision and try to link the imaging results to the unfolding elongation of the lamellae. Combining these observations to the multiscale model could help predict the results of LASIK surgery, which are nowadays mostly based on empirical results and surgeon experience.

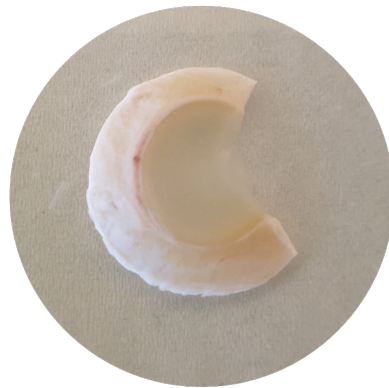


Figure 3.50: Human cornea cut with a scalpel to test the prestress. The cornea does not collapse on itself when a quarter (or more) is removed. The lamellar arrangement is able to support the entire structure, even when it is cut by a quarter.

Finally, all the hypotheses we have put forward during the modeling phase (affine behavior of the lamellae, quasi-incompressibility of the tissue, absence of remodeling...) had to be tested. To this end, we performed an experimental study with a double objective: (i) first we wanted to observe the macroscopic behavior of the cornea and thus complete the data available in the literature and (ii) secondly we wanted to use these data to identify parameters and thus validate or invalidate our hypotheses.

Conclusion on the experimental study The experimental study aimed to tackle the lack of data on full-field mechanical measurements of the non-pathological cornea under pressure. Creep tests and inflation tests have been performed to mimic transplant, to build a reference of strain maps of the cornea under a large range of pressure, and to study the mechanical response of human cornea at high pressure. Strain maps have been computed using DIC/DVC analysis on 2D/3D OCT images of the cornea taken all along the tests. The main outcome of the experimental study was unexpected for human corneas. Even though the cornea is usually modeled as a quasi-incompressible hyperelastic material, strain maps revealed a swelling of the cornea under low pressure that may lead to strain in the anterior-posterior direction reaching over 20% with time. Conversely, at high pressure the cornea seems to drain out its fluid content. In any case, an exchange of fluid/molecules seems to

happen through the endothelium, even though the mechanism governing the flow is not completely understood. Strain maps have also shown that three distinctive area can be defined, where the cornea has different responses. The middle part can even exhibit a negative apparent characteristic stiffness during inflation tests, leading to consider the idea that cornea is an auxetic material. But this is not sufficient to explain the high strains observed in the creep test at physiological pressure and also the temporal dependence of the response. A simple model combining the osmotic pressure effect and the elastic response of a material has been built to try to describe the mechanical response of human cornea. Although the osmotic exchange allows us to capture some observations such as positive strains or time evolution, it could not recreate the three observed zones. Thus, the experimental study has highlighted a number of mysteries that remain to be solved.

Perspectives of the experimental study Looking at the experimental results (especially the shear strain maps) and disregarding the swelling of the tissue, it seems that the cornea tends to compensate pressure variations through an adaptation process, mainly in its peripheral zone rather than its central part. These results are consistent with the fact that daily variations in intraocular pressure do not affect vision, and that physicians think that the curvature radii do not change much during the day. To check this, we could compute the radii of curvature of the anterior surface on 2D and 3D OCT images while varying the pressure (or at least during the creep test at physiological pressure). It could help confirm or discard this hypothesis. Similarly, on the 2D OCT images, it seems the stromal striae, which are located mainly on the posterior stroma, unfold while the pressure increases. It leads to a question I would like to explore: how does the cornea do to maintain its shape – with its focusing power – during the day? Experimental studies on the peripheral part and on the response of stromal striae under pressure could be a first step. What is challenging with studying the peripheral part of the cornea is that it is usually fixed to the anterior chamber, and the boundary conditions have to be taken into account very carefully. Using a whole eyeball could solve this problem, but in that case the main issues are first the availability of human samples (the grafts are always only corneal button, not the whole eyeball) and then the impact of the deformation of the rest of the eye, which would not necessarily be easy to measure. For stromal striae, the challenge is elsewhere, since they are visible on OCT images. The issue is more in quantifying the motion of these structures that are not really well known today. Image segmentation techniques could help isolate the structures, allowing them to be followed during the experiment.

The experiment at physiological pressure showed a swelling that does not occur anymore when the cornea has undergone a complete cycle of increasing and decreasing pressure steps. In the context of transplant, the graft is put under physiological pressure after being stored in the deturgescence medium. After transplant, the vision is blurry and useful vision comes back after a couple of days. It is not clear if swelling would appear after *in-vivo* transplant, but if it is the case, I would like to test if the lamellae are intact after the whole cycle of pressure steps, in which case a swelling-free, viable cornea could be obtained. In the context of this thesis, one cornea has been fixed in PFA and imaged by our colleague at Laboratoire d'Optique et Bioscience after having undergone a complete inflation test, and no significant differences were found compared to raw cornea. More corneas should be tested to conclude but it is a first step pointing in the direction of non-destructive pressure steps that could speed up the recovery process after transplant. Further, to complete this study and to ensure that the lamellae are not submitted to stress levels leading to irreversible damage, it would be very interesting

to couple the SHG imaging setup with the inflation experiment to follow the evolution of the collagen lamellae. In all cases, it is necessary to ensure the integrity of all the components of the cornea and not only the collagen lamellae, and in particular that the matrix is intact.

General perspectives of this work

Identification of the parameters One of the main perspectives of this work is the identification of the parameters of the multiscale model using the experimental results. Some of the parameters of the model – such as the unfolding elongations of the lamellae – are impossible (or extremely difficult) to measure experimentally. But, even if the identification loop is ready to run, experimental results have brought more questions than answers, so that the model has to be adapted beforehand to be able to represent the experimental data. First, swelling of the cornea has questioned the classical view of the tissue being a hyperelastic material only. Taking into account an osmotic exchange with the exterior medium in the model could solve the inflation problem, but the original way of deformation propagation seen during the experiment has to be investigated carefully. It is not obvious that the spatial arrangement of the lamellae would lead to the appearance of the three zones that were observed. Second, the creep test at high pressure has demonstrated draining of the fluid outside the cornea, which could be represented by a reverse osmotic effect. But then the pressure for which the pumping in becomes a pumping out should be identified properly, probably experimentally first, with creep tests at different pressures. Finally, the inflation tests highlighted a change in response of human cornea after a cycle of pressure step. To investigate this hysteresis in the context of transplant for example, the model has to be adapted too. In conclusion, to represent the experimental results the model should probably be able to adapt to each case.

In-vivo* VS *ex-vivo In this work, two parallel studies have been led: one *in-silico* and one *ex-vivo*. Even though the model is based on real patient geometries, the parameters used in the simulation are exclusively extracted from *ex-vivo* literature. And with good reason, since most of the experiments are destructive. The multiscale model was built to represent realistically the mechanical response of human cornea. But the *ex-vivo* experiments I conducted to fill in the sparse data available completely changed the prism through which I now see its modeling. If there is one thing that this work has taught me, is that the dialog between *in-vivo* data and *ex-vivo* or *in-silico* model is even more difficult, when it comes to human data. First, because *in-vivo* data are usually difficult to measure experimentally, even though the cornea is one of the external organ of the human body, so easily accessible. Then, because even when accessing human data *in-vivo*, they are always incomplete and the model should be able to fill in the gap between what is known and what is not. And finally, as experiments are often performed *ex-vivo*, the gap between what happens *ex-vivo* versus what happens *in-vivo* should be filled. Thus, the real question here is: how to fill in this gap between what we found *ex-vivo* and what we think happens *in-vivo*? As we are dealing with living tissues, reconciling *ex-vivo* experimental data with reality is also, in my point of view, one of the main challenges of biomechanics.

Bibliography

- [1] Aghamohammadzadeh, H., Newton, R. H., and Meek, K. M. (2004). X-Ray Scattering Used to Map the Preferred Collagen Orientation in the Human Cornea and Limbus. *Structure*, 12(2):249–256.
- [2] Akhtar, S., Bron, A. J., Salvi, S. M., Hawksworth, N. R., Tuft, S. J., and Meek, K. M. (2008). Ultrastructural analysis of collagen fibrils and proteoglycans in keratoconus. *Acta Ophthalmologica*, 86(7):764–772.
- [3] Alastrué, V., Calvo, B., Peña, E., and Doblaré, M. (2006). Biomechanical Modeling of Refractive Corneal Surgery. *Journal of Biomechanical Engineering*, 128(1):150–160.
- [4] Alastrué, V., Martínez, M., and Doblaré, M. (2008). Modelling adaptative volumetric finite growth in patient-specific residually stressed arteries. *Journal of Biomechanics*, 41(8):1773–1781.
- [5] Ambekar, R., Toussaint Jr., K. C., and Wagoner Johnson, A. (2011). The effect of keratoconus on the structural, mechanical, and optical properties of the cornea. *Journal of the Mechanical Behavior of Biomedical Materials*, 4(3):223–236.
- [6] Andreassen, T. T., Hjorth Simonsen, A., and Oxlund, H. (1980). Biomechanical Properties of Keratoconus and Normal Corneas. *Experimental Eye Research*, 31:435–441.
- [7] Ashofteh Yazdi, A., Melchor, J., Torres, J., Faris, I., Callejas, A., Gonzalez-Andrades, M., and Rus, G. (2020). Characterization of non-linear mechanical behavior of the cornea. *Scientific Reports*, 10(1):11549.
- [8] Ateshian, G. A., Rajan, V., Chahine, N. O., Canal, C. E., and Hung, C. T. (2009). Modeling the Matrix of Articular Cartilage Using a Continuous Fiber Angular Distribution Predicts Many Observed Phenomena. *Journal of Biomechanical Engineering*, 131.
- [9] Avril, S., Bonnet, M., Bretelle, A.-S., Grédiac, M., Hild, F., Ienny, P., Latourte, F., Lemosse, D., Pagano, S., Pagnacco, E., and Pierron, F. (2008). Overview of Identification Methods of Mechanical Parameters Based on Full-field Measurements. *Experimental Mechanics*, 48(4):381–402.
- [10] Barnett, M. and Mannis, M. J. (2011). Contact Lenses in the Management of Keratoconus. *Cornea*, 30(12):1510–1516.
- [11] Bay, B. K., Smith, T. S., Fyhrie, D. P., and Saad, M. (1999). Digital volume correlation: Three-dimensional strain mapping using X-ray tomography. *Experimental Mechanics*, 39(3):217–226.

BIBLIOGRAPHY

- [12] Belin, M. and Ambrósio, R. (2013). Scheimpflug imaging for keratoconus and ectatic disease. *Indian Journal of Ophthalmology*, 61(8):401.
- [13] Bell, J., Hayes, S., Whitford, C., Sanchez-Weatherby, J., Shebanova, O., Vergari, C., Winlove, C., Terrill, N., Sorensen, T., Elsheikh, A., and Meek, K. (2018). The hierarchical response of human corneal collagen to load. *Acta Biomaterialia*, 65:216–225.
- [14] Benoit, A., Latour, G., Marie-Claire, S.-K., and Allain, J.-M. (2016). Simultaneous microstructural and mechanical characterization of human corneas at increasing pressure. *Journal of the Mechanical Behavior of Biomedical Materials*, 60:93–105.
- [15] Bergmanson, J. P., Horne, J., Doughty, M. J., Garcia, M., and Gondo, M. (2005). Assessment of the Number of Lamellae in the Central Region of the Normal Human Corneal Stroma at the Resolution of the Transmission Electron Microscope. *Eye & Contact Lens: Science & Clinical Practice*, 31(6):281–287.
- [16] Billiar, K. L. and Sacks, M. S. (2000). Biaxial Mechanical Properties of the Natural and Glutaraldehyde Treated Aortic Valve Cusp—Part I: Experimental Results. *Journal of Biomechanical Engineering*, 122(1):23–30.
- [17] Bols, J., Degroote, J., Trachet, B., Verheghe, B., Segers, P., and Vierendeels, J. (2013). A computational method to assess the in vivo stresses and unloaded configuration of patient-specific blood vessels. *Journal of Computational and Applied Mathematics*, 246:10–17.
- [18] Boote, C., Hayes, S., Abahussin, M., and Meek, K. M. (2006). Mapping Collagen Organization in the Human Cornea: Left and Right Eyes Are Structurally Distinct. *Investigative Ophthalmology & Visual Science*, 47(3):901.
- [19] Bornert, M., Chaix, J.-M., Doumalin, P., Dupré, J.-C., Fournel, T., Jeulin, D., Maire, E., Moreaud, M., and Moulinec, H. (2004). Mesure tridimensionnelle de champs cinématiques par imagerie volumique pour l’analyse des matériaux et des structures. *Instrumentation, Mesure, Métrologie*, 4(3-4):43–88.
- [20] Bourne, W. M. (1998). Clinical estimation of corneal endothelial pump function. page 14.
- [21] Bourne, W. M. (2003). Biology of the corneal endothelium in health and disease. *Eye*, 17(8):912–918.
- [22] Boyce, B., Jones, R., Nguyen, T., and Grazier, J. (2007). Stress-controlled viscoelastic tensile response of bovine cornea. *Journal of Biomechanics*, 40(11):2367–2376.
- [23] Boyce, B. L., Grazier, J. M., Jones, R. E., and Nguyen, T. D. (2008). Full-field deformation of bovine cornea under constrained inflation conditions. *Biomaterials*, 29(28):3896–3904.
- [24] Buljac, A., Jailin, C., Mendoza, A., Neggens, J., Taillandier-Thomas, T., Bouterf, A., Smaniotto, B., Hild, F., and Roux, S. (2018). Digital Volume Correlation: Review of Progress and Challenges. *Experimental Mechanics*, 58(5):661–708.

- [25] Carvalho, L. A., Prado, M., Cunha, R. H., Costa Neto, A., Paranhos Jr, A., Schor, P., and Chamon, W. (2009). Keratoconus prediction using a finite element model of the cornea with local biomechanical properties. *Arquivos Brasileiros de Oftalmologia*, 72(2):139–145.
- [26] Cavas-Martínez, F., Bataille, L., Fernández-Pacheco, D. G., Cañavate, F. J. F., and Alió, J. L. (2017). A new approach to keratoconus detection based on corneal morphogeometric analysis. *PLOS ONE*, 12(9):e0184569.
- [27] Cavas-Martínez, F., Fernández-Pacheco, D. G., Parras, D., Cañavate, F. J. F., Bataille, L., and Alió, J. (2018). Study and characterization of morphogeometric parameters to assist diagnosis of keratoconus. *BioMedical Engineering OnLine*, 17(S1):161.
- [28] Chakraborty, S. and Ruiz, P. D. (2012). Measurement of all orthogonal components of displacement in the volume of scattering materials using wavelength scanning interferometry. *Journal of the Optical Society of America A*, 29(9):1776.
- [29] Chang, S.-H., Zhou, D., Eliasy, A., Li, Y.-C., and Elsheikh, A. (2020). Experimental evaluation of stiffening effect induced by UVA/Riboflavin corneal cross-linking using intact porcine eye globes. *PLOS ONE*, 15(11):e0240724.
- [30] Cheng, X., Petsche, S. J., and Pinsky, P. M. (2015). A structural model for the *in vivo* human cornea including collagen-swelling interaction. *Journal of The Royal Society Interface*, 12(109):20150241.
- [31] Choudhury, N., Bouchot, O., Rouleau, L., Tremblay, D., Cartier, R., Butany, J., Mongrain, R., and Leask, R. L. (2009). Local mechanical and structural properties of healthy and diseased human ascending aorta tissue. *Cardiovascular Pathology*, 18(2):83–91.
- [32] Ciarlet, P. and Geymonat, G. (1982). On constitutive equations in compressible non linear elasticity. *Comptes rendus des séances de l'Académie des Sciences.*, 295(4):423–426.
- [33] Davis, A. (2019). *Tomographie par cohérence optique confocale en ligne multimodale pour le diagnostic non invasif des cancers cutanés*. PhD thesis, Université Paris-Saclay.
- [34] De Stefano, V. S., Ford, M. R., Seven, I., and Dupps, W. J. (2020). Depth-Dependent Corneal Biomechanical Properties in Normal and Keratoconic Subjects by Optical Coherence Elastography. *Translational Vision Science & Technology*, 9(7):4.
- [35] den Toonder, J. M. J., Ramone, Y., van Dijken, A. R., Beijer, J. G. J., and Zhang, G. Q. (2005). Viscoelastic Characterization of Low-Dielectric Constant SiLK Films Using Nanoindentation in Combination With Finite Element Modeling. *Journal of Electronic Packaging*, 127(3):276–285.
- [36] Dias, J., Diakonis, V. F., Lorenzo, M., Gonzalez, F., Porrás, K., Douglas, S., Avila, M., Yoo, S. H., and Ziebarth, N. M. (2015). Corneal stromal elasticity and viscoelasticity assessed by atomic force microscopy after different cross linking protocols. *Experimental Eye Research*, 138:1–5.
- [37] Dias, J. M. and Ziebarth, N. M. (2013). Anterior and posterior corneal stroma elasticity assessed using nanoindentation. *Experimental Eye Research*, 115:41–46.

BIBLIOGRAPHY

- [38] Downie, L. E. and Lindsay, R. G. (2015). Contact lens management of keratoconus. *Clinical and Experimental Optometry*, 98(4):299–311.
- [39] Drexler, W., Liu, M., Kumar, A., Kamali, T., Unterhuber, A., and Leitgeb, R. A. (2014). Optical coherence tomography today: speed, contrast, and multimodality. *Journal of Biomedical Optics*, 19(7):071412.
- [40] Dua, H. S., Faraj, L. A., Said, D. G., Gray, T., and Lowe, J. (2013). Human Corneal Anatomy Redefined. *Ophthalmology*, 120(9):1778–1785.
- [41] Duncan, J. K., Belin, M. W., and Borgstrom, M. (2016). Assessing progression of keratoconus: novel tomographic determinants. *Eye and Vision*, 3(1):6.
- [42] Eberwein, P., Nohava, J., Schlunck, G., and Swain, M. (2014). Nanoindentation Derived Mechanical Properties of the Corneoscleral Rim of the Human Eye. *Key Engineering Materials*, 606:117–120.
- [43] Ehret, A. E., Bircher, K., Stracuzzi, A., Marina, V., Zündel, M., and Mazza, E. (2017). Inverse poroelasticity as a fundamental mechanism in biomechanics and mechanobiology. *Nature Communications*, 8(1):1002.
- [44] Eliasy, A., Chen, K.-J., Vinciguerra, R., Lopes, B. T., Abass, A., Vinciguerra, P., Ambrósio Jr., R., Roberts, C. J., and Elsheikh, A. (2019). Determination of Corneal Biomechanical Behavior in vivo for Healthy Eyes Using CorVis ST Tonometry: Stress-Strain Index. *Frontiers in Bioengineering and Biotechnology*, 7:105.
- [45] Elsheikh, A., Alhasso, D., and Rama, P. (2008). Biomechanical properties of human and porcine corneas. *Experimental Eye Research*, 86(5):783–790.
- [46] Elsheikh, A. and Anderson, K. (2005). Comparative study of corneal strip extensometry and inflation tests. *Journal of The Royal Society Interface*, 2(3):177–185.
- [47] Espana, E. M. and Birk, D. E. (2020). Composition, structure and function of the corneal stroma. *Experimental Eye Research*, 198:108137.
- [48] Fang, F. and Lake, S. P. (2016). Modelling approaches for evaluating multiscale tendon mechanics. *Interface Focus*, 6(1):20150044.
- [49] Feneck, E. M., Lewis, P. N., Ralphs, J., and Meek, K. M. (2018). A comparative study of the elastic fibre system within the mouse and human cornea. *Experimental Eye Research*, 177:35–44.
- [50] Ford, M. R., Dupps, W. J., Rollins, A. M., Roy, A. S., and Hu, Z. (2011). Method for optical coherence elastography of the cornea. *Journal of Biomedical Optics*, 16(1):016005.
- [51] Fratzl, P., Hulmes, D. J. S., Wess, T. J., Avery, N. C., Bailey, A. J., Ker, R., Silver, F. H., Landis, W. J., Gupta, H. S., Buehler, M. J., Kjaer, M., Magnusson, S. P., Biewener, A. A., Holzapfel, G. A., Purslow, P. P., Meek, K. M., Currey, J., Zalansky, P., Blank, R., Boskey, A. L., Sander, E. A., and Barocas, V. H. (2008). *Collagen: structure and mechanics*. Springer, New York. OCLC: ocn172979453.

- [Fu] Fu, J. Identification of corneal mechanical properties using optical tomography and digital volume correlation. page 201.
- [53] Fu, J., Pierron, F., and Ruiz, P. D. (2013). Elastic stiffness characterization using three-dimensional full-field deformation obtained with optical coherence tomography and digital volume correlation. *Journal of Biomedical Optics*, 18(12):121512.
- [54] Gasser, T. C., Ogden, R. W., and Holzapfel, G. A. (2006). Hyperelastic modelling of arterial layers with distributed collagen fibre orientations. *Journal of The Royal Society Interface*, 3(6):15–35.
- [55] Gatinel, D., Malet, J., Hoang-Xuan, T., and Azar, D. T. (2011). Corneal Elevation Topography: Best Fit Sphere, Elevation Distance, Asphericity, Toricity, and Clinical Implications:. *Cornea*, 30(5):508–515.
- [56] Gefen, A., Shalom, R., Elad, D., and Mandel, Y. (2009). Biomechanical analysis of the keratoconic cornea. *Journal of the Mechanical Behavior of Biomedical Materials*, 2(3):224–236.
- [57] Gilles, S. (2022). Gitlab MoReFEM.
- [58] Giraudet, C., Diaz, J., Le Tallec, P., and Allain, J.-M. (2022). Multiscale mechanical model based on patient-specific geometry: Application to early keratoconus development. *Journal of the Mechanical Behavior of Biomedical Materials*, page 105121.
- [59] Goulam Houssen, Y., Gusachenko, I., Schanne-Klein, M.-C., and Allain, J.-M. (2011). Monitoring micrometer-scale collagen organization in rat-tail tendon upon mechanical strain using second harmonic microscopy. *Journal of Biomechanics*, 44(11):2047–2052.
- [60] Greenwood, R. E. and Miller, J. J. (1948). Zeros of the Hermite polynomials and weights for Gauss’ mechanical quadrature formula. *Bulletin of the American Mathematical Society*, 54(8):765–770.
- [61] Grieve, K. (2019). Tomographie par Cohérence Optique. *La lumière et ses applications*, 95:19–23.
- [62] Grieve, K., Ghoubay, D., Georgeon, C., Latour, G., Nahas, A., Plamann, K., Crotti, C., Bocheux, R., Borderie, M., Nguyen, T.-M., Andreiuolo, F., Schanne-Klein, M.-C., and Borderie, V. (2017). Stromal striae: a new insight into corneal physiology and mechanics. *Scientific Reports*, 7(1):13584.
- [63] Guo, H., Hosseini-Moghaddam, S. M., and Hodge, W. (2019). Corneal biomechanical properties after SMILE versus FLEX, LASIK, LASEK, or PRK: a systematic review and meta-analysis. *BMC Ophthalmology*, 19(1):167.
- [64] Han, Z., Li, J., Singh, M., Wu, C., Liu, C.-h., Raghunathan, R., Aglyamov, S. R., Vantipalli, S., Twa, M. D., and Larin, K. V. (2017). Optical coherence elastography assessment of corneal viscoelasticity with a modified Rayleigh-Lamb wave model. *Journal of the Mechanical Behavior of Biomedical Materials*, 66:87–94.
- [65] Hansen, N. (2016). The CMA Evolution Strategy: A Tutorial. *arXiv:1604.00772 [cs, stat]*. arXiv:1604.00772.

- [66] Hashemi, H. (2005). Distribution of intraocular pressure in healthy Iranian individuals: the Tehran Eye Study. *British Journal of Ophthalmology*, 89(6):652–657.
- [67] Hayashi, S., Osawa, T., and Tohyama, K. (2002). Comparative observations on corneas, with special reference to bowman’s layer and descemet’s membrane in mammals and amphibians. *Journal of Morphology*, 254(3):247–258.
- [68] Holmes, D. F., Gilpin, C. J., Baldock, C., Ziese, U., Koster, A. J., and Kadler, K. E. (2001). Corneal collagen fibril structure in three dimensions: Structural insights into fibril assembly, mechanical properties, and tissue organization. *Proceedings of the National Academy of Sciences*, 98(13):7307–7312.
- [69] Holzapfel, G. A., Niestrawska, J. A., Ogden, R. W., Reinisch, A. J., and Schriefl, A. J. (2015). Modelling non-symmetric collagen fibre dispersion in arterial walls. *Journal of The Royal Society Interface*, 12(106):20150188.
- [70] Holzapfel, G. A. and Ogden, R. W. (2009). Constitutive modelling of passive myocardium: a structurally based framework for material characterization. *Philosophical Transactions of the Royal Society A: Mathematical, Physical and Engineering Sciences*, 367(1902):3445–3475.
- [71] Holzapfel, G. A., Ogden, R. W., and Sherifova, S. (2019). On fibre dispersion modelling of soft biological tissues: a review. *Proceedings of the Royal Society A: Mathematical, Physical and Engineering Sciences*, 475(2224):20180736.
- [72] Holzer, M. P., Rabsilber, T. M., and Auffarth, G. U. (2006). Femtosecond Laser-Assisted Corneal Flap Cuts: Morphology, Accuracy, and Histopathology. *Investigative Ophthalmology & Visual Science*, 47(7):2828.
- [73] Huang, L., Korhonen, R. K., Turunen, M. J., and Finnilä, M. A. (2019). Experimental mechanical strain measurement of tissues. *PeerJ*, 7:e6545.
- [74] Hughes, T., Cottrell, J., and Bazilevs, Y. (2005). Isogeometric analysis: CAD, finite elements, NURBS, exact geometry and mesh refinement. *Computer Methods in Applied Mechanics and Engineering*, 194(39-41):4135–4195.
- [75] Jaillet, F., Shariat, B., and Vandorpe, D. (1997). Periodic B-Spline Surface Skinning Of Anatomic Shapes. page 7.
- [76] Janunts, E., Kannengießer, M., and Langenbacher, A. (2015). Parametric fitting of corneal height data to a biconic surface. *Zeitschrift für Medizinische Physik*, 25(1):25–35.
- [77] Jin, Z., Khazaeinezhad, R., Zhu, J., Yu, J., Qu, Y., He, Y., Li, Y., Gomez Alvarez-Arenas, T. E., Lu, F., and Chen, Z. (2019). In-vivo 3D corneal elasticity using air-coupled ultrasound optical coherence elastography. *Biomedical Optics Express*, 10(12):6272.
- [78] Jor, J. W. Y., Nash, M. P., Nielsen, P. M. F., and Hunter, P. J. (2011). Estimating material parameters of a structurally based constitutive relation for skin mechanics. *Biomechanics and Modeling in Mechanobiology*, 10(5):767–778.

- [79] Kaufman, H., Barron, B., and McDonald, M. (1998). *The Cornea*. Woburn.
- [80] Kennedy, B. F., Kennedy, K. M., and Sampson, D. D. (2014). A Review of Optical Coherence Elastography: Fundamentals, Techniques and Prospects. *IEEE Journal of Selected Topics in Quantum Electronics*, 20(2):272–288.
- [81] Kennedy, B. F., Wijesinghe, P., and Sampson, D. D. (2017). The emergence of optical elastography in biomedicine. *Nature Photonics*, 11(4):215–221.
- [82] Khamar, P., Shetty, R., Vaishnav, R., Francis, M., M.M.A. Nuijts, R., and Sinha Roy, A. (2019). Biomechanics of LASIK Flap and SMILE Cap: A Prospective, Clinical Study. *Refract Surg.*, 35(5):324–332.
- [83] Kling, S. (2020). Optical coherence elastography by ambient pressure modulation for high-resolution strain mapping applied to patterned cross-linking. *Journal of The Royal Society Interface*, 17(162):20190786.
- [84] Kling, S., Bekesi, N., Dorronsoro, C., Pascual, D., and Marcos, S. (2014). Corneal Viscoelastic Properties from Finite-Element Analysis of In Vivo Air-Puff Deformation. *PLoS ONE*, 9(8):e104904.
- [85] Kling, S., Remon, L., Pérez-Escudero, A., Merayo-Llodes, J., and Marcos, S. (2010). Corneal Biomechanical Changes after Collagen Cross-Linking from Porcine Eye Inflation Experiments. *Investigative Ophthalmology & Visual Science*, 51(8):3961.
- [86] Klyce, S. D. (2020). 12. Endothelial pump and barrier function. *Experimental Eye Research*, 198:108068.
- [87] Komai, Y. and Ushikif, T. (1991). The Three-Dimensional Organization of Collagen Fibrils in the Human Cornea and Sclera. *Investigative Ophthalmology & Visual Science*, 32(8):2244–2258.
- [88] Lan, G., Aglyamov, S. R., Larin, K. V., and Twa, M. D. (2021). In Vivo Human Corneal Shear-wave Optical Coherence Elastography. *Optometry and Vision Science*, 98(1):58–63.
- [89] Larin, K. V. and Sampson, D. D. (2017). Optical coherence elastography – OCT at work in tissue biomechanics [Invited]. *Biomedical Optics Express*, 8(2):1172.
- [90] Last, J. A., Thomasy, S. M., Croasdale, C. R., Russell, P., and Murphy, C. J. (2012). Compliance profile of the human cornea as measured by atomic force microscopy. *Micron*, 43(12):1293–1298.
- [91] Latour, G., Gusachenko, I., Kowalczyk, L., Lamarre, I., and Schanne-Klein, M.-C. (2012). In vivo structural imaging of the cornea by polarization-resolved second harmonic microscopy. *Biomedical Optics Express*, 3(1):1.
- [92] Litwiller, D. V., Lee, S. J., Kolipaka, A., Mariappan, Y. K., Glaser, K. J., Pulido, J. S., and Ehman, R. L. (2010). MR elastography of the ex vivo bovine globe. *Journal of Magnetic Resonance Imaging*, 32(1):44–51.

BIBLIOGRAPHY

- [93] Lombardo, G., Serrao, S., Rosati, M., and Lombardo, M. (2014). Analysis of the Viscoelastic Properties of the Human Cornea Using Scheimpflug Imaging in Inflation Experiment of Eye Globes. *PLoS ONE*, 9(11):e112169.
- [94] Luyckx, T., Verstraete, M., De Roo, K., De Waele, W., Bellemans, J., and Victor, J. (2014). Digital image correlation as a tool for three-dimensional strain analysis in human tendon tissue. *Journal of Experimental Orthopaedics*, 1(1):7.
- [95] Lynch, B., Bancelin, S., Bonod-Bidaud, C., Gueusquin, J.-B., Ruggiero, F., Schanne-Klein, M.-C., and Allain, J.-M. (2017). A novel microstructural interpretation for the biomechanics of mouse skin derived from multiscale characterization. *Acta Biomaterialia*, 50:302–311.
- [96] Marchini, M., Morocutti, M., Ruggeri, A., Koch, M. H., Bigi, A., and Roveri, N. (1986). Differences in the Fibril Structure of Corneal and Tendon Collagen. An Electron Microscopy and X-Ray Diffraction Investigation. *Connective Tissue Research*, 15(4):269–281.
- [97] Markert, B., Ehlers, W., and Karajan, N. (2005). A general polyconvex strainenergy function for fiber-reinforced materials. 5:245–246.
- [98] Mashige, K. P. (2013). A review of corneal diameter, curvature and thickness values and influencing factors*. *African Vision and Eye Health*, 72(4):185–194.
- [99] Maurice, D. M. (1957). The structure and transparency of the cornea. *The Journal of Physiology*, 136(2):263–286.
- [100] McMonnies, C. W. and Boneham, G. C. (2010). Corneal Responses to Intraocular Pressure Elevations in Keratoconus. *Cornea*, 29(7):764–770.
- [101] Meek, K. M. and Boote, C. (2009). The use of X-ray scattering techniques to quantify the orientation and distribution of collagen in the corneal stroma. *Progress in Retinal and Eye Research*, 28(5):369–392.
- [102] Meek, K. M. and Knupp, C. (2015). Corneal structure and transparency. *Progress in Retinal and Eye Research*, 49:1–16.
- [103] Meek, K. M. and Quantock, A. J. (2001). The Use of X-ray Scattering Techniques to Determine Corneal Ultrastructure. *Progress in Retinal and Eye Research*, 20(1):95–137.
- [104] Meek, K. M., Tuft, S. J., Huang, Y., Gill, P. S., Hayes, S., Newton, R. H., and Bron, A. J. (2005). Changes in Collagen Orientation and Distribution in Keratoconus Corneas. *Investigative Ophthalmology & Visual Science*, 46(6):1948.
- [105] Meng, F., Chen, C., Hui, S., Wang, J., Feng, Y., and Sun, C. (2019). Three-dimensional static optical coherence elastography based on inverse compositional Gauss-Newton digital volume correlation. *Journal of Biophotonics*, 12(9).
- [106] Mercatelli, R., Ratto, F., Rossi, F., Tatini, F., Menabuoni, L., Malandrini, A., Nicoletti, R., Pini, R., Pavone, F. S., and Cicchi, R. (2017). Three-dimensional mapping of the orientation of collagen corneal lamellae in healthy and keratoconic human corneas using SHG microscopy. *Journal of Biophotonics*, 10(1):75–83.

-
- [107] Mergler, S. and Pleyer, U. (2007). The human corneal endothelium: New insights into electrophysiology and ion channels. *Progress in Retinal and Eye Research*, 26(4):359–378.
- [108] Merlini, G. (2021). Patient specific models with incomplete and mixed data: the example of the human cornea. Master’s thesis.
- [109] Mikula, E., Hollman, K., Chai, D., Jester, J. V., and Juhasz, T. (2014). Measurement of Corneal Elasticity with an Acoustic Radiation Force Elasticity Microscope. *Ultrasound in Medicine & Biology*, 40(7):1671–1679.
- [110] Mikula, E., Winkler, M., Juhasz, T., Brown, D. J., Shoa, G., Tran, S., Kenney, M. C., and Jester, J. V. (2018). Axial mechanical and structural characterization of keratoconus corneas. *Experimental Eye Research*, 175:14–19.
- [111] Mikula, E. R., Jester, J. V., and Juhasz, T. (2016). Measurement of an Elasticity Map in the Human Cornea. *Investigative Ophthalmology & Visual Science*, 57(7):3282.
- [112] Moilanen, J. A. O., Vesaluoma, M. H., Müller, L. J., and Tervo, T. M. T. (2003). Long-Term Corneal Morphology after PRK by In Vivo Confocal Microscopy. *Investigative Ophthalmology & Visual Science*, 44(3):1064.
- [113] Montanino, A., Gizzi, A., Vasta, M., Angelillo, M., and Pandolfi, A. (2018). Modeling the biomechanics of the human cornea accounting for local variations of the collagen fibril architecture. *ZAMM - Journal of Applied Mathematics and Mechanics / Zeitschrift für Angewandte Mathematik und Mechanik*, 98(12):2122–2134.
- [114] Naderan, M. (2017). Histopathologic findings of keratoconus corneas underwent penetrating keratoplasty according to topographic measurements and keratoconus severity. *International Journal of Ophthalmology*.
- [115] Nahas, A., Bauer, M., Roux, S., and Boccara, A. C. (2013). 3D static elastography at the micrometer scale using Full Field OCT. *Biomedical Optics Express*, 4(10):2138.
- [116] Nair, A., Singh, M., Aglyamov, S. R., and Larin, K. V. (2020). Heartbeat OCE: corneal biomechanical response to simulated heartbeat pulsation measured by optical coherence elastography. *Journal of Biomedical Optics*, 25(05):1.
- [117] Najmi, H. (2019). The correlation between keratoconus and eye rubbing: a review. *International Journal of Ophthalmology*, 12(11):1775–1781.
- [118] Napoli, P. E., Nioi, M., d’Aloja, E., Loy, F., and Fossarello, M. (2020). The architecture of corneal stromal striae on optical coherence tomography and histology in an animal model and in humans. *Scientific Reports*, 10(1):19861.
- [119] Nash, I. S., Greene, P. R., and Foster, C. (1982). Comparison of mechanical properties of keratoconus and normal corneas. *Experimental Eye Research*, 35(5):413–424.
- [120] Newton, R. H. and Meek, K. M. (1998). Circumcorneal Annulus of Collagen Fibrils in the Human Limbus. 39(7):8.

- [121] Nguyen, T. D. and Boyce, B. L. (2011). An inverse finite element method for determining the anisotropic properties of the cornea. *Biomechanics and Modeling in Mechanobiology*, 10(3):323–337.
- [122] Nguyen, T. D., Jones, R. E., and Boyce, B. L. (2008). A Nonlinear Anisotropic Viscoelastic Model for the Tensile Behavior of the Corneal Stroma. *Journal of Biomechanical Engineering*, 130(4):041020.
- [123] Nohava, J., Swain, M., Lang, S. J., Maier, P., Heinzlmann, S., Reinhard, T., and Eberwein, P. (2018). Instrumented indentation for determination of mechanical properties of human cornea after ultraviolet-A crosslinking: MECHANICAL PROPERTIES OF HUMAN CORNEA. *Journal of Biomedical Materials Research Part A*, 106(5):1413–1420.
- [Norouzpour and Mehdizadeh] Norouzpour, A. and Mehdizadeh, A. A Novel Insight into Keratoconus: Mechanical Fatigue of the Cornea. 1(1):4.
- [125] Okuyama, K. (2008). Revisiting the Molecular Structure of Collagen. *Connective Tissue Research*, 49(5):299–310.
- [126] Okuyama, K., Xu, X., Iguchi, M., and Noguchi, K. (2006). Revision of collagen molecular structure. *Biopolymers*, 84(2):181–191.
- [127] Pan, B., Qian, K., Xie, H., and Asundi, A. (2009). Two-dimensional digital image correlation for in-plane displacement and strain measurement: a review. *Measurement Science and Technology*, 20(6):062001.
- [128] Pandolfi, A., Gizzi, A., and Vasta, M. (2019). A microstructural model of cross-link interaction between collagen fibrils in the human cornea. *Philosophical Transactions of the Royal Society A: Mathematical, Physical and Engineering Sciences*, 377(2144):20180079.
- [129] Pandolfi, A. and Holzapfel, G. A. (2008). Three-Dimensional Modeling and Computational Analysis of the Human Cornea Considering Distributed Collagen Fibril Orientations. *Journal of Biomechanical Engineering*, 130(6):061006.
- [130] Pandolfi, A. and Manganiello, F. (2006). A model for the human cornea: constitutive formulation and numerical analysis. *Biomechanics and Modeling in Mechanobiology*, 5(4):237–246.
- [131] Pandolfi, A. and Vasta, M. (2012). Fiber distributed hyperelastic modeling of biological tissues. *Mechanics of Materials*, 44:151–162.
- [132] Park, S., Yoon, H., Larin, K. V., Emelianov, S. Y., and Aglyamov, S. R. (2017). The impact of intraocular pressure on elastic wave velocity estimates in the crystalline lens. *Physics in Medicine and Biology*, 62(3):N45–N57.
- [133] Pedersen, I. B., Bak-Nielsen, S., Vestergaard, A. H., Ivarsen, A., and Hjortdal, J. (2014). Corneal biomechanical properties after LASIK, ReLEx flex, and ReLEx smile by Scheimpflug-based dynamic tonometry. *Graefe’s Archive for Clinical and Experimental Ophthalmology*, 252(8):1329–1335.
- [134] Petsche, S. J. and Pinsky, P. M. (2013). The role of 3-D collagen organization in stromal elasticity: a model based on X-ray diffraction data and second harmonic-generated images. *Biomechanics and Modeling in Mechanobiology*, 12(6):1101–1113.

- [135] Piegl, L. and Tiller, W. (1995). *The NURBS Book*. Monographs in Visual Communications. Springer Berlin Heidelberg, Berlin, Heidelberg.
- [136] Pierce, D. M., Unterberger, M. J., Trobin, W., Ricken, T., and Holzapfel, G. A. (2016). A microstructurally based continuum model of cartilage viscoelasticity and permeability incorporating measured statistical fiber orientations. *Biomechanics and Modeling in Mechanobiology*, 15(1):229–244.
- [137] Pinsky, P. M., van der Heide, D., and Chernyak, D. (2005). Computational modeling of mechanical anisotropy in the cornea and sclera. *Journal of Cataract and Refractive Surgery*, 31(1):136–145.
- [138] Pitre, J. J., Kirby, M. A., Li, D. S., Shen, T. T., Wang, R. K., O’Donnell, M., and Pelivanov, I. (2020). Nearly-incompressible transverse isotropy (NITI) of cornea elasticity: model and experiments with acoustic micro-tapping OCE. *Scientific Reports*, 10(1):12983.
- [139] Piñero, D. P., Alió, J. L., Alesón, A., Vergara, M. E., and Miranda, M. (2010). Corneal volume, pachymetry, and correlation of anterior and posterior corneal shape in subclinical and different stages of clinical keratoconus. *Journal of Cataract and Refractive Surgery*, 36(5):814–825.
- [140] Qu, Y., Ma, T., He, Y., Zhu, J., Dai, C., Yu, M., Huang, S., Lu, F., Shung, K. K., Zhou, Q., and Chen, Z. (2016). Acoustic Radiation Force Optical Coherence Elastography of Corneal Tissue. *IEEE Journal of Selected Topics in Quantum Electronics*, 22(3):288–294.
- [141] Radner, W. and Mallinger, R. (2002). Interlacing of Collagen Lamellae in the Midstroma of the Human Cornea. *Cornea*, 21(6):598–601.
- [142] Radner, W., Zehetmayer, M., Skorpik, C., and Mallinger, R. (1998). Altered Organization of Collagen in the Apex of Keratoconus Corneas. *Ophthalmic Research*, 30(5):327–332.
- [143] Ramier, A., Eltony, A. M., Chen, Y., Clouser, F., Birkenfeld, J. S., Watts, A., and Yun, S.-H. (2020). In vivo measurement of shear modulus of the human cornea using optical coherence elastography. *Scientific Reports*, 10(1):17366.
- [144] Ramos, J. L. B., Li, Y., and Huang, D. (2009). Clinical and research applications of anterior segment optical coherence tomography - a review. *Clinical & Experimental Ophthalmology*, 37(1):81–89.
- [145] Raoux, C., Schmeltz, M., Bied, M., Alnawaiseh, M., Hansen, U., Latour, G., and Schanne-Klein, M.-C. (2021). Quantitative structural imaging of keratoconic corneas using polarization-resolved SHG microscopy. *Biomedical Optics Express*, 12(7):4163.
- [146] Roberts, C. J. and Dupps, W. J. (2014). Biomechanics of corneal ectasia and biomechanical treatments. *Journal of Cataract and Refractive Surgery*, 40(6):991–998.
- [147] Ruberti, J. W., Sinha Roy, A., and Roberts, C. J. (2011). Corneal Biomechanics and Biomaterials. *Annual Review of Biomedical Engineering*, 13(1):269–295.
- [148] Ruiz, P. D., Zhou, Y., Huntley, J. M., and Wildman, R. D. (2004). Depth-resolved whole-field displacement measurement using wavelength scanning interferometry. *Journal of Optics A: Pure and Applied Optics*, 6(7):679–683.

BIBLIOGRAPHY

- [149] Sacks, M. S. (2003). Incorporation of Experimentally-Derived Fiber Orientation into a Structural Constitutive Model for Planar Collagenous Tissues. *Journal of Biomechanical Engineering*, 125(2):280–287.
- [150] Salençon, J. (2016). *Mécanique des milieux continus Tome I Concepts généraux*. Ecole Polytechnique.
- [151] Salzer, H., Zucker, R., and Capuano, R. (1952). Table of the zeros and weight factors of the first 20 hermite polynomials. *Journal of Research of the National Bureau of Standards*, 48(2):111.
- [152] Sardar, D. K., Swanland, G.-Y., Yow, R. M., Thomas, R. J., and Tsin, A. T. C. (2007). Optical properties of ocular tissues in the near infrared region. *Lasers in Medical Science*, 22(1):46–52.
- [153] Scarcelli, G., Besner, S., Pineda, R., Kalout, P., and Yun, S. H. (2015). In Vivo Biomechanical Mapping of Normal and Keratoconus Corneas. *JAMA Ophthalmology*, 133(4):480.
- [154] Scarcelli, G., Besner, S., Pineda, R., and Yun, S. H. (2014). Biomechanical Characterization of Keratoconus Corneas Ex Vivo With Brillouin Microscopy. *Investigative Ophthalmology & Visual Science*, 55(7):4490.
- [155] Scarcelli, G., Kling, S., Quijano, E., Pineda, R., Marcos, S., and Yun, S. H. (2013). Brillouin Microscopy of Collagen Crosslinking: Noncontact Depth-Dependent Analysis of Corneal Elastic Modulus. *Investigative Ophthalmology & Visual Science*, 54(2):1418.
- [156] Scarcelli, G., Pineda, R., and Yun, S. H. (2012). Brillouin Optical Microscopy for Corneal Biomechanics. *Investigative Ophthalmology & Visual Science*, 53(1):185.
- [157] Sedaghat, M.-R., Askarizadeh, F., Narooie-Noori, F., Rakhshandadi, T., Ostadi-moghaddam, H., and Rajabi, S. (2018). Comparative evaluation of tomographic and biometric characteristics in bilateral keratoconus patients with unilateral corneal Vogt’s striae: a contralateral eye study. *Clinical Ophthalmology*, Volume 12:1383–1390.
- [158] Seiler, T. G., Shao, P., Eltony, A., Seiler, T., and Yun, S.-H. (2019). Brillouin Spectroscopy of Normal and Keratoconus Corneas. *American Journal of Ophthalmology*, 202:118–125.
- [159] Shao, P., Eltony, A. M., Seiler, T. G., Tavakol, B., Pineda, R., Koller, T., Seiler, T., and Yun, S.-H. (2019). Spatially-resolved Brillouin spectroscopy reveals biomechanical abnormalities in mild to advanced keratoconus in vivo. *Scientific Reports*, 9(1):7467.
- [160] Simonini, I. and Pandolfi, A. (2015). Customized Finite Element Modelling of the Human Cornea. *PLOS ONE*, 10(6):e0130426.
- [161] Singh, M., Li, J., Han, Z., Raghunathan, R., Nair, A., Wu, C., Liu, C.-H., Aglyamov, S., Twa, M. D., and Larin, K. V. (2017). Assessing the effects of riboflavin/UV-A crosslinking on porcine corneal mechanical anisotropy with optical coherence elastography. *Biomedical Optics Express*, 8(1):349.
- [162] Spoerl, E., Huhle, M., and Seiler, T. (1998). Induction of Cross-links in Corneal Tissue. *Experimental Eye Research*, 66(1):97–103.

- [163] Stracuzzi, A., Mazza, E., and Ehret, A. E. (2018). Chemomechanical models for soft tissues based on the reconciliation of porous media and swelling polymer theories. *ZAMM - Journal of Applied Mathematics and Mechanics / Zeitschrift für Angewandte Mathematik und Mechanik*, 98(12):2135–2154.
- [164] Studer, H., Larrea, X., Riedwyl, H., and Büchler, P. (2010). Biomechanical model of human cornea based on stromal microstructure. *Journal of Biomechanics*, 43(5):836–842.
- [165] Touboul, D., Gennisson, J.-L., Nguyen, T.-M., Robinet, A., Roberts, C. J., Tanter, M., and Grenier, N. (2014). Supersonic Shear Wave Elastography for the In Vivo Evaluation of Transepithelial Corneal Collagen Cross-Linking. *Investigative Ophthalmology & Visual Science*, 55(3):1976.
- [166] Venkateswaran, N., Galor, A., Wang, J., and Karp, C. L. (2018). Optical coherence tomography for ocular surface and corneal diseases: a review. *Eye and Vision*, 5(1):13.
- [167] Vesaluoma, M., Perez, J., Petroll, W. M., Linna, T., Alio, J., and Tervo, T. (2000). Corneal Stromal Changes Induced by Myopic LASIK. 41(2):8.
- [168] Vrana, N. E., Lavalle, P., Dokmeci, M. R., Dehghani, F., Ghaemmaghami, A. M., and Khademhosseini, A. (2013). Engineering Functional Epithelium for Regenerative Medicine and In Vitro Organ Models: A Review. *Tissue Engineering Part B: Reviews*, 19(6):529–543.
- [169] Väänänen, S. P., Amin Yavari, S., Weinans, H., Zadpoor, A. A., Jurvelin, J. S., and Isaksson, H. (2013). Repeatability of digital image correlation for measurement of surface strains in composite long bones. *Journal of Biomechanics*, 46(11):1928–1932.
- [170] Wang, S. and Hatami-Marbini, H. (2021). Constitutive Modeling of Corneal Tissue: Influence of Three-Dimensional Collagen Fiber Microstructure. *Journal of Biomechanical Engineering*, 143(3):031002.
- [171] Wang, S. and Larin, K. V. (2014). Noncontact depth-resolved micro-scale optical coherence elastography of the cornea. *Biomedical Optics Express*, 5(11):3807.
- [172] Wang, S. and Larin, K. V. (2015). Optical coherence elastography for tissue characterization: a review. *Journal of Biophotonics*, 8(4):279–302.
- [173] Whitford, C., Movchan, N. V., Studer, H., and Elsheikh, A. (2018). A viscoelastic anisotropic hyperelastic constitutive model of the human cornea. *Biomechanics and Modeling in Mechanobiology*, 17(1):19–29.
- [174] Whitford, C., Studer, H., Boote, C., Meek, K. M., and Elsheikh, A. (2015). Biomechanical model of the human cornea: Considering shear stiffness and regional variation of collagen anisotropy and density. *Journal of the Mechanical Behavior of Biomedical Materials*, 42:76–87.
- [175] Winkler, M., Chai, D., Kriling, S., Nien, C. J., Brown, D. J., Jester, B., Juhasz, T., and Jester, J. V. (2011). Nonlinear Optical Macroscopic Assessment of 3-D Corneal Collagen Organization and Axial Biomechanics. *Investigative Ophthalmology & Visual Science*, 52(12):8818.

BIBLIOGRAPHY

- [176] Winkler, M., Shoa, G., Xie, Y., Petsche, S. J., Pinsky, P. M., Juhasz, T., Brown, D. J., and Jester, J. V. (2013). Three-Dimensional Distribution of Transverse Collagen Fibers in the Anterior Human Corneal Stroma. *Investigative Ophthalmology & Visual Science*, 54(12):7293.
- [177] Wollensak, G., Spoerl, E., and Seiler, T. (2003). Stress-strain measurements of human and porcine corneas after riboflavin–ultraviolet-A-induced cross-linking. *Journal of Cataract and Refractive Surgery*, 29(9):1780–1785.
- [178] Yun, S. H. and Chernyak, D. (2018). Brillouin microscopy: assessing ocular tissue biomechanics. *Current Opinion in Ophthalmology*, 29(4):299–305.
- [179] Zeng, Y., Yang, J., Huang, K., Lee, Z., and Lee, X. (2001). A comparison of biomechanical properties between human and porcine cornea. *Journal of Biomechanics*, 34(4):533–537.
- [180] Zhang, D., Eggleton, C. D., and Arola, D. D. (2002). Evaluating the mechanical behavior of arterial tissue using digital image correlation. *Experimental Mechanics*, 42(4):409–416.
- [181] Zhou, D., Eliasy, A., Abass, A., Markov, P., Whitford, C., Boote, C., Movchan, A., Movchan, N., and Elsheikh, A. (2019). Analysis of X-ray scattering microstructure data for implementation in numerical simulations of ocular biomechanical behaviour. *PLOS ONE*, 14(4):e0214770.
- [182] Ávila, F. J., Artal, P., and Bueno, J. M. (2019). Quantitative Discrimination of Healthy and Diseased Corneas With Second Harmonic Generation Microscopy. *Translational Vision Science & Technology*, 8(3):51.

Appendix A

General framework of the multiscale modeling of the cornea

A.1 Continuum mechanics framework

A.1.1 Classical kinematics

The notations are inspired from [150]. The quantities related to the reference configuration are denoted with the subscript 0, whereas the quantities related to the deformed configuration are denoted with the subscript t . A Lagrangian description of the system is used: if O is the origin of the Cartesian coordinate system, for any material point: $\underline{OM}_0 := \underline{\xi}$ denotes its position in the reference configuration and $\underline{OM}_t := \underline{x}$ its position in the deformed configuration (see figure A.1).

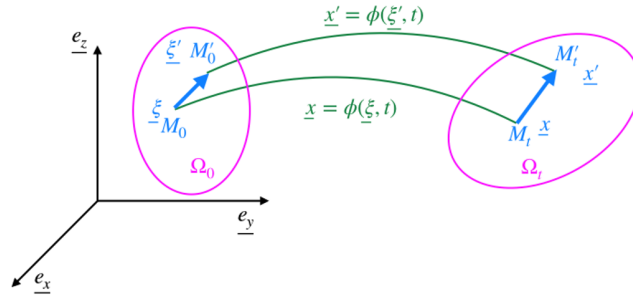


Figure A.1: Schematic view of the classical potato in the reference and deformed configurations. $\underline{OM}_0 := \underline{\xi}$ for the reference configuration Ω_0 and $\underline{OM}_t := \underline{x}$ for the deformed configuration Ω_t , $\underline{x} = \phi(\underline{\xi}, t)$ where ϕ is the mapping from the reference Ω_0 to the deformed Ω_t configurations.

Introducing the mapping ϕ sending the reference configuration into the deformed one:

$$\phi := \begin{cases} \Omega_0 \rightarrow \Omega_t, \\ \underline{\xi} \mapsto \underline{x} = \phi(\underline{\xi}, t), \end{cases} \quad (\text{A.1})$$

the displacement is defined as:

$$\underline{u} := \underline{x} - \underline{\xi} = \phi(\underline{\xi}, t) - \underline{\xi}. \quad (\text{A.2})$$

Then the deformation gradient tensor $\underline{\underline{F}}$ which transports material vectors is defined as:

$$\underline{\underline{F}}(\underline{\xi}, t) := \underline{\underline{\nabla}}_{\underline{\xi}} \phi = \underline{\underline{1}} + \underline{\underline{\nabla}}_{\underline{\xi}} \underline{u}. \quad (\text{A.3})$$

The volumetric dilatation is characterized by its Jacobian J :

$$J := \det(\underline{\underline{F}}), \quad (\text{A.4})$$

and the scalar product of two vectors after transport is characterized by the Cauchy-Green tensor $\underline{\underline{C}}$:

$$\underline{\underline{C}} := \underline{\underline{F}}^T \cdot \underline{\underline{F}}. \quad (\text{A.5})$$

Then we introduce the Green-Lagrange strain tensor $\underline{\underline{e}}$:

$$\underline{\underline{e}} := \frac{1}{2}(\underline{\underline{C}} - \underline{\underline{1}}), \quad (\text{A.6})$$

which is null for any rigid body motion. The three first invariants and reduced invariants of the Cauchy-Green tensor are defined as follows:

$$\begin{cases} I_1 := \text{tr}(\underline{\underline{C}}), & \bar{I}_1 := I_3^{-1/3} I_1, \\ I_2 := \frac{1}{2}((\text{tr}\underline{\underline{C}})^2 - \text{tr}(\underline{\underline{C}}^2)), & \bar{I}_2 := I_3^{-2/3} I_2, \\ I_3 := \det(\underline{\underline{C}}) = J^2. \end{cases} \quad (\text{A.7})$$

A.1.2 Weak formulation

The equilibrium written in a strong form write classically:

$$\begin{cases} \underline{\underline{div}}(\underline{\underline{\sigma}}) + \underline{\underline{f}} = \underline{\underline{0}}, & \text{in } \Omega_t, \\ \underline{\underline{\sigma}} \cdot \underline{\underline{n}} = \underline{\underline{g}}(\underline{\underline{x}}), & \text{on } \Gamma^N, \\ \underline{\underline{u}}(\underline{\underline{x}}) = \underline{\underline{0}}, & \text{on } \Gamma^D. \end{cases} \quad (\text{A.8})$$

with $\underline{\underline{\sigma}}$ the Cauchy-stress tensor, $\underline{\underline{f}}$ the volumetric forces and $\underline{\underline{g}}$ the surfacic forces on the boundary. Introducing a test field $\underline{\underline{w}} \in \mathcal{V}(\Omega_t)$ in the space $\mathcal{V}(\Omega_t)$ of kinematically admissible displacements with zero trace on Γ^D , the weak formulation is obtained integrating the strong form over the domain Ω_t :

$$\forall \underline{\underline{w}} \in \mathcal{V}(\Omega_t), \quad \int_{\Omega_t} \underline{\underline{div}}(\underline{\underline{\sigma}}) \cdot \underline{\underline{w}} d\Omega = - \int_{\Omega_t} \underline{\underline{f}} \cdot \underline{\underline{w}} d\Omega. \quad (\text{A.9})$$

Integrating by parts the first term of equation (A.9):

$$\forall \underline{\underline{w}} \in \mathcal{V}(\Omega_t), \quad \int_{\Omega_t} \underline{\underline{div}}(\underline{\underline{\sigma}}) \cdot \underline{\underline{w}} d\Omega = - \int_{\Omega_t} \underline{\underline{\sigma}} : \underline{\underline{\nabla}}_{\underline{\underline{x}}} \underline{\underline{w}} d\Omega + \int_{\Gamma^N} (\underline{\underline{\sigma}} \cdot \underline{\underline{n}}) \cdot \underline{\underline{w}} d\Gamma, \quad (\text{A.10})$$

the weak form, integrated over the deformed configuration becomes:

$$\forall \underline{\underline{w}} \in \mathcal{V}(\Omega_t), \quad \int_{\Omega_t} \underline{\underline{\sigma}} : \underline{\underline{\nabla}}_{\underline{\underline{x}}} \underline{\underline{w}} d\Omega = \int_{\Omega_t} \underline{\underline{f}} \cdot \underline{\underline{w}} d\Omega + \int_{\Gamma^N} \underline{\underline{g}} \cdot \underline{\underline{w}} d\Gamma. \quad (\text{A.11})$$

The computations are usually performed in the reference configuration, so the weak formulation has to be transported in a Lagrangian formulation, using the change of variable $\underline{x} \rightarrow \underline{\xi}$. Rewriting all derivatives in the reference configuration and introducing the second Piola-Kirchhoff tensor $\underline{\underline{\Sigma}}$, and the corresponding density of applied forces per unit measure of the reference configuration

$$\begin{cases} \underline{\underline{\nabla}}_{\underline{x}} \underline{w} = \underline{\underline{\nabla}}_{\underline{\xi}} \underline{w} \cdot \underline{F}^{-1}, \\ \underline{\underline{\Sigma}} = J \underline{F}^{-1} \cdot \underline{\underline{\sigma}} \cdot \underline{F}^{-T}, \\ \underline{f} = J \underline{f}_0, \quad \underline{g} = J \underline{F}^{-T} \cdot \underline{g}_0. \end{cases} \quad (\text{A.12})$$

yield the weak formulation on the reference configuration

$$\forall \underline{w} \in \mathcal{V}(\Omega_0), \quad \int_{\Omega_0} \underline{\underline{\Sigma}} : (\underline{F}^T \cdot \underline{\underline{\nabla}}_{\underline{\xi}} \underline{w}) d\Omega = \int_{\Omega_0} \underline{f}_0 \cdot \underline{w} d\Omega + \int_{\Gamma_0^N} \underline{g}_0 \cdot \underline{w} d\Gamma. \quad (\text{A.13})$$

Its compact form introduces the symmetric part of the gradient tensor of the test field in the current configuration brought back in the reference configuration

$$d_{\underline{u}} \underline{e} \cdot \underline{w} = \frac{1}{2} ((\underline{\underline{\nabla}}_{\underline{\xi}} \underline{w})^T \cdot \underline{F} + \underline{F}^T \cdot \underline{\underline{\nabla}}_{\underline{\xi}} \underline{w}), \quad (\text{A.14})$$

which finally yields:

$$\forall \underline{w} \in \mathcal{V}(\Omega_0), \quad \int_{\Omega_0} \underline{\underline{\Sigma}} : d_{\underline{u}} \underline{e} \cdot \underline{w} d\Omega = \int_{\Omega_0} \underline{f}_0 \cdot \underline{w} d\Omega + \int_{\Gamma_0^N} \underline{g}_0 \cdot \underline{w} d\Gamma. \quad (\text{A.15})$$

Defining the different virtual powers as:

$$\forall \underline{w} \in \mathcal{V}(\Omega_0), \quad \begin{cases} \mathcal{P}_i = \int_{\Omega_0} \underline{\underline{\Sigma}} : d_{\underline{u}} \underline{e} \cdot \underline{w} d\Omega, & \text{the internal power,} \\ \mathcal{P}_e = \int_{\Omega_0} \underline{f}_0 \cdot \underline{w} d\Omega, & \text{the power of bulk forces,} \\ \mathcal{P}_{BC} = \int_{\Gamma_0^N} \underline{g}_0 \cdot \underline{w} d\Gamma, & \text{the power induced by the boundary conditions,} \end{cases} \quad (\text{A.16})$$

it leads to the following energetic equilibrium

$$\mathcal{P}_i = \mathcal{P}_e + \mathcal{P}_{BC}. \quad (\text{A.17})$$

Internal power and 2nd Piola-Kirchhoff tensor are related to the energy potential ψ through its derivative with respect to the Green-Lagrange tensor

$$\underline{\underline{\Sigma}} := \frac{d\psi}{d\underline{e}}. \quad (\text{A.18})$$

A.2 Parametrization with B-splines

This part is largely based on the internship report of Giulia Merlini [108], who was in the M3DISIM team for nine months, under the supervision of Patrick Le Tallec and me on the topic: "Patient specific models with incomplete and mixed data: the example of the human cornea" and on the NURBS book [135].

Although some methods allow working with a large number of parameters (CMA-ES), the identification process should involve as few parameters as possible. Thus, in the case of highly heterogeneous materials for example, a global approximation approach may be necessary in order to reduce the number of independent parameters of a model, in particular when parameterizing experimental or local data. B-splines are a set of basic functions that allow for a global approach to parametrization. They are characterized by their smoothness (e.g., by filtering noise), flexibility (in terms of "settings") and control points for parametrization. Thus, they appear as a powerful tool that can be used to parameterize experimental data or local parameters.

A.2.1 Knot vector

B-splines are piecewise polynomial functions that form a basis for the vector space of all piecewise polynomial functions of the desired degree and continuity [135]. B-splines are defined in the parametric space, which is partitioned into knot spans by the knot vector $U = [u_1, \dots, u_r]$. Within the knot vector, we have a sequence of non-decreasing real numbers, the knots u_i , so that $u_i \leq u_{i+1}$, where i is the knot index. The knot spans are then defined as semi-open intervals $[u_i, u_{i+1})$. In the case where knots are repeated, the knot span has zero length and the number of repetitions is the multiplicity $m \geq 1$ of the knot. The B-splines are C^∞ within the knot span, while they are C^{p-m} across the knots, where p is the order of the B-spline. A knot vector is defined as open when the first and the last knots have multiplicity $m = p + 1$. In one dimension, basis functions formed from open knot vectors are interpolating at the ends of the parameter space interval – $[u_1$ and $u_r]$ – but they are not, in general, interpolating at interior knots. This is a distinguishing feature between knots and nodes in finite element analyses [74].

A.2.2 B-splines basis

Once the knot vector $U = [u_1, \dots, u_r]$ is chosen, the i -th p -degree B-spline basis function is computed with the Cox-de Boor formula:

$$N_{i,0}(u) = \begin{cases} 1 & \text{if } u_i \leq u < u_{i+1} \\ 0 & \text{otherwise} \end{cases} \quad (\text{A.19})$$

and

$$N_{i,p}(u) = \frac{u - u_i}{u_{i+p} - u_i} N_{i,p-1}(u) + \frac{u_{i+p+1} - u}{u_{i+p+1} - u_{i+1}} N_{i+1,p-1}(u). \quad (\text{A.20})$$

This recursive formula first builds the 0-degree basis functions, then linearly combines $(p - 1)$ -degree basis functions whose coefficients depend linearly on u in order to build B-splines $N_{i,p}(u)$ with $p > 0$. Figure A.2 presents the first three B-splines of the basis of the 0, 1 and 2 order functions for uniform knot vector $U = [0, 1, 2, 3, 4, 5]$.

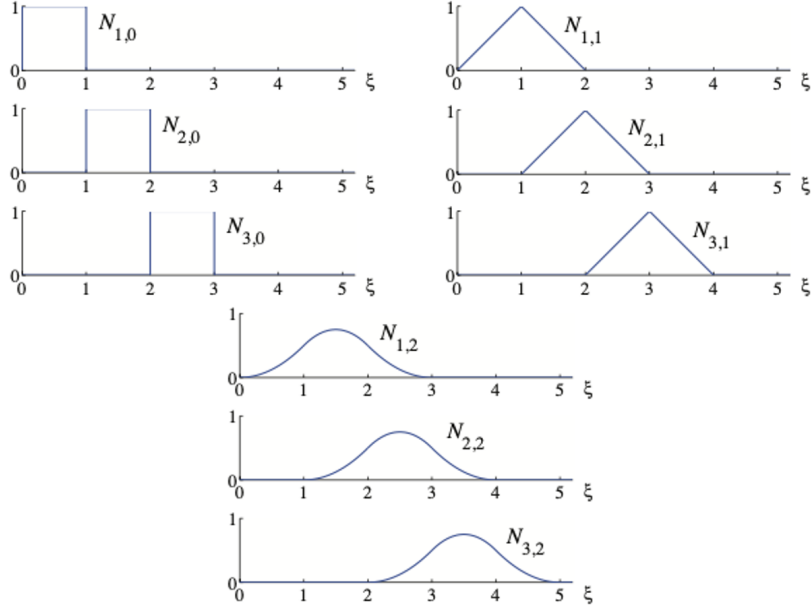


Figure A.2: Basis functions of order 0, 1 and 2 for uniform knot vector $U = [0, 1, 2, 3, 4, 5]$. Extracted from [74].

In the case of cornea, either Cartesian (u, v) or polar (ρ, ϕ) coordinates in the parametric space are used because the experimental data [1] are divided respectively into data at the center (a corneal disk with lamellae oriented along the naso-temporal and superior-inferior directions) and data at the periphery (a corneal annulus with lamellae oriented in the orthoradial direction). Periodic B-splines [75] are used to deal with the ϕ dependence of the data. The uniform knot vector has to be of the following form:

$$V = [v_{-q}, \dots, v_{-1}, v_0, \dots, v_{m-q}, v_{m-q+1}, \dots, v_m] \quad (\text{A.21})$$

with:

$$\begin{cases} v_0 = 0 & \text{and} & v_{m-q} = 1 \\ \forall j \in [1, q], & \begin{cases} v_{-j} = v_{-j+1} - (v_{m-q-j+1} - v_{m-q-j}) \\ v_{m-q+j} = v_{m-q+j-1} + (v_j - v_{j-1}) \end{cases} \end{cases} \quad (\text{A.22})$$

Let us denote $S^q = \text{span}\{N_{j,q} | j = 1, \dots, m\}$ the space spanned by m B-splines of degree q . On a uniform knot vector V , a periodic basis $\{N_{j,q}^{per}\}$ is built using:

$$N_{j,q}^{per} = \begin{cases} N_{j,q} + N_{m-q+j,q} & \forall j \in [1, q] \\ N_{j,q} & \forall j \in]q, m - q[\end{cases} \quad (\text{A.23})$$

The dimension of the periodic basis is $m - q + 1$ and as a consequence we will have $m - q + 1$ control points, because the last q control points correspond to the first q ones.

A.2.3 B-spline surfaces

As we are working with surface data (e.g. experimental data of [1] or local numerical data), B-spline surfaces will be used. Two types of B-splines will be used: Cartesian and periodic B-splines. The

first ones are obtained by taking two open knot vectors U and V , and the products of the univariate B-spline functions $N_{i,p}$ and $N_{j,q}$

$$Q(u, v) = \sum_{i=1}^m \sum_{j=1}^n N_{i,p}(u) N_{j,q}(v) P_{ij} \quad (\text{A.24})$$

with

$$\begin{cases} U = [0, \dots, 0, u_{p+1}, \dots, u_n, 1, \dots, 1] \\ V = [0, \dots, 0, v_{q+1}, \dots, v_n, 1, \dots, 1] \end{cases} \quad (\text{A.25})$$

with the knots 0 and 1 of multiplicity $p + 1$ for U and $q + 1$ for V and a vector P_{ij} that stores $(n \times m)$ control points. From now on, knot vectors within $[0, 1]$ will only be considered.

A periodic B-spline surface is built as:

$$Q(\rho, \phi) = \sum_{i=1}^n \sum_{j=1}^{m-q} N_{i,p}(\rho) N_{j,q}^{per}(\phi) P_{ij} \quad (\text{A.26})$$

with

$$\begin{cases} U = [0, \dots, 0, u_{p+1}, \dots, u_n, 1, \dots, 1] \\ V = [v_{-q}, \dots, v_{-1}, v_0, \dots, v_{m-q}, v_{m-q+1}, \dots, v_m] \end{cases} \quad \text{defined as in (A.22)}. \quad (\text{A.27})$$

Note that Q has no parametric form, it is just the value of the parameter at a given coordinate. The control points here are the set of coefficients P_{ij} (e.g., stiffness values if Q is a stiffness field) and are not associated with a notion of geometric points. Yet, once the control points P_{ij} are defined, Q can be computed at any point of coordinate (X_0, Y_0) or (R_0, Φ_0) in the reference space $((u_0, v_0)$ or (ρ_0, Φ_0) in the parametric space respectively). In this work the B-spline surfaces have been used to parameterize the anterior and posterior surfaces of the patient-specific geometry (Chap. 2).

A.3 Minimization of cost function: choice of the new set of parameters

A.3.1 Gradient-descent algorithm

The methods with gradient descent (Gauss-Newton, Levenberg-Marquardt...) are all based on the same principle: the choice of the set of parameters at iteration $k + 1$ depends on the set of parameters of iteration k and the Jacobian \underline{J} associated to the problem. Gauss-Newton algorithm is a generalized version of the 1D Newton's method, with a direct computation of the parameters at iteration $k + 1$ directly depending on the Jacobian and the residual (which gives the distance between the computed solution at iteration k and the data). Levenberg-Marquardt is an extension of the Gauss-Newton method with the adding of a damping parameter that accelerates convergence.

Here is a basic example of this two methods which are often used in the Finite Element Model Updating methods [9].

Let us assume:

$$J_{\underline{u}}(\tilde{\gamma}) = \sum_{i=1}^m [u_i^{exp} - f_i(u_i^{num}, \tilde{\gamma})]^2 \quad (\text{A.28})$$

be the form of the functional to be minimized. Let us define the residual vector \underline{r} such that:

$$\forall i \in [1, m], r_i(\underline{\tilde{\gamma}}) = u_i^{exp} - f_i(u_i^{num}, \underline{\tilde{\gamma}}). \quad (\text{A.29})$$

$J_{\underline{u}}(\underline{\tilde{\gamma}})$ rewrites $J_{\underline{u}}(\underline{\tilde{\gamma}}) = \underline{r}^T(\underline{\tilde{\gamma}}) \cdot \underline{r}(\underline{\tilde{\gamma}})$. Introducing

$$\underline{J}_f = \frac{\partial f}{\partial \underline{\tilde{\gamma}}}, \quad (\text{A.30})$$

the iterative $\underline{\tilde{\gamma}}^{k+1}$ with respect to iterative $\underline{\tilde{\gamma}}^k$ is given by the well-known definition of the new set of parameters for Gauss-Newton algorithm:

$$\underline{\tilde{\gamma}}^{k+1} = \underline{\tilde{\gamma}}^k + (\underline{J}_f^T \cdot \underline{J}_f)^{-1} \cdot \underline{J}_f^T \cdot \underline{r}(\underline{\tilde{\gamma}}^k) \quad (\text{A.31})$$

In the Levenberg-Marquardt algorithm, a changing damping factor λ^k that helps to accelerate convergence is added, giving the following form for $\underline{\tilde{\gamma}}^{k+1}$:

$$\underline{\tilde{\gamma}}^{k+1} = \underline{\tilde{\gamma}}^k + (\underline{J}_f^T \cdot \underline{J}_f + \lambda^k \text{diag}(\underline{J}_f^T \cdot \underline{J}_f))^{-1} \underline{J}_f^T \underline{r}(\underline{\tilde{\gamma}}). \quad (\text{A.32})$$

Gradient descent algorithms do not allow a large field of possibilities for the parameter sets to be explored and local optima to be found easily. The covariance matrix evolution strategy is one of the methods that makes it possible to overcome these weaknesses.

A.3.2 Covariance Matrix Evolution Strategy (CMA-ES)

This paragraph will present briefly the covariance matrix evolution strategy. Interested readers can refer to [65], this part is largely based on.

The Covariance Matrix Evolution Strategy (CMA-ES) is a stochastic method for real-parameter optimization of non-linear, non-convex functions. It computes the new parameter set $\underline{\tilde{\gamma}}^{k+1}$ from the old parameter set $\underline{\tilde{\gamma}}^k$ using a multivariate normal distribution $\mathcal{N}(\underline{m}, \underline{Covar})$ where \underline{Covar} is a positive definite matrix of covariances.

The principle is as follows: at each iteration of the identification loop, a number $\lambda > 1$ of parameter sets $[\underline{\tilde{\gamma}}_1^k, \dots, \underline{\tilde{\gamma}}_\lambda^k]$ will be tested, i.e. the cost function will be evaluated at these parameter sets. These are called the search points.

The l -th search point of the $k+1$ generation is chosen to follow the multivariate distribution of the k generation:

$$\underline{\tilde{\gamma}}_l^{k+1} \in \mathcal{R}^n \sim \underline{m}^k + \sigma^k \mathcal{N}(\underline{0}, \underline{Covar}^k) \quad (\text{A.33})$$

with \underline{m}^k the mean vector, \underline{Covar}^k the covariance matrix and σ^k the overall standard deviation at generation k . The challenge is to define the relationships between generations k and $k+1$ for the mean vector, the covariance matrix and the overall standard deviation. The mean \underline{m}^k is a weighted average of $\mu \leq \lambda$ selected points from the sample $[\underline{\tilde{\gamma}}_1^k, \dots, \underline{\tilde{\gamma}}_\lambda^k]$, for which the cost function estimate is the lowest. A typical value for μ is $\lambda/2$. \underline{m}^k also depends on the mean at the previous generation \underline{m}^{k-1} . Covariance matrices and overall standard deviations are less directly computed. Covariances matrix

at generation k is a combination the weighted covariances matrix at generation $k - 1$ and a update of this matrix using well chosen evolution paths, while overall standard deviation at generation k is computed using evolution paths.

This method presents several advantages, the main one being the ability to avoid premature convergence. Even if it does not guarantee to find the global optimum of the function, the stochastic process allows search points outside the classical range of the gradient method to be tested for example. Moreover, the size of the population (number of experimental points) can be chosen freely. A small population size allows for a fast computation, while a large population size helps to find the global optimum, or at least not to stop the convergence process too quickly at local optima.

Appendix B

Mesh Calculation

Considering the apex of the cornea at the center of a coordinates systems so the z -axis is oriented vertically and downwards (Fig. B.1), the anterior surface of the cornea is described by the **biconic function**:

$$z = \frac{\frac{x^2}{R_x} + \frac{y^2}{R_y}}{1 + \sqrt{1 - (1 + Q_x)\frac{x^2}{R_x^2} - (1 + Q_y)\frac{y^2}{R_y^2}}}, \quad (\text{B.1})$$

where R_x and R_y are the curvature radii of the flattest and the steepest meridian of the cornea and Q_x and Q_y are the the asphericities in the x and y directions.

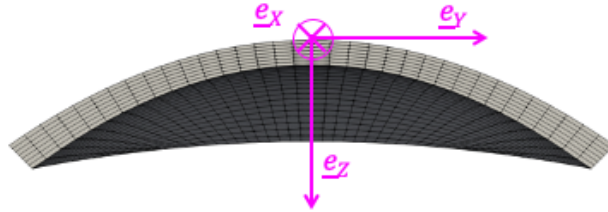


Figure B.1: Coordinate system associated with the creation of the mesh of the cornea where the anterior and posterior surfaces are defined by the biconic function (B.1). The center of the coordinate system is the apex of the cornea and the z axis is vertical and pointing downwards.

The following section will describe how the mesh is generated and relies on a Matlab code adapted from the C code kindly provided by A. Pandolfi [129].

B.1 Data used for the mesh creation

First, the number of nodes of the mesh in the three directions of space are defined. Table B.1 summarizes the different numbers used in the mesh: m_points and n_points correspond to the in-plane numbers of points and l_layers correspond to the number of layers of elements put in the thickness of the cornea (Fig. B.2).

m_points	Number of points in the horizontal (x) direction
n_points	Number of points in the vertical (y) direction
l_layers	Number of layers of elements (z direction)

Table B.1: Definition of the mesh geometry parameters.

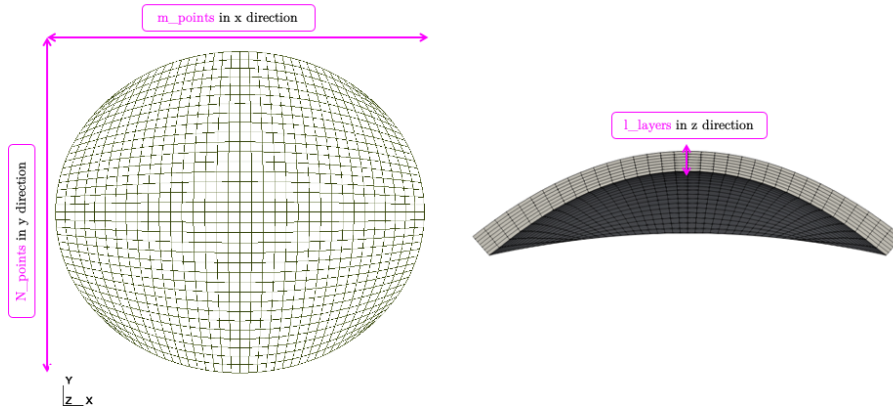


Figure B.2: Scheme of mesh parameters: m_points and n_points correspond to the in-plane numbers of points and l_layers corresponds to the number of layers of elements put in the thickness of the cornea

In the cornea, the meridians are defined as in the earth, i.e. "vertical virtual lines" (in the Inferior-Superior direction of the cornea). The flattest meridian is near the limbus (peripheral part of the cornea), whereas the steepest meridian is the one that pass by the apex of the cornea (Fig. B.3). The different meridians of the cornea have different curvatures, as the cornea can be slightly asymmetric. The external (corresponding to the external surface of the cornea) and the internal (corresponding to the internal surface of the cornea) curvatures of the steepest and the flattest meridians are defined in the code (Fig. B.3 and Table B.2).

curv_ext_min	External curvature along the flattest meridian
curv_ext_max	External curvature along the steepest meridian
curv_int_min	Internal curvature along the flattest meridian
curv_int_max	Internal curvature along the steepest meridian

Table B.2: Defintion of the different curvatures used to create the mesh

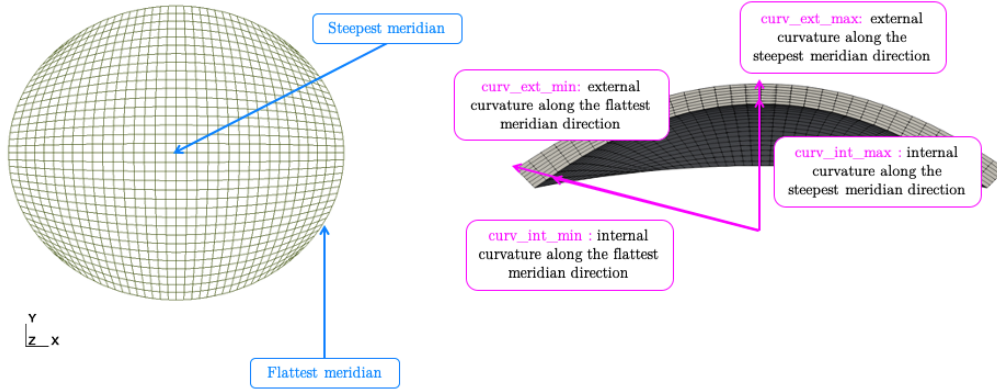


Figure B.3: Scheme of the different curvatures used to create the mesh. Two curvatures are taken into account for the flattest and the steepest meridian, which correspond to the curvature of the anterior and the posterior surfaces of the cornea.

Then the shape factor is a measure of corneal asphericity and a derivative of eccentricity. As for the meridian curvatures, the shape factors can be different for the flattest and steepest meridians (Table B.3 presents the convention used to name the different shape factors).

q_ext_min	Q factor external curvature along the flattest meridian
q_ext_max	Q factor external curvature along the steepest meridian
q_int_min	Q factor internal curvature along the flattest meridian
q_int_max	Q factor internal curvature along the steepest meridian

Table B.3: Shape factors of the different curvatures used to create the mesh.

Moreover, some physiological parameters are needed to be as close as possible to the real geometry of the patient cornea. Table B.4 and Fig. B.4 present the different physiological parameters used in the code to create the mesh.

Matlab denomination	Description
thickness	central thickness of the cornea - at the apex
limbus_thick	limbus thickness
hor_radius	external horizontal in plane radius
vert_radius	external vertical in plane radius

Table B.4: Table of the physical parameters used in the mesh (see figure B.4).

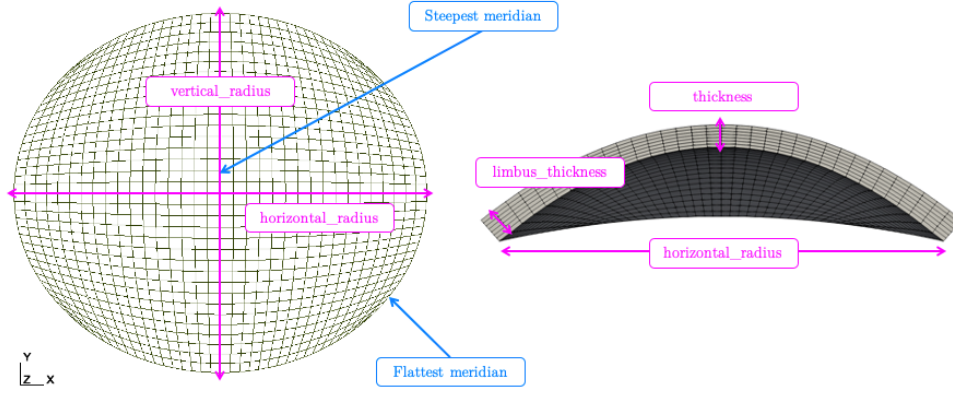


Figure B.4: View of a simplified mesh with the relevant parameters for its generation.

Once all the parameters are defined, the volumetric mesh of the cornea is created from a surface mesh based on the in-plane coordinates described in the following section (App. B.2).

B.2 Creation of the in-plane coordinates of the mesh

To create the in-plane coordinates (x, y) of the nodes of the surface, we create a quadrilateral mesh in a circle with 4 flat quadrilaterals at the 4 corners of the mesh.

B.2.1 Contour of the real space D

First the contour of the surface mesh has to be defined using only one radius and the number of in-plane points. This function discretizes the circle of center 0 and radius r with two quarters divided by n points and 2 quarters divided by m points.

A collections of angles t_1 , t_2 , t_3 and t_4 associated to the number of points in each direction is defined:

$$\begin{cases} t_1 = [\frac{3\pi}{2} : -\Delta\theta_n : \frac{3\pi}{2} - n\Delta\theta_n] \\ t_2 = [0 : \Delta\theta_n : n\Delta\theta_n] \end{cases} \quad \text{with} \quad \Delta\theta_n = \frac{\pi}{2(n-1)} \quad (\text{B.2})$$

$$\begin{cases} t_3 = [\frac{3\pi}{2} : \Delta\theta_m : \frac{3\pi}{2} + m\Delta\theta_m] \\ t_4 = [\pi : -\Delta\theta_m : \pi - m\Delta\theta_m] \end{cases} \quad \text{with} \quad \Delta\theta_m = \frac{\pi}{2(m-1)} \quad (\text{B.3})$$

Finally, the coordinates of the nodes (the cosine and sine of the value of t_1 , t_2 , t_3 and t_4) of the contour are stored in two vectors: \underline{Enxy} and \underline{Emxy} .

$$\underline{Enxy} = \begin{pmatrix} r \cos(t_1) \\ r \sin(t_1) \\ r \cos(t_2) \\ r \sin(t_2) \end{pmatrix}, \quad \underline{Emxy} = \begin{pmatrix} r \cos(t_3) \\ r \sin(t_3) \\ r \cos(t_4) \\ r \sin(t_4) \end{pmatrix} \quad (\text{B.4})$$

Figure B.5 shows the discretization of the circle. It gives a collection of points around the circle of radius r defined using their polar coordinates (here, $r = 1$ is used as the dilation in horizontal and vertical directions is done after to have the real dimension of the middle meridian and parallel).

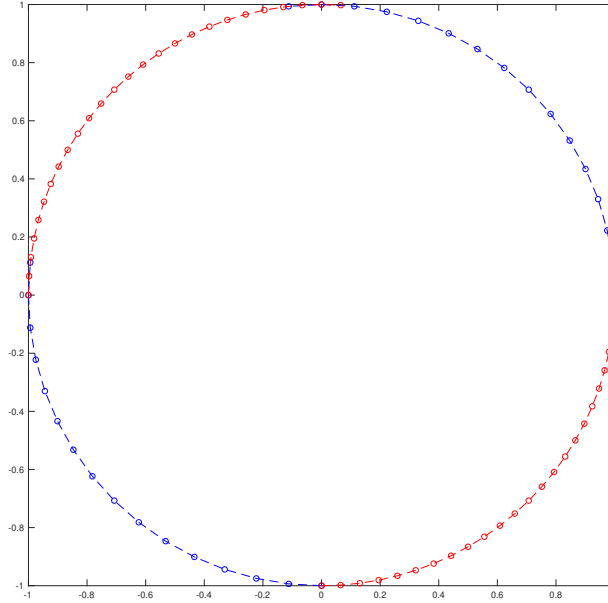


Figure B.5: Discretization of the circle of radius r . Plot of the different points stored in \underline{Enxy} and \underline{Emxy} : blue curve = $[r \cos(t_1), r \sin(t_1)]$ and $[r \cos(t_2), r \sin(t_2)]$ and red curve = $[r \cos(t_3), r \sin(t_3)]$ and $[r \cos(t_4), r \sin(t_4)]$.

B.2.2 Point in computational space

The points in the computational space are defined as follows:

$$\begin{cases} \xi = [0 : \delta\theta_m : (m-1)\delta\theta_m] \\ \eta = [0 : \delta\theta_n : (n-1)\delta\theta_n] \end{cases} \quad \text{with} \quad \delta\theta_m = \frac{1}{m-1} \quad \text{and} \quad \delta\theta_n = \frac{1}{n-1}. \quad (\text{B.5})$$

The points ξ and η created here are a discretization of the segment $[0 : 1]$ thanks to the number of points in horizontal and vertical directions.

B.2.3 Transfinite generation

The transfinite generation allows the circle to be transformed into a real geometry for the cornea. The transfinite interpolation method (Eq. (B.6)) is used to obtain $[x, y]$ started from the discretization of the circle shown in Sec. B.2.1 and the discretization of the horizontal and vertical unit-length segments in Sec. B.2.2. Figure B.6 shows the results of the discretized in-plane nodes used to create the quadrilateral in-plane mesh for the cornea.

$$\forall i \in [1 : m], \forall j \in [1 : n] \left\{ \begin{array}{l} x(i, j) = (1 - \xi(i))Enxy(1, j) + \xi(i)Enxy(3, j) + (1 - \eta(j))Emxy(1, i) + \\ \eta(j)Emxy(3, i) - (1 - \xi(i))(1 - \eta(j))Enxy(1, 1) - \xi(i)(1 - \eta(j))Enxy(3, 1) - \\ (1 - \xi(i))\eta(j)Emxy(3, 1) - \xi(i)\eta(j)Emxy(3, m) \\ y(i, j) = (1 - \xi(i))Enxy(2, j) + \xi(i)Enxy(4, j) + (1 - \eta(j))Emxy(2, i) + \\ \eta(j)Emxy(4, i) - (1 - \xi(i))(1 - \eta(j))Enxy(2, 1) - \\ \xi(i)(1 - \eta(j))Enxy(4, 1) - (1 - \xi(i))\eta(j)Emxy(4, 1) - \xi(i)\eta(j)Emxy(4, m). \end{array} \right. \quad (\text{B.6})$$

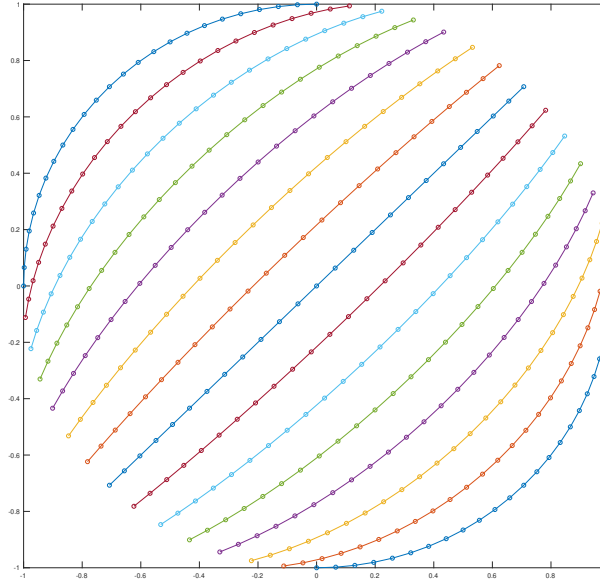


Figure B.6: Points $[x, y]$ created by the transfinite generation function.

B.3 Creation of the 3D mesh

From the in-plane nodes created by the transfinite generation and the parameters of the cornea, the volumetric mesh is then created. First, the in-plane coordinates (x, y) created in Sec. B.2 are rotated by an angle of 45° to have "vertical meridians" and "horizontal parallels" and not lines inclined at

45° from horizontal and vertical directions. Then, a loop over the layers is performed to redefine all physical parameters (Table B.5) at each layer using the ratio $= \frac{l-1}{l_layers}$, where l is the current layer and l_layers is the total number of layers.

Matlab denomination	formula	Description
ApexHigh	$ratio * thickness$	height of the Apex for the layer l
limbHigh	$ratio * vertical_limb_thick$	height of the limb for the layer l
h_radius	$horizontal_radius - ratio * inplane_limb_thick$	external horizontal in plane radius for the layer l
v_radius	$vertical_radius - ratio * inplane_limb_thick$	external vertical in plane radius for the layer l
q_f	$q_ext_f + ratio * (q_int_f - q_ext_f)$	asphericity factor for the layer l
q_s	$q_ext_s + ratio * (q_int_s - q_ext_s)$	asphericity factor for the layer l
curv_f	$curv_ext_f + ratio * (curv_int_f - curv_ext_f)$	external curvature of the flattest meridian for the layer l
curv_s	$curv_ext_s + ratio * (curv_int_s - curv_ext_s)$	external curvature of the steepest meridian for the layer l

Table B.5: Table of the physical parameters used in the mesh for each layer l

Then, the horizontal coordinates are multiplied by the h_radius and the vertical coordinate by the v_radius to have the real in-plane coordinates (and not only a circle of radius 1). And finally, the third coordinate (z) is computed for each node, using the biconic function defined in Eq. (B.1).

As the thicknesses of the limb and of apex areas are not the same, the thickness has to be interpolated between the apex and the limb. In our case, the interpolation is bi-linear. It gave the following thickness as a function of the in-plane points:

$$\forall i \in [1, m], \forall j \in [1, n], \quad thickness(i, j) = \frac{L - A}{2} (f_m(i) + f_n(j)) + L \quad \text{with:} \quad (\text{B.7})$$

$$\begin{cases} A = \text{height of the Apex at layer considered} \\ L = \text{height of the limb at layer considered} \\ f_m(i) = K_m(i^2 - (m-1) * i + m) \\ f_n(j) = K_n(j^2 - (n-1) * j + n) \\ K_m = \frac{1}{(\frac{m-1}{2})^2} \quad \text{and} \quad K_n = \frac{1}{(\frac{n-1}{2})^2} \end{cases}$$

Quadrilateral and hexahedral elements of the mesh, and the labels for each nodes/elements are defined. Finally, the mesh of figure B.7 is obtained.

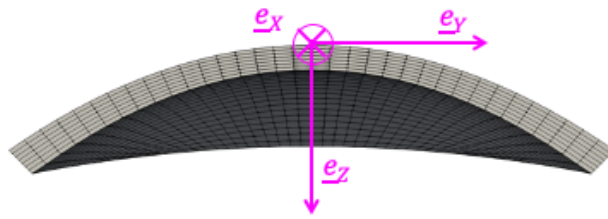


Figure B.7: Generic hexahedric corneal mesh obtained using a Matlab code adapted from the C-code kindly provided by A. Pandolfi

Appendix C

Technical developments related to the multiscale modeling of the cornea

C.1 Computation of the anisotropic 2nd Piola-Kirchhoff tensor

The material is considered hyperelastic, so the 2nd Piola Kirchhoff tensor $\underline{\underline{\Sigma}}$ is computed as:

$\underline{\underline{\Sigma}} = \frac{\partial \psi}{\partial \underline{\underline{e}}} = 2 \frac{\partial \psi}{\partial \underline{\underline{C}}}$ with $\psi = \psi^{iso} + \psi^{vol} + \psi^{lam}$. For the anisotropic part, this translates into:

$\underline{\underline{\Sigma}}_{aniso} = 2 \frac{\partial \psi^{lam}}{\partial \underline{\underline{C}}} = 2 \frac{\partial \psi^{lam}}{\partial \lambda} \frac{\partial \lambda}{\partial \lambda^2} \frac{\partial \lambda^2}{\partial \underline{\underline{C}}}$, with the state potential defined in Eq. (2.11):

$$\psi^{lam} = \int_{\theta=0}^{\pi} \int_{\phi=0}^{2\pi} (\rho_1(\theta, \phi) \delta \psi_1^{lam}(\theta, \phi) + \rho_2(\theta, \phi) \delta \psi_2^{lam}(\theta, \phi)) \sin \theta d\theta d\phi.$$

The only components that depend on $\underline{\underline{C}}$ and therefore on λ in Eq. (2.11) are $\delta \psi_1^{lam}$ and $\delta \psi_2^{lam}$, and they are the only which have to be differentiated with respect to λ . Furthermore, terms for fiber one and fiber two are independent so can be treated independently. The local contributions $\delta \underline{\underline{\Sigma}}_{aniso,1}$ and $\delta \underline{\underline{\Sigma}}_{aniso,2}$ are defined as:

$$\begin{cases} \delta \underline{\underline{\Sigma}}_{aniso,1} = 2 * \frac{\partial \delta \psi_1^{lam}}{\partial \lambda} \frac{\partial \lambda}{\partial \lambda^2} \frac{\partial \lambda^2}{\partial \underline{\underline{C}}}, \\ \delta \underline{\underline{\Sigma}}_{aniso,2} = 2 * \frac{\partial \delta \psi_2^{lam}}{\partial \lambda} \frac{\partial \lambda}{\partial \lambda^2} \frac{\partial \lambda^2}{\partial \underline{\underline{C}}}. \end{cases} \quad (C.1)$$

Thus $\underline{\underline{\Sigma}}_{aniso}$ can be computed by

$$\underline{\underline{\Sigma}}_{aniso} = \int_{\theta=0}^{\pi} \int_{\phi=0}^{2\pi} (\rho_1(\theta, \phi) \delta \underline{\underline{\Sigma}}_{aniso,1}(\theta, \phi) + \rho_2(\theta, \phi) \delta \underline{\underline{\Sigma}}_{aniso,2}(\theta, \phi)) \sin \theta d\theta d\phi. \quad (C.2)$$

Let us introduce the fiber tractions $t_{0,1}$ and $t_{0,2}$ and elongation given by:

$$\begin{cases} \frac{\partial \delta \psi_1^{lam}}{\partial l} = t_{0,1} = k_1 \left(\frac{\lambda}{\lambda_{u,1}} - 1 \right)_+ + t_{u,1} \\ \frac{\partial \delta \psi_2^{lam}}{\partial l} = t_{0,2} = k_2 \left(\frac{\lambda}{\lambda_{u,2}} - 1 \right)_+ + t_{u,2} \end{cases} \quad \text{with } \lambda(\theta, \phi)^2 = \underline{r_0}(\theta, \phi) \cdot \underline{\underline{C}} \cdot \underline{r_0}(\theta, \phi).$$

The two other useful partial derivatives are given by:

$$\frac{\partial \lambda}{\partial \lambda^2} = \frac{1}{2\lambda} \quad \text{and} \quad \frac{\partial \lambda^2}{\partial \underline{\underline{C}}} = \underline{\underline{r_0}} \otimes \underline{\underline{r_0}}. \quad (\text{C.3})$$

The computation for $\frac{\partial \lambda^2}{\partial \underline{\underline{C}}} = \underline{\underline{r_0}} \otimes \underline{\underline{r_0}}$ in Cartesian coordinates is detailed in Eq. (C.5). First the computation of $\lambda(\theta, \phi)$ in Cartesian coordinates is needed,

$$\lambda(\theta, \phi)^2 = \underline{\underline{r_0}}(\theta, \phi) \cdot \underline{\underline{C}} \cdot \underline{\underline{r_0}}(\theta, \phi) = C_{xx}r_x^2 + C_{yy}r_y^2 + C_{zz}r_z^2 + (C_{xy} + C_{yx})r_xr_y + (C_{yz} + C_{zy})r_yr_z + (C_{xz} + C_{zx})r_xr_z. \quad (\text{C.4})$$

yielding

$$\frac{\partial \lambda^2}{\partial \underline{\underline{C}}} = \begin{pmatrix} \frac{\partial(\lambda^2)}{\partial C_{xx}} & \frac{\partial(\lambda^2)}{\partial C_{xy}} & \frac{\partial(\lambda^2)}{\partial C_{xz}} \\ \frac{\partial(\lambda^2)}{\partial C_{xy}} & \frac{\partial(\lambda^2)}{\partial C_{yy}} & \frac{\partial(\lambda^2)}{\partial C_{yz}} \\ \frac{\partial(\lambda^2)}{\partial C_{xz}} & \frac{\partial(\lambda^2)}{\partial C_{yz}} & \frac{\partial(\lambda^2)}{\partial C_{zz}} \end{pmatrix} = \begin{pmatrix} r_x^2 & r_xr_y & r_xr_z \\ r_xr_y & r_y^2 & r_yr_z \\ r_xr_z & r_yr_z & r_z^2 \end{pmatrix} = \underline{\underline{r_0}} \otimes \underline{\underline{r_0}}. \quad (\text{C.5})$$

Altogether, $\delta \underline{\underline{\Sigma}}_{\text{aniso},1}$ and $\delta \underline{\underline{\Sigma}}_{\text{aniso},2}$ are computed as:

$$\begin{cases} \delta \underline{\underline{\Sigma}}_{\text{aniso},1} = 2 * \frac{\partial \delta \psi_1^{\text{lam}}}{\partial \lambda} \frac{\partial \lambda}{\partial \lambda^2} \frac{\partial \lambda^2}{\partial \underline{\underline{C}}} = 2 * l_{0,1} t_{0,1} \frac{1}{2\lambda} \underline{\underline{r_0}} \otimes \underline{\underline{r_0}} = \frac{l_{0,1}}{\lambda} (k_1 (\frac{\lambda}{\lambda_{u,1}} - 1)_+ + t_{u,1}) \underline{\underline{r_0}} \otimes \underline{\underline{r_0}}, \\ \delta \underline{\underline{\Sigma}}_{\text{aniso},2} = 2 * \frac{\partial \delta \psi_2^{\text{lam}}}{\partial \lambda} \frac{\partial \lambda}{\partial \lambda^2} \frac{\partial \lambda^2}{\partial \underline{\underline{C}}} = 2 * l_{0,2} t_{0,2} \frac{1}{2\lambda} \underline{\underline{r_0}} \otimes \underline{\underline{r_0}} = \frac{l_{0,2}}{\lambda} (k_2 (\frac{\lambda}{\lambda_{u,2}} - 1)_+ + t_{u,2}) \underline{\underline{r_0}} \otimes \underline{\underline{r_0}}. \end{cases} \quad (\text{C.6})$$

with $l_{0,i}$ the length of the fibers in the reference configuration.

C.2 Computation of the quadrature used in the micro-sphere model

C.2.1 Quadrature used in the FEM code to calculate the fiber contribution

At each Gauss point, Eq. (C.7) has to be computed:

$$\underline{\underline{\Sigma}}_{\text{aniso}} = \int_{\theta=0}^{\pi} \int_{\phi=0}^{2\pi} (\rho_1(\theta, \phi) \delta \underline{\underline{\Sigma}}_{\text{aniso},1}(\theta, \phi) + \rho_2(\theta, \phi) \delta \underline{\underline{\Sigma}}_{\text{aniso},2}(\theta, \phi)) \sin \theta d\theta d\phi. \quad (\text{C.7})$$

In classical FE code, the tangent stiffness tensor is also needed. The tangent stiffness tensor is the derivative of the 2nd Piola-Kirchhoff tensor with respect to $\underline{\underline{e}}$, or the 2nd derivative of ψ with respect to $\underline{\underline{e}}$. Using the same arguments as in App. C.1, the tangent stiffness tensor is computed as:

$$\underline{\underline{T}}_{\text{aniso}} = \int_{\theta=0}^{\pi} \int_{\phi=0}^{2\pi} (\rho_1(\theta, \phi) \delta \underline{\underline{T}}_{\text{aniso},1}(\theta, \phi) + \rho_2(\theta, \phi) \delta \underline{\underline{T}}_{\text{aniso},2}(\theta, \phi)) \sin \theta d\theta d\phi, \quad (\text{C.8})$$

where:

$$\left\{ \begin{array}{l} \delta \underline{\underline{T}}_{\equiv aniso,1} = \begin{cases} l_{0,1} \frac{k_1 - t_{u,1}}{\lambda^3} \underline{r_0} \otimes \underline{r_0} \otimes \underline{r_0} \otimes \underline{r_0} & \text{if } \lambda > \lambda_{u,1}, \\ -\frac{l_{0,1} t_{u,1}}{\lambda^3} \underline{r_0} \otimes \underline{r_0} \otimes \underline{r_0} \otimes \underline{r_0} & \text{if not,} \end{cases} \\ \delta \underline{\underline{T}}_{\equiv aniso,2} = \begin{cases} l_{0,2} \frac{k_2 - t_{u,2}}{\lambda^3} \underline{r_0} \otimes \underline{r_0} \otimes \underline{r_0} \otimes \underline{r_0} & \text{if } \lambda > \lambda_{u,2}, \\ -\frac{l_{0,2} t_{u,2}}{\lambda^3} \underline{r_0} \otimes \underline{r_0} \otimes \underline{r_0} \otimes \underline{r_0} & \text{if not.} \end{cases} \end{array} \right. \quad (C.9)$$

First, the above integrals are reduced thanks to the invariance in π of the probability density of the fiber with respect to the angle ϕ . We thus have

$$\underline{\underline{\Sigma}}_{aniso} = \int_{\theta=0}^{\pi} \int_{\phi=0}^{\pi} (\rho_1(\theta, \phi) \delta \underline{\underline{\Sigma}}_{aniso,1}(\theta, \phi) + \rho_2(\theta, \phi) \delta \underline{\underline{\Sigma}}_{aniso,2}(\theta, \phi)) \sin \theta d\theta d\phi,$$

and

$$\underline{\underline{T}}_{aniso} = \int_{\theta=0}^{\pi} \int_{\phi=0}^{\pi} (\rho_1(\theta, \phi) \delta \underline{\underline{T}}_{\equiv aniso,1}(\theta, \phi) + \rho_2(\theta, \phi) \delta \underline{\underline{T}}_{\equiv aniso,2}(\theta, \phi)) \sin \theta d\theta d\phi$$

where we recall hereafter the expression of the probability density functions

$$\left\{ \begin{array}{l} \rho_1(\theta, \phi) = K_1 e^{(\sigma_{p, fib1} \cos(2(\phi - \mu_{fib1})) + \sigma_{t, fib1} \cos(2(\theta - \nu_{fib1})))}, \quad \text{with: } K_1 = \frac{1}{K_{fib1}}, \\ \rho_2(\theta, \phi) = K_2 e^{(\sigma_{p, fib2} \cos(2(\phi - \mu_{fib2})) + \sigma_{t, fib2} \cos(2(\theta - \nu_{fib2})))}, \quad \text{with: } K_2 = \frac{1}{K_{fib2}}. \end{array} \right.$$

We make the following simplifying choices:

- the fiber coordinate system is chosen such that \underline{e}_x^{fib} coincides with the direction of one fiber family. It implies that:

$$\begin{aligned} - \rho_{fib1}(\theta, \phi) &= K_1 e^{\sigma_{p,1} \cos(2\phi) + \sigma_{t,1} \cos(2(\theta - \nu_1))}, \\ - \rho_{fib2}(\theta, \phi) &= K_2 e^{\sigma_{p,2} \cos(2(\phi + \mu_1 - \mu_2)) + \sigma_{t,2} \cos(2(\theta - \nu_2))}. \end{aligned}$$

- The fiber coordinate system is chosen such that the two families of fibers are mainly in the plane $(\underline{e}_x^{lam}, \underline{e}_y^{lam})$. It implies that $\nu_1 = \nu_2 = \pi/2$:

$$\begin{aligned} - \rho_{fib1}(\theta, \phi) &= K_1 e^{\sigma_{p,1} \cos(2\phi) + \sigma_{t,1} \cos(2(\theta - \pi/2))} = K_1 e^{\sigma_{p,1} \cos(2\phi) - \sigma_{t,1} \cos(2\theta)}, \\ - \rho_{fib2}(\theta, \phi) &= K_2 e^{\sigma_{p,2} \cos(2(\phi + \mu_1 - \mu_2)) + \sigma_{t,2} \cos(2(\theta - \pi/2))} = K_2 e^{\sigma_{p,2} \cos(2(\phi + \mu_1 - \mu_2)) - \sigma_{t,2} \cos(2\theta)}. \end{aligned}$$

The integrals that need to be computed reduce to:

$$\underline{\underline{\Sigma}}_{aniso} = \int_{\theta=0}^{\pi} \int_{\phi=0}^{\pi} (K_1 e^{\sigma_{p,1} \cos(2\phi) - \sigma_{t,1} \cos(2\theta)} \delta \underline{\underline{\Sigma}}_{aniso,1} + K_2 e^{\sigma_{p,2} \cos(2(\phi + \mu_1 - \mu_2)) - \sigma_{t,2} \cos(2\theta)} \delta \underline{\underline{\Sigma}}_{aniso,2}) \sin \theta d\theta d\phi,$$

and

$$\underline{\underline{T}}_{aniso} = \int_{\theta=0}^{\pi} \int_{\phi=0}^{\pi} (K_1 e^{\sigma_{p,1} \cos(2\phi) - \sigma_{t,1} \cos(2\theta)} \delta \underline{\underline{T}}_{\equiv aniso,1} + K_2 e^{\sigma_{p,2} \cos(2(\phi + \mu_1 - \mu_2)) - \sigma_{t,2} \cos(2\theta)} \delta \underline{\underline{T}}_{\equiv aniso,2}) \sin \theta d\theta d\phi,$$

which can each be decomposed into two parts, which are treated the same way:

- $\underline{\underline{\Sigma}}_{\text{aniso},1} = \int_{\theta=0}^{\pi} \int_{\phi=0}^{\pi} K_1 e^{\sigma_{p,1} \cos(2\phi) - \sigma_{t,1} \cos(2\theta)} \delta \underline{\underline{\Sigma}}_{\text{aniso},1}(\theta, \phi) \sin \theta d\theta d\phi,$
- $\underline{\underline{\Sigma}}_{\text{aniso},2} = \int_{\theta=0}^{\pi} \int_{\phi=0}^{\pi} K_2 e^{\sigma_{p,2} \cos(2(\phi+\mu_1-\mu_2)) - \sigma_{t,2} \cos(2\theta)} \delta \underline{\underline{\Sigma}}_{\text{aniso},2}(\theta, \phi) \sin \theta d\theta d\phi,$
- $\underline{\underline{T}}_{\text{aniso},1} = \int_{\theta=0}^{\pi} \int_{\phi=0}^{\pi} K_1 e^{\sigma_{p,1} \cos(2\phi) - \sigma_{t,1} \cos(2\theta)} \delta \underline{\underline{T}}_{\text{aniso},1}(\theta, \phi) \sin \theta d\theta d\phi,$
- $\underline{\underline{T}}_{\text{aniso},2} = \int_{\theta=0}^{\pi} \int_{\phi=0}^{\pi} K_2 e^{\sigma_{p,2} \cos(2(\phi+\mu_1-\mu_2)) - \sigma_{t,2} \cos(2\theta)} \delta \underline{\underline{T}}_{\text{aniso},2}(\theta, \phi) \sin \theta d\theta d\phi.$

Quadratures that will be chosen do not depend on the function that changes between the integrals from Eqs. (C.7) and (C.8) but on those that do not change: the densities ρ_1 and ρ_2 . Furthermore, the term depending on the two lamellae is independent. So, $\underline{\underline{\Sigma}}_{\text{aniso},1}$ will be chosen as an example, and the computation is similar for the other terms ($\underline{\underline{\Sigma}}_{\text{aniso},2}$, $\underline{\underline{T}}_{\text{aniso},1}$ and $\underline{\underline{T}}_{\text{aniso},2}$). Computation for $\underline{\underline{\Sigma}}_{\text{aniso},1}$ gives:

$$\underline{\underline{\Sigma}}_{\text{aniso},1} = \int_{\theta=0}^{\pi} \int_{\phi=0}^{\pi} K_1 e^{\sigma_{p,1} \cos(2\phi) - \sigma_{t,1} \cos(2\theta)} \delta \underline{\underline{\Sigma}}_{\text{aniso},1}(\theta, \phi) \sin \theta d\theta d\phi.$$

The integral is separated in θ and ϕ :

$$\underline{\underline{\Sigma}}_{\text{aniso},1} = K_1 \int_{\theta=0}^{\pi} e^{-\sigma_{t,1} \cos(2\theta)} \left(\int_{\phi=0}^{\pi} e^{\sigma_{p,1} \cos(2\phi)} \delta \underline{\underline{\Sigma}}_{\text{aniso},1}(\theta, \phi) d\phi \right) \sin \theta d\theta.$$

C.2.1.a Quadrature in ϕ

First, the integral in ϕ is considered:

$$I_1 = \int_{\phi=0}^{\pi} e^{\sigma_{p,1} \cos(2\phi)} \delta \underline{\underline{\Sigma}}_{\text{aniso},1}(\theta, \phi) d\phi. \quad (\text{C.10})$$

The function f_1 is defined as: $f_1(\phi) = e^{\sigma_{p,1} \cos(2\phi)} \delta \underline{\underline{\Sigma}}_{\text{aniso},1}(\theta, \phi)$, and then I_1 becomes:

$$I_1 = \int_{\phi=0}^{\pi} f_1(\phi) d\phi.$$

For the integral in ϕ , a uniformly distributed weight is used because a rather smooth distribution of $f_1(\phi) = e^{\sigma_{p,1} \cos(2\phi)} \delta \underline{\underline{\Sigma}}_{\text{aniso},1}(\theta, \phi)$ in terms of ϕ is expected. The function is integrated over the segment $[0, \pi]$ with a uniform distribution of the angle ϕ : $\forall i \in [1, m], \phi_i = \frac{(i-1)\pi}{m}$, with m the number of equatorial in-plane discretization points. Then, the rectangle rule is used to compute the integral in ϕ :

$$I_1 \approx \sum_{i=1}^m (\phi_{i+1} - \phi_i) f_1(\phi_i) \approx \frac{1}{m} \sum_{i=1}^m f_1(\phi_i) \approx \frac{1}{m} \sum_{i=1}^m e^{\sigma_{p,1} \cos(2\phi_i)} \delta \underline{\underline{\Sigma}}_{\text{aniso},1}(\theta, \phi_i).$$

At this point, $\underline{\underline{\Sigma}}_{\text{aniso},1}$ is:

$$\underline{\underline{\Sigma}}_{\text{aniso},1} = K_1 \int_{\theta=0}^{\pi} e^{-\sigma_{t,1} \cos(2\theta)} \left(\frac{1}{m} \sum_{i=1}^m e^{\sigma_{p,1} \cos(2\phi_i)} \delta \underline{\underline{\Sigma}}_{\text{aniso},1}(\theta, \phi_i) \right) \sin \theta d\theta,$$

which can be rearranged and rewritten as:

$$\underline{\underline{\Sigma}}_{\text{aniso},1} = \frac{K_1}{m} \sum_{i=1}^m e^{\sigma_{p,1} \cos(2\phi_i)} \int_{\theta=0}^{\pi} e^{-\sigma_{t,1} \cos(2\theta)} \delta \underline{\underline{\Sigma}}_{\text{aniso},1}(\theta, \phi_i) \sin \theta d\theta.$$

C.2.1.b Quadrature in θ

Second, the integral in θ is considered:

$$I_2 = \int_{\theta=0}^{\pi} e^{-\sigma_{t,1} \cos(2\theta)} \delta_{\underline{\Sigma}_{\text{aniso},1}}(\theta, \phi_i) \sin \theta d\theta. \quad (\text{C.11})$$

The well known trigonometry formula:

$$\cos(2\theta) = 2 \cos^2(\theta) - 1 \quad (\text{C.12})$$

helps us rewrite I_2 as:

$$I_2 = \int_{\theta=0}^{\pi} e^{-\sigma_{t,1}(2 \cos^2(\theta)-1)} \delta_{\underline{\Sigma}_{\text{aniso},1}}(\theta, \phi_i) \sin \theta d\theta = e^{\sigma_{t,1}} \int_{\theta=0}^{\pi} e^{-2\sigma_{t,1} \cos^2(\theta)} \delta_{\underline{\Sigma}_{\text{aniso},1}}(\theta, \phi_i) \sin \theta d\theta .$$

Then a change of variables is applied:

$$\begin{cases} x = \sqrt{2\sigma_{t,1}} \cos(\theta), \\ dx = -\sqrt{2\sigma_{t,1}} \sin(\theta) d\theta, \end{cases} \quad \text{and} \quad \begin{cases} \theta = 0 \Leftrightarrow x = \sqrt{2\sigma_{t,1}}, \\ \theta = \pi \Leftrightarrow x = -\sqrt{2\sigma_{t,1}}, \end{cases} \quad (\text{C.13})$$

and the following expression is found for I_2 :

$$I_2 = e^{\sigma_{t,1}} \int_{x=-\sqrt{2\sigma_{t,1}}}^{-\sqrt{2\sigma_{t,1}}} e^{-x^2} \delta_{\underline{\Sigma}_{\text{aniso},1}}(\cos^{-1}\left(\frac{x}{\sqrt{2\sigma_{t,1}}}\right), \phi_i) \left(-\frac{dx}{\sqrt{2\sigma_{t,1}}}\right).$$

The function f_2 is defined as: $f_2(x) = \delta_{\underline{\Sigma}_{\text{aniso},1}}(\cos^{-1}\left(\frac{x}{\sqrt{2\sigma_{t,1}}}\right), \phi_i)$, and then I_2 becomes:

$$I_2 = \frac{e^{\sigma_{t,1}}}{\sqrt{2\sigma_{t,1}}} \int_{x=-\sqrt{2\sigma_{t,1}}}^{\sqrt{2\sigma_{t,1}}} e^{-x^2} f_2(x) dx.$$

The Gauss-Hermite quadrature rule gives:

$$\int_{x=-\infty}^{+\infty} e^{-x^2} f(x) dx \approx \sum_{j=1}^n \frac{\sqrt{\pi} 2^{n+1} n!}{[H_n(x_j)]^2} f(x_j),$$

with x_j the root of the H_n Hermite polynomials that are defined recursively as:

$$\begin{cases} H_0(x) = 1, H_1(x) = 2x, \\ H_{k+1}(x) = 2xH_k(x) - 2kH_{k-1}(x). \end{cases}$$

The function \tilde{f}_2 is then defined as:

$$\begin{aligned} \tilde{f}_2 &: \mathbb{R} \rightarrow \mathbb{R}, \\ x &\mapsto \tilde{f}_2(x) = \begin{cases} f_2(x) & \forall x \in [-\sqrt{2\sigma_{t,1}}; \sqrt{2\sigma_{t,1}}], \\ 0 & \text{elsewhere.} \end{cases} \end{aligned} \quad (\text{C.14})$$

Gauss-Hermite quadrature is then applied to the \tilde{f}_2 function:

$$\int_{x=-\infty}^{+\infty} e^{-x^2} \tilde{f}_2 dx \approx \sum_{j=1}^n \frac{\sqrt{\pi} 2^{n+1} n!}{[H_n(x_j)]^2} \tilde{f}_2(x_j).$$

And I_2 becomes:

$$I_2 \approx \frac{e^{\sigma_{t,1}}}{\sqrt{2\sigma_{t,1}}} \sum_{j=1}^n \frac{\sqrt{\pi} 2^{n+1} n!}{[H_n(x_j)]^2} \tilde{f}_2(x_j). \quad (\text{C.15})$$

The last question that has to be answered is the validity of such interpolation, which can be improved by a proper scaling. The function \tilde{f}_2 is bounded (continuous in x on interval $[-\sqrt{2\sigma_{t,1}}; \sqrt{2\sigma_{t,1}}]$ and equal to 0 elsewhere) and so

$$I_2 = \frac{e^{\sigma_{t,1}}}{\sqrt{2\sigma_{t,1}}} \int_{x=-\sqrt{2\sigma_{t,1}}}^{\sqrt{2\sigma_{t,1}}} e^{-x^2} \tilde{f}_2(x) dx \leq \frac{M e^{\sigma_{t,1}}}{\sqrt{2\sigma_{t,1}}} \int_{x=-\sqrt{2\sigma_{t,1}}}^{\sqrt{2\sigma_{t,1}}} e^{-x^2} dx ,$$

with M the maximum of the \tilde{f}_2 function. Now, the upper bound looks like the integral of a normal distribution. Let us introduce the integral of a normal distribution, centered in 0 on the interval $[-a, a]$:

$$I_{t,a} = \int_{t=-a}^a \frac{1}{\sigma\sqrt{2\pi}} e^{-\left(\frac{t}{\sqrt{2\sigma}}\right)^2} dt .$$

For $a = 3\sigma$, this integral is more than 99% of the integral on the whole domain:

$$I_{t,3\sigma} = \int_{t=-3\sigma}^{3\sigma} \frac{1}{\sigma\sqrt{2\pi}} e^{-\left(\frac{t}{\sqrt{2\sigma}}\right)^2} dt \geq 0.99 I_{t,\infty} = 0.99 \int_{t=-\infty}^{\infty} \frac{1}{\sigma\sqrt{2\pi}} e^{-\left(\frac{t}{\sqrt{2\sigma}}\right)^2} dt .$$

The following change of variables:

$$\begin{cases} u = \frac{t}{\sqrt{2\sigma}}, \\ du = \frac{dt}{\sqrt{2\sigma}}, \end{cases}$$

for which we have $u = \pm \frac{3\sqrt{2}}{2}$ when $t = \pm 3\sigma$ is used in $I_{t,3\sigma}$:

$$I_{u, \frac{3\sqrt{2}}{2}} = \frac{1}{\sqrt{\pi}} \int_{u=-\frac{3\sqrt{2}}{2}}^{\frac{3\sqrt{2}}{2}} e^{-u^2} du \geq 0.99 I_{u,\infty} = 0.99 \frac{1}{\sqrt{\pi}} \int_{u=-\infty}^{\infty} e^{-u^2} du .$$

From this, we expect that the Hermite approximation of the integral will be accurate if we have:

$$\sqrt{2\sigma_{t,1}} \geq \frac{3\sqrt{2}}{2} \Leftrightarrow \sigma_{t,1} \geq \frac{9}{4} = 2.25 = \sigma_{t,min} .$$

Under the assumption of $\sigma_{t,1} \geq \sigma_{t,min}$, $\underline{\Sigma}_{aniso,1}$ becomes:

$$\underline{\Sigma}_{aniso,1} \approx \frac{K_1}{m} \frac{e^{\sigma_{t,1}}}{\sqrt{2\sigma_{t,1}}} \sum_{i=1}^m \sum_{j=1}^n e^{\sigma_{p,1} \cos(2\phi_i)} \frac{\sqrt{\pi} 2^{n+1} n!}{[H_n(x_j)]^2} f_2(x_j),$$

which is rearranged as:

$$\underline{\Sigma}_{aniso,1} \approx \frac{K_1}{m} \frac{e^{\sigma_{t,1}}}{\sqrt{2\sigma_{t,1}}} \sum_{i=1}^m \sum_{j=1}^n e^{\sigma_{p,1} \cos(2\phi_i)} \frac{\sqrt{\pi} 2^{n+1} n!}{[H_n(x_j)]^2} \delta_{\underline{\Sigma}_{aniso,1}} \left(\cos^{-1} \left(\frac{x_j}{\sqrt{2\sigma_{t,1}}} \right), \phi_i \right) .$$

And finally:

$$\underline{\Sigma}_{aniso,1} \approx \frac{K_1}{m} \frac{e^{\sigma_{t,1}}}{\sqrt{2\sigma_{t,1}}} \sum_{i=1}^m \sum_{j=1}^n e^{\sigma_{p,1} \cos(2\phi_i)} \frac{\sqrt{\pi} 2^{n+1} n!}{[H_n(\sqrt{2\sigma_{t,1}} \cos(\theta_j))]^2} \delta_{\underline{\Sigma}_{aniso,1}}(\theta_j, \phi_i) .$$

In the same way, $\underline{\Sigma}_{aniso,2}$ is computed as:

$$\underline{\Sigma}_{aniso,2} \approx \frac{K_2}{m} \frac{e^{\sigma_{t,2}}}{\sqrt{2\sigma_{t,2}}} \sum_{i=1}^m \sum_{j=1}^n e^{\sigma_{p,2} \cos(2(\phi_i + \mu_1 - \mu_2))} \frac{\sqrt{\pi} 2^{n+1} n!}{[H_n(\sqrt{2\sigma_{t,2}} \cos(\theta_j))]^2} \delta_{\underline{\Sigma}_{aniso,2}}(\theta_j, \phi_i) .$$

C.2.1.c Value of K_1 and K_2

The last thing that has to be known is the values of K_1 and K_2 , which guarantee that ρ_{fib1} and ρ_{fib2} are distribution densities such that:

$$\int_{\theta=0}^{\pi} \int_{\phi=0}^{\pi} \rho_{fib1}(\theta, \phi) \sin \theta d\theta d\phi = 1 \text{ and } \int_{\theta=0}^{\pi} \int_{\phi=0}^{\pi} \rho_{fib2}^M(\theta, \phi) \sin \theta d\theta d\phi = 1.$$

Rewritten in terms of K_1 and K_2 , we must have:

$$\int_{\theta=0}^{\pi} \int_{\phi=0}^{\pi} K_1 e^{\sigma_{p,1} \cos(2\phi) - \sigma_{t,1} \cos(2\theta)} \sin \theta d\theta d\phi = 1 \quad (\text{C.16})$$

and

$$\int_{\theta=0}^{\pi} \int_{\phi=0}^{\pi} K_2 e^{\sigma_{p,2} \cos(2(\phi+\mu_1-\mu_2)) - \sigma_{t,2} \cos(2\theta)} \sin \theta d\theta d\phi = 1, \quad (\text{C.17})$$

which yields in the absence of quadrature rules

$$K_1 = \frac{1}{\int_{\theta=0}^{\pi} \int_{\phi=0}^{\pi} e^{\sigma_{p,1} \cos(2\phi) - \sigma_{t,1} \cos(2\theta)} \sin \theta d\theta d\phi} \quad (\text{C.18})$$

and

$$K_2 = \frac{1}{\int_{\theta=0}^{\pi} \int_{\phi=0}^{\pi} e^{\sigma_{p,2} \cos(2(\phi+\mu_1-\mu_2)) - \sigma_{t,2} \cos(2\theta)} \sin \theta d\theta d\phi}. \quad (\text{C.19})$$

Using for consistency the same quadrature rules as in Sections C.2.1.a and C.2.1.b, this yields

$$\frac{1}{K_1} \approx \frac{e^{\sigma_{t,1}}}{m\sqrt{2\sigma_{t,1}}} \sum_{i=0}^m e^{\sigma_{p,1} \cos(2\phi_i)} \int_{x=-\sqrt{2\sigma_{t,1}}}^{\sqrt{2\sigma_{t,1}}} e^{-x^2} dx.$$

with a similar expression for K_2 . To compute exactly this term, the *erf* function is needed:

$$\begin{aligned} \frac{1}{K_1} &\approx \frac{e^{\sigma_{t,1}}}{m\sqrt{2\sigma_{t,1}}} \sum_{i=0}^m e^{\sigma_{p,1} \cos(2\phi_i)} \frac{\sqrt{\pi}}{2} (erf(\sqrt{2\sigma_{t,1}}) - erf(-\sqrt{2\sigma_{t,1}})) \approx \\ &\frac{e^{\sigma_{t,1}}}{m\sqrt{2\sigma_{t,1}}} \sum_{i=0}^m e^{\sigma_{p,1} \cos(2\phi_i)} \sqrt{\pi} erf(\sqrt{2\sigma_{t,1}}), \end{aligned}$$

yielding

$$K_1 \approx \frac{m\sqrt{2\sigma_{t,1}}}{e^{\sigma_{t,1}}} \frac{1}{\sqrt{\pi} erf(\sqrt{2\sigma_{t,1}}) \sum_{i=0}^m e^{\sigma_{p,1} \cos(2\phi_i)}}, \quad \text{with } \forall i \in [1, m], \phi_i = \frac{(i-1)\pi}{m}. \quad (\text{C.20})$$

From the previous expression of $\underline{\underline{\Sigma}}_{aniso,1}$:

$$\underline{\underline{\Sigma}}_{aniso,1} \approx \frac{K_1}{m} \frac{e^{\sigma_{t,1}}}{\sqrt{2\sigma_{t,1}}} \sum_{i=1}^m \sum_{j=1}^n e^{\sigma_{p,1} \cos(2\phi_i)} \frac{\sqrt{\pi} 2^{n+1} n!}{[H_n(\sqrt{2\sigma_{t,1}} \cos(\theta_j))]'^2} \delta \underline{\underline{\Sigma}}_{aniso,1}^{\sim}(\theta_j, \phi_i).$$

and under the definition:

$$\forall j \in [1, n], \lambda_{j,n} = \frac{\sqrt{\pi} 2^{n+1} n!}{[H_n(\sqrt{2\sigma_{t,1}} \cos(\theta_j))]'^2} = \frac{\sqrt{\pi} 2^{n+1} n!}{[H_n(x_j)]'^2}. \quad (\text{C.21})$$

the 2nd Piola-Kirchhoff tensor $\underline{\underline{\Sigma}}_{aniso,1}$ becomes:

$$\underline{\underline{\Sigma}}_{aniso,1} \approx \frac{K_1}{m} \frac{e^{\sigma_{t,1}}}{\sqrt{2\sigma_{t,1}}} \sum_{i=1}^m \sum_{j=1}^n e^{\sigma_{p,1} \cos(2\phi_i)} \lambda_{j,n} \delta \underline{\underline{\Sigma}}_{aniso,1}(\theta_j, \phi_i). \quad (\text{C.22})$$

Combining Eq. (C.22) and (C.20), we finally get

$$\underline{\underline{\Sigma}}_{aniso,1} \approx \frac{\sum_{i=1}^m \sum_{j=1}^n e^{\sigma_{p,1} \cos(2\phi_i)} \lambda_{j,n} \delta \underline{\underline{\Sigma}}_{aniso,1}(\theta_j, \phi_i)}{\sqrt{\pi} \operatorname{erf}(\sqrt{2\sigma_{t,1}}) \sum_{i=1}^m e^{\sigma_{p,1} \cos(2\phi_i)}}, \quad \text{with} \begin{cases} \forall i \in [1, m], \phi_i = \frac{(i-1)\pi}{m}, \\ \forall j \in [1, n], \cos(\theta_{j,k}) = \frac{x_j}{\sqrt{2\sigma_{t,k}}}, \\ \forall j \in [1, n], \lambda_{j,n} = \frac{\sqrt{\pi} 2^{n+1} n!}{[H_n(x_j)]^2}. \end{cases} \quad (\text{C.23})$$

C.2.2 Summary of the quadrature for Piola-Kirchhoff tensor

To sum up the computation of the 2nd Piola-Kirchhoff tensor, here is the final formula of the quadrature:

$$\left\{ \begin{array}{l} \underline{\underline{\Sigma}}_{aniso,1} \approx \frac{\sum_{i=1}^m \sum_{j=1}^n e^{\sigma_{p,1} \cos(2\phi_i)} \lambda_{j,n} \delta \underline{\underline{\Sigma}}_{aniso,1}(\theta_j, \phi_i)}{\sqrt{\pi} \operatorname{erf}(\sqrt{2\sigma_{t,1}}) \sum_{i=1}^m e^{\sigma_{p,1} \cos(2\phi_i)}}, \\ \underline{\underline{\Sigma}}_{aniso,2} \approx \frac{\sum_{i=1}^m \sum_{j=1}^n e^{\sigma_{p,2} \cos(2(\phi_i + \mu_1 - \mu_2))} \lambda_{j,n} \delta \underline{\underline{\Sigma}}_{aniso,2}(\theta_j, \phi_i)}{\sqrt{\pi} \operatorname{erf}(\sqrt{2\sigma_{t,2}}) \sum_{i=1}^m e^{\sigma_{p,2} \cos(2(\phi_i + \mu_1 - \mu_2))}}, \end{array} \right. \quad \text{with} \begin{cases} \forall i \in [1, m], \phi_i = \frac{(i-1)\pi}{m}, \\ \forall j \in [1, n], \cos(\theta_{j,k}) = \frac{x_j}{\sqrt{2\sigma_{t,k}}}, \\ \forall j \in [1, n], \lambda_{j,n} = \frac{\sqrt{\pi} 2^{n+1} n!}{[H_n(x_j)]^2}, \end{cases} \quad (\text{C.24})$$

with $\forall j \in [1, n]$, x_j the roots of the H_n Hermite polynomials (see Table C.1 for the five first polynomials), $\delta \underline{\underline{\Sigma}}_{aniso,1}$ and $\delta \underline{\underline{\Sigma}}_{aniso,2}$ defined using Eq. (C.14) and $\delta \underline{\underline{\Sigma}}_{aniso,1}$ and $\delta \underline{\underline{\Sigma}}_{aniso,2}$ defined in Eq. (C.25):

$$\left\{ \begin{array}{l} \delta \underline{\underline{\Sigma}}_{aniso,1} = \left(\frac{k}{\lambda l_0} \left(\frac{\lambda}{\lambda_{u,1}} - 1 \right)_+ + t_{u,1} \right) \underline{r}_0 \otimes \underline{r}_0, \\ \delta \underline{\underline{\Sigma}}_{aniso,2} = \left(\frac{k}{\lambda l_0} \left(\frac{\lambda}{\lambda_{u,2}} - 1 \right)_+ + t_{u,2} \right) \underline{r}_0 \otimes \underline{r}_0, \end{array} \right. \quad \text{with} \quad \lambda^2 = \underline{r}_0(\theta, \phi) \cdot \underline{C} \cdot \underline{r}_0(\theta, \phi). \quad (\text{C.25})$$

Finally, in the discrete form \underline{r}_0 is given by Eq. (C.26):

$$\begin{aligned} \underline{r}_0(\theta_{j,k}, \phi_i) &= (\sin \theta_{j,k} \cos \phi_i \underline{e}_x^{lam}(1) + \sin \theta_{j,k} \sin \phi_i \underline{e}_y^{lam}(1) + \cos \theta_{j,k} \underline{e}_z^{lam}(1)) \underline{e}_X \\ &\quad + (\sin \theta_{j,k} \cos \phi_i \underline{e}_x^{lam}(2) + \sin \theta_{j,k} \sin \phi_i \underline{e}_y^{lam}(2) + \cos \theta_{j,k} \underline{e}_z^{lam}(2)) \underline{e}_Y \\ &\quad + (\sin \theta_{j,k} \cos \phi_i \underline{e}_x^{lam}(3) + \sin \theta_{j,k} \sin \phi_i \underline{e}_y^{lam}(3) + \cos \theta_{j,k} \underline{e}_z^{lam}(3)) \underline{e}_Z. \end{aligned} \quad (\text{C.26})$$

C.2.3 First five Hermite polynomials, associated roots and weights

Tables C.1 and C.2 present the first five Hermite polynomials of order n , their associated roots $x_{j,n}$ and angles $\theta_{j,n}$ for $\sigma_{t,min} = 2.25$, first in an explicit form and then with the numerical values.

n	$H_n(x)$	$x_{j,n} : j \text{ roots of } H_n(x)$	$\theta_{j,n} = \cos^{-1}\left(\frac{x_{j,n}}{\sqrt{2\sigma_t}}\right)$ with $\sigma_t = 2.25$ (in degrees)	$\lambda_{j,n} = \frac{\sqrt{\pi}2^{n+1}n!}{[H_n(x_j)]'^2} = \frac{\sqrt{\pi}2^{n+1}n!}{[H_n(\sqrt{2\sigma_t}\cos(\theta_j))']^2}$
$n = 1$	$H_1(x) = 2x$	$x_{1,1} = 0$	$\theta_{1,1} = 90$	$\lambda_{1,1} = \sqrt{\pi}$
$n = 2$	$H_2(x) = 4x^2 - 2$	$x_{1,2} = -\frac{\sqrt{2}}{2}$	$\theta_{1,2} = 109.471220634504$	$\lambda_{1,2} = \frac{\sqrt{\pi}}{2}$
		$x_{2,2} = \frac{\sqrt{2}}{2}$	$\theta_{2,2} = 70.528779365496$	$\lambda_{2,2} = \frac{\sqrt{\pi}}{2}$
$n = 3$	$H_3(x) = 8x^3 - 12x$	$x_{1,3} = -\sqrt{\frac{3}{2}}$	$\theta_{1,3} = 125.264389669801$	$\lambda_{1,3} = \frac{\sqrt{\pi}}{6}$
		$x_{2,3} = 0$	$\theta_{2,3} = 90$	$\lambda_{2,3} = \frac{2\sqrt{\pi}}{3}$
		$x_{3,3} = \sqrt{\frac{3}{2}}$	$\theta_{3,3} = 54.735610317232$	$\lambda_{3,3} = \frac{\sqrt{\pi}}{6}$
$n = 4$	$H_4(x) = 16x^4 - 48x^2 + 12$	$x_{1,4} = -\sqrt{\frac{3+\sqrt{6}}{2}}$	$\theta_{1,4} = 141.090413810743$	$\lambda_{1,4} = \frac{\sqrt{\pi}(3-\sqrt{6})}{12}$
		$x_{2,4} = -\sqrt{\frac{3-\sqrt{6}}{2}}$	$\theta_{2,4} = 104.319054669049$	$\lambda_{2,4} = \frac{\sqrt{\pi}(3+\sqrt{6})}{12}$
		$x_{3,4} = \sqrt{\frac{3-\sqrt{6}}{2}}$	$\theta_{3,4} = 75.680945330951$	$\lambda_{3,4} = \frac{\sqrt{\pi}(3+\sqrt{6})}{12}$
		$x_{4,4} = \sqrt{\frac{3+\sqrt{6}}{2}}$	$\theta_{4,4} = 38.909586189258$	$\lambda_{4,4} = \frac{\sqrt{\pi}(3-\sqrt{6})}{12}$
$n = 5$	$H_5(x) = 32x^5 - 160x^3 + 120x$	$x_{1,5} = -\sqrt{\frac{5+\sqrt{10}}{2}}$	$\theta_{1,5} = 162.236386701988$	$\lambda_{1,5} = \frac{(7-2\sqrt{10})\sqrt{\pi}}{60}$
		$x_{2,5} = -\sqrt{\frac{5-\sqrt{10}}{2}}$	$\theta_{2,5} = 116.864071047785$	$\lambda_{2,5} = \frac{(7+2\sqrt{10})\sqrt{\pi}}{60}$
		$x_{3,5} = 0$	$\theta_{3,5} = 90$	$\lambda_{3,5} = \frac{8\sqrt{\pi}}{15}$
		$x_{4,5} = \sqrt{\frac{5-\sqrt{10}}{2}}$	$\theta_{4,5} = 63.135928952216$	$\lambda_{4,5} = \frac{(7+2\sqrt{10})\sqrt{\pi}}{60}$
		$x_{5,5} = \sqrt{\frac{5+\sqrt{10}}{2}}$	$\theta_{5,5} = 17.763613298012$	$\lambda_{5,5} = \frac{(7-2\sqrt{10})\sqrt{\pi}}{60}$

Table C.1: First five Hermite polynomials of order n , roots of Hermite polynomials $x_{j,n}$ and associated angles $\theta_{j,n}$ and weight for $\sigma_{t,min} = 2.25$. [60; 151]

n	$H_n(x)$	$x_{j,n} : j \text{ roots of } H_n(x)$	$\theta_{j,n} = \cos^{-1}\left(\frac{x_{j,n}}{\sqrt{2\sigma_t}}\right)$ with $\sigma_t = 2.25$ (in degrees)	$\lambda_{j,n} = \frac{\sqrt{\pi}2^{n+1}n!}{[H_n(x_j)]'^2} = \frac{\sqrt{\pi}2^{n+1}n!}{[H_n(\sqrt{2\sigma_t} \cos(\theta_j))]'^2}$
$n = 1$	$H_1(x) = 2x$	$x_{1,1} = 0.000000000000$	$\theta_{1,1} = 90$	$\lambda_{1,1} = 1.772453850906$
$n = 2$	$H_2(x) = 4x^2 - 2$	$x_{1,2} = -0.707106781187$	$\theta_{1,2} = 109.471220634504$	$\lambda_{1,2} = 0.886226925453$
		$x_{2,2} = 0.707106781187$	$\theta_{2,2} = 70.528779365496$	$\lambda_{2,2} = 0.886226925453$
$n = 3$	$H_3(x) = 8x^3 - 12x$	$x_{1,3} = -1.224744871392$	$\theta_{1,3} = 125.264389669801$	$\lambda_{1,3} = 0.295408975151$
		$x_{2,3} = 0.000000000000$	$\theta_{2,3} = 90$	$\lambda_{2,3} = 1.181635900604$
		$x_{3,3} = 1.224744871392$	$\theta_{3,3} = 54.735610317232$	$\lambda_{3,3} = 0.295408975151$
$n = 4$	$H_4(x) = 16x^4 - 48x^2 + 12$	$x_{1,4} = -1.650680123886$	$\theta_{1,4} = 141.090413810743$	$\lambda_{1,4} = 0.0813128354473$
		$x_{2,4} = -0.524647623275$	$\theta_{2,4} = 104.319054669049$	$\lambda_{2,4} = 0.804914090006$
		$x_{3,4} = 0.524647623275$	$\theta_{3,4} = 75.680945330951$	$\lambda_{3,4} = 0.804914090006$
		$x_{4,4} = 1.650680123886$	$\theta_{4,4} = 38.909586189258$	$\lambda_{4,4} = 0.0813128354473$
$n = 5$	$H_5(x) = 32x^5 - 160x^3 + 120x$	$x_{1,5} = -2.020182870456$	$\theta_{1,5} = 162.236386701988$	$\lambda_{1,5} = 0.0199532420590$
		$x_{2,5} = -0.958572464614$	$\theta_{2,5} = 116.864071047785$	$\lambda_{2,5} = 0.393619323152$
		$x_{3,5} = 0.000000000000$	$\theta_{3,5} = 90$	$\lambda_{3,5} = 0.945308720483$
		$x_{4,5} = 0.958572464614$	$\theta_{4,5} = 63.135928952216$	$\lambda_{4,5} = 0.393619323152$
		$x_{5,5} = 2.020182870456$	$\theta_{5,5} = 17.763613298012$	$\lambda_{5,5} = 0.0199532420590$

Table C.2: First five Hermite polynomials of order n , roots of Hermite polynomials $x_{j,n}$ and numerical value of associated angles $\theta_{j,n}$ and weight for $\sigma_{t,min} = 2.25$. [60; 151]

C.3 Technical development related to the identification process

Figure C.1 recalls the identification process presented in Sec. 1.5.1, while giving the tools and softwares (in pink) used in this work for its implementation.

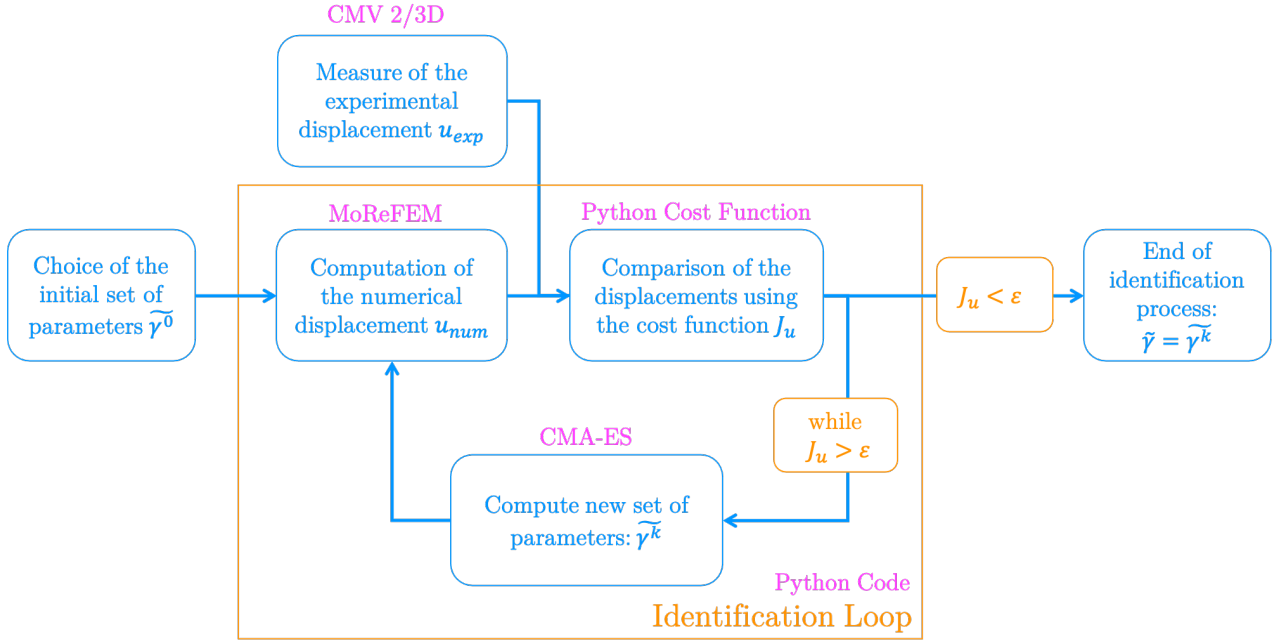


Figure C.1: General principle of the identification process. In blue are indicated the main steps of the process, orange box is the identification loop and in pink are specified the softwares used to perform the different steps of the process.

Experimental data are acquired using OCT and processed using a homemade DIC/DVC code: CMV2/3D (Chap. 3). The first set of active parameters $\tilde{\gamma}^0$ is chosen as in Chap. 2 and Sec. A.2. The other set of parameters should have been computed using the Covariance Matrix Evolution Strategy (CMA-ES) presented in Sec. A.3.2, which is a stochastic method for optimization. Numerical results are computed using a homemade finite element code MoReFEM (as in Chap. 2). The cost functions are computed using a Python Code adapted from the sensitivity analysis performed by G. Merlini [108]. The identification loop is managed using a Python code. The last ingredient of the identification process, which is not defined yet, is the cost function.

C.3.1 Reduction of the number of parameters to be identified using B-splines

As seen in Chap. 2, the number of independent parameters was reduced to 6 in the initial incompressible model (see table. 2.1): $\kappa_1^{apparent}$, α , K , k_{lam} , $\lambda_{u,max}$ and $\lambda_{u,min}$. Those lead to 6 independent parameters. We model the unfolding elongation as a function of the in-plane dispersion of the fiber, but in reality, we would like to be more precise and to identify these parameters at each node. It would lead to $2 \times 12250 = 24500$ independent parameters for the 12250-nodes mesh used in Chap. 2. To reduce drastically the number of independent parameters of the model, B-splines surfaces are used to parameterize the unfolding elongation of the two families of lamellae in the whole cornea. Parameters are then divided into two categories: the global parameters $\kappa_1^{apparent}$, α , K and k_{lam} and the control points of the B-spline surface parameterizing the unfolding elongation of the lamellae. K is fixed as it assures the "quasi-incompressibility" of the cornea and the other parameters will form from now on a set of active parameters $\tilde{\gamma} = \{\kappa_1^{apparent}, \alpha, k_{lam}, [P_{ij}]_{i=1..m, j=1..n}\}$

Using B-splines to describe the lamellae

The work done by Giulia Merlini [108] was first to approximate experimental data (stiffness, in-plane angle and dispersion of the two families of lamellae) using B-spline surfaces parametrization. This step allowed us to highlight trends concerning the organization of the lamellae within the cornea. First, the cornea can be split in two parts – the center VS the periphery – where lamellae arrange themselves in Naso-Temporal and Superior-Inferior directions or in tangential and radial directions respectively. Figure C.2 presents the division used for the different types of B-splines: in the central zone (delimited by the green circle), Cartesian B-splines are used to represent N–T and S–I lamellae while in the periphery (pink ring) polar B-splines are used to represent tangential and radial lamellae. Note that a recovery zone has been taken into account to smooth the transition between the two different representation. Then, the isotropic part of the intensity X-ray scattering signal I_{iso} is more regular than the lamellae part such that less control points are needed to parameterize the B-splines relative to I_{iso} than to control the B-splines relative to the anisotropic parameters.

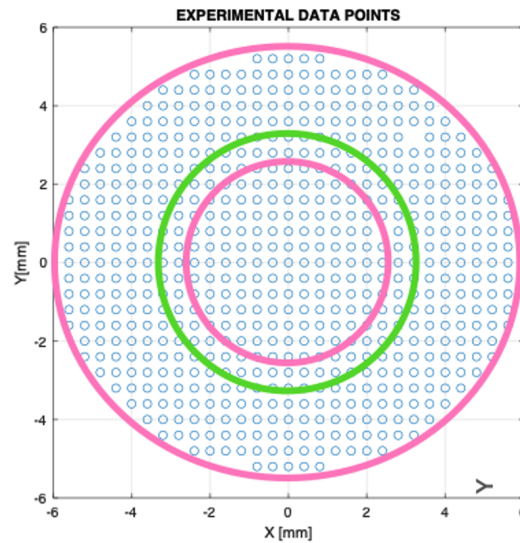


Figure C.2: Data division between optical and peripheral zone. The green circle circumscribes the optical region with $\rho_{max} = 3mm$ while the pink annulus delimits the peripheral fibers with $\rho_{min} = 2.5mm$. Extracted from [108].

A sensitivity analysis has been performed on B-spline settings to determine the best balance between a low number of control points (the less control point the better for the identification) and a good approximation of the data. For the two families of lamellae, it gave the following results for the scatter of the fiber (which is linked to the unfolding elongation):

	Central region	Periphery
Orders of the B-splines p, q	2	1
Number of knot spans x_u / x_p	5	2
Number of knot spans x_v / x_ϕ	5	8
Total number of Control Points	49	24

Table C.3: Recommended orders of B-splines for the parametrization of the data of the two families of lamellae.

With this B-spline setting, the total number of Control Points needed to describe the unfolding elongation of the two families of lamellae is $2 \times 49 + 2 \times 24 = 146$, which is still a large number of independent parameters but very small compared to the 24500 nodal values.

C.3.2 Cost function

In identification process, cost functions are used to compare two sets of data. In our case experimental data and numerical computation of different quantities during inflation tests are considered. Four cost functions (relatives to four numerical outputs) have been created for the sensitivity analysis to the B-spline settings by *G. Merlini* [108], which can be reused in the identification loop. The quantities are (i) the displacement of the anterior surface, (ii) the deformation gradient tensor \underline{F} , (iii) the Green-Lagrange strain tensor \underline{e} and (iv) the vertical apex displacement u_z^{apex} . The four cost functions associated to those quantities are:

$$\left\{ \begin{array}{l} J_{ant} = \|\underline{u}_{sim}(p) - \underline{u}_{exp}(p)\|_{L^2(S_{ant})} \\ J_{\underline{F}} = \|\underline{F}_{sim}(p) - \underline{F}_{exp}(p)\|_{L^2(\Omega)} \\ J_{\underline{e}} = \|\underline{e}_{sim}(p) - \underline{e}_{exp}(p)\|_{L^2(\Omega)} \\ J_{apex} = |u_{z,sim}^{apex}(p) - u_{z,exp}^{apex}(p)| \end{array} \right. \quad (C.27)$$

where $\|\cdot\|_L^2$ is the L^2 norm of the quantity considered over the anterior surface S_{ant} or the whole volume Ω , $\|\cdot\|$ is the absolute value of the quantity considered, p is the pressure, q_{sim} and q_{exp} are the simulated and experimental quantities respectively.

Appendix D

Supplementary experimental methods

D.1 Data on the corneas

Cornea Id	Age	Gender	Endothelial cell density (cell/mm ²)
23394	74	F	1650
23395	74	F	1650
23417	74	M	2650
23490	77	M	1300
23577	86	F	2250

Table D.1: Data on the corneas subjected to creep tests at physiological pressure.

Cornea Id	Age	Gender	Endothelial cell density (cell/mm ²)
23837	68	M	975
23850	82	M	1650
24046	46	M	2650
24055	85	F	2500
24082	64	F	2650
24083	58	M	1850
24105	86	M	1700

Table D.2: Data on the corneas subjected to creep tests at high pressure.

Cornea Id	Age	Gender	Endothelial cell density (cell/mm ²)
23769	72	F	1600
23809	81	F	2650
23831	66	M	2750
23849	82	M	1950
24109	87	F	2400
24149	74	M	1900
24167	76	M	Impossible to count

Table D.3: Data on the corneas subjected to the inflation tests.

D.2 Computation of the strain error due to difference of refractive index

The difference of refractive index causes an error in the strain computed using the image points when compared to the real one. In the image coordinates, the component of the 2D strain tensor $\underline{\underline{\varepsilon}}$ are:

$$\begin{cases} \varepsilon_{xx} = \frac{(x_{I'2} - x_{I'1}) - (x_{I2} - x_{I1})}{(x_{I2} - x_{I1})} = \frac{\Delta x_{I'} - \Delta x_I}{\Delta x_I} \\ \varepsilon_{xz} = \frac{1}{2} \left(\frac{(x_{I'2} - x_{I'1}) - (x_{I2} - x_{I1})}{(z_{I2} - z_{I1})} + \frac{(z_{I'2} - z_{I'1}) - (z_{I2} - z_{I1})}{(x_{I2} - x_{I1})} \right) = \frac{1}{2} \left(\frac{\Delta x_{I'} - \Delta x_I}{\Delta z_I} + \frac{\Delta z_{I'} - \Delta z_I}{\Delta x_I} \right) \\ \varepsilon_{zz} = \frac{(z_{I'2} - z_{I'1}) - (z_{I2} - z_{I1})}{(z_{I2} - z_{I1})} = \frac{\Delta z_{I'} - \Delta z_I}{\Delta z_I} \end{cases} \quad (\text{D.1})$$

while those of the real strain $\underline{\underline{\tilde{\varepsilon}}}$ are:

$$\begin{cases} \tilde{\varepsilon}_{xx} = \frac{(x_{B'2} - x_{B'1}) - (x_{B2} - x_{B1})}{(x_{B2} - x_{B1})} \\ \tilde{\varepsilon}_{xz} = \frac{1}{2} \left(\frac{(x_{B'2} - x_{B'1}) - (x_{B2} - x_{B1})}{(z_{B2} - z_{B1})} + \frac{(z_{B'2} - z_{B'1}) - (z_{B2} - z_{B1})}{(x_{B2} - x_{B1})} \right) \\ \tilde{\varepsilon}_{zz} = \frac{(z_{B'2} - z_{B'1}) - (z_{B2} - z_{B1})}{(z_{B2} - z_{B1})} \end{cases} \quad (\text{D.2})$$

Developing the real strain:

$$\begin{cases} \tilde{\varepsilon}_{xx} = \frac{(x_{I'2} + x'_2 - x_{I'1} - x'_1) - (x_{I2} + x_2 - x_{I1} - x_1)}{(x_{I2} + x_2 - x_{I1} - x_1)} \\ \tilde{\varepsilon}_{xz} = \frac{1}{2} \left(\frac{(x_{I'2} + x'_2 - x_{I'1} - x'_1) - (x_{I2} + x_2 - x_{I1} - x_1)}{(z_{I2} + z_2 - z_{I1} - z_1)} + \frac{(z_{I'2} + z'_2 - z_{I'1} - z'_1) - (z_{I2} + z_2 - z_{I1} - z_1)}{(x_{I2} + x_2 - x_{I1} - x_1)} \right) \\ \tilde{\varepsilon}_{zz} = \frac{(z_{I'2} + z'_2 - z_{I'1} - z'_1) - (z_{I2} + z_2 - z_{I1} - z_1)}{(z_{I2} + z_2 - z_{I1} - z_1)} \end{cases} \quad (\text{D.3})$$

which reorders:

$$\left\{ \begin{array}{l} \tilde{\varepsilon}_{xx} = \frac{(x_{I'2} - x_{I'1}) - (x_{I2} - x_{I1}) + (x'_2 - x_2) - (x'_1 - x_1)}{(x_{I2} - x_{I1}) + (x_2 - x_1)} \\ \tilde{\varepsilon}_{xz} = \frac{1}{2} \left(\frac{(x_{I'2} - x_{I'1}) - (x_{I2} - x_{I1}) + (x'_2 - x_2) - (x'_1 - x_1)}{(z_{I2} - z_{I1}) + (z_2 - z_1)} \right. \\ \left. + \frac{(z_{I'2} - z_{I'1}) - (z_{I2} - z_{I1}) + (z'_2 - z_2) - (z'_1 - z_1)}{(x_{I2} - x_{I1}) + (x_2 - x_1)} \right) \\ \tilde{\varepsilon}_{zz} = \frac{(z_{I'2} - z_{I'1}) - (z_{I2} - z_{I1}) + (z'_2 - z_2) - (z'_1 - z_1)}{(z_{I2} - z_{I1}) + (z_2 - z_1)} \end{array} \right. \quad . \quad (\text{D.4})$$

Denoting

$$\left\{ \begin{array}{l} \Delta x_I = x_{I2} - x_{I1}, \quad \Delta x_{I'} = x_{I'2} - x_{I'1} \\ \Delta z_I = z_{I2} - z_{I1}, \quad \Delta z_{I'} = z_{I'2} - z_{I'1} \\ \Delta x_1 = x'_1 - x_1, \quad \Delta x_2 = x'_2 - x_2 \\ \Delta z_1 = z'_1 - z_1, \quad \Delta z_2 = z'_2 - z_2 \end{array} \right. , \quad (\text{D.5})$$

the real strains become:

$$\left\{ \begin{array}{l} \tilde{\varepsilon}_{xx} = \frac{(\Delta x_{I'} - \Delta x_I) + (\Delta x_2 - \Delta x_1)}{(x_{I2} - x_{I1}) + (x_2 - x_1)} \\ \tilde{\varepsilon}_{xz} = \frac{1}{2} \left(\frac{(\Delta x_{I'} - \Delta x_I) + (\Delta x_2 - \Delta x_1)}{\Delta z_I + (z_2 - z_1)} + \frac{(\Delta z_{I'} - \Delta z_I) + (\Delta z_2 - \Delta z_1)}{(x_{I2} - x_{I1}) + (x_2 - x_1)} \right) \\ \tilde{\varepsilon}_{zz} = \frac{(\Delta z_{I'} - \Delta z_I) + (\Delta z_2 - \Delta z_1)}{\Delta z_I + (z_2 - z_1)} \end{array} \right. \quad . \quad (\text{D.6})$$

Or equivalently

$$\left\{ \begin{array}{l} \tilde{\varepsilon}_{xx} = \frac{\Delta x_{I'} - \Delta x_I}{\Delta x_I + (x_2 - x_1)} + \frac{(\Delta x_2 - \Delta x_1)}{\Delta x_I + (x_2 - x_1)} \\ \tilde{\varepsilon}_{xz} = \frac{1}{2} \left(\frac{\Delta x_{I'} - \Delta x_I}{\Delta z_I + (z_2 - z_1)} + \frac{\Delta z_{I'} - \Delta z_I}{\Delta x_I + (x_2 - x_1)} + \frac{(\Delta x_2 - \Delta x_1)}{\Delta z_I + (z_2 - z_1)} + \frac{(\Delta z_2 - \Delta z_1)}{\Delta x_I + (x_2 - x_1)} \right) \\ \tilde{\varepsilon}_{zz} = \frac{\Delta z_{I'} - \Delta z_I}{(z_{I2} - z_{I1}) + (z_2 - z_1)} + \frac{(\Delta z_2 - \Delta z_1)}{\Delta z_I + (z_2 - z_1)} \end{array} \right. \quad (\text{D.7})$$

and using the strain computed on image points, it finally becomes

$$\left\{ \begin{array}{l} \tilde{\varepsilon}_{xx} = \varepsilon_{xx} \frac{\Delta x_I}{\Delta x_I + (x_2 - x_1)} + \frac{(\Delta x_2 - \Delta x_1)}{\Delta x_I + (x_2 - x_1)} \\ \tilde{\varepsilon}_{xz} = \frac{1}{2} \left(\frac{\Delta x_{I'} - \Delta x_I}{\Delta z_I + (z_2 - z_1)} + \frac{\Delta z_{I'} - \Delta z_I}{\Delta x_I + (x_2 - x_1)} + \frac{(\Delta x_2 - \Delta x_1)}{\Delta z_I + (z_2 - z_1)} + \frac{(\Delta z_2 - \Delta z_1)}{\Delta x_I + (x_2 - x_1)} \right) \\ \tilde{\varepsilon}_{zz} = \varepsilon_{zz} \frac{\Delta z_I}{\Delta z_I + (z_2 - z_1)} + \frac{(\Delta z_2 - \Delta z_1)}{\Delta z_I + (z_2 - z_1)} \end{array} \right. \quad . \quad (\text{D.8})$$

Appendix E

Supplementary experimental results

E.1 Uncertainty quantification

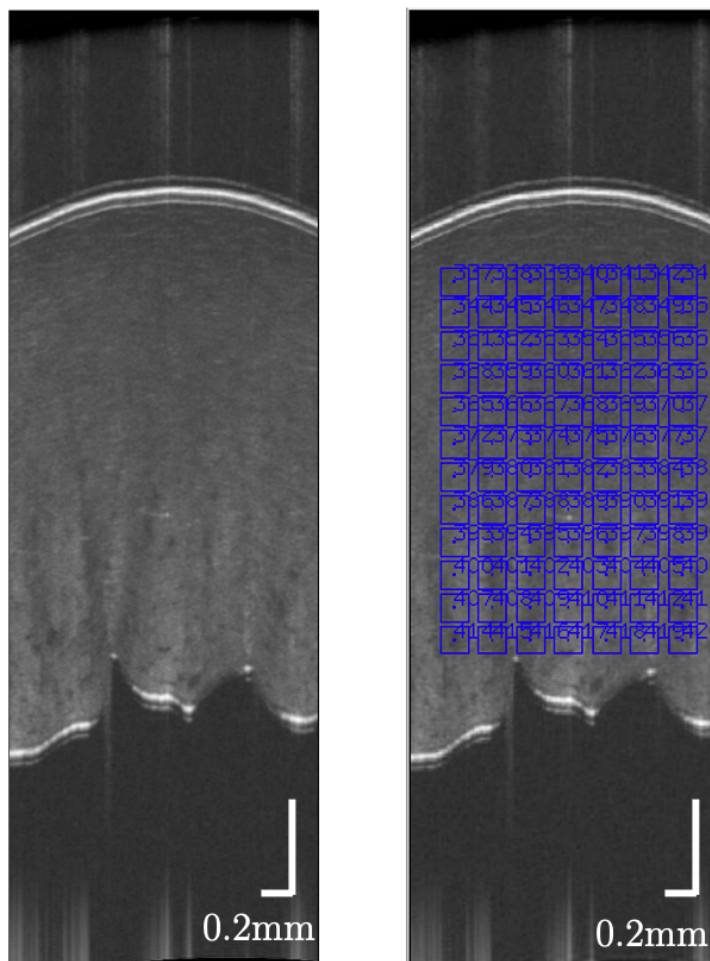


Figure E.1: Stack of 3D OCT image of a fixed cornea and corresponding correlation domains.

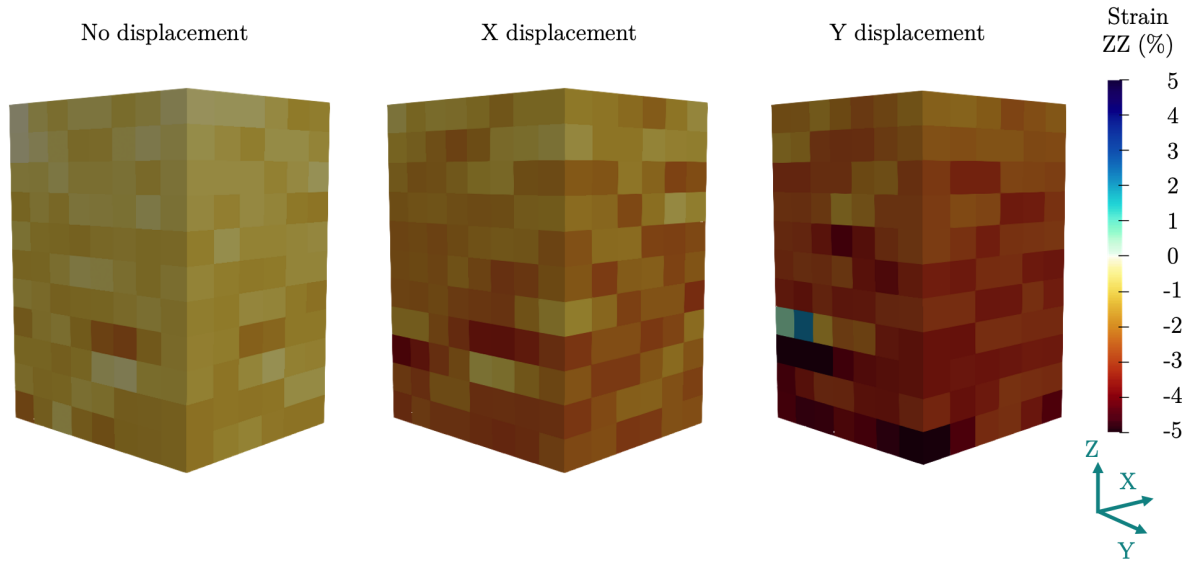


Figure E.2: Vertical strain computed on a fixed cornea while performing uncertainty quantification. A global contraction of the cornea is observed. Scale bar – [-5 %, 5 %].

Images 1 – 3	X	Z	Units
Size	166	1024	vx
FOV	1.00	2.00	mm
Voxel size	6.00	1.95	μm
Volumes 6 – 8	X	Z	Units
Size	250	1024	vx
FOV	1.00	2.00	mm
Voxel size	4.00	1.95	μm

Table E.1: Scanned zone information for the two cases of voxel sizes.

	Volume 2	Volume 3
Volume 1: Reference volume	No displacement	+ 60 μm = 10 vx in the x-direction
	Volume 7	Volume 8
Volume 6: Reference volume	No displacement	+ 60 μm = 15 vx in the x-direction

Table E.2: Volume considered for the uncertainty quantification. Volumes 1 and 6 are taken as reference states while the others are the deformed configuration with respect to volumes 1 and 6.

Im1 vs Im2	X	Z
\bar{T}	-0.036 vx = -0.217 μm	0.206 vx = 0.401 μm
σ	0.422 vx = 2.532 μm	0.108 vx = 0.211 μm
σ_{max}	0.585 vx = 3.510 μm	0.381 vx = 0.742 μm
L_0	32 vx = 192 μm	32 vx = 58.5 μm
Δd	0.621 vx = 3.726 μm	0.586 vx = 1.143 μm
Normal strain	XX	ZZ
Normal uncertainty (%)	2.79	1.41
Shear strain	XZ	
Shear uncertainty (%)	2.14	
Im6 vs Im7	X	Z
\bar{T}	0.076 vx = 0.305 μm	0.175 vx = 0.341 μm
σ	1.103 vx = 4.413 μm	0.188 vx = 0.367 μm
σ_{max}	3.282 vx = 13.129 μm	0.512 vx = 0.998 μm
L_0	32 vx = 128 μm	36 vx = 70.2 μm
Δd	3.359 vx = 13.434 μm	0.687 vx = 1.339 μm
Normal strain	XX	ZZ
Normal uncertainty (%)	7.13	1.53
Shear strain	XZ	
Shear uncertainty (%)	4.03	

Table E.3: Results for the correlation between two images taken at the same place: Im1 vs Im2 for the 6 μm voxel size in x direction and Im6 vs Im7 for the 4 μm voxel size in x direction.

Im1 vs Im3	X	Z
\bar{T}	-10.0 vx = -60.049 μm	-1.229 vx = -2.397 μm
σ	0.438 vx = 2.630 μm	0.170 vx = 0.332 μm
σ_{max}	0.561 vx = 3.365 μm	0.513 vx = 1.000 μm
L_0	32 vx = 192 μm	30 vx = 58.5 μm
Δd	0.569 vx = 3.414 μm	1.742 vx = 3.396 μm
Normal strain	XX	ZZ
Normal uncertainty (%)	2.81	5.23
Shear strain	XZ	
Shear uncertainty (%)	3.97	
Im6 vs Im8	X	Z
\bar{T}	-15.2 vx = -90.825 μm	-1.393 vx = -2.716 μm
σ	0.380 vx = 1.521 μm	0.079 vx = 0.154 μm
σ_{max}	0.691 vx = 2.763 μm	0.256 vx = 0.498 μm
L_0	32 vx = 128 μm	36 vx = 70.2 μm
Δd	0.897 vx = 3.587 μm	1.648 vx = 3.214 μm
Normal strain	XX	ZZ
Normal uncertainty (%)	3.02	4.31
Shear strain	XZ	
Shear uncertainty (%)	3.77	

Table E.4: Results for the correlation between two images with a 60 μm displacement in the x direction: Im1 vs Im3 for the 6 μm voxel size in x direction and Im6 vs Im8 for the 4 μm voxel size in x direction.

E.2 Supplementary results of the creep tests at physiological pressure

E.2.1 Histograms of the distributions

Here are given the histograms of the quantities considered in the t-tests of Sec. 3.3.1.c for the creep tests at physiological pressure.

Transect analysis

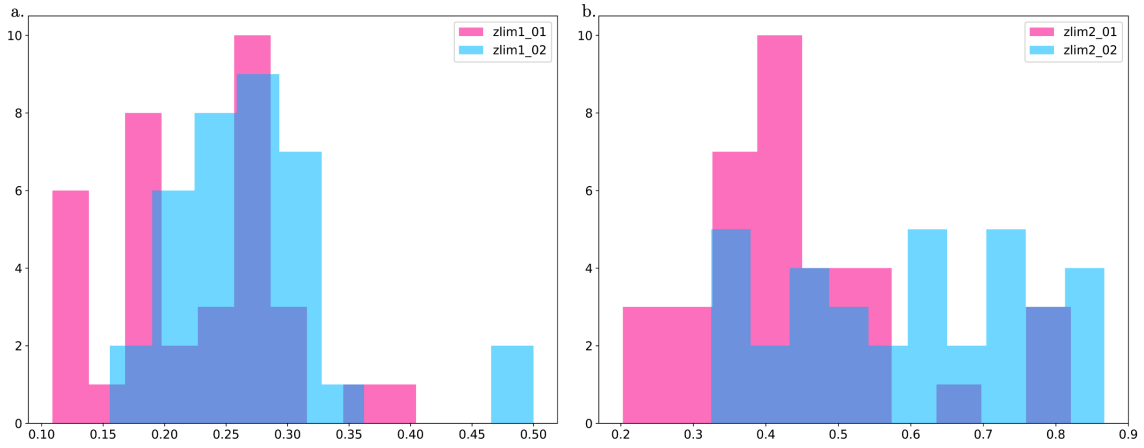


Figure E.3: Histograms of the limit depths – a. z_1 and b. z_2 for the two transects (pink and blue) corresponding to the T-test of Fig. 3.17.a.

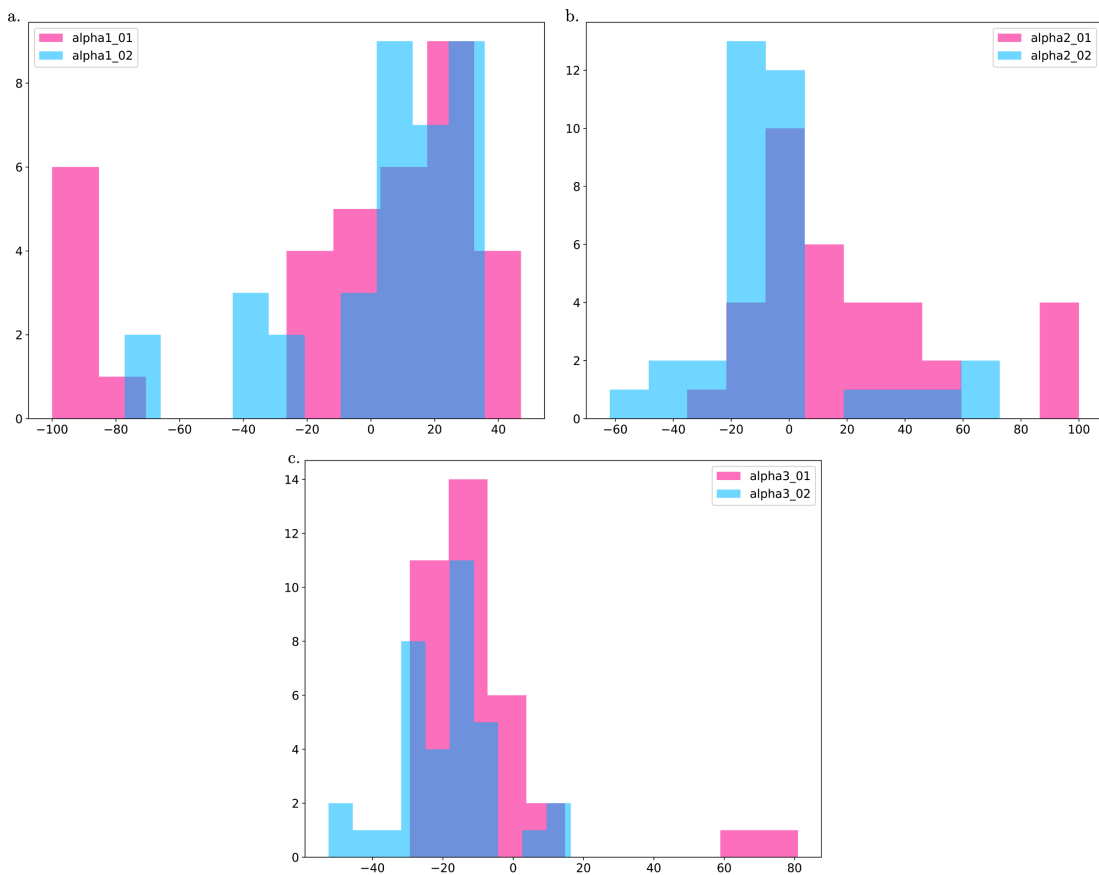


Figure E.4: Histograms of the slopes (in %) – a. α_1 , b. α_2 and c. α_3 for the two transects (pink and blue) corresponding to the T-test of Fig. 3.17.b.

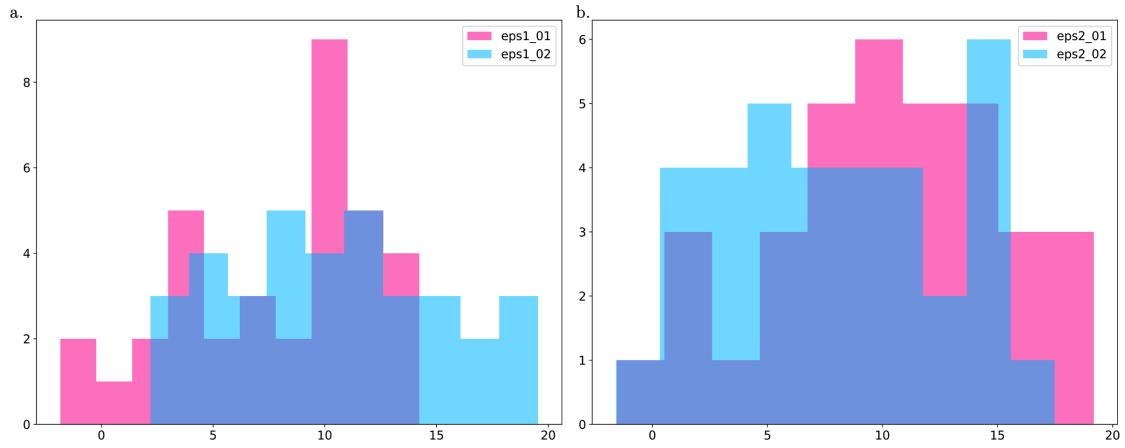


Figure E.5: Histograms of the limit strains (in %) – a. ε_1 and b. ε_2 for the two transects (pink and blue) corresponding to the T-test of Fig. 3.17.c.

E.2.2 Time dependence analyses

Here are given the time dependence analyses for the other corneas subjected to creep tests at physiological pressure considered in Sec. E.2.1 to complement Fig. 3.18.

Cornea 23395

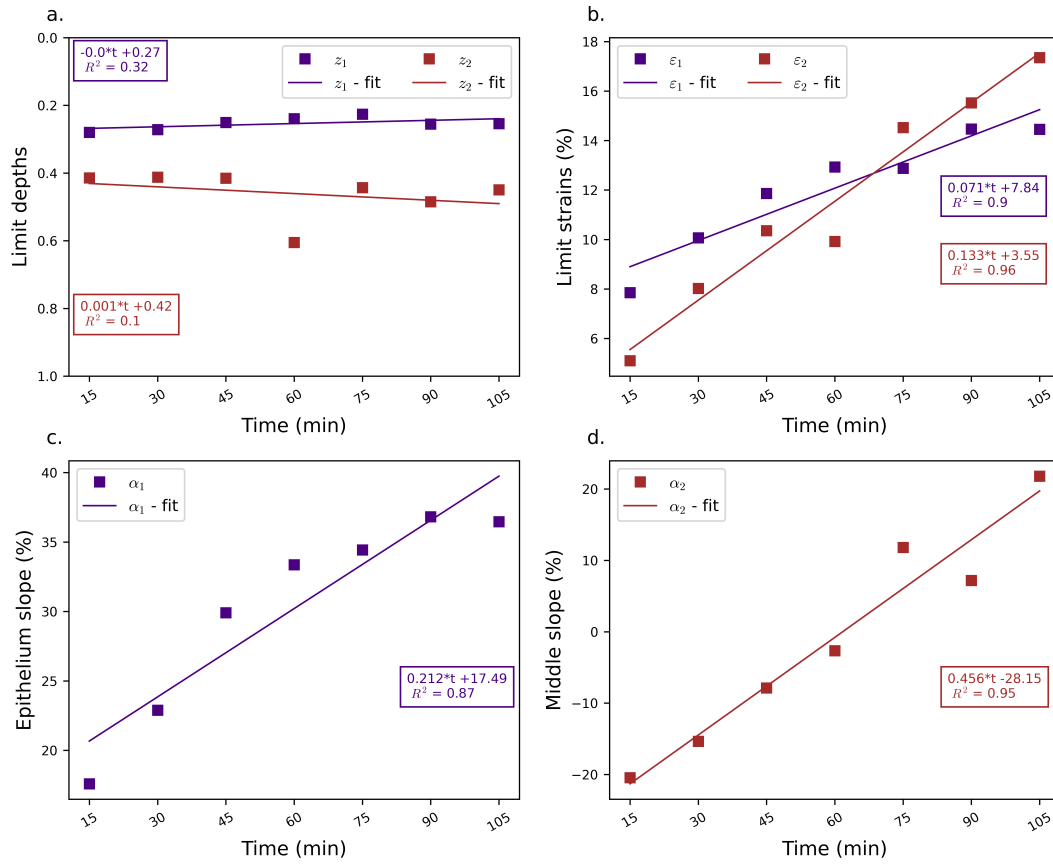


Figure E.6: Time dependence of the parameters for creep test at physiological pressure (cornea 23395). a. Limit depths, b. Limit strains (purple results indicates limit 1 and dark red indicates limit 2) and c. Epithelium slope and d. Middle slope.

Cornea 23417

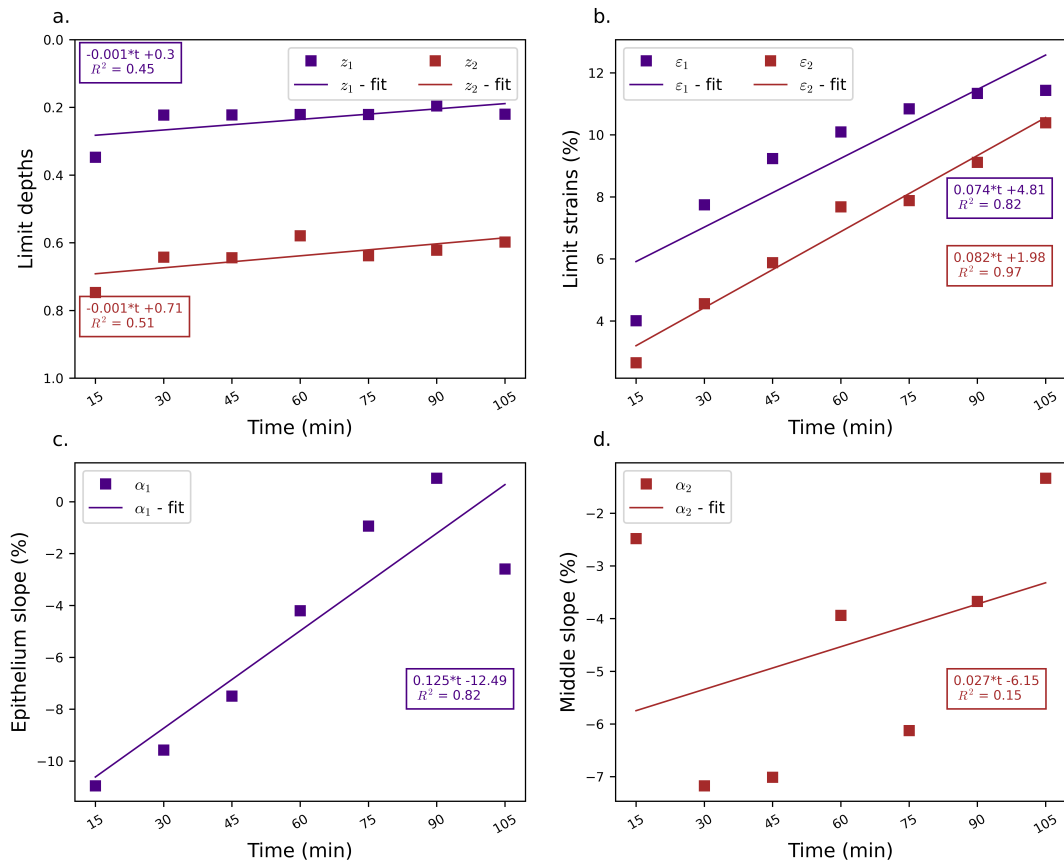


Figure E.7: Time dependence of the parameters for creep test at physiological pressure (cornea 23417). a. Limit depths, b. Limit strains (purple results indicates limit 1 and dark red indicates limit 2) and c. Epithelium slope and d. Middle slope.

Cornea 23490

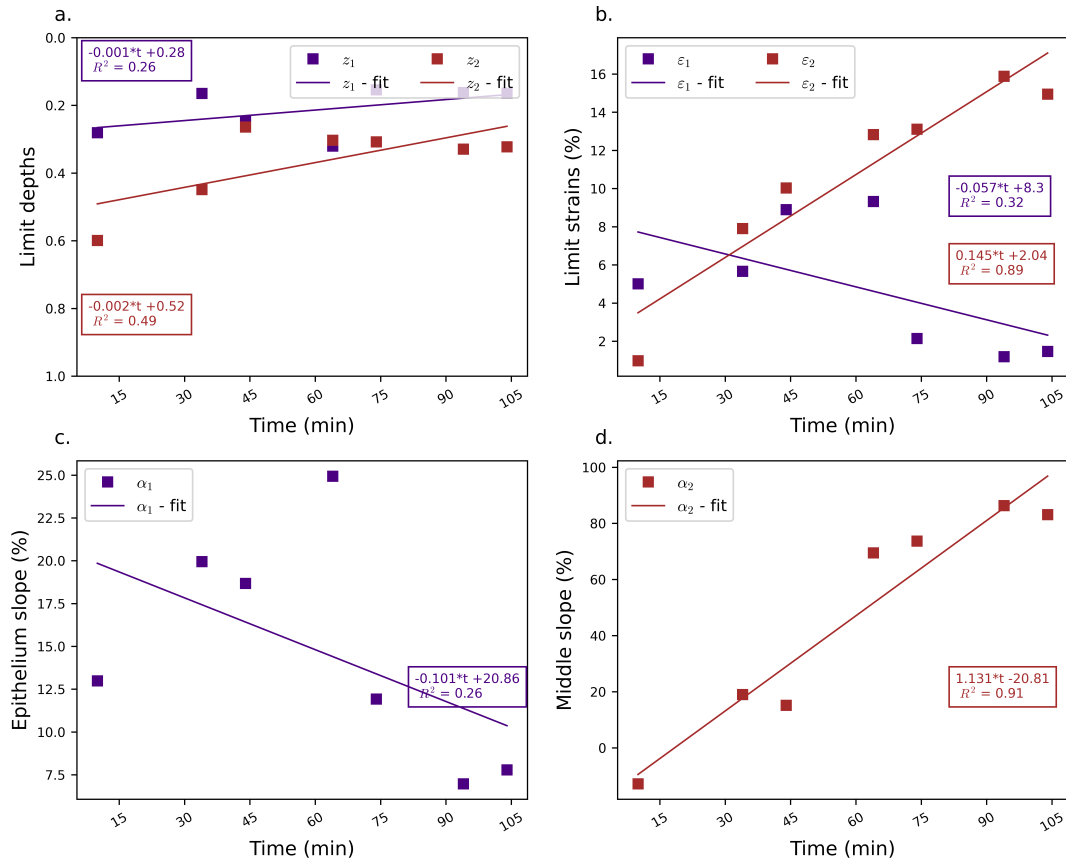


Figure E.8: Time dependence of the parameters for creep test at physiological pressure (cornea 23490). a. Limit depths, b. Limit strains (purple results indicates limit 1 and dark red indicates limit 2) and c. Epithelium slope and d. Middle slope.

Cornea 23577

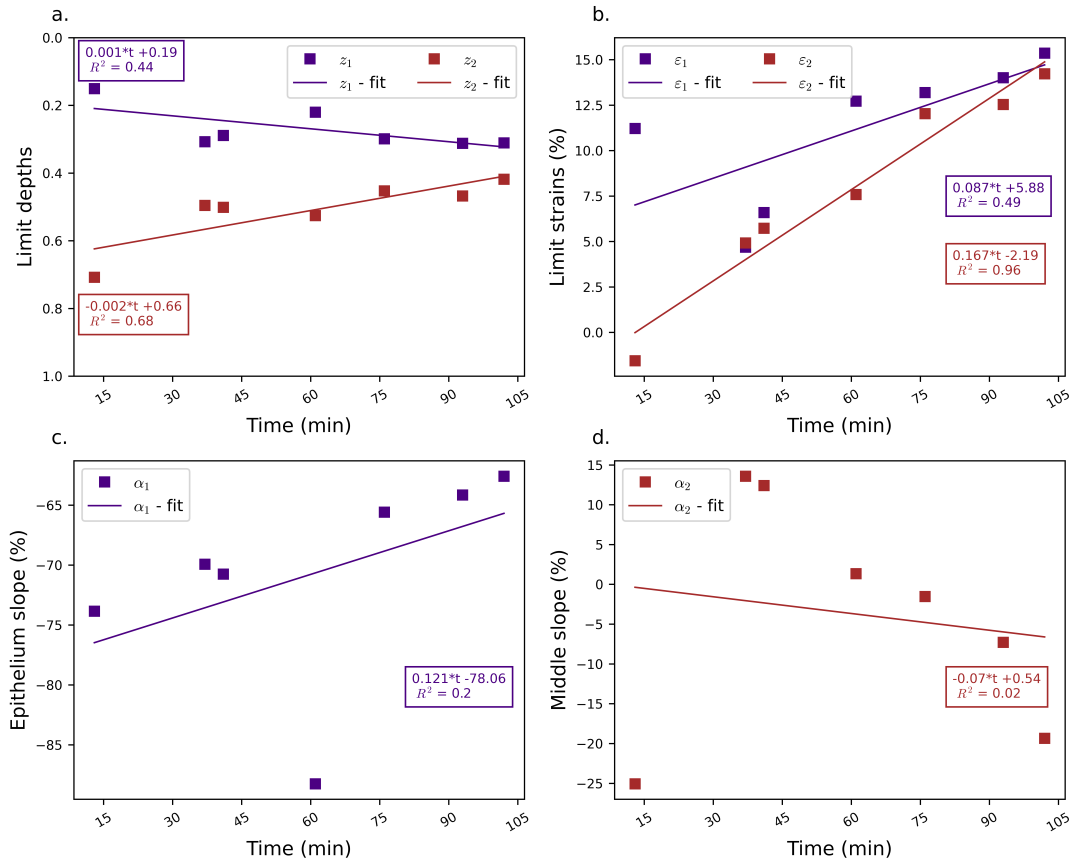


Figure E.9: Time dependence of the parameters for creep test at physiological pressure (cornea 23577). a. Limit depths, b. Limit strains (purple results indicates limit 1 and dark red indicates limit 2) and c. Epithelium slope and d. Middle slope.

E.3 Supplementary results of creep tests at high pressure

E.3.1 Histograms

Here are given the histograms of the quantities considered in the t-tests of Sec. 3.29 for the creep tests at high pressure.

Transect analysis

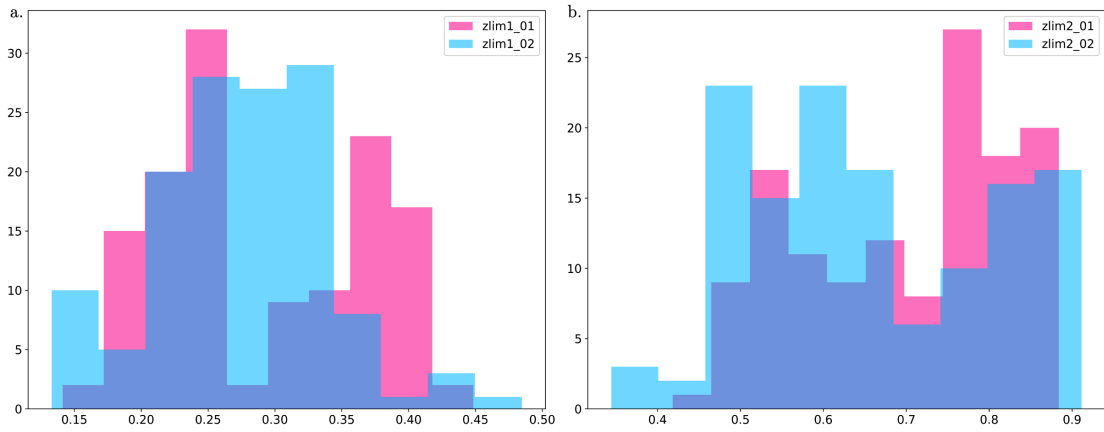


Figure E.10: Histograms of the limit depths – a. z_1 and b. z_2 for the two transects (pink and blue) corresponding to T-test of Fig. 3.29.a.

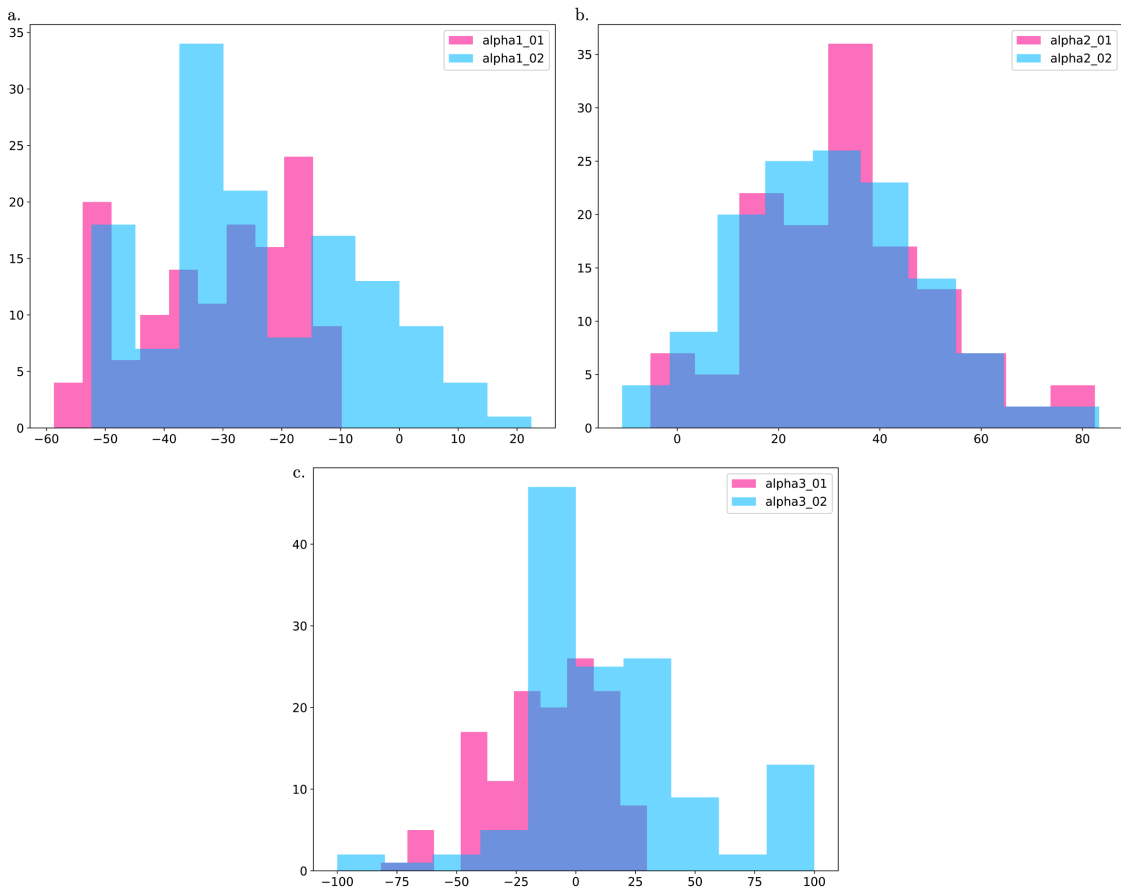


Figure E.11: Histograms of the slopes (in %) – a. α_1 , b. α_2 and c. α_3 for the two transects (pink and blue) corresponding to T-test of Fig. 3.29.b.

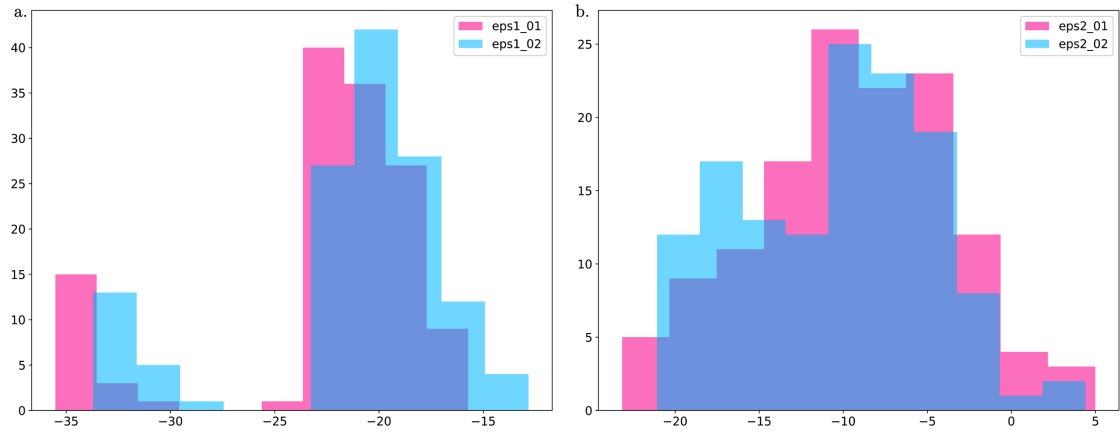


Figure E.12: Histograms of the limit strains (in %) – a. ϵ_1 and b. ϵ_2 for the two transects (pink and blue) corresponding to T-test of Fig. 3.29.c.

E.3.2 Time dependence analyses

Here are given the time dependence analyses for the other corneas subjected to creep tests at high pressure considered in Sec. 3.3.2.c to complement Fig. 3.30.

Cornea 23837

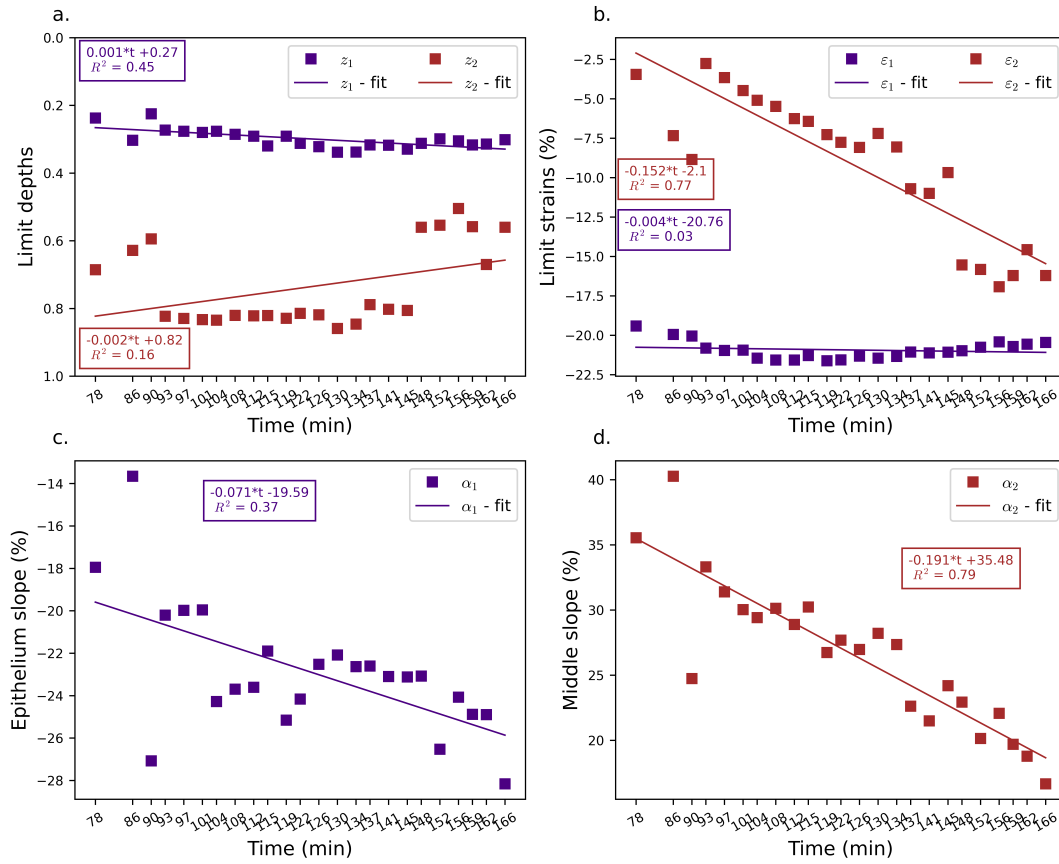


Figure E.13: Time dependence of the parameters for creep test at high pressure (cornea 23837). a. Limit depths, b. Limit strains (purple results indicates limit 1 and dark red indicates limit 2) and c. Epithelium slope and d. Middle slope.

Cornea 23850

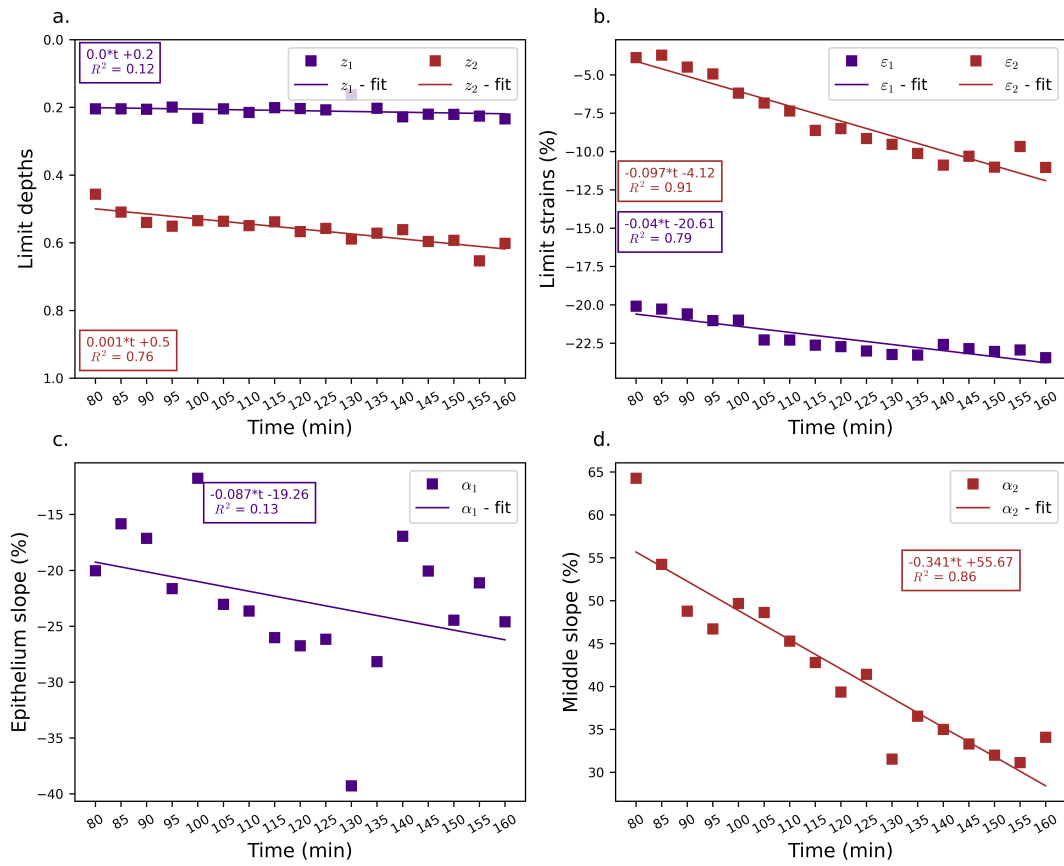


Figure E.14: Time dependence of the parameters for creep test at high pressure (cornea 23850). a. Limit depths, b. Limit strains (purple results indicates limit 1 and dark red indicates limit 2) and c. Epithelium slope and d. Middle slope.

Cornea 24046

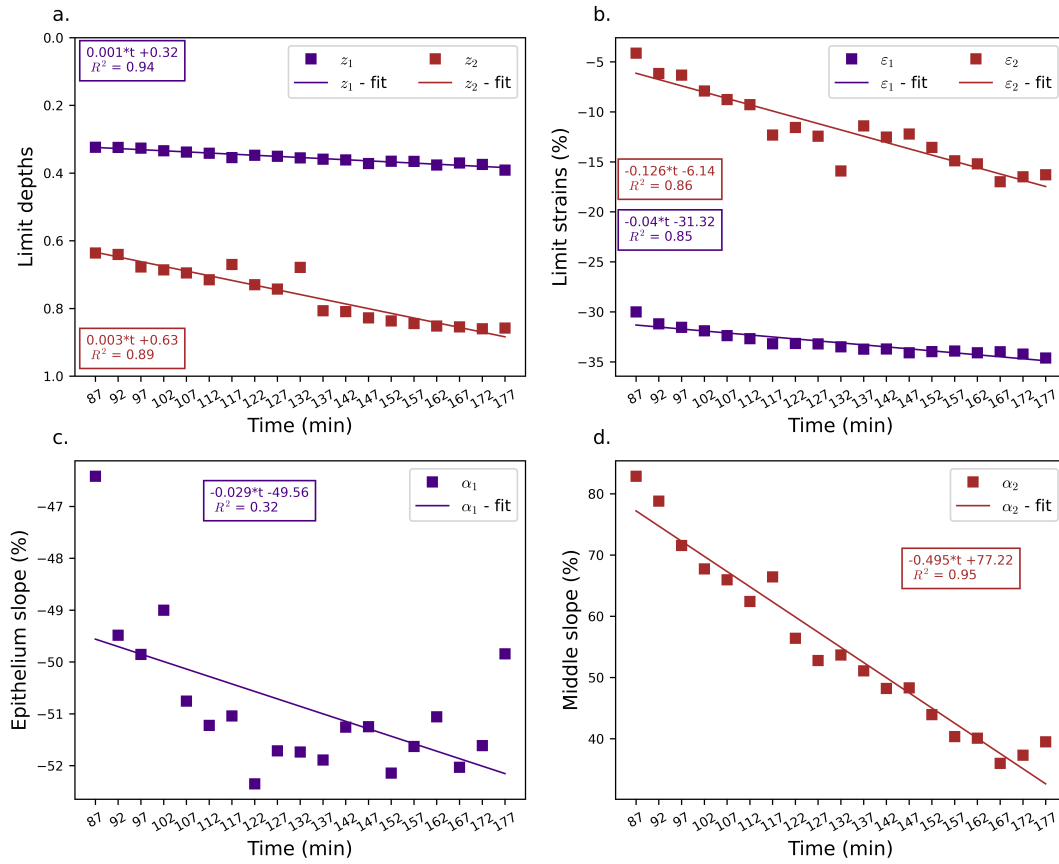


Figure E.15: Time dependence of the parameters for creep test at high pressure (cornea 24046). a. Limit depths, b. Limit strains (purple results indicates limit 1 and dark red indicates limit 2) and c. Epithelium slope and d. Middle slope.

Cornea 24055

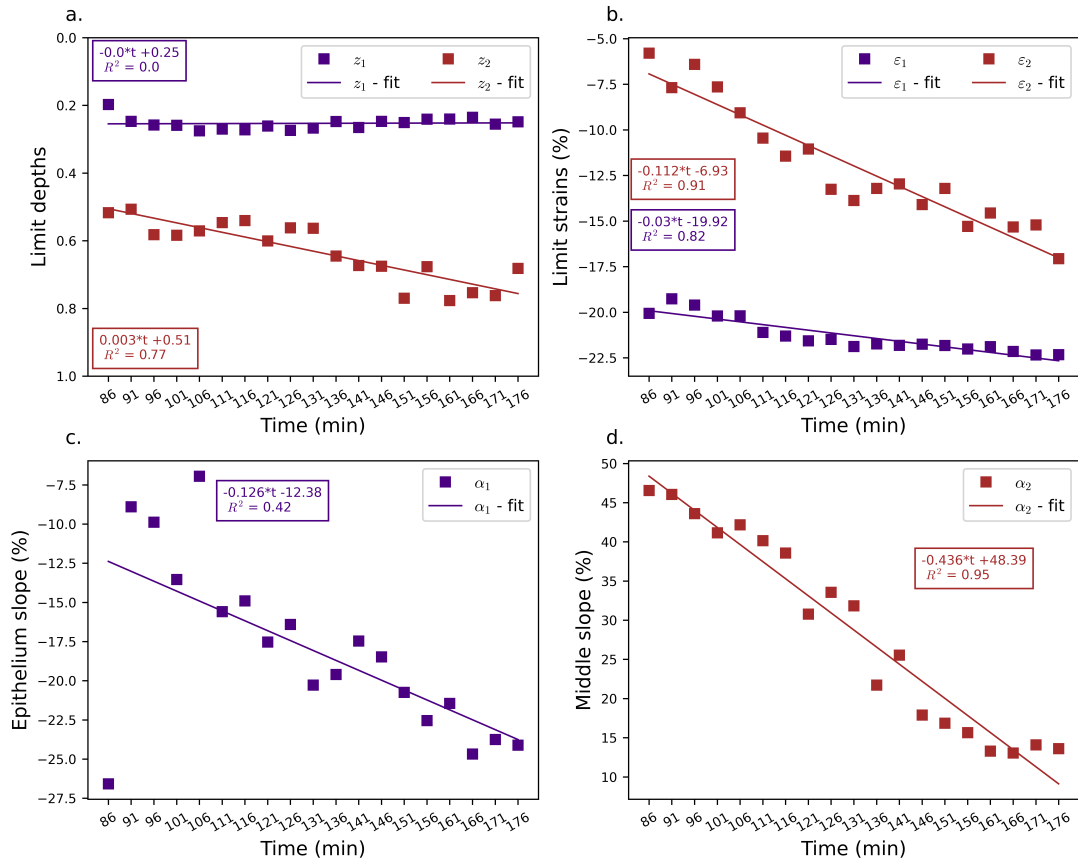


Figure E.16: Time dependence of the parameters for creep test at high pressure (cornea 24055). a. Limit depths, b. Limit strains (purple results indicates limit 1 and dark red indicates limit 2) and c. Epithelium slope and d. Middle slope.

Cornea 24082

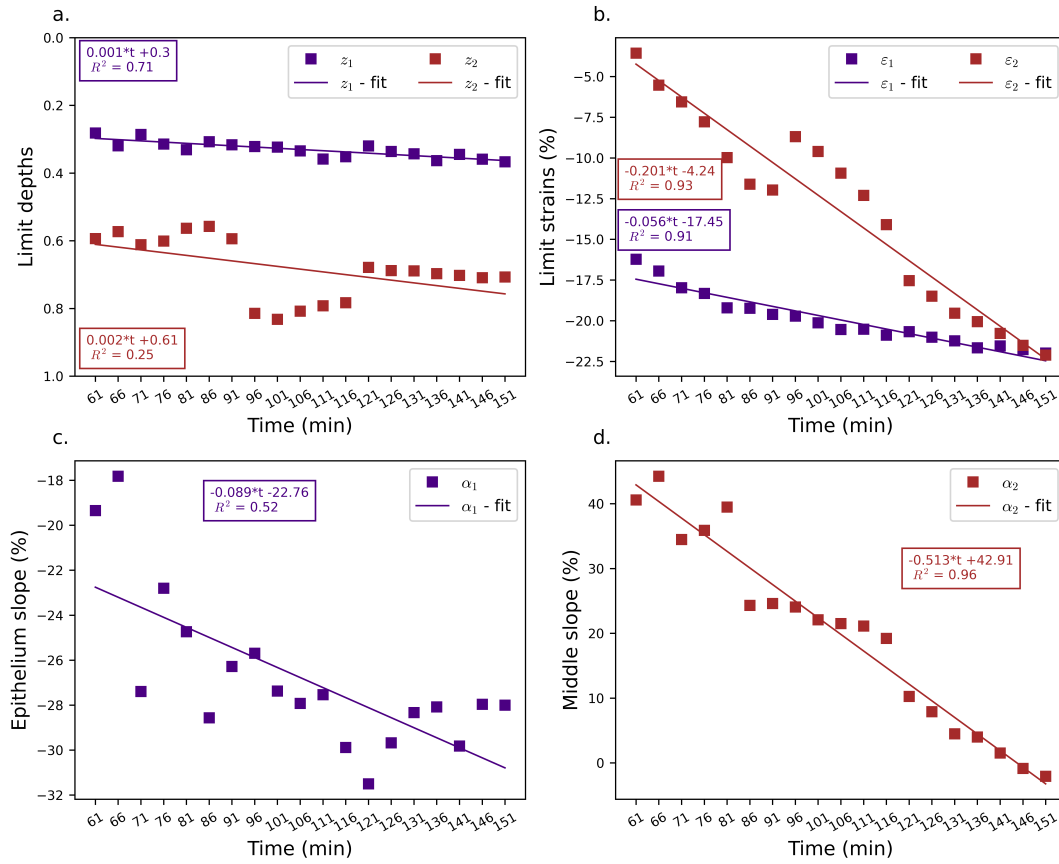


Figure E.17: Time dependence of the parameters for creep test at high pressure (cornea 24082). a. Limit depths, b. Limit strains (purple results indicates limit 1 and dark red indicates limit 2) and c. Epithelium slope and d. Middle slope.

Cornea 24083

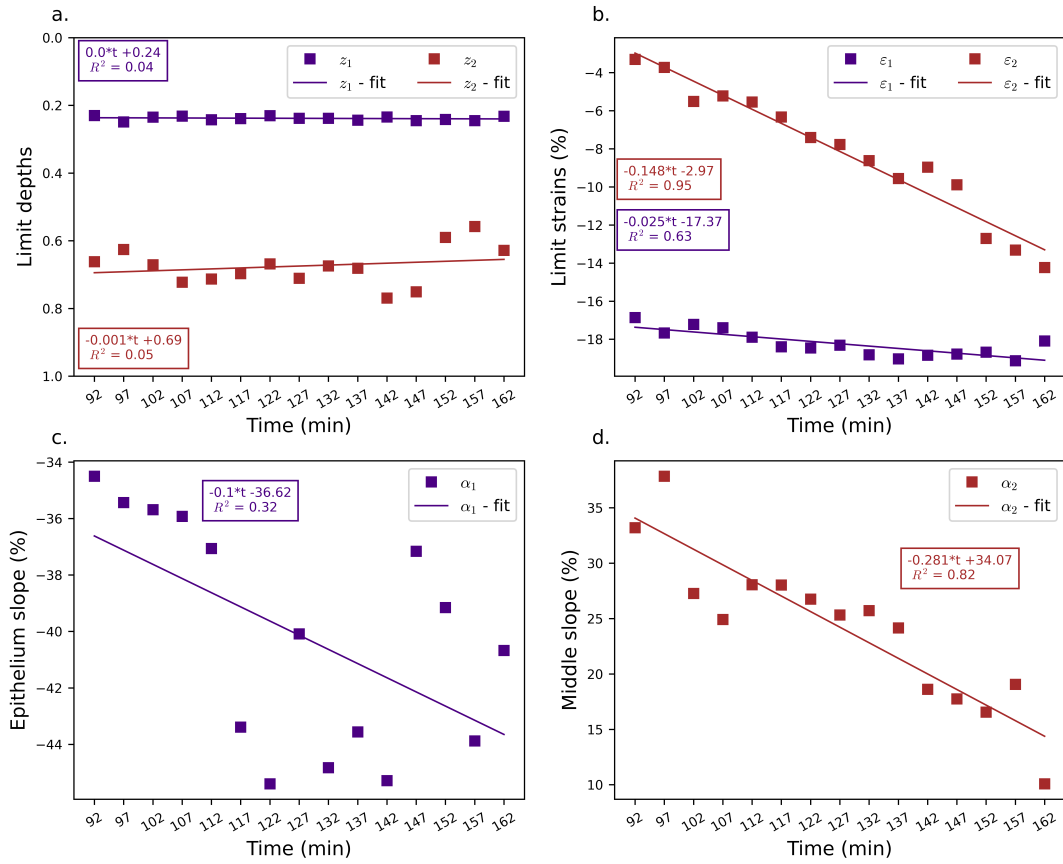


Figure E.18: Time dependence of the parameters for creep test at high pressure (cornea 24083). a. Limit depths, b. Limit strains (purple results indicates limit 1 and dark red indicates limit 2) and c. Epithelium slope and d. Middle slope.

E.4 Supplementary results for the comparison of the two creep tests

E.4.1 Histograms

Here are given the histograms of the quantities considered in the t-tests of Sec. 3.3.3 comparing the two creep tests.

4. Supplementary results for the comparison of the two creep tests

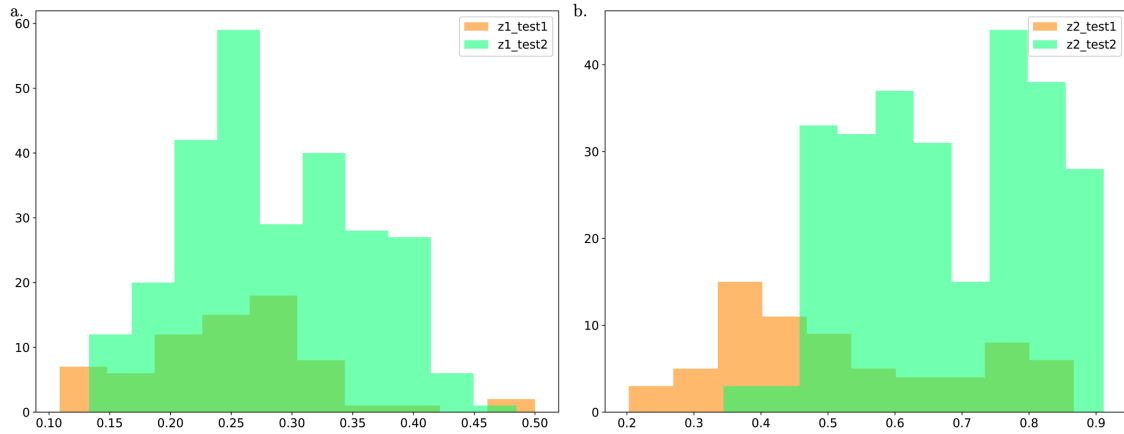


Figure E.19: Histograms of the limit depths – a. z_1 and b. z_2 for creep tests at physiological pressure (orange) and at high pressure (green) corresponding to the T-test of Fig. 3.31.a.

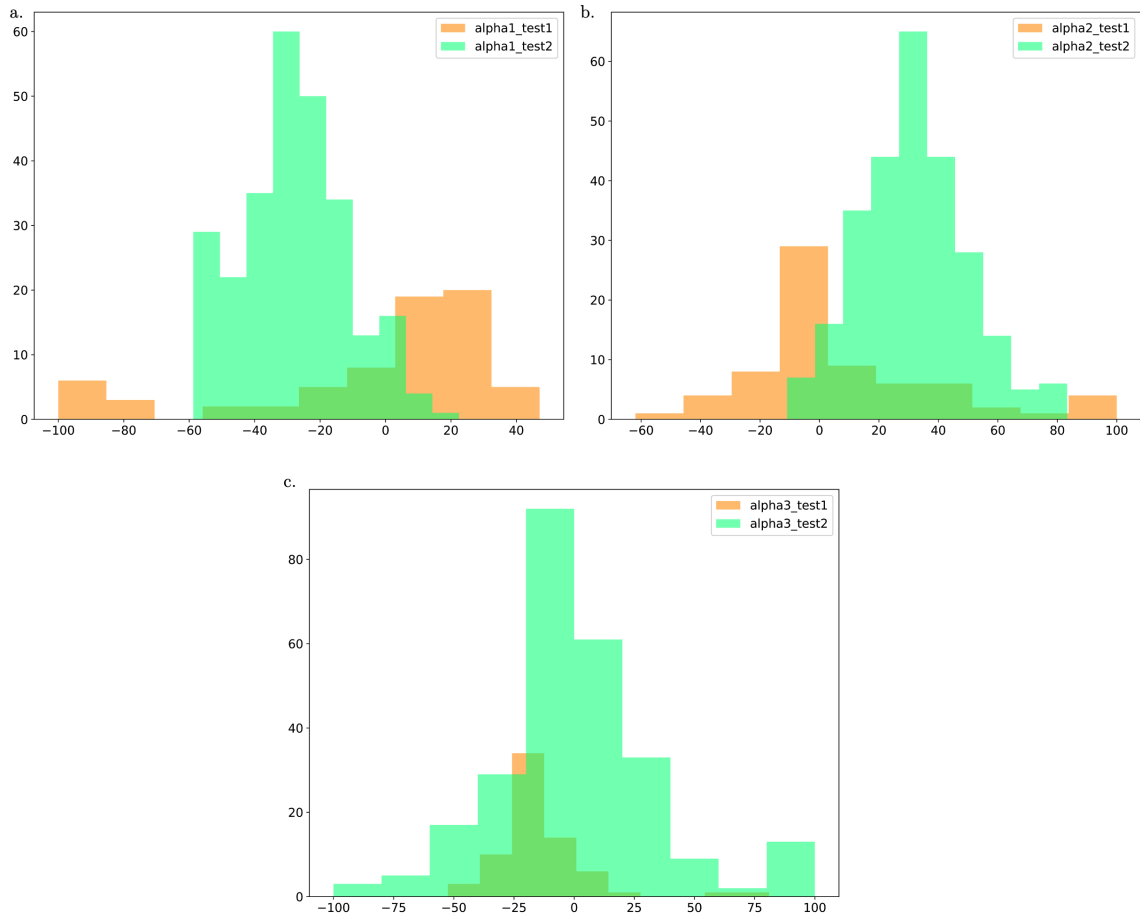


Figure E.20: Histograms of the slopes (in %) – a. α_1 , b. α_2 and c. α_3 for creep tests at physiological pressure (orange) and at high pressure (green) corresponding to the T-test of Fig. 3.31.b.

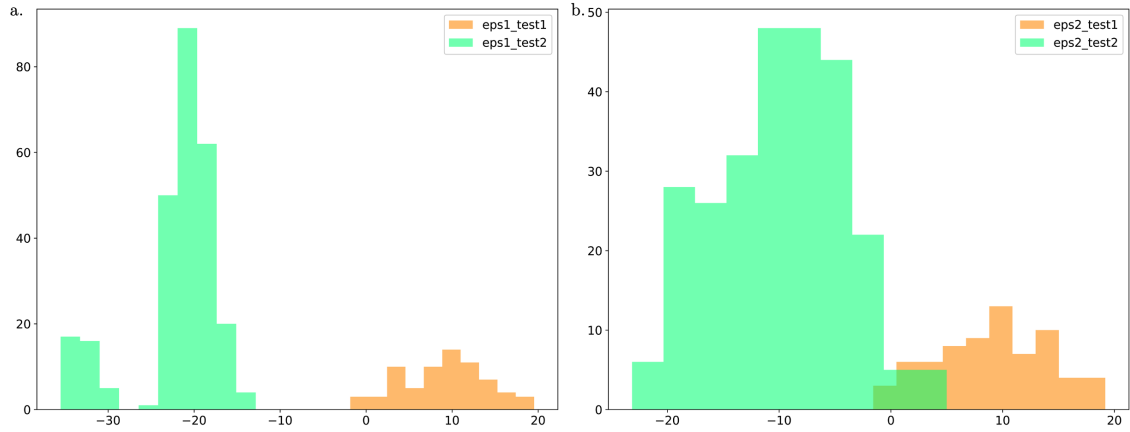


Figure E.21: Histograms of the limit strains (in %) – a. ϵ_1 and b. ϵ_2 for creep tests at physiological pressure (orange) and at high pressure (green) corresponding to the T-test of Fig. 3.31.c.

E.5 Supplementary results of the inflation tests

E.5.1 Histograms

Here are given the histograms of the quantities considered in the t-tests of Sec. 3.3.4 for the inflation tests.

Transect analysis

Here are given the histograms of the quantities considered in the transect analysis.

5. Supplementary results of the inflation tests

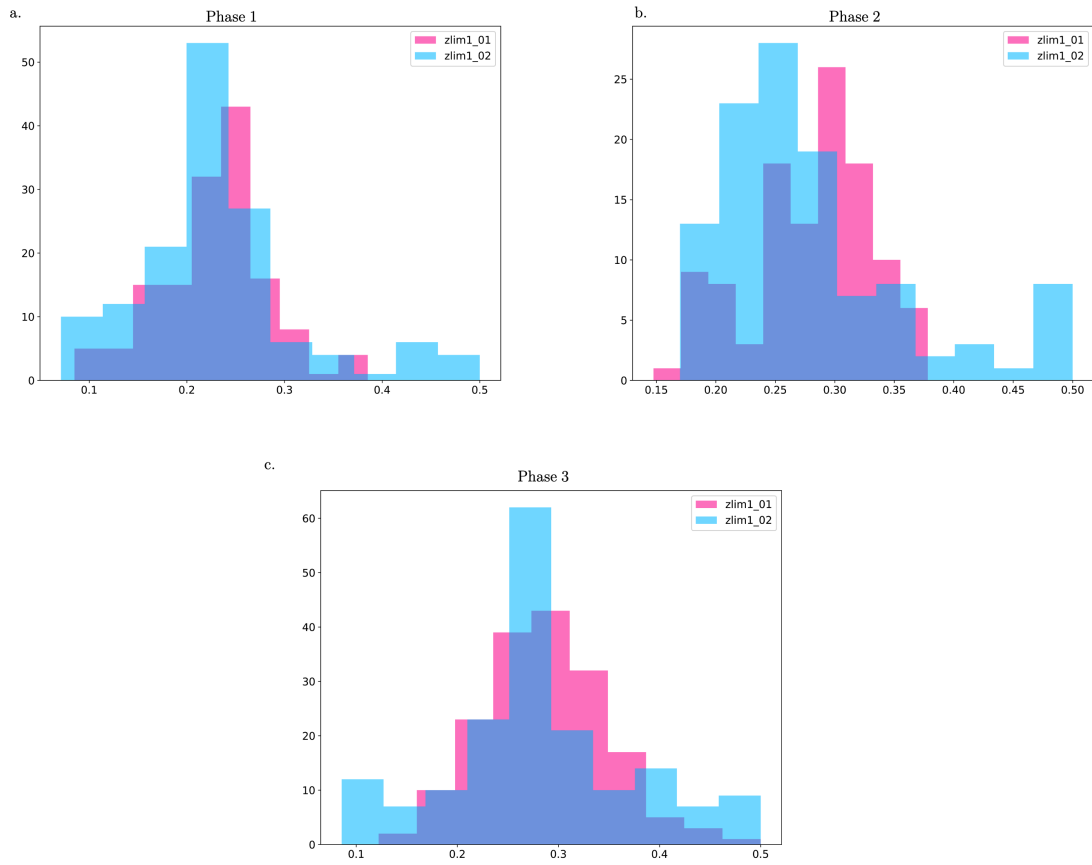


Figure E.22: Histograms of the limit depth 1 – a. Phase 1, b. Phase 2 and c. Phase 3 for the two transects (pink and blue) corresponding to the T-test of Fig. 3.41.a.

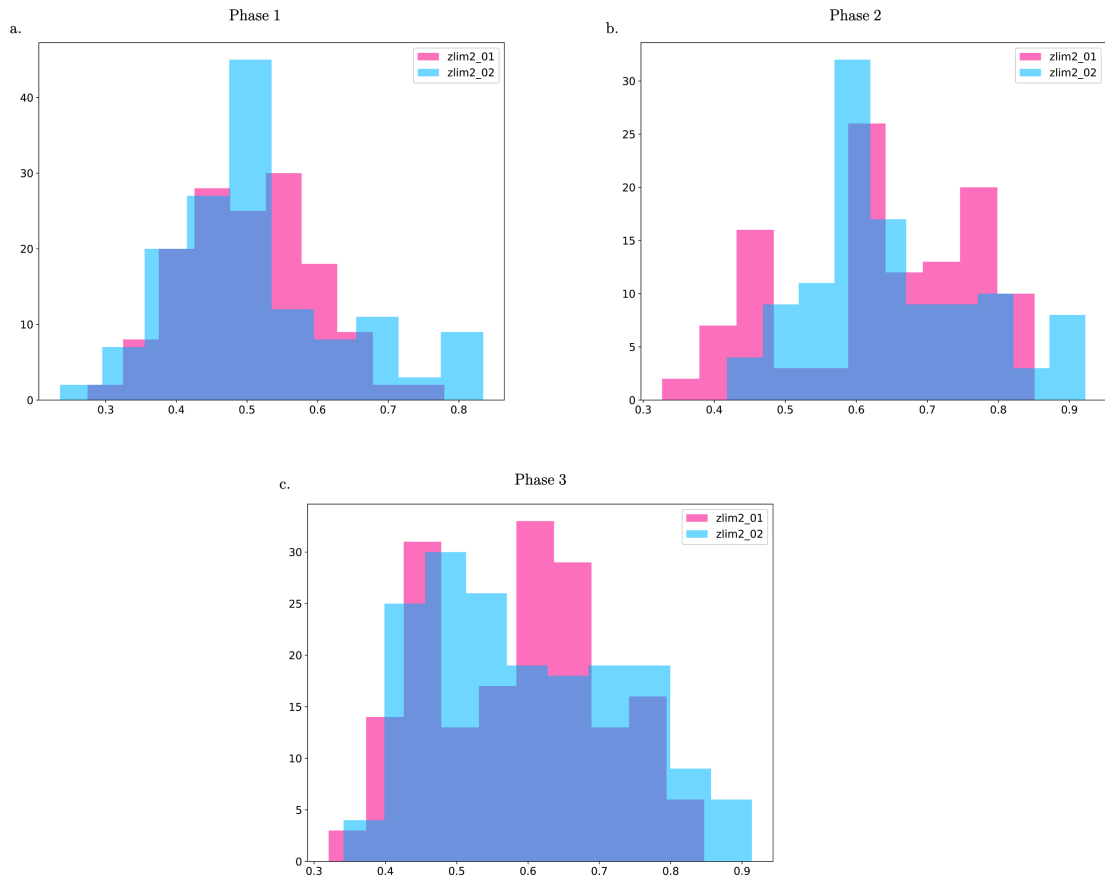


Figure E.23: Histograms of the limit depth 2 – a. Phase 1, b. Phase 2 and c. Phase 3 for the two transects (pink and blue) corresponding to the T-test of Fig. 3.41.b.

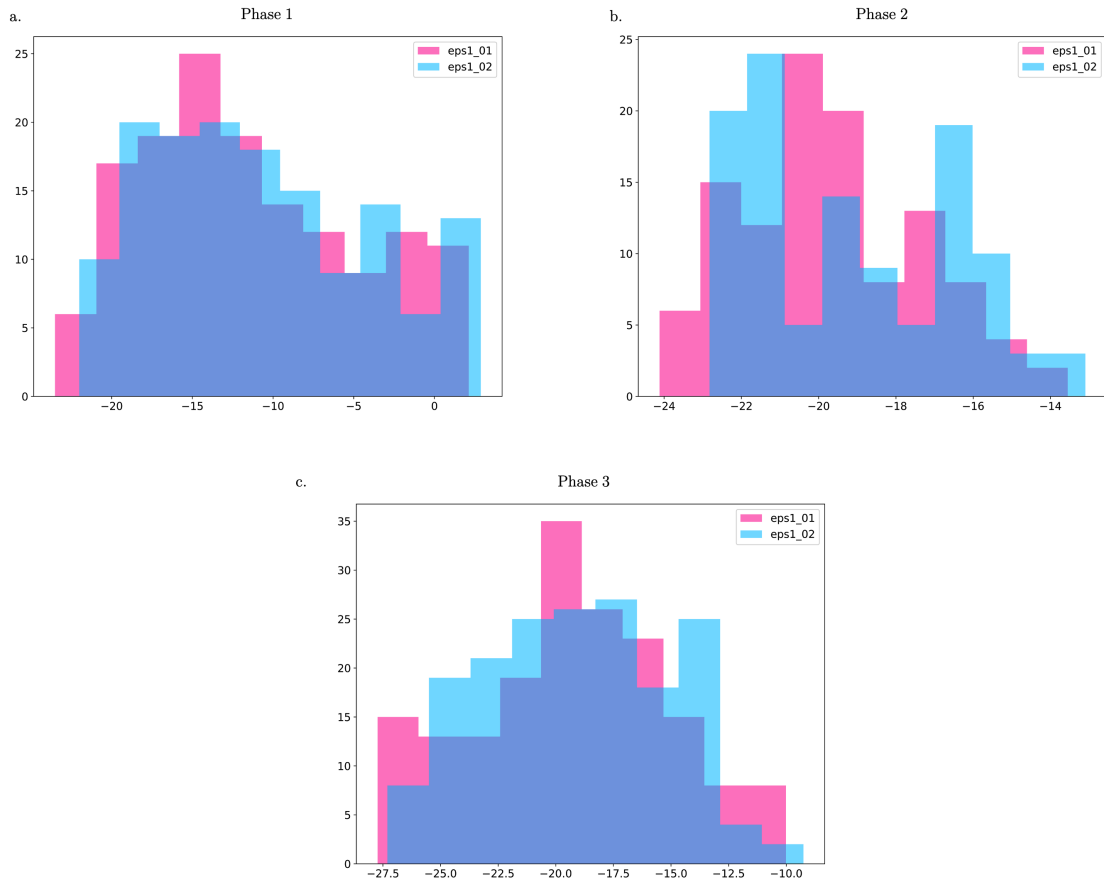


Figure E.24: Histograms of the limit strain 1 – a. Phase 1, b. Phase 2 and c. Phase 3 for the two transects (pink and blue) corresponding to the T-test of Fig. 3.41. c.

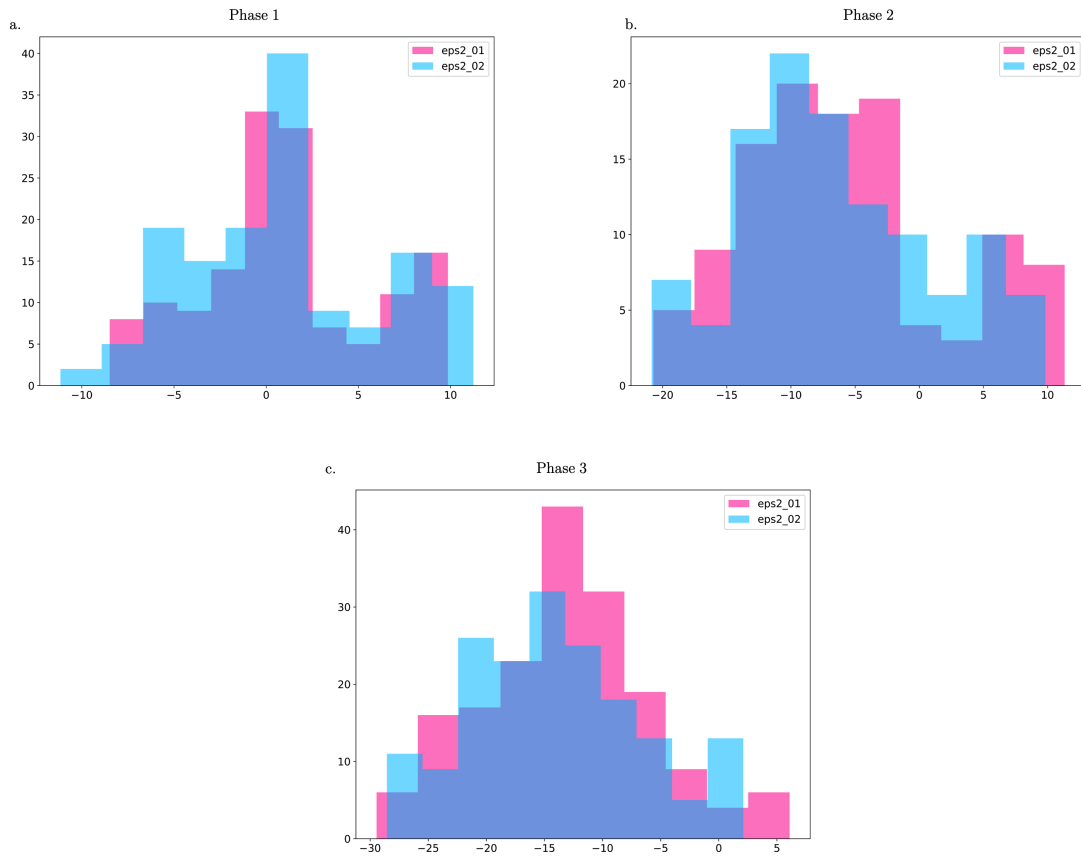


Figure E.25: Histograms of the limit strain 2 – a. Phase 1, b. Phase 2 and c. Phase 3 for the two transects (pink and blue) corresponding to the T-test of Fig. 3.41.d.

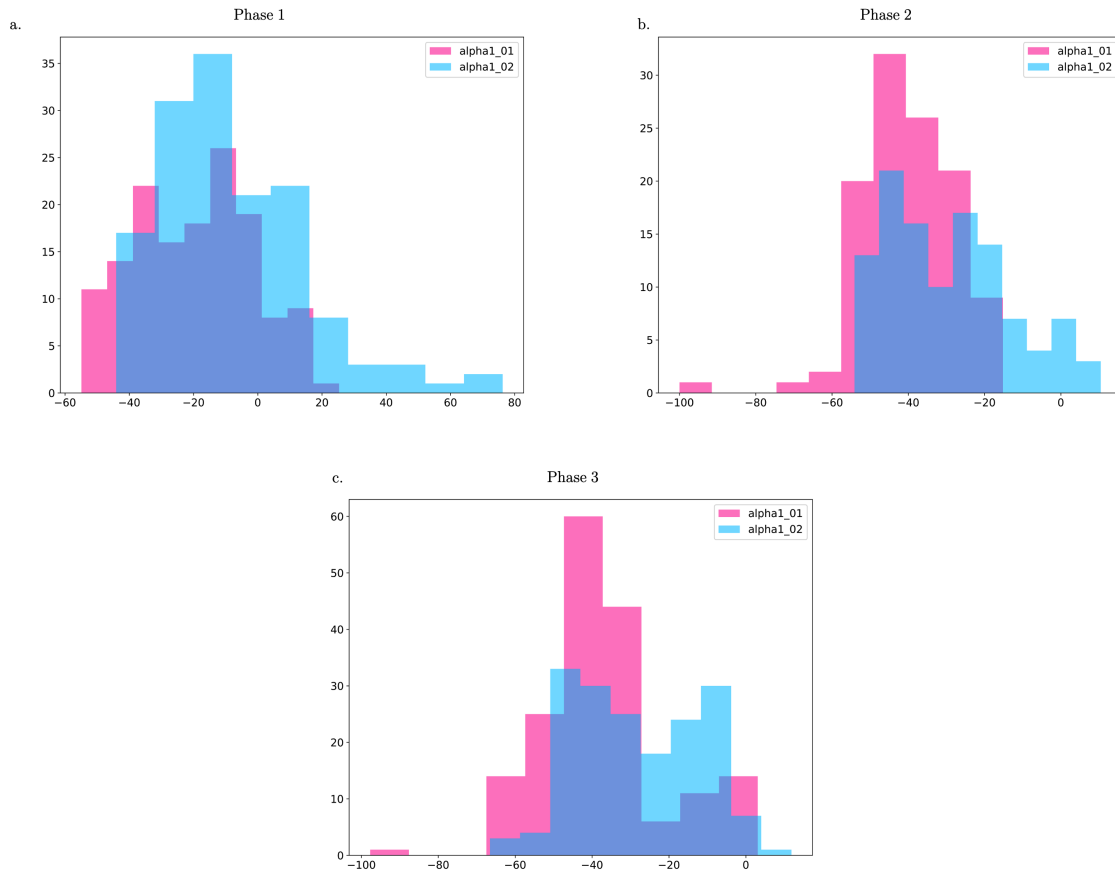


Figure E.26: Histograms of the epithelium slope – a. Phase 1, b. Phase 2 and c. Phase 3 for the two transects (pink and blue) corresponding to the T-test of Fig. 3.41.e.

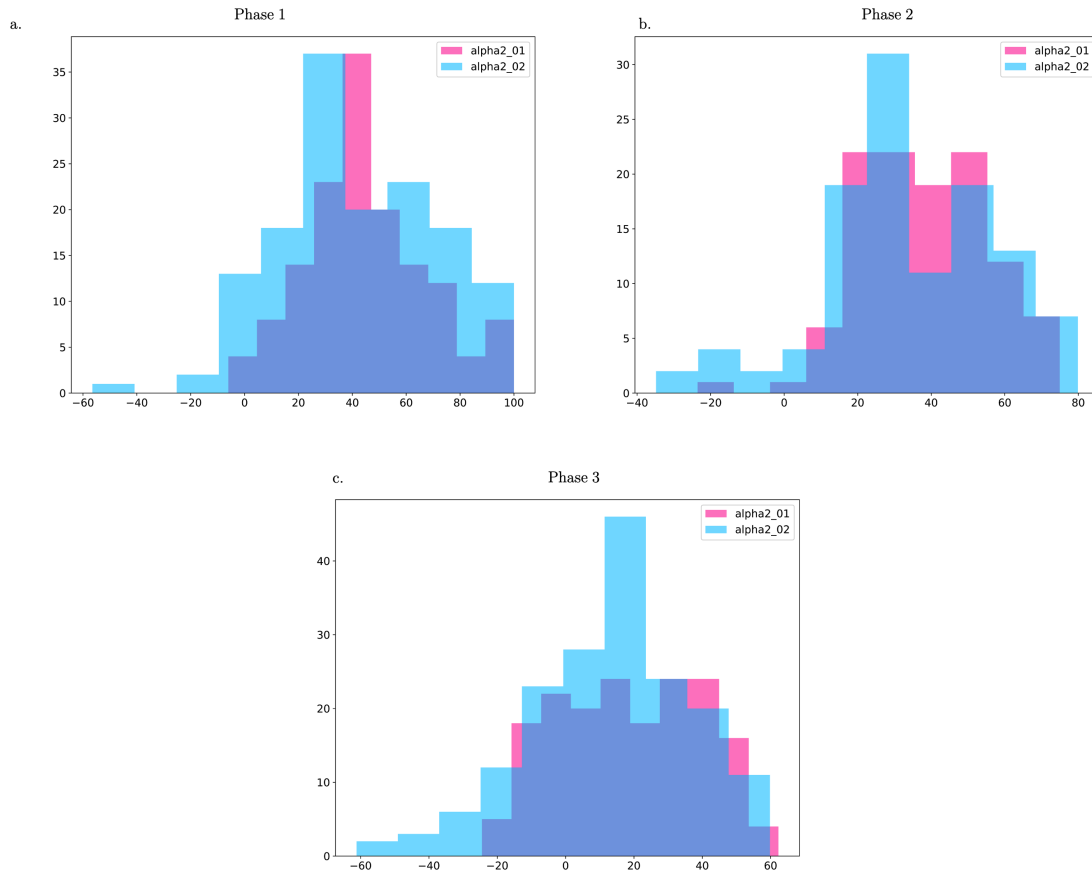


Figure E.27: Histograms of the middle slope – a. Phase 1, b. Phase 2 and c. Phase 3 for the two transects (pink and blue) corresponding to the T-test of Fig. 3.41.f.

E.5.2 Pressure dependence

Here are given the pressure dependence analyses for the other corneas subjected to inflation tests at high pressure considered in Sec. 3.3.4 to complement Fig. 3.42.

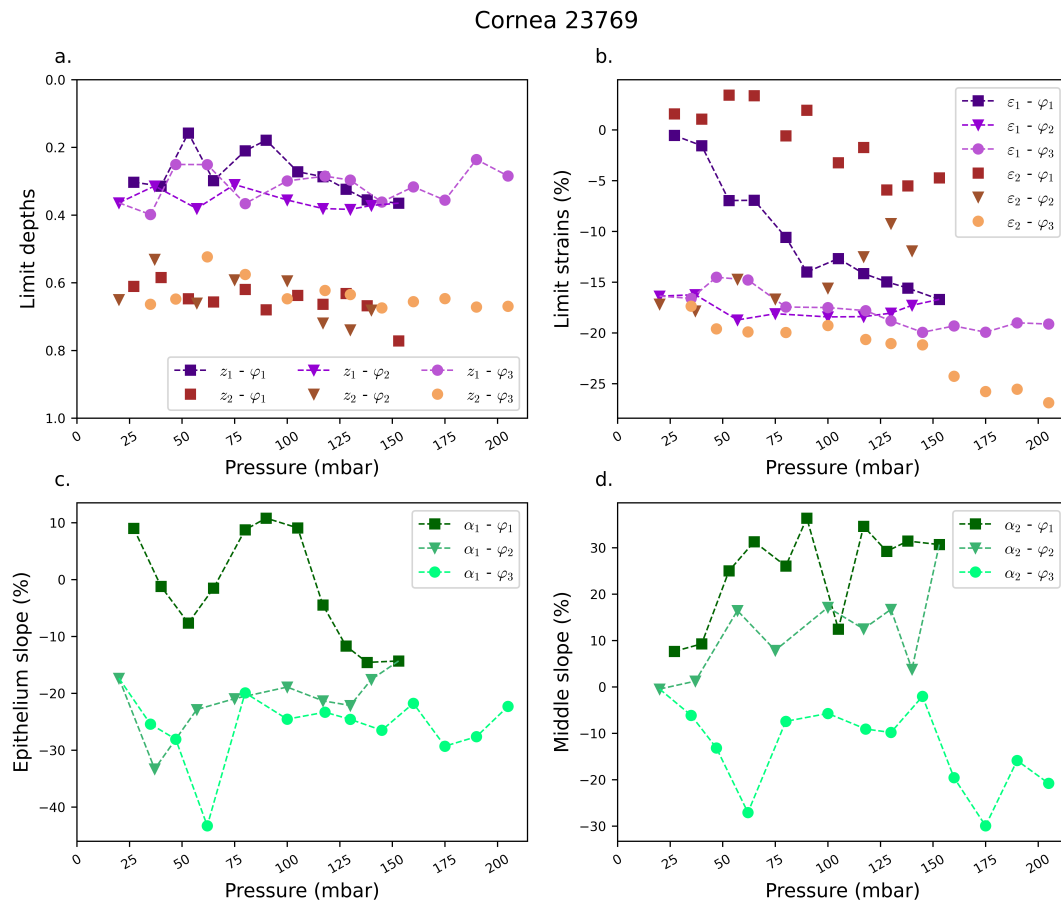


Figure E.28: Pressure dependence of the parameters for inflation test during the three phases (cornea 23769). a. Limit depths with pressure, b. Limit strains with pressure and c. Middle slope with pressure. Dark color squares indicate phase 1, middle color triangles indicate phase 2 and light color circle indicates phase 3.

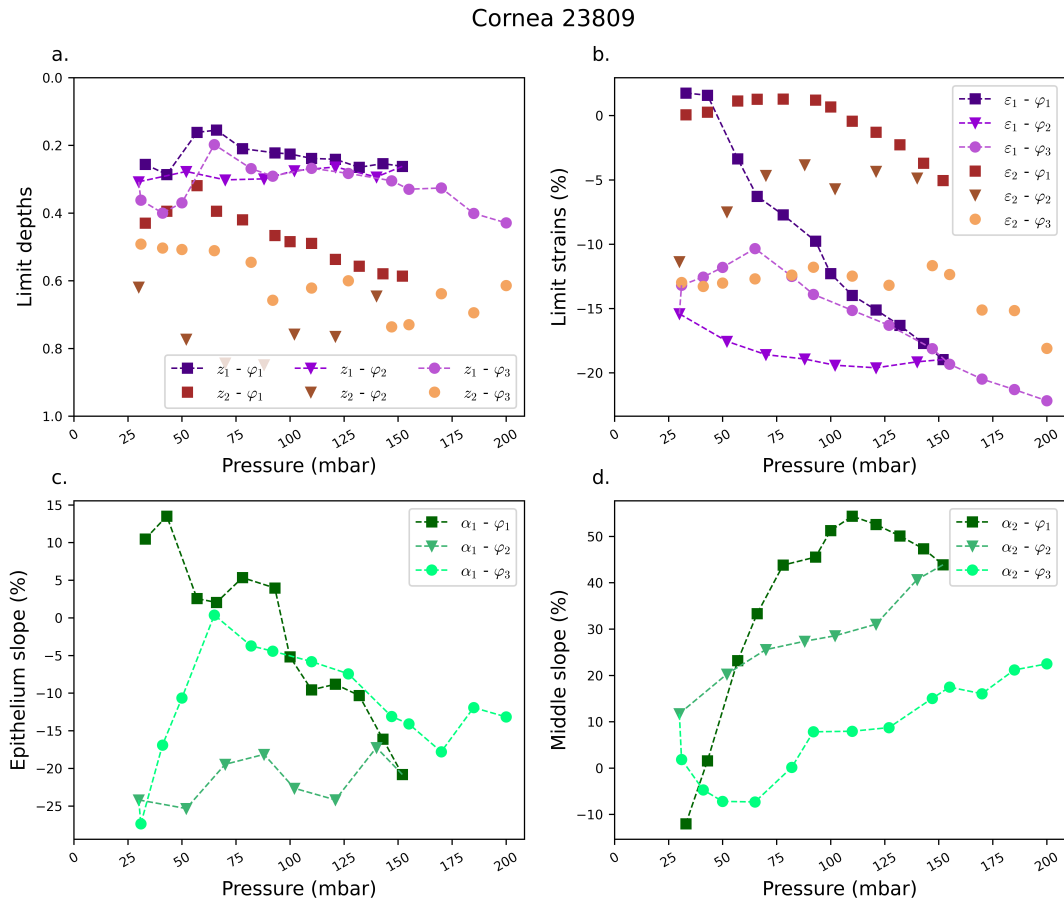


Figure E.29: Pressure dependence of the parameters for inflation test during the three phases (cornea 23809). a. Limit depths with pressure, b. Limit strains with pressure and c. Middle slope with pressure. Dark color squares indicate phase 1, middle color triangles indicate phase 2 and light color circle indicates phase 3.

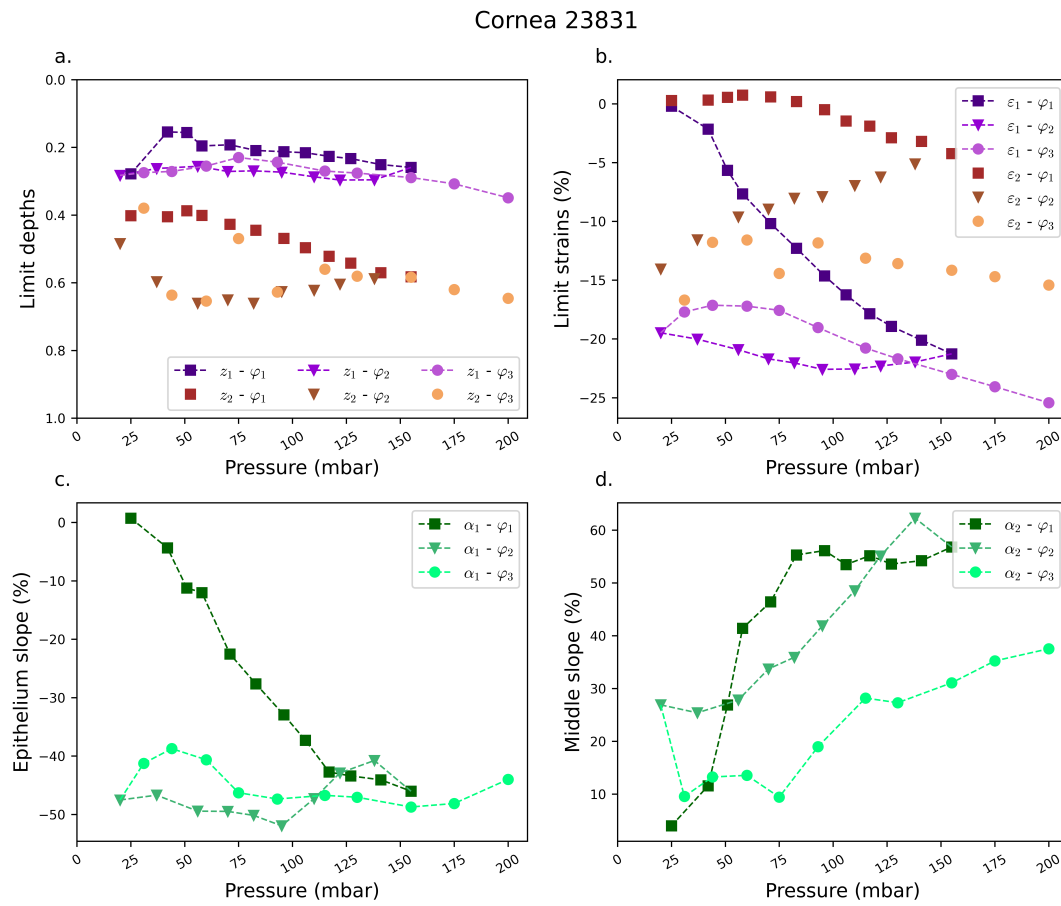


Figure E.30: Pressure dependence of the parameters for inflation test during the three phases (cornea 23831). a. Limit depths with pressure, b. Limit strains with pressure and c. Middle slope with pressure. Dark color squares indicate phase 1, middle color triangles indicate phase 2 and light color circle indicates phase 3.

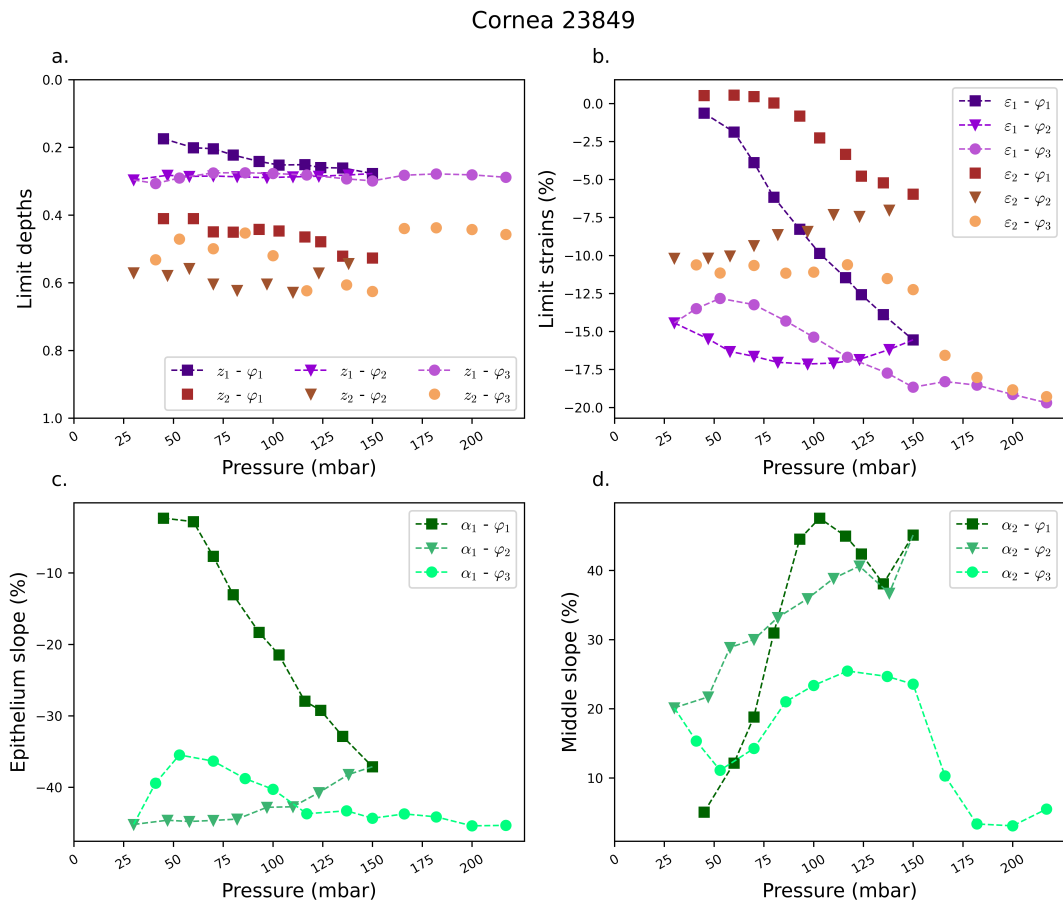


Figure E.31: Pressure dependence of the parameters for inflation test during the three phases (cornea 23849). a. Limit depths with pressure, b. Limit strains with pressure and c. Middle slope with pressure. Dark color squares indicate phase 1, middle color triangles indicate phase 2 and light color circle indicates phase 3.

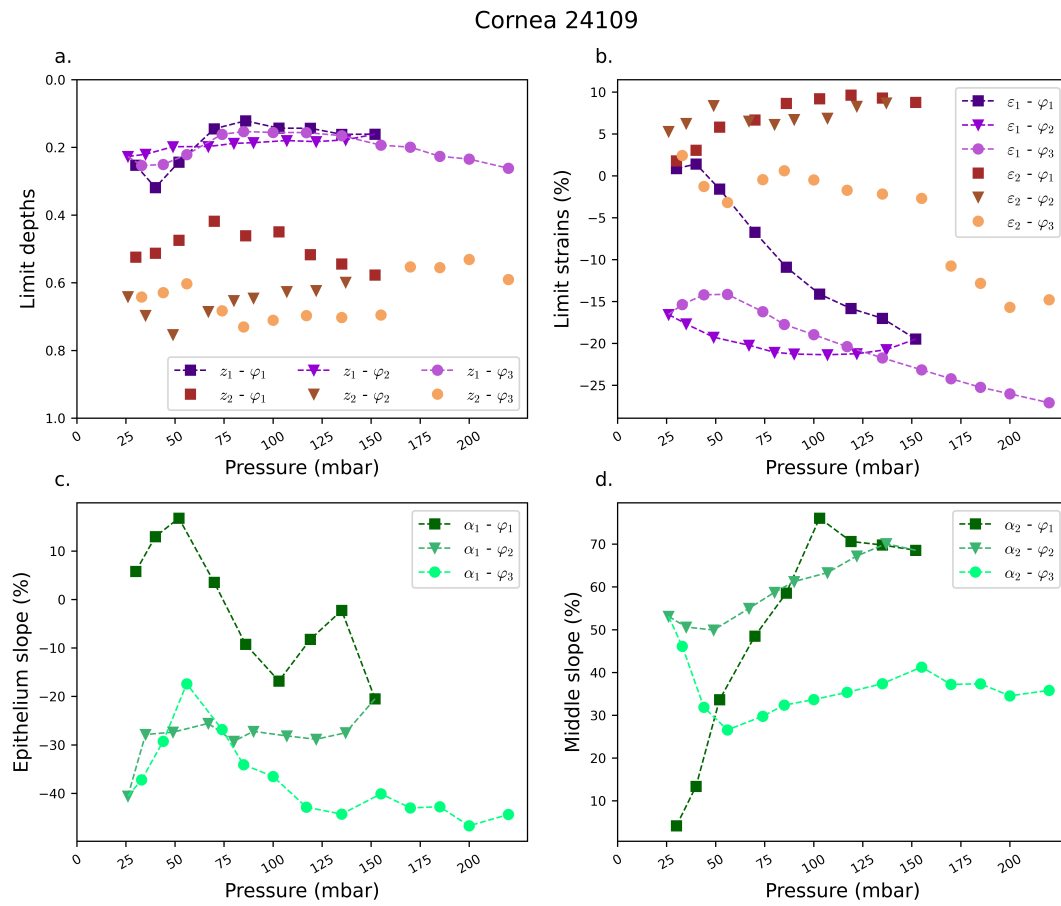


Figure E.32: Pressure dependence of the parameters for inflation test during the three phases (cornea 24109). a. Limit depths with pressure, b. Limit strains with pressure and c. Middle slope with pressure. Dark color squares indicate phase 1, middle color triangles indicate phase 2 and light color circle indicates phase 3.

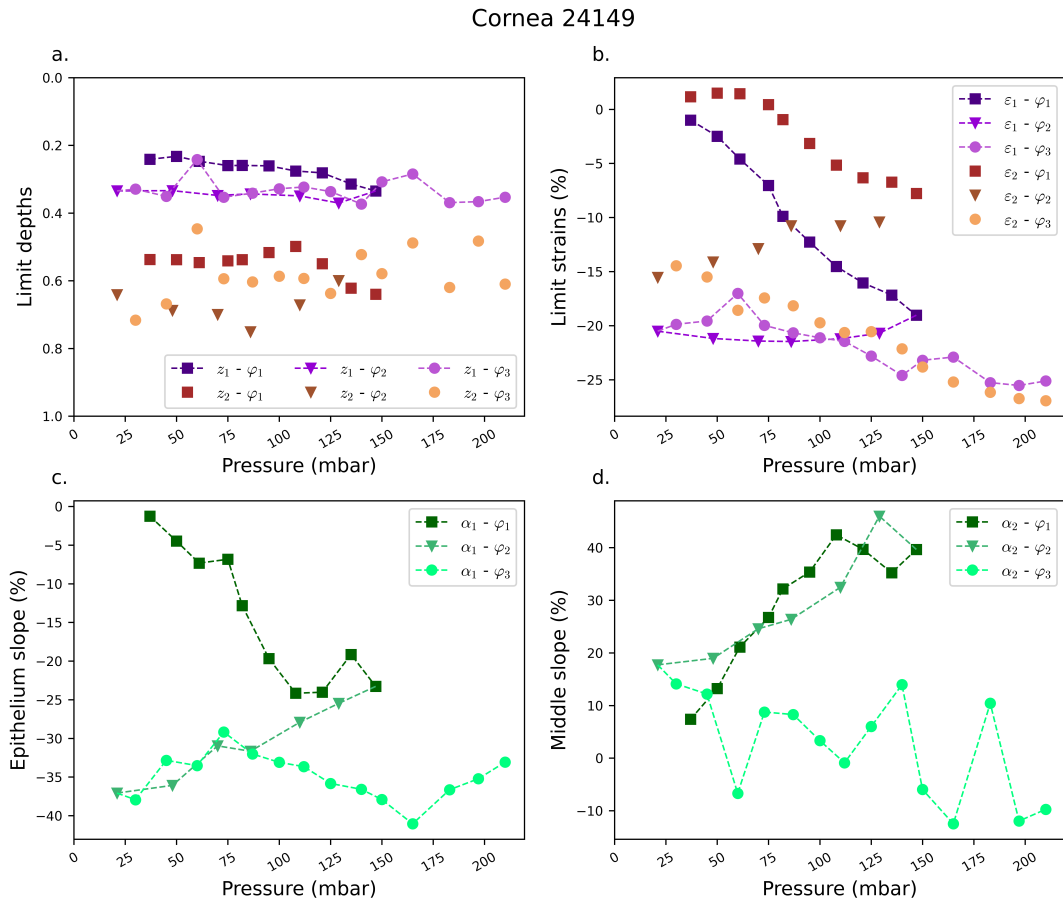


Figure E.33: Pressure dependence of the parameters for inflation test during the three phases (cornea 24149). a. Limit depths with pressure, b. Limit strains with pressure and c. Middle slope with pressure. Dark color squares indicate phase 1, middle color triangles indicate phase 2 and light color circle indicates phase 3.

E.5.3 Pressure - limit strain curves

Here are given the stress strain curves for the other corneas subjected to inflation tests at high pressure considered in Sec. 3.3.4 to complement Fig. 3.43.

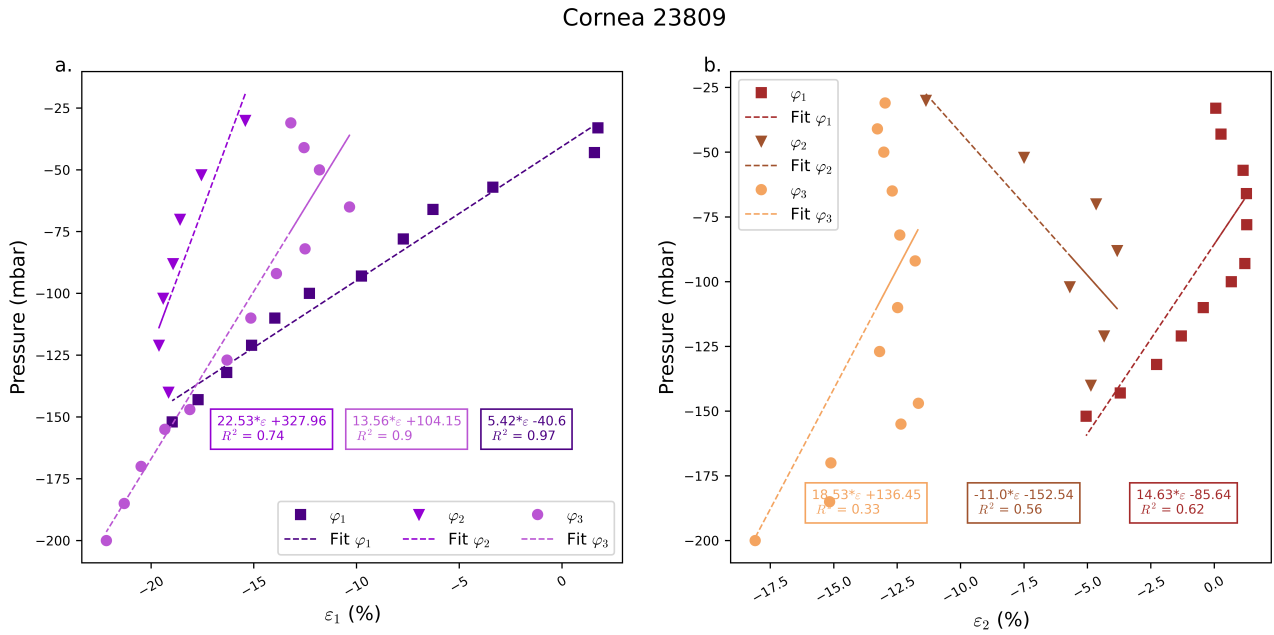


Figure E.34: Pressure VS strain and its linear fit during the three phases of the inflation test (cornea 23809). a. Pressure VS the first limit strain and b. Pressure VS the second limit strain.

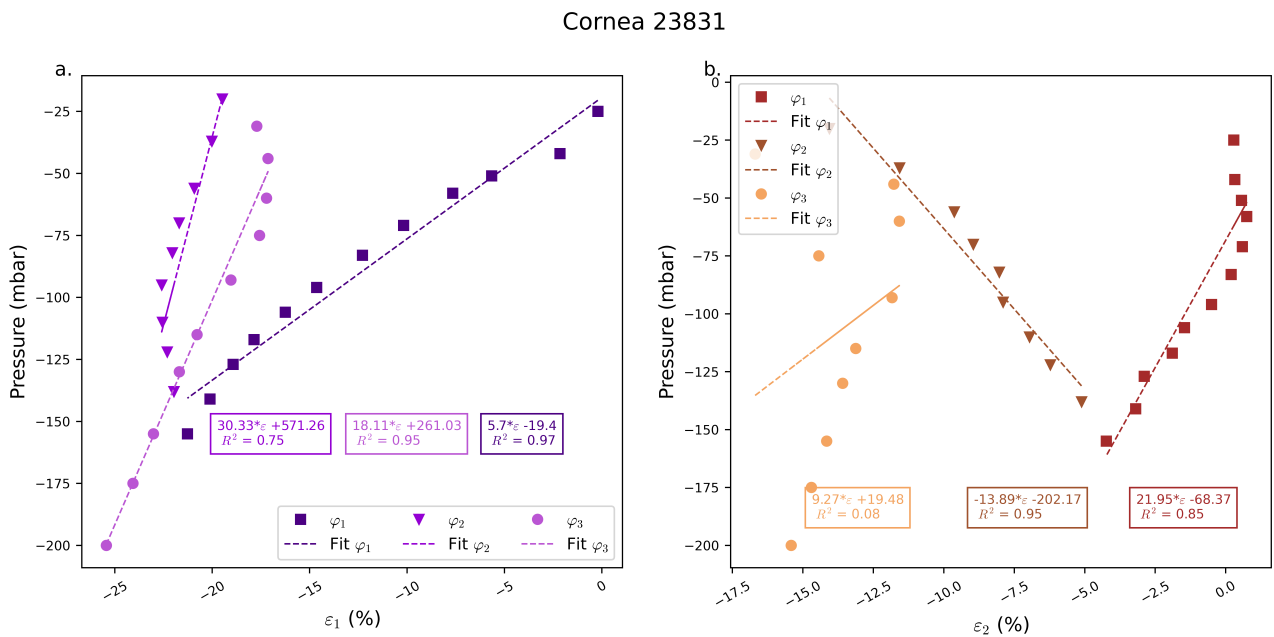


Figure E.35: Pressure VS strain and its linear fit during the three phases of the inflation test (cornea 23831). a. Pressure VS the first limit strain and b. Pressure VS the second limit strain.

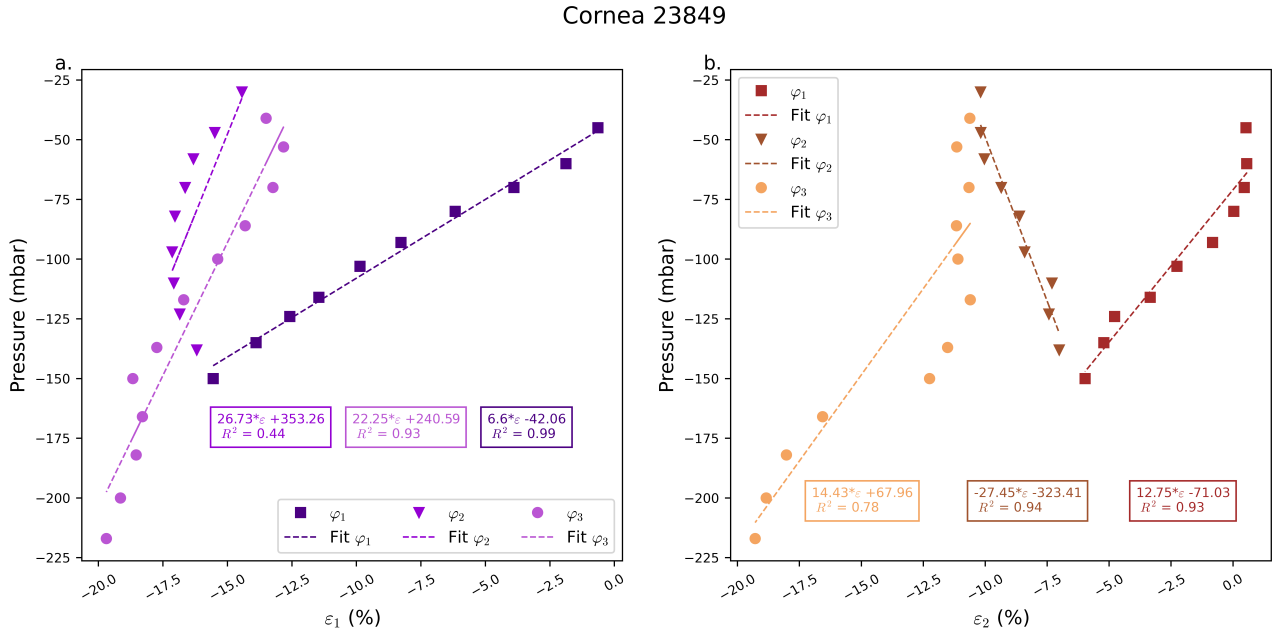


Figure E.36: Pressure VS strain and its linear fit during the three phases of the inflation test (cornea 23849). a. Pressure VS the first limit strain and b. Pressure VS the second limit strain.

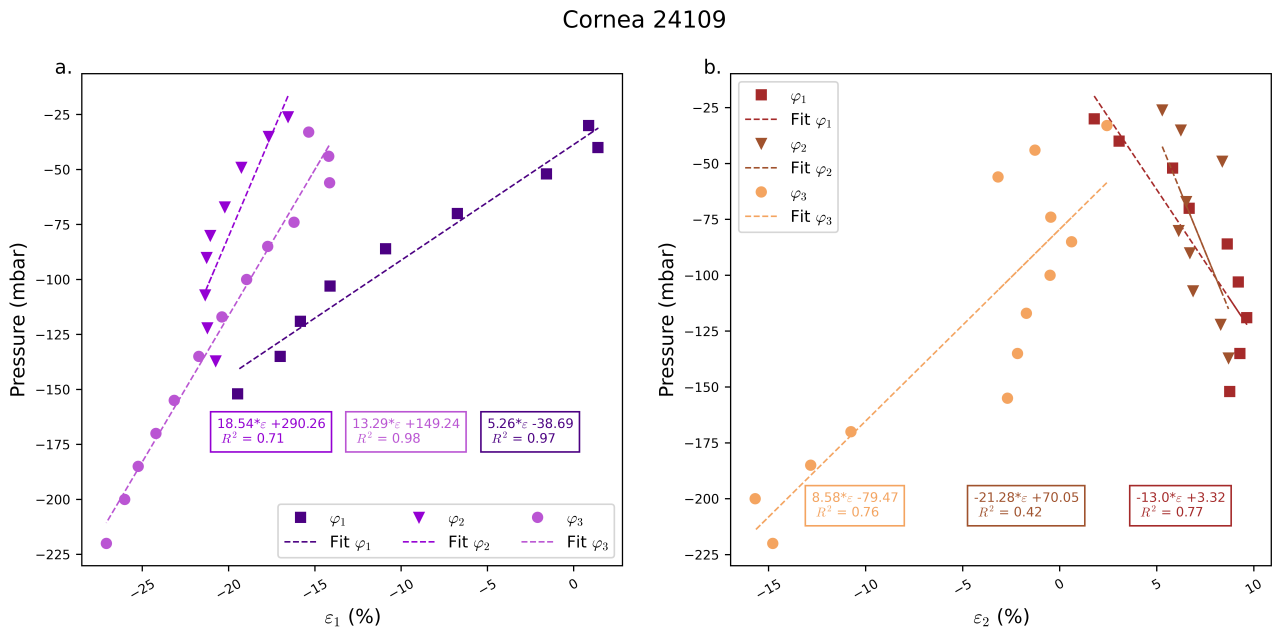


Figure E.37: Pressure VS strain and its linear fit during the three phases of the inflation test (cornea 24109). a. Pressure VS the first limit strain and b. Pressure VS the second limit strain.

Cornea 24149

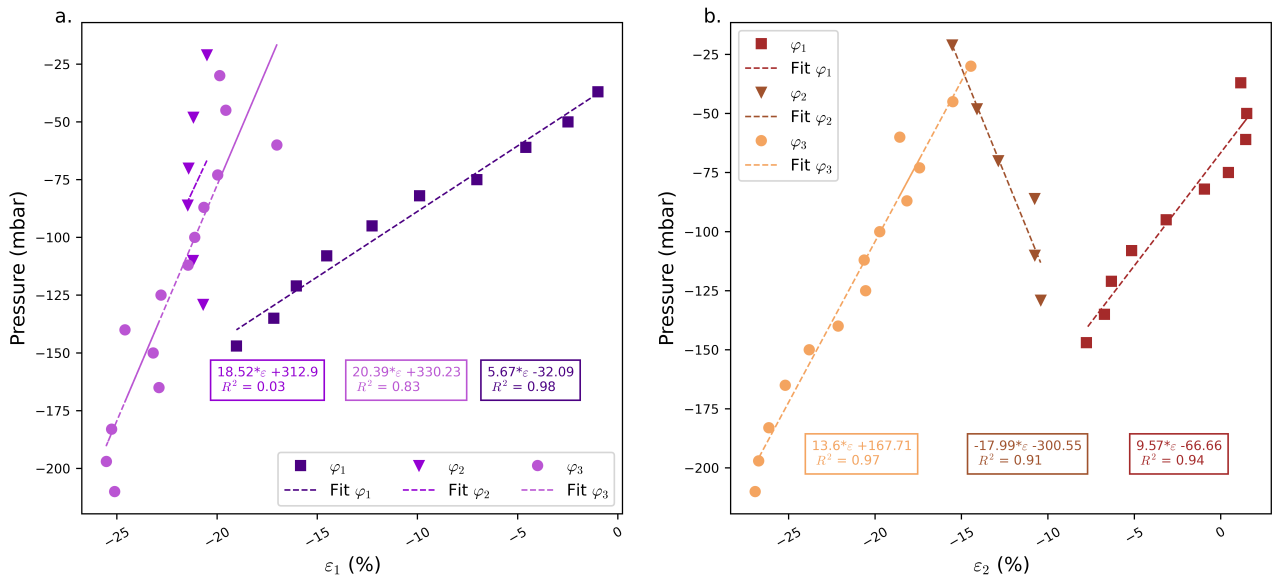


Figure E.38: Pressure VS strain and its linear fit during the three phases of the inflation test (cornea 24149). a. Pressure VS the first limit strain and b. Pressure VS the second limit strain.

Cornea 24167

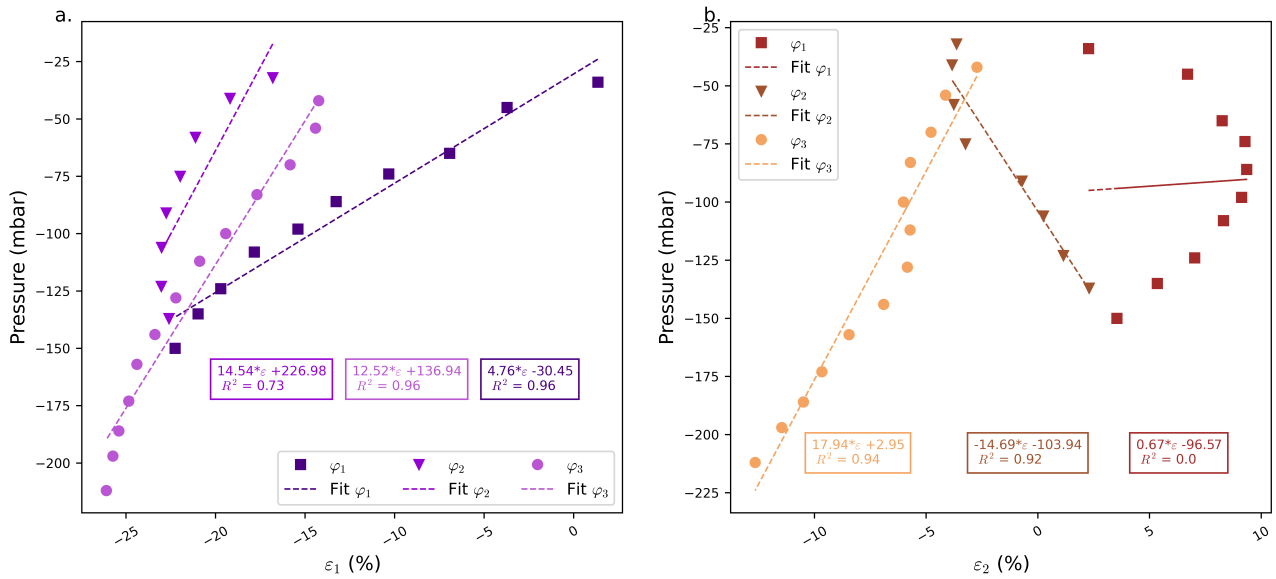


Figure E.39: Pressure VS strain and its linear fit during the three phases of the inflation test (cornea 24167). a. Pressure VS the first limit strain and b. Pressure VS the second limit strain.

Appendix F

Technical developments on the modeling of cornea following the experimental results

F.1 First hypothesis: a simple elastic model of an auxetic material

We first consider a sphere under pressure to model the cornea (Fig. F.1). The intraocular pressure is applied on the posterior surface (internal one) while the anterior surface is kept free of load.

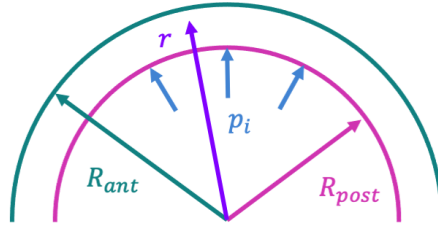


Figure F.1: Schematic view of the considered problem on a sphere. The sphere is subjected to internal pressure p_i on the posterior surface and is free of load on the anterior surface.

F.1.1 Infinitesimal strain tensor

The displacement is radial and considered to depend only on r , so the infinitesimal strain tensor is

$$\underline{\underline{\varepsilon}} = \begin{pmatrix} \frac{du_r}{dr} & 0 & 0 \\ 0 & \frac{u_r}{r} & 0 \\ 0 & 0 & \frac{u_r}{r} \end{pmatrix}, \quad (\text{F.1})$$

while its trace is defined as

$$tr(\underline{\underline{\varepsilon}}) = \frac{du_r}{dr} + 2\frac{u_r}{r} = \frac{1}{r^2} \frac{d(r^2 u_r)}{dr}. \quad (\text{F.2})$$

The spatial derivative of this trace is

$$\frac{d(\text{tr}(\underline{\underline{\varepsilon}}))}{dr} = \frac{d^2 u_r}{dr^2} + \frac{2}{r} \frac{du_r}{dr} - \frac{2u_r}{r^2}, \quad (\text{F.3})$$

and the Jacobian of the transformation is at first order

$$J = 1 + \text{tr}(\underline{\underline{\varepsilon}}) = 1 + \frac{du_r}{dr} + 2\frac{u_r}{r} = 1 + \frac{1}{r^2} \frac{d(r^2 u_r)}{dr}. \quad (\text{F.4})$$

F.1.2 Boundary conditions

The boundary conditions represent the internal pressure applied on posterior face and the absence of load on the anterior surface:

$$\sigma_{rr}(R_{ant}) = \sigma_{r\theta}(R_{ant}) = \sigma_{r\phi}(R_{ant}) = 0, \quad \sigma_{rr}(R_{post}) = -p_i \quad \text{and} \quad \sigma_{r\theta}(R_{post}) = \sigma_{r\phi}(R_{post}) = 0. \quad (\text{F.5})$$

F.1.3 Equilibrium

For an isotropic loading on an isotropic material, the equilibrium equations when written in spherical coordinates reduce to

$$\begin{cases} \frac{d\sigma_{rr}}{dr} + \frac{1}{r}(2\sigma_{rr} - \sigma_{\theta\theta} - \sigma_{\phi\phi}) = 0 \\ \frac{1}{r}(\sigma_{\theta\theta} - \sigma_{\phi\phi}) = 0 \end{cases} \quad (\text{F.6})$$

which yields

$$\frac{d\sigma_{rr}}{dr} + \frac{2}{r}(\sigma_{rr} - \sigma_{\theta\theta}) = 0. \quad (\text{F.7})$$

F.1.4 Constitutive law and computation of the strain

The constitutive law considered is the simplest one: an elastic material is considered with an elastic modulus E and a Poisson's ratio ν .

$$\underline{\underline{\sigma}} = \frac{E}{1+\nu}(\underline{\underline{\varepsilon}} + \frac{\nu}{1-2\nu}\text{tr}(\underline{\underline{\varepsilon}})\underline{\underline{1}}). \quad (\text{F.8})$$

Using the above expression of the strain tensor, we get

$$\begin{cases} \sigma_{rr} = \frac{E}{1+\nu} \left(\frac{du_r}{dr} + \frac{\nu}{1-2\nu} \text{tr}(\underline{\underline{\varepsilon}}) \right) \\ \sigma_{\theta\theta} = \frac{E}{1+\nu} \left(\frac{u_r}{r} + \frac{\nu}{1-2\nu} \text{tr}(\underline{\underline{\varepsilon}}) \right) \\ \sigma_{\phi\phi} = \sigma_{\theta\theta} \end{cases} \quad (\text{F.9})$$

We then compute the difference $\sigma_{rr} - \sigma_{\theta\theta}$

$$\sigma_{rr} - \sigma_{\theta\theta} = \frac{E}{1+\nu} \left(\frac{du_r}{dr} - \frac{u_r}{r} \right),$$

and the derivative of σ_{rr}

$$\frac{d\sigma_{rr}}{dr} = \frac{E}{1+\nu} \left(\frac{d^2u_r}{dr^2} + \frac{\nu}{1-2\nu} \frac{d(\text{tr}(\underline{\underline{\varepsilon}}))}{dr} \right).$$

We than look at equation (F.7):

$$\frac{E}{1+\nu} \left(\frac{d^2u_r}{dr^2} + \frac{\nu}{1-2\nu} \frac{d(\text{tr}(\underline{\underline{\varepsilon}}))}{dr} \right) + \frac{2}{r} \left(\frac{E}{1+\nu} \left(\frac{du_r}{dr} - \frac{u_r}{r} \right) \right) = 0$$

Since $\frac{d^2u_r}{dr^2} + \frac{2}{r} \frac{du_r}{dr} - \frac{2u_r}{r^2} = \frac{d(\text{tr}(\underline{\underline{\varepsilon}}))}{dr}$, we get that this equation reduces to

$$\frac{E(1-\nu)}{(1+\nu)(1-2\nu)} \frac{d(\text{tr}(\underline{\underline{\varepsilon}}))}{dr} = 0.$$

We define : $K_\nu = \frac{(1-\nu)}{(1+\nu)(1-2\nu)}$, and we have then:

$$K_\nu E \frac{d(\text{tr}(\underline{\underline{\varepsilon}}))}{dr} = 0 \Leftrightarrow \frac{d(\text{tr}(\underline{\underline{\varepsilon}}))}{dr} = 0. \quad (\text{F.10})$$

Integrating Eq. (F.10) gives

$$\text{tr}(\underline{\underline{\varepsilon}}) = K_1 \Leftrightarrow \frac{1}{r^2} \frac{d(r^2 u_r)}{dr} = K_1 \Leftrightarrow \frac{d(r^2 u_r)}{dr} = K_1 r^2 \Leftrightarrow r^2 u_r = K_1 \frac{r^3}{3} + K_2 \quad (\text{F.11})$$

that is

$$\begin{cases} u_r = K_1 \frac{r}{3} + \frac{K_2}{r^2} \\ \varepsilon_{rr} = \frac{K_1}{3} - \frac{2K_2}{r^3}, \quad \text{tr}(\underline{\underline{\varepsilon}}) = K_1 \end{cases} \quad (\text{F.12})$$

Applying the boundary conditions gives

$$\begin{cases} \sigma_{rr}(R_{post}) = -p_i \\ \sigma_{rr}(R_{ant}) = 0 \end{cases} \Leftrightarrow \begin{cases} \frac{E}{1+\nu} \left[\varepsilon_{rr}(R_{post}) + \frac{\nu}{1-2\nu} \text{tr}(\underline{\underline{\varepsilon}}(R_{post})) \right] = -p_i \\ \frac{E}{1+\nu} \left[\varepsilon_{rr}(R_{ant}) + \frac{\nu}{1-2\nu} \text{tr}(\underline{\underline{\varepsilon}}(R_{post})) \right] = 0 \end{cases} \quad (\text{F.13})$$

$$\Leftrightarrow \begin{cases} \frac{E}{1+\nu} \left(\frac{K_1}{3} - \frac{2K_2}{R_{post}^3} + \frac{\nu}{1-2\nu} K_1 \right) = -p_i \\ \frac{E}{1+\nu} \left(\frac{K_1}{3} - \frac{2K_2}{R_{ant}^3} + \frac{\nu}{1-2\nu} K_1 \right) = 0 \end{cases} \Leftrightarrow \begin{cases} \left(\frac{1}{3} + \frac{\nu}{1-2\nu} \right) K_1 - \frac{2}{R_{post}^3} K_2 = -\frac{1+\nu}{E} p_i \\ \left(\frac{1}{3} + \frac{\nu}{1-2\nu} \right) K_1 - \frac{2}{R_{ant}^3} K_2 = 0 \end{cases} \quad (\text{F.14})$$

$$\Leftrightarrow \begin{cases} \frac{K_1}{3} = \frac{1-2\nu}{E} p_i \frac{R_{post}^3}{R_{ant}^3 - R_{post}^3} \\ 2K_2 = \frac{1+\nu}{E} p_i \frac{R_{ant}^3 R_{post}^3}{R_{ant}^3 - R_{post}^3} \end{cases} \quad (\text{F.15})$$

$$\begin{cases} u_r = \frac{(1-2\nu)}{E} p_i \frac{R_{post}^3}{R_{ant}^3 - R_{post}^3} r + \frac{1+\nu}{E} p_i \frac{R_{ant}^3 R_{post}^3}{2(R_{ant}^3 - R_{post}^3) r^2} \\ \varepsilon_{rr} = \frac{(1-2\nu)}{E} + p_i \frac{R_{post}^3}{R_{ant}^3 - R_{post}^3} - \frac{1+\nu}{E} p_i \frac{R_{ant}^3 R_{post}^3}{(R_{ant}^3 - R_{post}^3) r^3} \end{cases} \quad (\text{F.16})$$

F.2 Second hypothesis: existence of an osmotic pressure

The second hypothesis we made was to take into account the exchange of water that can go through the endothelium. We then introduced a term of osmotic pressure in the model. As the analytical computation on a sphere leads to a second order equation with non constant coefficients, we use the 1D model described Fig. F.2 with the following constitutive law:

$$\underline{\underline{\sigma}} = \frac{E}{1+\nu} (\underline{\underline{\varepsilon}} + \frac{\nu}{1-2\nu} \text{tr}(\underline{\underline{\varepsilon}}) \underline{\underline{1}}) - (\mu + \pi(J)) \underline{\underline{1}}. \quad (\text{F.17})$$

yielding in particular

$$\sigma_{zz} = \frac{E}{1+\nu} \left(\frac{du_z}{dz} + \frac{\nu}{1-2\nu} \text{tr}(\underline{\underline{\varepsilon}}) \right) - (\mu + \pi(J)) \quad (\text{F.18})$$

with μ the chemical potential, $\pi(J)$ an osmotic pressure term defined in Eq. (F.19) [163]:

$$\pi(J) = \beta_0 \left(\frac{1 - \phi_s^{ref}}{J - \phi_s^{ref}} \right)^{\beta_1}, \quad (\text{F.19})$$

where β_0 is the reference osmotic pressure, ϕ_s^{ref} the solid volume fraction per unit reference volume, β_1 an exponent governing the non-linearity of the curve [43]. Defining the coefficient K_{osm} as

$$K_{osm} = \frac{\beta_0 \beta_1}{1 - \phi_s^{ref}}, \quad (\text{F.20})$$

the osmotic pressure function can be linearized under the infinitesimal strain assumption and becomes $\pi(z)$

$$\pi(z) \approx \beta_0 - K_{osm} \text{tr}(\underline{\underline{\varepsilon}}). \quad (\text{F.21})$$

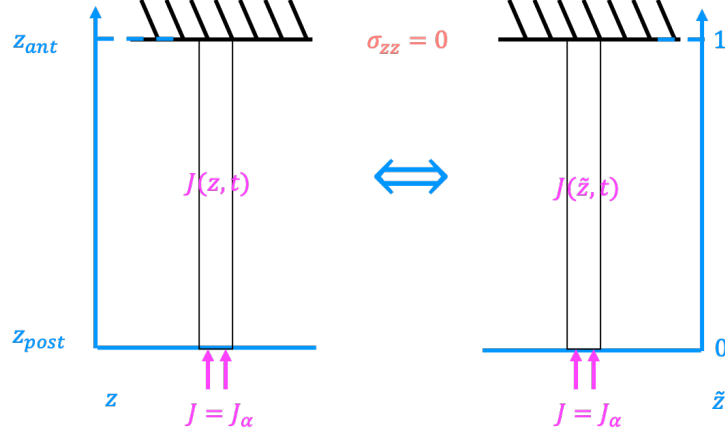


Figure F.2: Problem solved on the 1D domain

We then compute the derivative of σ_{zz}

$$\frac{d\sigma_{zz}}{dz} = \frac{E}{1+\nu} \left(\frac{d^2 u_z}{dz^2} + \frac{\nu}{1-2\nu} \frac{d(\text{tr}(\underline{\underline{\varepsilon}}))}{dz} \right) - \frac{d\mu}{dz} - \frac{d\pi}{dz} = \frac{E}{1+\nu} \left(\frac{d^2 u_z}{dz^2} + \frac{\nu}{1-2\nu} \frac{d(\text{tr}(\underline{\underline{\varepsilon}}))}{dz} \right) - \frac{d\mu}{dz} + K_{osm} \frac{d(\text{tr}(\underline{\underline{\varepsilon}}))}{dz}$$

Assuming a purely 1D motion $\underline{u} = u_z \underline{e}_z$ and setting $K_\nu = \frac{(1-\nu)}{(1+\nu)(1-2\nu)}$, the equilibrium equation becomes

$$(E.K_\nu + K_{osm}) \frac{\partial^2 u_z}{\partial z^2} - \frac{\partial \mu}{\partial z} = 0 \Leftrightarrow \frac{\partial \mu}{\partial z} = (E.K_\nu + K_{osm}) \frac{\partial^2 u_z}{\partial z^2}$$

or equivalently

$$\frac{\partial \mu}{\partial z} = (E.K_\nu + K_{osm}) \frac{\partial^2 u_z}{\partial z^2} = (E.K_\nu + K_{osm}) \frac{\partial \text{tr}(\underline{\underline{\varepsilon}})}{\partial z}.$$

Using a simplified version of the model described in [163] to relate the Jacobian to the chemical potential:

$$\frac{\partial J}{\partial t} = \text{div}(K \text{grad}(\mu)) \Leftrightarrow \frac{\partial J}{\partial t} = K \frac{\partial^2 \mu}{\partial z^2} \quad (\text{F.22})$$

and under the small strain assumption $J \simeq \text{tr}(\underline{\underline{\varepsilon}})$, the equilibrium equation can be written solely in term of Jacobian:

$$\frac{\partial J}{\partial t} = K(E.K_\nu + K_{osm}) \frac{\partial^2 J}{\partial z^2} = D \frac{\partial^2 J}{\partial z^2}. \quad (\text{F.23})$$

The resolution of this diffusion equation is carried out in App. F.2.1 and gives for a finite medium and a source term J_α :

$$J(\tilde{z}, t) \simeq J_\alpha + \sum_{k \in \mathbb{N}^*} B_k \sin\left(\frac{k\pi}{2} \tilde{z}\right) e^{-D\left(\frac{k\pi}{2}\right)^2 t} \quad \text{with} \quad B_k = \frac{2(J_\alpha - 1)}{k\pi} ((-1)^k - 1) \quad (\text{F.24})$$

F.2.1 Form of $J(z, t)$

F.2.1.a Boundary and initial conditions

The initial condition should reflect that the cornea has a constant volume as long as it is not subjected to the fluid, so that $J(\tilde{z}, 0) = 1$. The boundary conditions should reflect (i) that the cornea is subjected to a flux of fluid going through the endothelium such that $J(0, t) = J_\alpha$ and (ii) that the cornea is not

subjected to any stress at the epithelium barrier, such that $\sigma_{zz}(1, t) = 0$ or $\sigma_{zz}(\infty, t) = 0$ (considering an finite or infinite medium), leading to $\frac{\partial J}{\partial \tilde{z}}(1, t) = 0$ or $\frac{\partial J}{\partial \tilde{z}}(\infty, t) = 0$. The full problem considered is then

$$\begin{cases} \frac{\partial J(\tilde{z}, t)}{\partial t} - D \frac{\partial^2 J(\tilde{z}, t)}{\partial \tilde{z}^2} = 0 \\ J(\tilde{z}, 0) = 1 \\ J(0, t) = J_\alpha \quad \text{and} \quad \frac{\partial J}{\partial \tilde{z}}(1, t) = 0 \quad \text{or} \quad \frac{\partial J}{\partial \tilde{z}}(\infty, t) = 0 \end{cases} \quad (\text{F.25})$$

F.2.1.b Infinite thickness of the cornea

Assuming here that the cornea has an infinite thickness, i.e. the bar has an infinite length. This hypothesis could be valid if the thickness is large with respect to the radius of curvature. The system to solve is then:

$$\begin{cases} \frac{\partial J(\tilde{z}, t)}{\partial t} - D \frac{\partial^2 J(\tilde{z}, t)}{\partial \tilde{z}^2} = 0 \\ J(\tilde{z}, 0) = 1 \\ J(0, t) = J_\alpha \quad \text{and} \quad \frac{\partial J}{\partial \tilde{z}}(\infty, t) = 0 \end{cases} \quad (\text{F.26})$$

Searching J with the following form:

$$J(\tilde{z}, t) = f(\eta) \quad \text{with} \quad \eta = \frac{\tilde{z}}{2\sqrt{Dt}} \quad (\text{F.27})$$

The derivatives with respect to time and space are then:

$$\begin{cases} \frac{\partial J(\tilde{z}, t)}{\partial t} = \frac{\partial f}{\partial t} = \frac{\partial f}{\partial \eta} \frac{\partial \eta}{\partial t} = \frac{\partial f}{\partial \eta} \frac{\tilde{z}}{2\sqrt{Dt}} \frac{-1}{2t\sqrt{t}} = -\eta \frac{1}{2t} \frac{\partial f}{\partial \eta} \\ \frac{\partial J(\tilde{z}, t)}{\partial \tilde{z}} = \frac{\partial f}{\partial \tilde{z}} = \frac{\partial f}{\partial \eta} \frac{\partial \eta}{\partial \tilde{z}} = \frac{1}{2\sqrt{Dt}} \frac{\partial f}{\partial \eta} \\ \frac{\partial^2 J(\tilde{z}, t)}{\partial \tilde{z}^2} = \frac{\partial^2 f}{\partial \tilde{z}^2} = \frac{\partial}{\partial \eta} \left(\frac{\partial f}{\partial \tilde{z}} \right) \frac{\partial \eta}{\partial \tilde{z}} = \frac{\partial}{\partial \eta} \left(\frac{1}{2\sqrt{Dt}} \frac{\partial f}{\partial \eta} \right) \frac{1}{2\sqrt{Dt}} = \frac{1}{4Dt} \frac{\partial^2 f}{\partial \eta^2} \end{cases} \quad (\text{F.28})$$

This function f verifies the following Ordinary Differential Equation:

$$\frac{d^2 f}{d\eta^2} + 2\eta \frac{df}{d\eta} = 0 \quad (\text{F.29})$$

Integrating once, the form of the derivative $\frac{df}{d\eta}$ is:

$$\frac{df}{d\eta} = Ae^{-\eta^2}. \quad (\text{F.30})$$

Integrating twice, the form of function $f(\eta)$ is:

$$f(\eta) = B + A \int_0^\eta e^{-s^2} ds \quad (\text{F.31})$$

making appear two integration constants A and B , which will be determined using the limit and boundary conditions:

$$\begin{cases} J(\tilde{z}, 0) = 1 \\ J(0, t) = J_\alpha \\ \frac{\partial J}{\partial \tilde{z}}(\infty, t) = 0 \end{cases} \Leftrightarrow \begin{cases} \lim_{\eta \rightarrow \infty} f(\eta) = 1 \\ f(0) = J_\alpha \\ \frac{1}{2\sqrt{Dt}} \frac{\partial f}{\partial \eta}(\infty, t) = 0 \end{cases} \quad (\text{F.32})$$

which become the following equalities for A and B :

$$\begin{cases} B + A \int_0^\infty e^{-s^2} ds = 1 \\ B = J_\alpha \\ \frac{1}{2\sqrt{Dt}} A e^{-\infty^2} = 0 \end{cases} \Leftrightarrow \begin{cases} A = \frac{1 - B}{\int_0^\infty e^{-s^2} ds} \\ B = J_\alpha \\ \text{limits verified by comparative growth.} \end{cases} \quad (\text{F.33})$$

Using the *erf* function as:

$$\text{erf} : \begin{cases} \mathbf{R} & \longrightarrow & \mathbf{R} \\ x & \longmapsto & \frac{2}{\sqrt{\pi}} \int_0^x e^{-s^2} ds \end{cases} \quad \text{which satisfies} \quad \lim_{x \rightarrow \infty} \text{erf}(x) = 1, \quad (\text{F.34})$$

and solving for the constants A and B :

$$\begin{cases} B = J_\alpha \\ A = \frac{1 - B}{\frac{\sqrt{\pi}}{2}} \end{cases} \Leftrightarrow \begin{cases} B = J_\alpha \\ A = (1 - J_\alpha) \frac{2}{\sqrt{\pi}} \end{cases} \quad (\text{F.35})$$

gives the solution

$$f(\eta) = J_\alpha + (1 - J_\alpha) \frac{2}{\sqrt{\pi}} \int_0^\eta e^{-s^2} ds \quad (\text{F.36})$$

and hence the function $J(\tilde{z}, t)$:

$$J(\tilde{z}, t) = J_\alpha + (1 - J_\alpha) \text{erf}\left(\frac{\tilde{z}}{2\sqrt{Dt}}\right). \quad (\text{F.37})$$

Two constants to be identified appear:

$$\begin{cases} D & \text{the diffusion coefficient} \\ J_\alpha & \text{the change of volume due to the source} \end{cases} \quad (\text{F.38})$$

F.2.1.c Finite thickness of the cornea

Assuming here that the cornea has an finite thickness, i.e. the bar has an finite length (here normalized to 1), the system to solve is then:

$$\begin{cases} \frac{\partial J(\tilde{z}, t)}{\partial t} - D \frac{\partial^2 J(\tilde{z}, t)}{\partial \tilde{z}^2} = 0 \\ J(\tilde{z}, 0) = 1 \\ J(0, t) = J_\alpha \quad \text{and} \quad \frac{\partial J}{\partial \tilde{z}}(1, t) = 0 \end{cases} \quad (\text{F.39})$$

We look for a solution as a combination of independent functions of time $\hat{J}_k(t)$ and of space $\phi_k(\tilde{z})$ (harmonic analysis):

$$J(\tilde{z}, t) = B_0 + \sum_{k \in \mathbb{N}^*} \hat{J}_k(t) \phi_k(\tilde{z}) \quad \text{with} \quad \phi_k(\tilde{z}) = \sin\left(\frac{k\pi}{2} \tilde{z}\right) \quad (\text{F.40})$$

The derivatives in space of $\phi_k(\tilde{z})$ are then:

$$\frac{\partial \phi_k(\tilde{z})}{\partial \tilde{z}} = \frac{k\pi}{2} \cos\left(\frac{k\pi}{2} \tilde{z}\right), \quad \frac{\partial^2 \phi_k(\tilde{z})}{\partial \tilde{z}^2} = -\left(\frac{k\pi}{2}\right)^2 \sin\left(\frac{k\pi}{2} \tilde{z}\right) = -\left(\frac{k\pi}{2}\right)^2 \phi_k(\tilde{z}) \quad (\text{F.41})$$

and the derivative of $J(\tilde{z}, t)$ with respect to time and space are finally:

$$\frac{\partial J(\tilde{z}, t)}{\partial t} = \sum_{k \in \mathbb{N}^*} \frac{d\hat{J}_k(t)}{dt} \phi_k(\tilde{z}), \quad \frac{\partial^2 J(\tilde{z}, t)}{\partial \tilde{z}^2} = \sum_{k \in \mathbb{N}^*} \hat{J}_k(t) \frac{\partial^2 \phi_k(\tilde{z})}{\partial \tilde{z}^2} = - \sum_{k \in \mathbb{N}^*} \left(\frac{k\pi}{2}\right)^2 \hat{J}_k(t) \phi_k(\tilde{z}) \quad (\text{F.42})$$

The diffusion equation of system (F.39) becomes:

$$\begin{aligned} \frac{\partial J(\tilde{z}, t)}{\partial t} - D \frac{\partial^2 J(\tilde{z}, t)}{\partial \tilde{z}^2} = 0 &\Leftrightarrow \sum_{k \in \mathbb{N}^*} \frac{d\hat{J}_k(t)}{dt} \phi_k(\tilde{z}) + D \sum_{k \in \mathbb{N}^*} \left(\frac{k\pi}{2}\right)^2 \hat{J}_k(t) \phi_k(\tilde{z}) = 0 \Leftrightarrow \\ &\sum_{k \in \mathbb{N}^*} \left(\frac{d\hat{J}_k(t)}{dt} + D\left(\frac{k\pi}{2}\right)^2 \hat{J}_k(t)\right) \phi_k(\tilde{z}) = 0, \end{aligned}$$

and so, $\forall k \in \mathbb{N}^*$, we have to solve the equation

$$\frac{d\hat{J}_k(t)}{dt} + D\left(\frac{k\pi}{2}\right)^2 \hat{J}_k(t) = 0 \quad (\text{F.43})$$

with respect to time, which leads to the following solutions:

$$\forall k \in \mathbb{N}^*, \quad \hat{J}_k(t) = B_k e^{-D\left(\frac{k\pi}{2}\right)^2 t} \quad \text{where the constants } B_k \text{ are unknowns.} \quad (\text{F.44})$$

Altogether, $J(\tilde{z}, t)$ takes the following form:

$$J(\tilde{z}, t) = B_0 + \sum_{k \in \mathbb{N}^*} B_k \sin\left(\frac{k\pi}{2} \tilde{z}\right) e^{-D\left(\frac{k\pi}{2}\right)^2 t}. \quad (\text{F.45})$$

Now considering initial and boundary conditions, we obtain equations for the unknown coefficients B_k

$$\begin{cases} J(\tilde{z}, 0) = 1 \\ J(0, t) = J_\alpha \\ \frac{\partial J}{\partial \tilde{z}}(1, t) = 0 \end{cases} \Leftrightarrow \begin{cases} B_0 + \sum_{k \in \mathbb{N}^*} B_k \sin\left(\frac{k\pi}{2} \tilde{z}\right) = 1 \\ B_0 = J_\alpha \\ \sum_{k \in \mathbb{N}^*} B_k \cos\left(\frac{k\pi}{2}\right) e^{-D\left(\frac{k\pi}{2}\right)^2 t} = 0 \end{cases} \quad (\text{F.46})$$

The two first lines of Eq. (F.46) reduce to

$$1 - J_\alpha = \sum_{k \in \mathbb{N}^*} B_k \sin\left(\frac{k\pi}{2} \tilde{z}\right). \quad (\text{F.47})$$

A simple construction of B_k is obtained by taking the Fourier transform of the T-periodic function Π given by

$$\Pi : \begin{array}{l} \mathbf{R} \longrightarrow \mathbf{R} \\ \tilde{z} \longmapsto \forall k \in \mathbf{N} \begin{cases} -(1 - J_\alpha), & \forall \tilde{z} \in [-T/2 + kT, 0 + kT] \\ 1 - J_\alpha, & \forall \tilde{z} \in [0 + kT, T/2 + kT] \end{cases} \end{array} \quad (\text{F.48})$$

with $T = 4$. The function Π from equation (F.48) is presented Fig. F.3 in light purple for $J_\alpha = 1.2$. Π is a periodic odd function which can be decomposed in Fourier's series:

$$\Pi(\tilde{z}) = \sum_{k \in \mathbb{N}^*} B_k(\Pi) \sin\left(\frac{2k\pi}{T} \tilde{z}\right) = \sum_{k \in \mathbb{N}^*} B_k(\Pi) \sin\left(\frac{k\pi}{2} \tilde{z}\right), \quad (\text{F.49})$$

which corresponds to the initial condition (F.47).

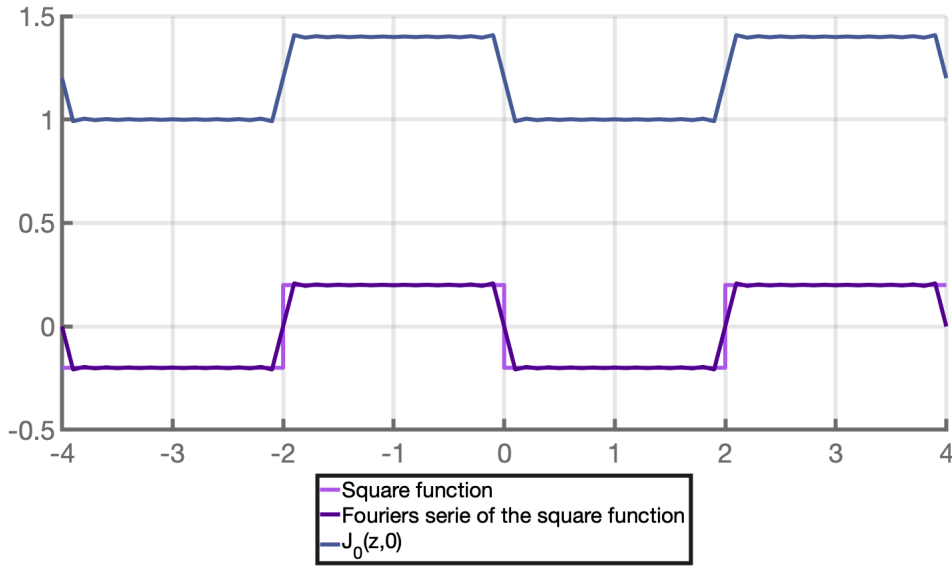


Figure F.3: Plot of the square function considered to compute the coefficient B_k as a Fourier's series (light purple), the associated Fourier's s (deep purple) and the function $J(\tilde{z}, 0)$ decomposed in Fourier's series (dark blue)

Let us compute $B_k(\Pi)$ the Fourier coefficients. Π is an odd function, so the coefficients reduce to:

$$B_k(\Pi) = \frac{4}{T} \int_0^{T/2} \Pi(x) \sin\left(\frac{k\pi}{2} x\right) dx = \frac{4}{4} \int_0^2 (1 - J_\alpha) \sin\left(\frac{k\pi}{2} x\right) dx = (1 - J_\alpha) \int_0^2 \sin\left(\frac{k\pi}{2} x\right) dx$$

$$B_k(\Pi) = (1 - J_\alpha) \left[\frac{-\cos\left(\frac{k\pi}{2} x\right)}{\frac{k\pi}{2}} \right]_0^2 = (J_\alpha - 1) \frac{2}{k\pi} (\cos\left(\frac{k\pi}{2} \cdot 2\right) - \cos(0)) = \frac{2(J_\alpha - 1)}{k\pi} (\cos(k\pi) - 1)$$

and then the Fourier coefficients become:

$$\forall k \in \mathbb{N}^*, \quad B_k(\Pi) = \frac{2(J_\alpha - 1)}{k\pi}((-1)^k - 1) \quad (\text{F.50})$$

As $\Pi(\tilde{z}) = 1 - J_\alpha$ for $\tilde{z} \in [0, 1]$, the Fourier coefficients satisfy the initial condition and then the expression of $J(\tilde{z}, t)$ becomes:

$$J(\tilde{z}, t) = J_\alpha + \sum_{k \in \mathbb{N}^*} B_k \sin\left(\frac{k\pi}{2}\tilde{z}\right)e^{-D\left(\frac{k\pi}{2}\right)^2 t} \quad \text{with} \quad B_k = \frac{2(J_\alpha - 1)}{k\pi}((-1)^k - 1) \quad (\text{F.51})$$

The boundary condition $\sum_{k \in \mathbb{N}^*} B_k \cos\left(\frac{k\pi}{2}\right)e^{-D\left(\frac{k\pi}{2}\right)^2 t} = 0$ at $\tilde{z} = 1$ remains to be checked. Let us decompose between even and odd numbers:

$$\forall k \in \mathbb{N}^*, \quad B_k(\Pi) = \frac{2(J_\alpha - 1)}{k\pi}((-1)^k - 1) \Leftrightarrow \forall l \in \mathbb{N} \begin{cases} B_{2l+1}(\Pi) = \frac{-4}{(2l+1)\pi}(J_\alpha - 1) \\ B_{2l+2}(\Pi) = 0 \end{cases} \quad (\text{F.52})$$

$$\forall k \in \mathbb{N}^*, \quad \cos\left(\frac{k\pi}{2}\right) \Leftrightarrow \forall l \in \mathbb{N} \begin{cases} \cos\left(\frac{(2l+1)\pi}{2}\right) = \cos\left(l\pi + \frac{\pi}{2}\right) = 0 \\ \cos\left(\frac{(2l+2)\pi}{2}\right) = \cos((l+1)\pi) = (-1)^{l+1} \end{cases} \quad (\text{F.53})$$

Finally,

$$\forall k \in \mathbb{N}^*, \quad B_k(\Pi) \cos\left(\frac{k\pi}{2}\right) = 0 \quad (\text{F.54})$$

and so the second boundary condition $\frac{\partial J}{\partial \tilde{z}}(1, t) = \sum_{k \in \mathbb{N}^*} B_k \cos\left(\frac{k\pi}{2}\right)e^{-D\left(\frac{k\pi}{2}\right)^2 t} = 0$ is satisfied. The final expression for $J(\tilde{z}, t)$ is thus

$$J(\tilde{z}, t) = J_\alpha + \sum_{k \in \mathbb{N}^*} B_k \sin\left(\frac{k\pi}{2}\tilde{z}\right)e^{-D\left(\frac{k\pi}{2}\right)^2 t} \quad \text{with} \quad B_k = \frac{2(J_\alpha - 1)}{k\pi}((-1)^k - 1) \quad (\text{F.55})$$

The same two constants to be identified appear:

$$\begin{cases} D & \text{the diffusion coefficient} \\ J_\alpha & \text{the change of volume close to the source} \end{cases} \quad (\text{F.56})$$

F.2.1.d Numerical comparison

Figure F.4 presents the results for the two cases (infinite thickness - up and finite thickness - down) with the following parameters: $J_\alpha = 1.2$, $D = 0.01 \text{ mm}^2 \cdot \text{s}^{-1}$ and $N_{\text{Fourier}} = 60$ (the maximum number of functions used in Fourier decomposition). The abscissa represents the space variable \tilde{z} and the time evolution is illustrated by the pink arrow. The second case with a volume change that propagates in the whole bar with time seems to better correspond to the real case of the cornea.

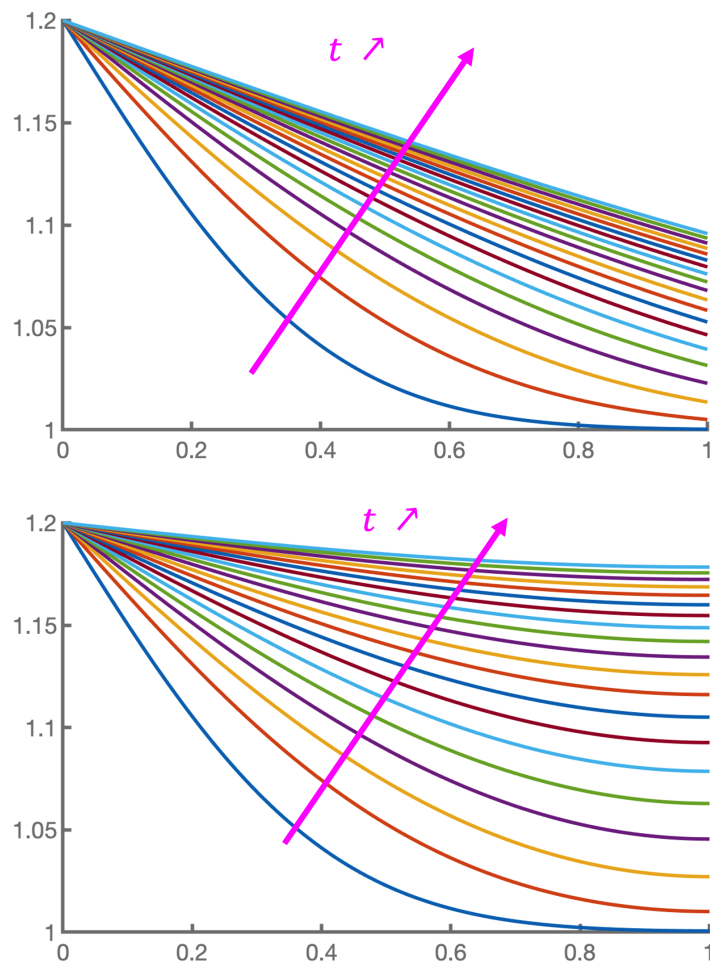


Figure F.4: Functions $J(\tilde{z}, t)$ for an infinite (up) and a finite (down) thickness of the cornea. Used parameters: the change of volume close to the source $J_\alpha = 1.2$, the diffusion coefficient $D = 0.01 \text{mm}^2 \cdot \text{s}^{-1}$ and the maximum number of functions used in Fourier decomposition $N_{\text{Fourier}} = 60$

Titre: Mécanique multi-échelle et structure de la cornée saine et pathologique

Mots clés: cornée, modélisation de tissus fibreux, tomographie par cohérence optique, corrélation d'images

Résumé: La cornée est la partie extérieure et transparente de l'œil et un des tissus essentiels à la vision. En effet, elle procure les 2/3 du pouvoir optique de l'œil tout en résistant aux variations de pression intraoculaire journalière auxquelles elle est soumise.

Le kératocône est une dystrophie cornéenne idiopathique caractérisée par une ectasie et un amincissement progressif du tissu dans la zone touchée par la pathologie. A ce jour, il n'existe pas d'origine claire et identifiée de la maladie. Une des hypothèses avancées est le changement de géométrie induit par un frottement oculaire répété.

Les propriétés mécaniques de la cornée sont liées à la microstructure très particulière de son stroma en contreplaqué de lamelles de collagène et il a été clairement identifié que cette microstructure se désorganise dans le cas d'un

kératocône. De nombreux modèles mécaniques ont été développés pour prendre en compte cette microstructure, dans des cas sains et pathologiques. Cependant, il n'existe à ce jour que très peu de données expérimentales sur la réponse mécanique macroscopique de la cornée pour les valider.

L'objectif de cette thèse est donc de caractériser la mécanique cornéenne afin de mieux comprendre l'apparition de la pathologie. Trois questions principales sont investiguées : quels sont les paramètres mécaniques qui influencent l'apparition du kératocône ? Peut-on mesurer la réponse mécanique de la cornée saine afin de compléter les données disponibles dans la littérature ? Quelle est la réponse mécanique de la cornée à la pression intraoculaire après une greffe ?

Title: Multiscale structure et biomechanics of healthy and pathological cornea

Keywords: cornea, fibrous tissue modeling, Optical Coherence Tomography, Digital Volume/Image Correlation

Abstract: The cornea is the external and transparent part of the eye and one of the essential tissues for vision. It provides 2/3 of the optical power of the eye while resisting the daily intraocular pressure variations to which it is subjected.

Keratoconus is an idiopathic corneal dystrophy characterized by an ectasia and progressive thinning of the tissue in the area affected by the pathology. To date, there is no clear and identified origin of the disease. One of the hypotheses put forward is the change in geometry induced by repeated ocular friction.

The mechanical properties of human cornea are linked to the very particular microstructure of its stroma made of a plywood of collagen lamellae and it has been clearly identified that this microstructure becomes disorga-

nized in the case of keratoconus. Numerous mechanical models have been developed to take into account this microstructure, in healthy and pathological cases. However, there are to date very little experimental data on the macroscopic mechanical response of cornea to validate them.

The objective of this thesis is therefore to characterize the corneal mechanics in order to better understand the pathology onset. Three main questions are investigated: what are the mechanical parameters that influence the inception of keratoconus? Can we measure the mechanical response of healthy cornea to complete the data available in the literature? What is the mechanical response of cornea to intraocular pressure after transplant?